

Advances in Mathematical Fluid Mechanics

Tomáš Bodnár  
Giovanni P. Galdi  
Šárka Nečasová  
Editors

# Particles in Flows

 Birkhäuser



# Advances in Mathematical Fluid Mechanics

## Series editors

Giovanni P. Galdi, Pittsburgh, USA

John G. Heywood, Vancouver, Canada

Rolf Rannacher, Heidelberg, Germany

*Advances in Mathematical Fluid Mechanics* is a forum for the publication of high quality monographs, or collections of works, on the mathematical theory of fluid mechanics, with special regards to the Navier-Stokes equations. Its mathematical aims and scope are similar to those of the *Journal of Mathematical Fluid Mechanics*. In particular, mathematical aspects of computational methods and of applications to science and engineering are welcome as an important part of the theory. So also are works in related areas of mathematics that have a direct bearing on fluid mechanics.

More information about this series at <http://www.springer.com/series/5032>

Tomáš Bodnár • Giovanni P. Galdi • Šárka Nečasová  
Editors

# Particles in Flows

 Birkhäuser



*Editors*

Tomáš Bodnár  
Department of Technical Mathematics  
Faculty of Mechanical Engineering  
Czech Technical University in Prague  
Prague, Czech Republic

Giovanni P. Galdi  
Department of Mechanical Engineering  
and Materials Science  
University of Pittsburgh  
Pittsburgh, Pennsylvania, USA

Šárka Nečasová  
Institute of Mathematics  
Czech Academy of Sciences  
Prague, Czech Republic

ISSN 2297-0320                      ISSN 2297-0339 (electronic)  
Advances in Mathematical Fluid Mechanics  
ISBN 978-3-319-60281-3              ISBN 978-3-319-60282-0 (eBook)  
DOI 10.1007/978-3-319-60282-0

Library of Congress Control Number: 2017953452

Mathematics Subject Classification (2010): 35Q70, 76M28, 35Q35, 76A02, 76D03, 76D05, 76T10

© Springer International Publishing AG 2017

This work is subject to copyright. All rights are reserved by the Publisher, whether the whole or part of the material is concerned, specifically the rights of translation, reprinting, reuse of illustrations, recitation, broadcasting, reproduction on microfilms or in any other physical way, and transmission or information storage and retrieval, electronic adaptation, computer software, or by similar or dissimilar methodology now known or hereafter developed.

The use of general descriptive names, registered names, trademarks, service marks, etc. in this publication does not imply, even in the absence of a specific statement, that such names are exempt from the relevant protective laws and regulations and therefore free for general use.

The publisher, the authors and the editors are safe to assume that the advice and information in this book are believed to be true and accurate at the date of publication. Neither the publisher nor the authors or the editors give a warranty, express or implied, with respect to the material contained herein or for any errors or omissions that may have been made. The publisher remains neutral with regard to jurisdictional claims in published maps and institutional affiliations.

Printed on acid-free paper

This book is published under the trade name Birkhäuser, [www.birkhauser-science.com](http://www.birkhauser-science.com)  
The registered company is Springer International Publishing AG  
The registered company address is: Gewerbestrasse 11, 6330 Cham, Switzerland

# Preface

The subject of particles in industrial, environmental and biomedical flows is a challenging topic with many practical applications in everyday life. It's a combination of fluid mechanics and solid body mechanics with various aspects of specific applications that make this multidisciplinary area so hard to address without a deep knowledge of a whole range of background topics.

The aim of this volume is to face the *Particles in Flows* from many different, but essentially interconnected sides and points of view. Thus the selection of authors and topics represented in the chapters ranges from deep mathematical analysis of the associated models, through the techniques of their numerical solution, towards real applications and physical implications.

The scope and structure of this book as well as the selection of authors is motivated by the very successful summer course and workshop “Particles in Flows” that was held in Prague in August 2014. This meeting has revealed a need for a book of this type, and thus we hope that this work will find its way to the scientific community dealing with this specific and challenging multidisciplinary subject.

The work on this book was partially supported by the Czech Science Foundation under the grant No. 201-16-03230S and by the project RVO 67985840 through the Institute of Mathematics of the Czech Academy of Sciences.

Prague, Czech Republic  
Pittsburgh, PA, USA  
Prague, Czech Republic  
April 2017

Tomáš Bodnár  
Giovanni Paolo Galdi  
Šárka Nečasová

# Contents

<b>1 A Maximal Regularity Approach to the Analysis of Some Particulate Flows</b> .....	1
D. Maity and M. Tucsnak	
1.1 Introduction and Hilbert Space Analysis of a Toy Model.....	1
1.1.1 The General Context.....	1
1.1.2 Introduction of a Toy Model .....	4
1.1.3 Change of Variables .....	5
1.1.4 Local in Time Existence and Uniqueness of Solutions .....	6
1.1.5 Proof of the Global Well-Posedness Result .....	15
1.1.6 Bibliographical Notes .....	22
1.2 Examples of Systems Modelling Fluid-Structure Interactions.....	22
1.2.1 Motion of a Piston in a Heat Conducting Gas; a 1D Model.....	23
1.2.2 Motion of a Rigid Body in a Viscous Incompressible Fluid .....	28
1.2.3 Motion of a Solid in a Compressible Fluid .....	30
1.3 Short Introduction to $\mathcal{R}$ -Sectorial Operators .....	32
1.3.1 Basic Definitions.....	33
1.3.2 Weis' Theorem.....	35
1.3.3 Abstract Framework Corresponding to Linear Fluid-Solid Interaction Problems .....	36
1.3.4 Bibliographical Notes .....	41
1.4 Existence and Uniqueness Results .....	42
1.4.1 Some Background .....	42
1.4.2 Back to the Toy Problem .....	47
1.4.3 A More Realistic 1D Model.....	53
1.4.4 Motion of a Solid in a Compressible Fluid .....	61
1.4.5 Bibliographical Notes .....	73
References .....	73

<b>2</b>	<b>Time-Periodic Linearized Navier–Stokes Equations: An Approach Based on Fourier Multipliers</b> .....	77
	T. Eiter and M. Kyed	
2.1	Introduction .....	77
2.2	Preliminaries .....	80
2.3	Transference Principle for Multipliers .....	86
2.3.1	Basic Properties of Fourier Multipliers .....	87
2.3.2	Approximation Results .....	89
2.3.3	Another Characterization of Multipliers .....	93
2.3.4	The Transference Principle .....	95
2.4	The Schwartz-Bruhat Space .....	101
2.4.1	Elementary Groups .....	102
2.4.2	Good and Compactly Generated Open Subgroups .....	109
2.4.3	The General Schwartz-Bruhat Space .....	113
2.4.4	Embedding Results .....	116
2.4.5	The Fourier Transform .....	119
2.5	Time-Periodic Linearized Navier–Stokes Equations .....	123
2.5.1	Maximal Regularity .....	123
2.5.2	Fundamental Solutions .....	131
	References .....	137
<b>3</b>	<b>Motion of a Particle Immersed in a Two Dimensional Incompressible Perfect Fluid and Point Vortex Dynamics</b> .....	139
	F. Sueur	
3.1	Introduction .....	139
3.2	Case of an Unbounded Irrotational Flow .....	152
3.2.1	Reduction to an ODE: Statement of Theorem 3.12 .....	152
3.2.2	Explicit Definition of the ODE Coefficients $\mathcal{M}_{a,\theta}$ , $\Gamma_{a,\theta}$ and $B_\theta$ .....	156
3.2.3	Reformulation as an ODE in the Body Frame: Statement of Theorem 3.18 .....	160
3.2.4	A Complex-Analytic Proof of Theorem 3.18 .....	163
3.2.5	A Real-Analytic Proof of Theorem 3.18 .....	175
3.2.6	Zero Radius Limit .....	178
3.3	Case of a Bounded Domain .....	180
3.3.1	Reduction to an ODE in the Case Where $\gamma = 0$ : Munnier’s Theorem .....	181
3.3.2	Proof of Munnier’s Result: Theorem 3.28 .....	182
3.3.3	Reduction to an ODE in the General Case: Statement of Theorem 3.32 .....	187
3.3.4	Proof of Theorem 3.32 .....	189
3.3.5	The Role of the Energy .....	190
3.3.6	Zero Radius Limit .....	192

3.4	Case of an Unbounded Flow with Vorticity.....	198
3.4.1	Statement of an Existence and Uniqueness Theorem à la Yudovich in the Body Frame .....	198
3.4.2	Proof of Theorem 3.40 .....	200
3.4.3	Energy Conservation .....	206
3.4.4	A Macroscopic Normal form Tailored for the Zero-Radius Limit .....	209
3.4.5	Zero Radius Limit .....	212
	References .....	215
<b>4</b>	<b>Stability of Permanent Rotations and Long-Time Behavior of Inertial Motions of a Rigid Body with an Interior Liquid-Filled Cavity</b> .....	<b>217</b>
	G.P. Galdi	
4.1	Introduction .....	217
4.2	Formulation of the Problem and Local Existence Theory .....	221
4.3	The Spectrum of the Linearized Operator .....	225
4.4	Global Existence and Stability of Permanent Rotations: A Full Explanation of Kelvin’s Experiment .....	236
4.5	Asymptotic Behavior for Large Data: A Full Proof of Zhukovsky Conjecture .....	241
4.6	Attainability of Permanent Rotations .....	248
	References .....	251
<b>5</b>	<b>Dissipative Particle Dynamics: Foundation, Evolution, Implementation, and Applications</b> .....	<b>255</b>
	Z. Li, X. Bian, X. Li, M. Deng, Y.-H. Tang, B. Caswell, and G.E. Karniadakis	
5.1	Introduction .....	255
5.2	Theoretical Formulation and Parameterization .....	257
5.2.1	Fokker-Planck Equation and Fluctuation-Dissipation Theorem .....	257
5.2.2	Bottom-Up and Top-Down Derivations .....	262
5.2.3	Transport Coefficients from Kinetic Theory.....	274
5.2.4	Parameterization .....	276
5.2.5	The Zwanzig Formalism for Coarse-Graining .....	281
5.3	Extensions of Dissipative Particle Dynamics .....	285
5.3.1	Energy-Conserving DPD (eDPD) for Non-Isothermal Systems.....	286
5.3.2	Many-Body DPD (mDPD) for Multiphase Flows.....	290
5.3.3	Transport DPD (tDPD) for Advection-Diffusion-Reaction ...	297
5.3.4	Other Extensions.....	304
5.4	Computer Implementation .....	306
5.4.1	Pairwise Search .....	306
5.4.2	Force Computation .....	306

5.4.3	Numerical Optimization .....	308
5.4.4	Time Integration .....	309
5.5	Applications .....	310
5.5.1	Single-Phase Fluid Flow .....	311
5.5.2	Blood Flow .....	313
5.5.3	Dynamics of Polymers in Shear Flow .....	318
5.6	Concluding Remarks .....	320
	References .....	321
<b>6</b>	<b>Numerical Methods for Dispersed Multiphase Flows</b> .....	<b>327</b>
	M. Sommerfeld	
6.1	Introduction to Multi-Phase Flows .....	328
6.2	Characterisation of Dispersed Multi-Phase Flows .....	330
6.3	Numerical Approaches for Single-Phase Flows .....	336
6.4	Hierarchy of Numerical Methods for Multi-Phase Flows .....	337
6.5	Particle-Scale Simulation Methods .....	340
6.5.1	Resolved Rigid Particles .....	340
6.5.2	Resolved Particles with Fluid Interfaces .....	343
6.6	Modelling of Dispersed Multi-Phase Flows .....	344
6.6.1	Two-Fluid or Euler/Euler Approach .....	346
6.6.2	Hybrid Euler/Lagrange Approach .....	349
6.6.3	Euler/Lagrange Coupling Approaches .....	355
6.6.4	Modelling of Particle-Scale Processes .....	359
6.7	Application Examples of Euler/Lagrange Approach .....	364
6.7.1	Unsteady Swirling Flow .....	365
6.7.2	Particle Dispersion in Stirred Vessel .....	371
6.7.3	Application: Horizontal Blade Filter .....	382
6.8	Conclusions and Outlook .....	389
	References .....	390
<b>7</b>	<b>Path Instabilities of Axisymmetric Bodies Falling or Rising Under the Action of Gravity and Hydrodynamic Forces in a Newtonian Fluid</b> .....	<b>397</b>
	J. Dušek	
7.1	Introduction .....	398
7.2	Wake of Fixed Bodies .....	400
7.2.1	Loss of Axisymmetry in Wakes .....	400
7.2.2	Linear Stability Analysis of an Axisymmetric Flow .....	402
7.2.3	Weakly Non-linear Theory .....	404
7.2.4	Some Examples of Bifurcation Scenarios in Wakes .....	408
7.3	Path Instabilities of Free Axisymmetric Bodies .....	411
7.3.1	Problem Formulation for a Homogeneous Spherical Body .....	411
7.3.2	Primary Path Instability of a Sphere .....	414
7.3.3	Weakly Non-linear Theory of the Interplay of a Regular and a Hopf Bifurcation .....	415

7.4	Transition Scenario of a Free Sphere .....	416
7.4.1	Early Stages .....	418
7.4.2	Onset of Chaos .....	421
7.4.3	Order in the Chaos: Vertical Oscillating Paths and Helical Paths .....	429
7.4.4	Conclusion .....	434
7.5	Homogeneous Thin Disc .....	435
7.5.1	Mathematical Formulation and Numerical Method .....	435
7.5.2	Description of Regimes of Falling Discs .....	437
7.5.3	Transition Scenario of Discs .....	444
7.5.4	Conclusion .....	449
7.6	General Conclusion and Perspectives .....	450
	References .....	450
<b>8</b>	<b>Microbubbles: Properties, Mechanisms of Their Generation</b> .....	<b>453</b>
	V. Tesař	
8.1	Basics of Gas Bubbles .....	454
8.1.1	Importance of Microbubbles .....	454
8.1.2	The Main Reason for Desirable Small Scale .....	456
8.1.3	Another Reason: Velocity .....	458
8.1.4	Surface Tension .....	461
8.1.5	Bubbles Generated by An Aerator .....	464
8.1.6	Bubble Shapes .....	466
8.1.7	Shape Oscillation .....	471
8.1.8	Oscillation Frequency .....	474
8.2	Problems and Solutions .....	476
8.2.1	Gas Diffusion from the Bubble .....	476
8.2.2	Surface Energy .....	481
8.2.3	Instability of Parallel Bubble Formation .....	483
8.2.4	Conjunction of Microbubbles .....	486
8.2.5	Microbubbles with Fluidic Oscillation .....	488
8.2.6	Consequences of the Discovered Effects .....	493
8.3	Fluidic Oscillators .....	494
8.3.1	Development History of Fluidics .....	494
8.3.2	The Key Component: Amplifier .....	495
8.3.3	Bistable Diverter with Jet Deflection Control .....	500
8.3.4	The Feedback .....	504
8.3.5	Other Oscillators: Usual and Unusual .....	506
8.3.6	Relaxation Oscillators .....	511
8.4	Conclusions .....	516
	References .....	517

# Chapter 1

## A Maximal Regularity Approach to the Analysis of Some Particulate Flows

D. Maity and M. Tucsnak

**Abstract** This work presents some recent advances in the mathematical analysis of particulate flows. The main idea we want to emphasize is that, for a variety of fluid models the corresponding coupled systems have a common structure, at least in the linearized case. Within this framework, several model problems are considered and studied in detail. This includes a simple toy model, motion of a piston in a heat conducting gas, motion of a rigid body in a viscous incompressible fluid and motion of a solid in a compressible fluid.

**Keywords** Compressible fluid • Existence • Fluid-structure interactions • Global well-posedness • Heat conducting gas • Navier-Stokes • Uniqueness • Viscous incompressible fluid

**MSC2010:** 35Q30, 76N10, 74F10

### 1.1 Introduction and Hilbert Space Analysis of a Toy Model

#### 1.1.1 The General Context

In the remaining part of this work the term *particulate flows* designs the coupled motion of a collection of rigid bodies and of a fluid surrounding them. Such systems occur, for instance, in aerodynamics (flow around an aircraft), medicine (blood flow in vessels), zoology (swimming of aquatic animals). The mathematical study of

---

D. Maity

Institut de Mathématiques, Université de Bordeaux, Bordeaux INP, CNRS, 351 cours de la Libération, F 33405 Talence, France

e-mail: [debayan.maity@u-bordeaux.fr](mailto:debayan.maity@u-bordeaux.fr)

M. Tucsnak (✉)

Institut de Mathématiques de Bordeaux UMR 5251, Université de Bordeaux, 351, cours de la Libération, F 33 405 Talence, France

e-mail: [marius.tucsnak@u-bordeaux.fr](mailto:marius.tucsnak@u-bordeaux.fr)



these problems rises several challenges, the main one being due to the fact that the domain filled by the fluid is one of the unknowns of the problem. Another difficulty which has to be tackled is that the dynamics of the system couples equations of different nature: ordinary differential or partial differential equations modeling the solid with the partial differential equations (compressible or incompressible Navier-Stokes) modeling the fluid.

A first important idea we want to develop in this work is that such a system can be mathematically tackled as a perturbation (in an appropriate sense) of the equations describing the fluid alone. More precisely, we see the coupled linearized fluid-structure system like a boundary controlled fluid system, with the boundary control given by an appropriate dynamic feedback which satisfies a “smallness” condition. For the considered applications, this smallness condition follows from a compactness type property of the operator describing the dynamic feedback. We first apply this methodology to a toy problem and then to systems describing particulate flows in a viscous compressible fluid. The incompressible case, a priori simpler, seems more difficult to be included in the general framework we have constructed. For this case we refer to the rich existing literature (see, for instance, Geissert et al. [17] or Martín and Tucsnak [27] and references therein).

A second important idea is that we study the wellposedness of the considered initial and boundary value problems in spaces of functions which are  $L^p$  with respect to time and  $L^q$  with respect to the space variable, with arbitrary  $p, q > 1$ . Most of the existing literature on the mathematical analysis of particulate flows consider the Hilbert space setting, corresponding to  $p = q = 2$ . (The only exceptions we are aware of are Geissert et al. [17] Hieber and Murata [19].) Quitting the Hilbert space setting clearly complicates the analysis. This is essentially due to the fact that the maximal regularity of the solutions of the linearized problems is no longer implied by the analytic character of the associated semigroup. Instead, a more sophisticated property of the generators, called  $\mathcal{R}$ -sectoriality, has to be investigated. One of the advantages of this approach is that the extra integrability properties obtained by taking  $p, q > 2$  allow us to avoid estimates on higher order derivatives and also to correctly define the changes of variables which naturally occur in the study of particulate flows (such as the equivalence of Eulerian and Lagrangian formulations for compressible flows).

Let us first describe those basic equations which are independent of the properties of the fluid. The domain occupied by the fluid and the particles is  $\Omega \subset \mathbb{R}^3$ , a connected open bounded set with  $C^2$  boundary. Let  $m \in \mathbb{N}$  be the number of particles let  $h_1, h_2, \dots, h_m$  be the (variable) positions of their centers of mass. For every  $k \in \{1, 2, \dots, m\}$  we denote by  $R_k$  the proper orthogonal matrix (also a variable one) giving the orientation of the  $k$ th particle, whose position is thus given by

$$S(h_j, R_j) = h_j + R_j(S_{0,j} - h_{0,j}) \quad (j \in \{1, \dots, m\}),$$

where  $S_{0,j}$  and  $h_{0,j}$  stand, for each  $j \in \{1, \dots, m\}$  for the set occupied by the  $j$ th solid, respectively the position of its center of mass, at  $t = 0$ . The fluid is supposed to be

incompressible, homogeneous with *density*  $\rho > 0$  and it occupies the domain

$$F(h_1, R_1 \dots h_m, R_m) := \Omega \setminus \bigcup_{k=1}^m S(h_k, R_k).$$

Regardless the considered type of fluid, we know that the *Cauchy equations* hold in fluid domain. More precisely, we have

$$\rho [\dot{v} + (v \cdot \nabla)v] - \operatorname{div} \sigma = \rho b \quad (t \geq 0, \quad x \in F(h_1(t), R_1(t), \dots, h_m(t), R_m(t))), \quad (1.1)$$

$v$  is the Eulerian velocity field of the fluid,  $\sigma$  is its Cauchy stress field and  $b$  is the density of exterior forces (supposed to be known). The equations of motion of the solids are given by Newton's laws and they can be written

$$M_j \ddot{h}_j = - \int_{\partial S(h_j(t), R_j(t))} \sigma n \, d\Gamma + \int_{S(h_j(t), R_j(t))} \rho_j b \, dx, \quad t \geq 0, \quad j = 1, \dots, m, \quad (1.2)$$

$$\begin{aligned} \frac{d}{dt}(J_j \omega_j) &= - \int_{\partial S(h_j(t), R_j(t))} (x - h_j) \times \sigma n \, d\Gamma \\ &+ \int_{S(h_j(t), R_j(t))} (x - h_j) \times \rho_j b \, dx, \quad t \geq 0, \quad j = 1, \dots, m, \end{aligned} \quad (1.3)$$

$$\frac{dR_j}{dt}(t) = A(\omega_j(t))R_j(t) \quad t \geq 0, \quad j = 1, \dots, m, \quad (1.4)$$

where  $\rho_j$  is the density of the solid  $S(h_j(t), R_j(t))$  (supposed to be a known constant),  $\omega_j(t)$  is its angular velocity, the notation  $\times$  stands for the usual vector product in  $\mathbb{R}^3$ , whereas  $n$  denotes the unitary normal vector field to  $\partial S(h_j(t), R_j(t))$  oriented towards the interior of each solid. The skew symmetric matrix  $A(\omega)$  is defined by

$$A(\omega) = \begin{pmatrix} 0 & -\omega_3 & \omega_2 \\ \omega_3 & 0 & -\omega_1 \\ -\omega_2 & \omega_1 & 0 \end{pmatrix} \quad \text{for all } \omega \in \mathbb{R}^3. \quad (1.5)$$

Moreover, for every  $j \in \{1, \dots, m\}$ ,  $M_j$  stands for the mass of  $S(h_j(t), R_j(t))$  and  $J(h_j(t), R_j(t))$  denotes the inertia matrix of  $S(h_j(t), R_j(t))$  defined by

$$\begin{aligned} &J(h_j(t), R_j(t))a \cdot b \\ &= \rho_j \int_{S(h_j(t), R_j(t))} [a \times (x - h_j(t))] \cdot [b \times (x - h_j(t))] \, dx \quad \text{for all } a, b \in \mathbb{R}^3. \end{aligned} \quad (1.6)$$

In order to close the system, Eqs. (1.1)–(1.4) have to be supplemented with a constitutive law for the fluid, with appropriate boundary conditions and with the

initial conditions, valid for  $j \in \{1, \dots, m\}$ ,

$$v(x, 0) = v_0(x) \quad (x \in F(h_{0,j}, R_{0,j})), \quad (1.7)$$

$$h_j(0) = h_{0,j}, \dot{h}_j(0) = g_{0,j}, R_j(0) = R_{0,j}, \omega_j(0) = \omega_{0,j} \quad (1.8)$$

The constitutive law and the boundary conditions in the case of a viscous incompressible fluid will be introduced in the following sections.

The outline of this work is as follows. In the next subsection, in order to give a flavour of the results to come, we introduce a toy model in one space dimension, in which the Navier-Stokes system is replaced by the viscous Burgers equations. The solid is replaced by a mass-point evolving under the action of the surrounding ‘‘Burgers’’ fluid. In the remaining part of the first section we develop the existence and uniqueness theory for the corresponding coupled PDE system, in a Hilbert space framework. The second section is devoted to the introduction of several more realistic models of fluid-structure interactions. More precisely we consider the systems modelling the motion of a piston in a 1D viscous heat conducting gas, then of a rigid body in a viscous incompressible fluid and finally the motion of a rigid body in a three dimensional viscous compressible fluid filling a bounded domain. Section 1.3 contains an introduction to the theory of maximal regularity for evolution equations, namely those which are associated to  $\mathcal{R}$ -sectorial operators. Moreover, we make precise here the common structure of the linearized problems for various particulate flow systems, and we prove a useful perturbation result. Section 1.4 first revisits the analysis of the toy problem introduced in Chap. 1, this time in an  $L^p - L^q$  setting. The last part of this chapter is devoted to local in time existence results, still in an  $L^p - L^q$  setting, for the two other systems introduced in Sect. 1.2.

### 1.1.2 Introduction of a Toy Model

The viscous Burgers equation is often used as a toy model for the Navier-Stokes equations. In this section we consider a similar simplification for the system describing the motion of a rigid body in a viscous fluid. Assuming that, instead of the Navier-Stokes equations, the fluid is described by the one dimensional viscous Burgers equation, the system writes

$$\begin{cases} \dot{v}(t, y) - v_{yy}(t, y) + v(t, y)v_y(t, y) = 0 & t \geq 0, y \in (-1, 1), y \neq h(t), \\ v(t, -1) = v(t, 1) = 0 & t \geq 0, \\ \dot{h}(t) = v(t, h(t)) & t \geq 0, \\ \ddot{h}(t) = [v_y](t, h(t)) & t \geq 0, \\ v(0, y) = v_0(y) & y \in (-1, 1), \\ h(0) = h_0, \quad \dot{h}(0) = g_0. & \end{cases} \quad (1.9)$$

In (1.9),  $v = v(t, y)$  denotes the Eulerian velocity field of the fluid filling the interval  $(-1, 1)$ , whereas  $h = h(t)$  indicates the position of the point mass and the derivative with respect to time is denoted by a dot. Moreover, the force exerted by the fluid on the mass is given by the jump of the derivative of  $v$  when crossing the mass, denoted by  $[v_y](t, h(t))$ . For the sake of simplicity, we have assumed that the mass of the body, the viscosity and the density of the fluid are equal to one.

The main result of this chapter reads as follows:

**Theorem 1.1** *Assume that  $v_0 \in H_0^1(-1, 1)$ ,  $h_0 \in (-1, 1)$  and  $g_0 \in \mathbb{R}$  are such that  $v_0(h_0) = g_0$ . Then the system (1.9) admits a unique solution  $\begin{bmatrix} v \\ h \end{bmatrix}$  with*

$$v \in C([0, \infty); H_0^1(-1, 1)) \cap H_{\text{loc}}^1((0, \infty); L^2(-1, 1)), \quad h \in H^2((0, T), (-1, 1)),$$

with the restriction of  $v$  to  $x \in (-1, h_0)$  (respectively to  $(h_0, 1)$ ) in  $L_{\text{loc}}^2((0, \infty); H^2(-1, h_0))$  (respectively in  $L_{\text{loc}}^2((0, \infty); H^2(h_0, 1))$ ).

Note that the global character of the wellposedness result above implies that the mass point does not reach the extremities of the interval, i.e. the solid will not touch the boundary. The methodology used in next section extends to the case of several point-masses and in this case we can show that the point-masses do not collide in finite time.

### 1.1.3 Change of Variables

An important step in proving our wellposedness results is to use a change of variables mapping the time dependent interval  $[-1, h(t)]$  (respectively  $[h(t), 1]$ ) on the fixed one  $[-1, h_0]$  (respectively  $[h_0, 1]$ ). More precisely, we set  $z(t, x) = v(t, y)$ , where

$$x = \begin{cases} \frac{(h_0+1)y+h_0-h(t)}{h(t)+1} & (y \in [-1, h(t)]), \\ \frac{(h_0-1)y+h(t)-h_0}{h(t)-1} & (y \in [h(t), 1]). \end{cases} \quad (1.10)$$

It is easily checked that (1.10) can be rewritten as

$$y = \frac{(1 - kh(t))x - h_0 + h(t)}{1 - kh_0}, \quad k = \text{sgn}(x - h_0). \quad (1.11)$$

The following proposition shows that by using the change of variable (1.10) the system (1.9) is equivalent with a system written in a fixed spatial domain.

**Proposition 1.2** *Let  $T > 0$ ,  $v_0 \in L^2[-1, 1]$ ,  $h_0 \in (-1, 1)$ ,  $g_0 \in \mathbb{R}$ , and assume that*

$$v \in C([0, T]; H_0^1(-1, 1)) \cap H^1((0, T); L^2(-1, 1)), \quad h \in H^2((0, T), (-1, 1)),$$

Then  $\begin{bmatrix} v \\ g \\ h \end{bmatrix}$  is a solution of (1.9) on  $[0, T]$  if and only if, the triplet  $\begin{bmatrix} z \\ g \\ h \end{bmatrix}$ , where  $z(t, x) = v(t, y)$ , with  $x$  given by (1.10), satisfies, for every  $t \in [0, T]$ ,

$$\begin{cases} \dot{z} - z_{xx} = \frac{k(h-h_0)}{1-kh} \left[ 2 + \frac{k(h-h_0)}{1-kh} \right] z_{xx} + \frac{1-kx}{1-kh} g z_x - \frac{1-kh_0}{1-kh} z z_x, & x \in (-1, 1) \setminus h_0 \\ z(t, -1) = z(t, 1) = 0 \\ z(t, h_0) = g(t) \\ \dot{g} - [z_x](t, h_0) = (h - h_0) \left[ \frac{kz_x}{1-kh} \right](t, h_0) & t \in (0, T) \\ \dot{h}(t) = g(t) \\ z(0, x) = z_0(x) & x \in (-1, 1) \\ h(0) = h_0, \quad g(0) = g_0. \end{cases} \quad (1.12)$$

*Proof* Using the change of variables (1.10)–(1.11), simple calculations show that (1.9) can be rewritten, for  $t \in [0, T]$ :

$$\begin{cases} (1 - kh)\dot{z} - \frac{(1-kh_0)^2}{1-kh} z_{xx} - (1 - kx)g z_x + (1 - kh_0)z z_x = 0, & x \in (-1, 1) \setminus h_0 \\ z(t, -1) = z(t, 1) = 0 \\ z(t, h_0) = g(t) \\ m\dot{g}(t) = \left[ \frac{1-kh_0}{1-kh} z_x \right](t, h_1) \\ \dot{h}(t) = g(t) \\ z(0, x) = z_0(x), & x \in (-1, 1), \\ h(0) = h_0, \quad g(0) = g_0. \end{cases} \quad (1.13)$$

After some simple calculations we see that the above equations are equivalent to the system (1.12).  $\square$

### 1.1.4 Local in Time Existence and Uniqueness of Solutions

The main result in this section states as follows.

**Proposition 1.3** *Assume that  $v_0 \in H_0^1(-1, 1)$ ,  $h_0 \in (-1, 1)$  and  $g_0 \in \mathbb{R}$  are such that  $v_0(h_0) = g_0$ . Then there exists  $T_{\max} > 0$  such that for every  $T \in (0, T_{\max})$ , the system (1.9) admits a unique solution*

$$v \in C([0, T]; H_0^1(-1, 1)) \cap H^1((0, T); L^2(-1, 1)), \quad h \in H^2((0, T), (-1, 1)), \quad (1.14)$$

with the restriction of  $v$  to  $x \in (-1, h_0)$  (respectively to  $(h_0, 1)$ ) in  $L^2((0, T); H^2(-1, h_0))$  (respectively in  $L^2((0, T); H^2(h_0, 1))$ ). Moreover, for every  $t \in [0, T_{\max})$

we have

$$\frac{1}{2} \int_{-1}^1 v^2(t, y) dy + \frac{1}{2} (\dot{h}(t))^2 = - \int_0^t \int_{-1}^1 v_y(\sigma, y)^2 dy d\sigma - \int_0^t \dot{h}^2(\sigma) d\sigma. \quad (1.15)$$

Finally, only one of the alternatives holds true

1. The solution is global, i.e.  $T_{max} = \infty$ .
2. We have either that  $\inf_{t \in [0, T_{max})} (1 - h(t)) = 0$  (which means that the mass touches the boundary) or that  $\sup_{t \in [0, T_{max})} \|v(t, \cdot)\|_{H_0^1(-1, 1)} = \infty$ .

An important role in the proof of the above proposition is played by a self-adjoint operator which we introduce below. Consider the Hilbert space

$$H = L^2(-1, 1) \times \mathbb{R},$$

endowed with the inner product

$$\left\langle \begin{bmatrix} \varphi_1 \\ p_1 \end{bmatrix}, \begin{bmatrix} \varphi_2 \\ p_2 \end{bmatrix} \right\rangle = \int_{-1}^1 \varphi_1(x) \varphi_2(x) dx + p_1 p_2. \quad (1.16)$$

We define the unbounded operator  $A_0 : \mathcal{D}(A_0) \rightarrow H$ ,

$$\mathcal{D}(A_0) = \left\{ \begin{bmatrix} \varphi \\ p \end{bmatrix} \in \begin{array}{c} H_0^1(-1, 1) \\ \times \\ \mathbb{R} \end{array} \mid \begin{array}{l} \varphi|_{(-1, h_0)} \in H^2(-1, h_0), \\ \varphi|_{(h_0, 1)} \in H^2(h_0, 1), \\ \varphi(h_0) = p \end{array} \right\}. \quad (1.17)$$

$$A_0 \begin{bmatrix} \varphi \\ p \end{bmatrix} = \begin{bmatrix} -\varphi_{xx} \\ -[\varphi_x](h_0) \end{bmatrix} \quad \left( \begin{bmatrix} \varphi \\ p \end{bmatrix} \in \mathcal{D}(A_0) \right). \quad (1.18)$$

**Proposition 1.4** *The operator  $A_0$  is positive in  $H$ . Moreover, the corresponding space  $H_{\frac{1}{2}}$  (i.e.,  $\mathcal{D}(A_0^{\frac{1}{2}})$  endowed with the graph norm of  $A_0^{\frac{1}{2}}$ ) is*

$$H_{\frac{1}{2}} = \left\{ \begin{bmatrix} \varphi \\ p \end{bmatrix} \in H_0^1(-1, 1) \times \mathbb{R} \mid \varphi(h_1) = p \right\}, \quad (1.19)$$

endowed with the inner product

$$\left\langle \begin{bmatrix} \varphi_1 \\ p_1 \end{bmatrix}, \begin{bmatrix} \varphi_2 \\ p_2 \end{bmatrix} \right\rangle_{\frac{1}{2}} = \int_{-1}^1 \varphi_{1,x}(x) \varphi_{2,x}(x) dx. \quad (1.20)$$

*Proof* We first check that  $A_0$  is symmetric. Indeed, for any  $\Phi_i = \begin{bmatrix} \varphi_i \\ p_i \end{bmatrix} \in D(A_0)$ ,  $i = 1, 2$ , we have that

$$\begin{aligned} \langle A_0 \Phi_1, \Phi_2 \rangle &= - \int_{-1}^{h_1} \varphi_{1,xx}(x) \varphi_2(x) \, dx \\ &\quad - \int_{h_1}^1 \varphi_{1,xx}(x) \varphi_2(x) \, dx - [\varphi_{1,x}](h_1) p_2 - [\varphi_{1,x}](h_1) r_2 \\ &= \int_{-1}^1 \varphi_{1,x}(x) \varphi_{2,x}(x) \, dx = \langle \Phi_1, A_0 \Phi_2 \rangle. \end{aligned} \quad (1.21)$$

We next check that  $A_0$  is onto. For  $F = \begin{bmatrix} f \\ g \end{bmatrix} \in H$ , the equation  $A_0 \Phi = F$ , of unknown  $\Phi = \begin{bmatrix} \varphi \\ p \end{bmatrix} \in \mathcal{D}(A_0)$  writes

$$\begin{cases} -\varphi_{xx}(x) = f(x) & x \in (-1, h_1) \cup (h_1, 1) \\ \varphi(a) = p \\ -[\varphi_x](h_1) = g. \end{cases}$$

Elementary considerations on the differential equation  $-\varphi_{xx} = f$  show that the above system has a unique solution  $\begin{bmatrix} \varphi \\ p \end{bmatrix} \in \mathcal{D}(A_0)$  so that  $A_0$  is onto. Since we have already shown that  $A_0$  is symmetric, a classical result (see, for instance, [34, Proposition 3.2.4]) implies that  $A_0$  is self-adjoint.

On the other hand, taking  $\Phi_1 = \Phi_2 = \Phi = \begin{bmatrix} \varphi \\ p \end{bmatrix}$  in (1.21) we see that,

$$\langle A_0 \Phi, \Phi \rangle = \int_{-1}^1 \varphi_x^2(x) \, dx,$$

which implies (1.20).  $\square$

As a consequence of the positivity  $A_0$  and of a classical result (see, for instance, Lemma 3.3 and Theorem 3.1 of [4]), we obtain:

**Corollary 1.5** *For every  $t_0, t_1 > 0$ ,  $Y_0 \in H$  and  $f \in L^2([t_0, t_1], H)$  there exists a unique  $Y \in C([t_0, t_1], H_{\frac{1}{2}}) \cap L^2([t_0, t_1], H_1)$  such that*

$$\begin{cases} \dot{Y}(t) + A_0 Y(t) = f(t) & t \in (t_0, t_1) \\ Y(t_0) = Y_0. \end{cases} \quad (1.22)$$

Moreover, there exists an absolute positive constant  $K$  such that, for every  $Y_0 \in H_{\frac{1}{2}}$  and  $f \in L^2([t_1, t_2], H)$ , we have

$$\begin{aligned} & \|Y\|_{C([t_1, t_2], H_{1/2})}^2 + \|A_0 Y\|_{L^2([t_1, t_2], H)}^2 \\ & \leq \|A_0^{\frac{1}{2}} Y_0\|_H^2 + K \|f\|_{L^2([t_1, t_2], H)}^2 \quad (Y_0 \in H_{1/2}, f \in L^2([t_1, t_2], H)). \end{aligned} \quad (1.23)$$

*Remark 1.6* In PDE terms the above corollary says that if  $T > 0$ ,  $z_0 \in H_0^1(-1, 1)$ ,  $g_0 \in \mathbb{R}$ ,  $f_1 \in L^2([0, T], L^2(-1, 1))$  and  $f_2 \in L^2[0, T]$ , are such that  $v_0(h_0) = g_0$  then then the solution  $\begin{bmatrix} z \\ g \end{bmatrix}$  of the system

$$\begin{cases} \dot{z}(t, x) - z_{xx}(t, x) = f_1(t, x), & x \in (-1, h_0) \cup (h_0, 1), \quad t \in (0, T), \\ z(t, -1) = z(t, 1) = 0, & t \in (0, T), \\ z(t, h_0) = g(t), & t \in (0, T), \\ \dot{g}(t) - [z_x](t, h_0) = f_2(t), & t \in (0, T), \\ z(0, x) = z_0(x), & x \in (-1, 1), \\ g(0) = g_0, \end{cases} \quad (1.24)$$

satisfies

$$\begin{aligned} & \|z\|_{C([0, T], H_0^1(-1, 1))}^2 + \|g\|_{C[0, T]}^2 + \|z\|_{L^2[0, T], H^2(-1, h_0)}^2 + \|z\|_{L^2[0, T], H^2(h_0, 1)}^2 \\ & \leq \|z_0\|_{H_0^1(-1, 1)}^2 + |g_0|^2 + K \left( \|f_1\|_{L^2([0, T], L^2(-1, 1))}^2 + \|f_2\|_{L^2[0, T]}^2 \right). \end{aligned} \quad (1.25)$$

Another important ingredient are the properties of the operators  $(\mathcal{G}_k)_{k=1}^4$  which are defined (as suggested by the right hand side of (1.12)) by

$$\mathcal{G}_1 \begin{bmatrix} f_1 \\ f_2 \end{bmatrix} (t, x) = \frac{k(h(t) - h_0)}{1 - kh(t)} \left[ 2 + \frac{k(h(t) - h_0)}{1 - kh(t)} \right] z_{xx}(t, x), \quad (1.26)$$

$$\mathcal{G}_2 \begin{bmatrix} f_1 \\ f_2 \end{bmatrix} (t, x) = \frac{1 - kx}{1 - kh(t)} g(t) z_x(t, x), \quad (1.27)$$

$$\mathcal{G}_3 \begin{bmatrix} f_1 \\ f_2 \end{bmatrix} (t, x) = -\frac{1 - kh_0}{1 - kh(t)} z(x, t) z_x(t, x), \quad (1.28)$$

$$\mathcal{G}_4 \begin{bmatrix} f_1 \\ f_2 \end{bmatrix} (t) = (h(t) - h_0) \left[ \frac{kz_x}{1 - kh} \right] (t, h_0), \quad (1.29)$$

where  $z, g$  satisfy (1.24) and

$$h(t) = h_0 + \int_0^t g(\sigma) d\sigma. \quad (1.30)$$



We give below some of the properties of these operators.

**Lemma 1.7** *Let  $T > 0$  and let  $\mathcal{G}_k$ , with  $k \in \{1, 2, 3, 4\}$ , be the operators defined in (1.26)–(1.29). Then, for every  $k \in \{1, 2, 3\}$ , the operator  $\mathcal{G}_k$  maps  $L^2([0, T], L^2[-1, 1])$  to  $L^2([0, T], L^2[-1, 1])$ , whereas  $\mathcal{G}_4$  maps  $L^2[0, T]$  to  $L^2[0, T]$ . Moreover, assume that*

$$\|f_1\|_{L^2([0, T], L^2[-1, 1])}^2 + \|f_2\|_{L^2([0, T])}^2 \leq R^2, \quad \|v_0\|_{H_0^1(-1, 1)}^2 + |g_0|^2 \leq M^2, \quad 1 - |h_0| \geq \varepsilon, \quad (1.31)$$

for some  $R, M, \varepsilon > 0$ . Then there exists a constant  $C = C(\varepsilon) > 0$  such that for every  $T \leq \frac{\varepsilon}{2\sqrt{M^2 + KR^2}}$  (with  $K$  being the constant in (1.25)) we have

$$\left\| \mathcal{G}_k \begin{bmatrix} f_1 \\ f_2 \end{bmatrix} \right\|_{L^2([0, T], L^2[-1, 1])} \leq TC(\varepsilon) (M^2 + KR^2) \quad (k \in \{1, 2, 3\}), \quad (1.32)$$

$$\left\| \mathcal{G}_4 \begin{bmatrix} f_1 \\ f_2 \end{bmatrix} \right\|_{L^2[0, T]} \leq \sqrt{T}C(\varepsilon) (M^2 + KR^2). \quad (1.33)$$

Finally, if  $h$  is defined by (1.30) we have that

$$|h(t)| \leq 1 - \frac{\varepsilon}{2} \quad (t \in [0, T]). \quad (1.34)$$

*Proof* In order to prove (1.34) it suffices to note that, using (1.25), we have

$$|h(t)| \leq |h_0| + \int_0^T |g(\sigma)| \, d\sigma \leq 1 - \varepsilon + T\sqrt{M^2 + KR^2} \leq 1 - \frac{\varepsilon}{2} \quad (t \in [0, T]).$$

The facts that  $\mathcal{G}_1, \mathcal{G}_2, \mathcal{G}_3$  map  $L^2([0, T], L^2[-1, 1])$  to  $L^2([0, T], L^2[-1, 1])$  and that  $\mathcal{G}_4$  maps  $L^2[0, T]$  to  $L^2[0, T]$  follow from (1.25) and from simple Sobolev embeddings.

In the remaining part of this proof we denote by  $\widetilde{C}(\varepsilon)$  a generic positive constant depending only on  $\varepsilon$ .

In order to prove (1.32) we first note that (1.34) implies that

$$\frac{1}{1 - kh(t)} \leq \frac{2}{2 - \varepsilon} \quad (t \in [0, T]). \quad (1.35)$$

By combining (1.26) and (1.35) it follows that

$$\left\| \mathcal{G}_1 \begin{bmatrix} f_1 \\ f_2 \end{bmatrix} \right\|_{L^2([0, T], L^2[-1, 1])} \leq T\widetilde{C}(\varepsilon) \|g\|_{C([0, T], L^2[-1, 1])} \|z_{xx}\|_{L^2(0, T, L^2(-1, 1))}.$$

Combining the last estimate with (1.25) we obtain that (1.32) holds for  $k = 1$ .

In order to prove (1.32) holds for  $k = 2$ , we note that the definition of  $\mathcal{G}_2$ , combined with (1.35) and the Cauchy-Schwarz inequality, imply that

$$\begin{aligned} & \left\| \mathcal{G}_2 \begin{bmatrix} f_1 \\ f_2 \end{bmatrix} (t, x) \right\|_{L^2[0,T], L^2(-1,1)} \leq \widetilde{C}(\varepsilon) \|g\|_{L^2[0,T]} \|z_x\|_{L^2(0,T, L^2[-1,1])} \\ & \leq T \widetilde{C}(\varepsilon) \|g\|_{C[0,T]} \|z_x\|_{C([0,T], L^2[-1,1])} \leq T \widetilde{C}(\varepsilon) \left( \|g\|_{C[0,T]}^2 + \|z_x\|_{C([0,T], L^2[-1,1])}^2 \right). \end{aligned}$$

The last estimate and (1.25) imply that (1.32) holds for  $k = 2$ .

The fact that (1.32) holds for  $k = 3$  can be proved in a completely similar manner, so we omit the details.

In order to prove (1.33) we note that the definition (1.29) of  $\mathcal{G}_4$ , estimate (1.35) and a classical trace theorem imply that

$$\begin{aligned} & \left| (h(t) - h_0) \left[ \frac{kz_x}{1 - kh} \right] (t, h_0) \right| \\ & \leq \widetilde{C}(\varepsilon) \int_0^T |g(t)| dt \left( \|z(t, \cdot)\|_{H^2(-1, h_0)} + \|z(t, \cdot)\|_{H^2(h_0, 1)} \right). \end{aligned}$$

The above estimate and (1.25) imply that

$$\begin{aligned} & \left\| (h(t) - h_0) \left[ \frac{kz_x}{1 - kh} \right] (t, h_0) \right\|_{L^2[0,T]} \\ & \leq \sqrt{T} \widetilde{C}(\varepsilon) \left( \|g\|_{C[0,T]}^2 + \|z(t, \cdot)\|_{H^2(-1, h_0)}^2 + \|z(t, \cdot)\|_{H^2(h_0, 1)}^2 \right), \end{aligned}$$

which, combined with (1.25), yields (1.33).  $\square$

**Lemma 1.8** *With the notation and assumptions in Lemma 1.8, suppose that  $\widetilde{f}_1, \widetilde{f}_2 \in L^2([0, T], L^2[-1, 1])$  satisfy*

$$\|\widetilde{f}_1\|_{L^2([0,T], L^2[-1,1])}^2 + \|\widetilde{f}_2\|_{L^2([0,T])}^2 \leq R^2, \quad (1.36)$$

*Then there exists a constant  $C = C(\varepsilon) > 0$  such that for every  $T \leq \frac{\varepsilon}{2\sqrt{M^2 + KR^2}}$  (with  $K$  being the constant in (1.25)) we have*

$$\begin{aligned} & \left\| \mathcal{G}_k \begin{bmatrix} f_1 \\ f_2 \end{bmatrix} - \mathcal{G}_k \begin{bmatrix} \widetilde{f}_1 \\ \widetilde{f}_2 \end{bmatrix} \right\|_{L^2([0,T], L^2[-1,1])} \\ & \leq TC(\varepsilon) \sqrt{M^2 + KR^2} \left( \|f_1 - \widetilde{f}_1\|_{L^2([0,T], L^2[-1,1])} + \|f_2 - \widetilde{f}_2\|_{L^2[0,T]} \right) \quad (k \in \{1, 2, 3\}), \end{aligned} \quad (1.37)$$

$$\begin{aligned} & \left\| \mathcal{G}_4 \begin{bmatrix} f_1 \\ f_2 \end{bmatrix} - \mathcal{G}_4 \begin{bmatrix} \tilde{f}_1 \\ \tilde{f}_2 \end{bmatrix} \right\|_{L^2[0,T]} \\ & \leq \sqrt{TC(\varepsilon)} \sqrt{M^2 + KR^2} (\|f_1 - \tilde{f}_1\|_{L^2([0,T],L^2[-1,1])} + \|f_2 - \tilde{f}_2\|_{L^2[0,T]}). \end{aligned} \quad (1.38)$$

*Proof* The proof is based on estimates which are very close to those used in proving Lemma 1.7. More precisely, we first note that, estimate (1.35) for  $h$  and for  $\tilde{h}$  implies that

$$\begin{aligned} & \left\| \mathcal{G}_1 \begin{bmatrix} f_1 \\ f_2 \end{bmatrix} - \mathcal{G}_1 \begin{bmatrix} \tilde{f}_1 \\ \tilde{f}_2 \end{bmatrix} \right\|_{L^2([0,T],L^2[-1,1])} \leq \tilde{C}(\varepsilon) \|h - h_0\|_{L^\infty[0,T]} \|z_{xx} - \tilde{z}_{xx}\|_{L^2([0,T],L^2[-1,1])} \\ & + \tilde{C}(\varepsilon) \|(h - h_0)z_{xx}(1 - k\tilde{h}) - (\tilde{h} - h_0)\tilde{z}_{xx}(1 - kh)\|_{L^2([0,T],L^2[-1,1])}. \end{aligned} \quad (1.39)$$

Using the inequality

$$\|h - h_0\|_{C[0,T]} \leq T\|g\|_{C[0,T]}, \quad (1.40)$$

together with (1.25) it follows that the first term in the right hand side of (1.39) satisfies

$$\begin{aligned} & \|h - h_0\|_{L^\infty[0,T]} \|z_{xx} - \tilde{z}_{xx}\|_{L^2([0,T],L^2[-1,1])} \\ & \leq T \sqrt{M^2 + KR^2} (\|f_1 - \tilde{f}_1\|_{L^2([0,T],L^2[-1,1])} + \|f_2 - \tilde{f}_2\|_{L^2[0,T]}). \end{aligned} \quad (1.41)$$

Concerning the second term in the right hand side of (1.39) we note that

$$\begin{aligned} & \|(h - h_0)z_{xx}(1 - k\tilde{h}) - (\tilde{h} - h_0)\tilde{z}_{xx}(1 - kh)\|_{L^2([0,T],L^2[-1,1])} \\ & \leq \|(h - h_0)z_{xx}\|_{L^2([0,T],L^2[-1,1])} \|h - \tilde{h}\|_{L^\infty[0,T]} \\ & + \|(h - h_0)(1 - kh)\|_{L^\infty[0,T]} \|z_{xx} - \tilde{z}_{xx}\|_{L^2([0,T],L^2[-1,1])} \\ & + \|\tilde{z}_{xx}(1 - kh)\|_{L^2([0,T],L^2[-1,1])} \|h - \tilde{h}\|_{L^\infty[0,T]}. \end{aligned}$$

Using in the above inequality the fact that

$$\|h - \tilde{h}\|_{L^\infty[0,T]} \leq T\|g - \tilde{g}\|_{L^\infty[0,T]}, \quad (1.42)$$

together with (1.42) and (1.25), we obtain that

$$\begin{aligned} & \|(h - h_0)z_{xx}(1 - k\tilde{h}) - (\tilde{h} - h_0)\tilde{z}_{xx}(1 - kh)\|_{L^2([0,T],L^2[-1,1])} \\ & \leq T\tilde{C}(\varepsilon) \sqrt{M^2 + KR^2} (\|f_1 - \tilde{f}_1\|_{L^2([0,T],L^2[-1,1])} + \|f_2 - \tilde{f}_2\|_{L^2[0,T]}). \end{aligned} \quad (1.43)$$

By combining (1.41) and (1.43) we obtain that (1.37) holds for  $k = 1$ . The proof of (1.37) for  $k \in \{2, 3\}$  is very similar (but quite tedious) so we omit it here.

In order to prove (1.38) we note that from the definition (1.29) of  $\mathcal{G}_4$  and from (1.35) it follows that

$$\begin{aligned} & \left\| \mathcal{G}_4 \begin{bmatrix} f_1 \\ f_2 \end{bmatrix} - \mathcal{G}_4 \begin{bmatrix} \tilde{f}_1 \\ \tilde{f}_2 \end{bmatrix} \right\|_{L^2[0,T]} \leq \|h(t) - h_0\|_{C[0,T]} \left\| \begin{bmatrix} k(z_x - \tilde{z}_x) \\ 1 - kh \end{bmatrix} (t, h_0) \right\|_{L^2[0,T]} \\ & + \|h - \tilde{h}\|_{C[0,T]} \left\| \begin{bmatrix} \tilde{z}_x \\ 1 - kh \end{bmatrix} (t, h_0) \right\|_{L^2[0,T]} + \gamma \sqrt{T} \|g - \tilde{g}\|_{C[0,T]} + \sqrt{T} \|h - \tilde{h}\|_{C[0,T]}. \end{aligned}$$

The above estimate, combined with (1.35), (1.40), (1.42) and (1.25), implies the conclusion (1.38).  $\square$

We are now in a proposition to prove the main result in this section.

*Proof of Proposition 1.3* Let

$$\mathcal{X} = L^2([0, T], L^2[-1, 1]) \times L^2[0, T],$$

and let  $\mathcal{N} : \mathcal{X} \rightarrow \mathcal{X}$  be defined by

$$\mathcal{N} = \begin{bmatrix} \mathcal{G}_1 + \mathcal{G}_2 + \mathcal{G}_3 \\ \mathcal{G}_4 \end{bmatrix},$$

where  $(\mathcal{G}_k)_{1 \leq k \leq 4}$  have been defined in (1.26)–(1.29).

Let  $M > 0$  be such that

$$\|z_0\|_{H_0^1(-1,1)}^2 + |g_0|^2 \leq M^2, \quad (1.44)$$

and let  $\varepsilon > 0$  such that

$$|h_0| \leq 1 - \varepsilon. \quad (1.45)$$

We denote by  $\mathcal{B}_M$  the ball in  $\mathcal{X}$  of radius  $M$ . From Lemma 1.7 it follows that

$$\left\| \mathcal{N} \begin{bmatrix} f_1 \\ f_2 \end{bmatrix} \right\|_{\mathcal{X}} \leq (T + \sqrt{T})C(\varepsilon)(M^2 + M + 1) \quad \left( \begin{bmatrix} f_1 \\ f_2 \end{bmatrix} \right) \in \mathcal{B}_M.$$

The last estimate implies that  $\mathcal{N}$  maps  $\mathcal{B}_M$  into  $\mathcal{B}_M$  if

$$T \leq [C(\varepsilon)M^2]^{-1}. \quad (1.46)$$

By applying Lemma 1.8 it follows that

$$\begin{aligned} & \left\| \mathcal{N} \begin{bmatrix} f_1 \\ f_2 \end{bmatrix} - \mathcal{N} \begin{bmatrix} \widetilde{f}_1 \\ \widetilde{f}_2 \end{bmatrix} \right\|_{\mathcal{X}} \\ & \leq \sqrt{T} \frac{C(\varepsilon)(M^2 + M + 1)}{M} \left\| \begin{bmatrix} f_1 \\ f_2 \end{bmatrix} - \begin{bmatrix} \widetilde{f}_1 \\ \widetilde{f}_2 \end{bmatrix} \right\|_{\mathcal{X}} \quad \left( \begin{bmatrix} f_1 \\ f_2 \end{bmatrix}, \begin{bmatrix} \widetilde{f}_1 \\ \widetilde{f}_2 \end{bmatrix} \in \mathcal{B}_M \right). \end{aligned}$$

The last estimate implies that the restriction of  $\mathcal{N}$  to  $\mathcal{B}_M$  is a strict contraction provided that

$$T \leq \frac{1}{2} \left[ \frac{C(\varepsilon)(M^2 + M + 1)}{M} \right]^{-1}. \quad (1.47)$$

Consequently, for every  $T$  satisfying (1.46) and (1.47) we have that  $\mathcal{N}$  has a unique fixed point  $\begin{bmatrix} \widehat{f}_1 \\ \widehat{f}_2 \end{bmatrix} \in \mathcal{B}_M$ . Denoting by  $\begin{bmatrix} \widehat{z} \\ \widehat{g} \end{bmatrix}$  the solution of (1.24) with  $f_1 = \widehat{f}_1$  and  $f_2 = \widehat{f}_2$  we clearly have that  $\begin{bmatrix} v \\ h \end{bmatrix}$  with

$$v(t, \cdot) = \widehat{z}(t, \cdot), \quad h(t) = h_0 + \int_0^t g(\sigma) \, d\sigma \quad (t \in [0, T]), \quad (1.48)$$

satisfy all the equations in (1.9), with the restriction of  $v$  to  $x \in (-1, h_0)$  (respectively to  $(h_0, 1)$ ) in  $L^2([0, T]; H^2(-1, h_0))$  (respectively in  $L^2([0, T]; H^2(h_0, 1))$ ). Moreover, according to (1.34) we have that  $h(t) \in (-1, 1)$  for every  $t \in [0, T]$ , so that  $\begin{bmatrix} v \\ h \end{bmatrix}$  is indeed the desired local in time solution of (1.9).

According to classical arguments, this solution can be extended to a solution defined on  $[0, T_{max})$ .

Finally, assume that both assertions in the second alternative in Proposition 1.3 are false. Denoting

$$M = \sup_{t \in [0, T_{max})} \|v(t, \cdot)\|_{H_0^1(-1, 1)}, \quad \varepsilon = \inf_{t \in [0, T_{max})} (1 - |h(t)|),$$

the first part of the proof shows that there exists  $\delta = \delta(\varepsilon, M) > 0$  such that for every  $t \in [0, T_{max})$  the solution can be extended on  $[t, T + \delta]$ . This clearly implies that  $T_{max} = \infty$ , i.e., that the solution is global.  $\square$

### 1.1.5 Proof of the Global Well-Posedness Result

The key estimates used to prove the above theorem are given in the result below.

**Proposition 1.9** *With the notation and assumptions in Proposition 1.3, let  $T \in [0, T_{max})$  and let  $\begin{bmatrix} v \\ h \end{bmatrix} : [0, T] \rightarrow H_0^1(-1, 1) \times \mathbb{R}$  be the local in time solution of (1.9) constructed in Proposition 1.3. Moreover, assume that the initial data  $v_0$  satisfies  $\|v_0\|_{H^1(-1,1)} \leq M$ , for some  $M > 0$ . Then there exists a constant  $K = K(M, T)$  such that*

$$\|v(t, \cdot)\|_{H_0^1(-1,1)} \leq K(M, T) \quad (t \in [0; T]). \quad (1.49)$$

$$\int_0^T \left[ \int_{-1}^{h(t)} v_{yy}^2(t, y) dy + \int_{h(t)}^1 v_{yy}^2(t, y) dy + |\ddot{h}(t)|^2 \right] dt \leq K(M, T). \quad (1.50)$$

*Proof* We follow step by step the method used in [36].

Multiplying the first equation in (1.9)  $v_{yy}$  and integrating on  $(-1, h_0)$  and  $(h_0, 1)$ , we obtain that for every  $t \in [0, T]$  we have

$$\int_{-1}^{h(t)} v_{yy}^2 dy = -\frac{1}{2} \int_{-1}^{h(t)} \frac{\partial}{\partial t} (v_y^2) dy + \dot{v}(t, h(t) - 0)v_y(t, h(t) - 0) + \int_{-1}^{h(t)} v v_y v_{yy} dy, \quad (1.51)$$

$$\int_{h(t)}^1 v_{yy}^2 dy = -\frac{1}{2} \int_{h(t)}^1 \frac{\partial}{\partial t} (v_y^2) dy - \dot{v}(t, h(t) + 0)v_y(t, h(t) + 0) + \int_{h(t)}^1 v v_y v_{yy}. \quad (1.52)$$

On the other hand, differentiating the third equation in (1.9) it follows that

$$\dot{v}(t, h(t) \pm 0) = \ddot{h}(t) - \dot{h}(t)v_y(t, h(t) \pm 0) \quad (t \geq 0),$$

so that

$$\dot{v}(t, h(t) \pm 0)v_y(t, h(t) \pm 0) = \ddot{h}(t)v_y(t, h(t) \pm 0) - \dot{h}(t)v_y^2(t, h(t) \pm 0). \quad (1.53)$$

On the other hand

$$\begin{aligned} \int_{-1}^{h(t)} \frac{\partial}{\partial t} (v_y^2) dy &= \frac{d}{dt} \int_{-1}^{h(t)} v_y^2 dy - \dot{h}(t)v_y(t, h(t) - 0), \\ \int_{h(t)}^1 \frac{\partial}{\partial t} (v_y^2) dy &= \frac{d}{dt} \int_{-1}^{h(t)} v_y^2 dy + \dot{h}(t)v_y(t, h(t) + 0), \end{aligned}$$

so that

$$-\frac{1}{2} \int_{-1}^{h(t)} \frac{\partial}{\partial t} (v_y^2) dy - \frac{1}{2} \int_{h(t)}^1 \frac{\partial}{\partial t} (v_y^2) dy = -\frac{1}{2} \frac{d}{dt} \int_{-1}^1 v_y^2 dy - \frac{1}{2} \dot{h}(t) [v_y](t, h(t)).$$

By combining the last formula with (1.51), (1.52) and (1.53) it follows that

$$\begin{aligned} \int_{-1}^{h(t)} v_{yy}^2 dy + \int_{h(t)}^1 v_{yy}^2 dy &= -\frac{1}{2} \frac{d}{dt} \int_{-1}^1 v_y^2 dy - \frac{1}{2} \dot{h}(t) [v_y](t, h(t)) \\ &\quad - \ddot{h}(t) [v_y](t, h(t)) + \dot{h}(t) [v_y^2](t, h(t)) + \int_{-1}^{h(t)} v v_y v_{yy} dy + \int_{h(t)}^1 v v_y v_{yy} dy. \end{aligned}$$

In the second term of the right hand side of the above formula we use the fact that

$$[v_y](t, h(t)) = \ddot{h}(t), \quad (1.54)$$

and we obtain that

$$\begin{aligned} \int_{-1}^{h(t)} v_{yy}^2 dy + \int_{h(t)}^1 v_{yy}^2 dy &= -\frac{1}{2} \frac{d}{dt} \int_{-1}^1 v_y^2 dy - \frac{1}{4} \frac{d}{dt} \dot{h}^2(t) \\ &\quad - \ddot{h}^2(t) + \dot{h}(t) [v_y^2](t, h(t)) + \int_{-1}^{h(t)} v v_y v_{yy} dy + \int_{h(t)}^1 v v_y v_{yy} dy. \end{aligned} \quad (1.55)$$

The last two terms in the right hand side of the above formula can be estimated, using the Cauchy-Schwarz inequality, to give

$$\begin{aligned} &\left| \int_{-1}^{h(t)} v v_y v_{yy} dy + \int_{h(t)}^1 v v_y v_{yy} dy \right| \\ &\leq \|v(t, \cdot) v_y(t, \cdot)\|_{L^2[-1,1]} \left( \|v_{yy}(t, \cdot)\|_{L^2[-1, h(t)]} + \|v_{yy}(t, \cdot)\|_{L^2[h(t), 1]} \right). \end{aligned} \quad (1.56)$$

Using the classical interpolation inequality

$$\|\psi\|_{C[-1,1]} \leq \|\psi'\|_{L^2[-1,1]}^{\frac{1}{2}} \|\psi\|_{L^2[-1,1]}^{\frac{1}{2}} \quad (\psi \in H_0^1(-1, 1)),$$

together with (1.15) it follows that

$$\|v(t, \cdot) v_y(t, \cdot)\|_{L^2[-1,1]} \leq M \|v_y(t, \cdot)\|_{L^2[-1,1]}^{\frac{3}{2}}.$$

Inserting the last inequality into (1.56) we obtain that

$$\left| \int_{-1}^{h(t)} v v_y v_{yy} dy + \int_{h(t)}^1 v v_y v_{yy} dy \right| \leq \frac{M^2}{2} \|v_y(t, \cdot)\|_{L^2[-1,1]}^3 + \frac{1}{2} \left( \|v_{yy}(t, \cdot)\|_{L^2[-1, h(t)]}^2 + \|v_{yy}(t, \cdot)\|_{L^2[h(t), 1]}^2 \right) \quad (t \in [0, T]). \quad (1.57)$$

By combining the last inequality and (1.55), it follows that

$$\begin{aligned} & \frac{d}{dt} \int_{-1}^1 v_y^2 dy + \int_{-1}^{h(t)} v_{yy}^2 dy + \int_{h(t)}^1 v_{yy}^2 dy + \frac{d}{dt} |\dot{h}(t)|^2 + |\ddot{h}(t)|^2 + \\ & \leq K_1 \left( 1 + \|v_y(t, \cdot)\|_{L^2[-1,1]}^3 + \dot{h}(t) [v_y^2](t, h(t)) \right) \quad (t \in [0, T]), \end{aligned} \quad (1.58)$$

with  $K_1$  depending only on  $M$ . In order to estimate the last term in the right hand side of (1.58) we note that, for almost every  $t \in [0, T]$ , we have

$$\begin{aligned} \dot{h}(t) [v_y^2](h(t), t) &= v(t, h(t)) [v_y^2(t, h(t) + 0) - v_y^2(t, h(t) - 0)] \\ &= \int_{-1}^{h(t)} (v(t, y) v_y^2(t, y))_y dy + \int_{h(t)}^1 (v(t, y) v_y^2(t, y))_y dy = \int_{-1}^1 v_y^3(t, y) dy \\ & \quad + 2 \int_{-1}^{h(t)} v(t, y) v_y(t, y) v_{yy}(t, y) dy + 2 \int_{h(t)}^1 v(t, y) v_y(t, y) v_{yy} dy \end{aligned}$$

Using (1.57) in the last inequality we deduce that

$$\begin{aligned} \dot{h}(t) [v_y^2](h(t), t) &\leq \int_{-1}^1 v_y^3(t, y) dy + M^2 \|v_y(t, \cdot)\|_{L^2[-1,1]}^3 \\ & \quad + \|v_{yy}(t, \cdot)\|_{L^2[-1, h(t)]}^2 + \|v_{yy}(t, \cdot)\|_{L^2[h(t), 1]}^2. \end{aligned}$$

Inserting the last inequality in (1.58) it follows that

$$\begin{aligned} & \frac{d}{dt} \int_{-1}^1 v_y^2 dy + \int_{-1}^{h(t)} v_{yy}^2 dy + \int_{h(t)}^1 v_{yy}^2 dy + \frac{d}{dt} |\dot{h}(t)|^2 + |\ddot{h}(t)|^2 \\ & \leq K_2 \left( 1 + \|v_y(t, \cdot)\|_{L^2[-1,1]}^3 + \int_{-1}^1 v_y^3 dy \right) \quad (t \in [0, T]), \end{aligned} \quad (1.59)$$



with  $K_2$  depending only on  $M$ . To estimate the last integral in the right-hand side of the above formula we use the interpolation inequality (4.13) from [36] which asserts the existence of a universal constant  $K > 0$  that

$$\|v_y\|_{L^\infty[-1,1]} \leq K \left[ \|v_y\|_{L^2[-1,1]}^{\frac{1}{2}} \left( \|v_{yy}\|_{L^2[-1,h(t)]}^{\frac{1}{2}} + \|v_{yy}\|_{L^2[h(t),1]}^{\frac{1}{2}} \right) + |\ddot{h}(t)| \right].$$

The above estimate, combined with Young's inequality, implies that for every  $\varepsilon > 0$  there exists a constant  $c > 0$  with

$$\begin{aligned} \int_{-1}^1 v_y^3 dy &\leq \varepsilon |\ddot{h}(t)|^2 + \varepsilon \left( \int_{-1}^{h(t)} v_{yy}^2 dy + \int_{h(t)}^1 v_{yy}^2 dy \right) \\ &\quad + c \left( \int_{-1}^1 v_y^2 dy \right)^{\frac{5}{3}} + c \left( \int_{-1}^1 v_y^2 dy \right)^2 \quad (t \in [0, T]). \end{aligned}$$

Choosing  $\varepsilon$  small enough and inserting the last inequality in (1.59) we obtain that

$$\begin{aligned} \frac{d}{dt} \int_{-1}^1 v_y^2 dy + \int_{-1}^{h(t)} v_{yy}^2 dy + \int_{h(t)}^1 v_{yy}^2 dy + \frac{d}{dt} |\dot{h}(t)|^2 + |\ddot{h}(t)|^2 \\ \leq K_3 \left[ 1 + \left( \int_{-1}^1 v_y^2 dy \right)^{\frac{3}{2}} + \left( \int_{-1}^1 v_y^2 dy \right)^{\frac{5}{3}} + \left( \int_{-1}^1 v_y^2 dy \right)^2 \right] \\ \leq K_4 \left[ 1 + \int_{-1}^1 v_y^2 dy + \left( \int_{-1}^1 v_y^2 dy \right)^2 \right], \quad (1.60) \end{aligned}$$

with  $K_3$  and  $K_4$  depending only on  $M$ . Integrating the above formula on  $[0, \tau]$ , with  $\tau \in [0, T]$ , it follows that

$$\begin{aligned} \int_{-1}^1 v_y^2(\tau, y) dy &\leq \int_{-1}^1 v_{0,y}^2(y) dy \\ &\quad + K_5 \left[ T + \int_0^\tau \left( 1 + \int_{-1}^1 v_y^2(t, y) dy \right) \int_{-1}^1 v_y^2(t, y) dy dt \right]. \end{aligned}$$

Using in the last estimate the fact, resulting from (1.15), that

$$\int_0^\tau \int_{-1}^1 v_y^2(t, y) dy dt \leq K_6,$$

the conclusion (1.49) follows by applying Gronwall's inequality.

In order to prove (1.50) it suffices to integrate (1.60) with respect to time and to use (1.49).  $\square$

We are now in a position to prove the main result of this section.

*Proof of Theorem 1.1* It suffices to prove that both assertions in the second alternative of Proposition 1.3 are false. The fact that the assertion

$$\lim_{t \rightarrow T_{\max}} \|v(t, \cdot)\|_{H_0^1(-1,1)} = \infty,$$

is false for every  $T_{\max} \in [0, \infty)$  is a direct consequence of Proposition 1.9. We show below that the assertion saying that

$$\lim_{t \rightarrow T_{\max}} |h(t)| = 1,$$

is false for every  $T_{\max} \in [0, \infty)$ . To accomplish this goal, we first note that from (1.49) and (1.50) it follows that  $v$  can be extended to a function, still denoted by  $v$ , such that

$$v \in C([0, T_{\max}], H_0^1(-1, 1)),$$

and  $v$  is Lipschitz with respect to  $x$ , uniformly with respect to  $t \in [0, T_{\max}]$ . We use now a contradiction argument. Indeed, assume that

$$\lim_{t \rightarrow T_{\max}} h(t) = 1.$$

This means that  $h$  can be extended to a function in  $C^1[0, T_{\max}]$  such that

$$\dot{h}(t) = v(t, h(t)) \quad (t \in [0, T_{\max}]), \quad h(T_{\max}) = 1.$$

On the other hand the function  $\tilde{h}(t) = 1$  for every  $t \in \mathbb{R}$  is also a solution of the above initial value problem. By the Cauchy-Lipschitz theorem it follows that  $h(t) = \tilde{h}(t) = 1$  for every  $t \in [0, T_{\max}]$ , which is clearly a contradiction.  $\square$

In order to study the concept of weak solution of (1.9) it is useful to note that that the distance from the mass point to the boundary is bounded from below by a function depending only on the initial kinetic energy of the fluid-mass particle system and of the initial position of the particle.

**Theorem 1.10** *Let  $M > 0$ . We assume that  $v_0$ ,  $h_0$  and  $g_0$  satisfy the assumptions in Theorem 1.1 and that*

$$\int_{-1}^1 v_0^2(y) dy + g_0^2 + |h_0 - h_1|^2 \leq M^2.$$

Let  $\begin{bmatrix} v \\ h \end{bmatrix}$  be the corresponding solution of (1.9). Then there exist the positive constants  $K_0$ , which depends only on  $M$ , and  $K_1$ , depending only on  $M$  and on  $h_0$ , such that

$$1 + h(t) \geq K_1 e^{-tK_0} \quad (t \geq 0). \quad (1.61)$$

$$1 - h(t) \geq K_1 e^{-tK_0} \quad (t \geq 0), \quad (1.62)$$

*Proof* We give below only the detailed proof of (1.62), since the proof of (1.61) can be obtained with obvious adaptations. Moreover, we note that it suffices to prove (1.61) only for the values of  $t$  for which  $h(t) \geq \frac{1}{2}$ , i.e. for values of  $t$  such that

$$h(t) \geq \frac{3}{2}. \quad (1.63)$$

Consider the function  $\varphi$  defined by

$$\varphi(t, y) = \begin{cases} \frac{1+y}{1+h(t)} & \text{if } y \in [-1, h(t)], \\ \frac{1-y}{1-h(t)} & \text{if } y \in [h(t), 1]. \end{cases}$$

Then

$$\begin{aligned} \int_{-1}^{h(t)} \dot{v}(t, y) \varphi(t, y) \, dy &= \int_{-1}^{h(t)} \frac{\partial}{\partial t} (v(t, y) \varphi(t, y)) \, dy - \int_{-1}^{h(t)} v(t, y) \dot{\varphi}(t, y) \, dy \\ &= \frac{d}{dt} \int_{-1}^{h(t)} v(t, y) \varphi(t, y) \, dy - \dot{h}^2(t) + \frac{\dot{h}(t)}{(1+h(t))^2} \int_{-1}^{h(t)} (1+y)v(t, y) \, dy \quad (t \geq 0), \\ &\quad - \int_{-1}^{h(t)} v_{yy}(t, y) \varphi(t, y) \, dy = \frac{\dot{h}(t)}{1+h(t)} - v_y(t, h(t) - 0) \quad (t \geq 0). \end{aligned}$$

Summing up the two above formulae it follows that

$$\begin{aligned} \frac{d}{dt} \int_{-1}^{h(t)} v(t, y) \varphi(t, y) \, dy - \dot{h}^2(t) + \frac{\dot{h}(t)}{(1+h(t))^2} \int_{-1}^{h(t)} (1+y)v(t, y) \, dy + \frac{\dot{h}(t)}{1+h(t)} \\ - v_y(t, h(t) - 0) + \int_{-1}^{h(t)} v(t, y) v_y(t, y) \varphi(t, y) \, dy = 0 \quad (t \geq 0). \quad (1.64) \end{aligned}$$

Similar calculations show that

$$\begin{aligned} & \int_{h(t)}^1 \dot{v}(t, y) \varphi(t, y) \, dy \\ &= \frac{d}{dt} \int_{h(t)}^1 v(t, y) \varphi(t, y) \, dy + \dot{h}^2(t) - \frac{\dot{h}(t)}{(1-h(t))^2} \int_{h(t)}^1 (1-y)v(t, y) \, dy \quad (t \geq 0), \\ & \quad - \int_{h(t)}^1 v_{yy}(t, y) \varphi(t, y) \, dy = \frac{\dot{h}(t)}{1-h(t)} + v_y(t, h(t) + 0) \quad (t \geq 0). \end{aligned}$$

Summing up the last two formulae we obtain that

$$\begin{aligned} & \frac{d}{dt} \int_{h(t)}^1 v(t, y) \varphi(t, y) \, dy + \dot{h}^2(t) - \frac{\dot{h}(t)}{(1-h(t))^2} \int_{-1}^{h(t)} (1-y)v(t, y) \, dy \\ & \quad + \frac{\dot{h}(t)}{1-h(t)} + v_y(t, h(t) + 0) + \int_{h(t)}^1 v(t, y) v_y(t, y) \varphi(t, y) \, dy = 0 \quad (t \geq 0). \end{aligned}$$

The above formula and (1.64) imply that

$$\begin{aligned} & \frac{d}{dt} \int_{-1}^1 v(t, y) \varphi(t, y) \, dy + \frac{\dot{h}(t)}{(1+h(t))^2} \int_{-1}^{h(t)} (1+y)v(t, y) \, dy \\ & \quad - \frac{\dot{h}(t)}{(1-h(t))^2} \int_{h(t)}^1 (1-y)v(t, y) \, dy + \frac{2\dot{h}(t)}{1-h^2(t)} \\ & \quad \quad + \ddot{h}(t) + \int_{-1}^1 v(t, y) v_y(t, y) \varphi(t, y) \, dy = 0 \quad (t \geq 0). \end{aligned}$$

The last formula implies that

$$\begin{aligned} & \frac{2\dot{h}(t)}{1-h^2(t)} = -\frac{d}{dt} \int_{-1}^1 v(t, y) \varphi(t, y) \, dy - \ddot{h}(t) - \frac{\dot{h}(t)}{(1+h(t))^2} \int_{-1}^{h(t)} (1+y)v(t, y) \, dy \\ & \quad + \frac{\dot{h}(t)}{(1-h(t))^2} \int_{h(t)}^1 (1-y)v(t, y) \, dy - \int_{-1}^1 v(t, y) v_y(t, y) \varphi(t, y) \, dy \quad (t \geq 0). \end{aligned}$$

It follows that

$$-\frac{2\dot{h}(t)}{1-h^2(t)} \leq \frac{d}{dt} \int_{-1}^1 v(t, y) \varphi(t, y) \, dy + \ddot{h}(t) + |\mathcal{A}_1(t)| + |\mathcal{A}_2(t)|, \quad (1.65)$$

where

$$\begin{aligned}\mathcal{A}_1(t) &= -\frac{\dot{h}(t)}{(1+h(t))^2} \int_{-1}^{h(t)} (1+y)v(t,y) dy + \frac{\dot{h}(t)}{(1-h(t))^2} \int_{h(t)}^1 (1-y)v(t,y) dy \quad (t \geq 0), \\ \mathcal{A}_2(t) &= -\int_{-1}^1 v(t,y)v_y(t,y)\varphi(t,y) dy \quad (t \geq 0).\end{aligned}$$

The expressions defined on the last two formulas can be estimated by

$$\begin{aligned}|\mathcal{A}_1(t)| &\leq 2|\dot{h}(t)| \|v\|_{L^\infty([0,T],L^2[-1,1])} \leq 2M|\dot{h}(t)| \leq 2M^2 \quad (t \geq 0), \\ |\mathcal{A}_2(t)| &\leq \sqrt{2} \|v_y(t, \cdot)\|_{L^2[-1,1]}^2 \|\varphi\|_{L^\infty([0,T] \times [-1,1])} \leq \sqrt{2} \|v_y(t, \cdot)\|_{L^2[-1,1]}^2 \quad (t \geq 0).\end{aligned}$$

The last two estimates and (1.65) imply that

$$-\frac{2\dot{h}(t)}{1-h^2(t)} \leq \frac{d}{dt} \int_{-1}^1 v(t,y)\varphi(t,y) dy + \ddot{h}(t) + 2M^2 + \sqrt{2} \|v_y(t, \cdot)\|_{L^2[-1,1]}^2 \quad (t \geq 0). \quad (1.66)$$

Integrating (1.66) on  $[0, t]$  it follows that for every  $t \geq 0$  we have

$$\begin{aligned}\ln\left(\frac{1-h(t)}{1+h(t)}\right) - \ln\left(\frac{1-h_0}{1+h_0}\right) &\leq \int_{-1}^1 v(t,y)\varphi(t,y) dy - \int_{-1}^1 v(0,y)\varphi(0,y) dy \\ &\quad + \dot{h}(t) - g_0 + 2M^2 t + \sqrt{2} \int_0^t \|v_y(\sigma, \cdot)\|_{L^2[-1,1]}^2 d\sigma \leq t\tilde{K}_0(M) + \tilde{K}_1(M).\end{aligned}$$

The last estimate, combined with (1.63), implies the conclusion (1.61).  $\square$

### 1.1.6 Bibliographical Notes

The first papers considering the coupling of viscous Burgers equation with Newton laws as a simplified fluid-structure interaction system are Vázquez and Zuazua [35, 36], where global wellposedness and long time behavior have been investigated. Similar models have been studied from a control theoretic viewpoint in Doubova and Fernández-Cara [15], Liu et al. [25] and Cîndea et al. [6]. Our presentation above follows [25] and [6].

## 1.2 Examples of Systems Modelling Fluid-Structure Interactions

In this chapter we introduce some systems modelling the motion of particles in a fluid, considering problems in one or several space dimensions. We also describe some change of variables allowing to consider the governing equations in a fixed

spatial domain and we postpone to the next chapters the study of the corresponding wellposedness results.

### 1.2.1 Motion of a Piston in a Heat Conducting Gas; a 1D Model

We consider a one dimensional model for the motion of a particle (piston) in a cylinder filled with a viscous compressible heat conducting gas. The extremities of the cylinder are fixed. The gas is modelled by the 1D compressible Navier-Stokes-Fourier equations, whereas the piston obeys Newton's second law. We assume that the piston is thermally conducting. More precisely, we consider the initial boundary value problem

$$\begin{aligned} \partial_t \varrho + \partial_\xi(\varrho w) &= 0, & (t \geq 0, \xi \in [-1, 1] \setminus \{h(t)\}) \\ \varrho (\partial_t w + w \partial_\xi w) - \partial_{\xi\xi} w + \partial_\xi(\varrho \vartheta) &= 0, & (t \geq 0, \xi \in [-1, 1] \setminus \{h(t)\}), \\ \varrho (\partial_t \vartheta + \partial_\xi \vartheta w) - \partial_{\xi\xi} \vartheta - (\partial_\xi w)^2 + \varrho \vartheta \partial_\xi w &= 0, & (t \geq 0, \xi \in [-1, 1] \setminus \{h(t)\}), \\ w(t, h(t) \pm 0) &= \dot{h}(t), \quad \vartheta(t, h(t) \pm 0) = Q(t) & (t \geq 0), \end{aligned} \tag{1.67}$$

$$\begin{aligned} m \ddot{h}(t) &= [\partial_\xi w - \varrho \vartheta](t, h(t)), \quad \dot{Q}(t) = [\partial_\xi \vartheta](t, h(t)), & (t \geq 0), \\ w(t, -1) &= 0 = w(t, 1), \quad \partial_\xi \vartheta(t, -1) = 0 = \partial_\xi \vartheta(t, 1), & (t \geq 0), \end{aligned}$$

with the initial conditions

$$\begin{aligned} h(0) &= h_0, \quad \dot{h}(0) = g_0, \quad Q(0) = Q_0 \\ w(0, \xi) &= w_0(\xi), \quad \varrho(0, \xi) = \rho_0(\xi), \quad \vartheta(0, \xi) = \vartheta_0(\xi) \quad (\xi \in [-1, 1] \setminus \{h_0\}). \end{aligned} \tag{1.68}$$

In the above equations,  $\varrho(t, \xi)$  is the density,  $w(t, \xi)$  is velocity of the fluid,  $\vartheta(t, \xi)$  is the temperature of the fluid (all in Eulerian coordinates),  $m$  is the mass of the particle and  $h$  is the trajectory of the mass point moving in the fluid. The symbol  $[f](\xi)$  denotes the jump of  $f$  at  $\xi$  i.e.

$$[f](\xi) = f(\xi+) - f(\xi-).$$

We now rewrite the system (1.67)–(1.68) in Lagrangian mass coordinates. This change of variables has been widely used in the literature devoted to the study of one dimensional compressible flows (see, for instance, [3] and references therein). One of the advantages of this change of coordinates is that the positions of the piston

becomes fixed. We begin by introducing the characteristic lines  $\chi(t; \eta)$  defined by

$$\partial_t \chi(t, \eta) = w(t, \chi(t, \eta)), \quad \chi(0, \eta) = \eta \quad (\eta \in [-1, 1]). \quad (1.69)$$

The first equation in (1.67) can be written

$$\rho_0(\eta) = \rho(t, \chi(t, \eta)) \frac{\partial \chi}{\partial \eta}(t, \eta) \quad (t \geq 0, X \in [-1, 1] \setminus \{h_0\}). \quad (1.70)$$

The *Lagrangian mass change of coordinates* consists in replacing the space variable  $\xi$  in (1.67) by

$$x = \Psi(t, \xi), \quad \Psi(t, \xi) = \int_{h(t)}^{\xi} \varrho(t, y) dy \quad (\xi \in [-1, 1]). \quad (1.71)$$

From (1.70) and (1.71) it follows that

$$\Psi(t, \chi(t, \eta)) = \int_{h_0}^{\eta} \rho_0(Y) dY \quad (\eta \in [-1, 1] \setminus \{h_0\}). \quad (1.72)$$

Using the facts that  $\chi(-t, 1) = -1$ ,  $\chi(t, 1) = 1$  and  $\chi(t, h(t)) = 0$ , it follows that

$$\Psi(t, -1) = -r_1, \quad \Psi(t, 1) = r_2, \quad (t \geq 0), \quad (1.73)$$

where

$$r_1 = \int_{-1}^{h_0} \rho_0(\eta) d\eta, \quad r_2 = \int_{h_0}^1 \rho_0(\eta) d\eta.$$

On the other hand, using the fact that the right hand side of (1.72) is time independent, together with (1.69), we obtain that

$$\partial_t \Psi(t, \xi) + \partial_\xi \Psi(t, \xi) w(t, \xi) = 0 \quad (t \geq 0, \xi \in [-1, 1] \setminus \{h(t)\}),$$

so that

$$\partial_t \Psi(t, \xi) = -\rho(t, \xi) w(t, \xi) \quad (t \geq 0, \xi \in [-1, 1] \setminus \{h(t)\}). \quad (1.74)$$

Using the above properties, it follows that, for every  $t \geq 0$ ,  $\Psi(t, \cdot)$  is a diffeomorphism from  $[-1, 1]$  onto  $[-r_1, r_2]$ , with  $\partial_\xi \Psi(t, \xi) = \varrho(t, \xi) > 0$  for every  $t \geq 0$  and for every  $\xi \in [-1, 1] \setminus \{h(t)\}$ .

For each  $t \geq 0$  we denote by  $\Phi(t, \cdot) = \Psi^{-1}(t, \cdot)$ . The *specific volume in mass lagrangian coordinates* is defined by

$$v(t, x) = \frac{1}{\varrho(t, \Phi(t, x))}, \quad \varrho(t, \xi) = \frac{1}{v(t, \Psi(t, \xi))}$$

$$(t \geq 0)$$

$$x \in [-r_1, r_2] \setminus \{0\}, \quad \xi \in [-1, 1] \setminus \{h(t)\}. \quad (1.75)$$

Similarly, the *velocity and temperature field in lagrangian mass coordinates* writes

$$u(t, x) = w(t, \Phi(t, x)), \quad w(t, \xi) = u(t, \Psi(t, \xi))$$

$$(t \geq 0, x \in [-r_1, r_2] \setminus \{0\}, \xi \in [-1, 1] \setminus \{h(t)\}), \quad (1.76)$$

$$\theta(t, x) = \vartheta(t, \Phi(t, x)), \quad \vartheta(t, \xi) = \theta(t, \Psi(t, \xi))$$

$$(t \geq 0, x \in [-r_1, r_2] \setminus \{0\}, \xi \in [-1, 1] \setminus \{h(t)\}) \quad (1.77)$$

From (1.71) and (1.74) it follows that for every  $t \geq 0$  and every  $\xi \in [-1, 1] \setminus \{h(t)\}$  we have

$$\partial_{\xi} \varrho(t, \xi) = -\frac{1}{v^3(t, \Psi(t, \xi))} \partial_x v(t, \Psi(t, \xi)), \quad (1.78)$$

$$\partial_t \varrho(t, \xi) = -\frac{1}{v^2(t, \Psi(t, \xi))} \partial_t v(t, \Psi(t, \xi)) + \frac{1}{v^3(t, \Psi(t, \xi))} \partial_x v(t, \Psi(t, \xi)) u(t, \Psi(t, \xi)).$$

$$(1.79)$$

From (1.71) we have for every  $t \geq 0$  and every  $\xi \in [-1, 1] \setminus \{h(t)\}$  we have

$$\partial_{\xi} w(t, \xi) = \partial_x u(t, \Psi(t, \xi)) \varrho(t, \xi) = \frac{\partial_x u(t, \Psi(t, \xi))}{v(t, \Psi(t, \xi))} \quad (\xi \in [-1, 1] \setminus \{h(t)\}).$$

$$(1.80)$$

By combining (1.78), (1.79) and (1.80) it follows that for every  $t \geq 0$  and every  $\xi \in [-1, 1] \setminus \{h(t)\}$  we have

$$\partial_t \varrho(t, \xi) + \partial_{\xi} (\varrho(t, \xi) w(t, \xi)) = -\frac{1}{v^2(t, \Psi(t, \xi))} (\partial_t v(t, \Psi(t, \xi)) - \partial_x u(t, \Psi(t, \xi))).$$

Consequently, using Lagrangian mass coordinates, Eq. (1.67)<sub>1</sub> writes

$$\partial_t v(t, x) - \partial_x u(t, x) = 0, \quad (t \geq 0, x \in [-r_1, r_2] \setminus \{0\}). \quad (1.81)$$



Using again (1.71) and (1.74), together with (1.80) it follows that

$$\partial_{\xi\xi} w(t, \xi) = \frac{\partial_{xx} u(t, \Psi(t, \xi))}{v^2(t, \Psi(t, \xi))} - \frac{\partial_x u(t, \Psi(t, \xi)) \partial_x v(t, \Psi(t, \xi))}{v^3(t, \Psi(t, \xi))} \quad (\xi \in [-1, 1] \setminus \{h(t)\}), \quad (1.82)$$

$$\partial_t w(t, \xi) = \partial_t u(t, \Psi(t, \xi)) - \frac{1}{v(t, \Psi(t, \xi))} \partial_x u(t, \Psi(t, \xi)) u(t, \Psi(t, \xi)) \quad (t \geq 0, x \in [-r_1, r_2] \setminus \{0\}). \quad (1.83)$$

The derivatives of  $\vartheta$  and  $\theta$  satisfy formulas similar to those satisfied by those of  $w$  and of  $u$ , that is

$$\partial_\xi \vartheta(t, \xi) = \partial_x \theta(t, \Psi(t, \xi)) \varrho(t, \xi) = \frac{\partial_x \theta(t, \Psi(t, \xi))}{v(t, \Psi(t, \xi))} \quad (\xi \in [-1, 1] \setminus \{h(t)\}), \quad (1.84)$$

$$\partial_{\xi\xi} \vartheta(t, \xi) = \frac{\partial_{xx} \theta(t, \Psi(t, \xi))}{v^2(t, \Psi(t, \xi))} - \frac{\partial_x \theta(t, \Psi(t, \xi)) \partial_x v(t, \Psi(t, \xi))}{v^3(t, \Psi(t, \xi))} \quad (\xi \in [-1, 1] \setminus \{h(t)\}), \quad (1.85)$$

$$\partial_t \vartheta(t, \xi) = \partial_t \theta(t, \Psi(t, \xi)) - \frac{1}{v(t, \Psi(t, \xi))} \partial_x \theta(t, \Psi(t, \xi)) u(t, \Psi(t, \xi)) \quad (\xi \in [-1, 1] \setminus \{h(t)\}). \quad (1.86)$$

By combining (1.78), (1.80), (1.82)–(1.84) we obtain that

$$\begin{aligned} & \varrho(t, \xi) (\partial_t w(t, \xi) + w(t, \xi) \partial_\xi w(t, \xi)) - \partial_{\xi\xi} w(t, \xi) + \partial_\xi [\varrho(t, \xi) \vartheta(t, \xi)] \\ &= \frac{1}{v(t, \Psi(t, \xi))} \left[ \partial_t u(t, \Psi(t, \xi)) - \partial_x \left( \frac{1}{v} \partial_x u - \frac{\theta}{v} \right) (t, \Psi(t, \xi)) \right]. \end{aligned}$$

Consequently, (1.67)<sub>2</sub> can be written as

$$\partial_t u(t, x) - \partial_x \left( \frac{\partial_x u}{v} - \frac{\theta}{v} \right) (t, x) = 0 \quad (t \geq 0, x \in [-r_1, r_2] \setminus \{0\}). \quad (1.87)$$

To write (1.67)<sub>3</sub> in mass Lagrangian coordinates we combine (1.80), (1.84)–(1.86) to get

$$\begin{aligned} & \rho(t, \xi) (\partial_t \vartheta(t, \xi) + \partial_\xi \vartheta(t, \xi) w(t, \xi)) - \partial_{\xi\xi} \vartheta - (\partial_\xi w)^2 + \varrho(t, \xi) \vartheta(t, \xi) \partial_\xi w \\ &= \frac{1}{v(t, \Psi(\xi, t))} \left[ \partial_t \theta(t, \Psi(t, \xi)) - \partial_x \left( \frac{1}{v} \partial_x \theta \right) (t, \Psi(t, \xi)) - \left( \frac{1}{v} |\partial_x u|^2 \right) (t, \Psi(t, \xi)) \right. \\ & \quad \left. + \left( \frac{\theta}{v} \partial_x u \right) (t, \Psi(t, \xi)) \right]. \end{aligned}$$

From the above formula, it follows that (1.67)<sub>3</sub> is satisfied iff

$$\partial_t \theta(t, x) - \partial_x \left( \frac{1}{v} \partial_x \theta \right) (t, x) - \frac{1}{v} (\partial_x u)^2 - \frac{\theta}{v} \partial_x u(t, x) = 0, \quad (t \geq 0, x \in [-r_1, r_2] \setminus \{0\}). \quad (1.88)$$

The fourth equation in (1.67) can obviously be rewritten as

$$u(t, \pm 0) = \dot{h}(t), \quad \frac{\partial \theta}{\partial x}(t, \pm 0) = Q(t) \quad (t \geq 0). \quad (1.89)$$

As for (1.67)<sub>5</sub>, using (1.80), we have

$$m\ddot{h}(t) = \left[ \frac{1}{v} \partial_x u - \frac{\theta}{v} \right] (t, 0), \quad \dot{Q}(t) = \left[ \frac{1}{v} \partial_x \theta \right] (t, 0) \quad (t \geq 0). \quad (1.90)$$

Using (1.84), it is easily seen that (1.67)<sub>6</sub> write in mass Lagrangian coordinates as

$$u(t, -r_1) = u(t, r_2) = 0, \quad \frac{\partial \theta}{\partial x}(-r_1, t) = \frac{\partial \theta}{\partial x}(r_1, t) = 0 \quad (t \geq 0). \quad (1.91)$$

Putting together (1.81) and (1.87)–(1.90), it follows that the system (1.67) writes in Lagrangian mass coordinates as

$$\begin{aligned} \partial_t v - \partial_x u &= 0, & (t \geq 0, x \in [-r_1, r_2] \setminus \{0\}), \\ \partial_t u - \partial_x \left( \frac{1}{v} \partial_x u \right) + \partial_x \left( \frac{\theta}{v} \right) &= 0, & (t \geq 0, x \in [-r_1, r_2] \setminus \{0\}), \\ \partial_t \theta - \partial_x \left( \frac{1}{v} \partial_x \theta \right) - \frac{1}{v} (\partial_x u)^2 + \frac{\theta}{v} \partial_x u &= 0, & (t \geq 0, x \in [-r_1, r_2] \setminus \{0\}), \\ u(t, \pm 0) = \dot{h}(t), \quad \theta(t, 0 \pm) &= Q(t), & (t \geq 0), \end{aligned} \quad (1.92)$$

$$m\ddot{h}(t) = \left[ \frac{1}{v} \partial_x u - \frac{\theta}{v} \right] (t, 0), \quad (t \geq 0),$$

$$\dot{Q}(t) = \left[ \frac{1}{v} \partial_x \theta \right] (t, 0), \quad (t \geq 0),$$

$$u(t, -r_1) = u(t, r_2) = 0, \quad \partial_x \theta(t, -r_1) = \partial_x \theta(t, r_2) = 0, \quad (t \geq 0),$$

$$v(0, x) = v_0(x), \quad u(0, x) = u_0(x), \quad \theta(0, x) = \theta_0(x), \quad x \in [-r_1, r_2] \setminus \{0\},$$

$$h(0) = h_0, \quad \dot{h}(0) = g_0,$$

where

$$v_0(x) := \frac{1}{\varrho_0(\Phi(0, x))}, \quad u_0(x) = w_0(\Phi(0, x)), \quad \theta_0(x) = \vartheta_0(\Phi(0, x)). \quad (1.93)$$

### 1.2.2 Motion of a Rigid Body in a Viscous Incompressible Fluid

In this section we describe the system modelling the motion of a rigid body immersed in a viscous incompressible fluid. Let us assume that the fluid and the rigid body are contained in a bounded domain with smooth boundary. At time  $t \geq 0$ , the rigid body occupies a smooth domain  $\Omega_S(t) \subset \Omega$ . We assume that

$$d(\Omega_S(0), \partial\Omega) > 0. \quad (1.94)$$

We denote by  $\Omega_F(t) = \Omega \setminus \Omega_S(t)$  the domain occupied by the fluid. The motion of the fluid is given by

$$\partial_t u + (u \cdot \nabla)u - \operatorname{div} \sigma(u, p) = 0, \quad \operatorname{div} u = 0, \quad x \in \Omega_F(t), t \in [0, T], \quad (1.95)$$

where the Cauchy stress tensor  $\sigma(u, p)$  is defined by

$$\sigma(u, p) = 2\nu Du - pI_3, \quad Du = \frac{1}{2}(\nabla u + \nabla u^T),$$

and  $I_3$  is the identity matrix.

At time  $t \geq 0$ , let  $h(t) \in \mathbb{R}^3$ ,  $Q(t) \in \mathbb{M}_{3 \times 3}(\mathbb{R})$  and  $\omega(t) \in \mathbb{R}^3$  denote the position of the center of mass, the orthogonal matrix giving the orientation of the solid and the angular velocity of the rigid body. Therefore we have,

$$\dot{Q}(t)Q(t)^{-1}y = A(\omega(t))y = \omega(t) \times y, \quad \forall y \in \mathbb{R}^3, \quad (1.96)$$

where the skew-symmetric matrix  $A(\omega)$  is given by

$$A(\omega) = \begin{pmatrix} 0 & -\omega_3 & \omega_2 \\ \omega_3 & 0 & -\omega_1 \\ -\omega_2 & \omega_1 & 0 \end{pmatrix}, \quad \omega \in \mathbb{R}^3.$$

Without loss of generality we can assume that

$$h(0) = 0 \quad \text{and} \quad Q(0) = I. \quad (1.97)$$

At time  $t$ , the domain occupied by the structure  $\Omega_S(t)$  is defined by

$$\Omega_S(t) = \chi_S(t, \Omega_S(0)) \quad (1.98)$$

where  $\chi_S$  denotes the flow associated to the motion of the structure:

$$\chi_S(t, y) = h(t) + Q(t)y, \quad \forall y \in \Omega_S(0), \quad \forall t > 0, \quad (1.99)$$

For each  $t > 0$ ,  $\chi_S(t, \cdot) : \Omega_S(0) \mapsto \Omega_S(t)$  is invertible and

$$\chi_S(t, \cdot)^{-1}(x) = Q(t)^{-1}(x - h(t)), \quad \forall x \in \Omega_S(t). \quad (1.100)$$

Thus the Eulerian velocity  $u_S$  of the structure is given by

$$u_S(t, x) = \partial_t \chi_S(t, \cdot) \circ \chi_S(t, \cdot)^{-1}(x) = \dot{h}(t) + \dot{Q}(t)Q(t)^{-1}(x - h(t)), \quad \forall x \in \Omega_S(t). \quad (1.101)$$

Therefore

$$u_S(t, x) = \dot{h}(t) + \omega(t) \times (x - h(t)), \quad \forall x \in \Omega_S(t). \quad (1.102)$$

We also assume the continuity of velocities at the fluid-solid interface, i.e.,

$$u(t, x) = \dot{h}(t) + \omega(t) \times (x - a(t)), \quad x \in \partial\Omega_S(t). \quad (1.103)$$

On the boundary of  $\Omega$  we prescribe no-slip boundary condition for fluid, i.e.,

$$u(t, x) = 0, \quad x \in \partial\Omega. \quad (1.104)$$

We denote by  $m > 0$  the mass of rigid structure and  $J(t) \in \mathcal{M}_{3 \times 3}(\mathbb{R})$  its tensor of inertia at time  $t$ . This tensor is given by

$$J(t)a \cdot b = \int_{\Omega_S(0)} \rho_S(y)(a \times Q(t)y) \cdot (b \times Q(t)y) dy, \quad \forall a, b \in \mathbb{R}^3, \quad (1.105)$$

where  $\rho_S > 0$  is the density of the structure. One can check that

$$J(t)a \cdot a \geq C_J |a|^2 > 0, \quad (1.106)$$

where  $C_J$  is independent of  $t > 0$ . The equation of the structure is given by

$$\begin{aligned} m\ddot{h} &= - \int_{\partial\Omega_S(t)} \sigma(u, p)n d\gamma, \\ J\dot{\omega} &= (J\omega) \times \omega - \int_{\partial\Omega_S(t)} (x - h(t)) \times \sigma(u, p)n d\gamma \end{aligned} \quad (1.107)$$

where  $n(t, x)$  the unit normal to  $\partial\Omega_S(t)$  at the point  $x$  directed toward the interior of the rigid body. The above system is completed by the following initial conditions

$$u(0) = u_0, \quad \text{in } \Omega_F(0), \quad h(0) = 0, \quad \dot{h}(0) = g_0, \quad \omega(0) = \omega_0. \quad (1.108)$$

### 1.2.3 Motion of a Solid in a Compressible Fluid

In this section, we consider a rigid structure immersed in a viscous compressible fluid. In this case, we assume that, the fluid and the rigid body are contained in a smooth bounded domain  $\Omega \subset \mathbb{R}^3$ . At time  $t \geq 0$ , the rigid body occupies a smooth bounded domain  $\Omega_S(t)$ . We assume that

$$d(\Omega_S(0), \partial\Omega) > 0. \quad (1.109)$$

For any time  $t \geq 0$ ,  $\Omega_F(t) = \Omega \setminus \overline{\Omega_S(t)}$  denotes the region occupied by the fluid. Let  $h(t) \in \mathbb{R}^3$ ,  $Q(t) \in \mathbb{M}_{3 \times 3}(\mathbb{R})$  and  $\omega(t) \in \mathbb{R}^3$  denote the position of the center of mass, the orthogonal matrix giving the orientation of the solid and the angular velocity of the rigid body satisfying (1.96) and (1.97). Let  $m$  denote the mass of the rigid body and  $J(t) \in \mathcal{M}_{3 \times 3}(\mathbb{R})$  its tensor of inertia at time  $t$  given by (1.105). The system modelling the motion of rigid body in a viscous compressible fluid can be written as

$$\begin{aligned} \partial_t \rho + \operatorname{div}(\rho u) &= 0, \quad t \in (0, T), x \in \Omega_F(t) \\ \rho(\partial_t u + (u \cdot \nabla)u) - \operatorname{div} \sigma(u, p) &= 0, \quad t \in (0, T), x \in \Omega_F(t) \\ u(t, x) &= \dot{h}(t) + \omega(t) \times (x - a(t)), \quad t \in (0, T), x \in \partial\Omega_S(t), \\ m\ddot{h} &= - \int_{\partial\Omega_S(t)} \sigma(u, p)n \, d\gamma, \quad t \in (0, T) \\ J\dot{\omega} &= (J\omega) \times \omega - \int_{\partial\Omega_S(t)} (x - h(t)) \times \sigma(u, p)n \, d\gamma \\ u(t, x) &= 0, \quad t \in (0, T), x \in \partial\Omega, \\ \rho(0) &= \rho_0, \quad u(0) = u_0, \quad \text{in } \Omega_F(0), \\ h(0) &= 0, \quad \dot{h}(0) = g_0, \quad \omega(0) = \omega_0, \end{aligned} \quad (1.110)$$

where

$$\begin{aligned} \sigma(u, p) &= 2\mu Du + (\alpha \operatorname{div} u - p)I_3, \quad Du = \frac{1}{2}(\nabla u + \nabla u^T) \\ \mu &\geq 0 \text{ and } \alpha + \frac{2}{3}\mu \geq 0, \quad p = \rho^\gamma, \quad \gamma \geq 1. \end{aligned}$$

Now we rewrite the above system in fixed domain. Here we use Lagrangian change of variable as it is well suited for the compressible fluids. We consider the characteristics  $X$  associated to the velocity fluid  $u$ , that is the solution of the Cauchy problem

$$\begin{cases} \partial_t X(t, y) = u(t, X(t, y)) & (t > 0), \\ X(0, y) = y \in \Omega. \end{cases} \quad (1.111)$$

Assume that  $X(t, \cdot)$  is a  $C^1$ -diffeomorphism from  $\Omega_F(0)$  onto  $\Omega_F(t)$  for all  $t \in (0, T)$  (see Lemma 1.60). For each  $t \in (0, T)$ , we denote by  $Y(t, \cdot) = [X(t, \cdot)]^{-1}$  the inverse of  $X(t, \cdot)$ . We consider the following change of variables

$$\tilde{\rho}(t, y) = \rho(t, X(t, y)), \quad \tilde{u}(t, y) = Q^{-1}(t)u(t, X(t, y)), \quad (1.112)$$

$$\tilde{g}(t) = Q^{-1}(t)\dot{h}(t), \quad \tilde{\omega}(t) = Q^{-1}(t)\omega(t), \quad (1.113)$$

for  $(t, y) \in (0, T) \times \Omega_F(0)$ . In particular,

$$\rho(t, x) = \tilde{\rho}(t, Y(t, x)), \quad u(t, x) = Q(t)\tilde{u}(t, Y(t, x)), \quad (1.114)$$

for  $(t, x) \in (0, T) \times \Omega_F(t)$ . The system satisfied by  $(\tilde{\rho}, \tilde{u}, \tilde{\ell}, \tilde{\omega})$  reads as follows

$$\begin{aligned} \partial_t \tilde{\rho} + \rho_0 \operatorname{div} \tilde{u} &= \mathcal{F}_1, \quad \text{in } (0, T) \times \Omega_F(0), \\ \partial_t \tilde{u} - \frac{\mu}{\rho_0} \Delta \tilde{u} - \frac{\alpha + \mu}{\rho_0} \nabla(\operatorname{div} \tilde{u}) &= \mathcal{F}_{2,1} + \mathcal{F}_{2,2} \quad \text{in } (0, T) \times \Omega_F(0), \\ \tilde{u} &= 0 \quad \text{on } (0, T) \times \partial\Omega, \quad \tilde{u} = g + \omega \times y \quad \text{on } (0, T) \times \partial\Omega_S(0), \\ m \frac{d}{dt} \tilde{g} &= - \int_{\Omega_S(0)} (\mu \nabla \tilde{u} + \mu \nabla \tilde{u}^\top + \alpha \operatorname{div} \tilde{u} l) n \, d\gamma + \mathcal{G}_1, \\ J(0) \frac{d}{dt} \tilde{\omega} &= - \int_{\Omega_S(0)} y \times (\mu \nabla \tilde{u} + \mu \nabla \tilde{u}^\top + \alpha \operatorname{div} \tilde{u} l) n + \mathcal{G}_2, \\ \tilde{\rho}(0) &= \rho_0, \quad \tilde{u}(0) = u_0, \quad \text{in } \Omega_F(0), \\ \tilde{g}(0) &= g_0, \quad \tilde{\omega}_0 = \omega_0, \end{aligned} \quad (1.115)$$

where

$$Q(t) = I + \int_0^t Q(s)(\tilde{\omega}(s) \times I), \quad Q^T = Q^{-1} \quad (1.116)$$

$$X(t, y) = y + \int_0^t Q(s)\tilde{u}(s) \, ds, \quad \text{and} \quad J_Y = J_X^{-1}, \quad (1.117)$$

$$\mathcal{F}_1(\tilde{\rho}, \tilde{u}, \tilde{g}, \tilde{\omega}) = -(\tilde{\rho} - \tilde{\rho}_0) \operatorname{div} \tilde{u} - \tilde{\rho}(Q - I) \nabla \tilde{u} : J_Y^\top - \tilde{\rho} \nabla \tilde{u} : (J_Y^\top - I), \quad (1.118)$$

$$\begin{aligned} \mathcal{F}_{2,1}(\tilde{\rho}, \tilde{u}, \tilde{g}, \tilde{\omega}) &= -\frac{\tilde{\rho}}{\rho_0} Q'(t) \tilde{u} - \frac{\tilde{\rho} - \rho_0}{\rho_0} Q(t) \partial_t \tilde{u} - (Q(t) - I) \partial_t \tilde{u} - \gamma \frac{\tilde{\rho}^{\gamma-1}}{\rho_0} J_Y^\top \nabla \tilde{\rho} \\ &\quad - \frac{\mu}{\rho_0} (Q - I) \Delta \tilde{u}, \end{aligned}$$

$$\begin{aligned}
(\mathcal{F}_{2,2})_i(\tilde{\rho}, \tilde{u}, \tilde{g}, \tilde{\omega}) &= \frac{\mu}{\rho_0} \sum_{j,k,l=1}^3 \partial_{y_l} (\partial_{y_k} (Q\tilde{u})_i [(J_Y)_{kj} - \delta_{kj}]) (J_Y)_{lj} \\
&\quad + \frac{\mu}{\rho_0} \sum_{k,l=1}^3 (\partial_{y_l y_k}^2 (Q\tilde{u})_i) [(J_Y)_{lk} - \delta_{lk}] \\
&\quad + \frac{\alpha + \mu}{\rho_0} \sum_{j,k,l=1}^3 \partial_{y_l} (\partial_{y_k} (Q\tilde{u})_j [(J_Y)_{kj} - \delta_{kj}]) (J_Y)_{li} \\
&\quad + \frac{\alpha + \mu}{\rho_0} \sum_{l,j=1}^3 (\partial_{y_l y_j}^2 (Q\tilde{u})_j) [(J_Y)_{li} - \delta_{li}] + (Q^\top - I) : \partial_{y_i} \nabla \tilde{u},
\end{aligned} \tag{1.119}$$

$$\mathcal{F}_3(\tilde{\rho}, \tilde{u}, \tilde{g}, \tilde{\omega}) = -m(\tilde{\omega} \times \tilde{\ell}) - \int_{\Omega_S(0)} \mathcal{G}n,$$

$$\mathcal{F}_4(\tilde{\rho}, \tilde{u}, \tilde{g}, \tilde{\omega}) = J(0)\tilde{\omega} \times \tilde{\omega} - \int_{\Omega_S(0)} y \times \mathcal{G}n,$$

$$\begin{aligned}
\mathcal{G}(\tilde{\rho}, \tilde{u}, \tilde{g}, \tilde{\omega}) &= (Q^\top - I) (\mu (Q\nabla\tilde{u}J_Y + J_Y^\top \nabla\tilde{u}^\top Q^\top) + (\alpha J_Y^\top : Q\nabla\tilde{u}^\top - \tilde{p}) I) \operatorname{cof} J_X \\
&\quad + (\mu (Q\nabla\tilde{u}J_Y + J_Y^\top \nabla\tilde{u}^\top Q^\top) + (\alpha J_Y^\top : Q\nabla\tilde{u}^\top - \tilde{p}) I) (\operatorname{cof} J_X - I) \\
&\quad + \mu(Q - I)\nabla\tilde{u}J_Y + \mu\nabla\tilde{u}(J_Y - I) + \mu(J_Y^\top - I)\nabla\tilde{u}^\top Q^\top + \mu\nabla\tilde{u}^\top(Q^\top - I) \\
&\quad + (\alpha(Q - I)\nabla\tilde{u} : J_Y^\top)I + (\alpha\nabla\tilde{u} : (J_Y^\top - I))I - R\tilde{\rho}^\nu I \tag{1.120}
\end{aligned}$$

### 1.3 Short Introduction to $\mathcal{R}$ -Sectorial Operators

Let  $X$  be a Banach space and  $A$  be a closed, densely defined linear unbounded operator in  $X$  with domain  $D(A)$ . We shall consider the abstract Cauchy problem

$$\dot{u}(t) = Au(t) + f(t), \quad t > 0, \quad u(0) = 0, \tag{1.121}$$

where  $f : \mathbb{R}^+ \mapsto X$  is a given function.

**Definition 1.11 (Maximal  $L^p$ -Regularity)** Let  $1 < p < \infty$ . The problem (1.121) has *maximal  $L^p$ -regularity* on  $[0, T)$ ,  $0 < T \leq \infty$ , if for every  $f \in L^p([0, T); X)$ , there exists a unique  $u$  satisfying the above equation almost everywhere and such that  $\dot{u} \in L^p([0, T); X)$ . In this case  $Au \in L^p([0, T); X)$  as well.

*Remark 1.12* In the above definition we do not assume that  $u \in L^p(0, T; X)$ . In fact, if  $T < \infty$  or  $0 \in \rho(A)$ , where  $\rho(A)$  is the resolvent set of  $A$ ,  $\dot{u} \in L^p(0, T; X)$  can be replaced by  $u \in W^{1,p}(0, T; X)$  [13].

Our aim is to give sufficient condition on the operator  $A$  so that the problem (1.121) has a maximal  $L^p$ -regularity. It is well known that, if (1.121) has a maximal  $L^p$ -regularity, then  $A$  generates an analytic semigroup in  $X$  (see [9] and [13]). On the other hand, if  $X$  is a Hilbert space, the above condition is enough to obtain maximal  $L^p$ -regularity, i.e., if  $A$  generates an analytic semigroup in  $X$ , then (1.121) has a maximal  $L^p$ -regularity (see de Simon [11] for more details). In fact, De Simon used Plancherel's theorem which is valid only in the Hilbert space setting and cannot be generalized. Since then, there has been considerable work in the general Banach space framework [10, 14, 20, 23, 24, 29]. We are interested in the recent result obtained by Weis [37]. He obtained a necessary and sufficient condition for maximal  $L^p$ -regularity when  $X$  is a UMD Banach space in terms of  $\mathcal{R}$ -boundedness of the operator  $A$  (for the precise definition of UMD spaces and  $\mathcal{R}$ -boundedness we refer to the next section). This result is very useful in order to obtain maximal  $L^p - L^q$  regularity of linearized fluid structure interaction problem.

In this chapter we recall some basic definitions and results on  $\mathcal{R}$ -sectorial operators and we prove a lemma, which seems to be new, on the  $\mathcal{R}$  sectoriality of a class of matrices of linear operators.

### 1.3.1 Basic Definitions

In this section we recall some basic definitions and results concerning maximal regularity and  $\mathcal{R}$ -boundedness in Banach spaces. For detailed information on these subjects we refer to [8, 12, 37] and references therein.

**Definition 1.13** Let  $X$  be a Banach space. The Hilbert transform of a function  $f \in \mathcal{S}(\mathbb{R}; X)$ , the Schwartz space of  $X$ -valued rapidly decreasing functions, is defined by

$$Hf(t) = \frac{1}{\pi} \lim_{\epsilon \rightarrow 0} \int_{|s| > \epsilon} \frac{f(t-s)}{s} ds, \quad t \in \mathbb{R}.$$

A Banach space  $X$  is said to be of class  $\mathcal{HT}$ , if the Hilbert transform is bounded on  $L^p(\mathbb{R}; X)$  for some (thus all)  $1 < p < \infty$ .

These spaces are also called *UMD* Banach spaces, where *UMD* stands for *unconditional martingale differences*. Hilbert spaces, all closed subspaces and quotient spaces of  $L^q(\Omega)$  with  $1 < q < \infty$  are examples of *UMD* spaces. In fact,  $X \in \mathcal{HT}$  implies that  $X$  is reflexive (see [1]). We next introduce the notion of  $\mathcal{R}$ -boundedness of family of operators and  $\mathcal{R}$ -sectoriality of a densely defined linear operator.

**Definition 1.14 ( $\mathcal{R}$ -Bounded Family of Operators)** Let  $X$  and  $Y$  be Banach spaces. A family of operators  $\mathcal{T} \subset \mathcal{L}(X, Y)$  is called  $\mathcal{R}$ -bounded on  $\mathcal{L}(X, Y)$ , if there exist constants  $C > 0$  and  $p \in [1, \infty)$  such that for every  $n \in \mathbb{N}$ ,  $\{T_j\}_{j=1}^n \subset \mathcal{T}$ ,



$\{x_j\}_{j=1}^n \subset X$  and for all sequences  $\{r_j(\cdot)\}_{j=1}^n$  of independent, symmetric,  $\{-1, 1\}$  valued random variables on  $[0, 1]$ , we have

$$\left\| \sum_{j=1}^n r_j(\cdot) T_j x_j \right\|_{L^p([0,1];Y)} \leq C \left\| \sum_{j=1}^n r_j(\cdot) x_j \right\|_{L^p([0,1];X)}.$$

The smallest such  $C$  is called  $\mathcal{R}$ -bound of  $\mathcal{T}$  on  $\mathcal{L}(X, Y)$  and denoted by  $\mathcal{R}_{\mathcal{L}(X,Y)}(\mathcal{T})$ .

*Remark 1.15*

(1) If  $\mathcal{T} \subset \mathcal{L}(X, Y)$  is  $\mathcal{R}$ -bounded then it is uniformly bounded with

$$\sup \{\|T\| \mid T \in \mathcal{T}\} \leq \mathcal{R}_{\mathcal{L}(X,Y)}(\mathcal{T}).$$

(2) If  $X = Y = L^q(\Omega)$  for some open set  $\Omega \subset \mathbb{R}^N$ , then  $\mathcal{T} \subset \mathcal{L}(X, Y)$  is  $\mathcal{R}$ -bounded if and only if there exists a constant  $C > 0$  such that for every  $n \in \mathbb{N}$ ,  $\{T_j\}_{j=1}^n \subset \mathcal{T}$ ,  $\{x_j\}_{j=1}^n \subset L^q(\Omega)$  the following estimate holds:

$$\left\| \left( \sum_{j=1}^n |T_j x_j|^2 \right)^{1/2} \right\|_{L^q(\Omega)} \leq C \left\| \left( \sum_{j=1}^n |x_j|^2 \right)^{1/2} \right\|_{L^q(\Omega)}.$$

(3) If  $X$  and  $Y$  are Hilbert spaces every set  $\mathcal{T}$  bounded in  $\mathcal{L}(X, Y)$  is  $\mathcal{R}$ -bounded.

For  $0 < \varepsilon \leq \pi/2$ , and  $\gamma \geq 0$  we define the sector  $\Sigma_{\varepsilon,\gamma}$  in the complex plane by

$$\Sigma_{\varepsilon,\gamma} = \{\lambda \in \mathbb{C} \setminus \{0\} \mid |\arg \lambda| \leq \pi - \varepsilon, \quad |\lambda| > \gamma\}. \quad (1.122)$$

When  $\gamma = 0$ ,  $\Sigma_{\varepsilon,\gamma}$  will be denoted by  $\Sigma_\varepsilon$ .

**Definition 1.16 ( $\mathcal{R}$ -Sectorial Operator)** Let  $A$  be a densely defined closed linear operator on a Banach space  $X$  with domain  $\mathcal{D}(A)$ . Then  $A$  is  $\mathcal{R}$ -sectorial operator in  $X$  if  $\Sigma_{\varepsilon,\gamma}$  contained in the resolvent set  $\rho(A)$  for some  $\varepsilon \in (0, \pi/2)$ ,  $\gamma \geq 0$  and  $\{\lambda(\lambda I - A)^{-1} \mid \lambda \in \Sigma_{\varepsilon,\gamma}\}$  is  $\mathcal{R}$  bounded on  $\mathcal{L}(X)$  with  $\mathcal{R}$ -bound  $M$ . In this case, the set  $\{A(\lambda I - A)^{-1} \mid \lambda \in \Sigma_{\varepsilon,\gamma}\}$  is  $\mathcal{R}$ -bounded with  $\mathcal{R}$ -bound at most  $1 + M$ .

We now state several useful propositions concerning  $\mathcal{R}$ -boundedness.

**Proposition 1.17**

(1) Let  $X$  and  $Y$  be Banach spaces and let  $\mathcal{T}$  and  $\mathcal{S}$  be  $\mathcal{R}$ -bounded families on  $\mathcal{L}(X, Y)$ . Then  $\mathcal{T} + \mathcal{S}$  is also  $\mathcal{R}$ -bounded on  $\mathcal{L}(X, Y)$ , and

$$\mathcal{R}_{\mathcal{L}(X,Y)}(\mathcal{T} + \mathcal{S}) \leq \mathcal{R}_{\mathcal{L}(X,Y)}(\mathcal{T}) + \mathcal{R}_{\mathcal{L}(X,Y)}(\mathcal{S}).$$

(2) Let  $X, Y$  and  $Z$  be Banach spaces and let  $\mathcal{T}$  and  $\mathcal{S}$  be  $\mathcal{R}$ -bounded families on  $\mathcal{L}(X, Y)$  and  $\mathcal{L}(Y, Z)$  respectively. Then  $\mathcal{ST}$  is  $\mathcal{R}$ -bounded on  $\mathcal{L}(X, Z)$ , and

$$\mathcal{R}_{\mathcal{L}(X,Z)}(\mathcal{ST}) \leq \mathcal{R}_{\mathcal{L}(X,Y)}(\mathcal{T})\mathcal{R}_{\mathcal{L}(Y,Z)}(\mathcal{S}).$$

(3) Let  $q \in (1, \infty)$ , let  $\Omega$  be a bounded domain in  $\mathbb{R}^n$  and let  $\Lambda$  be a domain in  $\mathbb{C}$ . Let  $m(\lambda)$  be a bounded function defined on  $\Lambda$  and let  $M_m(\lambda) \in \mathcal{L}(L^q(\Omega))$ , defined by  $M_m(\lambda)f = m(\lambda)f$ , for any  $f \in L^q(\Omega)$ . Then  $\{M_m(\lambda) \mid \lambda \in \Lambda\}$  is  $\mathcal{R}$ -bounded and

$$\mathcal{R}_{\mathcal{L}(L^q(\Omega))}\{M_m(\lambda) \mid \lambda \in \Lambda\} \leq C_{n,q,\Omega} \|m\|_{L^\infty(\Lambda)}. \quad (1.123)$$

*Proof* The proof of first two statement follows easily from the definition of  $\mathcal{R}$ -boundedness. The proof of Proposition 1.17 (3) follows from Remark 1.15 (2).  $\square$

### 1.3.2 Weis' Theorem

In this section we will discuss Weis' theorem concerning maximal  $L^p$ -regularity of the Cauchy problem (1.121). First, we will prove a proposition due to Kunstmann and Weis [22], which states that  $\mathcal{R}$ -sectoriality is preserved by  $A$  small perturbations.

**Proposition 1.18** *Let  $A$  be a  $\mathcal{R}$ -sectorial in a Banach space  $X$  with domain  $\mathcal{D}(A)$ . Assume that  $\Sigma_{\varepsilon_0, \gamma_0} \subset \rho(A)$ , for some  $\varepsilon_0 \in (0, \pi/2)$ ,  $\gamma_0 \geq 0$  and*

$$\mathcal{R}_{\mathcal{L}(X)}(\{A(\lambda I - A)^{-1} \mid \lambda \in \Sigma_{\varepsilon_0, \gamma_0}\}) \leq a < \infty. \quad (1.124)$$

*Let  $B$  be a linear operator such that  $\mathcal{D}(A) \subset \mathcal{D}(B)$  and*

$$\|Bx\| \leq \delta_1 \|Ax\| + \delta_2 \|x\|, \quad (1.125)$$

*with  $\delta_1 < 1/a$ . Then there exists  $\gamma_1 \geq \gamma_0$  such that*

$$\mathcal{R}_{\mathcal{L}(X)}(\{\lambda(\lambda I - (A + B))^{-1} \mid \lambda \in \Sigma_{\varepsilon_0, \gamma_1}\}) < \infty. \quad (1.126)$$

*Proof* From the definition of  $\mathcal{R}$ -boundedness, we have

$$\begin{aligned} \mathcal{R}_{\mathcal{L}(X)}\{B(\lambda I - A)^{-1}\} &\leq \delta_1 \mathcal{R}_{\mathcal{L}(X)}\{A(\lambda I - A)^{-1}\} + \delta_2 \mathcal{R}_{\mathcal{L}(X)}\{(\lambda I - A)^{-1}\} \\ &\leq \left( \delta_1 a + \frac{\delta_2 a}{|\lambda|} \right). \end{aligned}$$

Thus there exists  $\gamma_1 \geq \gamma_0$  such that  $\left(\delta_1 a + \frac{\delta_2 a}{|\lambda|}\right) \leq \delta < 1$  for  $\lambda \in \Sigma_{\varepsilon_0, \gamma_1}$  and hence  $I - B(\lambda I - A)^{-1}$  is invertible for  $\lambda \in \Sigma_{\varepsilon_0, \gamma_1}$ . Now

$$\begin{aligned} (\lambda I - (A + B))^{-1} &= (\lambda I - A)^{-1} (I - B(\lambda I - A)^{-1})^{-1} \\ &= (\lambda I - A)^{-1} \sum_{j=0}^{\infty} (B(\lambda I - A)^{-1})^j. \end{aligned}$$

By induction

$$\mathcal{R} \left( \lambda (\lambda I - A)^{-1} (B(\lambda I - A)^{-1})^j \right) \leq \mathcal{R} (\lambda (\lambda I - A)^{-1}) \delta^j$$

Therefore

$$\mathcal{R}_{\mathcal{L}(X)}(\{ \lambda (\lambda I - (A + B))^{-1} \mid \lambda \in \Sigma_{\varepsilon_0, \gamma_1} \}) \leq \frac{a}{1 - \delta}.$$

□

The Theorem of Weis is the following:

**Theorem 1.19** *Let  $X$  be a Banach space of class  $\mathcal{HT}$ ,  $1 < p < \infty$  and let  $A$  be a closed, densely defined unbounded operator with domain  $D(A)$ . Let  $A$  generates a bounded analytic semigroup on  $X$ , i.e.,*

$$\|\lambda (\lambda I - A)^{-1}\| \leq C, \text{ for } \lambda > 0.$$

*Then the following statements are equivalent.*

- (i) *The Cauchy problem (1.121) has maximal  $L^p$ -regularity.*
- (ii) *The set  $\{\lambda (\lambda I - A)^{-1} \mid \lambda \in \Sigma_\varepsilon\}$  is  $\mathcal{R}$  bounded for some  $\varepsilon \in (0, \pi/2)$ .*

### 1.3.3 Abstract Framework Corresponding to Linear Fluid-Solid Interaction Problems

In this section, we introduce an abstract framework which will correspond to the linear fluid-solid interactions problems. The main idea in elaborating this approach is that linearized fluid-solid interaction problems can be viewed as boundary controlled fluid systems with dynamic boundary feedback. To this aim we first recall, following [34, Chap. 10], some background on boundary control systems.

Systems described by linear partial differential equations with nonhomogeneous boundary conditions can be written in the form:

$$\dot{z}(t) = Lz(t), \quad Gz(t) = u(t). \quad (1.127)$$

Often  $L$  is a differential operator and  $G$  is a boundary trace operator. In the sequel, we assume that  $U, Z$  and  $X$  are reflexive Banach spaces such that

$$Z \subset X,$$

with continuous embedding. We shall call  $U$  the *input space*,  $Z$  the *solution space* and  $X$  the *state space*.

**Definition 1.20** A *boundary control system* on  $U, Z$  and  $X$  is a pair of operators  $(L, G)$ , where

$$L \in \mathcal{L}(Z, X), \quad G \in \mathcal{L}(Z, U),$$

if there exists a  $\beta \in \mathbb{C}$  such that the following properties hold:

- (i)  $G$  is onto,
- (ii)  $\text{Ker}G$  is dense in  $X$ ,
- (iii)  $\beta I - L$  restricted to  $\text{Ker}G$  is onto,
- (iv)  $\text{Ker}(\beta I - L) \cap \text{Ker}G = \{0\}$ .

With the assumptions of the last definition, we introduce the closed subspace  $X_1$  of  $Z$  and the operator  $A$  by

$$X_1 = \text{Ker}G, \quad A = L|_{X_1}. \quad (1.128)$$

Obviously,  $X_1$  is a closed subspace of  $Z$  and  $A \in \mathcal{L}(X_1, X)$ . Condition (iii) means that  $\beta I - A$  is onto. Condition (iv) means that  $\text{Ker}(\beta I - A) = \{0\}$ . Thus, (iii) and (iv) together are equivalent to the fact that  $\beta \in \rho(A)$ , where  $\rho(A)$  is the resolvent set of  $A$ , so that

$$(\beta I - A)^{-1} \in \mathcal{L}(X).$$

In fact,  $(\beta I - A)^{-1} \in \mathcal{L}(X, X_1)$ , so that the norm on  $X_1$  is equivalent to the norm

$$\|z\|_1 = \|(\beta I - A)z\|_X.$$

It is easy to see that  $\|\cdot\|_{X_1}$  on  $X_1$  is equivalent to the graph norm of  $A$ . Therefore, by closed graph theorem,  $(X_1, \|\cdot\|_1)$  is complete. Also, for any  $\beta' \in \rho(A)$ , we have an equivalent norm on  $X_1$ . We define the space  $X_{-1}$  as the completion of  $X$  with respect to the norm

$$\|z\|_{-1} = \|(\beta I - A)^{-1}z\|.$$

The space  $X_{-1}$  does not depend on the specific value of  $\beta$ . We have  $X_1 \subset X \subset X_1$ , with continuous and dense embedding. Then  $A$  has an extension, also denoted by  $A$ , such that  $A \in \mathcal{L}(X, X_{-1})$ .

Let  $X'$  denotes the dual of  $X$ . Let  $A^* : D(A)^* \mapsto X'$  denotes the adjoint of the operator  $(A, D(A))$ . We endow  $D(A^*)$  with the graph norm

$$\|z^*\|_{1,*} = \|(\beta I - A^*)z^*\|_{X'},$$

where  $\beta \in \rho(A) = \rho(A^*)$ . The following theorem holds (see [16, Chap. 2, Sect. 5]).

**Theorem 1.21** *Let  $X$  be a reflexive Banach space. Then  $X_{-1}$  is isomorphic to  $D(A^*)'$ .*

Also, if  $X$  is reflexive and if  $(S(t))_{t \geq 0}$  is a  $C^0$ -semigroup on  $X$  with generator  $A$ , then the adjoint semigroup  $(S(t)^*)_{t \geq 0}$  of  $(S(t))_{t \geq 0}$  is a  $C^0$ -semigroup on  $X'$  with generator  $A^*$  ([28, Corollary 10.6]).

**Proposition 1.22** *Let  $(L, G)$  be a boundary control system on  $U, Z$  and  $X$ . Let  $A$  and  $X_{-1}$  be as introduced earlier. Then there exists a unique operator  $B \in \mathcal{L}(U, X_{-1})$  such that*

$$L = A + BG, \tag{1.129}$$

where  $A$  is regarded as an operator from  $X$  to  $X_{-1}$ . For every  $\beta \in \rho(A)$  we have that  $(\beta I - A)^{-1}B \in \mathcal{L}(U, Z)$  and

$$G(\beta I - A)^{-1}B = I, \tag{1.130}$$

so that in particular,  $B$  is bounded from below.

*Proof* Since  $G$  is onto, it has at least one bounded right inverse  $H \in \mathcal{L}(U, Z)$ . We put

$$B = (L - A)H. \tag{1.131}$$

From  $G(I - HG) = 0$  we see that the range of  $I - HG$  is in  $\text{Ker}G = X_1$ , so that  $(L - A)(I - HG) = 0$ . Thus we get that  $BG = (L - A)HG = L - A$ , as required in (1.129). It is easy to see that  $B$  is unique. To prove (1.130), first we rewrite (1.131) in the form

$$(\beta I - A)H - (\beta I - L)H = B.$$

If we apply  $(\beta I - A)^{-1}$  to both sides, we get

$$H - (\beta I - A)^{-1}(\beta I - L)H = (\beta I - A)^{-1}B,$$

which shows that indeed  $(\beta I - A)^{-1}B \in \mathcal{L}(U, Z)$ . Therefore, we can apply  $G$  to both sides above and then the second term on the left-hand side disappears, due to  $X_1 = \text{Ker}G$ . Since  $GH = I$ , we obtain (1.130).  $\square$

When  $L, G, A$  and  $B$  are as in the above proposition, we say that  $A$  is the *generator* of the boundary control system  $(L, G)$  and  $B$  is the *control operator* of  $(L, G)$ .

*Remark 1.23* The following fact is an easy consequence of Proposition 1.22 (we use the notation of the proposition): For every  $v \in U$  and every  $\beta \in \rho(A)$ , the vector  $z = (\beta I - A)^{-1}Bv$  is the unique solution of the “abstract elliptic problem”

$$Lz = \beta z, \quad Gz = v.$$

For many  $L$  and  $G$ , this problem has a well known solution, and it is easier to describe  $z \in X$  than to describe  $Bv \in X_{-1}$ , since  $X$  is usually a more “natural” space than  $X_{-1}$  (see the other sections of this chapter).

We are now in a position to write a class of linearized fluid-structure interaction problems as boundary control systems with dynamic feedback.

Let  $Z, X, U$  be reflexive Banach spaces of class  $\mathcal{HT}$ . Let  $(L, G)$  be a boundary control system on  $U, Z$  and  $X$ . Let  $X_1$  and  $X_{-1}$  are defined as before. Let  $A = L|_{X_1}$  generates a  $C^0$  semigroup in  $X$ . Let  $K$  be a densely defined, closed unbounded operator in  $U$  with domain  $D(K)$  and  $K$  generates a  $C^0$  semigroup in  $U$ . Finally, let  $C \in \mathcal{L}(Z, U)$ . We consider the following abstract system

$$\begin{aligned} \dot{z} &= Lz, & Gz &= u, \\ \dot{u} &= Ku + Cz, \\ z(0) &= z_0, & u(0) &= u_0. \end{aligned} \tag{1.132}$$

Let us introduce the operator  $(A, D(A))$  in  $X \times U$  by

$$D(A) = \left\{ \begin{bmatrix} z \\ u \end{bmatrix} \in Z \times D(K) \mid Gz = u \right\} \tag{1.133}$$

and

$$A \begin{bmatrix} z \\ u \end{bmatrix} = \begin{bmatrix} Lz \\ Ku + Cz \end{bmatrix}. \tag{1.134}$$

**Lemma 1.24** *The map*

$$\begin{bmatrix} z \\ u \end{bmatrix} \mapsto \|z\|_Z + \|u\|_{D(K)}.$$

*is a norm on  $D(A)$  equivalent to the graph norm.*

*Proof* For  $(z, u) \in D(\mathcal{A})$ , and  $\beta \in \rho(A)$ , we note that

$$\begin{aligned} & \|z\|_Z + \|u\|_{D(K)} \\ & \leq \|z - (\beta I - A)^{-1}Bu\|_{X_1} + \|(\beta I - A)^{-1}Bu\|_Z + \|u\|_U + \|Ku\|_U \\ & \leq c(\|(\beta I - A)z - Bu\|_X + \|u\|_U + \|Ku\|_U) \\ & \leq c(\|z\|_X + \|Az + Bu\|_X + \|u\|_U + \|Ku\|_U) \leq c \left\| \begin{bmatrix} z \\ u \end{bmatrix} \right\|_{D(\mathcal{A})}, \end{aligned}$$

where  $c$  is a strictly positive constant, possibly depending on  $\beta$ . Since the reverse inequality is an obvious one, we obtain the claimed norm equivalence.  $\square$

The theorem below shows that if the operator  $A$  from (1.128) is  $\mathcal{R}$ -sectorial and if the operator  $C$  from the second equation in (1.132) is “small” with respect to  $A$  then the semigroup generator describing the system (1.132) is also  $\mathcal{R}$ -sectorial. In the applications we are interested in the first equation in (1.132) describes the fluid, with some boundary input. The second equation describes the motion of the structure. Our result below can be interpreted as asserting that, in some sense, the fluid structure system can be seen as a perturbation of the equations describing the fluid alone.

**Theorem 1.25** *Let  $Z, X, U$  be reflexive Banach spaces of class  $\mathcal{HT}$ . Let  $(L, G)$  be a boundary control system on  $U, Z$  and  $X$ . Assume that  $A = L|_{X_1}$  and  $K$  are  $\mathcal{R}$ -sectorial operators in  $X$  and  $U$ , respectively. More precisely, assume that there exists  $\varepsilon_1, \varepsilon_2 \in (0, \pi/2)$  and  $\gamma_1, \gamma_2 \geq 0$  such that*

$$\mathcal{R}_{\mathcal{L}(X)} \{ \lambda(\lambda I - A)^{-1} \mid \lambda \in \Sigma_{\varepsilon_1, \gamma_1} \} < \infty, \quad \mathcal{R}_{\mathcal{L}(U)} \{ \lambda(\lambda I - K)^{-1} \mid \lambda \in \Sigma_{\varepsilon_2, \gamma_2} \} < \infty. \quad (1.135)$$

*We also suppose that  $C \in \mathcal{L}(Z, U)$  satisfies the following condition: for every  $\delta > 0$ , there exists  $C(\delta) > 0$  such that*

$$\|Cz\|_U \leq \delta \|z\|_Z + C(\delta) \|z\|_X \quad (z \in Z). \quad (1.136)$$

*Then the operator  $(\mathcal{A}, D(\mathcal{A}))$  defined as in (1.134) is  $\mathcal{R}$ -sectorial in  $X \times U$ , i.e., here exists  $\varepsilon_0 \in (0, \pi/2)$  and  $\gamma_0 \geq 0$  such that*

$$\mathcal{R}_{\mathcal{L}(X \times U)} \{ \lambda(\lambda I - \mathcal{A})^{-1} \mid \lambda \in \Sigma_{\varepsilon_0, \gamma_0} \} < \infty. \quad (1.137)$$

*Proof* To prove this theorem we write  $\mathcal{A}$  in the form  $\mathcal{A} = \mathcal{A}_1 + \mathcal{B}$ , where

$$\mathcal{A}_1 \begin{pmatrix} z \\ u \end{pmatrix} = \begin{pmatrix} Lz \\ Ku \end{pmatrix}, \quad \mathcal{B} \begin{pmatrix} z \\ u \end{pmatrix} = \begin{pmatrix} 0 \\ Cz \end{pmatrix}.$$

We first show that  $(\mathcal{A}_1, D(\mathcal{A}))$  is a  $\mathcal{R}$ -sectorial operator in  $X \times U$ . Observe that

$$(\lambda - \mathcal{A}_1) \begin{pmatrix} z \\ u \end{pmatrix} = \begin{pmatrix} x \\ v \end{pmatrix}$$

if and only if,  $\lambda z - Az - Bu = x$  and  $\lambda u - Ku = v$ . Thus, for  $\lambda \in \Sigma_{\varepsilon_1, \gamma_1} \cap \Sigma_{\varepsilon_2, \gamma_2}$ ,

$$u = (\lambda - K)^{-1}v \quad \text{and} \quad z = (\lambda - A)^{-1}(x + B(\lambda - K)^{-1}v).$$

Fix  $\beta \in \rho(A)$  and set  $D = (\beta I - A)^{-1}B$ . Thus  $D \in \mathcal{L}(U, Z)$ . Therefore, for every  $v \in U$ ,

$$\begin{aligned} (\lambda I - A)^{-1}Bv &= (\lambda I - A)^{-1}(\beta I - A)Dv \\ &= -\lambda(\lambda I - A)^{-1}Dv + \beta(\lambda I - A)^{-1}Dv + Dv. \end{aligned}$$

This yields

$$\begin{aligned} &\lambda(\lambda I - \mathcal{A}_1)^{-1} \\ &= \begin{pmatrix} \lambda(\lambda I - A)^{-1}(\beta - \lambda)(\lambda I - A)^{-1}D\lambda(\lambda I - K)^{-1} + D\lambda(\lambda I - K)^{-1} \\ 0 & (\lambda I - K)^{-1} \end{pmatrix} \end{aligned}$$

Using Proposition 1.17 and (1.135), we can easily verify that, there exists  $\varepsilon_3 \in (0, \pi/2)$  and  $\gamma_3 > 0$ , such that

$$\begin{aligned} \mathcal{R}_{\mathcal{L}(X \times U)} \{ \lambda(\lambda I - \mathcal{A}_1)^{-1} \mid \lambda \in \Sigma_{\varepsilon_3, \gamma_3} \} &< \infty, \\ \mathcal{R}_{\mathcal{L}(X \times U)} \{ \mathcal{A}_1(\lambda I - \mathcal{A}_1)^{-1} \mid \lambda \in \Sigma_{\varepsilon_3, \gamma_3} \} &< \infty. \end{aligned}$$

Now, Lemma 1.24 and (1.136) gives, for any  $\delta > 0$

$$\left\| \mathcal{B} \begin{pmatrix} z \\ u \end{pmatrix} \right\|_{X \times U} \leq M\delta \left\| \mathcal{A}_1 \begin{pmatrix} z \\ u \end{pmatrix} \right\|_{X \times U} + C(\delta) \left\| \begin{pmatrix} z \\ u \end{pmatrix} \right\|_{X \times U}. \quad (1.138)$$

Therefore, by Proposition 1.18,  $\mathcal{A}$  is a  $\mathcal{R}$ -sectorial operator in  $X \times U$  and (1.137) holds.  $\square$

### 1.3.4 Bibliographical Notes

The importance of the maximal regularity property of linearized Navier-Stokes type systems in order to obtain existence and uniqueness for the original nonlinear problems is known for a long time (see Clément and Prüss [7] for an early reference). As previously mentioned, in a Hilbert space setting, this property holds



if  $A$  generates an analytic semigroup, see [11]. In a Banach space context, the analyticity of the semigroup is no longer sufficient to guarantee the maximal regularity property, see Kalton and Lancien [21]. In our notes we choose to remind the important necessary and sufficient condition for maximal regularity on  $\mathcal{HT}$  spaces due to Weis [37]. In our approach, an important role in passing from the maximal, regularity of linearized fluid problems to maximal regularity of associated fluid-structure systems is played by perturbations methods. The main results we have presented in this direction are Proposition 1.18, which is given in Kunstmann and Weis [22] and Theorem 1.25, which seems to be new.

## 1.4 Existence and Uniqueness Results

### 1.4.1 Some Background

In this section we will prove local in time existence and uniqueness results for the systems introduced in Sects. 1.1.2 and 1.2. The proofs of the local in time existence and uniqueness results are based on Banach fixed point theorem which is applied to the systems written in fixed spatial domain. In order to apply the Banach fixed point theorem, we need to study the regularity of linear systems with nonhomogeneous source term and non zero initial data on a compact time interval. In fact, to obtain local in time existence and uniqueness of solution, it is important to obtain estimate of solutions in terms of source term and initial data with precise dependence of the continuity constant with respect to time. To this aim, we first recall some basic facts about real interpolation spaces. The proofs can be found in [4, 18, 33].

Let  $X_0$  and  $X_1$  are two complex Banach spaces. The pair  $(X_0, X_1)$  is called interpolation couple if there is a linear, complex Hausdorff space  $Y$  such that  $X_0, X_1 \hookrightarrow Y$  with continuous embeddings.

**Lemma 1.26** *Let  $(X_0, X_1)$  be an interpolation couple. Then  $X_0 \cap X_1$  with the norm*

$$\|x\|_{X_0 \cap X_1} = \max(\|x\|_{X_0}, \|x\|_{X_1}),$$

*and  $X_0 + X_1$  with the norm*

$$\|x\|_{X_0 + X_1} = \inf_{\substack{x=x_0+x_1 \\ x_j \in X_j}} (\|x\|_{X_0} + \|x\|_{X_1}),$$

*are Banach spaces.*

We now introduce the real interpolation space  $(X_0, X_1)_{\theta, q}$  via  $K$  method. Let  $(X_0, X_1)$  be an interpolation couple. For  $0 < t < \infty, x \in X_0 + X_1$ ,

$$K(t, x) = K(t, x, X_0, X_1) = \inf_{\substack{x=x_0+x_1 \\ x_j \in X_j}} (\|x\|_{X_0} + t\|x\|_{X_1}),$$

is an equivalent norm in  $X_0 + X_1$ .

**Definition 1.27** Let  $(X_0, X_1)$  be an interpolation couple. Let  $0 < \theta < 1$  and  $1 < q < \infty$ . Then

$$(X_0, X_1)_{\theta, q} = \left\{ x \in X_0 + X_1 \mid \|x\|_{(X_0, X_1)_{\theta, q}} := \left( \int_0^\infty (t^{-\theta} K(t, x))^q \frac{dt}{t} \right)^{1/q} < \infty \right\}.$$

It is easy to verify that  $\|\cdot\|_{(X_0, X_1)_{\theta, q}}$  is a norm and that  $(X_0, X_1)_{\theta, q}$  is a linear subspace of  $X_0 + X_1$ . We recall some important properties of the space  $(X_0, X_1)_{\theta, q}$ .

**Proposition 1.28**

(1) *It holds that*

$$(X_0, X_1)_{\theta, q} = (X_1, X_0)_{1-\theta, q}.$$

(2) *There exists a constant  $C_{\theta, q}$ ,  $0 < \theta < \infty$ ,  $1 < q < \infty$  such that for all  $x \in X_0 \cap X_1$*

$$\|x\|_{(X_0, X_1)_{\theta, q}} \leq C_{\theta, q} \|x\|_{X_0}^{1-\theta} \|x\|_{X_1}^\theta.$$

Now we introduce another definition of interpolation spaces.

**Definition 1.29** Let  $(X_0, X_1)$  be an interpolation couple,  $\alpha \in \mathbb{R}$  and  $1 < q < \infty$ . Then

$$W(q, \alpha, X_0, X_1) = \left\{ u(t) \mid u(t) \text{ locally integrable functions defined on } (0, \infty) \text{ with} \right. \\ \left. \text{values in } X_0 + X_1 \text{ such that } t^\alpha u(t) \in L^q(0, \infty, X_0), \right. \\ \left. t^\alpha \dot{u} \in L^q(0, \infty, X_1) \right\},$$

where the derivative  $\dot{u} = \frac{du}{dt}$  is the distributional derivative of  $u$ .

The space  $W(q, \alpha, X_0, X_1)$  endowed with the norm

$$\|u\|_{W(q, \alpha, X_0, X_1)} := \|t^\alpha u\|_{L^q(0, \infty; X_0)} + \|t^\alpha \dot{u}\|_{L^q(0, \infty; X_1)}$$

is a Banach space. We define the space of traces as follows

**Definition 1.30** Let  $(X_0, X_1)$  be an interpolation couple. Let  $\alpha \in \mathbb{R}$  and  $1 < q < \infty$  are such that  $0 < \alpha + q^{-1} < 1$ . Then we define

$$T(q, \alpha, X_0, X_1) := \{x \in X_0 + X_1 \mid \text{there exists } u \in W(q, \alpha, X_0, X_1) \text{ with } u(0) = x\}.$$

The space  $T(q, \alpha, X_0, X_1)$  endowed with the norm

$$\|x\|_{T(q, \alpha, X_0, X_1)} := \inf \{ \|u\|_{W(q, \alpha, X_0, X_1)} \mid u(0) = x \},$$

is a Banach space. The following theorem shows the connection between the interpolation spaces  $(X_0, X_1)_{\theta, q}$  and  $T(q, \alpha, X_0, X_1)$ . This theorem will help us to determine the required space of initial conditions in order to obtain maximal  $L^p - L^q$  regularity for linear systems.

**Theorem 1.31** *Let  $(X_0, X_1)$  be an interpolation couple. Let  $\alpha \in \mathbb{R}$  and  $1 < q < \infty$  are such that  $0 < \alpha + q^{-1} < 1$ . Then we have*

$$T(q, \alpha, X_0, X_1) \cong (X_0, X_1)_{\theta, q}. \quad (1.139)$$

As discussed earlier in this chapter, we are now going to study the regularity of linear systems with nonhomogeneous source term and non zero initial data. Let  $0 < T < \infty$ . We consider the initial value problem

$$\dot{u}(t) = Au(t) + f(t), \quad t \in [0, T], \quad u(0) = u_0. \quad (1.140)$$

As a consequence of Theorem 1.19, we have the following result:

**Theorem 1.32** *Let  $X$  be a Banach space of class  $\mathcal{HT}$ ,  $1 < p < \infty$ , and let  $A$  be a closed, densely defined unbounded operator in  $X$  with domain  $D(A)$ . Let  $A$  be an  $\mathcal{R}$ -sectorial operator in  $X$ , i.e., there exists  $\varepsilon_0 \in (0, \pi/2)$  and  $\gamma_0 \geq 0$  such that*

$$\mathcal{R}_{\mathcal{L}(X)} \{ \lambda(\lambda - A)^{-1} \mid \lambda \in \Sigma_{\varepsilon_0, \gamma_0} \} < \infty. \quad (1.141)$$

*Then for every  $u_0 \in (X, D(A))_{1-1/p, p}$  and for every  $f \in L^p(0, T; X)$ , (1.140) admits a unique solution in  $L^p(0, T; D(A)) \cap W^{1,p}(0, T; X)$ . Moreover, there exists a constant  $C$  independent of  $T$  such that the following estimate holds*

$$\begin{aligned} & \|u\|_{L^p(0, T; D(A))} + \|u\|_{W^{1,p}(0, T; X)} \\ & \leq C(1 + 2\gamma_0)e^{2\gamma_0 T} (\|u_0\|_{(X, D(A))_{1-1/p, p}} + \|f\|_{L^p(0, T; X)}). \end{aligned} \quad (1.142)$$

*Proof* Let us set

$$f_T = \begin{cases} f & \text{if } 0 \leq t \leq T, \\ 0 & \text{if } t > T, \end{cases}$$

and

$$A_{\gamma_0} = A - 2\gamma_0 I, \quad f_{\gamma_0}(t) = e^{-2\gamma_0 t} f_T. \quad (1.143)$$

Therefore, obviously we have

$$D(A_{\gamma_0}) = D(A), \quad \mathcal{R}_{\mathcal{L}(X)} \{ \lambda(\lambda I - A_{\gamma_0})^{-1} \mid \lambda \in \Sigma_{\varepsilon_0} \} < \infty$$

and  $f_{\gamma_0}$  belongs to  $L^p(0, \infty; X)$ . Let us consider the problem

$$\dot{u}_{\gamma_0}(t) = A_{\gamma_0} u_{\gamma_0}(t) + f_{\gamma_0}(t), \quad t \geq 0, \quad u_{\gamma_0}(0) = u_0. \quad (1.144)$$

According to Theorem 1.31,

$$(X, D(A))_{1-1/p, p} \cong \{u(0) \mid u \in L^p(0, \infty; D(A)) \cap W^{1,p}(0, \infty; X)\}.$$

Therefore for every  $u_0 \in (X, D(A))_{1-1/p, p}$ , there exists  $u_1 \in L^p(0, \infty; D(A)) \cap W^{1,p}(0, \infty; X)$  such that  $u_1(0) = u_0$  and  $\dot{u}_1 - A_{\gamma_0} u_1$  belongs to  $L^p(0, \infty; X)$ . By Theorem 1.19 and using the fact that  $0 \in \rho(A_{\gamma_0})$ , we obtain existence and uniqueness strong solution  $u_2 \in L^p(0, \infty; D(A)) \cap W^{1,p}(0, \infty; X)$  to

$$\dot{u}_2 = A_{\gamma_0} u_2 + (f - \dot{u}_1 + A_{\gamma_0} u_1), \quad u_2(0) = 0.$$

Hence,  $u_{\gamma_0} = u_1 + u_2$  belongs to  $L^p(0, \infty; D(A)) \cap W^{1,p}(0, \infty; X)$  and  $u_{\gamma_0}$  solves (1.144). By closed graph theorem, there exists a constant  $C > 0$  such that

$$\|u_{\gamma_0}\|_{L^p(0, \infty; D(A))} + \|u_{\gamma_0}\|_{W^{1,p}(0, \infty; X)} \leq C(\|f_{\gamma_0}\|_{L^p(0, \infty; X)} + \|u_0\|_{(X, D(A))_{1-1/p, p}}). \quad (1.145)$$

Define

$$u(t) = e^{2\gamma_0 t} u_{\gamma_0}(t), \quad 0 \leq t \leq T.$$

Then  $u$  belongs to  $L^p(0, T; D(A)) \cap W^{1,p}(0, T; X)$  and  $u$  solves (1.140). Moreover,

$$\begin{aligned} & \|u\|_{L^p(0, T; D(A))} + \|u\|_{W^{1,p}(0, T; X)} \\ & \leq (1 + 2\gamma_0) e^{2\gamma_0 T} (\|u_{\gamma_0}\|_{L^p(0, T; D(A))} + \|u_{\gamma_0}\|_{W^{1,p}(0, T; X)}) \\ & \leq (1 + 2\gamma_0) e^{2\gamma_0 T} (\|u_{\gamma_0}\|_{L^p(0, \infty; D(A))} + \|u_{\gamma_0}\|_{W^{1,p}(0, \infty; X)}). \end{aligned}$$

Finally, by using the above estimate and (1.145), we obtain (1.142).  $\square$

For a smooth bounded domain  $\Omega \subset \mathbb{R}^n$ , the Sobolev spaces of order  $s > 0$  are denoted by  $W^{s,q}(\Omega)$ . Let  $m \in \mathbb{N}$ . For every  $0 < s < m$ ,  $1 \leq p < \infty$ ,  $1 \leq q < \infty$ , we define Besov spaces by real interpolation of Sobolev spaces

$$B_{q,p}^s(\Omega) = (L^q(\Omega), W^{m,q}(\Omega))_{s/m, p}. \quad (1.146)$$

In particular if  $p = q = 2$ , then  $B_{2,2}^s(\Omega) = W^{s,2}(\Omega)$ . We introduce the space

$$W_{q,p}^{2,1}((0, T) \times \Omega) := L^p(0, T; W^{2,q}(\Omega)) \cap W^{1,p}(0, T; L^q(\Omega)), \quad (1.147)$$

and

$$\|u\|_{W_{q,p}^{2,1}([0,T] \times \Omega)} := \|u\|_{L^p(0,T;W^{2,q}(\Omega))} + \|u\|_{W^{1,p}(0,T;L^q(\Omega))}. \quad (1.148)$$

We now state an important embedding theorem

**Theorem 1.33** ([1, Theorem 4.10.2]) *Let  $X_0$  and  $X_1$  be two Banach spaces such that  $X_1$  is densely embedded in  $X_0$ . Let  $0 < T \leq \infty$  and fix  $p \in (1, \infty)$ . Then*

$$L^p([0, T]; X_1) \cap W^{1,p}([0, T]; X_0) \hookrightarrow C([0, T]; (X_0, X_1)_{1-1/p, p}).$$

As a consequence of the above theorem, we obtain the following proposition

**Proposition 1.34** ([31, Proposition 4.2]) *Let  $1 < p, q < \infty$  and  $T$  be any positive number. Let  $\Omega$  be a smooth domain in  $\mathbb{R}^n$ . Then for any  $u \in W_{q,p}^{2,1}([0, T] \times \Omega)$ ,*

$$\sup_{t \in (0, T)} \|u(t)\|_{B_{q,p}^{2(1-1/p)}(\Omega)} \leq C \left( \|u(0)\|_{B_{q,p}^{2(1-1/p)}(\Omega)} + \|u\|_{W_{q,p}^{2,1}([0, T] \times \Omega)} \right), \quad (1.149)$$

where the constant  $C$  is independent of time  $T$ . In particular, if  $p = q = 2$ , then for any  $u \in L^2(0, T; W^{2,2}(\Omega)) \cap W^{1,2}(0, T; L^2(\Omega))$

$$\sup_{t \in (0, T)} \|u(t)\|_{W^{1,2}(\Omega)} \leq C \left( \|u(0)\|_{W^{1,2}(\Omega)} + \|u\|_{L^2(0, T; W^{2,2}(\Omega))} + \|u\|_{W^{1,2}(0, T; L^2(\Omega))} \right), \quad (1.150)$$

where the constant  $C$  is independent of  $T$ .

For any  $1 < p < \infty$ ,  $p'$  denotes the conjugate of  $p$ , i.e.,  $\frac{1}{p} + \frac{1}{p'} = 1$ . We recall some basic embedding estimates

$$\begin{aligned} \|f\|_{L^p(0, T)} &\leq T^{1/p-1/r} \|f\|_{L^r(0, T)}, & \text{for all } f \in L^r(0, T), r > p \\ \|f\|_{L^\infty(0, T)} &\leq T^{1/p'} \|f\|_{W^{1,p}(0, T)}, & \text{for all } f \in W^{1,p}(0, T), f(0) = 0. \end{aligned} \quad (1.151)$$

Let  $\Omega(t)$  be a time dependent domain. We define Sobolev spaces in the time dependent domain  $\Omega(t)$  as follows.

**Definition 1.35** We say that  $u \in W^{s_1, p}(0, T; W^{s_2, q}(\Omega(\cdot)))$  if for almost every  $t \in (0, T)$ ,  $u(t)$  belongs to  $W^{s_2, q}(\Omega(t))$  and  $t \mapsto \|u(t, \cdot)\|_{W^{s_2, q}(\Omega(t))}$  is in  $W^{s_1, p}(0, T)$ .

Other type of Sobolev spaces in the time dependent domain  $\Omega(t)$  can be defined similarly. Finally we recall the following useful lemma

**Lemma 1.36** ([32, Chap. 3, Lemma 2.1]) *Let  $X_i$ ,  $i = 1, 2, 3$  be Banach spaces with continuous inclusions*

$$X_1 \hookrightarrow X_2 \hookrightarrow X_3.$$

Assume that  $X_1$  is compactly embedded in  $X_2$ . Then for any given  $\epsilon > 0$ , there exists  $C(\epsilon) > 0$  such that for all  $x \in X_1$

$$\|x\|_{X_2} \leq \epsilon \|x\|_{X_1} + C(\epsilon) \|x\|_{X_3}.$$

### 1.4.2 Back to the Toy Problem

In this section we consider again the toy problem (1.9), this time in a  $L^p - L^q$  framework. The main result asserts the local in time existence and uniqueness of solutions for system (1.9) in this context. Let us set  $\Omega_h(t) = (-1, 1) \setminus \{h(t)\}$  and  $\Omega_{h_0} = (-1, 1) \setminus \{h_0\}$ . For every  $1 < p < \infty$  and  $1 < q < \infty$  the set  $\mathcal{I}_{p,q}$  is defined by

$$\mathcal{I}_{p,q} = \{(z_0, h_0, g_0) \mid z_0 \in B_{q,p}^{2(1-1/p)}(\Omega_{h_0}), h_0 \in (-1, 1), g_0 \in \mathbb{R}\} \quad (1.152)$$

and

$$\|(z_0, h_0, g_0)\|_{\mathcal{I}_{p,q}} := \|z_0\|_{B_{q,p}^{2(1-1/p)}(\Omega_{h_0})} + |h_0| + |g_0|.$$

For every  $p, q \in (1, \infty)$  satisfying the condition  $\frac{1}{p} + \frac{1}{2q} \neq 1$ , we introduce the space of initial data

$$\mathcal{I}_{p,q}^{cc} = \begin{cases} \mathcal{I}_{p,q} & \text{if } \frac{1}{p} + \frac{1}{2q} > 1, \\ \{(z_0, h_0, g_0) \in \mathcal{I}_{p,q} \mid z_0(h_0) = g_0, z_0(-1) = z_0(1) = 0\} & \text{if } \frac{1}{p} + \frac{1}{2q} < 1. \end{cases} \quad (1.153)$$

The main result of this section states as follows.

**Theorem 1.37** *Let  $1 < p, q < \infty$  satisfying the condition  $\frac{1}{p} + \frac{1}{2q} \neq 1$ . Assume that  $(v_0, h_0, g_0)$  belongs to  $\mathcal{I}_{p,q}^{cc}$ . Then there exists a  $T > 0$  such that the system (1.9) admits a unique strong solution*

$$\begin{aligned} v &\in L^p(0, T; W^{2,q}(\Omega_h(\cdot))) \cap W^{1,p}(0, T; L^q(\Omega_h(\cdot))) \cap C([0, T]; B_{q,p}^{2(1-1/p)}(\Omega_h(\cdot))), \\ h &\in W^{2,p}(0, T). \end{aligned}$$

Moreover,  $h(t) \in (-1, 1)$  for all  $t \in [0, T]$ .

In view of Proposition 1.2, it is enough to show local in time existence and uniqueness of solutions for system (1.12) which holds in a fixed spatial domain. Therefore, in this section, we prove the following theorem

**Theorem 1.38** *Let  $1 < p, q < \infty$  satisfying the condition  $\frac{1}{p} + \frac{1}{2q} \neq 1$ . Assume that  $(z_0, h_0, g_0)$  belongs to  $\mathcal{I}_{p,q}^{cc}$ . Then there exists a  $T > 0$  such that the system (1.12) admits a unique strong solution*

$$\begin{aligned} z &\in L^p(0, T; W^{2,q}(\Omega_{h_0})) \cap W^{1,p}(0, T; L^q(\Omega_{h_0})) \cap C([0, T]; B_{q,p}^{2(1-1/p)}(\Omega_{h_0})), \\ h &\in W^{2,p}(0, T). \end{aligned}$$

Moreover,  $h(t) \in (-1, 1)$  for all  $t \in [0, T]$ .

In order to prove the above theorem, we first rewrite (1.12) as follows

$$\begin{aligned} \dot{z} - z_{xx} &= \mathcal{F}_1(z, g, h), \quad t \in (0, T), \quad x \in (-1, 1) \setminus h_0, \\ z(t, -1) &= z(t, 1) = 0, \quad z(t, h_0) = g(t), \quad t \in (0, T) \\ \dot{g} &= [z_x](t, h_0) + \mathcal{F}_2(z, g, h), \quad t \in (0, T) \\ z(0, x) &= z_0(x) \quad x \in (-1, 1), \quad h(0) = h_0, \quad g(0) = g_0. \end{aligned} \tag{1.154}$$

where

$$\begin{aligned} h(t) &= h_0 + \int_0^t g(s) \, ds, \\ \mathcal{F}_1(z, g, h) &= \frac{k(h-h_0)}{1-kh} \left[ 2 + \frac{k(h-h_0)}{1-kh} \right] z_{xx} + \frac{1-kx}{1-kh} g z_x - \frac{1-kh_0}{1-kh} z z_x, \\ \mathcal{F}_2(z, g, h) &= (h-h_0) \left[ \frac{kz_x}{1-kh} \right] (t, h_0). \end{aligned} \tag{1.155}$$

We consider the following linear system

$$\begin{aligned} \dot{z} - z_{xx} &= f_1, \quad t \in (0, T), \quad x \in (-1, 1) \setminus h_0, \\ z(t, -1) &= z(t, 1) = 0, \quad z(t, h_0) = g(t), \quad t \in (0, T) \\ \dot{g} &= [z_x](t, h_0) + f_2, \quad t \in (0, T) \\ z(0, x) &= z_0(x) \quad x \in (-1, 1) \setminus \{h_0\}, \quad g(0) = g_0. \end{aligned} \tag{1.156}$$

We want to rewrite the above system as an evolution equation in an appropriate Banach space. Let  $\Omega_{h_0} = (-1, 1) \setminus \{h_0\}$  and  $q > 1$ . We introduce the following spaces

$$Z = W^{2,q}(\Omega_{h_0}) \cap W_0^{1,q}(-1, 1), \quad X = L^q(\Omega_{h_0}), \quad U = \mathbb{R}.$$

Let  $L \in \mathcal{L}(Z, X)$ ,  $G \in \mathcal{L}(Z, U)$  and  $C \in \mathcal{L}(Z, U)$  are defined as follows

$$Lz = z_{xx}, \quad Gz = z(h_0), \quad Cz = [z_x](h_0) \tag{1.157}$$

Let us introduce the unbounded operator  $(\mathcal{A}, D(\mathcal{A}))$  in  $X \times U$  by

$$D(\mathcal{A}) = \{(z, g) \in X \times U \mid Lz \in X, Gz = g\} \quad (1.158)$$

and

$$\mathcal{A} \begin{pmatrix} z \\ g \end{pmatrix} = \begin{pmatrix} Lz \\ Cz \end{pmatrix} \quad (1.159)$$

Thus (1.156) can be written as

$$\frac{d}{dt} \begin{pmatrix} z \\ g \end{pmatrix} = \mathcal{A} \begin{pmatrix} z \\ g \end{pmatrix} + \begin{pmatrix} f_1 \\ f_2 \end{pmatrix}, \quad \begin{pmatrix} z(0) \\ g(0) \end{pmatrix} = \begin{pmatrix} z_0 \\ g_0 \end{pmatrix}. \quad (1.160)$$

**Proposition 1.39** *There exists  $\varepsilon \in (0, \pi/2)$  and  $\gamma_0 > 0$  such that*

$$\mathcal{R}_{\mathcal{L}(X \times U)} \{ \lambda(\lambda - \mathcal{A})^{-1} \mid \lambda \in \Sigma_{\varepsilon_0, \gamma_0} \} < \infty. \quad (1.161)$$

*Proof* Let us set  $X_1 = \text{Ker}G = \{z \in Z \mid z(h_0) = 0\}$ , and  $A = L|_{X_1}$ . Then, by Denk et al. [12, Theorem 8.2],  $A$  is  $\mathcal{R}$ -sectorial in  $X$  and there exists  $\varepsilon_0$  and  $\tilde{\gamma} \geq 0$  such that

$$\mathcal{R}_{\mathcal{L}(X)} \{ \lambda(\lambda - A)^{-1} \mid \lambda \in \Sigma_{\varepsilon_0, \tilde{\gamma}} \} < \infty. \quad (1.162)$$

We also have, for  $s \in (1/q, 1)$

$$\|Cz\|_U \leq C\|z_x\|_{W^{s,q}(\Omega_{h_0})} \leq C\|z\|_{W^{1+s}(\Omega_{h_0})}. \quad (1.163)$$

Since  $W^{2,q}(\Omega_{h_0}) \hookrightarrow_{\text{compact}} W^{1+s,q}(\Omega_{h_0})$ , we obtain for any  $\delta > 0$ , there exists

$$\|z\|_{W^{1+s}(\Omega_{h_0})} \leq \delta\|z\|_{W^{2,q}(\Omega_{h_0})} + C(\delta)\|z\|_{L^q(\Omega_{h_0})},$$

holds for arbitrary small  $\delta$ . This completes the proof of the proposition.  $\square$

Combining the above proposition and Theorem 1.32, we obtain the following result

**Theorem 1.40** *Let  $1 < p, q < \infty$  and  $h_0 \in (-1, 1)$ . Then for every  $(z_0, g_0) \in (Z, D(\mathcal{A}))_{1-1/p, p}$  and for every  $(f_1, f_2) \in L^p(0, T; L^q(\Omega_{h_0})) \times L^p(0, T)$ , the system (1.156) admits a unique strong solution satisfying*

$$\begin{aligned} & \|z\|_{L^p(0, T; W^{2,q}(\Omega_{h_0}))} + \|z\|_{W^{1,p}(0, T; L^q(\Omega_{h_0}))} + \|g\|_{W^{1,p}(0, T)} \\ & \leq C(1 + e^{2\gamma_0 T}) \left( \|(z_0, h_0, g_0)\|_{(Z, D(\mathcal{A}))_{1-1/p, p}} + \|f_1\|_{L^p(0, T; L^q(\Omega_{h_0}))} + \|f_2\|_{L^p(0, T)} \right). \end{aligned}$$



In order to prove our local in time existence and uniqueness result we combine the above theorem with a fixed point procedure. In the above theorem, one requires initial conditions from a real interpolation space between  $\mathcal{D}(\mathcal{A})$  and  $Z$ . In order to identify this interpolation space, we prove the following lemma:

**Lemma 1.41** *Let  $p, q \in (1, \infty)$  satisfying the condition  $\frac{1}{p} + \frac{1}{2q} \neq 1$ . Let us assume that  $h_0 \in (-1, 1)$  and  $(z_0, g_0)$  belongs to  $(Z, D(\mathcal{A}))_{1-1/p, p}$ . Then  $(z_0, h_0, g_0)$  belongs to  $\mathcal{I}_{p, q}^{cc}$ , where  $\mathcal{I}_{p, q}^{cc}$  defined as in (1.153).*

*Proof* For proof we refer to [33, Sect. 4.3.3] and [2, Theorem 2.2].  $\square$

Next for  $T > 0$ , we define

$$\mathcal{B}_T = \left\{ (f_1, f_2) \in L^p(0, T; L^q(\Omega_{h_0})) \times L^p(0, T) \mid \right. \\ \left. \|f_1\|_{L^p(0, T; L^q(\Omega_{h_0}))} + \|f_2\|_{L^p(0, T)} \leq 1 \right\}. \quad (1.164)$$

**Proposition 1.42** *Let  $p, q \in (1, \infty)$  satisfying the condition  $\frac{1}{p} + \frac{1}{2q} \neq 1$ . Assume that  $(z_0, h_0, g_0)$  belongs to  $\mathcal{I}_{p, q}^{cc}$ . Let  $M > 0$  be such that*

$$\|(z_0, h_0, g_0)\|_{\mathcal{I}_{p, q}} \leq M. \quad (1.165)$$

*Then for every  $(f_1, f_2) \in \mathcal{B}_T$ , the system (1.156) admits a unique strong solution on  $[0, T]$ . Moreover, there exists a constant  $C$  depending only on  $M$  such that*

$$\|z\|_{L^p(0, T_*; W^{2, q}(\Omega_{h_0}))} + \|z\|_{W^{1, p}(0, T_*; L^q(\Omega_{h_0}))} + \|g\|_{W^{1, p}(0, T_*)} \leq C, \quad (1.166)$$

$$\|z\|_{L^\infty(0, T_*; L^q(\Omega_{h_0}))} \leq C, \quad \|g\|_{L^\infty(0, T_*)} \leq C, \quad (1.167)$$

$$\|z_x\|_{L^p(0, T_*; L^\infty(\Omega_{h_0}))} \leq CT_*^{(1-s)/2p}, \quad s \in (1/q, 1), \quad (1.168)$$

*holds for all  $T_* \in (0, 1]$ .*

*Proof* The first estimate follows directly from Theorem 1.40. Notice that,

$$\|z - z_0\|_{L^\infty(0, T; L^q(\Omega_{h_0}))} \leq T^{1/p'} \|z\|_{W^{1, p}(0, T; L^q(\Omega_{h_0}))},$$

which yields,

$$\|z\|_{L^\infty(0, T_*; L^q(\Omega_{h_0}))} \leq C, \quad T_* \in (0, 1]. \quad (1.169)$$

Similarly, we can show  $\|g\|_{L^\infty(0, T_*)} \leq C$ . Since  $1 < q < \infty$ , we have  $z_x \in L^p(0, T_*, W^{1, q}(\Omega_{h_0})) \hookrightarrow L^p(0, T_*, L^\infty(\Omega_{h_0}))$ . Let us fix,  $s \in (1/q, 1)$ . Therefore, we have

$$\|z_x(t, \cdot)\|_{L^\infty(\Omega_{h_0})} \leq C \|z_x(t, \cdot)\|_{W^{s, q}(\Omega_{h_0})} \leq C \|z(t, \cdot)\|_{W^{2, q}(\Omega_{h_0})}^{(1+s)/2} \|z(t, \cdot)\|_{L^q(\Omega_{h_0})}^{(1-s)/2}.$$

Thus, using (1.169) and Hölder's inequality we get

$$\begin{aligned} \|z_x\|_{L^p(0,T_*;L^\infty(\Omega_{h_0}))} &\leq C \|z\|_{L^\infty(0,T_*;L^q(\Omega_{h_0}))}^{(1-s)/2} \left( \int_0^{T_*} \|z(t, \cdot)\|_{W^{2,q}(\Omega_{h_0})}^{(1+s)p/2} dt \right)^{1/p} \\ &\leq CT_*^{(1-s)/2p}. \end{aligned}$$

□

**Lemma 1.43** *Let  $p, q \in (1, \infty)$  satisfying the condition  $\frac{1}{p} + \frac{1}{2q} \neq 1$ . For  $T_* \in (0, 1]$ , let  $\mathcal{B}_{T_*}$  be the ball defined in (1.164). Let  $(z_0, h_0, g_0)$  and  $M$  as in Proposition 1.42. Given  $(f_1, f_2) \in \mathcal{B}_{T_*}$ , let  $(z, g)$  be the solution of (1.156) on  $[0, T_*]$  constructed in Proposition 1.42.*

*Then there exists a constant  $C > 0$ , depending only on  $M$ , such that*

$$\begin{aligned} |h(t) - h(0)| &\leq CT_*^{1/p'}, \quad t \in [0, T_*] \\ \|\mathcal{F}_1(z, g, h)\|_{L^p(0,T_*;L^q(\Omega_{h_0}))} &\leq C(T_*^{1/p'} + T_*^{(1-s)/2p}), \quad s \in (1/q, 1) \\ \|\mathcal{F}_2(z, g, h)\|_{L^p(0,T_*)} &\leq CT_*^{1/p'}, \end{aligned} \quad (1.170)$$

where  $h, \mathcal{F}_1$  and  $\mathcal{F}_2$  have been defined in (1.155).

*Proof* Using (1.166), we get for all  $t \in [0, T_*]$ ,

$$|h(t) - h_0| \leq \int_0^{T_*} |g(s)| ds \leq T_*^{1/p'} \|g\|_{L^p(0,T_*)} \leq CT_*^{1/p'}. \quad (1.171)$$

Using the above estimate it is easy to see that, for all  $t \in [0, T_*]$

$$\left| \frac{1}{1 - \kappa h} \right| \leq C, \quad (1.172)$$

where the constant  $C$  is independent of  $T_*$ . Using (1.166), (1.171) and (1.172), the first term of  $\mathcal{F}_1(z, g, h)$  can be estimated as follows

$$\begin{aligned} &\left\| \frac{k(h - h_0)}{1 - kh} \left[ 2 + \frac{k(h - h_0)}{1 - kh} \right] z_{xx} \right\|_{L^p(0,T_*;L^q(\Omega_{h_0}))} \\ &\leq C|h - h_0| \|z_{xx}\|_{L^p(0,T_*;L^q(\Omega_{h_0}))} \leq CT_*^{1/p'}. \end{aligned} \quad (1.173)$$

Using (1.167), (1.168) and (1.172), it is easy to see that the second term of  $\mathcal{F}_1$  satisfy the following estimate

$$\begin{aligned} &\left\| \frac{1 - kx}{1 - kh} g z_x \right\|_{L^p(0,T_*;L^q(\Omega_{h_0}))} \leq C \|g\|_{L^\infty(0,T_*)} \|z_x\|_{L^p(0,T_*;L^q(\Omega_{h_0}))} \\ &\leq C \|z_x\|_{L^p(0,T_*;L^\infty(\Omega_{h_0}))} \leq CT_*^{(1-s)/2p}. \end{aligned} \quad (1.174)$$

Similarly, using (1.167), (1.168) and (1.172), we obtain

$$\begin{aligned} & \left\| \frac{1 - kh_0}{1 - kh} z z_x \right\|_{L^p(0, T_*; L^q(\Omega_{h_0}))} \leq C \|z\|_{L^\infty(0, T_*; L^q(\Omega_{h_0}))} \|z_x\|_{L^p(0, T_*; L^\infty(\Omega_{h_0}))} \\ & \leq CT_*^{(1-s)/2p}. \end{aligned} \quad (1.175)$$

Combining (1.173), (1.174) and (1.175), we get

$$\|\mathcal{F}_1(z, g, h)\|_{L^p(0, T_*; L^q(\Omega_{h_0}))} \leq C(T_*^{1/p'} + T_*^{(1-s)/2p}).$$

Finally, using (1.166), (1.171) and (1.172), one has

$$\begin{aligned} \|\mathcal{F}_2(z, g, h)\|_{L^p(0, T_*)} &= \left\| (h - h_0) \left[ \frac{kz_x}{1 - kh} \right] (\cdot, h_0) \right\|_{L^p(0, T_*)} \\ &\leq C \|h - h_0\|_{L^\infty(0, T_*)} \|z_x\|_{L^p(0, T_*; W^{1,q}(\Omega_{h_0}))} \leq CT_*^{1/p'}. \end{aligned}$$

□

**Lemma 1.44** *Let  $p, q \in (1, \infty)$  satisfying the condition  $\frac{1}{p} + \frac{1}{2q} \neq 1$ . For  $T_* \in (0, 1]$ , let  $\mathcal{B}_{T_*}$  be the ball defined in (1.164). Let  $(z_0, h_0, g_0)$  and  $M$  as in Proposition 1.42. Given  $(f_1^j, f_2^j) \in \mathcal{B}_{T_*}$ , for  $j = 1, 2$ , let  $(z^j, g^j)$  be the solution of (1.156) on  $[0, T_*]$  constructed in Proposition 1.42.*

*Then there exist a constant  $C > 0$  depending only on  $M$  and  $\delta > 0$  depending only on  $p$  and  $q$  such that*

$$\begin{aligned} & |h^1(t) - h^2(t)| + \|\mathcal{F}_1(z^1, g^1, h^1) - \mathcal{F}_1(z^2, g^2, h^2)\|_{L^p(0, T_*; L^q(\Omega_{h_0}))} \\ & \quad + \|\mathcal{F}_2(z^1, g^1, h^1) - \mathcal{F}_2(z^2, g^2, h^2)\|_{L^p(0, T_*)} \\ & \leq CT_*^\delta (\|f_1^1 - f_1^2\|_{L^p(0, T_*; L^q(\Omega_{h_0}))} + \|f_2^1 - f_2^2\|_{L^p(0, T_*)}) \end{aligned} \quad (1.176)$$

where  $h, \mathcal{F}_1$  and  $\mathcal{F}_2$  have been defined in (1.155).

We are now in a position to prove our main theorem.

*Proof of Theorem 1.38* We consider the map

$$\begin{cases} \mathcal{N} : \mathcal{B}_{T_*} \rightarrow \mathcal{B}_{T_*}, \\ \begin{bmatrix} f_1 \\ f_2 \end{bmatrix} \mapsto \begin{bmatrix} \mathcal{F}_1 \\ \mathcal{F}_2 \end{bmatrix}, \end{cases}$$

where  $\mathcal{F}_1$  and  $\mathcal{F}_2$  have been defined in (1.155). We want to show  $\mathcal{N}$  is a strict contraction of  $\mathcal{B}_{T_*}$ , with a Lipschitz constant  $\frac{1}{2}$  for small  $T_*$ . We first note that from

Lemma 1.43 , we obtain, for all  $(f_1, f_2) \in \mathcal{B}_{T_*}$

$$\|\mathcal{N}(f_1, f_2)\|_{L^p(0, T_*; L^q(\Omega_{h_0})) \times L^p(0, T_*)} \leq C(T_*^{1/p'} + T_*^{(1-s)/2p}),$$

where  $C$  is a constant depending only on  $M$ . Therefore by choosing  $T_* \leq 1$  small enough

$$\|\mathcal{N}(f_1, f_2)\|_{L^p(0, T_*; L^q(\Omega_{h_0})) \times L^p(0, T_*)} < 1. \quad (1.177)$$

Therefore  $\mathcal{N}$  maps  $\mathcal{B}_{T_*}$  into  $\mathcal{B}_{T_*}$  for small enough  $T_*$ . Next from Lemma 1.44, there exists  $C > 0$ , depending only on  $M$  such that

$$\begin{aligned} & \|\mathcal{N}(f_1^1, f_2^1) - \mathcal{N}(f_1^2, f_2^2)\|_{L^p(0, T_*; L^q(\Omega_{h_0})) \times L^p(0, T_*)} \\ & \leq C(T_*^{1/p'} + T_*^{(1-s)/2p}) \|(f_1^1, f_2^1) - (f_1^2, f_2^2)\|_{L^p(0, T_*; L^q(\Omega_{h_0})) \times L^p(0, T_*)}. \end{aligned}$$

Thus by choosing  $T_*$  small enough we obtain  $\mathcal{N}$  is a strict contraction, which implies the existence and uniqueness result.

### 1.4.3 A More Realistic 1D Model

In this section, we shall prove local in time existence and uniqueness of solutions for the system (1.67). Let us set  $\Omega_h(t) = (-1, 1) \setminus \{h(t)\}$  and  $\Omega_{h_0} = (-1, 1) \setminus \{h_0\}$ . For every  $1 < p < \infty$  and  $1 < q < \infty$  the set  $\mathcal{I}_{p,q,\Omega_{h_0}}$  is defined by

$$\begin{aligned} \mathcal{I}_{p,q,\Omega_{h_0}} = \{ & (\varrho_0, w_0, \vartheta_0, h_0, g_0, Q_0) \mid \varrho_0 \in W^{1,q}(\Omega_{h_0}), \quad w_0, \vartheta_0 \in B_{q,p}^{2(1-1/p)}(\Omega_{h_0}), \\ & h_0 \in (-1, 1), \quad g_0 \in \mathbb{R}, \quad Q_0 \in \mathbb{R}, \quad \min_{\xi \in \overline{\Omega_{h_0}}} \varrho_0(\xi) > 0\}, \end{aligned}$$

and

$$\begin{aligned} \|(\varrho_0, w_0, \vartheta_0, h_0, g_0, Q_0)\|_{\mathcal{I}_{p,q}} := & \|\varrho_0\|_{W^{1,q}(\Omega_{h_0})} + \|w_0\|_{B_{q,p}^{2(1-1/p)}(\Omega_{h_0})} + \|\vartheta_0\|_{B_{q,p}^{2(1-1/p)}(\Omega_{h_0})} \\ & + |h_0| + |g_0| + |Q_0|. \end{aligned}$$

Let  $p$  and  $q$  satisfy one of the following conditions:

$$\begin{aligned} & \text{either } 1 < q < \infty \text{ and } 2 < p < \infty \text{ satisfying } \frac{1}{p} + \frac{1}{2q} \neq 1 \text{ and } \frac{1}{p} + \frac{1}{2q} \neq \frac{1}{2}, \\ & \text{or } p = q = 2. \end{aligned} \quad (1.178)$$

Let  $p, q$  satisfy the condition (1.178). We introduce the space of initial data

$$\mathcal{I}_{p,q,\Omega_{h_0}}^{cc} = \begin{cases} \mathcal{I}_{p,q,\Omega_{h_0}} & \text{if } \frac{1}{p} + \frac{1}{2q} > 1, \\ \left\{ (\varrho_0, w_0, \vartheta_0, h_0, g_0, Q_0) \in \mathcal{I}_{p,q,\Omega_{h_0}} \mid w_0(h_0) = g_0, \right. \\ \quad \left. w_0(-1) = w_0(1) = 0, \vartheta_0(h_0) = Q_0 \right\} & \text{if } \frac{1}{2} < \frac{1}{p} + \frac{1}{2q} < 1, \\ \left\{ (\varrho_0, w_0, \vartheta_0, h_0, g_0, Q_0) \in \mathcal{I}_{p,q,\Omega_{h_0}} \mid w_0(h_0) = g_0, \right. \\ \quad \left. w_0(-1) = w_0(1) = 0, \vartheta_0(h_0) = Q_0, \right. \\ \quad \left. \partial_\xi \vartheta_0(-1) = \partial_\xi \vartheta_0(1) = 0 \right\} & \text{if } \frac{1}{p} + \frac{1}{2q} < \frac{1}{2}. \end{cases} \quad (1.179)$$

We prove the following theorem

**Theorem 1.45** *Let  $p, q$  satisfy the condition (1.178). Assume that  $(\varrho_0, w_0, \vartheta_0, h_0, g_0, Q_0)$  belongs to  $\mathcal{I}_{p,q,\Omega_{h_0}}^{cc}$ . Then there exists a  $T > 0$  such that the system (1.67) admits a unique strong solution*

$$\begin{aligned} \varrho &\in W^{1,p}(0, T; W^{1,q}(\Omega_h(\cdot))) \cap C([0, T]; W^{1,q}(\Omega_h(\cdot))) \\ w, \vartheta &\in L^p(0, T; W^{2,q}(\Omega_h(\cdot))) \cap W^{1,p}(0, T; L^q(\Omega_h(\cdot))) \cap C([0, T]; B_{q,p}^{2(1-1/p)}(\Omega_h(\cdot))), \\ h &\in W^{2,p}(0, T), \quad Q \in W^{1,p}(0, T). \end{aligned}$$

Moreover,  $h(t) \in (-1, 1)$  for all  $t \in [0, T]$  and  $\min_{\xi \in \Omega_{h_0}} \varrho(t, \xi) > 0$  for all  $t \in [0, T]$ ,  $\xi \in \Omega_h(t)$ .

Due to the change of variable introduced in Sect. 1.2.1, it is enough to prove local in time existence and uniqueness for the system (1.92). To this aim, let us set

$$\Omega = (-r_1, r_2) \setminus \{0\}.$$

Let  $p, q$  satisfy the condition (1.178). We introduce following space of initial conditions for system (1.92),

$$\mathcal{I}_{p,q,\Omega}^{cc} = \begin{cases} \mathcal{I}_{p,q,\Omega} & \text{if } \frac{1}{p} + \frac{1}{2q} > 1, \\ \left\{ (v_0, u_0, \theta_0, h_0, g_0, Q_0) \in \mathcal{I}_{p,q,\Omega} \mid u_0(0) = g_0, \right. \\ \quad \left. u_0(-r_1) = u_0(r_2) = 0, \theta_0(0) = Q_0 \right\} & \text{if } \frac{1}{2} < \frac{1}{p} + \frac{1}{2q} < 1, \\ \left\{ (v_0, u_0, \theta_0, h_0, g_0, Q_0) \in \mathcal{I}_{p,q,\Omega} \mid u_0(0) = g_0, \right. \\ \quad \left. u_0(-r_1) = u_0(r_2) = 0, \theta_0(0) = Q_0, \right. \\ \quad \left. \partial_x \theta_0(-r_1) = \partial_x \theta_0(r_2) = 0 \right\} & \text{if } \frac{1}{p} + \frac{1}{2q} < \frac{1}{2}. \end{cases} \quad (1.180)$$

In this section, we prove the following theorem

**Theorem 1.46** *Let  $p, q$  satisfy the condition (1.178). Assume that  $(v_0, u_0, \theta_0, h_0, g_0, Q_0)$  belongs to  $\mathcal{I}_{p,q,\Omega}^{cc}$ . Then there exists a  $T > 0$  such that the system (1.92) admits a unique strong solution*

$$\begin{aligned} v &\in W^{1,p}(0, T; W^{1,q}(\Omega)) \cap C([0, T]; W^{1,q}(\Omega)) \\ u, \theta &\in L^p(0, T; W^{2,q}(\Omega)) \cap W^{1,p}(0, T; L^q(\Omega)) \cap C([0, T]; B_{q,p}^{2(1-1/p)}(\Omega)), \\ h &\in W^{2,p}(0, T), \quad Q \in W^{1,p}(0, T). \end{aligned}$$

Moreover,  $h(t) \in (-r_1, r_2)$  for all  $t \in [0, T]$  and  $\min_{x \in \overline{\Omega}} v(t, x) > 0$  for all  $t \in [0, T]$ ,  $x \in \Omega$ .

To prove the above theorem, we rewrite (1.92) as follows

$$\begin{aligned} \partial_t v - \partial_x u &= 0, & (t \geq 0, x \in [-r_1, r_2] \setminus \{0\}), \\ \partial_t u - \partial_x \left( \frac{1}{v_0} \partial_x u \right) &= \mathcal{F}_1(v, u, \theta), & (t \geq 0, x \in [-r_1, r_2] \setminus \{0\}), \\ \partial_t \theta - \partial_x \left( \frac{1}{v_0} \partial_x \theta \right) &= \mathcal{F}_2(v, u, \theta), & (t \geq 0, x \in [-r_1, r_2] \setminus \{0\}), \\ u(t, \pm 0) &= \dot{h}(t), \quad \theta(t, 0 \pm) = Q(t), & (t \geq 0), \\ & & (1.181) \\ m\ddot{h}(t) &= \left[ \frac{1}{v_0} \partial_x u \right] (t, 0) + \mathcal{F}_3(v, u, \theta), & (t \geq 0), \\ \dot{Q}(t) &= \left[ \frac{1}{v_0} \partial_x \theta \right] (t, 0) + \mathcal{F}_4(v, u, \theta), & (t \geq 0), \\ u(t, -r_1) &= u(t, r_2) = 0, \quad \partial_x \theta(t, -r_1) = \partial_x \theta(t, r_2) = 0, & (t \geq 0), \\ v(0, x) &= v_0(x), \quad u(0, x) = u_0(x), \quad \theta(0, x) = \theta_0(x), & x \in [-r_1, r_2] \setminus \{0\}, \\ h(0) &= h_0, \quad \dot{h}(0) = g_0, \end{aligned}$$

where

$$\begin{aligned} \mathcal{F}_1(v, u, \theta) &= \partial_x \left( \left( \frac{1}{v} - \frac{1}{v_0} \right) \partial_x u \right) - \partial_x \left( \frac{\theta}{v} \right) \\ \mathcal{F}_2(v, u, \theta) &= \partial_x \left( \left( \frac{1}{v} - \frac{1}{v_0} \right) \partial_x \theta \right) + \frac{1}{v} (\partial_x u)^2 - \frac{\theta}{v} \partial_x u \\ \mathcal{F}_3(v, u, \theta) &= \left[ \left( \frac{1}{v} - \frac{1}{v_0} \right) \partial_x u - \frac{\theta}{v} \right] (t, 0), \quad \mathcal{F}_4(v, u, \theta) = \left[ \left( \frac{1}{v} - \frac{1}{v_0} \right) \partial_x \theta \right] (t, 0). \end{aligned} \tag{1.182}$$

We consider the following linear system

$$\begin{aligned}
\partial_t v - \partial_x u &= 0, & (t \geq 0, x \in [-r_1, r_2] \setminus \{0\}), \\
\partial_t u - \partial_x \left( \frac{1}{v_0} \partial_x u \right) &= f_1, & (t \geq 0, x \in [-r_1, r_2] \setminus \{0\}), \\
\partial_t \theta - \partial_x \left( \frac{1}{v_0} \partial_x \theta \right) &= f_2, & (t \geq 0, x \in [-r_1, r_2] \setminus \{0\}), \\
u(t, \pm 0) &= \dot{h}(t), \quad \theta(t, 0 \pm) = Q(t), & (t \geq 0), \\
& & (1.183) \\
m\ddot{h}(t) &= \left[ \frac{1}{v_0} \partial_x u \right] (t, 0) + f_3, & (t \geq 0), \\
\dot{Q}(t) &= \left[ \frac{1}{v_0} \partial_x \theta \right] (t, 0) + f_4, & (t \geq 0), \\
u(t, -r_1) &= u(t, r_2) = 0, \quad \partial_x \theta(t, -r_1) = \partial_x \theta(t, r_2) = 0, & (t \geq 0), \\
v(0, x) &= v_0(x), \quad u(0, x) = u_0(x), \quad \theta(0, x) = \theta_0(x), & x \in [-r_1, r_2] \setminus \{0\}, \\
h(0) &= h_0, \quad \dot{h}(0) = g_0.
\end{aligned}$$

We introduce the following spaces

$$\begin{aligned}
Z_1 &= W^{2,q}(\Omega) \cap W_0^{1,q}(-r_1, r_2), \quad Z_2 = \{\theta \in \times W^{2,q}(\Omega) \mid \partial_x \theta(-r_1) = \partial_x \theta(r_2) = 0\}, \\
Z &= W^{1,q}(\Omega) \times Z_1 \times Z_2, \quad X = W^{1,q}(\Omega) \times L^q(\Omega) \times L^q(\Omega), \quad U = \mathbb{R}^2.
\end{aligned}$$

Let  $L \in \mathcal{L}(Z, X)$ ,  $G \in \mathcal{L}(Z, U)$  and  $C \in \mathcal{L}(Z, U)$  are defined as follows

$$\begin{aligned}
L \begin{bmatrix} v \\ u \\ \theta \end{bmatrix} &= \begin{bmatrix} 0 & \partial_x & 0 \\ 0 & \partial_x \left( \frac{1}{v_0} \partial_x \right) & 0 \\ 0 & 0 & \partial_x \left( \frac{1}{v_0} \partial_x \right) \end{bmatrix} \begin{bmatrix} v \\ u \\ \theta \end{bmatrix}, \quad G \begin{bmatrix} v \\ u \\ \theta \end{bmatrix} = \begin{bmatrix} u(0) \\ \theta(0) \end{bmatrix}, \\
C \begin{bmatrix} v \\ u \\ \theta \end{bmatrix} &= \begin{bmatrix} m^{-1} \left[ \frac{1}{v_0} \partial_x u \right] (0) \\ \left[ \frac{1}{v_0} \partial_x \theta \right] (0) \end{bmatrix} \tag{1.184}
\end{aligned}$$

Let us introduce the unbounded operator  $(\mathcal{A}, D(\mathcal{A}))$  in  $X \times U$  by

$$D(\mathcal{A}) = \{(v, u, \theta, g, Q) \in Z \times U \mid G(v, u, \theta)^T = (g, Q)^T\} \tag{1.185}$$

and

$$\mathcal{A} \begin{pmatrix} v \\ u \\ \theta \\ g \\ Q \end{pmatrix} = \begin{pmatrix} L \begin{bmatrix} v \\ u \\ \theta \end{bmatrix} \\ C \begin{bmatrix} v \\ u \\ \theta \end{bmatrix} \end{pmatrix}. \quad (1.186)$$

Set  $\dot{h}(t) = g(t)$ . Then (1.183) can be written as

$$\frac{d}{dt} \begin{pmatrix} v \\ u \\ \theta \\ g \\ Q \end{pmatrix} = \mathcal{A} \begin{pmatrix} v \\ u \\ \theta \\ g \\ Q \end{pmatrix} + \begin{pmatrix} 0 \\ f_1 \\ f_2 \\ f_3 \\ f_4 \end{pmatrix}, \quad \begin{pmatrix} v(0) \\ u(0) \\ \theta(0) \\ g(0) \\ Q(0) \end{pmatrix} = \begin{pmatrix} v_0 \\ u_0 \\ \theta_0 \\ g_0 \\ Q_0 \end{pmatrix}. \quad (1.187)$$

**Proposition 1.47** *Let  $1 < q < \infty$  and  $v_0$  belongs to  $W^{1,q}(\Omega)$  such that  $v_0(y) > 0$  for all  $y \in [-r_1, r_2]$ . The operator  $(\mathcal{A}, D(\mathcal{A}))$  is  $\mathcal{R}$ -sectorial in  $X \times U$ , i.e., there exists  $\varepsilon \in (0, \pi/2)$  and  $\gamma_0 > 0$  such that*

$$\mathcal{R}_{\mathcal{L}(X \times U)} \{ \lambda(\lambda - \mathcal{A})^{-1} \mid \lambda \in \Sigma_{\varepsilon_0, \gamma_0} \} < \infty. \quad (1.188)$$

*Proof* Let us set  $X_1 = \text{Ker}G = \{(v, u, \theta) \in Z \mid u(0) = 0 = \theta(0)\}$ , and  $A = L|_{X_1}$ . We rewrite  $\mathcal{A}$  as  $\mathcal{A} = A_1 + B$ , where

$$A_1 = \begin{pmatrix} 0 & \partial_x & 0 \\ 0 & \frac{1}{v_0} \partial_{xx} & 0 \\ 0 & 0 & \frac{1}{v_0} \partial_{xx} \end{pmatrix}, \quad B = \begin{pmatrix} 0 & 0 & 0 \\ 0 & -\frac{\partial_x v_0}{v_0} \partial_x & 0 \\ 0 & 0 & -\frac{\partial_x v_0}{v_0} \partial_x \end{pmatrix} \quad (1.189)$$

By Denk et al. [12, Theorem 8.2], we first obtain that the operator  $A_1$  with  $D(A_1) = X_1$  is  $\mathcal{R}$ -sectorial in  $X \times U$ . Next, using Lemma 1.36, it is easy to see that the operator  $B$  with  $D(B) = D(A_1)$  satisfies the condition (1.125). Thus, by Proposition 1.18, we obtain  $\mathcal{A}$  is  $\mathcal{R}$ -sectorial in  $X \times U$ . Again, using Lemma 1.36 one can check that, the operator  $C$  satisfies the condition (1.136). Thus the  $\mathcal{R}$ -sectoriality of the operator  $(\mathcal{A}, D(\mathcal{A}))$  follows from Theorem 1.25.  $\square$

**Theorem 1.48** *Let  $1 < p, q < \infty$ . Then for every  $(v_0, u_0, \theta_0, g_0, Q_0) \in (Z, D(\mathcal{A}))_{1-1/p, p}$  and for every  $(f_1, f_2, f_3, f_4) \in L^p(0, T; L^q(\Omega)) \times L^p(0, T; L^q(\Omega)) \times$*



$L^p(0, T) \times L^p(0, T)$ , the system (1.183) admits a unique strong solution satisfying

$$\begin{aligned} & \|v\|_{W^{1,p}(0,T;W^{1,q}(\Omega))} + \|u\|_{W_{q,p}^{2,1}((0,T)\times\Omega)} + \|\theta\|_{W_{q,p}^{2,1}((0,T)\times\Omega)} + \|h\|_{W^{2,p}(0,T)} \\ & + \|\mathcal{Q}\|_{W^{1,p}(0,T)} \leq C(1 + e^{2\gamma_0 T}) \left( \|(v_0, u_0, \theta_0, g_0, \mathcal{Q}_0)\|_{(Z,D(\mathcal{A}))_{1-1/p,p}} \right. \\ & \left. + \|f_1\|_{L^p(0,T;L^q(\Omega))} + \|f_2\|_{L^p(0,T;L^q(\Omega))} + \|f_3\|_{L^p(0,T)} + \|f_4\|_{L^p(0,T)} \right), \end{aligned}$$

where the constant  $C$  is independent of time  $T$ .

Now we are in a position to get estimates required for fixed point argument. As before, at first we want to identify the space of initial conditions. We have the following lemma.

**Lemma 1.49** *Let  $p, q$  satisfy the condition (1.178). Let us assume that  $(v_0, u_0, \theta_0, g_0, \mathcal{Q}_0)$  belongs to  $(Z, D(\mathcal{A}))_{1-1/p,p}$ . Then  $(v_0, u_0, \theta_0, g_0, \mathcal{Q}_0)$  belongs to  $\mathcal{I}_{p,q,\Omega}^{cc}$ , where  $\mathcal{I}_{p,q,\Omega}^{cc}$  defined as in (1.180).*

*Proof* For proof we refer to [33, Sect. 4.3.3] and [2, Theorem 2.2].  $\square$

For  $T > 0$ , we define the space  $\mathcal{B}_T$  as follows

$$\begin{aligned} \mathcal{B}_T = & \left\{ (f_1, f_2, f_3, f_4) \in L^p(0, T; L^q(\Omega)) \times L^p(0, T; L^q(\Omega)) \times L^p(0, T) \times L^p(0, T) \mid \right. \\ & \left. \|f_1\|_{L^p(0,T;L^q(\Omega))} + \|f_2\|_{L^p(0,T;L^q(\Omega))} + \|f_3\|_{L^p(0,T)} + \|f_4\|_{L^p(0,T)} \leq 1 \right\}. \end{aligned} \quad (1.190)$$

**Proposition 1.50** *Let  $p, q$  satisfy the condition (1.178). Assume that  $(v_0, u_0, \theta_0, h_0, g_0, \mathcal{Q}_0)$  belongs to  $\mathcal{I}_{p,q,\Omega}^{cc}$ . Let  $M > 0$  be such that*

$$\|(v_0, u_0, \theta_0, h_0, g_0, \mathcal{Q}_0)\|_{\mathcal{I}_{p,q,\Omega}^{cc}} \leq M, \quad \frac{1}{M} \leq v_0(x) \leq M. \quad (1.191)$$

*Then for every  $(f_1, f_2, f_3, f_4) \in \mathcal{B}_T$ , the system (1.183) admits a unique strong solution on  $[0, T]$ . Moreover, there exist  $\tilde{T} \leq 1$  a constant  $C$ , both depending only on  $M$  such that*

$$\|v\|_{W^{1,p}(0,T_*;W^{1,q}(\Omega))} + \|v\|_{L^\infty(0,T_*;W^{1,q}(\Omega))} \leq C, \quad (1.192)$$

$$\frac{1}{C} \leq v(t, x) \leq C, \quad t \in (0, \tilde{T}), x \in (-r_1, r_2) \quad (1.193)$$

$$\|u\|_{W_{q,p}^{2,1}((0,T_*)\times\Omega)} + \|\theta\|_{W_{q,p}^{2,1}((0,T_*)\times\Omega)} \leq C, \quad (1.194)$$

$$\|u\|_{L^\infty(0,T_*;W^{1,q}(\Omega))} + \|\theta\|_{L^\infty(0,T_*;W^{1,q}(\Omega))} \leq C, \quad (1.195)$$

$$\|u\|_{L^p(0,T_*;L^\infty(\Omega))} + \|\theta\|_{L^p(0,T_*;L^\infty(\Omega))} \leq CT_*^{(2-s)/2p}, \quad s \in (1/q, 1), \quad (1.196)$$

$$\|\partial_x u\|_{L^p(0,T_*;L^\infty(\Omega))} + \|\partial_x \theta\|_{L^p(0,T_*;L^\infty(\Omega))} \leq CT_*^{(1-s)/2p}, \quad s \in (1/q, 1), \quad (1.197)$$

holds for all  $T_* \in (0, \tilde{T})$ .

*Proof* From Theorem 1.48, there exists a constant  $C$  depending only on  $M$  such that

$$\|v\|_{W^{1,p}(0,T;W^{1,q}(\Omega))} + \|u\|_{W_{q,p}^{2,1}((0,T) \times \Omega)} + \|\theta\|_{W_{q,p}^{2,1}((0,T) \times \Omega)} \leq C, \quad T_* \in (0, 1].$$

Since  $1 < q < \infty$ , we also have

$$\|v\|_{W^{1,q}(0,T_*;L^\infty(\Omega))} \leq C\|v\|_{W^{1,p}(0,T;W^{1,q}(\Omega))} \leq C, \quad T_* \in (0, 1].$$

Notice that, for every  $T_* \in (0, 1]$

$$\sup_{t \in (0, T_*)} \|v(t, \cdot) - v_0\|_{L^\infty(\Omega)} \leq T_*^{1/p'} \|v\|_{W^{1,q}(0,T_*;L^\infty(\Omega))} \leq CT_*^{1/p'}. \quad (1.198)$$

Thus there exist  $\tilde{T} \leq 1$  a constant  $C$ , both depending only on  $M$  such that

$$\frac{1}{C} \leq v(t, x) \leq C, \quad t \in (0, \tilde{T}), \quad x \in (-r_1, r_2).$$

To prove (1.195), note that  $W^{1,q}(\Omega) \hookrightarrow B_{q,p}^{2(1-1/p)}(\Omega)$  provided  $2 < p < \infty$ . Thus, Proposition 1.34 yields (1.195). In view of (1.150), estimate (1.195) also holds when  $p = q = 2$ . Proof of other estimates are similar to proof of estimates in Proposition 1.42.  $\square$

**Lemma 1.51** *Let  $p, q$  satisfy the condition (1.178). For  $T_* \in (0, \tilde{T}]$ , where  $\tilde{T}$  is a constant in Proposition 1.50, let  $\mathcal{B}_{T_*}$  be the ball defined in (1.190). Let  $(v_0, u_0, \theta_0, h_0, g_0, Q_0)$  and  $M$  as in Proposition 1.50. Given  $(f_1, f_2, f_3, f_4) \in \mathcal{B}_{T_*}$ , let  $(v, u, \theta, h, Q)$  be the solution of (1.183) on  $[0, T_*]$  constructed in Proposition 1.50.*

*Then there exist a constant  $C > 0$  depending only on  $M$  and a constant  $\delta$  depending only on  $p$  and  $q$ , such that*

$$\begin{aligned} & \|\mathcal{F}_1(v, u, \theta)\|_{L^p(0,T_*;L^q(\Omega))} + \|\mathcal{F}_2(v, u, \theta)\|_{L^p(0,T_*;L^q(\Omega))} \\ & + \|\mathcal{F}_3(v, u, \theta)\|_{L^p(0,T_*)} + \|\mathcal{F}_4(v, u, \theta)\|_{L^p(0,T_*)} \leq CT_*^\delta \end{aligned} \quad (1.199)$$

where  $\mathcal{F}_1, \mathcal{F}_2, \mathcal{F}_3$  and  $\mathcal{F}_4$  have been defined in (1.182).

*Proof* Using the estimates (1.192)–(1.197) and (1.198), we obtain the following estimate of  $\mathcal{F}_1$

$$\begin{aligned}
& \|\mathcal{F}_1(v, u, \theta)\|_{L^p(0, T_*; L^q(\Omega))} \\
&= \left\| \partial_x \left( \left( \frac{1}{v} - \frac{1}{v_0} \right) \partial_x u \right) \right\|_{L^p(0, T_*; L^q(\Omega))} + \left\| \partial_x \left( \frac{\theta}{v} \right) \right\|_{L^p(0, T_*; L^q(\Omega))} \\
&\leq \left\| \frac{v - v_0}{v v_0} \right\|_{L^\infty((0, T) \times \Omega)} \|\partial_{xx} u\|_{L^p(0, T_*; L^q(\Omega))} \\
&\quad + \left( \left\| \frac{\partial_x v}{v^2} - \frac{\partial_x v_0}{v_0^2} \right\|_{L^\infty(0, T_*; L^p(\Omega))} \right) \|\partial_x u\|_{L^p(0, T_*; L^\infty(\Omega))} \\
&\quad + \left\| \frac{1}{v} \right\|_{L^\infty(0, T_*; L^q(\Omega))} \|\partial_x \theta\|_{L^p(0, T_*; L^\infty(\Omega))} + \left\| \frac{\partial_x v}{v^2} \right\|_{L^\infty(0, T_*; L^q(\Omega))} \|\theta\|_{L^p(0, T_*; L^\infty(\Omega))} \\
&\leq C(T_*^{1/p'} + T_*^{(2-s)/2p} + T_*^{(1-s)/2p}), \quad s \in (1/q, 1).
\end{aligned}$$

Estimates of first and third term of  $\mathcal{F}_2$  are similar to the above estimate. Using (1.193), (1.194) and (1.197), it is easy to see that the second term of  $\mathcal{F}_2$  satisfy the following estimate

$$\begin{aligned}
& \left\| \frac{1}{v} (\partial_x u)^2 \right\|_{L^p(0, T_*; L^q(\Omega))} \\
&\leq \left\| \frac{1}{v} \right\|_{L^\infty((0, T) \times \Omega)} \|\partial_x u\|_{L^p(0, T_*; L^\infty(\Omega))} \|\partial_x u\|_{L^\infty(0, T_*; L^q(\Omega))} \\
&\leq C T_*^{(1-s)/2p}, \quad s \in (1/q, 1).
\end{aligned}$$

Thus there exist a constant  $C > 0$  depending only on  $M$  and a constant  $\delta$  depending only on  $p$  and  $q$ , such that

$$\|\mathcal{F}_2(v, u, \theta)\|_{L^p(0, T_*; L^q(\Omega))} \leq T_*^\delta. \quad (1.200)$$

Notice that

$$\left\| \left[ \left( \frac{1}{v} - \frac{1}{v_0} \right) \partial_x u - \frac{\theta}{v} \right] (\cdot, 0) \right\|_{L^p(0, T_*)} \leq C \left\| \left( \frac{1}{v} - \frac{1}{v_0} \right) \partial_x u - \frac{\theta}{v} \right\|_{L^p(0, T_*; W^{1,q}(\Omega))}.$$

Therefore, from the estimate of  $\mathcal{F}_1$  we obtain

$$\|\mathcal{F}_3(v, u, \theta)\|_{L^p(0, T_*)} \leq T_*^\delta, \quad (1.201)$$

where  $C > 0$  depends only on  $M$  and  $\delta$  depends only on  $p$  and  $q$ . The estimate of  $\mathcal{F}_4$  is similar.  $\square$

**Lemma 1.52** *Let  $p, q$  satisfy the condition (1.178). For  $T_* \in (0, \tilde{T}]$ , where  $\tilde{T}$  is a constant in Proposition 1.50, let  $\mathcal{B}_{T_*}$  be the ball defined in (1.190). Let  $(v_0, u_0, \theta_0, h_0, g_0, Q_0)$  and  $M$  as in Proposition 1.50. Given  $(f_1^i, f_2^i, f_3^i, f_4^i) \in \mathcal{B}_{T_*}$ ,  $i = 1, 2$ , let  $(v^i, u^i, \theta^i, h^i, Q^i)$  be the solution of (1.183) on  $[0, T_*]$  constructed in Proposition 1.50.*

*Then there exist a constant  $C > 0$  depending only on  $M$  and a constant  $\delta$  depending only on  $p$  and  $q$ , such that*

$$\begin{aligned} & \|\mathcal{F}_1(v^1, u^1, \theta^2) - \mathcal{F}_1(v^2, u^2, \theta^2)\|_{L^p(0, T_*; L^q(\Omega))} \\ & \quad + \|\mathcal{F}_2(v, u, \theta) - \mathcal{F}_2(v^2, u^2, \theta^2)\|_{L^p(0, T_*; L^q(\Omega))} \\ & + \|\mathcal{F}_3(v, u, \theta) - \mathcal{F}_3(v^2, u^2, \theta^2)\|_{L^p(0, T_*)} + \|\mathcal{F}_4(v, u, \theta) - \mathcal{F}_4(v^2, u^2, \theta^2)\|_{L^p(0, T_*)} \\ & \leq CT_*^\delta \left( \|f_1^1 - f_1^2\|_{L^p(0, T_*; L^q(\Omega))} + \|f_2^1 - f_2^2\|_{L^p(0, T_*; L^q(\Omega))} \right. \\ & \quad \left. + \|f_3^1 - f_3^2\|_{L^p(0, T_*)} + \|f_4^1 - f_4^2\|_{L^p(0, T_*)} \right) \end{aligned} \quad (1.202)$$

where  $\mathcal{F}_1, \mathcal{F}_2, \mathcal{F}_3$  and  $\mathcal{F}_4$  have been defined in (1.182).

*Proof of Theorem 1.46* We consider the map

$$\left\{ \begin{array}{l} \mathcal{N} : \mathcal{B}_{T_*} \rightarrow \mathcal{B}_{T_*}, \\ \left[ \begin{array}{c} f_1 \\ f_2 \\ f_3 \\ f_4 \end{array} \right] \mapsto \left[ \begin{array}{c} \mathcal{F}_1 \\ \mathcal{F}_2 \\ \mathcal{F}_3 \\ \mathcal{F}_4 \end{array} \right], \end{array} \right.$$

where  $\mathcal{F}_1, \mathcal{F}_2, \mathcal{F}_3$  and  $\mathcal{F}_4$  have been defined in (1.182). From Lemmas 1.51 and 1.52 and by choosing  $T_* \leq \tilde{T}$ , small enough it is easy to see that  $\mathcal{N}$  is a strict contraction of  $\mathcal{B}_{T_*}$ , with a Lipschitz constant  $\frac{1}{2}$ . This implies the existence and uniqueness result.

### 1.4.4 Motion of a Solid in a Compressible Fluid

In this section, we prove local in time existence and uniqueness of solution for the system (1.110). For every  $1 < p < \infty$  and  $1 < q < \infty$ , the space  $\mathcal{I}_{p,q,\Omega_F(0)}$  is

defined by

$$\begin{aligned} \mathcal{I}_{p,q,\Omega_F(0)} = \left\{ (\rho_0, u_0, \vartheta_0, \ell_0, \omega_0) \mid \rho_0 \in W^{1,q}(\Omega_F(0)) \cap L^\infty(\Omega_F(0)), \right. \\ \left. u_0 \in B_{q,p}^{2(1-1/p)}(\Omega_F(0))^3, g_0 \in \mathbb{R}^3, \omega_0 \in \mathbb{R}^3, \min_{y \in \Omega_F(0)} \rho_0(y) > 0 \right\}, \end{aligned} \quad (1.203)$$

and

$$\begin{aligned} \|(\rho_0, u_0, \vartheta_0, \ell_0, \omega_0)\|_{\mathcal{I}_{p,q,\Omega_F(0)}} &= \|\rho_0\|_{W^{1,q}(\Omega_F(0))} + \|u_0\|_{B_{q,p}^{2(1-1/p)}(\Omega_F(0))} \\ &\quad + \|g_0\|_{\mathbb{R}^3} + \|\omega_0\|_{\mathbb{R}^3}. \end{aligned}$$

We now state our main result.

**Theorem 1.53** *Let  $2 < p < \infty$  and  $3 < q < \infty$ . Assume that  $(\rho_0, u_0, g_0, \omega_0)$  belongs to  $\mathcal{I}_{p,q,\Omega_F(0)}$  satisfying the compatibility condition*

$$u_0 = 0 \text{ on } \partial\Omega, \quad u_0 = g_0 + \omega_0 \times y \text{ on } \partial\Omega_S(0). \quad (1.204)$$

Let  $M > 0$  be such that

$$\|(\rho_0, u_0, g_0, \omega_0)\|_{\mathcal{I}_{p,q,\Omega_F(0)}} \leq M, \quad \frac{1}{M} \leq \rho_0(x) \leq M \text{ for } x \in \Omega_F(0). \quad (1.205)$$

Then, there exists  $T > 0$  such that the system (1.110) admits a unique strong solution

$$\begin{aligned} \rho &\in W^{1,p}(0, T; W^{1,q}(\Omega_F(\cdot))) \cap C([0, T]; W^{1,q}(\Omega_F(\cdot))), \\ u &\in L^p(0, T; W^{2,q}(\Omega_F(\cdot))^3) \cap W^{1,p}(0, T; L^q(\Omega_F(\cdot))^3) \cap C([0, T]; B_{q,p}^{2(1-1/p)}(\Omega_F(\cdot))^3), \\ h &\in W^{2,p}(0, T; \mathbb{R}^3), \quad \omega \in W^{1,p}(0, T; \mathbb{R}^3). \end{aligned}$$

Moreover, there exists a constant  $M_T > 0$  such that  $\frac{1}{M_T} \leq \rho(t, x) \leq M_T$  for all  $t \in (0, T), x \in \Omega_F(t)$ .

As before, we first prove our result for a equivalent system in a fixed spatial domain.

**Theorem 1.54** *Let  $2 < p < \infty$  and  $3 < q < \infty$ . Assume that  $(\rho_0, u_0, g_0, \omega_0)$  belongs to  $\mathcal{I}_{p,q,\Omega_F(0)}$  such that (1.204)–(1.205) holds. Then, there exists  $T > 0$  such that the system (1.115)–(1.120) admits a unique strong solution*

$$\begin{aligned} \tilde{\rho} &\in W^{1,p}(0, T; W^{1,q}(\Omega_F(0))) \cap C([0, T]; W^{1,q}(\Omega_F(0))), \\ \tilde{u} &\in L^p(0, T; W^{2,q}(\Omega_F(0))^3) \cap W^{1,p}(0, T; L^q(\Omega_F(0))^3) \cap C([0, T]; B_{q,p}^{2(1-1/p)}(\Omega_F(0))^3), \\ \tilde{g} &\in W^{1,p}(0, T; \mathbb{R}^3), \quad \tilde{\omega} \in W^{1,p}(0, T; \mathbb{R}^3). \end{aligned}$$

Moreover, there exists a constant  $M_T > 0$ , such that  $\frac{1}{M_T} \leq \tilde{\rho}(t, y) \leq M_T$ , for all  $t \in (0, T), y \in \Omega_F(0)$ .

We start with the following linear system

$$\begin{aligned}
\partial_t \tilde{\rho} + \rho_0 \operatorname{div} \tilde{u} &= f_1, \quad \text{in } (0, T) \times \Omega_F(0), \\
\partial_t \tilde{u} - \frac{\mu}{\rho_0} \Delta \tilde{u} - \frac{\alpha + \mu}{\rho_0} \nabla(\operatorname{div} \tilde{u}) &= f_2 \quad \text{in } (0, T) \times \Omega_F(0), \\
\tilde{u} &= 0 \quad \text{on } (0, T) \times \partial\Omega, \quad \tilde{u} = g + \omega \times y \quad \text{on } (0, T) \times \partial\Omega_S(0), \\
m \frac{d}{dt} \tilde{\ell} &= - \int_{\Omega_S(0)} (\mu \nabla \tilde{u} + \mu \nabla \tilde{u}^\top + \alpha \operatorname{div} \tilde{u} l) n \, d\gamma + f_3, \quad t \in (0, T), \\
J(0) \frac{d}{dt} \tilde{\omega} &= - \int_{\Omega_S(0)} y \times (\mu \nabla \tilde{u} + \mu \nabla \tilde{u}^\top + \alpha \operatorname{div} \tilde{u} l) n + f_4, \quad t \in (0, T) \\
\tilde{\rho}(0) &= \rho_0, \quad \tilde{u}(0) = u_0, \quad \text{in } \Omega_F(0), \\
\tilde{g}(0) &= g_0, \quad \tilde{\omega}_0 = \omega_0.
\end{aligned} \tag{1.206}$$

We introduce the following spaces

$$\begin{aligned}
Z_1 &= \left\{ z \in W^{2,q}(\Omega_F(0))^3 \mid z = 0 \text{ on } \partial\Omega, \exists \ell, k \in \mathbb{R}^3 \text{ such that} \right. \\
&\quad \left. z = \ell + k \times y \text{ on } \partial\Omega_S(0) \right\} \\
Z &= W^{1,q}(\Omega) \times Z_1, \quad X = W^{1,q}(\Omega) \times L^q(\Omega)^3, \quad U = \mathbb{R}^6.
\end{aligned}$$

Let  $L \in \mathcal{L}(Z, X)$ ,  $G \in \mathcal{L}(Z, U)$  and  $C \in \mathcal{L}(Z, U)$  are defined as follows

$$\begin{aligned}
L \begin{bmatrix} \tilde{\rho} \\ \tilde{u} \end{bmatrix} &= \begin{bmatrix} 0 \\ \frac{\mu}{\rho_0} \Delta + \frac{\rho_0 \operatorname{div}}{\rho_0} + \frac{\alpha + \mu}{\rho_0} \nabla(\operatorname{div}) \end{bmatrix} \begin{bmatrix} \tilde{\rho} \\ \tilde{u} \end{bmatrix}, \quad G \begin{bmatrix} \tilde{\rho} \\ \tilde{u} \end{bmatrix} = \begin{bmatrix} \ell \\ k \end{bmatrix}, \\
C \begin{bmatrix} \tilde{\rho} \\ \tilde{u} \end{bmatrix} &= \begin{bmatrix} -m^{-1} \int_{\Omega_S(0)} (\mu \nabla \tilde{u} + \mu \nabla \tilde{u}^\top + \alpha \operatorname{div} \tilde{u} l) n \, d\gamma \\ -J(0)^{-1} \int_{\Omega_S(0)} y \times (\mu \nabla \tilde{u} + \mu \nabla \tilde{u}^\top + \alpha \operatorname{div} \tilde{u} l) n \end{bmatrix} \tag{1.207}
\end{aligned}$$

Let us introduce the unbounded operator  $(\mathcal{A}, D(\mathcal{A}))$  in  $X \times U$  by

$$D(\mathcal{A}) = \{ (\tilde{\rho}, \tilde{u}, \tilde{g}, \tilde{\omega}) \in Z \times U \mid G(\tilde{\rho}, \tilde{u})^T = (\tilde{g}, \tilde{\omega})^T \} \tag{1.208}$$

and

$$\mathcal{A} \begin{pmatrix} \widetilde{\rho} \\ \widetilde{u} \\ \widetilde{g} \\ \widetilde{\omega} \end{pmatrix} = \begin{pmatrix} L \begin{bmatrix} \widetilde{\rho} \\ \widetilde{u} \end{bmatrix} \\ C \begin{bmatrix} \widetilde{\rho} \\ \widetilde{u} \end{bmatrix} \end{pmatrix}. \quad (1.209)$$

Then (1.206) can be written as

$$\frac{d}{dt} \begin{pmatrix} \widetilde{\rho} \\ \widetilde{u} \\ \widetilde{g} \\ \widetilde{\omega} \end{pmatrix} = \mathcal{A} \begin{pmatrix} \widetilde{\rho} \\ \widetilde{u} \\ \widetilde{g} \\ \widetilde{\omega} \end{pmatrix} + \begin{pmatrix} f_1 \\ f_2 \\ f_3 \\ f_4 \end{pmatrix}, \quad \begin{pmatrix} \widetilde{\rho}(0) \\ \widetilde{u}(0) \\ \widetilde{g}(0) \\ \widetilde{\omega}(0) \end{pmatrix} = \begin{pmatrix} \rho_0 \\ u_0 \\ g_0 \\ \omega_0 \end{pmatrix}. \quad (1.210)$$

**Proposition 1.55** *Let  $3 < q < \infty$  and  $\rho_0$  belongs to  $W^{1,q}(\Omega_F(0))$  such that  $\rho_0(y) > 0$  for all  $y \in \Omega_F(0)$ . The operator  $(\mathcal{A}, D(\mathcal{A}))$  is  $\mathcal{R}$ -sectorial in  $X \times U$ , i.e., there exists  $\varepsilon \in (0, \pi/2)$  and  $\gamma_0 > 0$  such that*

$$\mathcal{R}_{\mathcal{L}(X \times U)} \{ \lambda(\lambda - \mathcal{A})^{-1} \mid \lambda \in \Sigma_{\varepsilon_0, \gamma_0} \} < \infty. \quad (1.211)$$

*Proof* The proof is similar to the proof of Proposition 1.47.  $\square$

As a consequence of the above proposition and Theorem 1.32 we obtain the following theorem

**Theorem 1.56** *Let  $3 < q < \infty$  and  $1 < p < \infty$ . Then for every  $(\rho_0, u_0, g_0, \omega_0) \in (Z, D(\mathcal{A}))_{1-1/p,p}$  and for every  $(f_1, f_2, f_3, f_4) \in L^p(0, T; L^q(\Omega_F(0))) \times L^p(0, T; L^q(\Omega_F(0))) \times L^p(0, T) \times L^p(0, T)$ , the system (1.206) admits a unique strong solution satisfying*

$$\begin{aligned} & \|\widetilde{\rho}\|_{W^{1,p}(0,T;W^{1,q}(\Omega_F(0)))} + \|\widetilde{u}\|_{W_{q,p}^{2,1}((0,T) \times \Omega_F(0))} + \|\widetilde{g}\|_{W^{1,p}(0,T)} + \|\widetilde{\omega}\|_{W^{1,p}(0,T)} \\ & \leq C(1 + e^{2\gamma_0 T}) \left( \|(\rho_0, u_0, g_0, \omega_0)\|_{(Z, D(\mathcal{A}))_{1-1/p,p}} + \|f_1\|_{L^p(0,T;L^q(\Omega_F(0)))} \right. \\ & \quad \left. + \|f_2\|_{L^p(0,T;L^q(\Omega_F(0)))} + \|f_3\|_{L^p(0,T)} + \|f_4\|_{L^p(0,T)} \right), \end{aligned}$$

where the constant  $C$  is independent of time  $T$ .

Now we characterize the space of initial conditions. As before, using [33, Sect. 4.3.3] and [2, Theorem 2.2] we obtain the following characterization of the initial conditions.

**Lemma 1.57** *Let  $3 < q < \infty$  and  $2 < p < \infty$ . Let us assume that  $(\rho_0, u_0, g_0, \omega_0)$  belongs to  $(Z, D(\mathcal{A}))_{1-1/p,p}$ . Then  $(\rho_0, u_0, g_0, \omega_0)$  belongs to  $\mathcal{I}_{p,q,\Omega_F(0)}$ , where  $\mathcal{I}_{p,q,\Omega_F(0)}$ , defined as in (1.203) satisfying the compatibility condition (1.204).*

For  $T > 0$ , we define the space  $\mathcal{B}_T$  as follows

$$\begin{aligned} \mathcal{B}_T = \Big\{ (f_1, f_2, f_3, f_4) \in L^p(0, T; L^q(\Omega_F(0))) \times L^p(0, T; L^q(\Omega_F(0))) \times L^p(0, T) \times \\ L^p(0, T) \mid \|f_1\|_{L^p(0, T; L^q(\Omega_F(0)))} + \|f_2\|_{L^p(0, T; L^q(\Omega_F(0)))} \\ + \|f_3\|_{L^p(0, T)} + \|f_4\|_{L^p(0, T)} \leq 1 \Big\}. \end{aligned} \quad (1.212)$$

**Proposition 1.58** *Let  $3 < q < \infty$  and  $2 < p < \infty$ . Assume that  $(\rho_0, u_0, g_0, \omega_0)$  belongs to  $\mathcal{I}_{p, q, \Omega_F(0)}$  such that (1.204)–(1.205) holds. Then for every  $(f_1, f_2, f_3, f_4) \in \mathcal{B}_T$ , the system (1.206) admits a unique strong solution  $[0, T]$ . Moreover, there exists a constant  $C$ , depending only on  $M$  such that*

$$\|\tilde{\rho}\|_{W^{1,p}(0, T_*; W^{1,q}(\Omega_F(0)))} + \|\tilde{u}\|_{W_{q,p}^{2,1}((0, T_*) \times \Omega_F(0))} \leq C \quad (1.213)$$

$$\|\tilde{g}\|_{W^{1,p}(0, T_*)} + \|\tilde{\omega}\|_{W^{1,p}(0, T_*)} \leq C, \quad (1.214)$$

$$\|\tilde{\rho} - \rho_0\|_{L^\infty(0, T_*; W^{1,q}(\Omega_F(0)))} \leq CT_*^{1/p'}, \quad \|\tilde{\rho}\|_{L^p(0, T_*; W^{1,q}(\Omega_F(0)))} \leq CT_*^{1/p}, \quad (1.215)$$

$$\|\tilde{u}\|_{L^\infty(0, T_*; W^{1,q}(\Omega_F(0)))} + \|\tilde{g}\|_{L^\infty(0, T_*)} + \|\tilde{\omega}\|_{L^\infty(0, T_*)} \leq C, \quad (1.216)$$

$$\|u\|_{L^p(0, T_*; L^\infty(\Omega_F(0)))} \leq CT_*^{(2-s)/2p}, \quad s \in (3/q, 1), \quad (1.217)$$

$$\|\nabla \tilde{u}\|_{L^p(0, T_*; L^\infty(\Omega_F(0)))}, \|\operatorname{div} \tilde{u}\|_{L^p(0, T_*; L^\infty(\Omega_F(0)))} \leq CT_*^{(1-s)/2p}, \quad s \in (3/q, 1), \quad (1.218)$$

$$\|\tilde{g}\|_{L^p(0, T_*)} + \|\tilde{\omega}\|_{L^p(0, T_*)} \leq CT_*^{1/p} \quad (1.219)$$

holds for all  $T_* \in (0, 1]$ .

*Proof* The proof is similar to the proof of Proposition 1.50. The main difference here is  $W^{1,q}(\Omega_F(0)) \hookrightarrow L^\infty(\Omega_F(0))$  if  $3 < q < \infty$ .  $\square$

Now we proof several lemmas required for fixed point argument.

**Lemma 1.59** *Let  $3 < q < \infty$  and  $2 < p < \infty$ . For  $T_* \in (0, 1]$ , let  $\mathcal{B}_{T_*}$  be the ball defined in (1.212). Let  $(\rho_0, u_0, \vartheta_0, a_0, \omega_0)$  and  $M$  as in Proposition 1.58. Given  $(f_1, f_2, f_3, f_4) \in \mathcal{B}_{T_*}$ , let  $(\tilde{\rho}, \tilde{u}, \tilde{g}, \tilde{\omega})$  be the solution of (1.206) constructed in Proposition 1.58. Let  $Q$  be defined as in (1.116). Then there exists a constant  $C > 0$  depending only on  $M$  such that*

$$\|Q\|_{L^\infty(0, T_*)} \leq C, \quad \|Q^T\|_{L^\infty(0, T_*)} \leq C, \quad (1.220)$$

$$\|Q - I\|_{L^\infty(0, T_*)} \leq CT_*^{1/p'}, \quad \|Q^T - I\|_{L^\infty(0, T_*)} \leq CT_*^{1/p'}, \quad (1.220)$$

$$\|\partial_t Q\|_{L^\infty(0, T_*)} \leq C. \quad (1.221)$$



*Proof* From (1.116) and Proposition 1.58, we have

$$|Q(t)| \leq 1 + C \int_0^t |Q(s)| ds, \quad \text{for all } t \in (0, T_*].$$

By Gronwall's lemma, we have

$$|Q(t)| \leq e^{Ct} \leq e^C \quad \text{for all } t \in (0, T_*].$$

Similarly, from (1.116) and Proposition 1.58, we have

$$\|Q - I\|_{L^\infty(0, T_*)} \leq \|Q\|_{L^\infty(0, T_*)} \int_0^{T_*} |(\tilde{\omega}(s) \times I)| ds \leq CT_*^{1/p'}.$$

□

**Lemma 1.60** *Let  $3 < q < \infty$  and  $2 < p < \infty$ . For  $T_* \in (0, 1]$ , let  $\mathcal{B}_{T_*}$  be the ball defined in (1.212). Let  $(\rho_0, u_0, \vartheta_0, a_0, \omega_0)$  and  $M$  as in Proposition 1.58. Given  $(f_1, f_2, f_3, f_4) \in \mathcal{B}_{T_*}$ , let  $(\tilde{\rho}, \tilde{u}, \tilde{g}, \tilde{\omega})$  be the solution of (1.206) constructed in Proposition 1.58. Let  $X$  be defined as in (1.117). Then there exists a constant  $C > 0$ , depending only on  $M$  such that*

$$\|J_X - I\|_{L^\infty((0, T_*) \times \Omega_F(0))} \leq CT_*^{1/p'}. \quad (1.222)$$

Moreover, there exists  $\tilde{T} \leq 1$  such that

$$\|J_X - I\|_{L^\infty((0, T_*) \times \Omega_F(0))} \leq \frac{1}{2}, \quad (T_* \in (0, \tilde{T}]). \quad (1.223)$$

*Proof* From the definition of  $X$  and Proposition 1.58, we obtain

$$\sup_{t \in (0, T_*)} \|J_X(t, \cdot) - I\|_{W^{1,q}(\Omega_F(0))} \leq C \int_0^{T_*} \|\nabla \tilde{u}\|_{W^{1,q}(\Omega_F(0))} \leq CT_*^{1/p'}.$$

Therefore

$$\|J_X - I\|_{L^\infty((0, T_*) \times \Omega_F(0))} \leq C \|J_X - I\|_{L^\infty(0, T_*; W^{1,q}(\Omega_F(0)))} \leq CT_*^{1/p'}.$$

□

**Lemma 1.61** *Let  $3 < q < \infty$  and  $2 < p < \infty$ . For  $T_* \in (0, \tilde{T}]$ , where  $\tilde{T}$  is the constant in Lemma 1.60, let  $\mathcal{B}_{T_*}$  be the ball defined in (1.212). Let  $(\rho_0, u_0, \vartheta_0, a_0, \omega_0)$  and  $M$  as in Proposition 1.58. Given  $(f_1, f_2, f_3, f_4) \in \mathcal{B}_{T_*}$ , let  $(\tilde{\rho}, \tilde{u}, \tilde{g}, \tilde{\omega})$  be the solution of (1.206) constructed in Proposition 1.58. Let  $X$  be defined as in (1.117).*

Then there exists a constant  $C > 0$  depending only on  $M$  such that

$$\begin{aligned}
& \|J_X\|_{W^{1,p}(0,T_*;W^{1,q}(\Omega_F(0)))} + \|J_X\|_{L^\infty(0,T_*;W^{1,q}(\Omega_F(0)))} \leq C, \\
& \|\operatorname{cof}J_X\|_{W^{1,p}(0,T_*;W^{1,q}(\Omega_F(0)))} + \|\operatorname{cof}J_X\|_{L^\infty(0,T_*;W^{1,q}(\Omega_F(0)))} \leq C \\
& \|\det J_X\|_{W^{1,p}(0,T_*;W^{1,q}(\Omega_F(0)))} + \|\det J_X\|_{L^\infty(0,T_*;W^{1,q}(\Omega_F(0)))} \leq C \\
& \|J_Y\|_{W^{1,p}(0,T_*;W^{1,q}(\Omega_F(0)))} + \|J_Y\|_{L^\infty(0,T_*;W^{1,q}(\Omega_F(0)))} \leq C, \tag{1.224}
\end{aligned}$$

*Proof* The estimate of  $J_X$  in  $L^\infty(0, T_*; W^{1,q}(\Omega_F(0)))$  norm follows from Lemma 1.60. Next we have,

$$\partial_r J_X = Q \nabla \tilde{u}.$$

Therefore  $\partial_r J_X \in L^p(0, T_*; W^{1,q}(\Omega_F(0)))$  and the estimate follows. The estimates of  $\operatorname{cof}J_X$  and  $\det J_X$  follows from the fact that  $W^{1,p}(0, T_*; W^{1,q}(\Omega_F(0)))$  and  $L^\infty(0, T_*; W^{1,q}(\Omega_F(0)))$  are algebras for  $p > 2$  and  $q > 3$ . In order to estimate the norms of  $J_Y$  we use the following relation

$$J_Y = \frac{1}{\det J_X} \operatorname{cof} J_X.$$

□

**Lemma 1.62** *Let  $3 < q < \infty$  and  $2 < p < \infty$ . For  $T_* \in (0, \tilde{T}]$ , where  $\tilde{T}$  is the constant in Lemma 1.60, let  $\mathcal{B}_{T_*}$  be the ball defined in (1.212). Let  $(\rho_0, u_0, \vartheta_0, a_0, \omega_0)$  and  $M$  as in Proposition 1.58. Given  $(f_1, f_2, f_3, f_4) \in \mathcal{B}_{T_*}$ , let  $(\tilde{\rho}, \tilde{u}, \tilde{g}, \tilde{\omega})$  be the solution of (1.206) constructed in Proposition 1.58. Let  $\tilde{\mathcal{F}}_1$  be defined as in (1.118). Then there exists a constant  $C > 0$  depending only on  $M$  such that*

$$\|\mathcal{F}_1\|_{L^p(0,T_*;W^{1,q}(\Omega_F(0)))} \leq CT_*^{1/p'}. \tag{1.225}$$

*Proof* Let us recall

$$\mathcal{F}_1 = -(\tilde{\rho} - \rho_0) \operatorname{div} \tilde{u} - \tilde{\rho}(Q - I) \nabla \tilde{u} : J_Y^\top - \tilde{\rho} \nabla \tilde{u} : (J_Y^\top - I).$$

Notice that  $W^{1,q}(\Omega_F(0))$  is an algebra for  $q > 3$ . Therefore, using Proposition 1.58, Lemmas 1.59 and 1.61 we estimate the first term of  $\mathcal{F}_1$  as follows

$$\begin{aligned}
& \|(\tilde{\rho} - \rho_0) \operatorname{div} \tilde{u}\|_{L^p(0,T_*;W^{1,q}(\Omega_F(0)))} \\
& \leq C \|\tilde{\rho} - \rho_0\|_{L^\infty(0,T_*;W^{1,q}(\Omega_F(0)))} \|\operatorname{div} \tilde{u}\|_{L^p(0,T_*;W^{1,q}(\Omega_F(0)))} \\
& \leq CT_*^{1/p'}.
\end{aligned}$$

Similarly, the second term of  $\mathcal{F}_1$  can be estimated as follows

$$\begin{aligned}
& \|\widetilde{\rho}(Q - I)\nabla\widetilde{u} : J_Y^\top\|_{L^p(0, T_*; W^{1,q}(\Omega_F(0)))} \\
& \leq C\|\widetilde{\rho}\|_{L^\infty(0, T_*; W^{1,q}(\Omega_F(0)))}\|Q - I\|_{L^\infty(0, T_*)} \\
& \quad \|\widetilde{u}\|_{L^p(0, T_*; W^{2,q}(\Omega_F(0)))}\|J_Y^\top\|_{L^\infty(0, T_*; W^{1,q}(\Omega_F(0)))} \\
& \leq CT_*^{1/p'}.
\end{aligned}$$

The last term of  $\mathcal{F}_1$  satisfies the following estimate

$$\begin{aligned}
& \|\widetilde{\rho}\nabla\widetilde{u} : (J_Y^\top - I)\|_{L^p(0, T_*; W^{1,q}(\Omega_F(0)))} \\
& \leq C\|\widetilde{\rho}\|_{L^\infty(0, T_*; W^{1,q}(\Omega_F(0)))}\|\widetilde{u}\|_{L^p(0, T_*; W^{2,q}(\Omega_F(0)))}\|J_Y^\top - I\|_{L^\infty(0, T_*; W^{1,q}(\Omega_F(0)))} \\
& \leq CT_*^{1/p'}.
\end{aligned}$$

□

**Lemma 1.63** *Let  $3 < q < \infty$  and  $2 < p < \infty$ . For  $T_* \in (0, \widetilde{T}]$ , where  $\widetilde{T}$  is the constant in Lemma 1.60, let  $\mathcal{B}_{T_*}$  be the ball defined in (1.212). Let  $(\rho_0, u_0, \vartheta_0, a_0, \omega_0)$  and  $M$  as in Proposition 1.58. Given  $(f_1, f_2, f_3, f_4) \in \mathcal{B}_{T_*}$ , let  $(\widetilde{\rho}, \widetilde{u}, \widetilde{g}, \widetilde{\omega})$  be the solution of (1.206) constructed in Proposition 1.58. Let  $\mathcal{F}_{2,1}$  be defined as in (1.119). Then there exist a constant  $C > 0$  depending only on  $M$  and a constant  $\delta$  depending only on  $p$  and  $q$  such that*

$$\|\mathcal{F}_{2,1}\|_{L^p(0, T_*; L^q(\Omega_F(0)))} \leq CT_*^\delta. \quad (1.226)$$

*Proof*

$$\mathcal{F}_{2,1} = -\frac{\widetilde{\rho}}{\rho_0}\partial_t Q(t)\widetilde{u} - \frac{\widetilde{\rho} - \rho_0}{\rho_0}Q(t)\partial_t\widetilde{u} - (Q(t) - I)\partial_t\widetilde{u} - \gamma\frac{\widetilde{\rho}^{\gamma-1}}{\rho_0}J_Y^\top\nabla\widetilde{\rho}$$

Using Proposition 1.58 and Lemmas 1.59–1.61, we estimate the various terms of  $\mathcal{F}_{2,1}$  as follows

$$\begin{aligned}
& \left\| \frac{\widetilde{\rho}}{\rho_0}\partial_t Q\widetilde{u} \right\|_{L^p(0, T_*; L^q(\Omega_F(0)))} \\
& \leq C\|\widetilde{\rho}\|_{L^\infty(0, T_*; W^{1,q}(\Omega_F(0)))}\|\partial_t Q\|_{L^\infty(0, T_*)}\|\widetilde{u}\|_{L^p(0, T_*; L^q(\Omega_F(0)))} \\
& \leq CT_*^{1/p}\|\widetilde{u}\|_{L^\infty(0, T_*; W^{1,q}(\Omega_F(0)))} \leq CT_*^{1/p'}, \\
& \left\| \frac{\widetilde{\rho} - \rho_0}{\rho_0}Q\partial_t\widetilde{u} \right\|_{L^p(0, T_*; L^q(\Omega_F(0)))} \\
& \leq C\|\widetilde{\rho} - \rho_0\|_{L^\infty(0, T_*; W^{1,q}(\Omega_F(0)))}\|Q\|_{L^\infty(0, T_*)}\|\partial_t\widetilde{u}\|_{L^p(0, T_*; L^q(\Omega_F(0)))} \\
& \leq CT_*^{1/p'},
\end{aligned}$$

$$\begin{aligned} \|(Q - I)\partial_t \tilde{u}\|_{L^p(0, T_*; L^q(\Omega_F(0)))} &\leq \|Q - I\|_{L^\infty(0, T_*)} \|\tilde{u}\|_{W^{1,p}(0, T_*; L^q(\Omega_F(0)))} \leq CT_*^{1/p'}, \\ \left\| \gamma \frac{\tilde{\rho}^{\gamma-1}}{\rho_0} J_Y^\top \nabla \tilde{\rho} \right\|_{L^p(0, T_*; L^q(\Omega_F(0)))} \\ &\leq C \|\tilde{\rho}\|_{L^\infty(0, T_*; W^{1,q}(\Omega_F(0)))} \|J_Y^\top\|_{L^\infty((0, T_*) \times \Omega_F(0))} \|\nabla \tilde{\rho}\|_{L^p(0, T_*; L^q(\Omega_F(0)))} \leq CT_*^{1/p}. \end{aligned}$$

□

**Lemma 1.64** *Let  $3 < q < \infty$  and  $2 < p < \infty$ . For  $T_* \in (0, \tilde{T}]$ , where  $\tilde{T}$  is the constant in Lemma 1.60, let  $\mathcal{B}_{T_*}$  be the ball defined in (1.212). Let  $(\rho_0, u_0, \vartheta_0, a_0, \omega_0)$  and  $M$  as in Proposition 1.58. Given  $(f_1, f_2, f_3, f_4) \in \mathcal{B}_{T_*}$ , let  $(\tilde{\rho}, \tilde{u}, \tilde{g}, \tilde{\omega})$  be the solution of (1.206) constructed in Proposition 1.58. Let  $\mathcal{F}_{2,2}$  be defined as in (1.119). Then there exist a constant  $C > 0$  depending only on  $M$  and a constant  $\delta$  depending only on  $p$  and  $q$  such that*

$$\|(\mathcal{F}_{2,2})_i\|_{L^p(0, T_*; L^q(\Omega_F(0)))} \leq CT_*^{1/p'}, \quad i = 1, 2, 3. \quad (1.227)$$

*Proof* We have

$$\begin{aligned} (\mathcal{F}_{2,2})_i &= \frac{\mu}{\rho_0} \sum_{j,k,l=1}^3 \partial_{y_l} (\partial_{y_k} (Q\tilde{u})_i [(J_Y)_{kj} - \delta_{kj}]) (J_Y)_{lj} \\ &\quad + \frac{\mu}{\rho_0} \sum_{k,l=1}^3 (\partial_{y_l y_k}^2 (Q\tilde{u})_i) [(J_Y)_{lk} - \delta_{lk}] \\ &\quad + \frac{\alpha + \mu}{\rho_0} \sum_{j,k,l=1}^3 \partial_{y_l} (\partial_{y_k} (Q\tilde{u})_j [(J_Y)_{kj} - \delta_{kj}]) (J_Y)_{li} \\ &\quad + \frac{\alpha + \mu}{\rho_0} \sum_{l,j=1}^3 (\partial_{y_l y_j}^2 (Q\tilde{u})_j) [(J_Y)_{li} - \delta_{li}] + (Q^\top - I) : \partial_{y_i} \nabla \tilde{u}, \end{aligned}$$

Let us notice that

$$(\partial_{y_k} J_Y)(0, \cdot) = 0.$$

Therefore, using the estimates in Lemma 1.61, we get

$$\|\partial_{y_k} J_Y\|_{L^\infty(0, T_*; L^q(\Omega_F(0)))} \leq T_*^{1/p'} \|\partial_{y_k} J_Y\|_{W^{1,p}(0, T_*; L^q(\Omega_F(0)))} \leq CT_*^{1/p'}. \quad (1.228)$$

The first term can be estimated as follows,

$$\begin{aligned}
& \left\| \frac{\mu}{\rho_0} \sum_{j,k,l=1}^3 \partial_{y_l} (\partial_{y_k} (\mathcal{Q}\tilde{u})_i [(J_Y)_{kj} - \delta_{kj}]) (J_Y)_{ij} \right\|_{L^p(0, T_*; L^q(\Omega_F(0)))} \\
& \leq C \sum_{j,k,l=1}^3 \left( \|\partial_{y_l y_k} (\mathcal{Q}\tilde{u})_i [(J_Y)_{kj} - \delta_{kj}]\|_{L^p(0, T_*; L^q(\Omega_F(0)))} \right. \\
& \quad \left. + \|\partial_{y_k} (\mathcal{Q}\tilde{u})_i [\partial_{y_l} (J_Y)_{kj}]\|_{L^p(0, T_*; L^q(\Omega_F(0)))} \right) \\
& \leq C \left( \|\mathcal{Q}\tilde{u}\|_{L^p(0, T_*; W^{2,q}(\Omega_F(0)))} \|J_Y - I\|_{L^\infty(0, T_*; W^{1,q}(\Omega_F(0)))} \right. \\
& \quad \left. + \|\mathcal{Q}\tilde{u}\|_{L^p(0, T_*; W^{2,q}(\Omega_F(0)))} \sum_{j,k,l=1}^3 \|\partial_{y_l} (J_Y)_{kj}\|_{L^\infty(0, T_*; L^q(\Omega_F(0)))} \right) \\
& \leq CT_*^{1/p'}.
\end{aligned}$$

Other terms in  $\mathcal{F}_{2,2}$  can be estimated similarly.  $\square$

**Lemma 1.65** *Let  $3 < q < \infty$  and  $2 < p < \infty$ . For  $T_* \in (0, \tilde{T}]$ , where  $\tilde{T}$  is the constant in Lemma 1.60, let  $\mathcal{B}_{T_*}$  be the ball defined in (1.212). Let  $(\rho_0, u_0, \vartheta_0, a_0, \omega_0)$  and  $M$  as in Proposition 1.58. Given  $(f_1, f_2, f_3, f_4) \in \mathcal{B}_{T_*}$ , let  $(\tilde{\rho}, \tilde{u}, \tilde{g}, \tilde{\omega})$  be the solution of (1.206) constructed in Proposition 1.58. Let  $\mathcal{G}$  be defined as in (1.120). Then there exist a constant  $C > 0$  depending only on  $M$  and a constant  $\delta$  depending only on  $p$  and  $q$  such that*

$$\|\mathcal{G}\|_{L^p(0, T_*; W^{1,q}(\Omega_F(0)))} \leq CT_*^{1/p'}. \quad (1.229)$$

*Proof* The proof is similar to the proof of Lemma 1.62. The only thing is left to check is the estimate  $\text{cof}J_X - I$  in  $L^\infty(0, T_*; W^{1,q}(\Omega_F(0)))$  norm. Since,  $(\text{cof}J_X - I)(0, \cdot) = 0$ , we have

$$\|\text{cof}J_X - I\|_{L^\infty(0, T_*; W^{1,q}(\Omega_F(0)))} \leq T_*^{1/p'} \|\text{cof}J_X - I\|_{W^{1,p}(0, T_*; W^{1,q}(\Omega_F(0)))}.$$

With the help of above estimate we can proceed as the proof of Lemma 1.62 to complete the proof of this Lemma.  $\square$

**Lemma 1.66** *Let  $3 < q < \infty$  and  $2 < p < \infty$ . For  $T_* \in (0, \tilde{T}]$ , where  $\tilde{T}$  is the constant in Lemma 1.60, let  $\mathcal{B}_{T_*}$  be the ball defined in (1.212). Let  $(\rho_0, u_0, \vartheta_0, a_0, \omega_0)$  and  $M$  as in Proposition 1.58. Given  $(f_1, f_2, f_3, f_4) \in \mathcal{B}_{T_*}$ , let  $(\tilde{\rho}, \tilde{u}, \tilde{g}, \tilde{\omega})$  be the solution of (1.206) constructed in Proposition 1.58. Let  $\mathcal{F}_3$  and  $\mathcal{F}_4$  be defined as*

in (1.120). Then there exists a constant  $C > 0$  depending only on  $M$  such that

$$\begin{aligned}\|\mathcal{F}_3\|_{L^p(0,T_*)} &\leq C(T_*^{1/p} + T_*^{1/p'}) \\ \|\mathcal{F}_4\|_{L^p(0,T_*)} &\leq C(T_*^{1/p} + T_*^{1/p'}).\end{aligned}\quad (1.230)$$

*Proof* Let us recall

$$\mathcal{F}_3 = -m(\tilde{\omega} \times \tilde{\ell}) - \int_{\Omega_S(0)} \mathcal{G}n$$

Therefore

$$\begin{aligned}\|\mathcal{F}_3\|_{L^p(0,T_*)} &\leq C\left(\|\tilde{\omega}\|_{L^p(0,T_*)}\|\tilde{g}\|_{L^\infty(0,T_*)} + \|\mathcal{G}\|_{L^p(0,T_*;L^q(\partial\Omega_S(0)))}\right) \\ &\leq C\left(T_*^{1/p'} + \|\mathcal{G}\|_{L^p(0,T_*;W^{1,q}(\Omega_F(0)))}\right) \\ &\leq CT_*^{1/p'}.\end{aligned}$$

The estimate of  $\|\mathcal{F}_4\|_{L^p(0,T_*)}$  is similar.  $\square$

**Proposition 1.67** *Let  $3 < q < \infty$  and  $2 < p < \infty$ . For  $T_* \in (0, \tilde{T}]$ , where  $\tilde{T}$  is the constant in Lemma 1.60, let  $\mathcal{B}_{T_*}$  be the ball defined in (1.212). Let  $(\rho_0, u_0, \vartheta_0, a_0, \omega_0)$  and  $M$  as in Proposition 1.58. Given  $(f_1^j, f_2^j, f_3^j, f_4^j) \in \mathcal{B}_{T_*}$ ,  $j = 1, 2$ , let  $(\tilde{\rho}^j, \tilde{u}^j, \tilde{g}^j, \tilde{\omega}^j)$  be the solution of (1.206) constructed in Proposition 1.58.*

*Let us set*

$$\begin{aligned}\mathcal{F}_1^j &= \mathcal{F}_1(\tilde{\rho}^j, \tilde{u}^j, \tilde{g}^j, \tilde{\omega}^j), \mathcal{F}_{2,1}^j = \mathcal{F}_{2,1}(\tilde{\rho}^j, \tilde{u}^j, \tilde{g}^j, \tilde{\omega}^j), \mathcal{F}_{2,2}^j = \mathcal{F}_{2,2}(\tilde{\rho}^j, \tilde{u}^j, \tilde{g}^j, \tilde{\omega}^j) \\ \mathcal{F}_3^j &= \mathcal{F}_3(\tilde{\rho}^j, \tilde{u}^j, \tilde{g}^j, \tilde{\omega}^j), \mathcal{F}_4^j = \mathcal{F}_4(\tilde{\rho}^j, \tilde{u}^j, \tilde{g}^j, \tilde{\omega}^j) \text{ for } j = 1, 2.\end{aligned}\quad (1.231)$$

Then there exists a constant  $C > 0$  depending only on  $M$  such that

$$\begin{aligned}\|\mathcal{F}_1^1 - \mathcal{F}_1^2\|_{L^p(0,T_*;W^{1,q}(\Omega_F(0)))} &+ \|\mathcal{F}_{2,1}^1 - \mathcal{F}_{2,1}^2\|_{L^p(0,T_*;L^q(\Omega_F(0)))} \\ &+ \|\mathcal{F}_{2,2}^1 - \mathcal{F}_{2,2}^2\|_{L^p(0,T_*;L^q(\Omega_F(0)))} + \|\mathcal{F}_3^1 - \mathcal{F}_3^2\|_{L^p(0,T_*)} + \|\mathcal{F}_4^1 - \mathcal{F}_4^2\|_{L^p(0,T_*)} \\ &\leq CT_*^\delta \left( \|f_1^1 - f_1^2\|_{L^p(0,T_*;L^q(\Omega_F(0)))} + \|f_2^1 - f_2^2\|_{L^p(0,T_*;L^q(\Omega_F(0)))} \right. \\ &\quad \left. + \|f_3^1 - f_3^2\|_{L^p(0,T_*)} + \|f_4^1 - f_4^2\|_{L^p(0,T_*)} \right)\end{aligned}\quad (1.232)$$

where  $\delta > 0$  is a positive constant depending only on  $p$  and  $q$ .

Now we give the proofs of main theorems of this section.

*Proof of Theorem 1.54* We consider the map

$$\left\{ \begin{array}{l} \mathcal{N} : \mathcal{B}_{T_*} \rightarrow \mathcal{B}_{T_*}, \\ \left[ \begin{array}{c} f_1 \\ f_2 \\ f_3 \\ f_4 \end{array} \right] \mapsto \left[ \begin{array}{c} \mathcal{F}_1 \\ \mathcal{F}_{2,1} + \mathcal{F}_{2,2} \\ \mathcal{F}_3 \\ \mathcal{F}_4 \end{array} \right], \end{array} \right.$$

By virtue of Lemmas 1.62–1.66 and Proposition 1.67, it is easy to see that  $\mathcal{N}$  is a strict contraction of  $\mathcal{B}_{T_*}$ , with a Lipschitz constant  $\frac{1}{2}$  for small  $T_*$ . Thus the proof follows from the Banach fixed point theorem.

*Proof of Theorem 1.53* Let us assume that  $(\rho_0, u_0, g_0, \omega_0) \in \mathcal{I}_{p,q,\Omega_F(0)}$  satisfying (1.204)–(1.205). Let  $\widehat{T} \leq \widetilde{T}$  be such that,  $(\widetilde{\rho}, \widetilde{u}, \widetilde{g}, \widetilde{\omega})$  be the solution to the system (1.115)–(1.120) satisfying

$$\begin{aligned} \widetilde{\rho} &\in W^{1,p}(0, \widehat{T}; W^{1,q}(\Omega_F(0))) \\ \widetilde{u} &\in L^p(0, \widehat{T}; W^{2,q}(\Omega_F(0))^3) \cap W^{1,p}(0, \widehat{T}; L^q(\Omega_F(0))^3) \\ \widetilde{g} &\in W^{1,p}(0, \widehat{T}; \mathbb{R}^3), \quad \widetilde{\omega} \in W^{1,p}(0, \widehat{T}; \mathbb{R}^3). \end{aligned}$$

Since  $\widehat{T} \leq \widetilde{T}$ ,  $X(t, \cdot)$  is  $C^1$ -diffeomorphism from  $\Omega_F(0)$  into  $\Omega_F(t)$ . Therefore, there is a unique  $Y(t, \cdot)$  from  $\Omega_F(t)$  into  $\Omega_F(0)$  such that  $Y(t, \cdot) = X^{-1}(t, \cdot)$ . We set

$$\begin{aligned} \rho(t, x) &= \widetilde{\rho}(t, Y(t, x)), \quad u(t, x) = Q(t)\widetilde{u}(t, Y(t, x)), \\ \dot{h}(t) &= Q(t)\widetilde{g}(t), \quad \omega(t) = Q(t)\widetilde{\omega}(t), \quad \text{for all } x \in \Omega_F(t), \quad t \geq 0. \end{aligned} \quad (1.233)$$

We can easily check that  $(\rho, u, \vartheta, h, \omega)$  satisfies the original system (1.110) and

$$\begin{aligned} \rho &\in W^{1,p}(0, T; W^{1,q}(\Omega_F(\cdot))) \cap C([0, T]; W^{1,q}(\Omega_F(\cdot))), \\ u &\in L^p(0, T; W^{2,q}(\Omega_F(\cdot))^3) \cap W^{1,p}(0, T; L^q(\Omega_F(\cdot))^3) \cap C([0, T]; B_{q,p}^{2(1-1/p)}(\Omega_F(\cdot))^3), \\ h &\in W^{2,p}(0, T; \mathbb{R}^3), \quad \omega \in W^{1,p}(0, T; \mathbb{R}^3). \end{aligned}$$

The uniqueness for the solution of (1.110) follows from uniqueness of solution to the system (1.115)–(1.120). This completes the proof of Theorem 1.53.

### 1.4.5 Bibliographical Notes

As far as we know, the first mathematical analysis approach of piston problems similar to the ones we have introduced in Sect. 1.4.3 was performed in Shelukhin [30], where global in time existence and uniqueness of classical solutions have been given. Less regular solutions, in a Hilbert space setting have been given in Maity et al. [26], which was our main source in Sect. 1.4.3. Our approach of the three dimensional case in Sect. 1.4.4 should be seen as a simplification of the methodology proposed in Hieber and Murata [19], which is also considering the  $L^p$ - $L^q$  setting. Earlier results in a Hilbert space framework, which require more derivability of the initial data, have been given in Boulakia and Guerrero [5].

**Acknowledgements** Many thanks to our Bernhard Haak and Takéo Takahashi for their help, via discussions and suggestions, in improving these notes.

### References

1. H. Amann, *Linear and Quasilinear Parabolic Problems. Vol. I: Abstract Linear Theory*. Monographs in Mathematics, vol. 89 (Birkhäuser Boston, Boston, MA, 1995)
2. H. Amann, On the strong solvability of the Navier-Stokes equations. *J. Math. Fluid Mech.* **2**(1), 16–98 (2000)
3. S.N. Antontsev, A.V. Kazhikhov, V.N. Monakhov, *Boundary Value Problems in Mechanics of Nonhomogeneous Fluids* (North-Holland Publishing, Amsterdam, 1990). Translated from the Russian
4. A. Bensoussan, G. Da Prato, M.C. Delfour, S.K. Mitter, *Representation and Control of Infinite Dimensional Systems*, vol. 1 (Birkhäuser Boston, Boston, MA, 1992)
5. M. Boulakia, S. Guerrero, A regularity result for a solid-fluid system associated to the compressible Navier-Stokes equations. *Ann. Inst. H. Poincaré Anal. Non Linéaire* **26**(3), 777–813 (2009)
6. N. Cîrdea, S. Micu, I. Roventă, M. Tucsnak, Particle supported control of a fluid-particle system. *J. Math. Pures Appl.* (9) **104**(2), 311–353 (2015)
7. P. Clément, J. Prüss, Global existence for a semilinear parabolic Volterra equation. *Math. Z.* **209**(1), 17–26 (1992)
8. P. Clément, J. Prüss, An operator-valued transference principle and maximal regularity on vector-valued  $L_p$ -spaces, in *Evolution Equations and Their Applications in Physical and Life Sciences (Bad Herrenalb, 1998)*. Lecture Notes in Pure and Applied Mathematics, vol. 215 (Dekker, New York, 2001), pp. 67–87
9. T. Coulhon, D. Lamberton, Régularité  $L^p$  pour les équations d'évolution, in *Séminaire d'Analyse Fonctionnelle 1984/1985*. Publications mathématiques de l'Université Paris VII, vol. 26 (Université Paris VII, Paris, 1986), pp. 155–165
10. G. Da Prato, P. Grisvard, Sommes d'opérateurs linéaires et équations différentielles opérationnelles. *J. Math. Pures Appl.* (9) **54**(3), 305–387 (1975)
11. L. de Simon, Un'applicazione della teoria degli integrali singolari allo studio delle equazioni differenziali lineari astratte del primo ordine. *Rend. Sem. Mat. Univ. Padova* **34**, 205–223 (1964)



12. R. Denk, M. Hieber, J. Prüss,  $\mathcal{R}$ -boundedness, Fourier multipliers and problems of elliptic and parabolic type. *Mem. Am. Math. Soc.* **166**(788), viii+114 (2003)
13. G. Dore,  $L^p$  regularity for abstract differential equations, in *Functional Analysis and Related Topics, 1991 (Kyoto)*. *Lecture Notes in Mathematics*, vol. 1540 (Springer, Berlin, 1993), pp. 25–38
14. G. Dore, A. Venni, On the closedness of the sum of two closed operators. *Math. Z.* **196**(2), 189–201 (1987)
15. A. Doubova, E. Fernández-Cara, Some control results for simplified one-dimensional models of fluid-solid interaction. *Math. Models Methods Appl. Sci.* **15**(5), 783–824 (2005)
16. K.-J. Engel, R. Nagel, *One-Parameter Semigroups for Linear Evolution Equations*. *Graduate Texts in Mathematics*, vol. 194 (Springer, New York, 2000). With contributions by S. Brendle, M. Campiti, T. Hahn, G. Metafune, G. Nickel, D. Pallara, C. Perazzoli, A. Rhandi, S. Romanelli and R. Schnaubelt
17. M. Geissert, K. Götze, M. Hieber,  $L^p$ -theory for strong solutions to fluid-rigid body interaction in Newtonian and generalized Newtonian fluids. *Trans. Am. Math. Soc.* **365**(3), 1393–1439 (2013)
18. P. Grisvard, Identités entre espaces de traces. *Math. Scand.* **13**, 70–74 (1963)
19. M. Hieber, M. Murata, The  $L^p$ -approach to the fluid-rigid body interaction problem for compressible fluids. *Evol. Equ. Control Theory* **4**(1), 69–87 (2015)
20. M. Hieber, J. Prüss, Heat kernels and maximal  $L^p$ - $L^q$  estimates for parabolic evolution equations. *Commun. Partial Differ. Equ.* **22**(9–10), 1647–1669 (1997)
21. N.J. Kalton, G. Lancien, A solution to the problem of  $L^p$ -maximal regularity. *Math. Z.* **235**(3), 559–568 (2000)
22. P.C. Kunstmann, L. Weis, Perturbation theorems for maximal  $L_p$ -regularity. *Ann. Scuola Norm. Sup. Pisa Cl. Sci. (4)*, **30**(2), 415–435 (2001)
23. O.A. Ladyženskaja, V.A. Solonnikov, N.N. Ural'ceva, *Linear and Quasilinear Equations of Parabolic Type*. Translated from the Russian by S. Smith. *Translations of Mathematical Monographs*, vol. 23 (American Mathematical Society, Providence, RI, 1968)
24. D. Lambertson, Équations d'évolution linéaires associées à des semi-groupes de contractions dans les espaces  $L^p$ . *J. Funct. Anal.* **72**(2), 252–262 (1987)
25. Y. Liu, T. Takahashi, M. Tucsnak, Single input controllability of a simplified fluid-structure interaction model. *ESAIM Control Optim. Calc. Var.* **19**(1), 20–42 (2013)
26. D. Maity, T. Takahashi, M. Tucsnak, Analysis of a system modelling the motion of a piston in a viscous gas. *J. Math. Fluid Mech.*, 1–29 (2016). doi:10.1007/s00021-016-0293-2
27. J.S. Martín, M. Tucsnak, Mathematical analysis of particulate flows, in *Fundamental Trends in Fluid-Structure Interaction*. *Contemporary Challenges in Mathematical Fluid Dynamics and its Applications*, vol. 1 (World Scientific Publishing, Hackensack, NJ, 2010), pp. 201–260
28. A. Pazy, *Semigroups of Linear Operators and Applications to Partial Differential Equations*. *Applied Mathematical Sciences*, vol. 44 (Springer, New York, 1983)
29. J. Prüss, H. Sohr, On operators with bounded imaginary powers in Banach spaces. *Math. Z.* **203**(3), 429–452 (1990)
30. V.V. Shelukhin, Motion with a contact discontinuity in a viscous heat conducting gas. *Dinamika Sploshn. Sredy* **57**, 131–152 (1982)
31. Y. Shibata, M. Murata, On the global well-posedness for the compressible Navier-Stokes equations with slip boundary condition. *J. Differ. Equ.* **260**(7), 5761–5795 (2016)
32. R. Temam, *Navier-Stokes Equations: Theory and Numerical Analysis*, With an appendix by F. Thomasset, 3rd edn. (North-Holland Publishing, Amsterdam, 1984)
33. H. Triebel, *Interpolation Theory, Function Spaces, Differential Operators*, 2nd edn. (Johann Ambrosius Barth, Heidelberg, 1995)
34. M. Tucsnak, G. Weiss, *Observation and Control for Operator Semigroups*. *Birkhäuser Advanced Texts: Basler Lehrbücher [Birkhäuser Advanced Texts: Basel Textbooks]* (Birkhäuser Verlag, Basel, 2009)

35. J.L. Vázquez, E. Zuazua, Large time behavior for a simplified 1D model of fluid-solid interaction. *Commun. Partial Differ. Equ.* **28**(9–10), 1705–1738 (2003)
36. J.L. Vázquez, E. Zuazua, Lack of collision in a simplified 1-dimensional model for fluid-solid interaction. *Math. Models Methods Appl. Sci.* **16**(5), 637–678 (2006)
37. L. Weis, Operator-valued Fourier multiplier theorems and maximal  $L_p$ -regularity. *Math. Ann.* **319**(4), 735–758 (2001)

# Chapter 2

## Time-Periodic Linearized Navier–Stokes Equations: An Approach Based on Fourier Multipliers

T. Eiter and M. Kyed

**Abstract** The Stokes and Oseen linearizations of the time-periodic Navier–Stokes equations in the  $n$ -dimensional whole space for  $n \geq 2$  are investigated. An approach based on Fourier multipliers is introduced to establish  $L^q$  estimates and to identify function spaces of maximal regularity for the corresponding operators. Moreover, the representation of a solution in terms of a Fourier multiplier is used to introduce the concept of a time-periodic fundamental solution. The main idea is to replace the time axis by a torus group and to study the system in a setting of functions defined on a locally compact abelian group  $G$ . For this purpose, we develop the required formalism. More specifically, we introduce the space  $\mathcal{S}(G)$  of Schwartz–Bruhat functions and investigate the Stokes and Oseen systems in the corresponding space of tempered distributions  $\mathcal{S}'(G)$ . Moreover, we give a detailed proof of the so-called Transference Principle, which enables us to employ Fourier multipliers in a group setting in order to establish  $L^q$  estimates.

**Keywords** Fourier multipliers on LCA groups • Maximal regularity • Oseen equations • Schwartz–Bruhat spaces • Stokes equations • Time-periodic fundamental solutions • Time-periodic solutions • Transference principle

**MSC2010:** 76D07, 35Q30, 76D05, 35B10, 35S30, 35A08

### 2.1 Introduction

Fourier multipliers play a significant role in the investigation of steady-state and initial-value fluid flow problems. Arguments based on multiplier theorems are typically used to establish  $L^q$  estimates of solutions to an appropriate linearization

---

T. Eiter • M. Kyed (✉)

Fachbereich Mathematik, Technische Universität Darmstadt, Schlossgartenstraße 7, 64289 Darmstadt, Germany

e-mail: [eiter@mathematik.tu-darmstadt.de](mailto:eiter@mathematik.tu-darmstadt.de); [kyed@mathematik.tu-darmstadt.de](mailto:kyed@mathematik.tu-darmstadt.de)

of the relevant equations of motion. For steady-state and initial-value problems of parabolic type, such arguments have become part of the standard literature. Recently, a technique has been developed by Kyed [12] to extend the approach based on Fourier multipliers to the corresponding time-periodic problems. The main idea behind the approach is to replace the time axis by a torus  $\mathbb{T}$  and to reformulate the equations on the locally compact abelian group  $G := \mathbb{T} \times \mathbb{R}^n$ . It is then possible to express solutions in terms of Fourier multipliers with respect to the abstract Fourier transform  $\mathcal{F}_G$ . In order for this approach to work, two tools from abstract harmonic analysis are needed. First of all, a setting of Schwartz functions  $\mathcal{S}(G)$  and corresponding tempered distributions  $\mathcal{S}'(G)$  are needed to reformulate the differential equations on the group  $G$  in such a way that a multiplier expression for the solution can be obtained by applying the Fourier transform  $\mathcal{F}_G$ . Secondly, a multiplier theorem is needed to establish the desired  $L^q$  estimates based on the characteristics of the multiplier. Although both tools have been available since the 1960s, they have only recently been combined in the analysis of partial differential equations. The so-called Schwartz-Bruhat space  $\mathcal{S}(G)$  was introduced by Bruhat [2]. The Transference Principle, which can be used to establish  $L^q$  estimates, was originally introduced by de Leeuw [3] and later generalized by Edwards and Gaudry [4]. In the following, a detailed description of the construction of Schwartz-Bruhat spaces  $\mathcal{S}(G)$  and a rigorous proof of the Transference Principle shall be given. As an application, we establish maximal  $L^q$  regularity for the time-periodic Stokes and Oseen linearizations of the Navier–Stokes equations. Moreover, we use the Fourier transform  $\mathcal{F}_G$  to introduce the concept of a time-periodic fundamental solution to these systems. Integrability properties of the fundamental solutions are established with the help of the Transference Principle.

The construction of Schwartz-Bruhat spaces  $\mathcal{S}(G)$  for general locally compact abelian groups was only sketched by Bruhat in [2]. Although these spaces can be used to investigate systems of partial differential equations where the unknowns are periodic in one or more (even infinitely many) coordinates, apart from the recent articles [12–15, 17, 20–22] there seems to be no applications of Schwartz-Bruhat spaces in this direction. In fact, with the exception of the alternative characterization of  $\mathcal{S}(G)$  by Osborne [18], a rigorous description of the construction is not available anywhere in literature. We have therefore chosen to include such a description in the following. The Schwartz-Bruhat space  $\mathcal{S}(G)$  on a general locally compact abelian group is defined as an inductive limit of Schwartz-Bruhat spaces on elementary groups  $\mathbb{R}^n \times \mathbb{T}^p \times \mathbb{Z}^q \times F$ , where  $F$  is a finite abelian group and  $n, p, q \in \mathbb{N}_0$ . In Sect. 2.4 we give a detailed explanation of this construction and show that the Fourier transform is a homeomorphism as a mapping  $\mathcal{F}_G: \mathcal{S}(G) \rightarrow \mathcal{S}(G)$ . We shall then introduce the space of tempered distributions  $\mathcal{S}'(G)$  and obtain, by duality, that also  $\mathcal{F}_G: \mathcal{S}'(G) \rightarrow \mathcal{S}'(G)$  is a homeomorphism, which enables us to study partial differential equations on  $G$  in terms of Fourier multipliers.

The Fourier multiplier corresponding to a linear differential operator (with constant coefficients) on a group  $G$  is a function  $M: \widehat{G} \rightarrow \mathbb{C}$  defined on the dual group  $\widehat{G}$ . There is no multiplier theory available in this abstract setting that can be used to determine directly from the characteristics of the multiplier  $M$  whether

the operator  $u \mapsto \mathcal{F}_G^{-1}[M \mathcal{F}_G(u)]$  is bounded on  $L^q(G)$ . Instead, the Transference Principle can be used. If  $\Phi: \widehat{G} \rightarrow \widehat{H}$  is a continuous homomorphism between  $\widehat{G}$  and the dual group  $\widehat{H}$  of some other locally compact abelian group  $H$ , the Transference Principle states that if  $M = m \circ \Phi$  for some  $L^q(H)$  multiplier  $m: \widehat{H} \rightarrow \mathbb{C}$ , then  $M$  is an  $L^q(G)$  multiplier. Provided therefore that one can find a continuous homomorphism  $\Phi: \widehat{G} \rightarrow \mathbb{R}^N$  such that  $M = m \circ \Phi$ , it becomes possible to “transfer” the investigation of a Fourier multiplier into the Euclidean setting, where a number of multiplier theorems are available. As in the case of the Schwartz-Bruhat spaces, the Transference Principle for general locally compact abelian groups has not been adapted into standard literature and does not seem to be widely know. In the following Sect. 2.3, we shall therefore provide a detailed proof of the Transference Principle.

Finally, in Sect. 2.5 we apply the theory to the linearized time-periodic Navier–Stokes equations. More specifically, we fix a time-period  $\mathcal{T} > 0$ , a constant  $\lambda \in \mathbb{R}$  and consider the system

$$\begin{cases} \partial_t u - \Delta u - \lambda \partial_{x_1} u + \nabla p = f & \text{in } \mathbb{R} \times \mathbb{R}^n, \\ \operatorname{div} u = 0 & \text{in } \mathbb{R} \times \mathbb{R}^n, \\ u(t, x) = u(t + \mathcal{T}, x), \end{cases} \quad (2.1)$$

which is a time-periodic Stokes system if  $\lambda = 0$ , and a time-periodic Oseen system if  $\lambda \neq 0$ . Here  $u: \mathbb{R} \times \mathbb{R}^n \rightarrow \mathbb{R}^n$  and  $p: \mathbb{R} \times \mathbb{R}^n \rightarrow \mathbb{R}$  denote the Eulerian velocity field and pressure term, respectively. Data  $f: \mathbb{R} \times \mathbb{R}^n \rightarrow \mathbb{R}^n$  with the same period, that is,  $f(t, x) = f(t + \mathcal{T}, x)$ , are considered. Moreover,  $t \in \mathbb{R}$  and  $x \in \mathbb{R}^n$  denote the time and spatial variable, respectively. Replacing in (2.1) the time axis  $\mathbb{R}$  with the torus  $\mathbb{R}/\mathcal{T}\mathbb{Z}$ , we shall reformulate (2.1) in a setting of distributions  $\mathcal{S}'(G)$  based on the locally compact group  $G := \mathbb{R}/\mathcal{T}\mathbb{Z} \times \mathbb{R}^n$ . We can then express the solution  $(u, p)$  in terms of an  $\mathcal{F}_G$  multiplier, which we shall estimate with the help of the Transference Principle. As a result, we can establish what is known as maximal  $L^q$  regularity for the problem, that is, we can identify a Banach space  $X_{\text{per}}^q(\mathbb{R} \times \mathbb{R}^n)$  of  $\mathcal{T}$ -time-periodic functions such that for any vector field  $f$  in a  $\mathcal{T}$ -time-periodic  $L^q$  space  $L_{\text{per}}^q(\mathbb{R} \times \mathbb{R}^n)^n$  there is a unique solution  $(u, p) \in X_{\text{per}}^q(\mathbb{R} \times \mathbb{R}^n)$  to (2.1), which satisfies

$$\|(u, p)\|_{X_{\text{per}}^q(\mathbb{R} \times \mathbb{R}^n)} \leq C \|f\|_{L_{\text{per}}^q(\mathbb{R} \times \mathbb{R}^n)}. \quad (2.2)$$

In other words, we identify a Banach space  $X_{\text{per}}^q(\mathbb{R} \times \mathbb{R}^n)$  that is mapped homeomorphically onto  $L_{\text{per}}^q(\mathbb{R} \times \mathbb{R}^n)^n$  by the differential operator on the left-hand side of (2.1)<sub>1</sub>.

As another application, we use the Fourier transform on  $G$  to introduce the concept of a time-periodic fundamental solution  $F$  to (2.1) in such a way that a solution  $u$  to (2.1) can be expressed as a convolution  $F * f$ , where the convolution is with respect to the group  $G$ . At the outset,  $F$  is defined as a tempered distribution in  $\mathcal{S}'(G)$ . However, using the Transference Principle, we shall establish integrability properties of  $F$  that allows us to identify it as a (locally) integrable function.

## 2.2 Preliminaries

In this section we introduce some notation, which will be used throughout the whole chapter. Moreover, we recall some results from Fourier analysis on locally compact abelian groups. For a comprehensive overview we refer to [10, 11, 19].

### *General Vector Spaces*

In the following, the symbol  $\mathbb{K}$  shall always denote one of the fields  $\mathbb{R}$  or  $\mathbb{C}$ . For  $n \in \mathbb{N}$  we equip the  $n$ -dimensional vector space  $\mathbb{K}^n$  with the Euclidean norm  $|\cdot|$ . When we consider two vectors  $x, \xi \in \mathbb{R}^n$ , we write  $x \cdot \xi$  for their standard scalar product.

For  $r > 0$  and  $x \in \mathbb{R}^n$  we denote the  $n$ -dimensional open ball of radius  $r$  with center  $x$  by  $B_r^n(x)$ , and for its closure we use the notation  $K_r^n(x)$ . For the  $n$ -dimensional ball with radius 1, the constants  $v_n$  and  $\omega_n$  denote its volume and its surface area, respectively, where we equip  $\mathbb{R}^n$  with the Lebesgue measure.

If  $V$  is a locally convex vector space, we denote its topological dual space by  $V'$ . In some cases we write  $\langle \psi, v \rangle := \psi(v)$  for  $v \in V$  and  $\psi \in V'$ .

Let  $M$  be a set and  $X(M)$  and  $Y(M)$  be vector spaces of functions  $M \rightarrow \mathbb{K}$ . Then we will occasionally use the abbreviation  $X \cap Y(M) := X(M) \cap Y(M)$ .

### *Spaces of Continuous Functions*

Let  $X$  and  $Y$  be topological spaces. We denote the set of all continuous functions  $X \rightarrow Y$  by  $C(X; Y)$ . In the case  $Y = \mathbb{K}$ , equipped with the standard topology, we always use the abbreviation  $C(X) := C(X; \mathbb{K})$ . Moreover, we write  $C_b(X)$  for the subset of bounded continuous functions, which is a Banach space when equipped with the supremum norm  $\|\cdot\|_\infty$ . In this case we also define the subspaces

$$C_c(X) := \{f \in C(X) : \text{supp } f \text{ compact}\},$$

$$C_0(X) := \{f \in C(X) : \forall \varepsilon > 0 \exists K \subseteq X \text{ compact } \forall x \in X \setminus K : |f(x)| < \varepsilon\}.$$

Let  $n \in \mathbb{N}$  and  $k \in \mathbb{N}_0 \cup \{\infty\}$ . We denote the space of all functions  $f: \mathbb{R}^n \rightarrow \mathbb{K}$  that are  $k$ -times continuously differentiable by  $C^k(\mathbb{R}^n)$ . Moreover, we introduce the spaces

$$C_c^\infty(\mathbb{R}^n) := C^\infty(\mathbb{R}^n) \cap C_c(\mathbb{R}^n),$$

$$C_b^\infty(\mathbb{R}^n) := \{f \in C^\infty(\mathbb{R}^n) : D^\alpha f \in C_b(\mathbb{R}^n) \text{ for all } \alpha \in \mathbb{N}_0^n\}.$$

## Lebesgue Spaces

Let  $X$  be a topological space. Then  $\mathcal{B}(X)$  denotes the Borel  $\sigma$ -algebra on  $X$ . Moreover, we set

$$M(X) := \{\mu: \mathcal{B}(X) \rightarrow \mathbb{C} \text{ regular Borel measure with } |\mu|(X) < \infty\},$$

where  $|\mu|$  denotes the total variation of the measure  $\mu$ . Then  $M(X)$  is a normed vector space if we define addition and scalar multiplication pointwise and the norm on  $M(X)$  by  $\|\mu\|_{M(X)} := |\mu|(X)$ .

Let  $p \in [1, \infty]$  and  $\mu: \mathcal{B}(X) \rightarrow [0, \infty]$  be a nonnegative Borel measure. Then  $L^p(X, \mu)$  denotes the corresponding Lebesgue space, which is equipped with the well-known Lebesgue norm  $\|\cdot\|_{L^p(X, \mu)}$ . Moreover, we may identify  $L^1(X, \mu)$  with a closed subspace of  $M(X)$  via the isometric embedding  $f \mapsto \mu_f$ , where

$$\mu_f(B) := \int_B f(x) \, d\mu(x)$$

for all  $B \in \mathcal{B}(X)$ .

If  $\mu$  is a regular Borel measure, the set  $C_c(X)$  is a dense subspace of the Banach space  $L^p(X, \mu)$  for all  $1 \leq p < \infty$ . This result will be very helpful in the following.

For  $p \in [1, \infty]$  we let  $p' := \frac{p}{p-1}$  denote the dual index, where  $1' := \infty$  and  $\infty' := 1$ . For  $1 < p < \infty$  it is well known that the mapping

$$\Phi: L^{p'}(X, \mu) \rightarrow (L^p(X, \mu))', \quad \Phi(g)(f) := \int_X f(x)g(x) \, d\mu(x),$$

defines an isometric isomorphism. In all cases considered in the following, this statement also holds for  $p = 1$ ; see [19, Subsection E10] for more details.

The space of locally integrable functions is denoted by  $L^1_{\text{loc}}(X, \mu)$ , where we identify functions that coincide  $\mu$ -almost everywhere.

Since in most cases it will be clear which measure we consider, we will usually write  $L^p(X)$  and  $L^1_{\text{loc}}(X)$  instead of  $L^p(X, \mu)$  and  $L^1_{\text{loc}}(X, \mu)$ , and we will sometimes use  $\|\cdot\|_p$  instead of  $\|\cdot\|_{L^p(X)}$ .

## Locally Compact Abelian Groups

Let  $G$  be a locally compact abelian group, i.e.,  $G$  is a topological and abelian group such that each element of  $G$  possesses a compact neighborhood. We always assume that such topological groups are Hausdorff spaces. If we equip  $\mathbb{R}$  with the standard topology and  $\mathbb{Z}$  with the discrete topology, both are locally compact abelian groups. Moreover, also the torus group  $\mathbb{T}$ , which consists of all complex numbers with

absolute value 1, equipped with the topology induced by the standard topology on  $\mathbb{C}$ , is a topological group of this kind. When we refer to topological properties of  $\mathbb{R}$ ,  $\mathbb{Z}$  and  $\mathbb{T}$ , we always assume that they are equipped with these topologies.

We normally use the additive notation for the group operation on  $G$ . Therefore, the neutral element is denoted by 0 in most cases. If  $A$  and  $B$  are subsets of  $G$ , then we define

$$\begin{aligned} A + B &:= \{a + b : a \in A, b \in B\}, \\ A - B &:= \{a - b : a \in A, b \in B\}, \\ -A &:= \{-a : a \in A\}. \end{aligned}$$

Furthermore, for an element  $x \in G$ , we set

$$A \pm x := A \pm \{x\} \quad \text{and} \quad x \pm A := \{x\} \pm A.$$

Moreover, we use the notation  $\langle A \rangle$  for the subgroup of  $G$  generated by  $A$ .

We denote the dual group of  $G$  by  $\widehat{G}$ . Recall that  $\widehat{G}$  consists of all continuous group homomorphisms  $\gamma: G \rightarrow \mathbb{T}$ , also called characters on  $G$ , and the group operation is defined via  $(\gamma_1 + \gamma_2)(x) := \gamma_1(x) \cdot \gamma_2(x)$  for all  $x \in G$  and  $\gamma_1, \gamma_2 \in \widehat{G}$ . Moreover,  $\widehat{G}$  is equipped with the so-called compact-open topology (see [19, Theorem 1.2.6]), which makes it a locally compact abelian group. The Pontryagin Duality Theorem states that the dual group of  $\widehat{G}$  is isomorphic to  $G$ . For this reason, we will identify these two groups in the following. This fact also justifies the notation  $(x, \gamma) := \gamma(x)$  for  $x \in G$ ,  $\gamma \in \widehat{G}$ , which will often be used throughout this chapter.

A locally compact abelian group  $G$  is compact if and only if  $\widehat{G}$  is discrete and vice versa. Additionally, one can show that the dual group of  $\mathbb{R}$  is isomorphic to  $\mathbb{R}$  itself and that the dual group of  $\mathbb{T}$  is isomorphic to  $\mathbb{Z}$  and vice versa.

## *Haar Measure*

Another important aspect in the treatment of locally compact abelian groups is the existence of the Haar measure. If  $G$  is a locally compact abelian group, there exists a nonvanishing regular Borel measure  $\mu_G: \mathcal{B}(G) \rightarrow [0, \infty]$  that is translation-invariant, i.e.,  $\mu_G(B + x) = \mu_G(B)$  for all  $x \in G$  and all  $B \in \mathcal{B}(G)$ . This measure is called Haar measure, and one can show that it is unique up to a positive constant factor. The Haar measure is reflection-invariant, i.e., it holds  $\mu_G(B) = \mu_G(-B)$  for all  $B \in \mathcal{B}(G)$ . Moreover, the Haar measure of a compact set is finite, and for a nonempty open set  $U$  it holds  $\mu_G(U) > 0$ . Therefore, we may introduce the following normalization convention: If  $G$  is a compact group, we choose  $\mu_G$  such that  $\mu_G(G) = 1$ , and in the case of a discrete group  $G$ , the condition  $\mu_G(\{0\}) = 1$  shall be valid. We remark that these conditions may contradict each other if  $G$  is



finite. For this reason, we do not demand any normalization assumptions in this case. For simplicity, we often write  $\mu$  for the Haar measure on  $G$ , and we also denote the Haar measure on  $\widehat{G}$  by  $\mu$  when no confusion can arise.

## Convolution

Now we may define convolution on the locally compact abelian group  $G$ . It is possible to define the convolution of two measures in  $M(G)$ ; see [19, Subsection 1.3.1]. This general case will not be necessary in the following, but we will need the convolution  $\nu * g$  of a measure  $\nu \in M(G)$  with a function  $g \in L^p(G)$  for some  $p \in [1, \infty]$ , which is given by

$$\nu * g(x) := g * \nu(x) := \int_G g(x - y) \, d\nu(y) \quad (2.3)$$

for  $\mu$ -almost all  $x \in G$ . This expression defines an element of  $L^p(G)$  with

$$\|\nu * g\|_{L^p(G)} \leq \|\nu\|_{M(G)} \|g\|_{L^p(G)};$$

see for example [11, Theorem 20.12]. Since we can interpret  $L^1(G)$  as a closed subspace of  $M(G)$ , (2.3) also defines the convolution with integrable functions. If we consider two functions  $f \in L^1(G)$  and  $g \in L^p(G)$  for some  $1 \leq p \leq \infty$ , we observe that

$$f * g(x) = g * f(x) = \int_G f(x - y)g(y) \, dy = \int_G g(x - y)f(y) \, dy$$

for  $\mu$ -almost all  $x \in G$ . The equality of the two integrals follows from the translation-invariance of the Haar measure. Furthermore, Young's inequality for convolutions states that  $f * g \in L^p(G)$  and

$$\|f * g\|_{L^p(G)} \leq \|f\|_{L^1(G)} \|g\|_{L^p(G)}.$$

Additionally, convolution is associative on  $L^1(G)$  and thus defines a continuous multiplication on this space, which makes  $L^1(G)$  a commutative Banach algebra. Moreover, we obtain

$$\text{supp}(f * g) \subseteq \text{supp} f + \text{supp} g.$$

If we assume  $f \in L^p(G)$  and  $g \in L^{p'}(G)$ , the expression  $f * g(x)$  does also exist for  $\mu$ -almost all  $x \in G$  by Hölder's inequality, and it holds  $f * g \in C_0(G)$ ; see also [19, Subsection 1.1.6].

Recall the following classical approximation statement: If  $1 \leq p < \infty$ ,  $f \in L^p(G)$  and  $\varepsilon > 0$ , then there exists a neighborhood  $U$  of 0 in  $G$  such that

$$\|g * f - f\|_{L^p(G)} < \varepsilon$$

for all  $g \in L^1(G)$  with  $\|g\|_{L^1(G)} = 1$  and  $\text{supp } g \subseteq U$ ; see [11, Theorem 20.15].

## Fourier Transform

For a regular finite Borel measure  $\nu \in M(G)$ , we define its Fourier transform  $\widehat{\nu}: \widehat{G} \rightarrow \mathbb{C}$  by

$$\widehat{\nu}(\gamma) := \int_G (-x, \gamma) \, d\nu(x) \quad \text{for } \gamma \in \widehat{G}.$$

Then  $\widehat{\nu}: \widehat{G} \rightarrow \mathbb{C}$  is a bounded and uniformly continuous function. Moreover, if we again identify  $L^1(G)$  with a subspace of  $M(G)$ , the Fourier transform of  $f \in L^1(G)$  is given by

$$\widehat{f}(\gamma) = \int_G f(x)(-x, \gamma) \, dx \quad \text{for } \gamma \in \widehat{G},$$

and it holds  $\widehat{f} \in C_0(\widehat{G})$ . In particular, the Fourier transform  $\mathcal{F}_G: L^1(G) \rightarrow L^\infty(\widehat{G})$ ,  $f \mapsto \widehat{f}$ , is a continuous linear operator with

$$\|\mathcal{F}_G[f]\|_{L^\infty(\widehat{G})} \leq \|f\|_{L^1(G)}.$$

As one readily verifies,  $\mathcal{F}_G[f * g] = \widehat{f}\widehat{g}$  as well as  $\mathcal{F}_G[\nu * g] = \widehat{\nu}\widehat{g}$  for all  $f, g \in L^1(G)$  and  $\nu \in M(G)$ .

It is possible to normalize the Haar measure  $\mu_{\widehat{G}}$  on  $\widehat{G}$  such that for all  $f \in L^1(G)$  with  $\widehat{f} \in L^1(\widehat{G})$  the so-called inversion formula

$$f(x) = \int_{\widehat{G}} \widehat{f}(\gamma)(x, \gamma) \, d\mu_{\widehat{G}}(\gamma)$$

holds for  $\mu$ -almost all  $x \in G$ . For this reason, the linear operator  $\mathcal{F}_G^{-1}: L^1(\widehat{G}) \rightarrow C_0(G)$  with

$$\mathcal{F}_G^{-1}[g](x) := g^\vee(x) := \int_{\widehat{G}} g(\gamma)(x, \gamma) \, d\mu_{\widehat{G}}(\gamma)$$

is called the inverse Fourier transform. In the following, we always assume that this normalization condition is satisfied. The normalization we fixed for (infinite) compact and discrete groups is compatible with this assumption. However, it is not compatible with the standard Lebesgue-Borel measure  $\lambda$  on  $\mathbb{R}$ . Therefore, if  $G = \mathbb{R}$ , we choose the Haar measure given by  $(2\pi)^{-1}\lambda$  on  $\widehat{G} = \mathbb{R}$  in the following. Then the inversion formula is also valid in this case.

Under the normalization assumptions above, Plancherel's Theorem states that the Fourier transform has an extension to an isometric isomorphism as a mapping  $\mathcal{F}_G: L^2(G) \rightarrow L^2(\widehat{G})$ . Clearly, an analogous statement holds for the operator  $\mathcal{F}_G^{-1}$ , which is the actual inverse of  $\mathcal{F}_G$  in this case. By the Riesz-Thorin Interpolation Theorem, this yields also an extension to  $L^p(G)$  for all  $1 < p < 2$ . As usual, we keep the notation  $\widehat{f}$  and  $\mathcal{F}_G$  for these extensions. Moreover, the Parseval formula is valid. Two of its versions read as

$$\int_G f(x)\overline{g(x)} \, dx = \int_{\widehat{G}} \widehat{f}(\gamma)\overline{\widehat{g}(\gamma)} \, d\gamma \quad \text{and} \quad \int_G f(x)g(x) \, dx = \int_{\widehat{G}} \widehat{f}(\gamma)\widehat{g}(-\gamma) \, d\gamma$$

for all  $f, g \in L^2(G)$ , and a third version is given by

$$\int_G f(x)\widehat{g}(x) \, dx = \int_{\widehat{G}} \widehat{f}(\gamma)g(\gamma) \, d\gamma$$

for  $f \in L^2(G)$  and  $g \in L^2(\widehat{G})$ . For the sake of convenience, we used the notation  $\widehat{g} = \mathcal{F}_{\widehat{G}}[g]$  here.

We sometimes leave out the index  $G$  and write  $\mathcal{F}$  instead of  $\mathcal{F}_G$  if it is obvious which group the Fourier transform relates to. Moreover, if  $X(G)$  is some vector space of objects on  $G$  for which the Fourier transform is well defined, we write

$$\mathcal{F}X(\widehat{G}) := \mathcal{F}[X(G)] = \{\widehat{f} : f \in X(G)\}.$$

## Finite Products

Consider finite products of locally compact abelian groups. Let  $G_1$  and  $G_2$  be such groups and  $G := G_1 \times G_2$  be the direct product of these groups equipped with the product topology. Then  $G$  is also a locally compact abelian group, and a Haar measure on  $G$  is given by the product measure of the Haar measures on  $G_1$  and  $G_2$ . Moreover, the dual group of  $G$  is isomorphic to  $\widehat{G}_1 \times \widehat{G}_2$ . In this case we always consider the corresponding product measures on  $G$  and  $\widehat{G}$ . Then the Fourier transform on  $G$  satisfies

$$\mathcal{F}_G = \mathcal{F}_{G_1}\mathcal{F}_{G_2} = \mathcal{F}_{G_2}\mathcal{F}_{G_1} \quad \text{and} \quad \mathcal{F}_G^{-1} = \mathcal{F}_{G_1}^{-1}\mathcal{F}_{G_2}^{-1} = \mathcal{F}_{G_2}^{-1}\mathcal{F}_{G_1}^{-1},$$

where, for instance,  $\mathcal{F}_{G_1}$  is applied to  $f \in L^p(G)$  for  $1 \leq p \leq 2$  by fixing the  $G_2$ -variable.

## Closed Subgroups and Quotient Groups

We recall some results on closed subgroups of locally compact abelian groups. Let  $G$  be a locally compact abelian group, and let  $H$  be a closed subgroup of  $G$  and  $\Gamma$  be a closed subgroup of  $\widehat{G}$ . Clearly, these are also locally compact abelian groups if we equip them with the corresponding subspace topology. Moreover, this is also the case for  $G/H$  and  $\widehat{G}/\Gamma$  equipped with the quotient topology.

The annihilator of  $H$  is given by

$$H^\perp := \{\gamma \in \widehat{G} : (x, \gamma) = 1 \text{ for all } x \in H\}.$$

Analogously, the set

$$\Gamma^\perp := \{x \in G : (x, \gamma) = 1 \text{ for all } \gamma \in \Gamma\}$$

is called the annihilator of  $\Gamma$ . One readily verifies that  $\Gamma^\perp$  and  $H^\perp$  are closed subgroups of  $G$  and  $\widehat{G}$ , respectively, and that  $(H^\perp)^\perp = H$  and  $(\Gamma^\perp)^\perp = \Gamma$ . Furthermore, there exist isomorphisms such that

$$\widehat{H} \cong \widehat{G}/H^\perp, \quad \widehat{H^\perp} \cong G/H, \quad \widehat{\Gamma} \cong G/\Gamma^\perp, \quad \widehat{\Gamma^\perp} \cong \widehat{G}/\Gamma$$

holds.

Now let  $K$  be a compact subgroup of  $G$ . We can normalize the Haar measures on  $K$  and on  $G/K$  such that for all  $f \in L^1(G)$  we have the identity

$$\int_G f(x) \, dx = \int_{G/K} \int_K f(x+k) \, dk \, d[x],$$

where  $[x]$  is the coset of  $x \in G$  under the quotient mapping  $G \rightarrow G/K$ . In the following, we will always assume that the corresponding Haar measures are chosen in this way. We remark that the inner integral really defines an integrable function on  $G/K$ ; see also [19, Subsection 2.7.3].

## 2.3 Transference Principle for Multipliers

In this section we give a proof of the Transference Principle for Fourier multipliers on locally compact abelian groups. In the classical setting, where the group  $\mathbb{R}^n$  is considered, there are several ways to determine if a Fourier multiplier induces a

bounded operator on  $L^p(\mathbb{R}^n)$ . For multipliers on general locally compact abelian groups, however, there are only a very limited number of tools available that can be used for this purpose. Instead, it is possible to “transfer” a multiplier from one group setting into another in such a way that the question of  $L^p$  boundedness can be answered in the new setting. This procedure is known as the Transference Principle.

The Transference Principle was originally introduced by de Leeuw [3] as a way to transfer Fourier multipliers between the torus group and  $\mathbb{R}$ . The theorem of de Leeuw was later generalized to multipliers on locally compact abelian groups by Edwards and Gaudry [4, Theorem B.2.1]. The proof presented in the following is based on the ideas in [4].

### 2.3.1 Basic Properties of Fourier Multipliers

Throughout this subsection we let  $G$  be a locally compact abelian group and  $\widehat{G}$  its dual group. We denote the Fourier transform on  $G$  by  $\mathcal{F}$ . We start by recalling the definition of Fourier multipliers on a Lebesgue space as they are introduced in [4, Sect. 1.2].

**Definition 2.1** Let  $1 \leq p < \infty$  and  $m \in L^\infty(\widehat{G})$ . We call  $m$  an  $L^p$  multiplier on  $G$  if there exists a constant  $C > 0$  such that

$$\|\mathcal{F}^{-1}[m\widehat{f}]\|_{L^p(G)} \leq C\|f\|_{L^p(G)} \quad (2.4)$$

for all  $f \in L^2 \cap L^p(G)$ . We define  $M_p(\widehat{G})$  as the set of all  $L^p$  multipliers on  $G$ . Furthermore, for  $m \in M_p(\widehat{G})$  we define the multiplier norm of  $m$  by

$$\|m\|_{M_p(\widehat{G})} := \inf \left\{ C > 0 : (2.4) \text{ holds for all } f \in L^2 \cap L^p(G) \right\},$$

and we write  $T_m$  for the operator  $f \mapsto \mathcal{F}^{-1}[m\widehat{f}]$ .

The expression on the left-hand side of inequality (2.4) is well defined since  $m\widehat{f} \in L^2(\widehat{G})$  for all  $f \in L^2(G)$  by Plancherel’s Theorem and Hölder’s inequality. Moreover, again by these two results, we see directly that  $M_2(\widehat{G}) = L^\infty(\widehat{G})$ .

*Remark 2.2* Because the space  $L^2 \cap L^p(G)$  is dense in  $L^p(G)$ , it follows from (2.4) that the operator  $T_m$  on  $L^2 \cap L^p(G)$  can be uniquely extended to a continuous linear operator  $L^p(G) \rightarrow L^p(G)$  with operator norm  $\|T_m\|_{L^p(G) \rightarrow L^p(G)} = \|m\|_{M_p(\widehat{G})}$ . In general, it suffices to verify (2.4) for  $f$  in some other dense subset of  $L^p(G)$  in order to show  $m \in M_p(G)$ .

One readily verifies that  $M_p(\widehat{G})$  is a vector space and  $\|\cdot\|_{M_p(\widehat{G})}$  is a norm on this space for all  $1 \leq p < \infty$ . In addition, we have the following embedding properties.

**Proposition 2.3** *Let  $1 < p < \infty$  and  $p'$  be its dual index. Then the normed vector spaces  $M_p(\widehat{G})$  and  $M_{p'}(\widehat{G})$  coincide and are subsets of  $M_2(\widehat{G})$ . Furthermore, the estimate*

$$\|m\|_{M_2(\widehat{G})} \leq \|m\|_{M_p(\widehat{G})}$$

holds for all  $m \in M_p(\widehat{G})$ .

*Proof* Let  $f, g \in L^p \cap L^{p'}(G)$  and  $m \in M_p(\widehat{G})$ . Then it is clear that also the function  $\widetilde{m}$ , defined by  $\widetilde{m}(\gamma) := m(-\gamma)$  for  $\gamma \in \widehat{G}$ , is an element of  $M_p(\widehat{G})$  with the same multiplier norm as  $m$ . Since we also have  $f, g \in L^2(G)$ , the functions  $T_{\widetilde{m}}f$  and  $T_m g$  are well defined in  $L^2(G)$ . Using Parseval's formula, we obtain

$$\begin{aligned} \int_G (T_{\widetilde{m}}f)g \, dx &= \int_{\widehat{G}} \widetilde{m}(-\gamma) \widehat{f}(-\gamma) \widehat{g}(\gamma) \, d\gamma = \int_{\widehat{G}} \widehat{f}(-\gamma) m(\gamma) \widehat{g}(\gamma) \, d\gamma \\ &= \int_G f(T_m g) \, dx \end{aligned}$$

and thus

$$\left| \int_G f(T_m g) \, dx \right| \leq \|T_{\widetilde{m}}f\|_{L^p(G)} \|g\|_{L^{p'}(G)} \leq \|m\|_{M_p(\widehat{G})} \|f\|_{L^p(G)} \|g\|_{L^{p'}(G)}.$$

This implies  $T_m g \in L^{p'}(G)$  and the estimate

$$\|T_m g\|_{L^{p'}(G)} \leq \|m\|_{M_p(\widehat{G})} \|g\|_{L^{p'}(G)}.$$

Since the space  $L^p \cap L^{p'}(G)$  is dense in  $L^{p'}(G)$ , according to Remark 2.2, we obtain  $m \in M_{p'}(\widehat{G})$  and

$$\|m\|_{M_{p'}(\widehat{G})} \leq \|m\|_{M_p(\widehat{G})}.$$

In total, if we exchange  $p$  and  $p'$  in the above argumentation, we have shown the identities  $M_p(\widehat{G}) = M_{p'}(\widehat{G})$  and

$$\|m\|_{M_p(\widehat{G})} = \|m\|_{M_{p'}(\widehat{G})}$$

for all  $m \in M_p(\widehat{G}) = M_{p'}(\widehat{G})$ . Now this implies that  $T_m$  can be extended to a continuous linear operator  $L^p(G) \rightarrow L^p(G)$  as well as  $L^{p'}(G) \rightarrow L^{p'}(G)$ . By the Riesz-Thorin Interpolation Theorem,  $T_m$  also has an extension to a continuous

operator  $L^2(G) \rightarrow L^2(G)$ , and we obtain

$$\begin{aligned} \|m\|_{M_2(\widehat{G})} &= \|T_m\|_{L^2(G) \rightarrow L^2(G)} \leq \|T_m\|_{L^p(G) \rightarrow L^p(G)}^{\frac{1}{2}} \|T_m\|_{L^{p'}(G) \rightarrow L^{p'}(G)}^{\frac{1}{2}} \\ &= \|m\|_{M_p(\widehat{G})}^{\frac{1}{2}} \|m\|_{M_{p'}(\widehat{G})}^{\frac{1}{2}} \\ &= \|m\|_{M_p(\widehat{G})}, \end{aligned}$$

again by Remark 2.2. This completes the proof.  $\square$

The Fourier transform of a regular finite measure is also an  $L^p$  multiplier for each  $1 \leq p < \infty$ . This is subject of the next proposition.

**Proposition 2.4** *For  $1 \leq p < \infty$  the inclusion  $\mathcal{FM}(\widehat{G}) \subseteq M_p(\widehat{G})$  holds.*

*Proof* By Proposition 2.3 it suffices to consider the case  $1 \leq p \leq 2$ . If  $m \in \mathcal{FM}(\widehat{G})$ , there exists a measure  $\nu \in M(G)$  with  $m = \widehat{\nu}$ . Therefore, for each  $f \in L^1 \cap L^2(G)$  we have  $\nu * f \in L^1 \cap L^2(G)$  and

$$(T_m f) = \mathcal{F}^{-1}[\widehat{\nu f}] = \nu * f.$$

This implies

$$\|T_m f\|_{L^p(G)} = \|\nu * f\|_{L^p(G)} \leq \|\nu\|_{M(G)} \|f\|_{L^p(G)}$$

for all  $f \in L^1 \cap L^2(G)$ . Since the space  $L^1 \cap L^2(G)$  is dense in  $L^p(G)$ , Remark 2.2 yields  $m \in M_p(\widehat{G})$ , and the assertion holds.  $\square$

One can even show the equality  $\mathcal{FM}(\widehat{G}) = M_1(\widehat{G})$ ; see for example [16, Corollary 0.1.1]. We will not need this stronger result in the following.

### 2.3.2 Approximation Results

In this subsection we establish a number of approximation statements. Again let  $G$  be a locally compact abelian group and  $\widehat{G}$  its dual group. Furthermore, let  $\mu$  denote the Haar measure on both  $G$  and  $\widehat{G}$ .

**Theorem 2.5** *Let  $K$  be a compact subset of  $G$  and  $\varepsilon > 0$ . Then there exists a Borel set  $V$  in  $G$  such that its closure is compact and*

$$\mu(K - V) < (1 + \varepsilon)\mu(V).$$

*Proof* A proof of this theorem relies on structure theory for locally compact abelian groups and can be found in [19, Theorem 2.6.7].  $\square$

**Theorem 2.6** *Let  $1 < p < \infty$  with dual index  $p'$ , and let  $K$  be a compact subset of  $G$ . For all  $\varepsilon > 0$ , there exist compactly supported bounded functions  $f, g: G \rightarrow \mathbb{R}$  such that*

- i.  $0 \leq f * g \leq 1$ ,
- ii.  $f * g = 1$  on  $K$ ,
- iii.  $\|f\|_{L^p(G)} \|g\|_{L^{p'}(G)} < 1 + \varepsilon$ .

*Proof* Let  $\varepsilon > 0$ . We define  $\delta := (1 + \varepsilon)^p - 1 > 0$ . By Theorem 2.5, there is a Borel set  $V \subseteq G$  with compact closure such that  $\mu(K - V) < (1 + \delta)\mu(V)$ . We set

$$f := \mathbb{1}_{K-V}, \quad g := \mu(V)^{-1} \mathbb{1}_V.$$

Then we have  $f, g \in L^1 \cap L^\infty(G)$  and clearly  $0 \leq f * g \leq 1$ . For  $y \in K$  we obtain

$$f * g(y) = \frac{1}{\mu(V)} \int_V \mathbb{1}_{K-V}(y-x) \, dx = \frac{1}{\mu(V)} \int_V 1 \, dx = 1,$$

which yields  $f * g = 1$  on  $K$ . Furthermore, we get

$$\|f\|_{L^p(G)} \|g\|_{L^{p'}(G)} = \mu(K-V)^{\frac{1}{p}} \frac{1}{\mu(V)^{\frac{1}{p'}}} \mu(V)^{\frac{1}{p'}} = \left( \frac{\mu(K-V)}{\mu(V)} \right)^{\frac{1}{p}} < (1 + \delta)^{\frac{1}{p}} = 1 + \varepsilon.$$

Consequently,  $f$  and  $g$  possess the desired properties.  $\square$

**Corollary 2.7** *Suppose  $K$  is a compact subset of  $\widehat{G}$  and  $\varepsilon > 0$ . Then there exists a function  $k \in L^1(G)$  such that  $\widehat{k} = 1$  on  $K$ ,  $\widehat{k}$  has compact support and  $\|k\|_{L^1(G)} < 1 + \varepsilon$ .*

*Proof* We apply Theorem 2.6 to the group  $\widehat{G}$  and the compact set  $K$ . Then there are compactly supported bounded functions  $f$  and  $g$  with the properties i. to iii. for  $p = 2$  and  $G$  replaced by  $\widehat{G}$ . In particular, we have  $f * g \in L^1 \cap L^\infty(\widehat{G}) \subseteq L^2(\widehat{G})$ , and we may define  $k := \mathcal{F}^{-1}[f * g] = \mathcal{F}^{-1}[f] \cdot \mathcal{F}^{-1}[g]$ . This leads to

$$\|k\|_{L^1(G)} \leq \|\mathcal{F}^{-1}[f]\|_{L^2(G)} \cdot \|\mathcal{F}^{-1}[g]\|_{L^2(G)} = \|f\|_{L^2(\widehat{G})} \|g\|_{L^2(\widehat{G})} < 1 + \varepsilon.$$

Since the other properties are clearly fulfilled, the proof is finished.  $\square$

**Lemma 2.8** *A locally compact abelian group is compact if and only if its Haar measure is finite.*

*Proof* If  $G$  is a compact abelian group, then  $\mu(G)$  is finite because each compact set has finite Haar measure. Conversely, let  $\mu(G)$  be finite. Then  $\mathbb{1}_G \in L^1(G)$  holds and thus  $\widehat{\mathbb{1}}_G \in C_0(\widehat{G})$ , but

$$\widehat{\mathbb{1}}_G(\gamma) = \mu(G) \mathbb{1}_{\{0\}}(\gamma) \tag{2.5}$$



for all  $\gamma \in \widehat{G}$ . This follows from

$$\widehat{\mathbb{1}}_G(0) = \int_G (-x, 0) \, dx = \int_G 1 \, dx = \mu(G)$$

and

$$\widehat{\mathbb{1}}_G(\gamma) = \int_G (-x + x_0, \gamma) \, dx = (x_0, \gamma) \int_G (-x, \gamma) \, dx = (x_0, \gamma) \widehat{\mathbb{1}}_G(\gamma)$$

for all  $x_0 \in G$  and  $\gamma \in \widehat{G}$  by the translation-invariance of the Haar measure. This equality implies  $\widehat{\mathbb{1}}_G(\gamma) = 0$  if  $\gamma \neq 0$ . Consequently,  $G$  is compact since the function  $\mathbb{1}_{\{0\}}: \widehat{G} \rightarrow \mathbb{C}$  is continuous if and only if the dual group  $\widehat{G}$  is discrete.  $\square$

**Theorem 2.9** *There exists a net  $(k_\alpha)_{\alpha \in A}$  of integrable functions on  $G$  with*

- i.  $\|k_\alpha\|_{L^1(G)} \leq 1$  for all  $\alpha \in A$ ,
- ii.  $\widehat{k}_\alpha \in C_c(\widehat{G})$  for all  $\alpha \in A$ ,
- iii.  $(\widehat{k}_\alpha)_{\alpha \in A}$  converges to 1 locally uniformly on  $\widehat{G}$ .

*Proof* At first we assume that  $G$  is discrete. Then  $\widehat{G}$  is compact. We can therefore define  $k := \mathcal{F}^{-1}[\mathbb{1}_{\widehat{G}}]$  because  $\mathbb{1}_{\widehat{G}} \in L^1(\widehat{G})$ . As in the proof of the previous lemma, we see that  $k = \mathbb{1}_{\{0\}}$ , where we assume that the Haar measure on  $\widehat{G}$  is normalized. Hence  $k \in L^1(G)$  and  $\|k\|_{L^1(G)} = 1$ . The remaining properties are trivially fulfilled if we set  $k_\alpha := k$  and let  $A$  be a singleton set.

Now assume that  $G$  is not discrete. Then  $\widehat{G}$  is not compact. By Lemma 2.8 it holds that  $\mu(\widehat{G})$  is not finite. Since the Haar measure  $\mu$  is a regular Borel measure, there exist compact sets with arbitrarily large Haar measure. We define the set

$$A := \{K \subseteq \widehat{G} : K \text{ is compact and } \mu(K) > 0\},$$

partially ordered by inclusion. By Corollary 2.7 for each  $K \in A$  there is a function  $\psi_K \in L^1(G)$  such that  $\widehat{\psi}_K = 1$  on  $K$ ,  $\widehat{\psi}_K \in C_c(\widehat{G})$  and  $\|\psi_K\|_{L^1(G)} < 1 + \mu(K)^{-1}$ . Then we define the function  $k_K: G \rightarrow \mathbb{C}$  by

$$k_K := \frac{\psi_K}{1 + \mu(K)^{-1}} = \frac{\mu(K)}{1 + \mu(K)} \psi_K.$$

The net  $(k_K)_{K \in A}$  has the desired properties. Indeed, properties i. and ii. are immediately clear. For the verification of iii., let  $K_1$  be an arbitrary compact subset of  $\widehat{G}$  and  $\varepsilon > 0$ . As mentioned above, there exists a compact set  $K_0 \in A$  with  $K_1 \subseteq K_0$  and  $\mu(K_0) > \varepsilon^{-1}$ . For  $K \in A$  with  $K_0 \subseteq K$  we obtain

$$|1 - \widehat{k}_K(\gamma)| = \frac{1 + \mu(K) - \mu(K)\widehat{\psi}_K(\gamma)}{1 + \mu(K)} = \frac{1}{1 + \mu(K)} \leq \frac{1}{\mu(K_0)} < \varepsilon$$

for all  $\gamma \in K_1$  because  $\widehat{\psi}_K(\gamma) = 1$  in this case. Hence the net  $(k_K)_{K \in A}$  converges to 1 locally uniformly, and the proof is finished.  $\square$

Finally, we construct an approximative unit in the Banach algebra  $L^1(G)$  with specific properties. For the statement concerning  $L^p$  functions, we proceed analogously to the proof of Theorem 20.27 in [11].

**Proposition 2.10** *There exists a net  $(k_\alpha)_{\alpha \in A}$  of functions in  $L^1 \cap L^\infty(G)$  with the following properties. It holds  $\|k_\alpha\|_{L^1(G)} = 1$  for all  $\alpha \in A$  and for  $1 \leq p < \infty$  the equation*

$$\lim_{\alpha \in A} \|f - f * k_\alpha\|_{L^p(G)} = 0$$

is valid for all  $f \in L^p(G)$ . Furthermore, for  $f \in C_0(G)$  it holds

$$\lim_{\alpha \in A} \|f - f * k_\alpha\|_{L^\infty(G)} = 0.$$

*Proof* We define  $A$  as the set of all compact neighborhoods of 0 in  $G$ , directed by  $K_1 \leq K_2$  if  $K_1 \supseteq K_2$ . For each  $K \in A$  we consider the function  $k_K := \mu(K)^{-1} \mathbb{1}_K$ . Clearly, then we have  $k_K \in L^1 \cap L^\infty(G)$  and  $\|k_K\|_{L^1(G)} = 1$  for all  $K \in A$ . Furthermore, if  $1 \leq p < \infty$  and  $f \in L^p(G)$ , for each  $\varepsilon > 0$  there exists an element  $K_p \in A$  such that

$$\|u * f - f\|_{L^p(G)} < \varepsilon$$

for all  $u \in L^1(G)$  with  $\|u\|_{L^1(G)} = 1$  and  $\text{supp } u \subseteq K_p$ . Since these conditions are fulfilled for all functions  $k_K$  with  $K \subseteq K_p$ , this yields the first of the desired convergence statements.

Now let  $f \in C_0(G)$  and  $\varepsilon > 0$  be arbitrary. Since  $f$  is uniformly continuous, see [19, B.10], there exists  $K_0 \in A$  such that

$$|f(x) - f(y)| < \varepsilon$$

for all  $x, y \in G$  with  $x - y \in K_0$ . Therefore, for  $x \in G$  arbitrary and  $K \in A$  with  $K \subseteq K_0$ , we obtain

$$\begin{aligned} |f(x) - (k_K * f)(x)| &= \left| \int_G (f(x) - f(x - y)) k_K(y) \, dy \right| \\ &\leq \frac{1}{\mu(K)} \int_K |f(x) - f(x - y)| \, dy \\ &\leq \sup_{y \in K_0} |f(x) - f(x - y)| \leq \varepsilon, \end{aligned}$$

which implies the second convergence result.  $\square$

### 2.3.3 Another Characterization of Multipliers

We shall now introduce a characterization of Fourier multipliers. Specifically, the aim of this subsection is to establish the following theorem.

**Theorem 2.11** *Let  $1 < p < \infty$  with dual index  $p'$ , and let  $m \in L^\infty(\widehat{G})$ . Then  $m \in M_p(\widehat{G})$  holds if and only if there is a constant  $C > 0$  such that*

$$\left| \int_{\widehat{G}} m(\gamma) \widehat{f}(\gamma) \widehat{g}(\gamma) \, d\gamma \right| \leq C \|f\|_{L^p(G)} \|g\|_{L^{p'}(G)} \quad (2.6)$$

for all  $f, g \in L^1(G)$  with compactly supported Fourier transforms. In this case  $\|m\|_{M_p(\widehat{G})}$  is the smallest constant such that estimate (2.6) is valid.

The verification of Theorem 2.11 mainly relies on the fact that the set

$$A(G) := \{f \in L^1(G) : \widehat{f} \text{ has compact support}\} \quad (2.7)$$

is a dense subset of  $L^p(G)$  for  $1 < p < \infty$  if  $G$  is a locally compact abelian group. Since we need this density result, we have to exclude the case  $p = 1$  because  $A(G)$  is not dense in  $L^\infty(G)$ . Indeed, if we consider a function  $f \in A(G)$ , its Fourier transform is continuous and compactly supported and thus an element of  $L^1(\widehat{G})$ . But then the Fourier inverse of  $\widehat{f}$  is also a continuous function, i.e., we have  $A(G) \subseteq C_0(G)$ . Hence  $A(G)$  cannot be a dense subset of  $L^\infty(G)$ , except for the case where  $G$  is finite. Furthermore, this argumentation implies that  $A(G) \subseteq L^\infty(G)$ . Using the standard interpolation inequality, we obtain  $A(G) \subseteq L^p(G)$  for all  $1 \leq p \leq \infty$ .

**Lemma 2.12** *For each  $f \in L^2(G)$  there exists a sequence  $(f_n) \subseteq L^2(G)$  such that  $\widehat{f}_n$  is compactly supported for each  $n \in \mathbb{N}$  and  $(f_n)$  converges to  $f$  in  $L^2(G)$ .*

*Proof* For  $f \in L^2(G)$  we have  $\widehat{f} \in L^2(\widehat{G})$  by Plancherel’s Theorem. Because  $C_c(\widehat{G})$  is a dense subspace of  $L^2(\widehat{G})$ , there is a sequence  $(g_n) \subseteq C_c(\widehat{G})$  that converges to the function  $\widehat{f}$  in  $L^2(\widehat{G})$ . We define  $f_n := \mathcal{F}^{-1}[g_n]$  for all  $n \in \mathbb{N}$ . Again by Plancherel’s Theorem, we obtain that  $(f_n)$  has the desired properties because the Fourier transform is an isometric isomorphism  $L^2(G) \rightarrow L^2(\widehat{G})$ .  $\square$

**Lemma 2.13** *The set  $A(G)$  is a dense subset of  $L^1(G)$ .*

*Proof* Let  $f \in L^1(G)$ . Let  $g := \sqrt{|f|}$  and  $h := \operatorname{sgn}(f) \sqrt{|f|}$ . Then we have  $f = gh$  and  $g, h \in L^2(G)$ . By Lemma 2.12, there are sequences  $(g_n), (h_n) \subseteq L^2(G)$  that converge in  $L^2(G)$  to  $g$  and  $h$ , respectively, and such that  $\widehat{g}_n$  and  $\widehat{h}_n$  are compactly supported functions for each  $n \in \mathbb{N}$ . If we define  $f_n := g_n h_n$ , we have  $f_n \in L^1(G)$  by Hölder’s inequality and  $\widehat{f}_n = \widehat{g}_n * \widehat{h}_n$  is compactly supported, i.e.,  $f_n \in A(G)$  for each  $n \in \mathbb{N}$ . Furthermore, we obtain

$$\|f - f_n\|_{L^1(G)} \leq \|g\|_{L^2(G)} \|h - h_n\|_{L^2(G)} + \|h_n\|_{L^2(G)} \|g - g_n\|_{L^2(G)} \rightarrow 0$$

as  $n \rightarrow \infty$  because  $(h_n)$  is convergent and thus bounded in  $L^2(G)$ . Consequently, we have found a sequence in  $A(G)$  that converges to  $f$ .  $\square$

**Theorem 2.14** *The set  $A(G)$  is a dense subspace of  $L^p(G)$  for all  $1 \leq p < \infty$ .*

*Proof* Let  $1 \leq p < \infty$ . Furthermore, let  $f \in L^p(G)$  and  $\varepsilon > 0$  be arbitrary. Then there exists  $\varphi \in C_c(G)$  with  $\|f - \varphi\|_{L^p(G)} < \frac{\varepsilon}{3}$ . Moreover, by Proposition 2.10 we may choose a function  $k \in L^1(G)$  such that  $\|\varphi - \varphi * k\|_{L^p(G)} < \frac{\varepsilon}{3}$ , and by Lemma 2.13 there exists a function  $\psi \in A(G)$  with  $\|k - \psi\|_{L^1(G)} < \frac{\varepsilon}{3C}$ , where  $C > 0$  is a constant such that  $\|\varphi\|_{L^p(G)} \leq C$ . Because  $\varphi, \psi \in L^1(G)$ , we also have  $\varphi * \psi \in L^1(G)$ . Furthermore, it holds  $\widehat{\varphi} \in C_0(\widehat{G})$  and  $\widehat{\psi} \in C_c(\widehat{G})$ , which implies  $\mathcal{F}[\varphi * \psi] = \widehat{\varphi}\widehat{\psi} \in C_c(\widehat{G})$ . Therefore, we have  $\varphi * \psi \in A(G)$ . Moreover, using Young's inequality we obtain the estimate

$$\begin{aligned} \|f - \varphi * \psi\|_{L^p(G)} &\leq \|f - \varphi\|_{L^p(G)} + \|\varphi - \varphi * k\|_{L^p(G)} + \|\varphi * k - \varphi * \psi\|_{L^p(G)} \\ &\leq \frac{\varepsilon}{3} + \frac{\varepsilon}{3} + \|\varphi\|_{L^p(G)} \|k - \psi\|_{L^1(G)} \\ &< \varepsilon. \end{aligned}$$

Since we have already observed that  $A(G) \subseteq L^p(G)$ , this proves the assertion.  $\square$

After these preparations, we finally come to the proof of Theorem 2.11.

*Proof of Theorem 2.11* First assume that  $m \in M_p(\widehat{G})$ . For  $f, g \in A(G)$  we obtain

$$\begin{aligned} \left| \int_{\widehat{G}} m(\gamma) \widehat{f}(\gamma) \widehat{g}(\gamma) \, d\gamma \right| &= \left| \int_G T_m f(x) g(-x) \, dx \right| \\ &\leq \|T_m f\|_{L^p(G)} \|g\|_{L^{p'}(G)} \\ &\leq \|m\|_{M_p(\widehat{G})} \|f\|_{L^p(G)} \|g\|_{L^{p'}(G)}, \end{aligned}$$

where we used Parseval's formula and Hölder's inequality. Thus estimate (2.6) is valid for a constant  $C \leq \|m\|_{M_p(\widehat{G})}$ . Conversely, assume there is a constant  $C > 0$  such that inequality (2.6) holds for all  $f, g \in A(G)$ . Since we have

$$\int_G T_m f(x) g(x) \, dx = \int_{\widehat{G}} m(\gamma) \widehat{f}(\gamma) \widehat{g}(-\gamma) \, d\gamma$$

by Parseval's formula, we obtain

$$\left| \int_G T_m f(x) g(x) \, dx \right| \leq C \|f\|_{L^p(G)} \|g\|_{L^{p'}(G)}$$

for all  $f, g \in A(G)$ . Since  $A(G)$  is dense in  $L^p(G)$  and  $L^{p'}(G)$  by Theorem 2.14, it follows that  $T_m: L^p(G) \rightarrow L^p(G)$  is a bounded operator, i.e., we have  $m \in M_p(\widehat{G})$  and  $\|m\|_{M_p(\widehat{G})} \leq C$ .  $\square$

### 2.3.4 The Transference Principle

**Theorem 2.15 (Transference Principle)** *Let  $G$  and  $H$  be locally compact abelian groups and let  $\Phi: \widehat{H} \rightarrow \widehat{G}$  be a continuous homomorphism. If  $1 < p < \infty$  and  $m \in M_p \cap C(\widehat{G})$ , then it holds  $m \circ \Phi \in M_p(\widehat{H})$  and*

$$\|m \circ \Phi\|_{M_p(\widehat{H})} \leq \|m\|_{M_p(\widehat{G})}. \quad (2.8)$$

For the remainder of this subsection,  $G$  and  $H$  will always be locally compact abelian groups.

**Definition 2.16** Let  $\Phi: \widehat{H} \rightarrow \widehat{G}$  be a continuous homomorphism. The function  $\widehat{\Phi}: G \rightarrow H$  that satisfies

$$\forall x \in G, \chi \in \widehat{H} : \quad (\widehat{\Phi}(x), \chi) = (x, \Phi(\chi)) \quad (2.9)$$

is called the *dual homomorphism* of  $\Phi$ .

Observe that the dual homomorphism is well defined by Eq.(2.9) due to Pontryagin’s Duality Theorem.

**Proposition 2.17 (Generalized Parseval Formula)** *Let  $\Phi: \widehat{H} \rightarrow \widehat{G}$  be a continuous homomorphism. For  $m \in \mathcal{FL}^1 \cap L^1(\widehat{G})$  and  $E \in \mathcal{FL}^1 \cap L^1(H)$ , it holds*

$$\int_G E(\widehat{\Phi}(x)) \widehat{m}(x) \, dx = \int_{\widehat{H}} m(\Phi(\chi)) \widehat{E}(\chi) \, d\chi.$$

*Proof* We define the measure  $\nu: \mathcal{B}(\widehat{G}) \rightarrow \mathbb{C}$  by

$$\nu(S) := \int_{\Phi^{-1}(S)} \widehat{E}(-\chi) \, d\chi.$$

Then  $\nu$  is a finite measure since  $\widehat{E} \in L^1(\widehat{H})$ . First we shall show that

$$\int_{\widehat{G}} f(\gamma) \, d\nu(\gamma) = \int_{\widehat{H}} f(\Phi(\chi)) \widehat{E}(-\chi) \, d\chi \quad (2.10)$$

for all bounded Borel functions  $f: \widehat{G} \rightarrow \mathbb{C}$ . If we consider the function  $f = \mathbb{1}_S$  for some  $S \in \mathcal{B}(\widehat{G})$ , starting from the right-hand side of Eq.(2.10), we obtain

$$\int_{\widehat{H}} \mathbb{1}_S(\Phi(\chi)) \widehat{E}(-\chi) \, d\chi = \int_{\Phi^{-1}(S)} \widehat{E}(-\chi) \, d\chi = \nu(S) = \int_{\widehat{G}} \mathbb{1}_S(\gamma) \, d\nu(\gamma),$$

so that Eq.(2.10) holds for the characteristic function of any Borel set. By linearity of the integral, this is also valid for simple functions on  $\widehat{G}$ . Finally, Eq.(2.10) holds for all bounded Borel functions  $f: \widehat{G} \rightarrow \mathbb{C}$  by the Monotone Convergence Theorem since we can monotonously approximate these by simple functions.

Now we consider  $x \in G$  and define  $f: \widehat{G} \rightarrow \mathbb{C}$  by  $f(\gamma) = (-x, \gamma)$ . Then we obtain the equality

$$\begin{aligned} \widehat{v}(x) &= \int_{\widehat{G}} (-x, \gamma) \, dv(\gamma) = \int_{\widehat{H}} (-x, \Phi(\chi)) \widehat{E}(-\chi) \, d\chi \\ &= \int_{\widehat{H}} (-\widehat{\Phi}(x), \chi) \widehat{E}(-\chi) \, d\chi = \int_{\widehat{H}} (\widehat{\Phi}(x), \chi) \widehat{E}(\chi) \, d\chi \\ &= E(\widehat{\Phi}(x)) \end{aligned}$$

by formula (2.10) and the Inversion Theorem, which is applicable due to the assumption  $E \in \mathcal{FL}^1 \cap L^1(H)$ . It follows that

$$\int_G E(\widehat{\Phi}(x)) \widehat{m}(x) \, dx = \int_G \widehat{v}(x) \widehat{m}(x) \, dx = \int_{\widehat{G}} \int_G (-x, \gamma) \widehat{m}(x) \, dx \, dv(\gamma),$$

where we used Fubini's Theorem. Using the inversion formula and equality (2.10) again, we can further transform the right-hand side and obtain

$$\int_{\widehat{G}} m(-\gamma) \, dv(\gamma) = \int_{\widehat{H}} m(-\Phi(\chi)) \widehat{E}(-\chi) \, d\chi = \int_{\widehat{H}} m(\Phi(\chi)) \widehat{E}(\chi) \, d\chi$$

by reflection-invariance of the Haar measure. In total, we have derived the equality we intended to show.  $\square$

We start with a special case of Theorem 2.15. Recall that  $L^1(G)$  can be identified with a subspace of  $M(G)$ , and thus it holds  $\mathcal{FL}^1(\widehat{G}) \subseteq M_p \cap C(\widehat{G})$  according to Proposition 2.4.

**Lemma 2.18** *Let the assumptions of Theorem 2.15 be fulfilled, and assume further that  $m \in \mathcal{FL}^1 \cap L^1(\widehat{G})$  holds. Then  $m \circ \Phi \in M_p(\widehat{H})$  and estimate (2.8) is valid.*

*Proof* By Theorem 2.11 the statement follows if we can show

$$\left| \int_{\widehat{H}} m \circ \Phi(\chi) \widehat{h}(\chi) \widehat{k}(\chi) \, d\chi \right| \leq \|m\|_{M_p(\widehat{G})} \|h\|_{L^p(H)} \|k\|_{L^{p'}(H)} \tag{2.11}$$

for all integrable functions  $h, k: H \rightarrow \mathbb{C}$  with compactly supported Fourier transforms. For this purpose, let  $h, k \in L^1(H)$  such that  $\widehat{h}$  and  $\widehat{k}$  have compact support. By the generalized Parseval formula, Proposition 2.17, we have the equality

$$\int_{\widehat{H}} m(\Phi(\chi)) \widehat{h}(\chi) \widehat{k}(\chi) \, d\chi = \int_G (h * k)(\widehat{\Phi}(x)) \widehat{m}(x) \, dx \tag{2.12}$$

because  $h * k \in L^1(H)$  and  $\mathcal{F}[h * k] = \widehat{h} \widehat{k} \in L^1(\widehat{H})$ .

Now let  $\varepsilon > 0$  be arbitrary. Since the integrand on the right-hand side of Eq. (2.12) is an integrable function, we may choose a compact subset  $K$  of  $G$  such that

$$\int_{G \setminus K} |(h * k)(\widehat{\Phi}(x)) \widehat{m}(x)| \, dx \leq \frac{\varepsilon}{2} \|m\|_{M_p(\widehat{G})} \|h\|_{L^p(H)} \|k\|_{L^{p'}(H)}. \quad (2.13)$$

Furthermore, by Theorem 2.6 we may choose compactly supported bounded functions  $f, g: G \rightarrow \mathbb{C}$  with the properties

- i.  $0 \leq f * g \leq 1$ ,
- ii.  $f * g = 1$  on  $K$ ,
- iii.  $\|f\|_{L^p(G)} \|g\|_{L^{p'}(G)} \leq 1 + \frac{\varepsilon}{2}$ .

If we are able to show

$$\left| \int_G (h * k)(\widehat{\Phi}(x)) (f * g)(x) \widehat{m}(x) \, dx \right| \leq \left(1 + \frac{\varepsilon}{2}\right) \|m\|_{M_p(\widehat{G})} \|h\|_{L^p(H)} \|k\|_{L^{p'}(H)}, \quad (2.14)$$

inequality (2.11) follows, which finishes the proof. Indeed, Eq. (2.12) and the estimates (2.13) and (2.14) lead to

$$\begin{aligned} \left| \int_{\widehat{H}} m \circ \Phi(\chi) \widehat{h}(\chi) \widehat{k}(\chi) \, d\chi \right| &= \left| \int_G (h * k)(\widehat{\Phi}(x)) \widehat{m}(x) \, dx \right| \\ &\leq \left| \int_G (h * k)(\widehat{\Phi}(x)) (f * g)(x) \widehat{m}(x) \, dx \right| \\ &\quad + \left| \int_G (h * k)(\widehat{\Phi}(x)) (1 - (f * g)(x)) \widehat{m}(x) \, dx \right| \\ &\leq \left(1 + \frac{\varepsilon}{2}\right) \|m\|_{M_p(\widehat{G})} \|h\|_{L^p(H)} \|k\|_{L^{p'}(H)} + \int_{G \setminus K} |(h * k)(\widehat{\Phi}(x))| |\widehat{m}(x)| \, dx \\ &\leq (1 + \varepsilon) \|m\|_{M_p(\widehat{G})} \|h\|_{L^p(H)} \|k\|_{L^{p'}(H)} \end{aligned}$$

because we have  $0 \leq 1 - f * g \leq 1$ . Since  $\varepsilon > 0$  was chosen arbitrarily, we obtain the desired estimate (2.11). Therefore, it remains to show inequality (2.14). To do so, for a function  $w: H \rightarrow \mathbb{C}$  and an element  $u \in H$ , we define the function  $\tau_u w$  by  $\tau_u w(x) := w(x - u)$  for all  $x \in H$ . By translation-invariance of the Haar measure, we now obtain the equality

$$\begin{aligned} (h * k)(\widehat{\Phi}(x)) (f * g)(x) &= \int_H h(\widehat{\Phi}(x) - u) k(u) \, du \int_G f(x - y) g(y) \, dy \\ &= \int_G \int_H h(\widehat{\Phi}(x) - \widehat{\Phi}(y) - u) k(u + \widehat{\Phi}(y)) f(x - y) g(y) \, du \, dy \end{aligned}$$

$$\begin{aligned}
&= \int_H \int_G [(\tau_u h \circ \widehat{\Phi})f](x-y) [(\tau_{-u} k \circ \widehat{\Phi})g](y) \, dy \, du \\
&= \int_H [(\tau_u h \circ \widehat{\Phi})f] * [(\tau_{-u} k \circ \widehat{\Phi})g](x) \, du,
\end{aligned}$$

where we used Fubini's Theorem. Therefore, again by Fubini's Theorem, we can rewrite the left-hand side of inequality (2.14) as

$$\left| \int_H \int_G [(\tau_u h \circ \widehat{\Phi})f] * [(\tau_{-u} k \circ \widehat{\Phi})g](x) \cdot \widehat{m}(x) \, dx \, du \right|.$$

By the (standard) Parseval formula, this is equal to

$$\left| \int_H \int_G m(\gamma) \mathcal{F}[(\tau_u h \circ \widehat{\Phi})f](\gamma) \cdot \mathcal{F}[(\tau_{-u} k \circ \widehat{\Phi})g](\gamma) \, d\gamma \, du \right|,$$

which can be estimated by

$$\int_H \left| \int_G m(\gamma) \mathcal{F}[(\tau_u h \circ \widehat{\Phi})f](\gamma) \cdot \mathcal{F}[(\tau_{-u} k \circ \widehat{\Phi})g](\gamma) \, d\gamma \right| \, du.$$

Since  $m$  is an  $L^p$  multiplier on  $G$ , see Proposition 2.4, we can use Theorem 2.11 in order to obtain

$$\int_H \|m\|_{M_p(\widehat{G})} \|(\tau_u h \circ \widehat{\Phi})f\|_{L^p(G)} \|(\tau_{-u} k \circ \widehat{\Phi})g\|_{L^{p'}(G)} \, du$$

as an upper bound for this term. By Hölder's inequality we can estimate this term by

$$\|m\|_{M_p(\widehat{G})} \left( \int_H \|(\tau_u h \circ \widehat{\Phi})f\|_{L^p(G)}^p \, du \right)^{\frac{1}{p}} \left( \int_H \|(\tau_{-u} k \circ \widehat{\Phi})g\|_{L^{p'}(G)}^{p'} \, du \right)^{\frac{1}{p'}},$$

and Fubini's Theorem implies that this is equal to

$$\|m\|_{M_p(\widehat{G})} \|f\|_{L^p(G)} \|h\|_{L^p(H)} \|g\|_{L^{p'}(G)} \|k\|_{L^{p'}(H)}.$$

Summarizing these estimates and using property iii. of  $f$  and  $g$ , we obtain

$$\left| \int_G (h * k)(\widehat{\Phi}(x))(f * g)(x) \widehat{m}(x) \, dx \right| \leq \left(1 + \frac{\varepsilon}{2}\right) \|m\|_{M_p(\widehat{G})} \|h\|_{L^p(H)} \|k\|_{L^{p'}(H)},$$

i.e., we verified inequality (2.14), which finishes the proof.  $\square$



**Lemma 2.19** *If  $m \in \mathcal{FL}^1(\widehat{G})$  and  $\Phi: \widehat{H} \rightarrow \widehat{G}$  is a continuous homomorphism, then  $m \circ \Phi \in \mathcal{FM}(\widehat{H})$ .*

*Proof* By assumption there is a function  $f \in L^1(G)$  with  $m = \widehat{f}$ . Hence we have

$$\begin{aligned} (m \circ \Phi)(\chi) &= \widehat{f}(\Phi(\chi)) = \int_G (-x, \Phi(\chi)) f(x) \, dx = \int_G (-\widehat{\Phi}(x), \chi) \, d\mu_f(x) \\ &= \int_H (-y, \chi) \, d(\mu_f \circ \widehat{\Phi}^{-1})(y) = \mathcal{F}[\mu_f \circ \widehat{\Phi}^{-1}](\chi) \end{aligned}$$

for all  $\chi \in \widehat{H}$ . Here  $\mu_f$  is the measure on  $G$  which is given by

$$\mu_f(S) = \int_S f(x) \, dx$$

for  $S \in \mathcal{B}(G)$ , and  $\mu_f \circ \widehat{\Phi}^{-1}$  is the image measure of  $\mu_f$  under  $\widehat{\Phi}$ . Since  $f$  is an integrable function, both of these measures are regular and finite, which implies the claimed statement.  $\square$

We can now establish Theorem 2.15 for multipliers  $m$  with compact support.

**Lemma 2.20** *Let the assumptions of Theorem 2.15 be fulfilled, and assume additionally that  $m$  is compactly supported. Then  $m \circ \Phi \in M_p(\widehat{H})$  and estimate (2.8) is valid.*

*Proof* Let  $m \in M_p \cap C_c(\widehat{G})$ . By Proposition 2.10 there exists an approximative unit  $(k_\alpha)_{\alpha \in A} \subseteq L^1 \cap L^\infty(\widehat{G})$  with  $\|k_\alpha\|_{L^1(\widehat{G})} = 1$  for all  $\alpha \in A$ . Then we have

- i.  $m * k_\alpha \in \mathcal{FL}^1 \cap L^1(\widehat{G})$  for all  $\alpha \in A$ ,
- ii.  $(m * k_\alpha)_{\alpha \in A}$  converges to  $m$  uniformly on  $\widehat{G}$ ,
- iii.  $m * k_\alpha \in M_p(\widehat{G})$  and  $\|m * k_\alpha\|_{M_p(\widehat{G})} \leq \|m\|_{M_p(\widehat{G})}$  for all  $\alpha \in A$ .

Property i. can be seen as follows. For  $\alpha \in A$  it is clear that  $m * k_\alpha$  is integrable since  $m$  and  $k_\alpha$  are so. In addition,  $\mathcal{F}[m * k_\alpha] = \widehat{m} \widehat{k}_\alpha$  is also integrable, which follows from  $m, k_\alpha \in L^1 \cap L^\infty(G) \subseteq L^2(\widehat{G})$  by Hölder's inequality and Plancherel's Theorem.

The validity of ii. follows directly from Proposition 2.10.

Because we can interpret  $L^1(G)$  as a subset of  $M(G)$ , the first statement of iii. is a direct consequence of i. and Proposition 2.4. In order to show the claimed inequality, we can use Theorem 2.11, i.e., it suffices to show

$$\left| \int_{\widehat{G}} m * k_\alpha(\gamma) \widehat{f}(\gamma) \widehat{g}(\gamma) \, d\gamma \right| \leq \|m\|_{M_p(\widehat{G})} \|f\|_{L^p(G)} \|g\|_{L^{p'}(G)}$$

for all integrable functions  $f, g: G \rightarrow \mathbb{C}$  with compactly supported Fourier transforms. If we choose such functions  $f, g$  and some  $\gamma_0 \in \widehat{G}$ , we obtain, again

by Theorem 2.11, that

$$\left| \int_{\widehat{G}} m(\gamma - \gamma_0) \widehat{f}(\gamma) \widehat{g}(\gamma) \, d\gamma \right| \leq \|m\|_{M_p(\widehat{G})} \|f\|_{L^p(G)} \|g\|_{L^{p'}(G)}$$

because  $m$  and thus also  $m(\cdot - \gamma_0)$  is an  $L^p$  multiplier on  $G$ . Together with Fubini's Theorem, this implies

$$\begin{aligned} \left| \int_{\widehat{G}} m * k_\alpha(\gamma) \widehat{f}(\gamma) \widehat{g}(\gamma) \, d\gamma \right| &= \left| \int_{\widehat{G}} \int_{\widehat{G}} m(\gamma - \gamma_0) k_\alpha(\gamma_0) \widehat{f}(\gamma) \widehat{g}(\gamma) \, d\gamma_0 \, d\gamma \right| \\ &\leq \int_{\widehat{G}} \left| \int_{\widehat{G}} m(\gamma - \gamma_0) k_\alpha(\gamma_0) \widehat{f}(\gamma) \widehat{g}(\gamma) \, d\gamma \right| \, d\gamma_0 \\ &\leq \int_{\widehat{G}} |k_\alpha(\gamma_0)| \|m\|_{M_p(\widehat{G})} \|f\|_{L^p(G)} \|g\|_{L^{p'}(G)} \, d\gamma_0 \\ &= \|m\|_{M_p(\widehat{G})} \|f\|_{L^p(G)} \|g\|_{L^{p'}(G)}, \end{aligned}$$

where we used Theorem 2.11 again. This yields statement iii.

Properties i. and iii. and Lemma 2.18 imply  $(m * k_\alpha) \circ \Phi \in M_p(\widehat{H})$  and

$$\|(m * k_\alpha) \circ \Phi\|_{M_p(\widehat{H})} \leq \|m * k_\alpha\|_{M_p(\widehat{G})} \leq \|m\|_{M_p(\widehat{G})}$$

for all  $\alpha \in A$ . Therefore, if we consider two integrable functions  $h, k: H \rightarrow \mathbb{C}$  such that  $\widehat{h}, \widehat{k}$  are compactly supported we have, by Theorem 2.11,

$$\left| \int_{\widehat{H}} (m * k_\alpha) \circ \Phi(\chi) \widehat{h}(\chi) \widehat{k}(\chi) \, d\chi \right| \leq \|m\|_{M_p(\widehat{G})} \|h\|_{L^p(H)} \|k\|_{L^{p'}(H)}.$$

Because of property ii., the sequence  $((m * k_\alpha) \circ \Phi)_{\alpha \in A}$  converges to  $m \circ \Phi$  uniformly on  $\widehat{H}$ . Since we have  $\widehat{h}, \widehat{k} \in C_c(\widehat{H})$ , Hölder's inequality implies that the left-hand side of this inequality converges, and we get

$$\left| \int_{\widehat{H}} m \circ \Phi(\chi) \widehat{h}(\chi) \widehat{k}(\chi) \, d\chi \right| \leq \|m\|_{M_p(\widehat{G})} \|h\|_{L^p(H)} \|k\|_{L^{p'}(H)}.$$

Now another application of Theorem 2.11 yields the claim.  $\square$

Finally, we can consider the general case and complete the proof of the Transference Principle.

*Proof of Theorem 2.15* Let  $m \in M_p \cap C(\widehat{G})$  and let  $(k_\alpha)_{\alpha \in A}$  be the net of integrable functions on  $G$  constructed in Theorem 2.9, i.e., with the properties

- i.  $\|k_\alpha\|_{L^1(G)} \leq 1$  for all  $\alpha \in A$ ,
- ii.  $\widehat{k}_\alpha \in C_c(\widehat{G})$  for all  $\alpha \in A$ ,
- iii.  $(\widehat{k}_\alpha)$  converges to 1 locally uniformly on  $\widehat{G}$ .

Because we have  $m \in M_p(\widehat{G})$ , Theorem 2.11 implies

$$\begin{aligned} \left| \int_{\widehat{G}} m(\gamma) \widehat{k}_\alpha(\gamma) \widehat{f}(\gamma) \widehat{g}(\gamma) \, d\gamma \right| &= \left| \int_{\widehat{G}} m(\gamma) \mathcal{F}[k_\alpha * f](\gamma) \widehat{g}(\gamma) \, d\gamma \right| \\ &\leq \|m\|_{M_p(\widehat{G})} \|k_\alpha * f\|_{L^p(G)} \|g\|_{L^{p'}(G)} \\ &\leq \|m\|_{M_p(\widehat{G})} \|f\|_{L^p(G)} \|g\|_{L^{p'}(G)} \end{aligned}$$

for all integrable functions  $f, g: G \rightarrow \mathbb{C}$  with compactly supported Fourier transforms and for all  $\alpha \in A$ . Here we used Young's inequality as well as the fact that the function  $\mathcal{F}[k_\alpha * f] = \widehat{k}_\alpha \widehat{f}$  is compactly supported and  $\|k_\alpha\|_{L^1(G)} \leq 1$ . Together with Theorem 2.11, this estimate yields  $m\widehat{k}_\alpha \in M_p(\widehat{G})$  and

$$\|m\widehat{k}_\alpha\|_{M_p(\widehat{G})} \leq \|m\|_{M_p(\widehat{G})}$$

for all  $\alpha \in A$ . We also have  $m\widehat{k}_\alpha \in C_c(\widehat{G})$ . Therefore, it follows from the inequality above and Lemma 2.20 that  $(m\widehat{k}_\alpha) \circ \Phi \in M_p(\widehat{H})$  and

$$\|(m\widehat{k}_\alpha) \circ \Phi\|_{M_p(\widehat{H})} \leq \|m\widehat{k}_\alpha\|_{M_p(\widehat{G})} \leq \|m\|_{M_p(\widehat{G})}.$$

Using Theorem 2.11 once more, we get

$$\left| \int_{\widehat{H}} ((m\widehat{k}_\alpha) \circ \Phi)(\chi) \widehat{h}(\chi) \widehat{k}(\chi) \, d\chi \right| \leq \|m\|_{M_p(\widehat{G})} \|h\|_{L^p(H)} \|k\|_{L^{p'}(H)} \quad (2.15)$$

for all integrable functions  $h, k: H \rightarrow \mathbb{C}$  with compactly supported Fourier transforms. By property iii., the net  $((m\widehat{k}_\alpha) \circ \Phi)_{\alpha \in A}$  converges to  $m \circ \Phi$  locally uniformly on  $\widehat{H}$ . Therefore, Hölder's inequality implies that the left-hand side of inequality (2.15) converges. We thus obtain the estimate

$$\left| \int_{\widehat{H}} (m \circ \Phi)(\chi) \widehat{h}(\chi) \widehat{k}(\chi) \, d\chi \right| \leq \|m\|_{M_p(\widehat{G})} \|h\|_{L^p(H)} \|k\|_{L^{p'}(H)}.$$

A final application of Theorem 2.11 yields  $m \circ \Phi \in M_p(\widehat{H})$  and the validity of estimate (2.8). This completes the proof.  $\square$

## 2.4 The Schwartz-Bruhat Space

The Schwartz-Bruhat space  $\mathcal{S}(G)$  is a generalization of the classical Schwartz space  $\mathcal{S}(\mathbb{R}^n)$  to a setting of functions defined on a locally compact abelian group  $G$ . Analogously to the classical case, this topological vector space and its dual space

can be used to investigate partial differential equations with the help of the Fourier transform.

The construction of Schwartz-Bruhat spaces is due to Bruhat, who first introduced these spaces in 1961 [2, Sect. 9]. The construction in [2] is based on properties of Lie groups. In order to give a more self-contained introduction to  $\mathcal{S}(G)$ , we shall avoid the notion of Lie groups below.

At first we will construct the Schwartz-Bruhat space for elementary groups, i.e., for the case that the group is isomorphic to  $\mathbb{R}^n \times \mathbb{T}^p \times \mathbb{Z}^q \times F$ , where  $F$  is a finite abelian group and  $n, p, q \in \mathbb{N}_0$ . In this case we will derive a number of results that are completely analogous to the classical case. Subsequently, we will establish some results concerning compactly generated subgroups and so-called good subgroups. Finally, we will define the Schwartz-Bruhat space on an arbitrary locally compact abelian group as an inductive limit of Schwartz-Bruhat spaces on elementary groups. A space of tempered distributions  $\mathcal{S}'(G)$  can then be defined as the topological dual space to  $\mathcal{S}(G)$ . We shall verify that the Fourier transform acts on  $\mathcal{S}(G)$  and  $\mathcal{S}'(G)$  in the expected way.

### 2.4.1 Elementary Groups

**Definition 2.21** A topological group  $G$  is called *elementary* if it is isomorphic to  $\mathbb{R}^n \times \mathbb{T}^p \times \mathbb{Z}^q \times F$  for some  $n, p, q \in \mathbb{N}_0$ , where  $F$  is a finite abelian group. In this case we call the triple  $(n, p, q)$  *the type of  $G$* .

The type of an elementary group is unique. This can be seen by using [11, Corollary 9.13], which tells us that the numbers  $n$  and  $q$  are unique. By the fact that  $\mathbb{T}^p \times F$  consists of  $|F|$  many connected components, we also obtain the uniqueness of  $p$ . For simplicity, in the rest of this subsection we identify an elementary group of type  $(n, p, q)$  directly with  $\mathbb{R}^n \times \mathbb{T}^p \times \mathbb{Z}^q \times F$ .

The occurring product space is equipped with the usual product topology. Therefore, elementary groups are, in particular, locally compact abelian groups. Furthermore, the dual group of an elementary group of type  $(n, p, q)$  is an elementary group of type  $(n, q, p)$ .

It is clear that not every locally compact abelian group is elementary, consider  $\mathbb{T}^{\mathbb{N}}$  for example. But we will see later that we can approximate each such group by elementary groups in a certain way. We shall use such an approximation to define the Schwartz-Bruhat space on arbitrary locally compact abelian groups.

The definition of the Schwartz-Bruhat space on an elementary group is a straightforward generalization of the classical case, i.e., of the case where the group is  $\mathbb{R}^n$ . We first define a differentiability structure on elementary groups. Let  $G$  be an elementary group of type  $(n, p, q)$  and  $f: G \rightarrow \mathbb{C}$ . For each  $k \in \mathbb{Z}^q$  and each  $a \in F$ , we define the function

$$f^{(k,a)}: \mathbb{R}^n \times \mathbb{R}^p \rightarrow \mathbb{C}, \quad f^{(k,a)}(t, x) := f(x, [t], k, a). \quad (2.16)$$

Here  $[t]$  is the image of  $t$  under the quotient mapping  $\mathbb{R}^p \rightarrow \mathbb{T}^p \cong (\mathbb{R}/2\pi\mathbb{Z})^p$ . We define the set  $C^\infty(G)$  as the set of all  $f: G \rightarrow \mathbb{C}$  such that  $f^{(k,a)} \in C^\infty(\mathbb{R} \times \mathbb{R}^{np})$  for all  $k \in \mathbb{Z}^q$  and all  $a \in F$ . Hence for  $f \in C^\infty(G)$  the derivative  $D_x^\beta D_t^\gamma f$  for  $\beta \in \mathbb{N}_0^n$  and  $\gamma \in \mathbb{N}_0^q$  is a well-defined function and it is also an element of  $C^\infty(G)$ . Now we can define the expressions

$$\rho_{\alpha,\beta,\gamma,\delta}^{\mathcal{S}(G)}(f) := \rho_{\alpha,\beta,\gamma,\delta}(f) := \sup_{(t,x,k,a) \in G} |x^\alpha k^\delta D_x^\beta D_t^\gamma f(t, x, k, a)| \tag{2.17}$$

for each  $\alpha, \beta \in \mathbb{N}_0^n, \gamma \in \mathbb{N}_0^q$  and  $\delta \in \mathbb{N}_0^q$ , which enable us to give the definition of the Schwartz-Bruhat space in this setting.

**Definition 2.22** Let  $G$  be an elementary group of type  $(n, p, q)$ . The *Schwartz-Bruhat space*  $\mathcal{S}(G)$  on  $G$  is defined by

$$\mathcal{S}(G) := \{f \in C^\infty(G) : \rho_{\alpha,\beta,\gamma,\delta}(f) < \infty \text{ for all } \alpha, \beta \in \mathbb{N}_0^n, \gamma \in \mathbb{N}_0^q, \delta \in \mathbb{N}_0^q\}$$

and equipped with the locally convex topology induced by the family  $\{\rho_{\alpha,\beta,\gamma,\delta}\}$  of seminorms defined in (2.17).

Observe that the Schwartz-Bruhat space is not trivial. For example, the function

$$f: G \rightarrow \mathbb{C}, \quad f(t, x, k, a) := e^{-|x|^2 - |k|^2} \tag{2.18}$$

is an element of  $\mathcal{S}(G)$ , which one may easily verify. Moreover, the Schwartz-Bruhat space embeds continuously into  $L^r(G)$ .

**Theorem 2.23** Let  $G$  be an elementary group and  $1 \leq r \leq \infty$ . Then  $\mathcal{S}(G)$  is continuously embedded into  $L^r(G)$ .

*Proof* The case  $r = \infty$  is clear since we have  $\|f\|_{L^\infty(G)} = \rho_{0,0,0,0}(f)$  for all  $f \in \mathcal{S}(G)$ . Therefore, it remains to consider the case  $1 \leq r < \infty$ . Furthermore, we assume  $n, q > 0$  since the cases  $n = 0$  and  $q = 0$  are quite similar and less difficult. Let  $f \in \mathcal{S}(G)$  and define the sets

$$\begin{aligned} M_1 &:= B_1^n(0) \times \mathbb{T}^p \times \{0\}^q \times F, \\ M_2 &:= B_1^n(0)^c \times \mathbb{T}^p \times \{0\}^q \times F, \\ M_3 &:= B_1^n(0) \times \mathbb{T}^p \times (\{0\}^q)^c \times F, \\ M_4 &:= B_1^n(0)^c \times \mathbb{T}^p \times (\{0\}^q)^c \times F. \end{aligned}$$

Then  $G$  is the disjoint union of the family  $\{M_i : i = 1, \dots, 4\}$ . By the normalization assumptions, the set  $M_1$  has the Haar measure  $\mu(M_1) = v_n \mu_F(F)$ , where  $\mu_F$  is the Haar measure on  $F$ . We obtain

$$\int_{M_1} |f(x)|^r dx \leq \mu(M_1) \cdot \|f\|_{L^\infty(G)}^r = v_n \mu_F(F) \cdot \rho_{0,0,0,0}(f)^r. \tag{2.19}$$

With the help of Fubini's Theorem, on the set  $M_4$  we derive the estimate

$$\begin{aligned} \int_{M_4} |f(x)|^r dx &= \int_{M_4} |x|^{-n-1} |k|^{-q-1} |x|^{n+1} |k|^{q+1} |f(t, x, k, a)|^r d(t, x, k, a) \\ &\leq \mu_F(F) \int_{B_1^n(0)^c} |x|^{-n-1} dx \cdot \sum_{\substack{k \in \mathbb{Z}^q \\ k \neq 0}} |k|^{-q-1} \cdot \sup_{(t,x,k,a) \in M_4} |x|^{n+1} |k|^{q+1} |f(t, x, k, a)|^r. \end{aligned}$$

For the remaining integral, we have

$$\int_{B_1^n(0)^c} |x|^{-n-1} dx = \omega_n \int_1^\infty s^{-n-1} s^{n-1} ds = \omega_n \int_1^\infty s^{-2} ds = \omega_n.$$

The occurring sum is also finite and thus equal to a constant  $c_q > 0$ . Moreover, we define  $n_0 := \lceil \frac{n+1}{r} \rceil + 1$  and  $q_0 := \lceil \frac{q+1}{r} \rceil + 1$ . For the last factor we use that

$$|x|^d \leq C_{m,d} \sum_{\beta \in \mathbb{N}_0^m, |\beta|=d} |x^\beta|$$

in order to obtain

$$\begin{aligned} |x|^{\frac{n+1}{r}} |k|^{\frac{q+1}{r}} |f(t, x, k, a)| &\leq |x|^{n_0} |k|^{q_0} |f(t, x, k, a)| \\ &\leq C_{n,n_0} \sum_{|\alpha|=n_0} |x^\alpha| C_{q,q_0} \sum_{|\delta|=q_0} |k^\delta| |f(t, x, k, a)| \\ &\leq C_{n,n_0} C_{q,q_0} \sum_{|\alpha|=n_0} \sum_{|\delta|=q_0} \rho_{\alpha,0,0,\delta}(f) \end{aligned}$$

for all  $(t, x, k, a) \in M_4$ . In total, we have

$$\int_{M_4} |f(x)|^r dx \leq C_{n,q,F,r} \left( \sum_{|\alpha|=n_0} \sum_{|\delta|=q_0} \rho_{\alpha,0,0,\delta}(f) \right)^r \quad (2.20)$$

for some constant  $C_{n,q,F,r} > 0$ . For the sets  $M_2$  and  $M_3$  we proceed in a similar way. Using the same estimates as before, on the one hand, we have

$$\begin{aligned} \int_{M_2} |f(x)|^r dx &= \int_{M_2} |x|^{-n-1} |x|^{n+1} |f(t, x, k, a)|^r d(t, x, k, a) \\ &\leq \mu_F(F) \int_{B_1^n(0)^c} |x|^{-n-1} dx \cdot \sup_{(t,x,k,a) \in M_2} |x|^{n+1} |f(t, x, k, a)|^r \\ &\leq \mu_F(F) \omega_n \left( C_{n,n_0} \sum_{|\alpha|=n_0} \rho_{\alpha,0,0,0}(f) \right)^r \end{aligned}$$

and, on the other hand, we obtain

$$\begin{aligned} \int_{M_3} |f(x)|^r \, dx &= \int_{M_3} |k|^{-q-1} |k|^{q+1} |f(t, x, k, a)|^r \, d(t, x, k, a) \\ &\leq \mu_F(F) \nu_n \cdot \sum_{\substack{k \in \mathbb{Z}^q \\ k \neq 0}} |k|^{-q-1} \cdot \sup_{(t,x,k,a) \in M_3} |k|^{q+1} |f(t, x, k, a)|^r \\ &\leq \mu_F(F) \nu_n c_q \left( C_{q,q_0} \sum_{|\delta|=q_0} \rho_{0,0,0,\delta}(f) \right)^r. \end{aligned}$$

Putting these estimates together with the inequalities (2.19) and (2.20), we obtain  $f \in L^r(G)$  and

$$\|f\|_{L^r(G)} \leq C \sum_{|\alpha| \leq n_0} \sum_{|\delta| \leq q_0} \rho_{\alpha,0,0,\delta}(f)$$

for some constant  $C > 0$ . Finally, this estimate yields also the continuity of the embedding.  $\square$

In particular, we have seen that elements of the Schwartz-Bruhat space are integrable functions. Therefore, we can now investigate the Fourier transform  $\mathcal{F}$  as an operator on this space. For this purpose, for  $\alpha \in \mathbb{N}_0^n$  we will simply write  $x^\alpha$  for both functions

$$G \rightarrow G, (t, x, k, a) \mapsto x^\alpha \quad \text{and} \quad \widehat{G} \rightarrow \widehat{G}, (t, x, k, a) \mapsto x^\alpha.$$

Analogously, for  $\gamma \in \mathbb{N}_0^p$  and  $\delta \in \mathbb{N}_0^q$ , the symbols  $k^\delta$  and  $k^\gamma$  denote the functions

$$G \rightarrow G, (t, x, k, a) \mapsto k^\delta \quad \text{and} \quad \widehat{G} \rightarrow \widehat{G}, (t, x, k, a) \mapsto k^\gamma,$$

respectively.

**Theorem 2.24** *Let  $G$  be an elementary group of type  $(n, p, q)$  and  $\mathcal{S}(G)$  the Schwartz-Bruhat space on  $G$ . Then the following statements hold.*

- i.  $\mathcal{S}(G)$  is a Fréchet space.
- ii. For  $\alpha \in \mathbb{N}_0^n$ ,  $\gamma \in \mathbb{N}_0^p$  and  $\delta \in \mathbb{N}_0^q$ , the mappings

$$\begin{aligned} f &\mapsto D_x^\alpha f, \quad f \mapsto x^\alpha f, \\ f &\mapsto D_i^\gamma f, \quad f \mapsto k^\delta f, \end{aligned}$$

define continuous functions  $\mathcal{S}(G) \rightarrow \mathcal{S}(G)$ , and we have the identities

$$\mathcal{F}[D_x^\alpha f] = i^{|\alpha|} x^\alpha \widehat{f}, \quad \mathcal{F}[x^\alpha f] = i^{|\alpha|} D_x^\alpha \widehat{f},$$

$$\mathcal{F}[D_i^\gamma f] = i^{|\gamma|} k^\gamma \widehat{f}, \quad \mathcal{F}[k^\delta f] = i^{|\delta|} D_i^\delta \widehat{f}$$

for all  $f \in \mathcal{S}(G)$ .

iii. The Fourier transform is a topological isomorphism  $\mathcal{S}(G) \rightarrow \mathcal{S}(\widehat{G})$ .

*Proof* By definition  $\mathcal{S}(G)$  is a locally convex Hausdorff space, whose topology is induced by a countable family of seminorms. Therefore, for the proof of i., it remains to show that  $\mathcal{S}(G)$  is complete. For this, let  $(f_j)$  be a Cauchy sequence in  $\mathcal{S}(G)$ . For all multi-indices  $\alpha, \beta \in \mathbb{N}_0^n$ ,  $\gamma \in \mathbb{N}_0^q$  and  $\delta \in \mathbb{N}_0^q$ , we define the functions  $g_{j,\alpha,\beta,\gamma,\delta}: G \rightarrow \mathbb{C}$  by

$$g_{j,\alpha,\beta,\gamma,\delta}(t, x, k, a) := x^\alpha k^\delta D_x^\beta D_i^\gamma f_j(t, x, k, a).$$

Then  $(g_{j,\alpha,\beta,\gamma,\delta})_{j \in \mathbb{N}}$  is a Cauchy sequence in  $C_b(G)$  and thus converges uniformly to a function  $g_{\alpha,\beta,\gamma,\delta}$ . With the notation introduced in Eq. (2.16), this implies that also the sequence  $(g_{j,\alpha,\beta,\gamma,\delta}^{(k,a)})_{j \in \mathbb{N}} \subseteq C_b^\infty(\mathbb{R}^n \times \mathbb{R}^p)$  converges uniformly to  $g_{\alpha,\beta,\gamma,\delta}^{(k,a)}$  for each  $(k, a) \in \mathbb{Z}^q \times F$ . Now we define  $f := g_{0,0,0,0}$ . Since

$$g_{j,\alpha,\beta,\gamma,\delta}^{(k,a)}(t, x) = x^\alpha k^\delta D_x^\beta D_i^\gamma f_j^{(k,a)}(t, x),$$

we obtain by uniform convergence that  $f^{(k,a)} \in C^\infty(\mathbb{R}^n \times \mathbb{R}^p)$  and

$$g_{\alpha,\beta,\gamma,\delta}^{(k,a)}(t, x) = x^\alpha k^\delta D_x^\beta D_i^\gamma f^{(k,a)}(t, x)$$

for each  $(k, a) \in \mathbb{Z}^q \times F$ . This yields  $f \in \mathcal{S}(G)$  and  $f$  is the limit of  $(f_j)$  in  $\mathcal{S}(G)$ . Hence  $\mathcal{S}(G)$  is complete and thus a Fréchet space.

Now we continue with the proof of ii., where it is clear that for each  $f \in \mathcal{S}(G)$  also the functions  $D_x^\alpha f$ ,  $D_i^\gamma f$  and  $k^\delta f$  are elements of  $\mathcal{S}(G)$ . It follows directly from Leibniz's rule for higher derivatives of products that this is also the case for  $x^\alpha f$ . This also implies the continuity of the considered mappings  $\mathcal{S}(G) \rightarrow \mathcal{S}(G)$ . The remaining formulas follow directly from decomposing the Fourier transform on  $G$  as  $\mathcal{F}_G = \mathcal{F}_{\mathbb{R}^n} \mathcal{F}_{\mathbb{T}^p} \mathcal{F}_{\mathbb{Z}^q} \mathcal{F}_F$  and using the behavior of polynomials and derivatives under the Fourier transform on  $\mathbb{R}^n$  as well as on  $\mathbb{Z}^q$  and  $\mathbb{T}^p$ .

In order to show iii., let  $f \in \mathcal{S}(G)$ . For  $\alpha \in \mathbb{N}_0^n$  and  $\delta \in \mathbb{N}_0^q$ , we define

$$g_{\alpha,\delta} := (-i)^{|\alpha|+|\delta|} x^\alpha k^\delta f.$$

By ii. we obtain  $g_{\alpha,\delta} \in \mathcal{S}(G)$  and  $\widehat{g_{\alpha,\delta}} = D_x^\alpha D_i^\delta \widehat{f}$ . Thus for  $\beta \in \mathbb{N}_0^n$  and  $\gamma \in \mathbb{N}_0^q$ , we have

$$x^\beta k^\gamma D_x^\alpha D_i^\delta \widehat{f} = x^\beta k^\gamma \widehat{g_{\alpha,\delta}} = (-i)^{|\beta|+|\gamma|} \mathcal{F}[D_x^\beta D_i^\gamma g_{\alpha,\delta}] \in L^\infty(\widehat{G})$$

since  $D_x^\beta D_i^\gamma g_{\alpha,\delta} \in \mathcal{S}(G) \subseteq L^1(G)$ ; see Theorem 2.23. Because the multi-indices were chosen arbitrarily, this implies  $\widehat{f} \in \mathcal{S}(\widehat{G})$ .



Now we shall show that the Fourier transform is also continuous as a mapping  $\mathcal{S}(G) \rightarrow \mathcal{S}(\widehat{G})$ . Let  $(f_j) \subseteq \mathcal{S}(G)$  be a convergent sequence with limit  $f \in \mathcal{S}(G)$ . By statement ii., for each  $\alpha, \beta \in \mathbb{N}_0^n$ ,  $\gamma \in \mathbb{N}_0^p$  and  $\delta \in \mathbb{N}_0^q$ , the sequence  $(h_{j,\alpha,\beta,\gamma,\delta})_{j \in \mathbb{N}}$  defined by

$$\widehat{h_{j,\alpha,\beta,\gamma,\delta}}(t, x, k, a) := D_x^\beta D_t^\gamma (x^\alpha k^\delta f_j(t, x, k, a))$$

is a sequence in  $\mathcal{S}(G)$  and converges in the topology of  $\mathcal{S}(G)$  to the function  $h_{\alpha,\beta,\gamma,\delta}: G \rightarrow \mathbb{C}$  given by

$$h_{\alpha,\beta,\gamma,\delta}(t, x, k, a) := D_x^\beta D_t^\gamma (x^\alpha k^\delta f(t, x, k, a)).$$

Since  $\mathcal{S}(G)$  is continuously embedded into  $L^1(G)$  by Theorem 2.23, this convergence also holds in  $L^1(G)$ . The continuity of the Fourier transform  $\mathcal{F}$  as a mapping  $\mathcal{F}: L^1(G) \rightarrow L^\infty(\widehat{G})$  implies that the sequence  $(\widehat{h_{j,\alpha,\beta,\gamma,\delta}})_{j \in \mathbb{N}}$  converges to  $\widehat{h_{\alpha,\beta,\gamma,\delta}}$  in  $L^\infty(\widehat{G})$ . Because this holds for all multi-indices, the sequence  $(\widehat{f_j})$  converges to  $\widehat{f}$  in  $\mathcal{S}(\widehat{G})$ .

In exactly the same way, we can derive that  $\mathcal{F}^{-1}: \mathcal{S}(\widehat{G}) \rightarrow \mathcal{S}(G)$  is a continuous mapping. Furthermore, the Inversion Theorem now implies that  $\mathcal{F}^{-1}$  is the actual inverse of  $\mathcal{F}$  and thus  $\mathcal{F}$  is a topological isomorphism. This finishes the proof.  $\square$

The space  $C_b^\infty(G)$  on an elementary group  $G$  is defined as the space of all functions  $f \in C^\infty(G)$  such that  $f$  and all derivatives of  $f$  are bounded. In particular, it holds  $\mathcal{S}(G) \subseteq C_b^\infty(G)$ . For these functions we obtain the following result.

**Proposition 2.25** *Let  $G$  be an elementary group of type  $(n, p, q)$ . If  $u \in C_b^\infty(G)$  and  $f \in L^1(G)$ , then  $u * f \in C_b^\infty(G)$  and  $D_x^\alpha D_t^\beta (u * f) = (D_x^\alpha D_t^\beta u) * f$  for all  $\alpha \in \mathbb{N}_0^n$  and  $\beta \in \mathbb{N}_0^p$ .*

*Proof* At first we consider derivatives in the  $\mathbb{R}^n$  variables. For  $j \in \{1, \dots, n\}$  and  $h > 0$ , the  $j$ -th difference quotient  $D_j^h$  is defined by

$$D_j^h u(t, x, k, a) = \frac{1}{h} (u(x + h e_j, t, k, a) - u(t, x, k, a))$$

for all  $(t, x, k, a) \in G$ . With this notation, we obtain

$$D_j^h (u * f)(t, x, k, a) = \int_G D_j^h u(x - y, t - s, k - l, a - b) f(y, s, l, b) \, d(y, s, l, b).$$

Since  $\|\partial_j u\|_\infty f$  is an integrable upper bound to this integrand, we can take the limit  $h \rightarrow 0$  in this equation, and the Dominated Convergence Theorem yields the existence of  $\partial_j(u * f)$  and the formula  $\partial_j(u * f) = (\partial_j u) * f$ .

The same argument leads to the analogous result for partial derivatives concerning the  $\mathbb{T}^p$  variables. Iterating this procedure, we obtain  $u * f \in C^\infty(G)$  and the

desired formula for the derivatives. Furthermore, by Young's inequality we have

$$\|D_x^\alpha D_t^\beta(u * f)\|_\infty = \|(D_x^\alpha D_t^\beta u) * f\|_\infty \leq \|D_x^\alpha D_t^\beta u\|_\infty \|f\|_{L^1(G)}$$

and thus also  $u * f \in C_b^\infty(G)$ .  $\square$

**Proposition 2.26** *Let  $G$  be an elementary group,  $u \in \mathcal{S}(G)$  and  $f: G \rightarrow \mathbb{C}$  a compactly supported integrable function. Then we have  $u * f \in \mathcal{S}(G)$ .*

*Proof* By Proposition 2.25 we have  $u * f \in C^\infty(G)$ . Now let  $\alpha, \beta \in \mathbb{N}_0^n$ ,  $\gamma \in \mathbb{N}_0^p$  and  $\delta \in \mathbb{N}_0^q$ . Since  $f$  is compactly supported, we may choose a number  $N \in \mathbb{N}$  such that  $\text{supp } f$  is contained in

$$M_1 := [-N, N]^n \times \mathbb{T}^p \times \{-N, -N + 1, \dots, N - 1, N\}^q \times F.$$

We define the set

$$M_2 := [-2N, 2N]^n \times \mathbb{T}^p \times \{-2N, -2N + 1, \dots, 2N - 1, 2N\}^q \times F,$$

which is a compact subset of  $G$ . Hence the continuous function  $x^\alpha k^\delta D_x^\beta D_t^\gamma(u * f)$  is bounded on this set. Now let  $(t, x, k, a) \in M_2^c$ . Using Proposition 2.25 again, we obtain

$$\begin{aligned} |x^\alpha k^\delta D_x^\beta D_t^\gamma(u * f)(t, x, k, a)| &= |x^\alpha k^\delta (D_x^\beta D_t^\gamma u) * f(t, x, k, a)| \\ &\leq \int_{M_1} |x^\alpha| |k^\delta| |D_x^\beta D_t^\gamma u(x - y, t - s, k - l, a - b)| |f(y, s, l, b)| \, d(y, s, l, b) \\ &\leq \int_{M_1} 2^{|\alpha|+|\delta|} |(x - y)^\alpha (k - l)^\delta| \\ &\quad \cdot |D_x^\beta D_t^\gamma u(x - y, t - s, k - l, a - b)| |f(y, s, l, b)| \, d(y, s, l, b) \\ &\leq 2^{|\alpha|+|\delta|} \rho_{\alpha, \beta, \gamma, \delta}(u) \cdot \|f\|_{L^1(G)}, \end{aligned}$$

where we used the estimate  $|c| \leq 2|c - d|$  for  $c, d \in \mathbb{R}$  with  $|c| \geq 2N$  and  $|d| \leq N$ . Since the multi-indices were chosen arbitrarily, we have shown  $u * f \in \mathcal{S}(G)$ .  $\square$

In order to derive density results, we will also need the existence of infinitely differentiable functions with arbitrarily small support.

**Proposition 2.27** *Let  $G$  be an elementary group and  $U \subseteq G$  be a nonempty open subset of  $G$ . Then there exists a function  $u \in C^\infty(G)$ ,  $u \neq 0$ , such that  $\text{supp } u \subseteq U$ .*

*Proof* We define the function  $\varphi: \mathbb{R}^n \times \mathbb{R}^p \rightarrow \mathbb{C}$  by

$$\varphi(x, y) = \begin{cases} e^{\frac{-1}{1-|x|^2}} e^{\frac{-1}{1-|y|^2}}, & \text{if } |x| < 1 \text{ and } |y| < 1, \\ 0, & \text{otherwise.} \end{cases}$$

It is well known that this defines an element of  $C^\infty(\mathbb{R}^n \times \mathbb{R}^p)$  with compact support  $K_1^n(0) \times K_1^p(0)$ . Since  $U$  is an open subset of  $G$ , there exist  $(x_0, t_0, k_0, a_0) \in U$  and  $r \in (0, 1)$  such that  $\bar{V} \subseteq U$  if we define

$$V := B_r^n(x_0) \times \pi(B_r^p(t'_0)) \times \{k_0\} \times \{a_0\}.$$

Here  $\pi$  denotes the quotient mapping  $\mathbb{R}^p \rightarrow \mathbb{T}^p \cong (\mathbb{R}/2\pi\mathbb{Z})^p$  and  $t'_0 \in [-\pi, \pi)^p$  is the unique representative of  $t_0$ . We can now define the function  $u: G \rightarrow \mathbb{C}$  by

$$u(t, x, k, a) = \begin{cases} \varphi(r^{-1}x, r^{-1}t'), & \text{if } (k, a) = (k_0, a_0), \\ 0, & \text{otherwise,} \end{cases}$$

where  $t'$  is the unique representative in  $[-\pi, \pi)^p$  for  $t \in \mathbb{T}^p$ . Then  $u \in C^\infty(G)$  and we have  $\text{supp } u \subseteq \bar{V} \subseteq U$ . Hence  $u$  possesses the desired properties.  $\square$

## 2.4.2 Good and Compactly Generated Open Subgroups

In order to define the Schwartz-Bruhat space on a general locally compact abelian group  $G$  and to investigate the action of the Fourier transform  $\mathcal{F}_G$ , we consider certain pairs of subgroups and their behavior with regard to duality. We will see that the quotient group of such a pair is elementary, which will enable us to apply the results of the previous subsection.

### Definition 2.28

- i. We say that a topological group  $H$  has no small subgroups if there exists an open neighborhood  $U$  of the zero element such that  $U$  contains no subgroup of  $H$  but the trivial one.
- ii. We call a subgroup  $K$  of  $G$  good if  $K$  is compact and  $G/K$  contains no small subgroups.
- iii. A subgroup  $\Gamma$  of  $G$  is called compactly generated if there exists a compact set  $C$  in  $G$  with  $\Gamma = \langle C \rangle$ .
- iv. We define  $\mathcal{A}$  as the set of all pairs  $(K, \Gamma)$  of subgroups of  $G$ , where  $K$  is good,  $\Gamma$  is compactly generated and open and  $K \subseteq \Gamma$ . The set  $\widehat{\mathcal{A}}$  denotes the corresponding set of pairs of subgroups of  $\widehat{G}$ .

The quotient group  $G/K$  is a locally compact abelian group if  $K$  is a closed subgroup. Hence the condition that  $K$  is good is equivalent to the claim that  $K$  is compact and  $G/K$  is a (finite-dimensional) Lie group; see [7]. Thus the above definition of good subgroups coincides with the one given in [2].

In the following, we want to investigate the behavior of the annihilator operation on the good and the compactly generated subgroups.

**Lemma 2.29** *Let  $H$  be a subgroup of  $G$ . Then  $H$  is compact if and only if the annihilator  $H^\perp$  is open.*

*Proof*  $H$  is compact if and only if its dual group  $\widehat{H}$  is discrete. Since this group is isomorphic to the quotient group  $\widehat{G}/H^\perp$ , this is equivalent to the statement that  $H^\perp$  is an open subgroup. Hence we have proved the desired equivalence.  $\square$

In the paper [2] by Bruhat, the theory of Lie groups was used in order to introduce the good subgroups. In the following, we shall avoid the notion of Lie groups and instead use the following lemma due to Osborne [18].

**Lemma 2.30** *The group  $G$  is compactly generated if and only if  $\widehat{G}$  has no small subgroups.*

*Proof* For each compact subset  $C \subseteq G$  and  $r > 0$ , define the set

$$N(C, r) := \left\{ \gamma \in \widehat{G} : |1 - (x, \gamma)| < r \text{ for all } x \in C \right\}.$$

The family of these sets is a neighborhood base of 0 in  $\widehat{G}$ .

At first let  $G$  be compactly generated, i.e.,  $G = \langle C \rangle$  for some compact set  $C \subseteq G$ . We take  $r > 0$  such that  $U := \{z \in \mathbb{T} : |1 - z| < r\}$  contains no nontrivial subgroups of  $\mathbb{T}$ . For example, this is valid for  $r = 1$ . We consider the open set  $N(C, r)$  and a subgroup  $H$  of  $\widehat{G}$  with  $H \subseteq N(C, r)$ . Then for all  $\gamma \in H$  the multiples of  $\gamma$  are also elements of  $N(C, r)$ , and thus we have  $\gamma(x)^k \in U$  for all  $k \in \mathbb{Z}$  and all  $x \in C$ . Since these elements of  $\mathbb{T}$  form a subgroup contained in  $U$ , we obtain  $\gamma(x) = 1$  by the choice of  $r$ . Because  $x \in C$  was arbitrary, this implies that  $\gamma(\langle C \rangle) = \{1\}$  and thus  $\gamma \in \langle C \rangle^\perp = \{0\}$ . Hence  $H$  is the trivial group, and we have found an open set in  $\widehat{G}$  that contains no nontrivial subgroups. Therefore,  $\widehat{G}$  has no small subgroups.

Conversely, assume that  $G$  is not compactly generated. Let  $V \subseteq \widehat{G}$  be an open neighborhood of 0. As we remarked above, there exists a compact set  $C \subseteq G$  and some  $r > 0$  such that  $N(C, r) \subseteq V$ . If  $\gamma \in \langle C \rangle^\perp$ , we have  $(x, \gamma) = 1$  for all  $x \in C$ , hence  $\langle C \rangle^\perp \subseteq N(C, r) \subseteq V$ . Since  $G$  is not compactly generated,  $\langle C \rangle^\perp$  is a nontrivial subgroup of  $\widehat{G}$ . As  $V$  was an arbitrary open neighborhood of 0,  $\widehat{G}$  has small subgroups.  $\square$

Now we are able to state the following duality result, which we will need for the investigation of the Fourier transform on the Schwartz-Bruhat space.

**Theorem 2.31** *A pair  $(K, \Gamma)$  of subgroups of  $G$  is an element of  $\mathcal{A}$  if and only if the pair  $(\Gamma^\perp, K^\perp)$  belongs to  $\widehat{\mathcal{A}}$ .*

*Proof* Let  $H$  be a subgroup of  $G$ . By definition  $H$  is good if it is compact and  $G/H$  has no small subgroups. By Lemma 2.29 the set  $H$  is compact if and only if  $H^\perp$  is open. Furthermore, using Lemma 2.30 and the Pontryagin Duality Theorem,  $G/H$  has no small subgroups if and only if its dual group, which is isomorphic to  $H^\perp$ , is compactly generated. All in all, we have shown that an arbitrary subgroup  $H$  is good if and only if  $H^\perp$  is open and compactly generated. Applying this result to  $K$  and  $\Gamma$  and using  $(\Gamma^\perp)^\perp = \Gamma$  completes the proof.  $\square$

Finally, we want to connect the results presented here with those of the previous subsection and justify the special role the set  $\mathcal{A}$  plays in our approach. At first we examine the quotient  $\Gamma/K$  for  $(K, \Gamma) \in \mathcal{A}$ .

**Proposition 2.32** *Let  $K$  be a compact and  $\Gamma$  be an open subgroup of  $G$  with  $K \subseteq \Gamma$ . Then  $(K, \Gamma) \in \mathcal{A}$  if and only if  $\Gamma/K$  is compactly generated and has no small subgroups.*

*Proof* Let  $\pi: \Gamma \rightarrow \Gamma/K$  be the quotient mapping, and assume that  $(K, \Gamma) \in \mathcal{A}$ . Then there is a compact set  $C \subseteq \Gamma$  with  $\Gamma = \langle C \rangle$ . As  $\pi$  is continuous,  $\pi(C)$  is a compact subset of  $\Gamma/K$ . Furthermore, since  $\pi$  is a homomorphism, we have

$$\langle \pi(C) \rangle = \pi(\langle C \rangle) = \pi(\Gamma) = \Gamma/K.$$

Hence  $\Gamma/K$  is compactly generated.

Now consider the canonical embedding  $\iota: \Gamma/K \rightarrow G/K$ , which is a continuous homomorphism. By assumption, there is an open neighborhood  $V \subseteq G/K$  of  $0 \in G/K$  which contains no nontrivial subgroups. Then  $\iota^{-1}(V)$  is an open neighborhood of  $0 \in \Gamma/K$ . If  $H \subseteq \iota^{-1}(V)$  is a subgroup of  $\Gamma/K$ , then  $\iota(H)$  is a subgroup of  $V$ . Hence  $\iota(H) = \{0\}$  and, by the injectivity of  $\iota$ , we have  $H = \{0\}$ . Consequently,  $\Gamma/K$  has no small subgroups.

Conversely, assume that  $\Gamma/K$  has no small subgroups, i.e., that there is an open subset  $U \subseteq \Gamma/K$  which contains no subgroup but the trivial one. Since  $\Gamma$  is an open subgroup of  $G$ , the quotient group  $\Gamma/K$  is an open subgroup of  $G/K$ . Therefore,  $U$  is also an open subset of  $G/K$ . Hence  $G/K$  has no small subgroups and  $K$  is a good subgroup of  $G$ .

If  $\Gamma/K$  is compactly generated, then there is a compact subset  $C \subseteq \Gamma/K$  such that  $\Gamma/K = \langle C \rangle$ . Then  $\Gamma$  is isomorphic to  $\langle C \rangle \times K$ , which is generated by the compact set  $C \times K$ . Thus  $\Gamma$  is also compactly generated.  $\square$

The paper [2] by Bruhat contains the statement that  $(K, \Gamma) \in \mathcal{A}$  implies that  $\Gamma/K$  is a (compactly generated abelian) Lie group. Moreover, there exists a characterization theorem for this kind of Lie groups, namely that they are isomorphic to elementary groups. This result can, for instance, be found in [1, Proposition 3, Sect. II.2]. A characterization theorem for compactly generated groups without small subgroups can also be shown without the application of Lie group theory. For instance, this is done in [25, Theorem 21.18], which we rephrased below in order to make it fit in our setting.

**Theorem 2.33** *The elementary groups are exactly those locally compact abelian groups that are compactly generated and have no small subgroups.*

*Proof* We refer the reader to [25, Theorem 21.18].  $\square$

Combining this result with Proposition 2.32 directly leads us to the following statement, which shows the connection between this subsection and the previous one.

**Theorem 2.34** *Let  $K$  be a compact and  $\Gamma$  be an open subgroup of  $G$  such that  $K \subseteq \Gamma$ . Then  $(K, \Gamma) \in \mathcal{A}$  if and only if  $\Gamma/K$  is an elementary group.*

This theorem will be the key for the introduction of the Schwartz-Bruhat space on an arbitrary locally compact abelian group because it enables us to expand the definition from elementary groups.

Until now, we have not ensured that the set  $\mathcal{A}$  is nonempty. In order to guarantee the existence of good subgroups and compactly generated subgroups containing them, we need the following theorem.

**Theorem 2.35** *Let  $\Gamma$  be an open compactly generated subgroup of  $G$ . Every neighborhood  $U$  of 0 in  $\Gamma$  contains a compact subgroup  $K$  such that  $\Gamma/K$  is elementary.*

*Proof* See [11, Theorem 9.6]. □

We remark that in the above setting each open subset of  $\Gamma$  is also an open subset of  $G$  since  $\Gamma$  is open. Using Theorem 2.34, we can directly derive the following.

**Corollary 2.36** *Let  $\Gamma$  be an open compactly generated subgroup of  $G$ . Every neighborhood  $U$  of 0 in  $\Gamma$  contains a good subgroup.*

If we take a compact subset  $C$  of  $G$  with nonempty interior, for example, a compact neighborhood of 0, we directly obtain that  $\Gamma := \langle C \rangle$  is an open compactly generated subgroup of  $G$ . Together with Corollary 2.36, this yields the following result.

**Corollary 2.37** *The set  $\mathcal{A}$  is nonempty.*

Later we will need another property of the set  $\mathcal{A}$ , which is subject of the next proposition.

**Proposition 2.38** *The set  $\mathcal{A}$  is a directed set if we define the order on  $\mathcal{A}$  by*

$$(K_1, \Gamma_1) \leq (K_2, \Gamma_2) \iff \Gamma_1 \subseteq \Gamma_2 \text{ and } K_1 \supseteq K_2.$$

*Proof* It is clear that the relation  $\leq$  is a partial order on  $\mathcal{A}$ . Let us consider  $(K_1, \Gamma_1), (K_2, \Gamma_2) \in \mathcal{A}$ . We have to find  $(K, \Gamma) \in \mathcal{A}$  such that  $(K_j, \Gamma_j) \leq (K, \Gamma)$  for  $j = 1, 2$ . We set  $K := K_1 \cap K_2$  and  $\Gamma := \Gamma_1 + \Gamma_2$  and have to show that these elements form a pair in  $\mathcal{A}$ . We see directly that  $\Gamma$  is an open subgroup of  $G$ . For  $j = 1, 2$  the group  $\Gamma_j$  is compactly generated so that there is a compact set  $C_j \subseteq G$  with  $\Gamma_j = \langle C_j \rangle$ . Hence  $\Gamma$  is generated by the set  $C_1 + C_2$ , which is again a compact subset of  $G$ . Therefore,  $\Gamma$  is also compactly generated. Furthermore,  $K$  is a compact subgroup of  $G$ . It remains to show that  $G/K$  has no small subgroups. We have seen in Lemma 2.30 that this is the case if and only if  $K^\perp = (K_1 \cap K_2)^\perp = K_1^\perp + K_2^\perp$  is compactly generated. But this fact follows in the same way as above since  $K_1^\perp$  and  $K_2^\perp$  are so, again by Lemma 2.30. Finally, we have shown  $(K, \Gamma) \in \mathcal{A}$ . It is trivial that this element is greater than  $(K_1, \Gamma_1)$  and  $(K_2, \Gamma_2)$ . Thus the proof is complete. □

### 2.4.3 The General Schwartz-Bruhat Space

We shall define the general Schwartz-Bruhat space as an inductive limit of function spaces on  $G$ . To do so, we consider the Schwartz-Bruhat space for the groups of the form  $\Gamma/K$ , where  $(K, \Gamma) \in \mathcal{A}$ . Since this quotient is an elementary group, as seen in Theorem 2.34, we have already defined and examined these spaces. They do not consist of functions on the considered group  $G$ , but we can identify each such function with a function on  $G$ , which is invariant under the subgroup  $K$ . Throughout this subsection, let  $G$  be a locally compact abelian group and  $\mathcal{A}$  the set of pairs as in Definition 2.28.

**Definition 2.39** Let  $(K, \Gamma) \in \mathcal{A}$  and  $\pi: \Gamma \rightarrow \Gamma/K$  be the canonical quotient mapping. We define the space  $\mathcal{S}(K, \Gamma)$  as the set of all functions  $f: G \rightarrow \mathbb{C}$  for which there exists a function  $u_f \in \mathcal{S}(\Gamma/K)$  such that

$$f(x) = \begin{cases} u_f(\pi(x)), & \text{if } x \in \Gamma, \\ 0, & \text{otherwise.} \end{cases} \quad (2.21)$$

The vector space  $\mathcal{S}(K, \Gamma)$  inherits the topology of  $\mathcal{S}(\Gamma/K)$  by defining  $V \subseteq \mathcal{S}(K, \Gamma)$  as open if and only if the set  $\{u_f : f \in V\}$  is open in  $\mathcal{S}(\Gamma/K)$ .

Note that  $\mathcal{S}(K, \Gamma)$  and  $\mathcal{S}(\Gamma/K)$  are isomorphic as topological vector spaces, which is a direct consequence of the definition given above. Thus  $\mathcal{S}(K, \Gamma)$  is also a Fréchet space and thus, in particular, a locally convex topological vector space.

If  $\Gamma/K$  is elementary of type  $(n, p, q)$ , we define

$$\rho_{\alpha, \beta, \gamma, \delta}^{\mathcal{S}(K, \Gamma)}(f) := \rho_{\alpha, \beta, \gamma, \delta}(f) := \rho_{\alpha, \beta, \gamma, \delta}^{\mathcal{S}(\Gamma/K)}(u_f)$$

for  $f \in \mathcal{S}(K, \Gamma)$  and  $\alpha, \beta \in \mathbb{N}_0^n$ ,  $\gamma \in \mathbb{N}_0^p$  and  $\delta \in \mathbb{N}_0^q$ , where  $u_f$  is chosen as in (2.21). We see that the topology on  $\mathcal{S}(K, \Gamma)$  is induced by the family  $\{\rho_{\alpha, \beta, \gamma, \delta}\}$  of seminorms. Moreover, since the set  $\Gamma$  is an open and closed subset of  $G$ , the spaces  $\mathcal{S}(K, \Gamma)$  consist of continuous functions.

We shall now show that Schwartz-Bruhat spaces corresponding to elements  $(K, \Gamma)$  in  $\mathcal{A}$  are ordered by inclusion according to the order  $\leq$  on  $\mathcal{A}$  defined in Proposition 2.38.

**Proposition 2.40** For  $(K_1, \Gamma_1), (K_2, \Gamma_2) \in \mathcal{A}$  with  $(K_1, \Gamma_1) \leq (K_2, \Gamma_2)$ , the space  $\mathcal{S}(K_1, \Gamma_1)$  is a topological linear subspace of  $\mathcal{S}(K_2, \Gamma_2)$ .

*Proof* For  $j \in \{1, 2\}$  we denote the canonical projection by  $\pi_j: \Gamma_j \rightarrow \Gamma_j/K_j$ . Let  $f \in \mathcal{S}(K_1, \Gamma_1)$  and  $u_f \in \mathcal{S}(\Gamma_1/K_1)$  as in Definition 2.39. Furthermore, we consider the mapping  $\tilde{\pi}: \Gamma_2/K_2 \rightarrow \Gamma_2/K_1, x + K_2 \mapsto x + K_1$ , which is well defined because  $K_2 \subseteq K_1$ . We define

$$v: \Gamma_2/K_2 \rightarrow \mathbb{C}, \quad v(x) = \begin{cases} u_f(\tilde{\pi}(x)), & \text{if } x \in \Gamma_1/K_2, \\ 0, & \text{otherwise.} \end{cases}$$

Since  $(\tilde{\pi} \circ \pi_2)|_{\Gamma_1} = \pi_1$ , we obtain

$$f(x) = \begin{cases} v(\pi_2(x)), & \text{if } x \in \Gamma_2, \\ 0, & \text{otherwise.} \end{cases}$$

In order to show  $f \in \mathcal{S}(K_2, \Gamma_2)$ , it remains to verify  $v \in \mathcal{S}(\Gamma_2/K_2)$ .

Since the subgroups  $\Gamma_1, \Gamma_2, K_1, K_2$  of  $G$  are closed, we have

$$\Gamma_2/K_2 \cong \Gamma_2/\Gamma_1 \times \Gamma_1/K_1 \times K_1/K_2$$

as an isomorphism of topological groups.  $\Gamma_2/K_2$  is an elementary group, and closed subgroups of elementary groups are elementary; see [25, Theorem 21.19]. Hence  $\Gamma_2/\Gamma_1$  and  $K_1/K_2$  are also elementary. Because  $\Gamma_1$  is an open subset of  $\Gamma_2$ , the quotient  $\Gamma_2/\Gamma_1$  is also discrete and thus isomorphic to  $\mathbb{Z}^{q_0} \times F_1$  for some  $q_0 \in \mathbb{N}_0$  and a finite abelian group  $F_1$ . Moreover,  $K_1$  is a compact subgroup of  $G$  and, therefore,  $K_1/K_2$  is also compact and hence isomorphic to  $\mathbb{T}^{p_0} \times F_2$  for some  $p_0 \in \mathbb{N}_0$  and a finite abelian group  $F_2$ . By Theorem 2.34 we can identify  $\Gamma_1/K_1$  with the group  $\mathbb{R}^n \times \mathbb{T}^p \times \mathbb{Z}^q \times F$  for some  $n, p, q \in \mathbb{N}_0$  and a finite abelian group  $F$ . Using the isomorphisms above, we obtain that  $\Gamma_2/K_2$  is isomorphic to  $\mathbb{R}^n \times \mathbb{T}^{p+p_0} \times \mathbb{Z}^{q+q_0} \times F_0$ , where  $F_0 = F \times F_1 \times F_2$ .

In the following, in order to avoid unnecessary complicated notation, we identify each of the considered quotient groups with the product group it is isomorphic to. Then the mapping  $\tilde{\pi}: \mathbb{R}^n \times \mathbb{T}^{p+p_0} \times \mathbb{Z}^{q+q_0} \times F_0 \rightarrow \mathbb{R}^n \times \mathbb{T}^p \times \mathbb{Z}^{q+q_0} \times F \times F_1$  is given by

$$\tilde{\pi}(t, x, k, a) = (x, [t], k, [a]),$$

where  $[(t_1, t_2)] = t_1$  for  $(t_1, t_2) \in \mathbb{T}^{p+p_0}$  and  $[(a_0, a_1, a_2)] = (a_0, a_1)$  for  $(a_0, a_1, a_2) \in F_0$ . With this notation, we obtain the identities

$$\begin{aligned} v(x+y, t, k, a) - v(t, x, k, a) &= u_f(x+y, [t], k, [a]) - u_f(x, [t], k, [a]), \\ v(t, x+s, k, a) - v(t, x, k, a) &= u_f(x, [t+s], k, [a]) - u_f(x, [t], k, [a]) \end{aligned}$$

for all  $x, y \in \mathbb{R}^n$ ,  $t, s \in \mathbb{T}^{p+p_0}$ ,  $k \in \mathbb{Z}^{q+q_0}$  and  $a \in F_0$ . Considering differential quotients, we infer that  $v$  inherits the regularity properties of  $u_f$ . Therefore, it holds  $v \in C^\infty(\Gamma_2/K_2)$ . Moreover, for  $\alpha \in \mathbb{N}_0^n$  and  $\gamma = (\gamma_1, \gamma_2) \in \mathbb{N}_0^{p+p_0}$ , we thus have

$$\begin{aligned} D_x^\alpha v &= D_x^\alpha u_f \circ \tilde{\pi}, \\ D_i^\gamma v &= \begin{cases} D_i^{\gamma_1} u_f \circ \tilde{\pi}, & \text{if } \gamma_2 = 0, \\ 0, & \text{if } \gamma_2 \neq 0. \end{cases} \end{aligned}$$



Furthermore, for  $\alpha, \beta \in \mathbb{N}_0^n$ ,  $\gamma = (\gamma_1, \gamma_2) \in \mathbb{N}_0^{p+p_0}$  and  $\delta = (\delta_1, \delta_2) \in \mathbb{N}_0^{q+q_0}$ , we obtain the equality

$$\begin{aligned} \rho_{\alpha, \beta, \gamma, \delta}^{\mathcal{S}(K_2, \Gamma_2)}(f) &= \rho_{\alpha, \beta, \gamma, \delta}^{\mathcal{S}(\Gamma_2/K_2)}(v) = \sup_{(t, x, k, a) \in \Gamma_2/K_2} |x^\alpha k^\delta D_x^\beta D_t^\gamma v(t, x, k, a)| \\ &= \sup_{\substack{(t, x_1, k_1, a_0) \in \Gamma_1/K_1 \\ (k_2, a_1) \in \Gamma_2/\Gamma_1 \\ (t_2, a_2) \in K_1/K_2}} |x^\alpha k_1^{\delta_1} k_2^{\delta_2} D_x^\beta D_{t_1}^{\gamma_1} D_{t_2}^{\gamma_2} v(t, x_1, t_2, k_1, k_2, a_0, a_1, a_2)|, \end{aligned}$$

where we distinguish several cases. If  $\gamma_2 \neq 0$ , we have

$$\rho_{\alpha, \beta, \gamma, \delta}^{\mathcal{S}(K_2, \Gamma_2)}(f) = 0$$

since  $D_{t_2}^{\gamma_2} v = 0$ , as we have already seen above. If  $\delta_2 \neq 0$ , we have

$$\rho_{\alpha, \beta, \gamma, \delta}^{\mathcal{S}(K_2, \Gamma_2)}(f) = 0$$

since  $v$  (and all its derivatives) are supported in  $\{(t, x, k_1, k_2, a) \in \Gamma_2/K_2 : k_2 = 0\}$  by definition. But on this set the factor  $k_2^{\delta_2}$  vanishes. If  $\gamma_2 = 0$  and  $\delta_2 = 0$ , we have

$$\begin{aligned} \rho_{\alpha, \beta, \gamma, \delta}^{\mathcal{S}(K_2, \Gamma_2)}(f) &= \sup_{(t, x_1, k_1, a_0) \in \Gamma_1/K_1} |x^\alpha k_1^{\delta_1} D_x^\beta D_{t_1}^{\gamma_1} u_f(t, x_1, k_1, a_0)| \\ &= \rho_{\alpha, \beta, \gamma_1, \delta_1}^{\mathcal{S}(K_1, \Gamma_1)}(f) < \infty. \end{aligned}$$

Therefore, we obtain  $f \in \mathcal{S}(K_2, \Gamma_2)$ , and the space  $\mathcal{S}(K_1, \Gamma_1)$  is a subspace of  $\mathcal{S}(K_2, \Gamma_2)$  and is equipped with the subspace topology. Hence the claim is proved.  $\square$

After these preparations, we recall the definition of the inductive limit topology for locally convex spaces.

**Definition 2.41** Let  $(A, \leq)$  be a directed set and  $\{E_\alpha : \alpha \in A\}$  be a family of locally convex Hausdorff spaces. Furthermore, let  $E_\alpha$  be continuously embedded into  $E_\beta$  for all  $\alpha, \beta \in A$  such that  $\alpha \leq \beta$ . Then the *inductive limit topology* on the vector space  $E := \bigcup_{\alpha \in A} E_\alpha$  is defined as the finest locally convex topology for which each of the embeddings  $\iota_\alpha : E_\alpha \rightarrow E$  is continuous. We call the locally convex vector space  $E$  the *inductive limit* of the family  $\{E_\alpha : \alpha \in A\}$ .

The following proposition will be very useful for the derivation of continuity properties. Classically, it is called the universal property of the inductive limit.

**Proposition 2.42 (Universal Property)** *Let  $\{E_\alpha : \alpha \in A\}$  be a family of locally convex Hausdorff spaces as in Definition 2.41 with inductive limit  $E$ , and let  $F$  be a locally convex space. A linear mapping  $v : E \rightarrow F$  is continuous if and only if the restriction  $v|_{E_\alpha} = v \circ \iota_\alpha$  is continuous for each  $\alpha \in A$ .*

*Proof* See [23, Subsection II.6.1]. □

We can now introduce the general Schwartz-Bruhat space as an inductive limit of Schwartz-Bruhat spaces on elementary groups.

**Definition 2.43** The *Schwartz-Bruhat space*  $\mathcal{S}(G)$  on  $G$  is the inductive limit of the family  $\{\mathcal{S}(K, \Gamma) : (K, \Gamma) \in \mathcal{A}\}$ , i.e.,

$$\mathcal{S}(G) := \bigcup_{(K, \Gamma) \in \mathcal{A}} \mathcal{S}(K, \Gamma)$$

equipped with the inductive limit topology of the family  $\{\mathcal{S}(K, \Gamma) : (K, \Gamma) \in \mathcal{A}\}$ .

We have seen in Theorem 2.24 and Proposition 2.40 that the conditions of Definition 2.41 are fulfilled, and thus  $\mathcal{S}(G)$  is a well-defined locally convex space. Analogously to the classical case, we can now define the space of tempered distributions on the group  $G$ .

**Definition 2.44** The *space of tempered distributions*  $\mathcal{S}'(G)$  on  $G$  is defined as the topological dual space of  $\mathcal{S}(G)$ .

In order to utilize the space  $\mathcal{S}'(G)$  in the theory of partial differential equations, we also have to introduce derivatives of a tempered distribution. For a general locally compact abelian group, we cannot distinguish between different directions. Therefore, we are also not able to define partial derivatives. However, when we consider an elementary group  $G$  and identify it with  $\mathbb{R}^n \times \mathbb{T}^p \times \mathbb{Z}^q \times F$  for a finite abelian group  $F$  and  $n, p, q \in \mathbb{N}_0$ , this problem does not occur and we have already defined derivatives for functions in  $\mathcal{S}(G)$  at the beginning of Sect. 2.4.1. In the same way as in the classical case, we can thus define derivatives by duality. For  $\psi \in \mathcal{S}'(G)$  and  $f \in \mathcal{S}(G)$  we set

$$\langle D_x^\alpha D_t^\beta \psi, f \rangle := (-1)^{|\alpha|+|\beta|} \langle \psi, D_x^\alpha D_t^\beta f \rangle \tag{2.22}$$

for  $\alpha \in \mathbb{N}_0^n$  and  $\beta \in \mathbb{N}_0^p$ . In the same way, partial derivatives can even be defined on groups of the form  $\mathbb{R}^n \times \mathbb{T}^n \times \mathbb{Z}^n \times F$ , where  $\alpha, \beta \in \mathbb{N}_0^{\mathbb{N}}$  with  $|\alpha|, |\beta|$  finite.

### 2.4.4 Embedding Results

For the extension of the Fourier transform on a locally compact abelian group to each  $L^p$  space, we proceed as in the classical case. To do so, we have to show that these spaces can be embedded into the space of tempered distributions, where we can define the Fourier transform via duality. Beforehand, we have to investigate the Schwartz-Bruhat space further. As in the previous subsection, let  $G$  be a locally compact abelian group.

**Theorem 2.45** *Let  $1 \leq p \leq \infty$ . Then the Schwartz-Bruhat space  $\mathcal{S}(G)$  is continuously embedded into  $L^p(G)$ .*

*Proof* Let  $f \in \mathcal{S}(G)$ . Then there is a pair  $(K, \Gamma) \in \mathcal{A}$  with  $f \in \mathcal{S}(K, \Gamma)$ , and hence there exists  $u \in \mathcal{S}(\Gamma/K)$  such that

$$f(x) = \begin{cases} u(\pi(x)), & \text{if } x \in \Gamma, \\ 0, & \text{otherwise,} \end{cases}$$

where  $\pi: \Gamma \rightarrow \Gamma/K$  is the quotient mapping. If  $p < \infty$ , we get

$$\begin{aligned} \int_G |f(x)|^p dx &= \int_\Gamma |u(\pi(x))|^p dx = \int_{\Gamma/K} \int_K |u(\pi(x+k))|^p dk d[x] \\ &= \int_{\Gamma/K} \int_K |u([x])|^p dk d[x] = \mu(K) \cdot \|u\|_{L^p(\Gamma/K)}^p, \end{aligned}$$

where  $\mu$  denotes the Haar measure on the group  $G$ . For  $p = \infty$ , we have

$$\operatorname{ess\,sup}_{x \in G} |f(x)| = \operatorname{ess\,sup}_{x \in \Gamma} |u(\pi(x))| = \|u\|_{L^\infty(\Gamma/K)}.$$

In total, we obtain  $f \in L^p(G)$  and

$$\|f\|_{L^p(G)} = \mu(K)^{\frac{1}{p}} \|u\|_{L^p(\Gamma/K)} \quad (2.23)$$

for each  $p \in [1, \infty]$ , where we set  $\frac{1}{\infty} := 0$ . Since  $u$  is an element of the Schwartz–Bruhat space on the elementary group  $\Gamma/K$ , we have  $u \in L^p(\Gamma/K)$ ; compare Theorem 2.23. Therefore, (2.23) implies  $\mathcal{S}(G) \subseteq L^p(G)$  for all  $1 \leq p \leq \infty$ . In order to show continuity of this embedding, we can use the universal property from Proposition 2.42. Hence it remains to show that the embedding  $\mathcal{S}(K, \Gamma) \hookrightarrow L^p(G)$  is continuous for all  $(K, \Gamma) \in \mathcal{A}$ . By using Theorem 2.23 and Eq. (2.23) again, this follows directly and completes the proof.  $\square$

We shall now show that the embedding above is dense. The case  $p = \infty$  must be excluded (as in the classical setting).

**Theorem 2.46** *For  $1 \leq p < \infty$  the space  $\mathcal{S}(G)$  is a dense subset of  $L^p(G)$ .*

*Proof* Let  $f \in C_c(G)$  and  $\varepsilon > 0$  be arbitrary, and let  $C \subseteq G$  be a compact set with nonempty interior such that  $\operatorname{supp} f \subseteq C$ . We define the group  $\Gamma := \langle C \rangle$ . Then  $\Gamma$  is open and compactly generated. Since  $\Gamma$  is a locally compact abelian group, there is an open neighborhood  $U \subseteq \Gamma$  of 0 (which is, in particular, an open neighborhood of 0 in  $G$ ) such that

$$\|f - \varphi * f\|_{L^p(G)} = \|f - \varphi * f\|_{L^p(\Gamma)} < \varepsilon$$

for all  $\varphi \in L^1(G)$  with  $\operatorname{supp} \varphi \subseteq U$  and  $\|\varphi\|_{L^1(G)} = \|\varphi\|_{L^1(\Gamma)} = 1$ . By Corollary 2.36 there exists a good subgroup  $K$  of  $\Gamma$  with  $K \subseteq U$ . Hence we have

$(K, \Gamma) \in \mathcal{A}$ . If  $\pi: \Gamma \rightarrow \Gamma/K$  denotes the usual quotient mapping,  $\pi(U)$  is an open neighborhood of 0 in  $\Gamma/K$ . Since  $\Gamma/K$  is elementary, by Proposition 2.27 there exists a function  $u \in C^\infty(\Gamma/K)$  with  $\text{supp } u \subseteq \pi(U)$  and  $u \neq 0$ . Moreover, we can re-norm this function such that  $\|u\|_{L^1(\Gamma/K)} = \mu(K)^{-1}$ . Now we define  $\varphi: G \rightarrow \mathbb{C}$  by

$$\varphi(x) = \begin{cases} u(\pi(x)), & \text{if } x \in \Gamma, \\ 0, & \text{otherwise.} \end{cases}$$

Then  $\varphi \in \mathcal{S}(K, \Gamma)$  because  $u \in \mathcal{S}(\Gamma/K)$ , and  $\text{supp } \varphi \subseteq U$ . Furthermore, by Eq. (2.23) we have

$$\|\varphi\|_{L^1(\Gamma)} = \|\varphi\|_{L^1(G)} = \mu(K) \|u\|_{L^1(\Gamma/K)} = 1.$$

Therefore, we obtain  $\|f - \varphi * f\|_{L^p(G)} < \varepsilon$ , and it remains to check that  $\varphi * f \in \mathcal{S}(G)$ . Since  $\text{supp}(\varphi * f) \subseteq \text{supp } \varphi + \text{supp } f \subseteq U + \Gamma = \Gamma$ , we have  $\varphi * f(x) = 0$  for  $x \in G \setminus \Gamma$ . For  $x \in \Gamma$  we obtain

$$\begin{aligned} \varphi * f(x) &= \int_{\Gamma} u(\pi(y))f(x - y) \, dy = \int_{\Gamma/K} \int_K u(\pi(y + k))f(x - (y + k)) \, dk \, d[y] \\ &= \int_{\Gamma/K} u([y])F([x] - [y]) \, d[y] = (u * F)(\pi(x)), \end{aligned}$$

where the functions  $\tilde{F}: \Gamma \rightarrow \mathbb{C}$  and  $F: \Gamma/K \rightarrow \mathbb{C}$  are given by

$$\tilde{F}(z) := \int_K f(z - k) \, dk$$

and  $F([z]) := \tilde{F}(z)$ . The question arises if these functions are well defined. Indeed, since the function  $(z, k) \mapsto f(z - k)$  is integrable on  $\Gamma \times K$ , the function  $\tilde{F}$  is also measurable and integrable by Fubini's Theorem. Furthermore, we have

$$\tilde{F}(z + k_0) = \int_K f(z + k_0 - k) \, dk = \int_K f(z - k) \, dk = \tilde{F}(z)$$

for all  $k_0 \in K$  and  $z \in \Gamma$  by translation-invariance of the Haar measure. Therefore,  $F$  is also a well-defined, integrable function on  $\Gamma/K$ . Hence  $u * F$  is well defined, too.

Now let  $z \in \Gamma$  with  $[z] \notin \pi(C + K)$ . Then  $z \notin C + K$ , hence  $z - k \notin C$  for all  $k \in K$  and so

$$F([z]) = \tilde{F}(z) = \int_K f(z - k) \, dk = 0$$

since  $\text{supp } f \subseteq C$ . Thus we have shown that  $\text{supp } F$  is contained in  $\pi(C + K)$ , which is a compact set since  $C + K$  is a compact set and  $\pi$  is a continuous mapping.

Because it holds  $u \in \mathcal{S}(\Gamma/K)$  and  $F$  is integrable and compactly supported, we obtain  $u * F \in \mathcal{S}(\Gamma/K)$  by Proposition 2.26. Thus we have  $\varphi * f \in \mathcal{S}(K, \Gamma) \subseteq \mathcal{S}(G)$ . Consequently, we have shown that each function in  $C_c(G)$  can be approximated by elements of  $\mathcal{S}(G)$  in  $L^p(G)$  for  $1 \leq p < \infty$ . By density of  $C_c(G)$  in  $L^p(G)$ , we obtain the desired result.  $\square$

The embedding of  $L^p(G)$  into  $\mathcal{S}'(G)$  is defined in the same way as in the classical case.

**Theorem 2.47** *Let  $1 \leq p \leq \infty$ . The mapping  $f \mapsto \psi_f$ , where  $\psi_f: \mathcal{S}(G) \rightarrow \mathbb{C}$  is given by*

$$\psi_f(\varphi) = \int_G f(x)\varphi(x) \, dx, \quad (2.24)$$

*defines a continuous embedding  $L^p(G) \hookrightarrow \mathcal{S}'(G)$ .*

*Proof* Let  $p, p' \in [1, \infty]$ , where  $p'$  is the dual index of  $p$ , and let  $f \in L^p(G)$ . By Theorem 2.45 we have  $\mathcal{S}(G) \subseteq L^{p'}(G)$ . Using Hölder's inequality, we obtain

$$|\psi_f(\varphi)| \leq \int_G |f\varphi| \leq \|f\|_{L^p(G)} \|\varphi\|_{L^{p'}(G)}. \quad (2.25)$$

Hence  $\psi_f$  is well defined and also a continuous linear functional on  $\mathcal{S}(G)$  since the embedding  $\mathcal{S}(G) \hookrightarrow L^{p'}(G)$  is continuous; see Theorem 2.45. Furthermore, the linearity of  $f \mapsto \psi_f$  is clear, and it remains to show the continuity and the injectivity of this mapping. The continuity follows directly from estimate (2.25). For the proof of the injectivity, let  $f, g \in L^p(G)$  with  $\psi_f = \psi_g$ , i.e.,

$$\int_G (f - g)\varphi = 0$$

for all  $\varphi \in \mathcal{S}(G)$ . Since the space  $\mathcal{S}(G)$  is dense in  $L^q(G)$  for any  $1 \leq q < \infty$  by Theorem 2.46, we obtain  $f - g = 0$  almost everywhere and hence  $f = g$  as  $L^p(G)$  functions. This finishes the proof.  $\square$

## 2.4.5 The Fourier Transform

We shall now investigate the Fourier transform on  $\mathcal{S}(G)$  and  $\mathcal{S}'(G)$ . We will see that the continuity properties, which are well known in the classical case, still hold in our generalized setting. Consequently, by using the results of the previous subsection, the Fourier transform of an  $L^p$  function is also well defined for any  $p \in [1, \infty]$ .

Throughout this subsection, let  $G$  be a locally compact abelian group, and let  $\mathcal{A}$  be given as in Definition 2.28. Let  $\mathcal{F}$  denote the Fourier transform on  $G$ . For the sake of convenience, we also use the notation  $\widehat{f}$  instead of  $\mathcal{F}[f]$  if the latter is well defined.

**Lemma 2.48** *Let  $(K, \Gamma) \in \mathcal{A}$ . Then the Fourier transform on  $G$  is a topological isomorphism  $\mathcal{F}: \mathcal{S}(K, \Gamma) \rightarrow \mathcal{S}(\Gamma^\perp, K^\perp)$ .*

*Proof* In Theorem 2.45 we have already seen that  $\mathcal{S}(K, \Gamma)$  is a subspace of  $L^1(G)$ . Hence  $\widehat{f}$  is well defined for any  $f \in \mathcal{S}(K, \Gamma)$ . At first we want to show that  $\widehat{f}$  is, in fact, an element of  $\mathcal{S}(\Gamma^\perp, K^\perp)$ . We denote the canonical quotient mapping by  $\pi: \Gamma \rightarrow \Gamma/K$ . By definition, there is  $u = u_f \in \mathcal{S}(\Gamma/K)$  such that (2.39) is valid. We thus obtain the equality

$$\widehat{f}(\gamma) = \int_G f(x)(-x, \gamma) \, dx = \int_\Gamma u(\pi(x))(-x, \gamma) \, dx$$

for all  $\gamma \in \widehat{G}$ . On the one hand, the identity

$$\begin{aligned} \widehat{f}(\gamma) &= \int_\Gamma u(\pi(x))(-x, \gamma) \, dx = \int_\Gamma u(\pi(x+k))(-x+k, \gamma) \, dx \\ &= (-k, \gamma) \int_\Gamma u(\pi(x))(-x, \gamma) \, dx = (-k, \gamma) \widehat{f}(\gamma) \end{aligned}$$

for any  $\gamma \in \widehat{G}$  and any  $k \in K$  implies that we have  $\widehat{f}(\gamma) = 0$  if  $(k, \gamma) \neq 1$ , i.e.,  $\text{supp } \widehat{f} \subseteq K^\perp$ . On the other hand, for all  $x \in \Gamma, k \in K, \gamma \in K^\perp, \gamma_0 \in \Gamma^\perp$ , we have the equality

$$(x+k, \gamma+\gamma_0) = (x, \gamma)(x, \gamma_0)(k, \gamma)(k, \gamma_0) = (x, \gamma).$$

Thus the identity  $([x], [\gamma]) = (x, \gamma)$  does not depend on the chosen representatives. Here we set  $[x] := \pi(x)$ , and  $[\gamma]$  denotes the coset in  $K^\perp/\Gamma^\perp$  containing  $\gamma$ . Therefore, for all  $\gamma \in K^\perp$ , a direct computation yields

$$\begin{aligned} \widehat{f}(\gamma) &= \int_\Gamma u(\pi(x))(-x, \gamma) \, dx = \int_{\Gamma/K} \int_K u(\pi(x+k))(-x-k, \gamma) \, dk \, d[x] \\ &= \int_{\Gamma/K} \int_K u([x])(-x, \gamma) \, dk \, d[x] = \mu(K) \int_{\Gamma/K} u([x])(-[x], [\gamma]) \, d[x] \\ &= \mu(K) \widehat{u}([\gamma]), \end{aligned}$$

where  $\mu$  denotes the Haar measure on  $G$  and  $\widehat{u} := \mathcal{F}_{\Gamma/K}[u]$ . In total, we obtain the equality

$$\widehat{f}(\gamma) = \begin{cases} \mu(K) \cdot \widehat{u}(\widehat{\pi}(\gamma)), & \text{if } \gamma \in K^\perp, \\ 0, & \text{otherwise,} \end{cases} \quad (2.26)$$

where  $\widehat{\pi}: K^\perp \rightarrow K^\perp/\Gamma^\perp$  denotes the quotient mapping. Theorem 2.24 implies that  $\widehat{u}$  is a Schwartz-Bruhat function on the dual group of  $\Gamma/K$ , i.e., on  $K^\perp/\Gamma^\perp$ , and hence we have  $\widehat{f} \in \mathcal{S}(\Gamma^\perp, K^\perp)$ . Furthermore, we obtain that the Fourier transform is continuous since the convergence of a sequence  $(f_n) \subseteq \mathcal{S}(K, \Gamma)$  to a function  $f \in \mathcal{S}(K, \Gamma)$  implies that the associated sequence  $(u_n) \subseteq \mathcal{S}(\Gamma/K)$  converges to the function  $u$  chosen as above. By continuity of the Fourier transform on  $\mathcal{S}(\Gamma/K)$ , compare Theorem 2.24, we obtain that the sequence  $(\widehat{u}_n)$  converges to  $\widehat{u}$ . Now equality (2.26) implies that  $(\widehat{f}_n)$  converges to  $\widehat{f}$ .

With the same argument, we obtain that the mapping  $\mathcal{F}_G^{-1}$  possesses the same mapping properties and is, up to a constant, the inverse mapping to  $\mathcal{F}$ . Since we may modify the Haar measure and thus the Fourier transform on  $\Gamma/K$  by a constant factor, we may omit this factor, and we have proved the statement.  $\square$

Now we can consider the Fourier transform on the Schwartz-Bruhat space on  $G$  and use the universal property of the inductive limit, compare Proposition 2.42, in order to obtain its continuity.

**Theorem 2.49** *The Fourier transform  $\mathcal{F}: \mathcal{S}(G) \rightarrow \mathcal{S}(\widehat{G})$  is a topological isomorphism.*

*Proof* For any  $f \in \mathcal{S}(G)$  there exists a pair  $(K, \Gamma) \in \mathcal{A}$  such that  $f \in \mathcal{S}(K, \Gamma)$ . By Lemma 2.48 this implies that  $\widehat{f} \in \mathcal{S}(\Gamma^\perp, K^\perp) \subseteq \mathcal{S}(\widehat{G})$ . Hence  $\mathcal{F}$  maps  $\mathcal{S}(G)$  to  $\mathcal{S}(\widehat{G})$  and  $\mathcal{F}^{-1}$  is its actual inverse. It remains to show that these two mappings are continuous. We have already seen that  $\mathcal{F}: \mathcal{S}(K, \Gamma) \rightarrow \mathcal{S}(\Gamma^\perp, K^\perp)$  is continuous for each pair  $(K, \Gamma) \in \mathcal{A}$ . Furthermore, by the definition of the topology on  $\mathcal{S}(\widehat{G})$ , the embedding  $\mathcal{S}(\Gamma^\perp, K^\perp) \hookrightarrow \mathcal{S}(\widehat{G})$  is continuous. Therefore, the Fourier transform considered as a mapping  $\mathcal{S}(K, \Gamma) \rightarrow \mathcal{S}(\widehat{G})$  is also continuous. By the universal property of the inductive limit, see Proposition 2.42, we obtain the continuity of  $\mathcal{F}: \mathcal{S}(G) \rightarrow \mathcal{S}(\widehat{G})$ . The same argument leads to the analogous result for  $\mathcal{F}^{-1}: \mathcal{S}(\widehat{G}) \rightarrow \mathcal{S}(G)$ .  $\square$

As in the classical case, we can define the Fourier transform on the space of tempered distributions via duality.

**Definition 2.50** The Fourier transform on the space of tempered distributions is defined by

$$\mathcal{F}: \mathcal{S}'(G) \rightarrow \mathcal{S}'(\widehat{G}), \quad \langle \mathcal{F}[\psi], f \rangle := \langle \widehat{\psi}, f \rangle := \langle \psi, \widehat{f} \rangle,$$

and the inverse Fourier transform by

$$\mathcal{F}^{-1}: \mathcal{S}'(\widehat{G}) \rightarrow \mathcal{S}'(G), \quad \langle \mathcal{F}^{-1}[\psi], f \rangle := \langle \psi, \mathcal{F}^{-1}[f] \rangle.$$

Observe that these mappings are well defined since  $\mathcal{F}[f] \in \mathcal{S}(G)$  for all  $f \in \mathcal{S}(\widehat{G})$  and vice versa by the previous theorem (and the Pontryagin Duality Theorem). Furthermore, we can prove the following statement, which shows that the mapping properties of  $\mathcal{F}$  on  $\mathcal{S}'(G)$  are the same as on  $\mathcal{S}(G)$ .

**Theorem 2.51** *The Fourier transform  $\mathcal{F}: \mathcal{S}'(G) \rightarrow \mathcal{S}'(\widehat{G})$  is a topological isomorphism and its inverse is given by  $\mathcal{F}^{-1}$ .*

*Proof* It follows directly from the definition that  $\mathcal{F}$  is a linear mapping on  $\mathcal{S}'(G)$ . We have to verify that it is continuous. Let  $(\psi_\alpha) \subseteq \mathcal{S}'(G)$  be a convergent net with limit  $\psi \in \mathcal{S}'(G)$ . We obtain

$$\lim_\alpha \langle \mathcal{F}[\psi_\alpha], f \rangle = \lim_\alpha \langle \psi_\alpha, \widehat{f} \rangle = \langle \psi, \widehat{f} \rangle = \langle \mathcal{F}[\psi], f \rangle$$

for each  $f \in \mathcal{S}(\widehat{G})$ , and thus  $(\widehat{\psi}_\alpha)$  converges to  $\widehat{\psi}$ , which yields continuity. The same is true for  $\mathcal{F}^{-1}$ , and we have

$$\langle \mathcal{F}^{-1} \mathcal{F}[\psi], f \rangle = \langle \psi, \mathcal{F} \mathcal{F}^{-1}[f] \rangle = \langle \psi, f \rangle$$

for all  $\psi \in \mathcal{S}'(G)$  and all  $f \in \mathcal{S}(G)$ . □

Since we have seen in Theorem 2.47 that we can embed the space  $L^p(G)$  into  $\mathcal{S}'(G)$  continuously for any  $1 \leq p \leq \infty$ , the restriction of the Fourier transform to  $L^p(G)$  is also a continuous mapping  $L^p(G) \rightarrow \mathcal{S}'(\widehat{G})$ . The question arises if this notion of Fourier transform is consistent to the already defined Fourier transform of a function  $f \in L^p(G)$  for  $p \in [1, 2]$ . The next proposition gives a positive answer.

**Proposition 2.52** *Let  $1 \leq p \leq 2$ . Then the equality*

$$\widehat{\psi}_f = \psi_{\widehat{f}} \tag{2.27}$$

*holds for all  $f \in L^p(G)$ , where  $\psi_f$  is defined in Eq. (2.24).*

*Proof* At first let  $f \in \mathcal{S}(G)$  and  $\varphi \in \mathcal{S}(\widehat{G})$ . We obtain

$$\langle \widehat{\psi}_f, \varphi \rangle = \langle \psi_f, \widehat{\varphi} \rangle = \int_G f \widehat{\varphi} = \int_{\widehat{G}} \widehat{f} \varphi = \langle \psi_{\widehat{f}}, \varphi \rangle,$$

where we applied Parseval's formula. Hence Eq. (2.27) holds for all  $f \in \mathcal{S}(G)$ . By Theorem 2.46 the set  $\mathcal{S}(G)$  is a dense subspace of  $L^p(G)$  for  $1 \leq p \leq 2$ , and the embedding  $L^p(G) \hookrightarrow \mathcal{S}'(G), f \mapsto \psi_f$  is continuous by Theorem 2.47. Thus equality (2.27) holds for all  $f \in L^p(G)$ . □



## 2.5 Time-Periodic Linearized Navier–Stokes Equations

We now return to the investigation of the linearized time-periodic Navier–Stokes system (2.1). In the first step we replace the time axis by the torus group  $\mathbb{T} := \mathbb{R}/\mathcal{T}\mathbb{Z}$ , equipped with the quotient topology, and formulate (2.1) on the locally compact abelian group  $G := \mathbb{T} \times \mathbb{R}^n$  as

$$\begin{cases} \partial_t u - \Delta u - \lambda \partial_{x_1} u + \nabla p = f & \text{in } G, \\ \operatorname{div} u = 0 & \text{in } G \end{cases} \quad (2.28)$$

with unknowns  $u: G \rightarrow \mathbb{R}^n$  and  $p: G \rightarrow \mathbb{R}$ , and data  $f: G \rightarrow \mathbb{R}^n$ . Observe that in this formulation the periodicity condition is not needed anymore. Indeed, all functions defined on  $G$  are intrinsically  $\mathcal{T}$ -time-periodic. We shall investigate (2.28) in the setting of Schwartz-Bruhat distributions  $\mathcal{S}'(G)$  and a posteriori reformulate the results in a setting of classical periodic functions.

### 2.5.1 Maximal Regularity

The Transference Principle can be used to establish maximal  $L^q$  regularity, that is, to identify a function space  $X^q(G)$  such that the differential operator on the left-hand side of (2.28)<sub>1</sub> maps  $X^q(G)$  homeomorphically onto  $L^q(G)^n$ . For this purpose, we shall need to decompose the problem into two parts, which will be analyzed separately. We therefore introduce the projections

$$\mathcal{P}: \mathcal{S}'(G) \rightarrow \mathcal{S}'(G), \quad \mathcal{P}f := \mathcal{F}_G^{-1}[\delta_{\mathbb{Z}} \mathcal{F}_G(f)], \quad (2.29)$$

$$\mathcal{P}_{\perp}: \mathcal{S}'(G) \rightarrow \mathcal{S}'(G), \quad \mathcal{P}_{\perp}f := \mathcal{F}_G^{-1}[(1 - \delta_{\mathbb{Z}}) \cdot \mathcal{F}_G(f)], \quad (2.30)$$

where

$$\delta_{\mathbb{Z}}: \widehat{G} \rightarrow \mathbb{C}, \quad \delta_{\mathbb{Z}}(k, \xi) := \begin{cases} 1 & \text{if } k = 0, \\ 0 & \text{if } k \neq 0, \end{cases}$$

denotes the delta distribution. It is immediately clear that  $\mathcal{P}$  and  $\mathcal{P}_{\perp}$  are complementary projections. Moreover, for any sufficiently regular function  $f: G \rightarrow \mathbb{R}$  one readily verifies that

$$\mathcal{P}f(t, x) = \int_{\mathbb{T}} f(s, x) \, ds. \quad (2.31)$$

Since  $\mathcal{P}f$  is independent of time, we call it the *steady-state* part of  $f$  and implicitly treat it as a function that only depends on the spatial variable  $x \in \mathbb{R}^n$ . We call  $\mathcal{P}_{\perp}f$

the *purely periodic* part of  $f$ . It turns out that the steady-state part and the purely periodic part of a solution to (2.28) have different regularity properties.

We define appropriate Sobolev spaces to characterize the maximal regularity of a solution to (2.28). For this purpose, we recall that the  $L^q(G)$  spaces are continuously embedded into  $\mathcal{S}'(G)$  by Theorem 2.47. Hence the derivatives of an  $L^q$  function are well defined by (2.22). For  $q \in (1, \infty)$  we let

$$\begin{aligned} W^{1,2,q}(G) &:= \{u \in L^q(G) : \partial_t u \in L^q(G), D_x^\alpha u \in L^q(G) \forall |\alpha| \leq 2\}, \\ \|u\|_{W^{1,2,q}(G)} &:= \|u\|_{1,2,q} := \left( \|\partial_t u\|_q^q + \sum_{|\alpha| \leq 2} \|D_x^\alpha u\|_q^q \right)^{\frac{1}{q}}, \end{aligned}$$

and introduce the subspace

$$W_{\sigma,\perp}^{1,2,q}(G) := \{u \in W^{1,2,q}(G)^n : \mathcal{P}u = 0, \operatorname{div} u = 0\}$$

of purely periodic, solenoidal  $W^{1,2,q}$  vector fields. Moreover, put

$$L_{\sigma,\perp}^q(G) := \{u \in L^q(G)^n : \mathcal{P}u = 0, \operatorname{div} u = 0\}.$$

As in the classical Euclidean case, one can employ ‘‘Bogovskii’s formula’’ (see for example [6]) in combination with a mollifier argument to show that the space of compactly supported, smooth, solenoidal vector fields

$$C_{c,\sigma,\perp}^\infty(G) := \{u \in C_c^\infty(G)^n : \mathcal{P}u = 0, \operatorname{div} u = 0\}$$

is dense in  $L_{\sigma,\perp}^q(G)$  and in  $W_{\sigma,\perp}^{1,2,q}(G)$ . In the following theorem, we establish maximal  $L^q$  regularity for purely periodic data in  $L_{\sigma,\perp}^q(G)$ .

**Theorem 2.53** *Let  $q \in (1, \infty)$ . For any  $f \in L_{\sigma,\perp}^q(G)$  there is a unique solution  $u \in \mathcal{P}_\perp \mathcal{S}'(G)^n$  and  $\mathfrak{p} = 0$  to (2.28). The solution  $u$  belongs to  $W_{\sigma,\perp}^{1,2,q}(G)$  and satisfies the estimate*

$$\|u\|_{1,2,q} \leq CP(\lambda, \mathcal{T}) \|f\|_q, \tag{2.32}$$

where  $P(\lambda, \mathcal{T}) > 0$  is a polynomial in  $\lambda$  and  $\mathcal{T}$ , and  $C = C(n, q) > 0$ .

*Proof* It suffices to establish the theorem for  $f \in C_{c,\sigma,\perp}^\infty(G)$ . Clearly, we then have  $f \in \mathcal{S}(G)^n$ . Let

$$M: \widehat{G} \rightarrow \mathbb{C}, \quad M(k, \xi) := \frac{(1 - \delta_{\mathbb{Z}}(k, \xi))}{i\frac{2\pi}{\mathcal{T}}k + |\xi|^2 - \lambda i\xi_1}.$$

Observe that  $M$  is bounded since the numerator vanishes in a neighborhood of the only zero  $(k, \xi) = (0, 0)$  of the denominator  $|\xi|^2 + i(\frac{2\pi}{T}k - \lambda\xi_1)$ . In fact, we have  $M \in C^\infty(G) \cap L^\infty(G)$ . Define

$$u := \mathcal{F}_G^{-1}[M(k, \xi) \mathcal{F}_G(f)]. \tag{2.33}$$

Since  $f = \mathcal{P}_\perp f$ , we observe that  $\mathcal{F}_G[f] = (1 - \delta_{\mathbb{Z}}(k, \xi)) \mathcal{F}_G[f]$ . It follows that

$$\begin{aligned} \partial_t u - \Delta u - \lambda \partial_{x_1} u &= \mathcal{F}_G^{-1} \left[ \left( i \frac{2\pi}{T} k + |\xi|^2 - \lambda i \xi_1 \right) \mathcal{F}_G[u] \right] \\ &= \mathcal{F}_G^{-1} \left[ (1 - \delta_{\mathbb{Z}}(k, \xi)) \mathcal{F}_G[f] \right] = f. \end{aligned}$$

We obtain directly from (2.33) that  $\operatorname{div} u = 0$  and  $\mathcal{P}u = 0$ . Thus,  $u$  is a solution in  $\mathcal{P}_\perp \mathcal{S}'(G)^n$  to (2.28). If  $v \in \mathcal{P}_\perp \mathcal{S}'(G)^n$  is another solution, we have

$$\left( i \frac{2\pi}{T} k + |\xi|^2 - \lambda i \xi_1 \right) \mathcal{F}_G[u - v] = 0.$$

We conclude that  $\operatorname{supp} \mathcal{F}_G[u - v] \subseteq \{(0, 0)\}$ . However, since  $\delta_{\mathbb{Z}} \mathcal{F}_G[u - v] = \mathcal{F}_G[\mathcal{P}(u - v)] = 0$ , we have  $(0, 0) \notin \operatorname{supp} \mathcal{F}_G[u - v]$ . Consequently,  $\operatorname{supp} \mathcal{F}_G[u - v] = \emptyset$ . It follows that  $\mathcal{F}_G[u - v] = 0$  and thus  $u = v$ . Therefore,  $u$  is a unique solution in  $\mathcal{P}_\perp \mathcal{S}'(G)^n$ . It remains to show (2.32), for which we shall use the Transference Principle. Let  $\chi$  be a ‘‘cut-off’’ function with

$$\chi \in C_c^\infty(\mathbb{R}; \mathbb{R}), \quad \chi(\eta) = 1 \text{ for } |\eta| \leq \frac{1}{2}, \quad \chi(\eta) = 0 \text{ for } |\eta| \geq 1. \tag{2.34}$$

Define

$$m: \mathbb{R} \times \mathbb{R}^n \rightarrow \mathbb{C}, \quad m(\eta, \xi) := \frac{1 - \chi(\frac{T}{2\pi}\eta)}{|\xi|^2 + i(\eta - \lambda\xi_1)}. \tag{2.35}$$

We can consider  $\mathbb{R} \times \mathbb{R}^n$  as a group  $H$  with addition as group operation. Endowed with the Euclidean topological,  $H$  becomes a locally compact abelian group. It is well known that the dual group  $\widehat{H}$  can also be identified with  $\mathbb{R} \times \mathbb{R}^n$  equipped with the Euclidean topology. We can thus consider  $m$  as a mapping  $m: \widehat{H} \rightarrow \mathbb{C}$ . In order to employ Theorem 2.15, we define  $\Phi: \widehat{G} \rightarrow \widehat{H}$ ,  $\Phi(k, \xi) := (\frac{2\pi}{T}k, \xi)$ . Clearly,  $\Phi$  is a continuous homomorphism. Moreover,  $M = m \circ \Phi$ . Consequently, if we can show that  $m$  is a continuous  $L^q(\mathbb{R} \times \mathbb{R}^n)$  multiplier, we may conclude from Theorem 2.15 that  $M$  is an  $L^q(G)$  multiplier. We first observe that the only zero of the denominator  $|\xi|^2 + i(\eta - \lambda\xi_1)$  in definition (2.35) of  $m$  is  $(\eta, \xi) = (0, 0)$ . Since the numerator  $1 - \chi(\frac{T}{2\pi}\eta)$  in (2.35) vanishes in a neighborhood of  $(0, 0)$ , we see that  $m$  is continuous; in fact  $m$  is smooth. We shall now apply Marcinkiewicz’s multiplier theorem, see for example [8, Corollary 5.2.5] or [24, Chap. IV, §6], to show that  $m$

is an  $L^q(\mathbb{R} \times \mathbb{R}^n)$ -multiplier. Note that Marcinkiewicz’s multiplier theorem can be employed at this point since  $m$  is a Fourier multiplier in the Euclidean  $\mathbb{R} \times \mathbb{R}^n$  setting. To employ Marcinkiewicz’s multiplier theorem, we must verify that

$$\sup_{\varepsilon \in \{0,1\}^{n+1}} \sup_{(\eta, \xi) \in \mathbb{R} \times \mathbb{R}^n} \left| \xi_1^{\varepsilon_1} \cdots \xi_n^{\varepsilon_n} \eta^{\varepsilon_{n+1}} \partial_1^{\varepsilon_1} \cdots \partial_n^{\varepsilon_n} \partial_\eta^{\varepsilon_{n+1}} m(\eta, \xi) \right| \leq c_0 \tag{2.36}$$

for some constant  $c_0 > 0$ . Since  $m$  is smooth, (2.36) follows if we can show that all functions of type

$$(\eta, \xi) \rightarrow \xi_1^{\varepsilon_1} \cdots \xi_n^{\varepsilon_n} \eta^{\varepsilon_{n+1}} \partial_1^{\varepsilon_1} \cdots \partial_n^{\varepsilon_n} \partial_\eta^{\varepsilon_{n+1}} m(\eta, \xi)$$

stay bounded for  $|(\eta, \xi)| \rightarrow \infty$ . Because  $m$  is a rational function with nonvanishing denominator away from  $(0, 0)$ , this is easy to verify. Consequently, we conclude (2.36). If we analyze the bound on the functions more carefully, we find that  $c_0$  can be chosen such that  $c_0 = P_1(\lambda, \mathcal{T})$  with  $P_1(\lambda, \mathcal{T})$  a polynomial in  $\lambda$  and  $\mathcal{T}$ . By Marcinkiewicz’s multiplier theorem, see for example [8, Corollary 5.2.5] or [24, Chap. IV, §6],  $m$  is an  $L^q(\mathbb{R} \times \mathbb{R}^n)$ -multiplier. We now recall Theorem 2.15 and conclude that  $M = m \circ \Phi$  is an  $L^q(G)$ -multiplier. Since  $u = \mathcal{F}_G^{-1}[M(k, \xi) \mathcal{F}_G(f)]$ , we thus obtain

$$\|u\|_q \leq c_1 P_1(\lambda, \mathcal{T}) \|f\|_q, \tag{2.37}$$

with  $c_1 = c_1(q, n)$ . Differentiating  $u$  in the equation  $u = \mathcal{F}_G^{-1}[M(k, \xi) \mathcal{F}_G(f)]$  with respect to time and space, we further obtain the identities

$$\partial_t u = \mathcal{F}_G^{-1} \left[ \left( i \frac{2\pi}{\mathcal{T}} k \right) M(k, \xi) \mathcal{F}_G(f) \right]$$

and

$$D_x^\alpha u = \mathcal{F}_G^{-1} \left[ (i\xi)^\alpha M(k, \xi) \mathcal{F}_G(f) \right],$$

respectively. We can now repeat the argument above with  $(i\frac{2\pi}{\mathcal{T}}k)M(k, \xi)$  in the role of the multiplier  $M$  and  $(i\frac{2\pi}{\mathcal{T}}\eta)m(\eta, \xi)$  in the role of  $m$  in order to conclude

$$\|\partial_t u\|_q \leq c_2 P_2(\lambda, \mathcal{T}) \|f\|_q, \tag{2.38}$$

with  $c_2 = c_2(q, n)$ . Similarly, for  $|\alpha| \leq 2$  we repeat the argument above with  $(i\xi)^\alpha M(k, \xi)$  in the role of  $M$  and  $(i\xi)^\alpha m(\eta, \xi)$  in the role of  $m$  in order to obtain

$$\|D_x^\alpha u\|_q \leq c_3 P_3(\lambda, \mathcal{T}) \|f\|_q. \tag{2.39}$$

Collecting (2.37)–(2.39), we thus conclude  $u \in W_{\sigma,\perp}^{1,2,q}(G)$  with

$$\|u\|_{1,2,q} \leq c_4 P_4(\lambda, \mathcal{T}) \|f\|_q, \quad (2.40)$$

where  $c_4 = c_4(q, n)$ . □

Next, we consider data  $f$  in the subspace

$$L_\sigma^q(G) := \{u \in L^q(G)^n : \operatorname{div} u = 0\}.$$

of solenoidal  $L^q(G)^n$  vector fields. It is easy to verify that  $\mathcal{P}$  is a continuous projection  $\mathcal{P}: L_\sigma^q(G) \rightarrow L_\sigma^q(G)$ . Since  $\mathcal{P}f$  is time-independent, we can identify  $\mathcal{P}L_\sigma^q(G)$  with  $L_\sigma^q(\mathbb{R}^n)$ . Consequently,  $\mathcal{P}$  induces the decomposition

$$L_\sigma^q(G) = L_\sigma^q(\mathbb{R}^n) \oplus L_{\sigma,\perp}^q(G). \quad (2.41)$$

We can therefore combine the maximal regularity obtained in Theorem 2.53 for data in  $L_{\sigma,\perp}^q(G)$  with a similar result for data in  $L_\sigma^q(\mathbb{R}^n)$  to obtain maximal regularity for data in  $L_\sigma^q(G)$ . For data in  $L_\sigma^q(\mathbb{R}^n)$ , however, the system (2.28) reduces to the steady-state Stokes ( $\lambda = 0$ ) or Oseen ( $\lambda \neq 0$ ) system

$$\begin{cases} -\Delta u - \lambda \partial_{x_1} u + \nabla p = f & \text{in } \mathbb{R}^n, \\ \operatorname{div} u = 0 & \text{in } \mathbb{R}^n. \end{cases} \quad (2.42)$$

In order to characterize the space of maximal  $L^q$  regularity, we have to distinguish between  $\lambda = 0$  and  $\lambda \neq 0$ . Moreover, the case  $n = 2$  has to be treated separately. For  $n \geq 3$ ,  $\lambda = 0$ ,  $q \in (1, \frac{n}{2})$  put

$$\begin{aligned} X_{\sigma,\text{Stokes}}^q(\mathbb{R}^n) &:= \{v \in L_{\text{loc}}^1(\mathbb{R}^n)^n : \operatorname{div} v = 0, \|v\|_{q,\text{Stokes}} < \infty\}, \\ \|v\|_{q,\text{Stokes}} &:= \|v\|_{\frac{nq}{n-2q}} + \|\nabla v\|_{\frac{nq}{n-q}} + \|\nabla^2 v\|_q. \end{aligned}$$

For  $n \geq 3$ ,  $\lambda \neq 0$ ,  $q \in (1, \frac{n+1}{2})$  put

$$\begin{aligned} X_{\sigma,\text{Oseen}}^q(\mathbb{R}^n) &:= \{v \in L_{\text{loc}}^1(\mathbb{R}^n)^n : \operatorname{div} v = 0, \|v\|_{q,\lambda,\text{Oseen}} < \infty\}, \\ \|v\|_{q,\lambda,\text{Oseen}} &:= |\lambda|^{\frac{2}{n+1}} \|v\|_{\frac{(n+1)q}{n+1-2q}} + |\lambda|^{\frac{1}{n+1}} \|\nabla v\|_{\frac{(n+1)q}{n+1-q}} + |\lambda| \|\partial_1 v\|_q + \|\nabla^2 v\|_q. \end{aligned}$$

For  $n = 2$ ,  $\lambda \neq 0$ ,  $q \in (1, \frac{3}{2})$  put

$$\begin{aligned} X_{\sigma,\text{Oseen2D}}^q(\mathbb{R}^2) &:= \{v \in L_{\text{loc}}^1(\mathbb{R}^2)^2 : \operatorname{div} v = 0, \|v\|_{q,\lambda,\text{Oseen2D}} < \infty\}, \\ \|v\|_{q,\lambda,\text{Oseen2D}} &:= |\lambda|^{\frac{2}{3}} \|v\|_{\frac{3q}{3-2q}} + |\lambda|^{\frac{1}{3}} \|\nabla v\|_{\frac{3q}{3-q}} + |\lambda| \|\partial_1 v\|_q + \|\nabla^2 v\|_q \\ &\quad + |\lambda| \|\nabla v_2\|_q + |\lambda| \|v_2\|_{\frac{2q}{2-q}}. \end{aligned}$$

The two-dimensional Stokes problem, that is, the case  $n = 2$ ,  $\lambda = 0$ , is not well posed in  $L^q_\sigma(\mathbb{R}^n)$  for any  $q \in (1, \infty)$  in the sense that the kernel of operator on the left-hand side in (2.42) is non-trivial; see [6, Lemma V.4.4]. This phenomenon is also known as the Stokes Paradox. We shall not consider this case here. Recall the following well-known result:

**Theorem 2.54** *Let*

$$X^q_S(\mathbb{R}^n) := X^q_{\sigma, \text{Stokes}}(\mathbb{R}^n) \quad \text{if } n \geq 3, \lambda = 0, q \in \left(1, \frac{n}{2}\right), \quad (2.43)$$

$$X^q_S(\mathbb{R}^n) := X^q_{\sigma, \text{Oseen}}(\mathbb{R}^n) \quad \text{if } n \geq 3, \lambda \neq 0, q \in \left(1, \frac{n+1}{2}\right), \quad (2.44)$$

$$X^q_S(\mathbb{R}^n) := X^q_{\sigma, \text{Oseen2D}}(\mathbb{R}^2) \quad \text{if } n = 2, \lambda \neq 0, q \in \left(1, \frac{3}{2}\right). \quad (2.45)$$

For any  $f \in L^q_\sigma(\mathbb{R}^n)$  there is a unique solution  $u \in X^q_S(\mathbb{R}^n)$  and  $\mathbf{p} = 0$  to (2.42). This solution satisfies

$$\|u\|_{X^q_S(\mathbb{R}^n)} \leq C\|f\|_q, \quad (2.46)$$

where  $C = C(n, q) > 0$ .

*Proof* See [6, Theorem IV.2.1] and [6, Theorem VII.4.1].  $\square$

In order to consider data  $f \in L^q(G)^n$  that are not necessarily divergence-free, we introduce what is sometimes referred to as the Helmholtz projection:

$$\mathcal{P}_H: \mathcal{S}(G)^n \rightarrow \mathcal{S}'(G)^n, \quad \mathcal{P}_H f := \mathcal{F}_G^{-1} \left[ \left( I - \frac{\xi \otimes \xi}{|\xi|^2} \right) \widehat{f} \right].$$

**Lemma 2.55** *Let  $q \in (1, \infty)$ . Then  $\mathcal{P}_H$  extends uniquely to a continuous projection  $\mathcal{P}_H: L^q(G)^n \rightarrow L^q(G)^n$ . Moreover,  $\mathcal{P}_H L^q(G)^n = L^q_\sigma(G)$ .*

*Proof* Clearly,

$$\mathcal{F}_G^{-1} \left[ \left( I - \frac{\xi \otimes \xi}{|\xi|^2} \right) \widehat{f} \right] = \mathcal{F}_{\mathbb{R}^n}^{-1} \left[ \left( I - \frac{\xi \otimes \xi}{|\xi|^2} \right) \mathcal{F}_{\mathbb{R}^n}(f) \right].$$

The classical Helmholtz projection on  $L^q(\mathbb{R}^n)^n$ , which one recognizes on the right-hand side, can be written as a sum of Riesz operators and is therefore bounded on  $L^q(\mathbb{R}^n)^n$ . It follows directly that  $\mathcal{P}_H$  is also bounded on  $L^q(G)^n$ . One readily verifies that  $\mathcal{P}_H$  is a projection, and that  $\operatorname{div} \mathcal{P}_H f = 0$ . Consequently,  $\mathcal{P}_H L^q(G)^n \subseteq L^q_\sigma(G)$  follows. On the other hand, since  $\operatorname{div} f = 0$  implies  $\xi_j f_j = 0$ , we have  $\mathcal{P}_H f = f$  for all  $f \in L^q_\sigma(G)$ . Hence we conclude  $\mathcal{P}_H L^q(G)^n = L^q_\sigma(G)$ .  $\square$

Since  $\mathcal{P}_H: L^q(G)^n \rightarrow L^q(G)^n$  is a continuous projection, it decomposes  $L^q(G)$  into a direct sum

$$L^q(G) = L^q(G) \oplus \mathcal{G}^q(G) \tag{2.47}$$

of closed subspaces with

$$\mathcal{G}^q(G) := (\text{Id} - \mathcal{P}_H)L^q(G)^n. \tag{2.48}$$

**Theorem 2.56** *Let  $q \in (1, n)$ . Put*

$$\begin{aligned} X_p^q(G) &:= \{p \in \mathcal{S}'(G) \cap L^1_{\text{loc}}(G) : \|p\|_{X_p^q} < \infty\}, \\ \|p\|_{X_p^q} &:= \left( \int_{\mathbb{T}} \|p(t, \cdot)\|_{\frac{nq}{n-q}}^q dt + \|\nabla p\|_q^q \right)^{1/q}. \end{aligned} \tag{2.49}$$

Then

$$\text{grad}: X_p^q(G) \rightarrow \mathcal{G}^q(G), \quad \text{grad } p := \nabla p \tag{2.50}$$

is a homeomorphism. Moreover,  $\|\text{grad}^{-1}\|$  depends only on  $n$  and  $q$ .

*Proof* Clearly, grad is bounded. Consider  $p \in \ker \text{grad}$ . Then  $\nabla p = 0$  and it thus follows that  $p(t, x) = c(t)$ . Since  $\|p\|_{X_p^q} < \infty$ , we must have  $p = 0$ . Consequently, grad is injective. To show that grad is onto, we consider the mapping

$$\mathcal{I}: \mathcal{S}(G)^n \rightarrow \mathcal{S}'(G), \quad \mathcal{I}(f) := \mathcal{F}_{\mathbb{R}^n}^{-1} \left[ \sum_{j=1}^n \frac{\xi_j}{|\xi|^2} \mathcal{F}_{\mathbb{R}^n}(f_j) \right].$$

Observe that

$$\nabla \mathcal{I}(f) = (\text{Id} - \mathcal{P}_H)f. \tag{2.51}$$

Since  $\mathcal{I}$  can be expressed as a Riesz potential composed with a sum of Riesz operators, well-known properties of the Riesz potential (see for example [9, Theorem 6.1.3]) and the Riesz operators (see for example [8, Corollary 4.2.8]) yield

$$\frac{1}{\mathcal{T}} \int_0^{\mathcal{T}} \|\mathcal{I}(f)(t, \cdot)\|_{\frac{nq}{n-q}}^q dt \leq c_1 \frac{1}{\mathcal{T}} \int_0^{\mathcal{T}} \|f(t, \cdot)\|_q^q dt = c_1 \|f\|_q^q \tag{2.52}$$

with  $c_1 = c_1(n, q)$ . In combination with (2.51), (2.52) implies  $\|\mathcal{I}(f)\|_{X_p^q} \leq c_2 \|f\|_q$ . By a density argument, we can extend  $\mathcal{I}$  uniquely to a bounded map  $\mathcal{I}: L^q(G)^n \rightarrow X_p^q(G)$  that satisfies (2.51) for all  $f \in L^q(G)^n$ . We can now show that grad is onto. If namely  $f \in \mathcal{G}^q(G)$ , then  $\nabla \mathcal{I}(f) = f$ . We conclude by the open mapping theorem

that  $\text{grad}$  is a homeomorphism. In fact, the inverse is given by  $\mathcal{I}$ , whence by (2.52)  $\|\text{grad}^{-1}\|$  depends only on  $n$  and  $q$ .  $\square$

We can finally combine Theorems 2.53, 2.54 and 2.56 to identify the function spaces of maximal  $L^q$  regularity for (2.28).

**Theorem 2.57** *Let  $X_s^q(\mathbb{R}^n)$  be as in Theorem 2.54. For every  $f \in L^q(G)^n$  there is a unique solution*

$$(u, \mathbf{p}) = (v \oplus w, \mathbf{p}) \in \left( X_s^q(\mathbb{R}^n) \oplus W_{\sigma, \perp}^{1,2,q}(G) \right) \times X_p^q(G)$$

to (2.28). Moreover,

$$\|v\|_{X_s^q} + \|w\|_{1,2,q} + \|\mathbf{p}\|_{X_p^q} \leq C \|f\|_q,$$

where  $C = C(\lambda, \mathcal{T}, n, q) > 0$ .

*Proof* Utilizing the decompositions (2.41) and (2.47) induced by  $\mathcal{P}$  and  $\mathcal{P}_H$ , respectively, we deduce the statements directly from Theorems 2.53, 2.54 and 2.56.  $\square$

At this point we can abandon the abstract formalism and reformulate Theorem 2.57 in a setting of classical Sobolev spaces of time-periodic functions. Let

$$C_{\text{per}}^\infty(\mathbb{R} \times \mathbb{R}^n) := \{u \in C^\infty(\mathbb{R} \times \mathbb{R}^n) : \forall t \in \mathbb{R}: u(\cdot, t + \mathcal{T}) = u(\cdot, t)\},$$

$$C_{\text{c,per}}^\infty(\mathbb{R} \times \mathbb{R}^n) := \{u \in C_{\text{per}}^\infty(\mathbb{R} \times \mathbb{R}^n) : u \in C_c^\infty([0, \mathcal{T}] \times \mathbb{R}^n)\}.$$

By construction, the canonical quotient mapping  $\pi: \mathbb{R} \times \mathbb{R}^n \rightarrow \mathbb{T} \times \mathbb{R}^n$  induces, by lifting, a homeomorphism between  $C^\infty(G)$  and  $C_{\text{per}}^\infty(\mathbb{R} \times \mathbb{R}^n)$  as well as between  $C_c^\infty(G)$  and  $C_{\text{c,per}}^\infty(\mathbb{R} \times \mathbb{R}^n)$ . Analogously to (2.31), we introduce the projection

$$\mathcal{P}: C_{\text{c,per}}^\infty(\mathbb{R} \times \mathbb{R}^n) \rightarrow C_{\text{c,per}}^\infty(\mathbb{R} \times \mathbb{R}^n), \quad \mathcal{P}f(t, x) = \frac{1}{\mathcal{T}} \int_0^{\mathcal{T}} f(s, x) \, ds \quad (2.53)$$

and observe that lifting by  $\pi$  also furnishes a homeomorphism between  $C_{\text{c,}\sigma,\perp}^\infty(G)$  and the space

$$C_{\text{c,per},\perp}^\infty(\mathbb{R} \times \mathbb{R}^n) := \{u \in C_{\text{c,per}}^\infty(\mathbb{R} \times \mathbb{R}^n) : \text{div } u = 0, \mathcal{P}u = 0\}.$$

Consequently,  $W_{\sigma,\perp}^{1,2,q}(G)$  and

$$W_{\text{per},\sigma,\perp}^{1,2,q}(\mathbb{R} \times \mathbb{R}^n) := \overline{C_{\text{c,per},\perp}^\infty(\mathbb{R} \times \mathbb{R}^n)}^{\|\cdot\|_{1,2,q}},$$

$$\|u\|_{1,2,q} := \left( \frac{1}{\mathcal{T}} \int_0^{\mathcal{T}} \int_{\mathbb{R}^n} |\partial_t u|^q + \sum_{|\alpha| \leq 2} |D_x^\alpha u|^q \, dx dt \right)^{\frac{1}{q}}$$



are homeomorphic via  $\pi$  by density. Similarly,  $L^q(G)$  and

$$L^q_{\text{per}}(\mathbb{R} \times \mathbb{R}^n) := \overline{C^\infty_{\text{c,per}}(\mathbb{R} \times \mathbb{R}^n)}^{\|\cdot\|_q}, \quad \|u\|_q := \left( \frac{1}{\mathcal{T}} \int_0^{\mathcal{T}} \int_{\mathbb{R}^n} |u|^q \, dx dt \right)^{\frac{1}{q}}$$

as well as  $X^q_{\text{p}}(G)$  and

$$X^q_{\text{p,per}}(\mathbb{R} \times \mathbb{R}^n) := \{\mathfrak{p} \in L^1_{\text{loc}}(\mathbb{R} \times \mathbb{R}^n) : \|\mathfrak{p}\|_{X^q_{\text{p}}} < \infty\},$$

$$\|\mathfrak{p}\|_{X^q_{\text{p}}} := \left( \frac{1}{\mathcal{T}} \int_0^{\mathcal{T}} \|\mathfrak{p}(\cdot, t)\|_{\frac{nq}{n-q}}^q + \|\nabla \mathfrak{p}(\cdot, t)\|_q^q \, dt \right)^{1/q}$$

are homeomorphic via  $\pi$ . By construction of the differentiable structure on  $G$ , a pair  $(u, \mathfrak{p})$  is a solution to (2.28) with data  $f$  if and only if  $(u \circ \pi, \mathfrak{p} \circ \pi)$  is a solution to (2.1) with data  $f \circ \pi$ . Consequently, we can reformulate Theorem 2.57 as follows:

**Theorem 2.58** *Let  $X^q_{\text{s}}(\mathbb{R}^n)$  be as in Theorem 2.54. For every  $f \in L^q_{\text{per}}(\mathbb{R} \times \mathbb{R}^n)^n$  there is a unique solution*

$$(u, \mathfrak{p}) = (v \oplus w, \mathfrak{p}) \in \left( X^q_{\text{s}}(\mathbb{R}^n) \oplus W^{1,2,q}_{\text{per},\sigma,\perp}(\mathbb{R} \times \mathbb{R}^n) \right) \times X^q_{\text{p,per}}(\mathbb{R} \times \mathbb{R}^n)$$

to (2.1). Moreover,

$$\|v\|_{X^q_{\text{s}}} + \|w\|_{1,2,q} + \|\mathfrak{p}\|_{X^q_{\text{p}}} \leq C \|f\|_q,$$

where  $C = C(\lambda, \mathcal{T}, n, q) > 0$ .

### 2.5.2 Fundamental Solutions

In order to define a fundamental solution to (2.1), we employ the approach from [15] and [5] and again consider the reformulation (2.28). In the setting of tempered distributions  $\mathcal{S}'(G)$ , we can then define a fundamental solution  $F$  to (2.1) as a tensor-field

$$F := \begin{pmatrix} \Gamma_{11}^{\text{TP}} & \cdots & \Gamma_{1n}^{\text{TP}} \\ \vdots & \ddots & \vdots \\ \Gamma_{n1}^{\text{TP}} & \cdots & \Gamma_{nn}^{\text{TP}} \\ \gamma_1^{\text{TP}} & \cdots & \gamma_n^{\text{TP}} \end{pmatrix} \in \mathcal{S}'(G)^{(n+1) \times n} \tag{2.54}$$

that satisfies<sup>1</sup>

$$\begin{cases} \partial_t \Gamma_{ij}^{\text{TP}} - \Delta \Gamma_{ij}^{\text{TP}} - \lambda \partial_{x_1} \Gamma_{ij}^{\text{TP}} + \partial_i \gamma_j^{\text{TP}} = \delta_{ij} \delta_G, \\ \partial_i \Gamma_{ij}^{\text{TP}} = 0 \end{cases} \tag{2.55}$$

in the sense of  $\mathcal{S}'(G)$ -distributions. Here,  $\delta_{ij}$  and  $\delta_G$  denote the Kronecker delta and delta distribution, respectively. A solution to the time-periodic system (2.1) is then given by

$$\begin{pmatrix} u \\ p \end{pmatrix} := F * f, \tag{2.56}$$

where the component-wise convolution is taken over the group  $G$ .

Similarly to the previous subsection, we split the fundamental solution into a steady-state and a purely periodic part. More precisely, we shall identify a fundamental solution  $F$  to (2.1) as the sum of a fundamental solution to the corresponding steady-state system

$$\begin{cases} -\Delta \Gamma_{ij} - \lambda \partial_{x_1} \Gamma_{ij} + \partial_i \gamma_j = \delta_{ij} \delta_{\mathbb{R}^n}, \\ \partial_i \Gamma_{ij} = 0, \end{cases} \tag{2.57}$$

and a second purely periodic part. Recall that in the Stokes case ( $\lambda = 0$ ) a fundamental solution to (2.57) is given by (see for example [6, IV.2])

$$\Gamma_{ij}^s(x) := \begin{cases} \frac{1}{2\omega_n} \left( \delta_{ij} \log(|x|^{-1}) + \frac{x_i x_j}{|x|^2} \right) & \text{if } n = 2, \\ \frac{1}{2\omega_n} \left( \delta_{ij} \frac{1}{n-2} |x|^{2-n} + \frac{x_i x_j}{|x|^n} \right) & \text{if } n \geq 3. \end{cases} \tag{2.58}$$

In the Oseen case ( $\lambda \neq 0$ ), a fundamental solution to (2.57) is given by (see for example [6, VII.3])

$$\Gamma_{ij}^o(x) := \frac{1}{\lambda} (\delta_{ij} \Delta - \partial_{x_i} \partial_{x_j}) \int_0^{x_1} [\Gamma_L(y_1, x_2, \dots, x_n) - \Psi(y_1, \dots, x_n)] dy_1, \tag{2.59}$$

where

$$\Gamma_L(x) := \begin{cases} -\frac{1}{2\pi} \log|x| & \text{if } n = 2, \\ \frac{1}{(n-2)\omega_n} |x|^{2-n} & \text{if } n > 2, \end{cases}$$

---

<sup>1</sup>We make use of the Einstein summation convention and implicitly sum over all repeated indices.

is the fundamental solution to the Laplace equation  $\Delta \Gamma_L = \delta_{\mathbb{R}^n}$  in  $\mathbb{R}^n$  and

$$\Psi(x) := -\frac{1}{2\pi} \left( \frac{\lambda}{4\pi|x|} \right)^{\frac{n-2}{2}} K_{\frac{n-2}{2}} \left( \frac{\lambda}{2}|x| \right) e^{-\frac{\lambda}{2}|x|}.$$

Here  $K_\nu$ ,  $\nu \in \mathbb{C}$ , denotes the modified Bessel function of the second kind. In both the Stokes and Oseen case the pressure term in the fundamental solution is given by

$$\gamma_i(x) := \frac{1}{\omega_n} \frac{x_i}{|x|^n}. \tag{2.60}$$

In order to identify the second part of F, that is, the purely periodic part, we utilize the Fourier transform  $\mathcal{F}_G$  on the group  $G$ . Similarly to the previous subsection, the fact that  $\mathcal{F}_G: \mathcal{S}'(G) \rightarrow \mathcal{S}'(\widehat{G})$  is a homeomorphism allows us to express the purely periodic part in terms of a Fourier multiplier defined on the dual group  $\widehat{G} = \mathbb{Z} \times \mathbb{R}^n$ . This representation enables us to establish integrability properties and pointwise decay estimates.

**Theorem 2.59** *Let  $n \geq 2$  and  $\lambda \in \mathbb{R}$ . Put*

$$\Gamma := \begin{cases} \Gamma^s & \text{if } \lambda = 0 \quad (\text{Stokes case}), \\ \Gamma^o & \text{if } \lambda \neq 0 \quad (\text{Oseen case}). \end{cases}$$

*Then the elements of  $\mathcal{S}'(G)$  given by*

$$\Gamma^{\text{TP}} := \Gamma \otimes 1_{\mathbb{T}} + \Gamma^\perp, \tag{2.61}$$

$$\gamma^{\text{TP}} := \gamma \otimes \delta_{\mathbb{T}}, \tag{2.62}$$

*with*

$$\Gamma^\perp := \mathcal{F}_G^{-1} \left[ \frac{1 - \delta_{\mathbb{Z}}(k)}{|\xi|^2 + i(\frac{2\pi}{\lambda}k - \lambda\xi_1)} \left( I - \frac{\xi \otimes \xi}{|\xi|^2} \right) \right] \in \mathcal{S}'(G)^{n \times n} \tag{2.63}$$

*define a fundamental solution  $F \in \mathcal{S}'(G)^{(n+1) \times n}$  to (2.55) of the form (2.54) satisfying*

$$\forall q \in \left( 1, \frac{n+2}{n} \right) : \quad \Gamma^\perp \in L^q(G)^{n \times n}, \tag{2.64}$$

$$\forall q \in \left[ 1, \frac{n+2}{n+1} \right) : \quad \partial_j \Gamma^\perp \in L^q(G)^{n \times n} \quad (j = 1, \dots, n), \tag{2.65}$$

$$\forall \alpha \in \mathbb{N}_0^n \quad \forall r \in [1, \infty) \quad \forall \varepsilon > 0 \quad \exists C > 0 \quad \forall |x| \geq \varepsilon : \|D_x^\alpha \Gamma^\perp(\cdot, x)\|_{L^r(\mathbb{T})} \leq \frac{C}{|x|^{n+|\alpha|}}, \quad (2.66)$$

$$\forall q \in (1, \infty) \quad \exists C > 0 \quad \forall f \in \mathcal{S}(G)^n : \|\Gamma^\perp * f\|_{W^{1,2,q}(G)} \leq C \|f\|_{L^q(G)}, \quad (2.67)$$

where  $\delta_{\mathbb{T}} \in \mathcal{S}'(\mathbb{T})$  denotes the delta distribution and  $1_{\mathbb{T}} \in \mathcal{S}'(\mathbb{T})$  the constant 1 distribution.

*Remark 2.60* Consider data  $f \in C_c(G)^n$ . The integrability of  $\Gamma^\perp$  obtained in (2.64) implies, in combination with well-known integrability properties of the steady-state fundamental solutions (2.58) and (2.59), that the solution  $u$  to (2.1) given by the convolution (2.56) can be written in terms of classical integrals as

$$\begin{aligned} u_i(t, x) &= (\Gamma \otimes 1_{\mathbb{T}})_{ij} * f_j(t, x) + \Gamma_{ij}^\perp * f_j(t, x) \\ &= \int_{\mathbb{R}^n} \Gamma_{ij}(x-y) \int_{\mathbb{T}} f_j(s, y) \, ds \, dy + \int_G \Gamma_{ij}^\perp(t-s, x-y) f_j(s, y) \, d(s, y) \\ &=: u_i^s(x) + u_i^p(t, x) \end{aligned}$$

for  $i = 1, \dots, n$ . Observe that  $u^s$  is a solution to a steady-state Stokes ( $\lambda = 0$ ) or Oseen ( $\lambda \neq 0$ ) problem. Consequently, the pointwise asymptotic structure at spatial infinity of  $u^s$  is well known; see for example [6, Theorems V.3.2 and VII.6.2]. From (2.64) and (2.66) it follows that  $u^p(t, x) = O(|x|^{-n})$ , which means that the decay rate of  $u^p(t, x)$  as  $|x| \rightarrow \infty$  is actually *faster* than the decay rate of the leading term in the asymptotic expansion of  $u^s(x)$ . In other words, the leading term in an asymptotic expansion of  $u$  coincides with the (known) leading term in the expansion of  $u^s$ . This direct consequence of Theorem 2.59 is by no means trivial.

*Proof of Theorem 2.59* In the proof of Theorem 2.53 we have already seen that the function

$$M: \widehat{G} \rightarrow \mathbb{C}, \quad M(k, \xi) := \frac{1 - \delta_{\mathbb{Z}}(k)}{|\xi|^2 + i\left(\frac{2\pi}{\mathcal{T}}k - \lambda\xi_1\right)} \quad (2.68)$$

is an element of  $L^\infty(G)$ . Thus (2.63) is a well-defined object in  $\mathcal{S}'(G)^{n \times n}$ . Since it holds  $\mathcal{F}_{\mathbb{R}^n}[\gamma] = -i\frac{\xi}{|\xi|^2}$ , we obtain

$$\mathcal{F}_G[\nabla \gamma^{\text{TP}}] = \mathcal{F}_{\mathbb{R}^n}[\nabla \gamma] \otimes \mathcal{F}_{\mathbb{T}}[\delta_{\mathbb{T}}] = \frac{\xi \otimes \xi}{|\xi|^2} \cdot \mathbf{1}_{\mathbb{Z}}.$$

Because we also have  $(|\xi|^2 - i\lambda\xi_1) \cdot \mathcal{F}_{\mathbb{R}^n}[\Gamma] = \left(I - \frac{\xi \otimes \xi}{|\xi|^2}\right)$ , we further deduce

$$\left(|\xi|^2 + i\left(\frac{2\pi}{\mathcal{T}}k - \lambda\xi_1\right)\right) \cdot \mathcal{F}_G[\Gamma \otimes 1_{\mathbb{T}}] = \left(I - \frac{\xi \otimes \xi}{|\xi|^2}\right) \delta_{\mathbb{Z}}(k),$$

which finally leads us to

$$\left( |\xi|^2 + i\left(\frac{2\pi}{T}k - \lambda\xi_1\right) \right) \cdot \mathcal{F}_G[\Gamma^{\text{TP}}] + \mathcal{F}_G[\nabla\gamma^{\text{TP}}] = I.$$

Applying the inverse Fourier transformation to this equality, we conclude that  $(\Gamma^{\text{TP}}, \gamma^{\text{TP}})$  is, in fact, a fundamental solution to (2.55) since clearly  $\text{div } \Gamma = \text{div } \Gamma^\perp = 0$ .

For the proof of (2.66) we refer to [5]. We proceed with the derivation of (2.64). Equation (2.63) leads to the representation

$$\Gamma_{jl}^\perp = [\delta_{jl}(\mathfrak{R}_n\mathfrak{R}_n) - \mathfrak{R}_j\mathfrak{R}_l] \circ \mathcal{F}_G^{-1} \left[ M_0 \cdot \mathcal{F}_G[\mathcal{F}_G^{-1}(\mathcal{K})] \right],$$

where  $\mathfrak{R}_j, j \in \{1, \dots, n\}$ , denotes the Riesz transformation

$$\mathfrak{R}_j: \mathcal{S}(G) \rightarrow \mathcal{S}'(G), \quad \mathfrak{R}_j(f) := \mathcal{F}_{\mathbb{R}^n}^{-1} \left[ \frac{\xi_j}{|\xi|} \mathcal{F}_{\mathbb{R}^n}(f) \right]$$

and  $M_0$  and  $\mathcal{K}$  are given by

$$M_0: \widehat{G} \rightarrow \mathbb{C}, \quad M_0(k, \xi) := \frac{(1 - \delta_{\mathbb{Z}}(k))|k|^{\frac{2}{n+2}}(1 + |\xi|^2)^{\frac{n}{n+2}}}{|\xi|^2 + i\left(\frac{2\pi}{T}k - \lambda\xi_1\right)}$$

and

$$\mathcal{K}: \widehat{G} \rightarrow \mathbb{C}, \quad \mathcal{K}(k, \xi) := (1 - \delta_{\mathbb{Z}}(k))|k|^{-\frac{2}{n+2}}(1 + |\xi|^2)^{-\frac{n}{n+2}},$$

respectively. It is well known that the Riesz operator  $\mathfrak{R}_j$  extends to a bounded linear operator  $L^q(G) \rightarrow L^q(G)$  for all  $q \in (1, \infty)$ ; see for example [8, Corollary 4.2.8]. In order to obtain that  $M_0$  is an  $L^q(G)$  multiplier, we adapt the method from the proof of Theorem 2.53. We again consider the locally compact abelian group  $H := \mathbb{R} \times \mathbb{R}^n$  with dual group  $\widehat{H} = \mathbb{R} \times \mathbb{R}^n$ , and we introduce a “cut-off” function  $\chi \in C_c^\infty(\mathbb{R}; \mathbb{R})$  as in (2.34) and define

$$m_0: \mathbb{R} \times \mathbb{R}^n \rightarrow \mathbb{C}, \quad m_0(\eta, \xi) := \frac{\chi(\eta)|\eta|^{\frac{2}{n+2}}(1 + |\xi|^2)^{\frac{n}{n+2}}}{|\xi|^2 + i\left(\frac{2\pi}{T}\eta - \lambda\xi_1\right)}.$$

Moreover, we define the natural homomorphism  $\Phi: \widehat{G} \rightarrow \widehat{H}, \Phi(k, \xi) := (k, \xi)$ . Observe that  $m_0$  is a continuous and bounded function since the numerator vanishes in a neighborhood of 0, which is the only zero of the denominator. With the help of Marcinkiewicz’s Multiplier Theorem (see for instance [8, Corollary 5.2.5]), one readily verifies that  $m_0$  is an  $L^q(\widehat{H})$  multiplier for all  $q \in (1, \infty)$ . Additionally, we have  $M_0 = m_0 \circ \Phi$ . Thus an application of the Transference Principle, Theorem 2.15,

implies that  $M_0$  is an  $L^q(G)$  multiplier for all  $q \in (1, \infty)$ . Hence we obtain (2.63) if we can show  $\mathcal{F}_G^{-1}(\mathcal{K}) \in L^r(G)$ . If we identify  $\mathbb{T}$  with the interval  $(-\frac{1}{2}\mathcal{T}, \frac{1}{2}\mathcal{T}]$ , we obtain

$$\mathcal{F}_{\mathbb{T}}^{-1} \left[ (1 - \delta_{\mathbb{Z}}(k)) |k|^{-\frac{2}{n+2}} \right] (t) = c_0 |t|^{-\frac{n}{n+2}} + h(t)$$

for some function  $h \in C^\infty(\mathbb{R}/\mathcal{T}\mathbb{Z})$ ; see for instance [8, Example 3.1.19]. Furthermore, one can derive the estimate

$$\left| \mathcal{F}_{\mathbb{R}^n}^{-1} \left[ (1 + |\xi|^2)^{-\frac{n}{n+2}} \right] (x) \right| \leq c_1 \left( |x|^{-\frac{n}{n+2}} \chi_{B_2}(x) + e^{-\frac{|x|}{2}} \right);$$

see for example [9, Proposition 6.1.5]. Therefore, we conclude

$$\mathcal{F}_G^{-1}(\mathcal{K}) = \mathcal{F}_{\mathbb{T}}^{-1} \left[ (1 - \delta_{\mathbb{Z}}(k)) |k|^{-\frac{2}{n+2}} \right] \otimes \mathcal{F}_{\mathbb{R}^n}^{-1} \left[ (1 + |\xi|^2)^{-\frac{n}{n+2}} \right] \in L^r(G)$$

for all  $r \in (1, \frac{n+2}{n})$ , and we have verified (2.64). In order to show (2.65), we proceed in a similar way. We consider the identity

$$\partial_m \Gamma_{jl}^\perp = [\delta_{jl}(\mathfrak{R}_h \mathfrak{R}_h) - \mathfrak{R}_j \mathfrak{R}_l] \circ \mathcal{F}_G^{-1} \left[ M_m \cdot \mathcal{F}_G[\mathcal{F}_G^{-1}(\mathcal{J})] \right],$$

where

$$M_m: \widehat{G} \rightarrow \mathbb{C}, \quad M_m(k, \xi) := \frac{(1 - \delta_{\mathbb{Z}}(k)) |k|^{\frac{1}{n+2}} (1 + |\xi|^2)^{\frac{n}{2(n+2)}} i \xi_m}{|\xi|^2 + i(\frac{2\pi}{\mathcal{T}}k - \lambda \xi_1)}$$

and

$$\mathcal{J}: \widehat{G} \rightarrow \mathbb{C}, \quad \mathcal{J}(k, \xi) := (1 - \delta_{\mathbb{Z}}(k)) |k|^{-\frac{1}{n+2}} (1 + |\xi|^2)^{-\frac{n}{2(n+2)}}.$$

With the same arguments as above, we conclude  $\partial_m \Gamma^\perp \in L^r(G)$  for all  $r \in (1, \frac{n+2}{n+1})$ . In particular, this yields  $\partial_m \Gamma^\perp \in L^1_{\text{loc}}(G)$ , which finally leads to  $\partial_m \Gamma^\perp \in L^1(G)$  by the asymptotic behavior from (2.66). Consequently, we have also shown (2.65).

The convolution  $\Gamma^\perp * f$  can be expressed in terms of a Fourier multiplier

$$\Gamma^\perp * f = \mathcal{F}_G^{-1} \left[ M(k, \xi) \left( I - \frac{\xi \otimes \xi}{|\xi|^2} \right) \mathcal{F}_G[f] \right],$$

with  $M$  given by (2.68). In the same way as in the proof of Theorem 2.53, one readily verifies that the function  $M \in L^\infty(\widehat{G})$  as well as the functions  $(k, \xi) \mapsto (i\xi)^\alpha M(k, \xi)$  for  $|\alpha| \leq 2$  and  $(k, \xi) \mapsto ik M(k, \xi)$  are  $L^q(G)$  multipliers for all  $q \in (1, \infty)$ . This directly yields (2.67) and finishes the proof.  $\square$

## References

1. N. Bourbaki, *Éléments de mathématique. Fasc. XXXII. Théories spectrales.* Actualités Scientifiques et Industrielles, No. 1332 (Hermann, Paris, 1967)
2. F. Bruhat, Distributions sur un groupe localement compact et applications à l'étude des représentations des groupes  $p$ -adiques. *Bull. Soc. Math. Fr.* **89**, 43–75 (1961)
3. K. de Leeuw, On  $L_p$  multipliers. *Ann. Math. (2)* **81**, 364–379 (1965)
4. R.E. Edwards, G.I. Gaudry, *Littlewood-Paley and Multiplier Theory.* Ergebnisse der Mathematik und ihrer Grenzgebiete, Band 90 (Springer, Berlin, 1977)
5. T. Eiter, M. Kyed, Estimates of time-periodic fundamental solutions to the linearized Navier–Stokes equations. *J. Math. Fluid Mech.* (2017). doi:[10.1007/s00021-017-0332-7](https://doi.org/10.1007/s00021-017-0332-7)
6. G.P. Galdi, *An Introduction to the Mathematical Theory of the Navier–Stokes Equations. Steady-State Problems*, 2nd edn. (Springer, New York, 2011)
7. A.M. Gleason, Groups without small subgroups. *Ann. Math. (2)* **56**, 193–212 (1952)
8. L. Grafakos, *Classical Fourier Analysis*, 2nd edn. (Springer, New York, 2008)
9. L. Grafakos, *Modern Fourier Analysis*, 2nd edn. (Springer, New York, 2009)
10. E. Hewitt, K.A. Ross, *Abstract Harmonic Analysis. Volume II: Structure and Analysis for Compact Groups. Analysis on Locally Compact Abelian Groups.* Grundlehren der mathematischen Wissenschaften, vol. 152 (Springer, Berlin, 1970)
11. E. Hewitt, K.A. Ross, *Abstract Harmonic Analysis. Volume I: Structure of Topological Groups, Integration Theory, Group Representations*, 2nd edn. Grundlehren der Mathematischen Wissenschaften, vol. 115 (Springer, Berlin, 1979)
12. M. Kyed, Time-periodic solutions to the Navier–Stokes equations. Habilitationsschrift, Technische Universität Darmstadt (2012)
13. M. Kyed, Existence and regularity of time-periodic solutions to the three-dimensional Navier–Stokes equations. *Nonlinearity* **27**(12), 2909–2935 (2014)
14. M. Kyed, Maximal regularity of the time-periodic linearized Navier–Stokes system. *J. Math. Fluid Mech.* **16**(3), 523–538 (2014)
15. M. Kyed, A fundamental solution to the time-periodic Stokes equations. *J. Math. Anal. Appl.* **437**(1), 708–719 (2016)
16. R. Larsen, *An Introduction to the Theory of Multipliers.* Die Grundlehren der mathematischen Wissenschaften, Band 175 (Springer, New York, 1971)
17. Y. Maekawa, J. Sauer, Maximal regularity of the time-periodic stokes operator on unbounded and bounded domains. *J. Math. Soc. Jpn.* (2016, to appear)
18. M.S. Osborne, On the Schwartz-Bruhat space and the Paley-Wiener theorem for locally compact abelian groups. *J. Funct. Anal.* **19**, 40–49 (1975)
19. W. Rudin, *Fourier Analysis on Groups.* Interscience Tracts in Pure and Applied Mathematics, vol. 12 (Interscience Publishers (a division of Wiley), New York, 1962)
20. J. Sauer, An extrapolation theorem in non-euclidean geometries and its application to partial differential equations. *J. Elliptic Parabol. Equ.* **1**, 403–418 (2015)
21. J. Sauer, Weighted resolvent estimates for the spatially periodic stokes equations. *Ann. Univ. Ferrara* **61**(2), 333–354 (2015)
22. J. Sauer, Maximal regularity of the spatially periodic stokes operator and application to nematic liquid crystal flows. *Czechoslov. Math. J.* **66**(1), 41–55 (2016)
23. H.H. Schaefer, M.P. Wolff, *Topological Vector Spaces*, 2nd edn. Graduate Texts in Mathematics, vol. 3 (Springer, New York, 1999)
24. E.M. Stein, *Singular Integrals and Differentiability Properties of Functions* (Princeton University Press, Princeton, NJ, 1970)
25. M. Stroppel, *Locally Compact Groups.* EMS Textbooks in Mathematics (European Mathematical Society, Zürich, 2006)

# Chapter 3

## Motion of a Particle Immersed in a Two Dimensional Incompressible Perfect Fluid and Point Vortex Dynamics

F. Sueur

**Abstract** In these notes, we expose some recent works by the author in collaboration with Olivier Glass, Christophe Lacave and Alexandre Munnier, establishing point vortex dynamics as zero-radius limits of motions of a rigid body immersed in a two dimensional incompressible perfect fluid in several inertia regimes.

**Keywords** 2D incompressible perfect fluid • Motion of an immersed rigid body • Point vortex dynamics • Zero-radius limit

**MSC2010:** 35Q31, 35Q35, 35Q70, 76D99, 34E05, 34E15, 70E99

### 3.1 Introduction

The rigid body is assumed to be only accelerated by the force exerted by the fluid pressure on its boundary according to the Newton equations, the fluid velocity and pressure being given by the incompressible Euler equations. The equations at stake then read:

$$\frac{\partial u}{\partial t} + (u \cdot \nabla)u + \nabla \pi = 0 \quad \text{and} \quad \operatorname{div} u = 0, \quad (3.1)$$

$$mh''(t) = \int_{\partial S(t)} \pi n \, ds \quad \text{and} \quad \mathcal{J}r'(t) = \int_{\partial S(t)} (x - h(t))^\perp \cdot \pi n \, ds. \quad (3.2)$$

---

F. Sueur (✉)

Institut de Mathématiques de Bordeaux UMR 5251, Université de Bordeaux, 351, cours de la Libération, F 33 405 Talence, France

e-mail: [franck.sueur@math.u-bordeaux.fr](mailto:franck.sueur@math.u-bordeaux.fr)



Here

- $u = (u_1, u_2)$  and  $\pi$  respectively denote the velocity and pressure fields (the fluid is supposed to be homogeneous, of density 1 in order to simplify the notations),
- $m > 0$  and  $\mathcal{J} > 0$  denote respectively the mass and the momentum of inertia of the body,
- $h'(t)$  is the velocity of the center of mass  $h(t)$  of the body and  $r(t)$  is the angular velocity. The body rigidly moves so that at times  $t$  it occupies a domain  $\mathcal{S}(t)$  which is isometric to its initial position  $\mathcal{S}_0$  which is supposed to be a simply connected smooth compact subset of  $\mathbb{R}^2$ . Indeed, there exists a rotation matrix

$$R(\theta(t)) := \begin{pmatrix} \cos \theta(t) & -\sin \theta(t) \\ \sin \theta(t) & \cos \theta(t) \end{pmatrix} \quad (3.3)$$

such that

$$\mathcal{S}(t) = \{h(t) + R(\theta(t))x, x \in \mathcal{S}_0\}.$$

Furthermore, the angle satisfies  $\theta'(t) = r(t)$ .

- when  $x = (x_1, x_2)$  the notation  $x^\perp$  stands for  $x^\perp = (-x_2, x_1)$ ,
- $n$  denotes the unit normal vector pointing outside the fluid domain, which of course depends on the solid position.

We assume that the boundary of the solid is impermeable so that the fluid cannot penetrate into the solid and we assume that there is no cavitation as well. The natural boundary condition at the fluid-solid interface is therefore

$$u \cdot n = \left( h'(t) + r(t)(x - h(t))^\perp \right) \cdot n \quad \text{for } x \in \partial\mathcal{S}(t). \quad (3.4)$$

Let us emphasize that this condition extends the usual condition  $u \cdot n = 0$  on a fixed boundary and involves only the normal part of the fluid velocity. As usual with perfect fluids no pointwise boundary condition needs to be prescribed for the tangential part of the fluid velocity. However because the domain occupied by the solid is a hole in the fluid domain there is a global condition on the tangential part of the fluid velocity involving the circulation  $\gamma$  defined as

$$\gamma = \int_{\partial\mathcal{S}_0} u \cdot \tau \, ds$$

where  $u$  is the fluid velocity and  $\tau$  the unit counterclockwise tangential vector so that  $n = \tau^\perp$ . Indeed when considering a fluid velocity  $u$  which has a good enough regularity, what we will always do in these notes, the so-called Kelvin's theorem applies and  $\gamma$  is preserved over time. The circulation somehow encodes the amount of vorticity hidden in the particle from the fluid viewpoint. Indeed by Green Theorem the circulation can be recast as the integral over  $\mathcal{S}_0$  of the vorticity

$\text{curl } \bar{u} = \partial_1 \bar{u}_2 - \partial_2 \bar{u}_1$  of any smooth vector field  $\bar{u}$  in  $\mathcal{S}_0$  such that  $\bar{u} \cdot \tau = u \cdot \tau$  on  $\partial \mathcal{S}_0$ . Therefore the limit where the body radius converges to zero corresponds to a singular perturbation problem (in space) for the fluid velocity when this latter has to accommodate with a condition of non-vanishing  $\gamma$  around a shrinking solid. Indeed it is well understood since the works [15] and [22] that for a solid obstacle held fixed in a perfect incompressible fluid, with a nonzero given circulation and with possibly nonzero vorticity in the fluid, in the limit where the obstacle shrinks into a fixed pointwise particle, the Euler equation driving the fluid evolution has to be modified: in the Biot-Savart law providing the fluid velocity generated by the fluid vorticity, a Dirac mass at the fixed position of the pointwise obstacle with an amplitude equal to the circulation has to be added to the fluid vorticity. We will refer to the background fluid velocity in the sequel and we will denote it by  $u_{\text{bd}}$ . The genuine fluid vorticity  $\omega$  (that is without the Dirac mass) is convected by the background fluid velocity  $u_{\text{bd}}$ . In the case of a moving body one may wonder if the divergence of the fluid velocity has to be modified in the zero-radius limit as well in order to accommodate with the non-homogeneous condition (3.4). In the sequel we will consider some cases where the solid radius  $\varepsilon$  shrinks to 0 with  $(h', \varepsilon \theta')$  bounded so that the limit fluid velocity is divergence free including in the region where the solid has disappeared.<sup>1</sup> Still the analysis of the dynamics of immersed rigid particles requires a more precise analysis, in particular because it is driven by the fluid pressure, a quantity which depends in a non linear and non local way on the fluid velocity. Hence to understand the limit dynamics one has to precisely evaluate the pressure field on the boundary of the solid, that is, where the singularity is concentrated.

One main goal of this line of research is prove another derivation of the point vortex dynamics as motions of immersed particles. In particular we will consider, in some appropriate settings, the limit of the dynamics of an immersed rigid body when its size and its mass go to zero and recover the equation of a point vortex. Let us recall that the point vortex system is a classical model which goes back to Helmholtz [12], Kirchhoff [16], Poincaré [26], Routh [27], Kelvin [30], and Lin [20, 21]. In these works it was thought as an idealized fluid model where the vorticity of an ideal incompressible two-dimensional fluid is discrete. Although it does not constitute a solution of the incompressible Euler equations, even in the sense of distributions, point vortices can be viewed as Dirac masses obtained as limits of concentrated smooth vortices which evolve according to the Euler equations. In particular in the case of a single vortex moving in a bounded and simply-connected domain this was proved by Turkington in [31] and an extension to the case of several vortices, including in the case where there is also a part of the vorticity which is

---

<sup>1</sup>Let us observe that since

$$\int_{\partial \mathcal{S}(t)} \left( h'(t) + r(t)(x - h(t))^\perp \right) \cdot n \, ds = 0,$$

see (3.25) below, should the behaviour of the solid velocity with  $\varepsilon$  be worse the resulting singularity would be rather a dipole than a Dirac mass.

absolutely continuous with respect to Lebesgue measure (the so-called wave-vortex system), was given by Marchioro and Pulvirenti, see [23]. Let us also mention that Gallay has recently proven in [3] that the point vortex system can also be obtained as vanishing viscosity limits of concentrated smooth vortices evolving according to the incompressible Navier-Stokes equations. Our main goal is to prove that this classical point vortex motion can also be viewed as the limit of the dynamics of a solid, shrinking into a pointwise massless particle with fixed circulation, in free motion. Indeed, our analysis also covers the case where the mass is kept fixed positive in the limit, one then obtains a second-order ordinary differential equation for the particle's position, that we will refer to as a "massive" point vortex system.

Let us precise more the two kinds of inertia regimes we are going to consider in the small radius limit with the following definitions.

**Definition 3.1 (Massive and Massless Particles)** We define

- a massive particle as the limit of a rigid body when its radius  $\varepsilon$  goes to 0 with its mass  $m^\varepsilon$  and its momentum of inertia  $\mathcal{J}^\varepsilon$  respectively satisfying  $m^\varepsilon = m$  and  $\mathcal{J}^\varepsilon = \varepsilon^2 \mathcal{J}$ ,
- a massless particle as the limit of a rigid body when its radius  $\varepsilon$  goes to 0 with its mass  $m^\varepsilon$  and its momentum of inertia  $\mathcal{J}^\varepsilon$  respectively satisfying  $m^\varepsilon = \varepsilon^\alpha m$  and  $\mathcal{J}^\varepsilon = \varepsilon^{\alpha+2} \mathcal{J}$ ,

where  $\alpha > 0$ ,  $m > 0$  and  $\mathcal{J} > 0$  are fixed independent of  $\varepsilon$ .

Five remarks are in order:

- it is understood that we consider a self-similar shrinking of the rigid body into its center of mass. Choosing the origin 0 of the frame as the center of mass of  $\mathcal{S}_0$  it means that we will as initial domain, for every  $\varepsilon \in (0, 1]$ ,

$$\mathcal{S}_0^\varepsilon := \varepsilon \mathcal{S}_0, \quad (3.5)$$

- one observes, of course, that the case of a massive particle corresponds to the limit case  $\alpha = 0$ ,
- the scaling of momentum of inertia  $\mathcal{J}^\varepsilon$  may look surprising at first sight, but it is quite natural since it corresponds to a second order moment whereas the mass is a zeroth order moment of the body's density,
- it is understood that the circulation  $\gamma^\varepsilon$  around the body satisfies  $\gamma^\varepsilon = \gamma$ , where  $\gamma$  is fixed. The amount of circulation is therefore supposed to be independent of the size of the body in our problem. Moreover we assume that  $\gamma \neq 0$  in the case of a massless particle.
- the case where  $\mathcal{S}_0$  is a homogeneous disk is the most simple whereas the case where  $\mathcal{S}_0$  is a non-homogeneous disk involves some adapted tools in particular in order to deal with the case where  $\alpha \geq 2$ . We refer to [11] for a detailed treatment of these cases and we will consider only here the case where  $\mathcal{S}_0$  is not a disk.

Let us have a deeper look at Newton's equations (3.2) and anticipate that in the case of a massless particle the prefactor  $m$  and  $\mathcal{J}$  in front of the second-order

time derivative converge to zero in the zero radius limit so that one faces a singular perturbation problem in time of a non linear dynamics. We will make use of geodesic and gyroscopic features of the system in order to overcome this difficulty. Let us mention from now on that the use of the geodesic structure is more subtle than one may expect at first glance. Indeed the full system “fluid + rigid body” is conservative and enjoys a geodesic structure as a whole in the sense that if on a time interval  $(0, T)$  the initial and final configurations are prescribed, then the PDE’s system “fluid + rigid body” is satisfied on  $(0, T)$  if and only if the couple of flow maps associated with the fluid and solid velocities is a critical point of the action obtained by time integration of the total kinetic energy, cf. [4]. This gives some credit to the belief that the energy conservation drives the dynamics of the system, still some important transfers of energy from one phase to another may occur and this leads to a lack of bound of the solid velocity in the case of a light body. Since the fluid velocity corresponding to a point vortex is not square integrable a renormalization of the energy is necessary in the zero radius limit. Indeed one main feature of the point vortex equation is that the self-induced velocity of the vortex is discarded, or more precisely the self-induced velocity as if the point vortex was alone in the plane. Let us therefore introduce  $K_{\mathbb{R}^2}[\cdot]$  the Biot-Savart law in the full plane that is the operator which maps any reasonable scalar function  $\omega$  to the unique vector field  $\widehat{K}_{\mathbb{R}^2}[\omega]$  vanishing at infinity and satisfying  $\operatorname{div} K_{\mathbb{R}^2}[\omega] = 0$  and  $\operatorname{curl} K_{\mathbb{R}^2}[\omega] = \omega$  in  $\mathbb{R}^2$ , which is given by the convolution formula

$$K_{\mathbb{R}^2}[\omega] := \frac{1}{2\pi} \int_{\mathbb{R}^2} \frac{(x-y)^\perp}{|x-y|^2} \omega(t,y) dy. \tag{3.6}$$

We believe that the following statement is true in a very general setting.

*Conjecture (C)* A massive particle immersed in a two dimensional incompressible perfect fluid moves according to Newton’s law with a gyroscopic force orthogonally proportional to its relative velocity and proportional to the circulation around the body. A massless particle immersed in a two dimensional incompressible perfect fluid with non-vanishing circulation moves as a point vortex, its vortex strength being given by the circulation. More precisely, the position  $h(t)$  of a massive (respectively massless) particle satisfies the equation

$$mh'' = \gamma(h' - u_d(h))^\perp \quad (\text{resp. } h' = u_d(h)), \tag{3.7}$$

with  $u_d(h) = (u_{\text{bd}} - K_{\mathbb{R}^2}[\gamma\delta_h])(h)$  where  $u_{\text{bd}}$  denotes the background fluid velocity hinted above. On the other hand the genuine fluid vorticity  $\omega$  is convected by the background fluid velocity  $u_{\text{bd}}$ .

---

<sup>2</sup>The index “d” of  $u_d$  can be either interpreted as drift or desingularized as it is obtained from  $u_{\text{bd}}$  by removing its orthoradial singular part in  $h$ .

Let us mention that in [2, Chap. 3] Friedrichs already evoked a similar conjecture with a massive point vortex system in the case of two point vortices in the whole plane under the terminology of *bound vortices* (as opposed to *free vortices*). The gyroscopic force appearing in the right hand side of the first equation in (3.7) is a generalisation of the Kutta-Joukowski lift force which attracted a huge interest at the beginning of the twentieth century during the first mathematical investigations in aeronautics, and which will be recalled in Sect. 3.2.

Observe that the conjecture above does not mention any sensitivity to the body's shape. Indeed it is expected that a more accurate description of the asymptotic behaviour thanks to a multi-scale asymptotic expansion of the body's dynamics in the limit  $\varepsilon \rightarrow 0$  will reveal an influence of the body's shape on some corrector terms which appears as subprincipal in the limit  $\varepsilon \rightarrow 0$  for coarse topologies.

Indeed this conjecture has already been proved in a few cases and this is precisely the goal of these notes to give an account of these results.

- **In Sect. 3.2**, we will start with a review of the case, well-known since more than one century, of the motion of one single rigid body immersed in an irrotational fluid filling the rest of the plane. In this setting the equations at stake are the incompressible Euler equations (3.13) on the fluid domain  $\mathcal{F}(t) := \mathbb{R}^2 \setminus \mathcal{S}(t)$ , the Newton equations (3.14), the interface condition (3.4) and the following condition of decay at infinity:  $\lim_{|x| \rightarrow \infty} |u(t, x)| = 0$ . Regarding the initial conditions we observe that there is no loss of generality in assuming that the center of mass (respectively rotation angle) of the solid coincides at the initial time with the origin  $(0, 0)$  (resp.  $0$ ) and we therefore prescribe some initial position and velocity of the solid of the form  $(h, h', \theta, \theta')(0) = (0, \ell_0, 0, r_0)$ . On the other hand we prescribe the initial value of the velocity  $u|_{t=0} = u_0$  in the initial domain  $\mathcal{F}_0 = \mathcal{F}(0) = \mathbb{R}^2 \setminus \mathcal{S}_0$  occupied by the fluid. Of course since we aim at considering smooth solutions we assume that the fluid and solid initial data are compatible. We may therefore consider that the solid translation and rotation velocities  $\ell_0$  and  $r_0$  are arbitrarily given and that the fluid velocity  $u_0$  is the unique vector field compatible in the sense of the following definition.

**Definition 3.2 (Compatible Initial Fluid Velocity)** Given the initial domain  $\mathcal{S}_0$  occupied by the body,  $\ell_0$  and  $r_0$  respectively in  $\mathbb{R}^2$  and  $\mathbb{R}$ , and  $\gamma$  in  $\mathbb{R}$ , we say that a vector field  $u_0$  on the closure of  $\mathcal{F}_0 = \mathbb{R}^2 \setminus \mathcal{S}_0$  with values in  $\mathbb{R}^2$  is compatible if it is the unique vector field satisfying the following div/curl type system:

$$\begin{aligned} \operatorname{div} u_0 &= 0 \text{ and } \operatorname{curl} u_0 = 0 \text{ in } \mathcal{F}_0, \\ u_0 \cdot n &= (\ell_0 + r_0 x^\perp) \cdot n \text{ for } x \in \partial \mathcal{S}_0, \quad \int_{\partial \mathcal{S}_0} u_0 \cdot \tau \, ds = \gamma, \\ \lim_{x \rightarrow \infty} u_0 &= 0. \end{aligned}$$

Indeed the vanishing vorticity condition propagates from  $t = 0$  according to Helmholtz's third theorem so that at any time  $t > 0$  the fluid velocity  $u(t, \cdot)$  can indeed be recovered from the solid's dynamics by an elliptic-type problem similar to the one given above for the initial data. Since time appears only as a parameter rather than in the differential operators, the fluid state may be seen as only solving an auxiliary steady problem rather than an evolution equation. The Newton equations can therefore be rephrased as a second-order differential equation whose coefficients are determined by the auxiliary fluid problem. In particular the prefactor of the translation and angular accelerations is the sum of the inertia of the solid and of the so-called "added inertia" which is a symmetric positive-semidefinite matrix depending only on the body's shape and which encodes the amount of incompressible fluid that the rigid body has also to accelerate around itself. Remarkably enough in the case where the circulation is 0 it turns out that the solid equations can be recast as a geodesic equation associated with the metric given by the total inertia. Unlike the geodesic structure of the full system "fluid + rigid body" hinted above, the configuration manifold only encodes here the solid's dynamics and is therefore of finite dimensions. This echoes that the equations of motion of point vortices embedded in incompressible flow are usually thought as a reduction of an infinite-dimensional dynamical system, namely the incompressible Euler equation, to a finite-dimensional system. Another celebrated feature of the body's dynamics is due to a gyroscopic force, proportional to the circulation around the body, known as the Kutta-Joukowski lift force. In order to make these features appear, cf. Theorem 3.12, and to make as explicit as possible the quantities genuinely involved in this ODE two approaches were followed in the literature: the first one dates back to Blasius, Kutta, Joukowski, Chaplygin and Sedov, cf. for instance [28], and relies on complex analysis whereas the second one is real-analytic and was initiated by Lamb, cf. [19]. We will report here these two methods.<sup>3</sup> A trivial consequence of this reformulation is that a global-in-

---

<sup>3</sup>On the one hand the presentation of the complex-analytic method is extracted from the use we made of it in our first investigations of the rotational case, cf. Sect. 3.4 which reports the results of [8, 9]. On the other hand the presentation of the real-analytic method is extracted from the use we made of it in our investigation of the case where fluid-solid system occupies a bounded domain, cf. Sect. 3.3 which reports the results of [11]. Arguably the length comparison and the temporary occurrence of Archimedes' type quantities (like the volume of the body, its geometric center..) in some intermediate computations leading to Lemma 3.23 (where they cancel out) emphasize the superiority of Lamb's method for our purposes. Indeed in our forthcoming paper [10] Lamb's approach is extended to tackle the general case where several bodies move in a bounded rotational perfect flow when some of the rigid bodies shrink to pointwise particles, some of them with constant mass, the others with vanishing mass. Still the complex-analytic method is known to be useful to deal with the case of a body whose boundary has singularities thanks to conformal mapping. It could be that it appears relevant as well to investigate the motion of a rigid curve resulting from an anisotropic shrinking. In this direction let us mention the paper [17] which deals with the influence of a fixed curve on the fluid around.

time smooth solution to the Cauchy problem exists and is unique. Therefore in Sect. 3.2 (cf. below Proposition 3.14) we will prove the following classical result.

**Theorem 3.3** *Given the initial domain  $S_0$  occupied by the body, the initial solid translation and rotation velocities  $(\ell_0, r_0)$  in  $\mathbb{R}^2 \times \mathbb{R}$ , the circulation  $\gamma$  in  $\mathbb{R}$ , and  $u_0$  the associated compatible initial fluid velocity (according to Definition 3.2), there exists a unique smooth global-in-time solution to the problem compound of the incompressible Euler equations (3.1) on the fluid domain, of the Newton equations (3.2), of the interface condition (3.4), of the condition at infinity:  $\lim_{|x| \rightarrow \infty} |u(t, x)| = 0$ , and of the initial conditions  $(h, h', \theta, \theta')(0) = (0, \ell_0, 0, r_0)$  and  $u|_{t=0} = u_0$ .*

Moreover the structure of the reduced ODE hinted above allows to investigate the zero-radius limit quite easily and to obtain the following result.

**Theorem 3.4** *Let be given a rescaled initial domain  $S_0$  occupied by the body, some initial solid translation and rotation velocities  $(\ell_0, r_0)$  in  $\mathbb{R}^2 \times \mathbb{R}$  and a circulation  $\gamma$  in  $\mathbb{R}$  in the case of a massive particle and in  $\mathbb{R}^*$  in the case of a massless particle, all of them independent of  $\varepsilon$ . Let, for each  $\varepsilon > 0$ ,  $u_0^\varepsilon$  the associated compatible initial fluid velocity associated (according to Definition 3.2) with the initial solid domain  $S_0^\varepsilon$  defined by (3.5),  $(\ell_0, r_0)$  and  $\gamma$ ; and consider the corresponding solution given by Theorem 3.3. Then in the zero radius limit  $\varepsilon \rightarrow 0$ , with the inertia scaling described in Definition 3.1, one respectively obtains for the position  $h(t)$  of the pointwise limit particle the equations  $mh'' = \gamma(h')^\perp$  in the massive limit and  $h' = 0$  in the massless limit.*

Therefore, in this historical setting, Conjecture (C) is validated with  $u_d = 0$ . Of course Theorem 3.4 is a quite informal statement put here for sake of exposition, we will provide a rigorous statement in Sect. 3.2, cf. Theorem 3.26.

- **In Sect. 3.3**, we consider the case where the fluid-solid system occupies a bounded domain  $\Omega$ , still in the irrotational case. We assume that  $\Omega$  is a bounded open regular connected and simply connected domain  $\Omega$  of  $\mathbb{R}^2$  and that the center of mass of the solid coincides at the initial time with the origin 0 which is assumed to be in  $\Omega$ .

Again the fluid velocity can be recovered from the solid's dynamics by an elliptic-type problem for which time is only a parameter and the Newton equations can therefore be rephrased as a second-order differential equation with geodesic and gyroscopic features involving some coefficients determined by this auxiliary fluid problem.

Still some extra difficulties show up in this process. In particular the way the fluid domain depends on the body motion is more intricate and so are the variations of the added inertia and therefore of the metric given by the total inertia. Indeed even in the case where the circulation  $\gamma$  is zero the reformulation of the system as an geodesic equation was proven only recently in [24]. The general case, with nonzero  $\gamma$  is obtained in [8]. One another main new feature with respect to the unbounded case is that the Kutta-Joukowski lift force is superseded by a more sophisticated force term which has the form of the Lorentz force in electromagnetism. Indeed the magnetic part of the Lorentz force,

being gyroscopic and proportional to the circulation around the body, is a quite natural extension of the Kutta-Joukowski lift force of the unbounded case. Still it depends on the body position in a more subtle way. On the other hand the electric-type force which may seem very damaging in order to obtain uniform estimates in the zero-radius limit as it does not disappear in an energy estimate.

At least for fixed radius we will be able to infer straightforwardly from this reformulation the local-in-time existence and uniqueness of smooth solution to the Cauchy problem. Unlike the unbounded case of Sect. 3.2, cf. Theorem 3.3, the result is only local-in-time since collision of the body with the external may occur in finite time (at least as far as it concerns smooth solutions), see [13, 14] for some examples of collisions of a disk moving in a potential flow (that is in the case where the circulation  $\gamma$  satisfies  $\gamma = 0$ ) with the fixed external boundary of the fluid domain. Indeed an energy argument, cf. Corollary 3.36, proves that the life-time of such a smooth solution can only be limited by a collision. In order to obtain smooth solutions, even for small time, it is necessary to consider some compatible initial data. We therefore adapt the notion of compatible initial fluid velocity introduced in Definition 3.2 to the bounded case.

**Definition 3.5 (Compatible Initial Fluid Velocity)** Given the open regular connected and simply connected bounded cavity  $\Omega$  and the initial closed regular domain  $\mathcal{S}_0 \subset \Omega$  occupied by the body,  $\ell_0$  and  $r_0$  respectively in  $\mathbb{R}^2$  and  $\mathbb{R}$ , and  $\gamma$  in  $\mathbb{R}$ , we say that a vector field  $u_0$  on the closure of  $\mathcal{F}_0 = \Omega \setminus \mathcal{S}_0$  with values in  $\mathbb{R}^2$  is compatible if it is the unique vector field satisfying the following div/curl type system:

$$\begin{aligned} \operatorname{div} u_0 &= 0 \text{ and } \operatorname{curl} u_0 = 0 \text{ in } \mathcal{F}_0, \\ u_0 \cdot n &= (\ell_0 + r_0 x^\perp) \cdot n \text{ for } x \in \partial \mathcal{S}_0, \quad \int_{\partial \mathcal{S}_0} u_0 \cdot \tau \, ds = \gamma, \\ u_0 \cdot n &= 0 \text{ for } x \in \partial \Omega. \end{aligned}$$

Therefore in Sect. 3.3 we will prove the following.

**Theorem 3.6** *Given the open regular connected and simply connected bounded cavity  $\Omega$ , the initial closed domain  $\mathcal{S}_0 \subset \Omega$  occupied by the body, the initial solid translation and rotation velocities  $(\ell_0, r_0)$  in  $\mathbb{R}^2 \times \mathbb{R}$ , the circulation  $\gamma$  in  $\mathbb{R}$ , and  $u_0$  the associated compatible initial fluid velocity (according to Definition 3.5), there exists a unique smooth local-in-time solution to the problem compound of the incompressible Euler equations (3.1) on the fluid domain, of the Newton equations (3.2), of the interface condition (3.4), of the impermeability condition  $u \cdot n = 0$  on  $\partial \Omega$ , and the initial conditions  $(h, h', \theta, \theta')(0) = (0, \ell_0, 0, r_0)$  and  $u|_{t=0} = u_0$ . Moreover the life-time of such a smooth solution can only be limited by a collision.*



This result by itself belongs to the mathematical folklore.<sup>4</sup> Here it will be easily deduced from the normal form hinted above in order to introduce the solutions which will be tackled in the zero radius limit and because this normal form is precisely the first step of our strategy in order to tackle the singular features of the body’s dynamics in the zero radius limit.

Then we expand the coefficients of the previous normal form in the zero-radius limit and repeatedly use Lamb’s lemma to reformulate under an asymptotic normal form closer to the one of the unbounded case where the leading terms of the electric-type force are absorbed in the other terms by a modulation of the unknown. Indeed we will consider in particular as new unknown a quantity obtained by subtracting a drift velocity given by the leading terms of the electric-type potential from the translation velocity. This will allow to extend to this case the vanishingly small limit, still in both cases of a limit pointwise particle which is massive or massless. Indeed we will obtain both the massive point vortex system and the classical point vortex system in a cavity as limit equations for respectively a massive and a massless particle, that is from the dynamics of a shrinking solid in the inertia regime mentioned above.

Let us recall that the Kirchhoff-Routh velocity  $u_\Omega$  is defined as  $u_\Omega := \nabla^\perp \psi_\Omega$ , where  $\nabla^\perp := (-\partial_2, \partial_1)$  and where the Kirchhoff-Routh stream function  $\psi_\Omega$  is defined as  $\psi_\Omega(x) := \frac{1}{2} \psi^0(x, x)$ , where  $\psi^0(h, \cdot)$  is the solution to the Dirichlet problem:  $\Delta \psi^0(h, \cdot) = 0$  in  $\Omega$ ,  $\psi^0(h, \cdot) = -\frac{1}{2\pi} \ln |\cdot - h|$  on  $\partial\Omega$ . Let us now introduce the limit equation for the case of a massive particle.

$$mh'' = \gamma(h' - \gamma u_\Omega(h))^\perp \text{ on } [0, T], \text{ with } (h, h')(0) = (0, \ell_0). \tag{3.8}$$

The existence of the maximal solution  $(h, T)$  follows from classical ODE theory. Moreover it follows from the conservation of the energy  $\frac{1}{2}mh' \cdot h' - \gamma^2 \psi_\Omega(h)$  for any  $h \in C^\infty([0, T]; \Omega)$  satisfying (3.8), and from the continuity of the Kirchhoff-Routh stream function  $\psi_\Omega$  in  $\Omega$  that  $T$  is the time of the first collision of  $h$  with the outer boundary  $\partial\Omega$  of the fluid domain. If there is no collision, then  $T = +\infty$ .

Let us also recall the point vortex equation:

$$h' = \gamma u_\Omega(h) \text{ for } t > 0, \text{ with } h(0) = 0. \tag{3.9}$$

It is well-known that the solution  $h$  is global in time, and in particular that there is no collision of the vortex point with the external boundary  $\partial\Omega$ . This follows from the conservation of the energy  $\gamma^2 \psi_\Omega(h)$  for any  $h \in C^\infty([0, T]; \Omega)$  satisfying (3.9), and the fact that  $\psi_\Omega(h) \rightarrow +\infty$  when  $h$  comes close to  $\partial\Omega$ .

Next result states the convergence of  $h^\varepsilon$  to the solutions to these Eqs. (3.8) and (3.9).

---

<sup>4</sup>Indeed a stronger result has been obtained in [7], where the rotational case (with curl  $u_0$  in  $L^\infty$ ) is handled with pure PDE’s methods.

**Theorem 3.7** *Let  $\mathcal{S}_0 \subset \Omega$ ,  $(\ell_0, r_0) \in \mathbb{R}^2 \times \mathbb{R}$ , and  $(m, \mathcal{J}) \in (0, +\infty) \times (0, +\infty)$ . Let, in the case of a massive (respectively massless) particle,  $\gamma$  in  $\mathbb{R}$  (resp. in  $\mathbb{R}^*$ ). Let  $(h, T)$  be the maximal solution to (3.8) (resp.  $h$  be the global solution to (3.9)). For every  $\varepsilon \in (0, 1]$  small enough to ensure that the set  $\mathcal{S}_0^\varepsilon$  defined by (3.5) satisfies  $\mathcal{S}_0^\varepsilon \subset \Omega$ , we consider  $u_0^\varepsilon$  the associated compatible initial fluid velocity associated (according to Definition 3.5) with the initial solid domain  $\mathcal{S}_0^\varepsilon$  defined by (3.5),  $\Omega$ ,  $(\ell_0, r_0)$  and  $\gamma$ , and we denote  $T^\varepsilon$  the life-time of the associated smooth solution  $(h^\varepsilon, \theta^\varepsilon, u^\varepsilon)$  given by Theorem 3.6, with the inertia scaling described in Definition 3.1 and the initial conditions  $(h^\varepsilon, (h^\varepsilon)', \theta^\varepsilon, (\theta^\varepsilon)')(0) = (0, \ell_0, 0, r_0)$  and  $u^\varepsilon|_{t=0} = u_0^\varepsilon$ . Then in the zero radius limit  $\varepsilon \rightarrow 0$ , there holds  $\liminf T^\varepsilon \geq T$  (resp.  $\liminf T^\varepsilon \rightarrow +\infty$ ) and  $h^\varepsilon \rightharpoonup h$  in  $W^{2,\infty}([0, T]; \mathbb{R}^2)$  weak- $\star$  (resp.  $W^{1,\infty}([0, T]; \mathbb{R}^2)$  weak- $\star$ ).*

Therefore, in this setting, Conjecture (C) is also true with  $u_d = \gamma u_\Omega$  (and a easy byproduct of the analysis is that  $u_{bd} = K_\Omega[\gamma \delta_h]$  where  $K_\Omega$  denotes the Biot-Savart law associated with the simply connected domain  $\Omega$ ). Theorem 3.7 will be proven as a consequence of Theorems 3.32 and 3.37. This result was obtained in [11].

- **In Sect. 3.4**, we will consider the motion of a rigid body immersed in a two dimensional incompressible perfect fluid with vorticity. In order to focus on the interaction between the rigid body and the fluid vorticity we go back to the unbounded setting of Sect. 3.2 so that the fluid-solid system occupies again the whole plane. We first recall a result obtained in [8] establishing a global in time existence and uniqueness result similar to the celebrated result [32] by Yudovich about the case of a fluid alone. Yudovich’s theory relies on the transport of the fluid vorticity in particular to the preservation of  $L^\infty$ -in space bound of the vorticity when time proceeds and we therefore extend Definition 3.2 to this setting.

**Definition 3.8 (Compatible Initial Fluid Velocity)** Given the initial domain  $\mathcal{S}_0$  occupied by the body, the initial solid velocities  $\ell_0$  and  $r_0$  respectively in  $\mathbb{R}^2$  and  $\mathbb{R}$ , an initial fluid vorticity  $\omega_0$  in  $L_c^\infty(\mathbb{R}^2 \setminus \{0\})$  and  $\gamma$  in  $\mathbb{R}$ , we say that a vector field  $u_0$  on the closure of  $\mathcal{F}_0 = \mathbb{R}^2 \setminus \mathcal{S}_0$  with values in  $\mathbb{R}^2$  is compatible if it is the unique vector field in  $C^0(\overline{\mathcal{F}_0}; \mathbb{R}^2)$  satisfying the following div/curl type system:

$$\begin{aligned} \operatorname{div} u_0 &= 0 \text{ and } \operatorname{curl} u_0 = \omega_0 \text{ in } \mathcal{F}_0, \\ u_0 \cdot n &= (\ell_0 + r_0 x^\perp) \cdot n \text{ for } x \in \partial \mathcal{S}_0, \quad \int_{\partial \mathcal{S}_0} u_0 \cdot \tau \, ds = \gamma, \\ \lim_{x \rightarrow \infty} u_0 &= 0. \end{aligned}$$

We are now ready to state the existence and uniqueness result with bounded vorticity.

**Theorem 3.9** *For any  $(\ell_0, r_0) \in \mathbb{R}^2 \times \mathbb{R}$ ,  $\omega_0 \in L_c^\infty(\overline{\mathcal{F}_0})$ , there exists a unique solution to the problem compound of the incompressible Euler equations (3.1) on*

the fluid domain, of the Newton equations (3.2), of the interface condition (3.4), of the condition at infinity:  $\lim_{|x| \rightarrow \infty} |u(t, x)| = 0$ , and of the initial conditions  $(h, h', \theta, \theta')(0) = (0, \ell_0, 0, r_0)$  and  $u|_{t=0} = u_0$ , with  $u_0$  the compatible initial velocity associated with  $\ell_0, r_0$  and  $\omega_0$  by Definition 3.8. Moreover  $(h, \theta) \in C^2(\mathbb{R}^+; \mathbb{R}^2 \times \mathbb{R})$  and for all  $t > 0$ ,  $\omega(t) := \text{curl } u(t) \in L_c^\infty(\overline{\mathcal{F}(t)})$ .

A key of Yudovich’s approach is that a  $L^\infty$ -in space bound of the vorticity is enough to control the log-Lipschitz regularity of the fluid velocity.<sup>5</sup> We will see in Sect. 3.4 that this is still true for the case with an immersed body. Moreover this amount of regularity is sufficient in order to insure convenient a priori bounds regarding the solid motion. We refer to [5, 6, 29] for some other results regarding the existence of solutions with less regularity. Indeed we will slightly modify the proof of Theorem 3.9 given in [8] regarding the a priori estimates of the rigid body’s acceleration. We will use here an argument from [6, 29] which requires pretty much only a  $L^2$  type a priori estimate of the fluid velocity.

This setting will allow to investigate the zero radius limit. In [8] and [9] we have obtained respectively the following results corresponding to the massive and massless cases.

**Theorem 3.10** *Let be given a circulation  $\gamma$  in  $\mathbb{R}$  in the case of a massive particle and in  $\mathbb{R}^*$  in the case of a massless particle,  $(\ell_0, r_0) \in \mathbb{R}^3$ ,  $\omega_0$  in  $L_c^\infty(\mathbb{R}^2 \setminus \{0\})$  and consider as initial fluid velocity  $u_0^\varepsilon$  is then defined as the unique vector field  $u_0^\varepsilon$  compatible with  $S_0^\varepsilon, \ell_0, r_0, \gamma$  and  $\omega_0^\varepsilon := \omega_0|_{\mathcal{F}_0^\varepsilon}$ . For any  $\varepsilon \in (0, 1]$ , let us denote  $(h^\varepsilon, r^\varepsilon, u^\varepsilon)$  the corresponding solution of the system. Then in the zero radius limit  $\varepsilon \rightarrow 0$ , with the inertia scaling described in Definition 3.1, one respectively obtains the following equation for the position  $h(t)$  of the pointwise limit particle:*

$$mh''(t) = \gamma \left( h'(t) - K_{\mathbb{R}^2}[\omega(t, \cdot)](h(t)) \right)^\perp, \tag{3.10}$$

in the massive limit and

$$h'(t) = K_{\mathbb{R}^2}[\omega(t, \cdot)](h(t)), \tag{3.11}$$

in the massless limit. Regarding the fluid state, one obtain at the limit the following transport equation for the fluid vorticity:

$$\frac{\partial \omega}{\partial t} + \text{div}(\omega K_{\mathbb{R}^2}[\omega + \gamma \delta_h]) = 0. \tag{3.12}$$

Therefore, in the bounded setting, Conjecture (C) is also true with  $u_d = K_{\mathbb{R}^2}[\omega]$  and  $u_{bd} = K_{\mathbb{R}^2}[\omega + \gamma \delta_h]$ .

---

<sup>5</sup>Indeed the uniqueness part of the result above has to be understood to hold in the class of solutions with such a regularity.

The fluid equation (3.12) is the same whether the body shrinks to a massive or a massless pointwise particle. Equation (3.12) describes the evolution of the vorticity of the fluid: it is transported by a velocity obtained by the usual Biot-Savart law in the plane, but from a vorticity which is the sum of the fluid vorticity and of a point vortex placed at the (time-dependent) position  $h(t)$  where the solid shrinks, with a strength equal to the circulation  $\gamma$  around the body. Equation (3.12) and its corresponding initial condition hold in the sense that for any test function  $\psi \in C_c^\infty([0, T) \times \mathbb{R}^2)$  we have

$$\int_0^\infty \int_{\mathbb{R}^2} \psi_t \omega \, dx \, dt + \int_0^\infty \int_{\mathbb{R}^2} \nabla_x \psi \cdot K_{\mathbb{R}^2}[\omega + \gamma \delta_h] \omega \, dx \, dt + \int_{\mathbb{R}^2} \psi(0, x) \omega_0(x) \, dx = 0.$$

The uniqueness of the solution to the massive limit system (3.10)–(3.12) is an interesting question. Observe that a putative uniqueness result would entail the convergence of the whole sequence. This is the case for the massless limit system (3.11)–(3.12) for which uniqueness does hold according to a result due to Marchioro and Pulvirenti, cf. [23] and revisited by Lacave and Miot, cf. [18].

We will take advantage of the approach developed in [10] and exposed in Sect. 3.3 to provide a sketch of a more simple proof of the results claimed in Theorem 3.10 than the ones achieved in [8] for the massive case and most of all in [9] for the massless case. In order to do so we will start with an exact reformulation of the body's dynamics for fixed radius into an ODE with a geodesic feature, a Lorentz type force of the same form than the one mentioned above in the irrotational case, but with an extra dependence to the fluid vorticity, and a new term describing a somehow more direct influence of the vorticity but which does not enjoy much structure, cf. Theorem 3.49. Then we expand the coefficients of the previous ODE in the zero-radius limit using in particular an irrotational approximation of the fluid velocity on the body's boundary in order to use Lamb's lemma. This provides in particular the leading terms in the expansion of the Lorentz type force with less effort than by the complex-analytic method used in [8] and [9]. Another simplification comes from the extra term encoding a direct influence of the vorticity to the body's dynamics which is more simple to estimate than its counterpart in [9].<sup>6</sup> We thus obtain an asymptotic normal form once again close to the one of Sect. 3.2 where the leading terms of the electric-type force are absorbed in the other terms by a modulation of the solid translation velocity by a drift velocity of the particle under the influence of the fluid vorticity. This will allow to extend to this case the vanishingly small limit, still in both cases of a limit pointwise particle which is massive or massless. Indeed Theorem 3.10 will be proven in Sect. 3.3.6 as a consequence of Theorem 3.50.

---

<sup>6</sup>In particular it avoids again the temporary occurrence of Archimedes' type quantities.

We aim at extending this analysis to the case where both interactions of a body with an external boundary and with the fluid vorticity are considered in the same time, for several massive and massless particles, which will provide a positive answer to Conjecture (C) in a wide setting, cf. the ongoing work [10].

## 3.2 Case of an Unbounded Irrotational Flow

In this section we assume that the system “fluid + solid” is unbounded so that the domain occupied by the fluid at time  $t$  is  $\mathcal{F}(t) := \mathbb{R}^2 \setminus \mathcal{S}(t)$  starting from the initial domain  $\mathcal{F}_0 := \mathbb{R}^2 \setminus \mathcal{S}_0$ . The equations at stake then read :

$$\frac{\partial u}{\partial t} + (u \cdot \nabla)u + \nabla \pi = 0 \quad \text{and} \quad \operatorname{div} u = 0 \quad \text{for } x \in \mathcal{F}(t), \quad (3.13)$$

$$mh''(t) = \int_{\partial \mathcal{S}(t)} \pi n \, ds \quad \text{and} \quad \mathcal{J}\theta''(t) = \int_{\partial \mathcal{S}(t)} (x - h(t))^\perp \cdot \pi n \, ds, \quad (3.14)$$

$$u \cdot n = \left( h'(t) + r(t)(x - h(t))^\perp \right) \cdot n \quad \text{for } x \in \partial \mathcal{S}(t), \quad (3.15)$$

$$\lim_{|x| \rightarrow \infty} |u(t, x)| = 0, \quad (3.16)$$

$$u|_{t=0} = u_0 \quad \text{for } x \in \mathcal{F}_0 \quad \text{and} \quad (h, h', \theta, \theta')(0) = (0, \ell_0, 0, r_0). \quad (3.17)$$

### 3.2.1 Reduction to an ODE: Statement of Theorem 3.12

In the irrotational case, the system above can be recast as an ODE whose unknowns are the degrees of freedom of the solid, namely  $h$  and  $\theta$ . In particular the motion of the fluid is completely determined by the solid position and velocity. In order to state this, let us introduce the variable  $q := (h, \theta) \in \mathbb{R}^3$ . Since the fluid and solid domains only depend on  $t$  through the solid position, we will rather denote them respectively  $\mathcal{F}(q)$  and  $\mathcal{S}(q)$  instead of  $\mathcal{F}(t)$  and  $\mathcal{S}(t)$ .

Let us gather the mass and moment of inertia of the solid into the following matrix:

$$\mathcal{M}_g := \begin{pmatrix} m & 0 & 0 \\ 0 & m & 0 \\ 0 & 0 & \mathcal{J} \end{pmatrix}. \quad (3.18)$$

Observe that  $\mathcal{M}_g$  is diagonal and in the set  $S_3^{++}(\mathbb{R})$  of the real symmetric positive definite  $3 \times 3$  matrices. As already mentioned in the introduction the reformulation relies on the phenomenon of added mass, which, loosely speaking, measures how

much the surrounding fluid resists the acceleration as the body moves through it. This will be encoded by a matrix  $\mathcal{M}_a$  in the set  $S_3^+(\mathbb{R})$  of the real symmetric positive-semidefinite  $3 \times 3$  matrices. The index  $a$  refers to “added”, by opposition to the genuine inertia  $\mathcal{M}_g$ . This matrix  $\mathcal{M}_a$  depends on the shape of the domain occupied by the solid and therefore on the solid position. Still since the system “fluid + solid” occupies the full plane the added inertia is invariant by translation and therefore only depends on  $\theta$ . In order to measure its variations let us denote by  $\mathcal{BL}(\mathbb{R}^3 \times \mathbb{R}^3; \mathbb{R}^3)$  the space of bilinear mappings from  $\mathbb{R}^3 \times \mathbb{R}^3$  to  $\mathbb{R}^3$ .

**Definition 3.11 (a-Connection)** Given a  $C^\infty$  mapping  $\theta \in \mathbb{R} \mapsto \mathcal{M}_{a,\theta} \in S_3^+(\mathbb{R})$ , we say that the  $C^\infty$  mapping  $\theta \in \mathbb{R} \mapsto \Gamma_{a,\theta} \in \mathcal{BL}(\mathbb{R}^3 \times \mathbb{R}^3; \mathbb{R}^3)$  is the associated a-connection if for any  $p \in \mathbb{R}^3$ ,

$$\langle \Gamma_{a,\theta}, p, p \rangle := \left( \sum_{1 \leq i, j \leq 3} (\Gamma_{a,\theta})_{i,j}^k p_i p_j \right)_{1 \leq k \leq 3} \in \mathbb{R}^3, \quad (3.19a)$$

with for every  $i, j, k \in \{1, 2, 3\}$  and for any  $q = (h, \theta)$ ,

$$(\Gamma_{a,\theta})_{i,j}^k(q) := \frac{1}{2} \left( (\mathcal{M}_{a,\theta})_{k,j}^i + (\mathcal{M}_{a,\theta})_{k,i}^j - (\mathcal{M}_{a,\theta})_{i,j}^k \right)(q), \quad (3.19b)$$

where  $(\mathcal{M}_{a,\theta})_{i,j}^k$  denotes the partial derivative with respect to  $q_k$  of the entry of indexes  $(i, j)$  of the matrix  $\mathcal{M}_{a,\theta}$ , that is

$$(\mathcal{M}_{a,\theta})_{i,j}^k := \frac{\partial (\mathcal{M}_{a,\theta})_{i,j}}{\partial q_k}. \quad (3.19c)$$

As already mentioned in the introduction another celebrated feature of the body’s dynamics in the case of an unbounded irrotational flow is the Kutta-Joukowski force. This force also depends on the shape of the domain occupied by the solid and in particular on the solid position through  $\theta$  only. Since this force is gyroscopic, i.e. orthogonal to the velocity  $q'$  (which gathers both translation and rotation velocities), and proportional to the circulation around the body, it will be encoded by a vector  $B_\theta$  in  $\mathbb{R}^3$ .

The first main result of this section is the following reformulation of Eqs. (3.13)–(3.16) into an ODE for the degrees of freedom of the solid only.

**Theorem 3.12** *There exists a  $C^\infty$  mapping  $\theta \in \mathbb{R} \mapsto (\mathcal{M}_{a,\theta}, B_\theta) \in S_3^+(\mathbb{R}) \times \mathbb{R}^3$  depending only on  $\mathcal{S}_0$  such that Eqs. (3.13)–(3.16) are equivalent to the following ODE for  $q = (h, \theta)$ :*

$$(\mathcal{M}_g + \mathcal{M}_{a,\theta}) q'' + \langle \Gamma_{a,\theta}, q', q' \rangle = \gamma q' \times B_\theta, \quad (3.20)$$

where  $\Gamma_{a,\theta}$  denotes the a-connection associated with  $\mathcal{M}_{a,\theta}$ , the fluid velocity  $u$  being given with respect to  $q$  and  $q' = (h', \theta')$  as the unique solution to the following

*div/curl type system:*

$$\begin{aligned} \operatorname{div} u &= 0 \text{ and } \operatorname{curl} u = 0 \text{ in } \mathcal{F}(q), \\ u \cdot n &= \left( h' + \theta'(x-h)^\perp \right) \cdot n \text{ for } x \in \partial\mathcal{S}(q), \quad \int_{\partial\mathcal{S}(q)} u \cdot \tau \, ds = \gamma, \\ \lim_{x \rightarrow \infty} u &= 0. \end{aligned}$$

Indeed the matrix  $\mathcal{M}_{a,\theta}$ , its associated a-connection  $\Gamma_{a,\theta}$  and  $B_\theta$  will be given by some precise formulas in the next section, cf. (3.27), (3.29) and (3.36). Let us already mention here that the dependence on  $\theta$  of  $(\mathcal{M}_{a,\theta}, B_\theta)$  is quite simple since

$$\mathcal{M}_{a,\theta} = \mathcal{R}(\theta)\mathcal{M}_{a,0}\mathcal{R}(\theta)^t \text{ and } B_\theta = \mathcal{R}(\theta)B_0,$$

where we associate the  $3 \times 3$  rotation matrix

$$\mathcal{R}(\theta) := \begin{pmatrix} R(\theta) & 0 \\ 0 & 1 \end{pmatrix} \in \operatorname{SO}(3) \quad (3.21)$$

with the  $2 \times 2$  rotation matrix  $R(\theta)$  defined in (3.3).

*Remark 3.13* Let us emphasize that the coefficients  $(\Gamma_{a,\theta})_{ij}^k$  defined in (3.19b) are not the Christoffel symbols associated with  $\mathcal{M}_{a,\theta}$  nor  $\mathcal{M}_g + \mathcal{M}_{a,\theta}$ . Indeed, one should multiply by  $(\mathcal{M}_g + \mathcal{M}_{a,\theta})^{-1}$  the column vector of the  $(\Gamma_{a,\theta})_{ij}^k$  indexed by  $k$  to get the standard Christoffel symbols:

$$\left( \Gamma_{ij}^k(q) \right)_{k \in \{1,2,3\}} = (\mathcal{M}_g + \mathcal{M}_{a,\theta})^{-1} \left( (\Gamma_{a,\theta})_{ij}^k(q) \right)_{k \in \{1,2,3\}}, \quad (3.22)$$

for any  $i, j \in \{1, 2, 3\}$ . The reason for deviating from the standard notations is that we want to keep track of the two types of inertia for the subsequent asymptotic analysis of the zero-radius limit. Observe that the a-connection only involves the added inertia. Still it is worth highlighting that should its right hand side vanish (3.20) would be the geodesic equation associated with the metric  $\mathcal{M}_g + \mathcal{M}_{a,\theta}$ :

$$(q^k)'' + \Gamma_{ij}^k(q)(q^i)'(q^j)' = 0,$$

where the  $\Gamma_{ij}^k$  are the standard Christoffel symbols defined in (3.22) and where Einstein summation notation is used.

We will prove Theorem 3.12 in the sequel but we first deduce and prove the following result.

**Proposition 3.14** *Given some initial data  $(q, q')(0) = (0, \ell_0, 0, r_0)$  there exists a unique global solution  $q \in C^\infty([0, +\infty); \mathbb{R}^3)$  to (3.20). Moreover the quantity*

$$\frac{1}{2}(\mathcal{M}_g + \mathcal{M}_{a,\theta}) q' \cdot q' \quad (3.23)$$

*is conserved.*

Theorem 3.3 is then a consequence of Theorem 3.12 and Proposition 3.14.

*Remark 3.15* The quantity (3.23) corresponds to the sum of the kinetic energy of the solid associated with its genuine inertia and of the one associated with the added inertia. It will become apparent in the sequel, cf. Sect. 3.2.3, that the kinetic energy associated with the added inertia of the rigid body can be also interpreted as a renormalization of the kinetic energy of the fluid by retaining only the potential contribution and discarding the term due to the circulation around the body.

*Proof* Local existence and uniqueness follow from classical ODE theory. Global existence would be a consequence of the energy conservation. Indeed defining for any  $\theta$  in  $\mathbb{R}$ , for any  $p$  in  $\mathbb{R}^3$ , the matrix

$$S_{a,\theta}(p) := \left( \sum_{1 \leq i \leq 3} (\Gamma_{a,\theta})_{ij}^k p_i \right)_{1 \leq k, j \leq 3} \quad \text{so that } \langle \Gamma_{a,\theta}, p, p \rangle = S_{a,\theta}(p)p,$$

then, an explicit computation proves that for any  $\theta$  in  $\mathbb{R}$ , for any  $p$  in  $\mathbb{R}^3$ ,

$$\frac{1}{2} \frac{\partial \mathcal{M}_{a,\theta}}{\partial q}(\theta) \cdot p - S_{a,\theta}(p) \text{ is skew-symmetric.}$$

Therefore for any  $\theta$  in  $\mathbb{R}$ , for any  $p$  in  $\mathbb{R}^3$ ,

$$\langle \Gamma_{a,\theta}, p, p \rangle \cdot p = (S_{a,\theta}(p)p) \cdot p = \frac{1}{2} \left( \frac{\partial \mathcal{M}_{a,\theta}}{\partial q}(\theta) p \right) \cdot p,$$

so that taking the inner product of (3.20) with  $q'$  yields on the one hand

$$(\mathcal{M}_g + \mathcal{M}_{a,\theta}) q'' \cdot q' = \frac{1}{2} ((\mathcal{M}_g + \mathcal{M}_{a,\theta}) q' \cdot q')' - \frac{1}{2} \left( \frac{\partial \mathcal{M}_{a,\theta}}{\partial q}(\theta) q' \right) \cdot q'$$

and on the other hand

$$\langle \Gamma_{a,\theta}, q', q' \rangle \cdot q' = \frac{1}{2} \left( \frac{\partial \mathcal{M}_{a,\theta}}{\partial q}(\theta) q' \right) \cdot q',$$

Therefore when doing the energy estimate the term coming from the a-connection exactly compensates the term coming from the commutation of one time derivative in the acceleration term, and the conservation of the energy follows by observing that the contribution of the right hand side of (3.20) is 0.  $\square$



### 3.2.2 *Explicit Definition of the ODE Coefficients $\mathcal{M}_{a,\theta}$ , $\Gamma_{a,\theta}$ and $B_\theta$*

In this section we are going to provide some precise formulas for the matrix  $\mathcal{M}_{a,\theta}$  (and for its associated a-connection  $\Gamma_{a,\theta}$  as well) and for the vector  $B_\theta$  thanks to some elementary flows corresponding respectively to potential and circulatory type flows. Indeed we will see in Sect. 3.2.3 (in a different frame, moving with the body) that the real flow can be decomposed thanks to these elementary flows.

#### **Kirchhoff Potentials**

The following so-called Kirchhoff potentials  $\Phi := (\Phi_i)_{i=1,2,3}$  will play a major role. They are defined as the solutions of the following problems:

$$-\Delta\Phi_i = 0 \quad \text{in } \mathcal{F}_0, \quad \Phi_i \longrightarrow 0 \quad \text{when } x \rightarrow \infty, \quad \frac{\partial\Phi_i}{\partial n} = K_i \quad \text{on } \partial\mathcal{F}_0, \quad (3.24)$$

where  $(K_1, K_2, K_3) := (n_1, n_2, x^\perp \cdot n)$ . The compatibility condition for this Neumann Problem is satisfied i.e. we check that

$$\int_{\partial\mathcal{S}_0} K_i ds = 0, \quad (3.25)$$

for  $i = 1, 2, 3$ , which is obvious by the Stokes formula :

$$\int_{\partial\mathcal{S}_0} n_1 ds = - \int_{\mathcal{S}_0} \operatorname{div}(e_1) dx = 0 \quad \text{and similarly} \quad \int_{\partial\mathcal{S}_0} n_2 ds = 0,$$

$$\text{whereas} \quad \int_{\partial\mathcal{S}_0} x^\perp \cdot n ds = - \int_{\mathcal{S}_0} \operatorname{div}(x^\perp) dx = 0.$$

Above  $e_1$  and  $e_2$  are the unit vectors of the canonical basis of  $\mathbb{R}^2$ .

We have that for all  $i = 1, 2, 3$ :

$$\Phi_i(x) = \mathcal{O}\left(\frac{1}{|x|}\right) \quad \text{and} \quad \nabla\Phi_i(x) = \mathcal{O}\left(\frac{1}{|x|^2}\right) \quad \text{as } |x| \rightarrow +\infty, \quad (3.26)$$

and consequently that  $\nabla\Phi_i$  are in  $L^2(\mathcal{F}_0)$ .

For instance in the case where  $\mathcal{S}_0$  is a disk one has  $\Phi_1(x) = -\frac{x_1}{|x|^2}$ ,  $\Phi_2(x) = -\frac{x_2}{|x|^2}$  and  $\Phi_3(x) = 0$ . If  $\mathcal{S}_0$  is not a disk then these three functions are linearly independent; this can be easily be proved by using a smooth arc length parameterization of the boundary and the usual Frenet equations, see for instance Lemma 6.1. of [25].

### Added Inertia

Let us define the matrices

$$\mathcal{M}_a := (m_{ij})_{i,j \in \{1,2,3\}} \quad \text{and} \quad \mathcal{M}_{a,\theta} := \mathcal{R}(\theta)\mathcal{M}_a\mathcal{R}(\theta)^t, \quad (3.27)$$

where for  $i, j \in \{1, 2, 3\}$

$$m_{i,j} := \int_{\mathcal{F}_0} \nabla \Phi_i \cdot \nabla \Phi_j \, dx, \quad (3.28)$$

and  $\mathcal{R}(\theta)$  is the  $3 \times 3$  rotation matrix defined in (3.21). Let us mention from now on that the matrix  $\mathcal{M}_{a,\theta}$  is positive definite if and only if  $\mathcal{S}_0$  is not a disk. When  $\mathcal{S}_0$  is a disk then  $\mathcal{M}_{a,\theta}$  has the form  $\text{diag}(m_a, m_a, 0)$  with  $m_a > 0$ . The case where  $\mathcal{S}_0$  is a disk is therefore peculiar, indeed by combining the translation and rotation equations one can observe that  $\mathcal{J}\theta'' = mh'' \cdot (h_c - h)^\perp$ , where  $h_c$  denotes the position of the center of the disk  $\mathcal{S}(q)$ , which can be different from  $h$  if the body is not homogeneous. As a consequence, in this case where  $\mathcal{S}_0$  is a disk, a particular reduction of the dynamics is possible and is indeed very helpful in order to tackle the case of massless particles. In the sequel we will focus on the case where  $\mathcal{S}_0$  is not a disk, and we refer to [11] for a full treatment of the case where  $\mathcal{S}_0$  is a disk.

### Added Inertia Connection

Let us define for  $p = (\ell, r)^t$ ,

$$\langle \Gamma_{a,\theta}, p, p \rangle := - \begin{pmatrix} P_{a,\theta} \\ 0 \end{pmatrix} \times p - r \mathcal{M}_{a,\theta} \begin{pmatrix} 0 \\ \ell^\perp \end{pmatrix}, \quad (3.29)$$

where  $P_{a,\theta}$  are the two first coordinates of  $\mathcal{M}_{a,\theta} p$ . A tedious computation reveals that  $\Gamma_{a,\theta}$  is the a-connection associated with  $\mathcal{M}_{a,\theta}$ .

### Harmonic Field

To take the velocity circulation around the body into account, we introduce the following harmonic field: let  $H$  be the unique solution vanishing at infinity of

$$\text{div } H = 0 \quad \text{and} \quad \text{curl } H = 0 \quad \text{in } \mathcal{F}_0, \quad H \cdot n = 0 \quad \text{on } \partial\mathcal{S}_0, \quad \int_{\partial\mathcal{S}_0} H \cdot \tau \, ds = 1.$$

The vector field  $H$  admits a harmonic stream function  $\Psi_H(x)$ :

$$H = \nabla^\perp \Psi_H,$$

which vanishes on the boundary  $\partial S_0$ , and behaves like  $\frac{1}{2\pi} \ln |x|$  as  $x$  goes to infinity. One way to get more information on the far-field behaviour of  $H$  is to use a little bit of complex analysis. We identify  $\mathbb{C}$  and  $\mathbb{R}^2$  through

$$(x_1, x_2) = x_1 + ix_2 = z. \tag{3.30}$$

We also use the notation

$$\widehat{f} = f_1 - if_2 \text{ for any } f = (f_1, f_2). \tag{3.31}$$

The reason of this notation is the following: if  $f$  is divergence and curl free if and only if  $\widehat{f}$  is holomorphic. In particular the function  $\widehat{H}$  is holomorphic (as a function of  $z = x_1 + ix_2$ ), and can be decomposed in Laurent Series :

$$\widehat{H}(z) = \frac{1}{2i\pi z} + \mathcal{O}(1/z^2) \text{ as } z \rightarrow \infty. \tag{3.32}$$

Coming back to the variable  $x \in \mathbb{R}^2$ , the previous decomposition implies

$$H(x) = \mathcal{O}\left(\frac{1}{|x|}\right) \text{ and } \nabla H = \mathcal{O}\left(\frac{1}{|x|^2}\right). \tag{3.33}$$

Moreover, we deduce from (3.32) that

$$x^\perp \cdot H = \frac{1}{2\pi} + \mathcal{O}\left(\frac{1}{|x|}\right) \text{ and } (H)^\perp - x^\perp \cdot \nabla H = \mathcal{O}\left(\frac{1}{|x|^2}\right).$$

**Conformal Center**

The harmonic field  $H$  allows to define the following geometric constant, known as the conformal center of  $S_0$ :

$$\xi_1 + i\xi_2 := \int_{\partial S_0} z \widehat{H} dz, \tag{3.34}$$

which depends only on  $S_0$ . In the particular case of a disk, the harmonic field  $H$  is given by  $\frac{1}{2\pi} \frac{x^\perp}{|x|^2}$  so that the conformal center  $\xi$  of a disk is obviously 0. In the general case one proves the following real-analytic characterization.

**Proposition 3.16** *There holds:*

$$\xi = \int_{\partial S_0} (H \cdot \tau) x ds. \tag{3.35}$$

In order to prove Proposition 3.16 we will use the following result which relates the integral  $\int_C \widehat{f} dz$  associated with a tangent vector field  $f$  to its flux and its circulation.

**Lemma 3.17** *Let  $C$  be a smooth Jordan curve,  $f := (f_1, f_2)$  a smooth vector fields on  $C$ :*

$$\int_C \widehat{f} dz = \int_C f \cdot \tau ds - i \int_C f \cdot n ds.$$

*Proof of Lemma 3.17* Denoting by  $\gamma = (\gamma_1, \gamma_2)$  a arc-length parametrization of  $C$  then  $\tau = (\gamma'_1, \gamma'_2)/|\gamma'|$ ,  $n = (-\gamma'_2, \gamma'_1)/|\gamma'|$ ,  $ds = |\gamma'(t)|dt$  and  $dz = (\gamma'_1(t) + i\gamma'_2(t))dt$ . Hence the conclusion follows from

$$\int_C (f_1 - if_2) dz = \int_C (f_1\gamma'_1 + f_2\gamma'_2) dt - i \int_C (-f_1\gamma'_2 + f_2\gamma'_1) dt.$$

□

*Proof of Proposition 3.16* Observe that  $z(H_1 - iH_2) = f_1 - if_2$  with  $f_1 = x \cdot H$  and  $f_2 = x^\perp \cdot H$  so that applying Lemma 3.17 we have that

$$\int_{\partial\mathcal{S}_0} z\widehat{H} dz = \int_{\partial\mathcal{S}_0} g ds, \text{ with } g := \begin{pmatrix} x \cdot H \\ x^\perp \cdot H \end{pmatrix} \cdot \tau - i \begin{pmatrix} x \cdot H \\ x^\perp \cdot H \end{pmatrix} \cdot n.$$

Moreover, for  $x \in \partial\mathcal{S}_0$ , we have

$$\begin{aligned} g &= (x_1H_1 + x_2H_2)\tau_1 + (-x_2H_1 + x_1H_2)\tau_2 \\ &\quad -i(x_1H_1 + x_2H_2)n_1 - i(-x_2H_1 + x_1H_2)n_2 \\ &= x_1(H_1\tau_1 + H_2\tau_2) + x_2(H_2\tau_1 - H_1\tau_2) \\ &\quad -ix_1(H_1n_1 + H_2n_2) - ix_2(H_2n_1 - H_1n_2), \end{aligned}$$

and using that  $(n_1, n_2) = (-\tau_2, \tau_1)$ , we deduce that  $g = z(H \cdot \tau) - iz(H \cdot n)$ . It is then sufficient to recall that  $H \cdot n = 0$  to conclude. □

### Kutta-Joukowski Field

Then the vector field  $B_\theta$  is defined by the following formula:

$$B_\theta := \mathcal{R}(\theta) \begin{pmatrix} \xi^\perp \\ -1 \end{pmatrix}. \quad (3.36)$$

Observe that the corresponding force in the left hand side of (3.20) is therefore

$$q' \times B_\theta = \begin{pmatrix} (h')^\perp - \theta' R(\theta) \xi^\perp \\ R(\theta) \xi \cdot h' \end{pmatrix}.$$

### 3.2.3 Reformulation as an ODE in the Body Frame: Statement of Theorem 3.18

In order to transfer the equations in the body frame we apply the following isometric change of variable:

$$\begin{cases} v(t, x) = R(\theta(t))^T u(t, R(\theta(t))x + h(t)), \\ \tilde{\pi}(t, x) = \pi(t, R(\theta(t))x + h(t)), \\ \ell(t) = R(\theta(t))^T h'(t), \end{cases} \quad (3.37)$$

where we recall that  $R(\theta(t))$  is the  $2 \times 2$  rotation matrix defined in (3.3) so that Eqs. (3.13)–(3.17) become

$$\frac{\partial v}{\partial t} + [(v - \ell - rx^\perp) \cdot \nabla] v + rv^\perp + \nabla \tilde{\pi} = 0 \text{ and } \operatorname{div} v = 0 \quad \text{for } x \in \mathcal{F}_0, \quad (3.38)$$

$$m\ell'(t) = \int_{\partial \mathcal{S}_0} \tilde{\pi} n \, ds - mr\ell^\perp \text{ and } \mathcal{J}r'(t) = \int_{\partial \mathcal{S}_0} x^\perp \cdot \tilde{\pi} n \, ds, \quad (3.39)$$

$$v \cdot n = (\ell + rx^\perp) \cdot n \quad \text{for } x \in \partial \mathcal{S}_0, \quad (3.40)$$

$$v(0, x) = v_0(x) \text{ for } x \in \mathcal{F}_0 \text{ and } (\ell, r)(0) = (\ell_0, r_0), \quad (3.41)$$

where  $r(t) = \theta'(t)$ .

In order to state recast the system above as an ODE in the body frame we are going to introduce now a few objects. Let  $\Gamma_g : \mathbb{R}^3 \times \mathbb{R}^3 \rightarrow \mathbb{R}^3$  and  $\Gamma_a : \mathbb{R}^3 \times \mathbb{R}^3 \rightarrow \mathbb{R}^3$  be the bilinear symmetric mappings defined, for all  $p = (\ell, r) \in \mathbb{R}^3$ , by

$$\langle \Gamma_g, p, p \rangle = mr \begin{pmatrix} \ell^\perp \\ 0 \end{pmatrix} \text{ and } \langle \Gamma_a, p, p \rangle = \begin{pmatrix} r(\mathcal{M}_b \ell)^\perp \\ \ell^\perp \cdot \mathcal{M}_b \ell \end{pmatrix} + rp \times \mu, \quad (3.42)$$

where

$$\mu := \begin{pmatrix} m_{1,3} \\ m_{2,3} \\ 0 \end{pmatrix} \text{ and } \mathcal{M}_b := (m_{i,j})_{i,j \in \{1,2\}}. \quad (3.43)$$

Note that

$$\forall p \in \mathbb{R}^3, \quad \langle \Gamma_g, p, p \rangle \cdot p = 0 \text{ and } \langle \Gamma_a, p, p \rangle \cdot p = 0, \quad (3.44)$$

and that  $\Gamma_a$  is depending only on  $\mathcal{S}_0$ . Because of (3.44) we will refer to the quadratic mappings  $\Gamma_g$  and  $\Gamma_a$  as *gyroscopic terms*.

One will deduce Theorem 3.12 from the following result by going back in the original frame.

**Theorem 3.18** *Equations (3.38)–(3.39) are equivalent to the following ODE for  $p := (\ell, r)^T$ :*

$$[\mathcal{M}_g + \mathcal{M}_a]p' + \langle \Gamma_g, p, p \rangle + \langle \Gamma_a, p, p \rangle = \gamma p \times B, \quad (3.45)$$

*the fluid velocity  $v$  being given as the unique solution to the following div/curl type system:*

$$\operatorname{div} v = 0 \text{ and } \operatorname{curl} v = 0 \text{ in } \mathcal{F}_0, \quad (3.46)$$

$$v \cdot n = (\ell + rx^\perp) \cdot n \text{ on } \partial\mathcal{S}_0, \quad \int_{\partial\mathcal{S}_0} v \cdot \tau \, ds = \gamma, \quad (3.47)$$

$$\lim_{x \rightarrow \infty} v = 0. \quad (3.48)$$

Let us recall that  $\mathcal{M}_g$  and  $\mathcal{M}_a$  are respectively the genuine and added inertia, see (3.27) and (3.18), and that  $B$  is a fixed vector defined in (3.36).

Observe that one may also obtain from this formulation the conservative feature of the system since it suffices to multiply (3.45) by  $p$ , to use the symmetry of the matrices  $\mathcal{M}_g$  and  $\mathcal{M}_a$  and the properties (3.44) to deduce that the total energy  $\frac{1}{2}p \cdot (\mathcal{M}_g + \mathcal{M}_a)p$  is conserved along time.

The rest of the section is devoted to the proof of Theorem 3.18. Indeed after a slight reformulation of the solid equations and the decomposition of the velocity into several pieces corresponding to the various sources in the right hand sides of the system (3.46)–(3.48), we will compare two methods, one based on complex argument and the other one on real analysis only.

## Reformulation of the Solid Equations

The first step of the proof of Theorem 3.18 uses the Euler equations and the Kirchhoff potentials in order to get rid of the pressure and to make appear the added inertia.

**Lemma 3.19** *Equations (3.39) can be rewritten in the form*

$$(\mathcal{M}_g + \mathcal{M}_a)p' + \langle \Gamma_g, p, p \rangle = -\left(\frac{1}{2} \int_{\partial\mathcal{S}_0} |v|^2 K_i \, ds - \int_{\partial\mathcal{S}_0} (\ell + rx^\perp) \cdot v K_i \, ds\right)_i, \quad (3.49)$$

where  $i$  runs over the integers 1, 2, 3.

*Proof* Using the following equality for two vector fields  $a$  and  $b$  in  $\mathbb{R}^2$ :

$$\nabla(a \cdot b) = a \cdot \nabla b + b \cdot \nabla a - (a^\perp \operatorname{curl} b + b^\perp \operatorname{curl} a), \quad (3.50)$$

Eq. (3.38) can be written as

$$\frac{\partial v}{\partial t} + \frac{1}{2} \nabla(v^2) - \nabla((\ell + rx^\perp) \cdot v) + \nabla \tilde{\pi} = 0. \quad (3.51)$$

We use this equation to deduce the force/torque acting on the body:

$$\left( \int_{\partial S_0} \tilde{\pi} n \, ds, \int_{\partial S_0} \tilde{\pi} x^\perp \cdot n \, ds \right) = \left( \int_{\mathcal{F}_0} \nabla \tilde{\pi} \cdot \nabla \Phi_i \, dx \right)_{i=1,2,3}.$$

One can check that the above integration by parts is licit by using the decay properties of  $v$  and  $\nabla \Phi_i$ . Using an integration by parts, the boundary condition (3.40) and another integration by parts, one observes that the contribution of  $\partial_t v$  is

$$\int_{\mathcal{F}_0} \partial_t v \cdot \nabla \Phi_i(x) \, dx = \mathcal{M}_a \left( \frac{\ell}{r} \right)', \quad (3.52)$$

and one obtains the result.  $\square$

### Decomposition of the Velocity Field

Finally, for  $\ell$  in  $\mathbb{R}^2$ ,  $r$  and  $\gamma$  in  $\mathbb{R}$  given, there exists a unique vector field  $v$  verifying (3.46)–(3.48) and it is given by the law:

$$v = \gamma H + \ell_1 \nabla \Phi_1 + \ell_2 \nabla \Phi_2 + r \nabla \Phi_3, \quad (3.53)$$

We will denote by

$$\tilde{v} := v - \gamma H. \quad (3.54)$$

the part without circulation, that we will decomposed sometimes into

$$\tilde{v} = v_\# + r \nabla \Phi_3, \quad (3.55)$$

with

$$v_\# := \ell_1 \nabla \Phi_1 + \ell_2 \nabla \Phi_2, \quad (3.56)$$

in order to analyse separately the effects of the body translation and of the body rotation.

Observe that in the particular case the fluid velocity is assumed to be globally a gradient (the so-called potential case corresponding to  $\gamma = 0$ ) it may be expanded with respect to the Kirchoff potentials only.

Another crucial observation is that the first term in the right hand side of (3.49) is quadratic in  $v$  and that  $v$  is decomposed into a potential part and a circulatory part, cf. (3.53). Roughly speaking the a-connection (the last term in the right hand side of (3.45)) will result from the quadratic self-interaction of the potential part and the Kutta-Joukowski term (the left hand side of (3.45)) from the crossed interaction between the potential part and the circulatory part. There will be a cancellation of the quadratic self-interaction of the circulatory part, cf. (3.81) and Lemma 3.25. Indeed this cancellation echoes the renormalization hinted in Remark 3.15. The kinetic energy of the fluid should be  $\frac{1}{2} \int_{\mathcal{F}_0} v^2 dx$  but the term  $\frac{1}{2} (\mathcal{M}_{a,\theta} q') \cdot q'$  included in (3.23) is equal to  $\frac{1}{2} \int_{\mathcal{F}_0} \tilde{v}^2 dx$ . Since  $\tilde{v}$  and  $H$  are orthogonal in  $L^2(\mathcal{F}_0)$  this renormalization therefore formally consists in discarding the contribution to the fluid kinetic energy due to the fluid velocity associated with the circulation around the body. Observe that this contribution is infinite because of the slow decay at infinity of this part of the fluid velocity but depends only on the body's shape, not on its position or velocity.

### 3.2.4 A Complex-Analytic Proof of Theorem 3.18

We will follow here a strategy based on complex analysis after Blasius, Kutta, Joukowski, Chaplygin and Sedov. A key lemma is the following Blasius formula about tangent vector fields where we use the identifications (3.30) and (3.31).

**Lemma 3.20** *Let  $\mathcal{C}$  be a smooth Jordan curve,  $f := (f_1, f_2)$  and  $g := (g_1, g_2)$  two smooth tangent vector fields on  $\mathcal{C}$ . Then*

$$\int_{\mathcal{C}} (f \cdot g) n ds = i \left( \int_{\mathcal{C}} \widehat{f} \widehat{g} dz \right)^* , \tag{3.57}$$

$$\int_{\mathcal{C}} (f \cdot g) (x^\perp \cdot n) ds = \operatorname{Re} \left( \int_{\mathcal{C}} z \widehat{f} \widehat{g} dz \right) . \tag{3.58}$$

Above  $(\cdot)^*$  denotes the complex conjugation.

*Proof of Lemma 3.20* Thanks to the polarization identity, it is sufficient to consider the case where  $f = g$ . Let us consider  $\gamma = (\gamma_1, \gamma_2) : [0, 1] \rightarrow \mathbb{R}^2$  a smooth arc length parameterization of the Jordan curve  $\mathcal{C}$ . On one side, one has

$$\int_{\mathcal{C}} (f \cdot f) n ds = \int_0^1 (f_1(\gamma(t))^2 + f_2(\gamma(t))^2) \begin{pmatrix} -\gamma_2'(t) \\ \gamma_1'(t) \end{pmatrix} dt . \tag{3.59}$$



On the other side, one has

$$\begin{aligned} & \int_{\mathcal{C}} (f_1(z) - if_2(z))^2 dz \\ &= \int_0^1 \left( f_1(\gamma(t)) - if_2(\gamma(t)) \right) \left[ (f_1(\gamma(t)) - if_2(\gamma(t))) (\gamma_1'(t) + i\gamma_2'(t)) \right] dt. \end{aligned}$$

But since  $f$  is tangent to  $\mathcal{C}$ , one sees that the expression inside the brackets above is real, and hence is equal to its complex conjugate. It follows that

$$\int_{\mathcal{C}} (f_1(z) - if_2(z))^2 dz = \int_0^1 |f_1(\gamma(t)) - if_2(\gamma(t))|^2 (\gamma_1'(t) - i\gamma_2'(t)) dt,$$

and (3.57) follows.

The proof of (3.58) is analogous: using again

$$(f_1(\gamma(t)) - if_2(\gamma(t))) (\gamma_1'(t) + i\gamma_2'(t)) = (f_1(\gamma(t)) + if_2(\gamma(t))) (\gamma_1'(t) - i\gamma_2'(t)),$$

we deduce

$$\begin{aligned} & \int_{\mathcal{C}} (f_1(z) - if_2(z))^2 z dz \\ &= \int_0^1 |f_1(\gamma(t)) - if_2(\gamma(t))|^2 (\gamma_1(t) + i\gamma_2(t)) (\gamma_1'(t) - i\gamma_2'(t)) dt, \end{aligned}$$

so that

$$\begin{aligned} & \operatorname{Re} \left( \int_{\mathcal{C}} (f_1(z) - if_2(z))^2 z dz \right) \\ &= \int_0^1 \left( f_1(\gamma(t))^2 + f_2(\gamma(t))^2 \right) (\gamma_1(t)\gamma_1'(t) + \gamma_2(t)\gamma_2'(t)) dt \\ &= \int_{\mathcal{C}} (f \cdot f)(x^\perp \cdot n) ds. \end{aligned}$$

□

The idea of the complex-analytic approach of the computation of the terms in the right hand side of the equation in Lemma 3.19 is to decompose them in order to make appear some vector fields tangent to the boundary  $\partial\mathcal{S}_0$ , to use Blasius' lemma and then Cauchy's residue theorem.

In this process of computing the residue we will use the Laurent series of  $\widehat{\nabla}\Phi_i$ . Because of the decay property at infinity in (3.24) the Laurent series of  $\widehat{\nabla}\Phi_i$  has to start at least with a term in  $\mathcal{O}(1/z)$ , and this term is

$$\frac{1}{2i\pi} \int_{\partial\mathcal{S}_0} \widehat{\nabla}\Phi_i dz.$$

Thanks to Lemma 3.17 we get that  $\int_{\partial S_0} \widehat{\nabla \Phi}_i dz = 0$  since the circulation of a gradient around  $\partial S_0$  vanishes and the flux as well according to (3.25).

Moreover Lemma 3.17 also allows to compute the second term in the Laurent series:

**Corollary 3.21** *Let  $\mathcal{C}$  be a smooth Jordan curve,  $f := (f_1, f_2)$  a smooth vector fields on  $\mathcal{C}$ :*

$$\begin{aligned} \int_{\mathcal{C}} \widehat{z} f dz &= \int_{\mathcal{C}} \begin{pmatrix} x \cdot f \\ x^\perp \cdot f \end{pmatrix} \cdot \tau ds - i \int_{\mathcal{C}} \begin{pmatrix} x \cdot f \\ x^\perp \cdot f \end{pmatrix} \cdot n ds \\ &= \int_{\mathcal{C}} (x_1 + ix_2)(f \cdot \tau) ds - i \int_{\mathcal{C}} (x_1 + ix_2)(f \cdot n) ds. \end{aligned}$$

*Proof* To apply the previous lemma, we have to identify a function  $g$  such that  $z(f_1 - if_2) = g_1 - ig_2$ . Hence, to get the first equality, it is sufficient to check that

$$(x_1 + ix_2)(f_1 - if_2) = (x_1 f_1 + x_2 f_2) - i(-x_2 f_1 + x_1 f_2) = (x \cdot f) - i(x^\perp \cdot f).$$

To obtain the second equality, we simply use  $(n_1, n_2) = (-\tau_2, \tau_1)$ :

$$\begin{aligned} \begin{pmatrix} x \cdot f \\ x^\perp \cdot f \end{pmatrix} \cdot \tau - i \begin{pmatrix} x \cdot f \\ x^\perp \cdot f \end{pmatrix} \cdot n &= (x_1 f_1 + x_2 f_2) \tau_1 + (-x_2 f_1 + x_1 f_2) \tau_2 \\ &\quad - i(x_1 f_1 + x_2 f_2) n_1 - i(-x_2 f_1 + x_1 f_2) n_2 \\ &= x_1(f_1 \tau_1 + f_2 \tau_2) + x_2(f_2 \tau_1 - f_1 \tau_2) \\ &\quad - ix_1(f_1 n_1 + f_2 n_2) - ix_2(f_2 n_1 - f_1 n_2) \\ &= x_1(f_1 \tau_1 + f_2 \tau_2) + x_2(f_2 n_2 + f_1 n_1) \\ &\quad - ix_1(f_1 n_1 + f_2 n_2) - ix_2(-f_2 \tau_2 - f_1 \tau_1) \\ &= (x_1 + ix_2)(f_1 \tau_1 + f_2 \tau_2) \\ &\quad - i(x_1 + ix_2)(f_1 n_1 + f_2 n_2) \end{aligned}$$

which ends the proof. □

Replacing  $x_2$  by  $-x_2$  in the previous proof, we note that we obtain

$$\int_{\mathcal{C}} \widehat{z} f dz = \int_{\mathcal{C}} (x_1 - ix_2)(f \cdot \tau) ds - i \int_{\mathcal{C}} (x_1 - ix_2)(f \cdot n) ds. \quad (3.60)$$

We apply the previous results to the function  $\nabla\Phi_i$ :

**Lemma 3.22** *One has:*

$$\int_{\partial\mathcal{S}_0} z\widehat{\nabla\Phi_i} dz = -(m_{i,2} + |\mathcal{S}_0|\delta_{i,2}) + i(m_{i,1} + |\mathcal{S}_0|\delta_{i,1}), \quad \text{for } i = 1, 2;$$

$$\int_{\partial\mathcal{S}_0} z\widehat{\nabla\Phi_3} dz = -(m_{3,2} + |\mathcal{S}_0|x_{G,1}) + i(m_{3,1} - |\mathcal{S}_0|x_{G,2});$$

where  $m_{i,j}$  is defined in (3.28).

*Proof* We use the previous corollary with  $f = \nabla\Phi_i$ :

$$\int_{\partial\mathcal{S}_0} z\widehat{\nabla\Phi_i} dz = \int_{\partial\mathcal{S}_0} (x_1 + ix_2)\partial_\tau\Phi_i ds - i \int_{\partial\mathcal{S}_0} (x_1 + ix_2)\partial_n\Phi_i ds.$$

We can integrate by part in the first integral:

$$\begin{aligned} \int_{\partial\mathcal{S}_0} (x_1 + ix_2)\partial_\tau\Phi_i ds &= - \int_{\partial\mathcal{S}_0} \partial_\tau(x_1 + ix_2)\Phi_i ds \\ &= - \int_{\partial\mathcal{S}_0} (\tau_1 + i\tau_2)\Phi_i ds \\ &= - \int_{\partial\mathcal{S}_0} (n_2 - in_1)\Phi_i ds \\ &= - \int_{\mathcal{F}_0} \nabla\Phi_2 \cdot \nabla\Phi_i ds + i \int_{\mathcal{F}_0} \nabla\Phi_1 \cdot \nabla\Phi_i ds \\ &= -m_{i,2} + im_{i,1}. \end{aligned}$$

The second integral can be computed thanks to the boundary condition and (3.66):

$$\begin{aligned} \int_{\partial\mathcal{S}_0} x_j\partial_n\Phi_i ds &= \int_{\partial\mathcal{S}_0} x_jn_i ds = -\delta_{i,j}|\mathcal{S}_0| \quad \text{for } i, j = 1, 2, \\ \int_{\partial\mathcal{S}_0} x_1\partial_n\Phi_3 ds &= \int_{\partial\mathcal{S}_0} x_1(x^\perp \cdot n) ds = |\mathcal{S}_0|x_{G,2} \text{ and} \\ \int_{\partial\mathcal{S}_0} x_2\partial_n\Phi_3 ds &= \int_{\partial\mathcal{S}_0} x_2(x^\perp \cdot n) ds = -|\mathcal{S}_0|x_{G,1}. \end{aligned}$$

□

Using (3.60), we can reproduce exactly the previous proof to establish that:

$$\int_{\partial\mathcal{S}_0} \bar{z}\widehat{\nabla\Phi_i} dz = (-m_{i,2} + |\mathcal{S}_0|\delta_{i,2}) + i(-m_{i,1} + |\mathcal{S}_0|\delta_{i,1}), \quad \text{for } i = 1, 2;$$

$$\int_{\partial\mathcal{S}_0} \bar{z}\widehat{\nabla\Phi_3} dz = (-m_{3,2} + |\mathcal{S}_0|x_{G,1}) - i(m_{3,1} + |\mathcal{S}_0|x_{G,2}).$$

We are now almost ready to start the proof by itself. The last preparation consists in using the decomposition (3.54) to deduce from Lemma 3.19 that Eq. (3.39) can be rewritten in the form

$$(\mathcal{M}_g + \mathcal{M}_a)p' + \langle \Gamma_g, p, p \rangle = -(A_i + B_i + C_i)_{i=1,2,3}, \quad (3.61)$$

where for  $i = 1, 2, 3$ ,

$$\begin{aligned} A_i &:= \frac{1}{2} \int_{\partial \mathcal{S}_0} |\tilde{v}|^2 K_i ds - \int_{\partial \mathcal{S}_0} (\ell + rx^\perp) \cdot \tilde{v} K_i ds, \\ B_i &:= \gamma \int_{\partial \mathcal{S}_0} (\tilde{v} - (\ell + rx^\perp)) \cdot HK_i ds, \end{aligned} \quad (3.62)$$

$$C_i := \frac{\gamma^2}{2} \int_{\partial \mathcal{S}_0} |H|^2 K_i ds. \quad (3.63)$$

We start with the computation of the terms  $(A_i)_{i=1,2,3}$ .

**Lemma 3.23**

$$\begin{pmatrix} A_1 \\ A_2 \end{pmatrix} = r^2 \begin{pmatrix} -m_{3,2} \\ m_{3,1} \end{pmatrix} + r(\mathcal{M}_b \ell)^\perp \quad (3.64)$$

and

$$A_3 = \ell^\perp \mathcal{M}_b \ell - r\ell \cdot \begin{pmatrix} -m_{3,2} \\ m_{3,1} \end{pmatrix}. \quad (3.65)$$

*Proof* We start with the following observation:

$$A_i = \frac{1}{2} \int_{\partial \mathcal{S}_0} |\tilde{v} - (\ell + rx^\perp)|^2 K_i ds - \frac{1}{2} \int_{\partial \mathcal{S}_0} |\ell + rx^\perp|^2 K_i ds,$$

which makes appear at least one term with the wished tangence property. Since Blasius' lemma is different for the torque, we replace  $\tilde{v}$  by the decomposition (3.55) to get

$$\begin{aligned} A_i &= \frac{1}{2} \int_{\partial \mathcal{S}_0} |v_\# - \ell|^2 K_i ds + \frac{1}{2} \int_{\partial \mathcal{S}_0} |r(\nabla \Phi_3 - x^\perp)|^2 K_i ds \\ &\quad + \int_{\partial \mathcal{S}_0} r(v_\# - \ell) \cdot (\nabla \Phi_3 - x^\perp) K_i ds - \frac{1}{2} \int_{\partial \mathcal{S}_0} |\ell + rx^\perp|^2 K_i ds \\ &=: A_{i,a} + A_{i,b} + A_{i,c} + A_{i,d}. \end{aligned}$$

The first three terms have a form appropriated for the strategy mentioned above. One may worry about the last one but it benefits from a special structure resembling the Archimedes' force (despite the absence of gravity in our setting). Let us see first how this term can be simply computed thanks to the Stokes formula so that we will then be serene to implement the complex-analytic approach to the three other terms.

**An Archimedes' Type Term** In order to compute the term  $A_{i,d}$  we first expand

$$\begin{aligned} \int_{\partial\mathcal{S}_0} |\ell + rx^\perp|^2 K_i ds &= |\ell|^2 \int_{\partial\mathcal{S}_0} K_i ds - 2\ell_1 r \int_{\partial\mathcal{S}_0} x_2 K_i ds \\ &\quad + 2\ell_2 r \int_{\partial\mathcal{S}_0} x_1 K_i ds + r^2 \int_{\partial\mathcal{S}_0} |x|^2 K_i ds. \end{aligned}$$

Thanks to the Stokes formula:

$$\int_{\partial\mathcal{S}_0} x_j n_i ds = - \int_{\mathcal{S}_0} \operatorname{div}(x_j e_i) dx = -\delta_{ij} |\mathcal{S}_0|, \quad \text{for } i, j = 1, 2; \quad (3.66a)$$

$$\int_{\partial\mathcal{S}_0} x_1 (x^\perp \cdot n) ds = - \int_{\mathcal{S}_0} \operatorname{div}(x_1 x^\perp) dx = - \int_{\mathcal{S}_0} (-x_2) dx = |\mathcal{S}_0| x_{G,2}; \quad (3.66b)$$

$$\int_{\partial\mathcal{S}_0} x_2 (x^\perp \cdot n) ds = - \int_{\mathcal{S}_0} \operatorname{div}(x_2 x^\perp) dx = - \int_{\mathcal{S}_0} x_1 dx = -|\mathcal{S}_0| x_{G,1}; \quad (3.66c)$$

and

$$\begin{aligned} \int_{\partial\mathcal{S}_0} |x|^2 n_i ds &= - \int_{\mathcal{S}_0} \operatorname{div}(|x|^2 e_i) dx = - \int_{\mathcal{S}_0} 2x_i dx \\ &= -2x_{G,i} |\mathcal{S}_0|, \quad \text{for } i = 1, 2; \end{aligned} \quad (3.67a)$$

$$\int_{\partial\mathcal{S}_0} |x|^2 x^\perp \cdot n ds = - \int_{\mathcal{S}_0} \operatorname{div}(|x|^2 x^\perp) dx = 0, \quad (3.67b)$$

where  $|\mathcal{S}_0|$  is the Lebesgue measure of  $\mathcal{S}_0$  and  $x_G = (x_{G,1}, x_{G,2})$  is the position of the geometrical center of  $\mathcal{S}_0$  (which can be different of the mass center 0 if the solid is not homogenous):

$$x_G := \frac{1}{|\mathcal{S}_0|} \int_{\mathcal{S}_0} x dx. \quad (3.68)$$

Then, using also (3.25), we check easily that

$$(A_{i,d})_{i=1,2} = -r\ell^\perp |\mathcal{S}_0| + r^2 x_G |\mathcal{S}_0| \text{ and } A_{3,d} = -r(\ell \cdot x_G) |\mathcal{S}_0|. \quad (3.69)$$

**Computation of the Three Other Terms** Recalling the definition (3.56) and using the notation (3.31) we first remark that

$$\widehat{v_{\#} - \ell}(z) = -\ell_1 + i\ell_2 + \ell_1 \widehat{\nabla \Phi_1} + \ell_2 \widehat{\nabla \Phi_2}. \quad (3.70)$$

**Computation of  $A_{i,a}$**  We compute separately the case where  $i = 1, 2$  and the case where  $i = 3$ .

- As  $v_{\#} - \ell$  is tangent to the boundary, we can apply the Blasius formula (see Lemma 3.20), (3.70), Cauchy's residue theorem, to obtain

$$(A_{i,a})_{i=1,2} = 0. \quad (3.71)$$

- We proceed in the same way for  $i = 3$ :

$$\begin{aligned} A_{3,a} &= \frac{1}{2} \int_{\partial \mathcal{S}_0} |v_{\#} - \ell|^2 K_3 ds = \frac{1}{2} \operatorname{Re} \left( \int_{\partial \mathcal{S}_0} z \widehat{(v_{\#} - \ell)^2} dz \right) \\ &= \operatorname{Re} \left( \left[ (-\ell_1) - i(-\ell_2) \right] \int_{\partial \mathcal{S}_0} z \left( \ell_1 \widehat{\nabla \Phi_1} + \ell_2 \widehat{\nabla \Phi_2} \right) dz \right). \end{aligned}$$

so that, thanks to Lemma 3.22,

$$A_{3,a} = (-\ell_1) \left[ -\ell_1 m_{1,2} - \ell_2 (m_{2,2} + |\mathcal{S}_0|) \right] + (-\ell_2) \left[ \ell_1 (m_{1,1} + |\mathcal{S}_0|) + \ell_2 m_{2,1} \right]$$

which finally can be simplified as follows:

$$A_{3,a} = \ell^\perp \mathcal{M}_b \ell. \quad (3.72)$$

**Computation of  $A_{i,b}$**  Once again we distinguish the case where  $i = 1, 2$  and the case where  $i = 3$ .

- As  $\nabla \Phi_3 - x^\perp$  is tangent to the boundary, we can write for  $i = 1, 2$  by Lemma 3.20 and by Cauchy's residue theorem:

$$\begin{aligned} (A_{i,b})_{i=1,2} &= \frac{r^2}{2} \int_{\partial \mathcal{S}_0} |\nabla \Phi_3 - x^\perp|^2 n ds = \frac{ir^2}{2} \left( \int_{\partial \mathcal{S}_0} \widehat{(\nabla \Phi_3 - x^\perp)^2} dz \right)^* \\ &= \frac{ir^2}{2} \left( \int_{\partial \mathcal{S}_0} 2i\bar{z} \widehat{\nabla \Phi_3} dz - \int_{\partial \mathcal{S}_0} \bar{z}^2 dz \right)^*, \end{aligned}$$

where we have noted that  $-\widehat{x^\perp} = i\bar{z}$ . Let us observe that

$$\begin{aligned}
 \int_{\partial\mathcal{S}_0} \bar{z}^2 dz &= \int (\gamma_1 - i\gamma_2)^2 (\gamma'_1 + i\gamma'_2) \\
 &= \int (\gamma_1^2 \gamma'_1 - \gamma_2^2 \gamma'_1 + 2\gamma_1 \gamma_2 \gamma'_2) + i \int (\gamma_1^2 \gamma'_2 - \gamma_2^2 \gamma'_2 - 2\gamma_1 \gamma_2 \gamma'_1) \\
 &= - \int_{\partial\mathcal{S}_0} \begin{pmatrix} 2x_1 x_2 \\ x_2^2 \end{pmatrix} \cdot n ds - i \int_{\partial\mathcal{S}_0} \begin{pmatrix} x_1^2 \\ 2x_1 x_2 \end{pmatrix} \cdot n ds \\
 &= \int_{\mathcal{S}_0} \operatorname{div} \begin{pmatrix} 2x_1 x_2 \\ x_2^2 \end{pmatrix} dx + i \int_{\mathcal{S}_0} \operatorname{div} \begin{pmatrix} x_1^2 \\ 2x_1 x_2 \end{pmatrix} dx \\
 &= 4|\mathcal{S}_0|_{x_{G,2}} + 4i|\mathcal{S}_0|_{x_{G,1}}.
 \end{aligned}$$

Therefore thanks to Lemma 3.22 we state that:

$$\begin{aligned}
 (A_{i,b})_{i=1,2} &= ir^2 \left( i(-m_{3,2} + |\mathcal{S}_0|_{x_{G,1}}) + (m_{3,1} + |\mathcal{S}_0|_{x_{G,2}}) \right. \\
 &\quad \left. - 2(|\mathcal{S}_0|_{x_{G,2}} + i|\mathcal{S}_0|_{x_{G,1}}) \right)^* \\
 &= r^2 \left( (-m_{3,2} - |\mathcal{S}_0|_{x_{G,1}}) + i(m_{3,1} - |\mathcal{S}_0|_{x_{G,2}}) \right) \\
 &= r^2 \left( \begin{pmatrix} -m_{3,2} \\ m_{3,1} \end{pmatrix} - |\mathcal{S}_0|_{x_G} \right),
 \end{aligned}$$

and thus

$$(A_{i,b})_{i=1,2} = 0. \quad (3.73)$$

- For  $i = 3$ , we have that:

$$\begin{aligned}
 A_{3,b} &= \int_{\partial\mathcal{S}_0} |\nabla\Phi_3 - x^\perp|^2 (x^\perp \cdot n) ds \\
 &= \int_{\partial\mathcal{S}_0} |\nabla\Phi_3|^2 x^\perp \cdot n ds - 2 \int_{\partial\mathcal{S}_0} (\nabla\Phi_3 \cdot x^\perp) (x^\perp \cdot n) ds + \int_{\partial\mathcal{S}_0} |x|^2 x^\perp \cdot n ds \\
 &= \int_{\mathcal{F}_0} \operatorname{div}(|\nabla\Phi_3|^2 x^\perp) dx - 2 \int_{\mathcal{F}_0} \nabla(\nabla\Phi_3 \cdot x^\perp) \cdot \nabla\Phi_3 dx - \int_{\mathcal{S}_0} \operatorname{div}(|x|^2 x^\perp) dx,
 \end{aligned}$$

where there is no boundary term at infinity because  $\nabla\Phi_3 = \mathcal{O}(1/|x|^2)$ . Next we use the general relation (3.50) to obtain that

$$\begin{aligned}\nabla(\nabla\Phi_3 \cdot x^\perp) \cdot \nabla\Phi_3 &= [(\nabla\Phi_3 \cdot \nabla)x^\perp + (x^\perp \cdot \nabla)\nabla\Phi_3] \cdot \nabla\Phi_3 \\ &= -(\nabla\Phi_3)^\perp \cdot \nabla\Phi_3 + \frac{1}{2}(x^\perp \cdot \nabla)|\nabla\Phi_3|^2 = \frac{1}{2}\operatorname{div}(x^\perp|\nabla\Phi_3|^2).\end{aligned}$$

Hence,

$$A_{3,b} = 0. \quad (3.74)$$

### Computation of $A_{i,c}$

- We use again the Blasius formula together with (3.70) and the Cauchy's residue theorem:

$$\begin{aligned}(A_{i,c})_{i=1,2} &= \int_{\partial\mathcal{S}_0} r(v_\# - \ell) \cdot (\nabla\Phi_3 - x^\perp)n \, ds \\ &= ir \left( \int_{\partial\mathcal{S}_0} (\widehat{v_\# - \ell})(\widehat{\nabla\Phi_3 + i\bar{z}}) \, dz \right)^* \\ &= ir \left( i(-\ell_1 + i\ell_2) \int_{\partial\mathcal{S}_0} \bar{z} \, dz + i\ell_1 \int_{\partial\mathcal{S}_0} \widehat{\nabla\Phi_1} \bar{z} \, dz + i\ell_2 \int_{\partial\mathcal{S}_0} \widehat{\nabla\Phi_2} \bar{z} \, dz \right)^*.\end{aligned}$$

Let us observe that

$$\begin{aligned}\int_{\partial\mathcal{S}_0} \bar{z} \, dz &= \int (\gamma_1 - i\gamma_2)(\gamma'_1 + i\gamma'_2) = \int (\gamma_1\gamma'_1 + \gamma_2\gamma'_2) + i \int (\gamma_1\gamma'_2 - \gamma_2\gamma'_1) \\ &= -i \int_{\partial\mathcal{S}_0} \begin{pmatrix} x_1 \\ x_2 \end{pmatrix} \cdot n \, ds \\ &= i \int_{\mathcal{S}_0} \operatorname{div} \begin{pmatrix} x_1 \\ x_2 \end{pmatrix} \, dx = 2i|\mathcal{S}_0|;\end{aligned} \quad (3.75)$$

$$\begin{aligned}\int_{\partial\mathcal{S}_0} |z|^2 \, dz &= \int (\gamma_1^2 + \gamma_2^2)(\gamma'_1 + i\gamma'_2) \\ &= \int_{\partial\mathcal{S}_0} \begin{pmatrix} 0 \\ x_2^2 \end{pmatrix} \cdot n \, ds - i \int_{\partial\mathcal{S}_0} \begin{pmatrix} x_1^2 \\ 0 \end{pmatrix} \cdot n \, ds \\ &= - \int_{\mathcal{S}_0} \operatorname{div} \begin{pmatrix} 0 \\ x_2^2 \end{pmatrix} \, dx + i \int_{\mathcal{S}_0} \operatorname{div} \begin{pmatrix} x_1^2 \\ 0 \end{pmatrix} \, dx \\ &= -2|\mathcal{S}_0|x_{G,2} + 2i|\mathcal{S}_0|x_{G,1}.\end{aligned} \quad (3.76)$$



Therefore, it suffices to write the value obtained in Lemma 3.22 to get:

$$\begin{aligned} (A_{i,c})_{i=1,2} &= r \left[ (-\ell_2)2|\mathcal{S}_0| - \ell_1 m_{1,2} + \ell_2(-m_{2,2} + |\mathcal{S}_0|) \right] \\ &\quad + ir \left[ \ell_1 2|\mathcal{S}_0| - \ell_1(-m_{1,1} + |\mathcal{S}_0|) + \ell_2 m_{2,1} \right], \end{aligned}$$

which can be simplified as

$$(A_{i,c})_{i=1,2} = r \left[ (\mathcal{M}_b + |\mathcal{S}_0| \mathbf{I}_2) \ell \right]^\perp. \quad (3.77)$$

- For  $i = 3$ , Lemma 3.20, (3.70) and Cauchy's residue theorem imply that

$$\begin{aligned} A_{3,c} &= \int_{\partial \mathcal{S}_0} r(v_\# - \ell) \cdot (\nabla \Phi_3 - x^\perp) K_3 ds \\ &= r \operatorname{Re} \left( \int_{\partial \mathcal{S}_0} z(\widehat{v_\#} - \ell)(\widehat{\nabla \Phi_3} + i\bar{z}) dz \right) \\ &= r \operatorname{Re} \left[ \left( -\ell_1 + i\ell_2 \right) \int_{\partial \mathcal{S}_0} (z \widehat{\nabla \Phi_3} + i|z|^2) dz \right. \\ &\quad \left. + \ell_1 i \int_{\partial \mathcal{S}_0} \widehat{\nabla \Phi_1} |z|^2 dz + \ell_2 i \int_{\partial \mathcal{S}_0} \widehat{\nabla \Phi_2} |z|^2 dz \right]. \end{aligned}$$

Now applying Lemma 3.17 to  $(|z|^2 \partial_1 \Phi_i, |z|^2 \partial_2 \Phi_i)$  we have

$$\int_{\partial \mathcal{S}_0} |z|^2 (\partial_1 \Phi_i - i \partial_2 \Phi_i) dz = \int_{\partial \mathcal{S}_0} |x|^2 \partial_\tau \Phi_i ds - i \int_{\partial \mathcal{S}_0} |x|^2 \partial_n \Phi_i ds$$

where we easily verify that

$$\int_{\partial \mathcal{S}_0} |x|^2 \partial_\tau \Phi_i ds = - \int_{\partial \mathcal{S}_0} \Phi_i 2x \cdot \tau ds = - \int_{\partial \mathcal{S}_0} \Phi_i 2(x^\perp \cdot n) ds = -2m_{i,3}.$$

The value of  $\int_{\partial \mathcal{S}_0} |x|^2 \partial_n \Phi_i ds$  has already been computed in (3.67). We therefore obtain:

$$\int_{\partial \mathcal{S}_0} |z|^2 \widehat{\nabla \Phi_i} dz = -2m_{i,3} + 2i|\mathcal{S}_0|_{x_{G,i}} \text{ for } i = 1, 2 \text{ and } \int_{\partial \mathcal{S}_0} |z|^2 \widehat{\nabla \Phi_3} dz = -2m_{3,3}.$$

Hence, we deduce from this, (3.76) and Lemma 3.22 that

$$A_{3,c} = r \left[ \begin{aligned} & -(-\ell_1)(m_{3,2} + |\mathcal{S}_0|x_{G,1} + 2|\mathcal{S}_0|x_{G,1}) \\ & \quad (-\ell_2)(m_{3,1} - |\mathcal{S}_0|x_{G,2} - 2|\mathcal{S}_0|x_{G,2}) \\ & \quad - \ell_1 2|\mathcal{S}_0|x_{G,1} - \ell_2 2|\mathcal{S}_0|x_{G,2} \end{aligned} \right],$$

so that

$$A_{3,c} = -r\ell \cdot \left( \begin{pmatrix} -m_{3,2} \\ m_{3,1} \end{pmatrix} - |\mathcal{S}_0|x_G \right). \quad (3.78)$$

**Conclusion** Gathering (3.69), (3.71)–(3.74), (3.77) and (3.78) we obtain (3.64) and (3.65). This ends the proof of Lemma 3.23.  $\square$

Let us continue with the term  $B_i$ . Let us prove the following.

**Lemma 3.24** *One has*

$$\begin{pmatrix} B_1 \\ B_2 \end{pmatrix} = -\gamma\ell^\perp + \gamma r\xi \text{ and } B_3 = -\gamma\xi \cdot \ell, \quad (3.79)$$

where  $\xi$  was defined in (3.34).

*Proof* Putting the decomposition (3.55) in the definition of  $B_i$ , we write:

$$B_i = \gamma \int_{\partial\mathcal{S}_0} (v_\# - \ell) \cdot HK_i ds + \gamma \int_{\partial\mathcal{S}_0} r(\nabla\Phi_3 - x^\perp) \cdot HK_i ds.$$

Concerning the second integral, as  $v_\# - \ell$  and  $H$  are tangent to the boundary, we apply the Blasius formula (see Lemma 3.20), then we compute by (3.70) and Cauchy's residue theorem and (3.32):

$$\begin{aligned} \left( \gamma \int_{\partial\mathcal{S}_0} (v_\# - \ell) \cdot HK_i ds \right)_{i=1,2} &= \gamma \int_{\partial\mathcal{S}_0} (v_\# - \ell) \cdot Hn ds \\ &= i\gamma \left( \int_{\partial\mathcal{S}_0} \widehat{(v_\# - \ell)} \widehat{H} dz \right)^* \\ &= i\gamma \left( (-\ell_1 + i\ell_2) \int_{\partial\mathcal{S}_0} \widehat{H} dz \right)^* \\ &= i\gamma \left( (-\ell_1 + i\ell_2) \right)^* \\ &= -\gamma\ell^\perp. \end{aligned}$$

For  $i = 3$ , we compute by Lemma 3.20 and the Cauchy's residue theorem that

$$\begin{aligned} \gamma \int_{\partial S_0} (v_{\#} - \ell) \cdot HK_3 ds &= \gamma \operatorname{Re} \left( \int_{\partial S_0} z \widehat{(v_{\#} - \ell)} \widehat{H} dz \right) \\ &= \gamma \operatorname{Re} \left( (-\ell_1 + i\ell_2) \int_{\partial S_0} z \widehat{H} dz \right) \\ &= \gamma \operatorname{Re} \left( (-\ell_1 + i\ell_2) (\xi_1 + i\xi_2) \right) \\ &= -\gamma \ell \cdot \xi. \end{aligned}$$

For the last term, we use that  $\nabla \Phi_3 - x^\perp$  and  $H$  are tangent to the boundary, and we write by Lemma 3.20 and by the Cauchy's residue theorem:

$$\begin{aligned} \left( \gamma r \int_{\partial S_0} (\nabla \Phi_3 - x^\perp) \cdot HK_i ds \right)_{i=1,2} &= i\gamma r \left( \int_{\partial S_0} \widehat{(\nabla \Phi_3 - x^\perp)} \widehat{H} dz \right)^* \\ &= i\gamma r \left( i \int_{\partial S_0} \bar{z} \widehat{H} dz \right)^* \\ &= \gamma r \left( \int_{\partial S_0} \bar{z} \widehat{H} dz \right)^* = \gamma r \xi, \end{aligned}$$

where we have used that  $\widehat{-x^\perp} = i\bar{z}$  and

$$\left( \int_{\partial S_0} \bar{z} \widehat{H} dz \right)^* = \int_{\partial S_0} z \widehat{H} dz, \quad (3.80)$$

the latter being easily shown by using a parametrization. For  $i = 3$ , we have that:

$$\begin{aligned} \gamma r \int_{\partial S_0} (\nabla \Phi_3 - x^\perp) \cdot HK_3 ds &= \gamma r \operatorname{Re} \left( \int_{\partial S_0} z \widehat{(\nabla \Phi_3 - x^\perp)} \widehat{H} dz \right) \\ &= \gamma r \operatorname{Re} \left( i \int_{\partial S_0} \bar{z} \widehat{H} dz \right) = 0, \end{aligned}$$

which can also be shown by using a parametrization. Gathering the equalities above yields (3.79). This ends the proof of Lemma 3.24.  $\square$

We now turn to  $C_i$  (see (3.63)). From Lemma 3.20, (3.32) and Cauchy's Residue Theorem, we deduce that

$$C_1 = C_2 = C_3 = 0. \quad (3.81)$$

Indeed, we can verify that  $\int_{\partial S_0} z(\widehat{H})^2 dz = -i/(2\pi)$  is purely imaginary.

Plugging (3.64), (3.65), (3.79) and (3.81) in (3.61) and using that for any  $p_a := (\ell_a, \omega_a)$  and  $p_b := (\ell_b, \omega_b)$  in  $\mathbb{R}^2 \times \mathbb{R}$ ,  $p_a \times p_b = (\omega_a \ell_b^\perp - \omega_b \ell_a^\perp, \ell_a^\perp \cdot \ell_b)$ , yields (3.45). This ends the complex-analytic proof of Theorem 3.18.

### 3.2.5 A Real-Analytic Proof of Theorem 3.18

We now consider another approach which dates back to Lamb. We therefore go back to Lemma 3.19 and provide an alternative real-analytic end of the proof of Theorem 3.18. Of crucial importance is the following identity which we will use instead of Blasius’ lemma though to different terms.

Let

$$\zeta_1(x) := e_1, \quad \zeta_2(x) := e_2 \quad \text{and} \quad \zeta_3(x) := x^\perp.$$

denote the elementary rigid velocities. The following lemma seems to originate from Lamb’s work.

**Lemma 3.25** *For any pair of vector fields  $(u, v)$  in  $C^\infty(\overline{\mathbb{R}^2 \setminus \mathcal{S}_0}; \mathbb{R}^2)$  satisfying*

- $\operatorname{div} u = \operatorname{div} v = \operatorname{curl} u = \operatorname{curl} v = 0$ ,
- $u(x) = O(1/|x|)$  and  $v(x) = O(1/|x|)$  as  $|x| \rightarrow +\infty$ ,

one has, for any  $i = 1, 2, 3$ ,

$$\int_{\partial \mathcal{S}_0} (u \cdot v) K_i ds = \int_{\partial \mathcal{S}_0} \zeta_i \cdot \left( (u \cdot n)v + (v \cdot n)u \right) ds. \tag{3.82}$$

*Proof of Lemma 3.25* Let us start with the case where  $i = 1$  or  $2$ . Then

$$\int_{\partial \mathcal{S}_0} (u \cdot v) K_i ds = \int_{\partial \mathcal{S}_0} ((u \cdot v)\zeta_i) \cdot n ds = \int_{\mathbb{R}^2 \setminus \mathcal{S}_0} \operatorname{div} ((u \cdot v)\zeta_i) dx, \tag{3.83}$$

by using that  $u(x) = O(1/|x|)$  and  $v(x) = O(1/|x|)$  when  $|x| \rightarrow +\infty$ . Therefore

$$\int_{\partial \mathcal{S}_0} (u \cdot v) K_i ds = \int_{\mathbb{R}^2 \setminus \mathcal{S}_0} \zeta_i \cdot \nabla(u \cdot v) dx = \int_{\mathbb{R}^2 \setminus \mathcal{S}_0} \zeta_i \cdot (u \cdot \nabla v + v \cdot \nabla u) dx, \tag{3.84}$$

using that  $\operatorname{curl} u = \operatorname{curl} v = 0$ . Now, integrating by parts, using that  $\operatorname{div} u = \operatorname{div} v = 0$  and once again that  $u(x) = O(1/|x|)$  and  $v(x) = O(1/|x|)$  as  $|x| \rightarrow +\infty$ , we obtain (3.82) when  $i = 1$  or  $2$ .

We now tackle the case where  $i = 3$ . We follow the same lines as above, with two precisions. First we observe that there is no contribution at infinity in (3.83) and (3.84) when  $i = 3$  as well. Indeed  $\zeta_3$  and the normal to a centered circle are orthogonal. Moreover there is no additional distributed term coming from the

integration by parts in (3.84) when  $i = 3$  since

$$\int_{\mathbb{R}^2 \setminus \mathcal{S}_0} v \cdot (u \cdot \nabla_x \zeta_i) + u \cdot (v \cdot \nabla_x \zeta_i) \, dx = \int_{\mathbb{R}^2 \setminus \mathcal{S}_0} (v \cdot u^\perp + u \cdot v^\perp) \, dx = 0.$$

□

As a consequence, using Lamb's lemma and the boundary conditions (3.40) we obtain for any  $i = 1, 2, 3$ ,

$$\begin{aligned} \frac{1}{2} \int_{\partial \mathcal{S}_0} |v|^2 K_i \, ds &= \int_{\partial \mathcal{S}_0} (v \cdot n)(v \cdot \zeta_i) \, ds \\ &= \int_{\partial \mathcal{S}_0} ((\ell + rx^\perp) \cdot n)(v \cdot \zeta_i) \, ds \\ &= \int_{\partial \mathcal{S}_0} ((\ell + rx^\perp) \cdot n)(v \cdot n) K_i \, ds \\ &\quad + \int_{\partial \mathcal{S}_0} ((\ell + rx^\perp) \cdot n)(v \cdot \tau)(\zeta_i \cdot \tau) \, ds \end{aligned}$$

so that the right hand side of (3.49) can be recast as follows:

$$\begin{aligned} &\frac{1}{2} \int_{\partial \mathcal{S}_0} |v|^2 K_i \, ds - \int_{\partial \mathcal{S}_0} (\ell + rx^\perp) \cdot v K_i \, ds \\ &= - \int_{\partial \mathcal{S}_0} ((\ell + rx^\perp) \cdot \tau)(v \cdot \tau) K_i \, ds + \int_{\partial \mathcal{S}_0} ((\ell + rx^\perp) \cdot n)(v \cdot \tau)(\zeta_i \cdot \tau) \, ds \\ &= \sum_k p_k \int_{\partial \mathcal{S}_0} (v \cdot \tau)[(\zeta_i \cdot \tau) K_k - (\zeta_k \cdot \tau) K_i] \, ds, \end{aligned}$$

for any  $i = 1, 2, 3$ , where the sum runs for  $k$  over  $1, 2, 3$  and  $p = (\ell, r)^T$ .

### Computation of the Brackets

We now compute the brackets  $[(\zeta_i \cdot \tau) K_k - (\zeta_k \cdot \tau) K_i]$ , for  $i, k = 1, 2, 3$ , in order to make explicit the previous integrals.

- For  $i = 1$ , we therefore obtain that

$$\begin{aligned} &\frac{1}{2} \int_{\partial \mathcal{S}_0} |v|^2 K_i \, ds - \int_{\partial \mathcal{S}_0} (\ell + rx^\perp) \cdot v K_i \, ds = \\ &p_2 \int_{\partial \mathcal{S}_0} (v \cdot \tau)[(\zeta_1 \cdot \tau) K_2 - (\zeta_2 \cdot \tau) K_1] \, ds \\ &+ p_3 \int_{\partial \mathcal{S}_0} (v \cdot \tau)[(\zeta_1 \cdot \tau) K_3 - (\zeta_3 \cdot \tau) K_1] \, ds. \end{aligned}$$

Using that

$$\begin{aligned} (\zeta_1 \cdot \tau)K_2 - (\zeta_2 \cdot \tau)K_1 &= (\zeta_1 \cdot \tau)(\zeta_2 \cdot n) - (\zeta_2 \cdot \tau)(\zeta_1 \cdot n) \\ &= (\zeta_2 \cdot n)^2 + (\zeta_2 \cdot \tau)^2 \\ &= 1 \end{aligned}$$

and

$$\begin{aligned} (\zeta_1 \cdot \tau)(\zeta_3 \cdot n) - (\zeta_3 \cdot \tau)(\zeta_1 \cdot n) &= (\zeta_2 \cdot n)(\zeta_3 \cdot n) + (\zeta_3 \cdot \tau)(\zeta_2 \cdot \tau) \\ &= \zeta_2 \cdot \zeta_3, \end{aligned}$$

we infer, using the decomposition (3.53) and (3.35), that

$$\begin{aligned} \frac{1}{2} \int_{\partial S_0} |v|^2 K_i ds - \int_{\partial S_0} (\ell + rx^\perp) \cdot v K_i ds &= \gamma \ell_2 + \gamma r \zeta_2 \cdot \xi^\perp \\ &+ r \sum_{j=1}^3 p_j \zeta_2 \cdot \int_{\partial S_0} (\nabla \Phi_j \cdot \tau) x^\perp ds. \end{aligned}$$

- For  $i = 2$ ,

$$\begin{aligned} \frac{1}{2} \int_{\partial S_0} |v|^2 K_i ds - \int_{\partial S_0} (\ell + rx^\perp) \cdot v K_i ds &= \\ p_1 \int_{\partial S_0} (v \cdot \tau) [(\zeta_2 \cdot \tau)K_1 - (\zeta_1 \cdot \tau)K_2] ds & \\ + p_3 \int_{\partial S_0} (v \cdot \tau) [(\zeta_2 \cdot \tau)K_3 - (\zeta_3 \cdot \tau)K_2] ds & \end{aligned}$$

But

$$(\zeta_2 \cdot \tau)K_1 - (\zeta_1 \cdot \tau)K_2 = -(\zeta_2 \cdot \tau)^2 - (\zeta_1 \cdot \tau)^2 = -1,$$

and

$$(\zeta_2 \cdot \tau)K_3 - (\zeta_3 \cdot \tau)K_2 = -(\zeta_1 \cdot n)(\zeta_3 \cdot n) - (\zeta_3 \cdot \tau)(\zeta_1 \cdot \tau) = -\zeta_1 \cdot \zeta_3,$$

so that

$$\begin{aligned} \frac{1}{2} \int_{\partial S_0} |v|^2 K_i ds - \int_{\partial S_0} (\ell + rx^\perp) \cdot v K_i ds &= -\gamma \ell_1 - \gamma r \zeta_1 \cdot \xi^\perp \\ &- r \sum_{j=1}^3 p_j \zeta_1 \cdot \int_{\partial S_0} (\nabla \Phi_j \cdot \tau) x^\perp ds. \end{aligned}$$

Moreover, by an integration by parts,

$$\int_{\partial S_0} (\nabla \Phi_j \cdot \tau) x^\perp ds = - \int_{\partial S_0} \Phi_j \cdot n ds = - \left( \int_{\partial S_0} \Phi_j \partial_n \Phi_i ds \right)_i = - (m_{ij})_i,$$

where  $i$  runs over 1, 2, so that

$$\begin{aligned} - \left( \frac{1}{2} \int_{\partial S_0} |v|^2 K_i ds - \int_{\partial S_0} (\ell + rx^\perp) \cdot v K_i ds \right)_{i=1,2} &= -r (\mathcal{M}^b \ell + r \begin{pmatrix} m_{1,3} \\ m_{2,3} \end{pmatrix})^\perp \\ &\quad + \gamma (\ell^\perp - r\xi). \end{aligned}$$

- Proceeding in the same way for  $i = 3$  and using the definitions (3.42) and (3.43) we finally arrive at (3.45). This ends the real-analytic proof of Theorem 3.18.

### 3.2.6 Zero Radius Limit

We now assume that, for every  $\varepsilon \in (0, 1]$ , the domain occupies (3.5) and for every  $q = (h, \theta) \in \mathbb{R}^3$ ,

$$S^\varepsilon(q) := R(\theta)S_0^\varepsilon + h \text{ and } \mathcal{F}^\varepsilon(q) = \mathbb{R}^2 \setminus \bar{S}^\varepsilon(q). \tag{3.85}$$

We will treat at once both the massive and massless cases. The following statement implies Theorem 3.4.

**Theorem 3.26** *Let a rescaled initial domain  $S_0$  occupied by the body, some initial solid translation and rotation velocities  $(\ell_0, r_0)$  and a circulation  $\gamma$  in  $\mathbb{R}$  in the case of a massive particle and in  $\mathbb{R}^*$  in the case of a massless particle, all independent of  $\varepsilon$ . Let, for each  $\varepsilon > 0$ , the solution  $h^\varepsilon$  associated with an initial solid domain  $S_0^\varepsilon$  defined by (3.5) with the inertia scaling described in Definition 3.1, and initial data  $q(0) = 0$  and  $q'(0) = (\ell_0, r_0)$ , given by Proposition 3.14. Then for all  $T > 0$ , as  $\varepsilon \rightarrow 0$  one has in the case of massive particle (respectively massless particle)  $h^\varepsilon \rightharpoonup h$  in  $W^{2,\infty}([0, T]; \mathbb{R}^2)$  weak- $\star$  (resp.  $W^{1,\infty}([0, T]; \mathbb{R}^2)$  weak- $\star$ ) and  $\varepsilon\theta^\varepsilon \rightharpoonup 0$  in  $W^{2,\infty}([0, T]; \mathbb{R})$  weak- $\star$  (resp.  $W^{1,\infty}([0, T]; \mathbb{R})$  weak- $\star$ ). Moreover the limit time-dependent vector  $h$  satisfies the equations  $mh'' = \gamma(h')^\perp$  (resp.  $h' = 0$ ).*

*Proof* In order to compare the influence of the circulation and of the solid velocity on the dynamics in the zero-radius limit we first consider the harmonic field  $H^\varepsilon$  and the Kirchhoff potentials  $(\nabla \Phi_i^\varepsilon)_{i=1,2,3}$  associated with the rigid body  $S^\varepsilon(0)$  as the harmonic field  $H$  and the Kirchhoff potentials  $(\nabla \Phi_i)_{i=1,2,3}$  were associated with the rigid body  $S_0$  in Sect. 3.2.2. They satisfy the following scaling law  $H^\varepsilon(x) = \varepsilon^{-1}H(x/\varepsilon)$ , whereas the Kirchhoff potentials obey:  $\Phi_i^\varepsilon(x) = \varepsilon \Phi_i^1(x/\varepsilon)$  for  $i = 1, 2$ ,  $\Phi_3^\varepsilon(x) = \varepsilon^2 \Phi_3^1(x/\varepsilon)$ . Therefore the harmonic field  $H^\varepsilon$  is more singular than the Kirchhoff potentials  $\nabla \Phi_i^\varepsilon(x)$  in the vanishingly small limit. On the other hand we

deduce that the added inertia is given by the following matrix

$$\mathcal{M}_{a,\theta}^\varepsilon = \varepsilon^2 I_\varepsilon \mathcal{M}_{a,\theta} I_\varepsilon, \quad (3.86)$$

where  $I_\varepsilon$  is the diagonal matrix  $I_\varepsilon := \text{diag}(1, 1, \varepsilon)$ . This has to be compared with the genuine inertia matrix which, according to Definition 3.1, scales as follows:

$$\mathcal{M}_g^\varepsilon := \text{diag}(m^\varepsilon, m^\varepsilon, \mathcal{J}^\varepsilon) = \varepsilon^\alpha I_\varepsilon \mathcal{M}_g I_\varepsilon, \quad (3.87)$$

where the matrix  $\mathcal{M}_g$  is given in terms of  $m > 0$  and  $\mathcal{J} > 0$  by (3.18). Recall that  $\alpha > 0$ ,  $m > 0$  and  $\mathcal{J} > 0$  are defined in Definition 3.1 and fixed independent of  $\varepsilon$ .

Two remarks are in order.

- First we observe from the comparison of (3.86) and (3.87) that the physical case  $\alpha = 2$  appears as critical.
- Secondly because of the matrix  $I_\varepsilon$  in the right hand sides of the two inertia matrices  $\mathcal{M}_g^\varepsilon$  and  $\mathcal{M}_{a,\theta}^\varepsilon$ , it is natural to introduce the vector  $p^\varepsilon = ((h^\varepsilon)', \varepsilon(\theta^\varepsilon)')^t$ . Hence the natural counterpart to  $(h^\varepsilon)'$  for what concerns the angular velocity is rather  $\varepsilon(\theta^\varepsilon)'$  than  $(\theta^\varepsilon)'$ . This can also be seen on the boundary condition (3.91d): when  $x$  belongs to  $\partial\mathcal{S}^\varepsilon(t)$ , the term  $(\theta^\varepsilon)'(x - h^\varepsilon)^\perp$  is of order  $\varepsilon(\theta^\varepsilon)'$  and is added to  $(h^\varepsilon)'$ .

Examining how the other terms scale with  $\varepsilon$  one obtains:

$$(\varepsilon^\alpha \mathcal{M}_g + \varepsilon^2 \mathcal{M}_{a,\theta^\varepsilon})(p^\varepsilon)' + \varepsilon \langle \Gamma_{a,\theta^\varepsilon}, p^\varepsilon, p^\varepsilon \rangle = \gamma p^\varepsilon \times B_{\theta^\varepsilon}. \quad (3.88)$$

The energy associated with this scaling is twice  $(\varepsilon^\alpha \mathcal{M}_g + \varepsilon^2 \mathcal{M}_{a,\theta^\varepsilon})p^\varepsilon \cdot p^\varepsilon$  and its conservation provides that  $p^\varepsilon$  is bounded uniformly with respect to  $\varepsilon$  on the time interval  $[0, +\infty)$ , whatever is  $\alpha$ . Now our goal is to pass to the limit in (3.88). Let  $T > 0$ . Computing the right-hand-side of (3.88) gives

$$(\varepsilon^\alpha \mathcal{M}_g + \varepsilon^2 \mathcal{M}_{a,\theta^\varepsilon})(p^\varepsilon)' + \varepsilon \langle \Gamma_{a,\theta^\varepsilon}, p^\varepsilon, p^\varepsilon \rangle = \gamma \begin{pmatrix} ((h^\varepsilon)')^\perp - \varepsilon(\theta^\varepsilon)'R(\theta^\varepsilon)\xi \\ R(\theta^\varepsilon)\xi \cdot (h^\varepsilon)' \end{pmatrix}. \quad (3.89)$$

We start with the massive case for which  $\alpha = 0$ . Using the equation we deduce some uniform  $W^{2,\infty}$  bounds on  $h_\varepsilon$  and  $\varepsilon\theta^\varepsilon$  and this entails the existence of a subsequence of  $(h^\varepsilon, \varepsilon\theta^\varepsilon)$  converging to  $(h, \Theta)$  in  $W^{2,\infty}$  weak- $\star$ . Moreover the left hand side of (3.89) (with  $\alpha = 0$ ) converges to  $\mathcal{M}_g(h'', \Theta'')^t$  in  $L^\infty$  weak- $\star$ , and using that

$$\varepsilon(\theta^\varepsilon)'R(\theta^\varepsilon)\xi = \varepsilon(R(\theta^\varepsilon) - \pi/2)\xi' \quad (3.90)$$

converges in  $W^{-1,\infty}$  weak- $\star$  up to a subsequence and that the weak- $\star$  convergence in  $W^{2,\infty}$  entails the strong  $W^{1,\infty}$  one, we get from the two first lines of (3.89) that  $mh'' = \gamma(h')^\perp$  and  $(h(0), h'(0)) = (0, \ell_0)$ . In order to prove that  $\Theta = 0$  one may use a stationary phase argument, cf. Lemma 10 in [8] for more on this.



In the massless case, that is when  $\alpha > 0$ , a few modifications in the arguments are in order. First, thanks to the energy estimate,  $\varepsilon \mathcal{M}_{a, \theta^\varepsilon}$  is bounded in  $W^{1, \infty}$  and since  $\mathcal{M}_g$  is constant and  $(p^\varepsilon)'$  is bounded uniformly with respect to  $\varepsilon$  in  $W^{-1, \infty}$ , we can conclude that the left hand side of (3.89) converges to 0 in  $W^{-1, \infty}$  due to the extra powers of  $\varepsilon$ . Next, concerning the right hand side, the term  $\varepsilon \langle \Gamma_{a, \theta^\varepsilon}, (p^\varepsilon), (p^\varepsilon) \rangle$  converges to 0 in  $L^\infty$  since the terms inside the brackets are bounded. As before the last term in the two first lines of Eq. (3.89), converges weakly to 0 in  $W^{-1, \infty}$ . Hence we infer that  $(h^\varepsilon)'$  converges weakly- $\star$  to 0 in  $W^{-1, \infty}$ . Due to the a priori estimate, this convergences occurs in  $L^\infty$  weak- $\star$ . Again this is sufficient to deduce the strong convergence of  $h^\varepsilon$  towards some  $h$  in  $L^\infty$ , and that  $h' = 0$  and  $h(0) = 0$ . This concludes the proof of Theorem 3.26.  $\square$

### 3.3 Case of a Bounded Domain

We consider now the case where the system fluid-solid occupies a bounded open regular connected and simply connected domain  $\Omega$  of  $\mathbb{R}^2$ . We assume that the body initially occupies the closed domain  $\mathcal{S}_0 \subset \Omega$ , so that the domain of the fluid is  $\mathcal{F}_0 = \Omega \setminus \mathcal{S}_0$  at the initial time, and (without loss of generality) that the center of mass of the solid coincides at the initial time with the origin and that  $0 \in \Omega$ . Let be given the initial solid translation and rotation velocities  $(\ell_0, r_0)$  in  $\mathbb{R}^2 \times \mathbb{R}$ , the circulation  $\gamma$  in  $\mathbb{R}$ , and  $u_0$  the associated compatible initial fluid velocity (according to Definition 3.5). We therefore still consider the case without any initial vorticity that it follows from Definition 3.5 that the initial fluid velocity  $u_0$  is assumed to satisfy  $\text{curl } u_0 = 0$  in  $\mathcal{F}_0$ . The domain of the fluid is denoted by  $\mathcal{F}(t) = \Omega \setminus \mathcal{S}(t)$  at time  $t > 0$ . The fluid-solid system is governed by the following set of coupled equations:

$$\frac{\partial u}{\partial t} + (u \cdot \nabla)u + \nabla \pi = 0 \quad \text{in } \mathcal{F}(t), \quad (3.91a)$$

$$\text{div } u = 0 \quad \text{in } \mathcal{F}(t), \quad (3.91b)$$

$$mh'' = \int_{\partial \mathcal{S}(t)} \pi n \, ds \quad \text{and} \quad \mathcal{J}\theta'' = \int_{\partial \mathcal{S}(t)} (x - h(t))^\perp \cdot \pi n \, ds, \quad (3.91c)$$

$$u \cdot n = (\ell + r(\cdot - h)^\perp) \cdot n \quad \text{on } \partial \mathcal{S}(t), \quad (3.91d)$$

$$u \cdot n = 0 \quad \text{on } \partial \Omega, \quad (3.91e)$$

$$u_{t=0} = u_0 \quad \text{in } \mathcal{F}_0 \quad \text{and} \quad (h, h', \theta, \theta')(0) = (0, \ell_0, 0, r_0). \quad (3.91f)$$

Here again on the one hand the fluid velocity remains irrotational for every time, that is

$$\text{curl } u(t, \cdot) = 0 \quad \text{in } \mathcal{F}(t), \quad (3.92)$$

according to Helmholtz's theorem and on the other hand the circulation around the body is constant in time equal to  $\gamma$  according to Kelvin's theorem. Since the domains  $\mathcal{S}(t)$  and  $\mathcal{F}(t)$  depend on  $q := (h, \theta) \in \mathbb{R}^3$ . Only, we shall rather denote them  $\mathcal{S}(q)$  and  $\mathcal{F}(q)$  in the sequel. Since we will not consider any collision here, we introduce:  $\mathcal{Q} := \{q \in \mathbb{R}^3 : d(\mathcal{S}(q), \partial\Omega) > 0\}$ , where  $d(A, B)$  denotes for two sets  $A$  and  $B$  in the plane that is  $d(A, B) := \min \{|x - y|_{\mathbb{R}^2}, x \in A, y \in B\}$ . Above the notation stands  $|\cdot|_{\mathbb{R}^d}$  for the Euclidean norm in  $\mathbb{R}^d$ . Since  $\mathcal{S}_0$  is a closed subset in the open set  $\Omega$  the initial position  $q(0) = 0$  of the solid belongs to  $\mathcal{Q}$ .

As in the unbounded case of the previous section, our analysis here will rely on a reformulation of the system above as an second-order differential ODE for  $q$  together with an auxiliary div-curl type system for the fluid velocity. Indeed, here again, the solid drives the dynamics of the coupled system as a consequence of the added inertia phenomenon. However in the case where the system occupies a bounded domain the matrix  $\mathcal{M}_a$  encoding the added inertia depends not only on  $\theta$  but on the three components of  $q$ . We therefore extend Definition 3.11 to this new setting.

**Definition 3.27 (a-Connection)** Given a  $C^\infty$  mapping  $q \in \mathcal{Q} \mapsto \mathcal{M}_a(q) \in \mathcal{S}_3^+(\mathbb{R})$ , we say that the  $C^\infty$  mapping  $q \in \mathcal{Q} \mapsto \Gamma_a(q) \in \mathcal{BL}(\mathbb{R}^3 \times \mathbb{R}^3; \mathbb{R}^3)$  is the a-connection associated with this mapping if for any  $p \in \mathbb{R}^3$ ,

$$\langle \Gamma_a(q), p, p \rangle := \left( \sum_{1 \leq i, j \leq 3} (\Gamma_a(q))_{i,j}^k p_i p_j \right)_{1 \leq k \leq 3} \in \mathbb{R}^3, \quad (3.93)$$

with for every  $i, j, k \in \{1, 2, 3\}$ ,

$$(\Gamma_a(q))_{i,j}^k(q) := \frac{1}{2} \left( (\mathcal{M}_a(q))_{k,j}^i + (\mathcal{M}_a(q))_{k,i}^j - (\mathcal{M}_a(q))_{i,j}^k \right)(q), \quad (3.94)$$

where  $(\mathcal{M}_a(q))_{i,j}^k$  denotes the partial derivative with respect to  $q_k$  of the entry of indexes  $(i, j)$  of the matrix  $\mathcal{M}_a(q)$ , that is

$$(\mathcal{M}_a(q))_{i,j}^k := \frac{\partial (\mathcal{M}_a(q))_{i,j}}{\partial q_k}. \quad (3.95)$$

Remark 3.13 is still in order for the definition above.

### 3.3.1 Reduction to an ODE in the Case Where $\gamma = 0$ : Munnier's Theorem

Let us start with the case where the circulation  $\gamma$  is zero. Then the initial fluid velocity and therefore the velocity at any time is potential (that is a gradient globally

on  $\mathcal{F}(q)$ ). The following result was proven surprisingly only recently, by Munnier in [24]. This result consists in a reformulation of the system (3.91) in terms of an ordinary differential equation for the motion of the rigid body which corresponds to geodesics associated with the Riemann metric induced on  $\mathcal{Q}$  by the matrix  $\mathcal{M}_g + \mathcal{M}_a(q)$ , where we recall that  $\mathcal{M}_g$  is the genuine inertia defined in Definition 3.18. This reformulation therefore establishes an equivalence of the Newtonian and the Lagrangian points of view in the potential case.

**Theorem 3.28** *Let be given the open regular connected and simply connected bounded cavity  $\Omega$ , the initial closed domain  $\mathcal{S}_0 \subset \Omega$  occupied by the body, the initial solid translation and rotation velocities  $(\ell_0, r_0)$  in  $\mathbb{R}^2 \times \mathbb{R}$ . Assume that the circulation  $\gamma$  is 0. Let  $u_0$  be the associated compatible initial fluid velocity according to Definition 3.5. Then there exists a  $C^\infty$  mapping  $q \in \mathcal{Q} \mapsto \mathcal{M}_a(q) \in \mathcal{S}_3^+(\mathbb{R})$ , depending only on  $\mathcal{S}_0$  and  $\Omega$ , such that up to the first collision, System (3.91) is equivalent to the second order differential equation:*

$$(\mathcal{M}_g + \mathcal{M}_a(q))q'' + \langle \Gamma_a(q), q', q' \rangle = 0,$$

with Cauchy data  $q(0) = 0 \in \mathcal{Q}$ ,  $q'(0) = (\ell_0, r_0) \in \mathbb{R}^2 \times \mathbb{R}$ , where  $\Gamma_a$  is the  $a$ -connection associated with  $\mathcal{M}_a$  by Definition 3.27. For any  $q \in \mathcal{Q}$  the fluid velocity  $u(q, \cdot)$  is the unique solution of the div-curl type system in the doubly-connected domain  $\mathcal{F}(q)$ , constituted of (3.91b), (3.92), (3.91d), (3.91e), together with the prescription of zero circulation.

Indeed we are going to provide a quite explicit expression of  $\mathcal{M}_a(q)$ . Consider the functions  $\zeta_j$ , for  $j = 1, 2, 3$ , defined for  $q = (h, \theta) \in \mathcal{Q}$  and  $x \in \mathcal{F}(q)$ , by the formula  $\zeta_j(q, x) := e_j$ , for  $j = 1, 2$  and  $\zeta_3(q, x) := (x - h)^\perp$ . Above  $e_1$  and  $e_2$  are the unit vectors of the canonical basis. We introduce  $\Phi := (\Phi_1, \Phi_2, \Phi_3)'$  where the Kirchhoff's potentials  $\Phi_j(q, \cdot)$ , for  $j = 1, 2, 3$ , are the unique (up to an additive constant) solutions in  $\mathcal{F}(q)$  of the following Neumann problem:

$$\Delta \Phi_j = 0 \text{ in } \mathcal{F}(q), \quad \frac{\partial \Phi_j}{\partial n}(q, \cdot) = n \cdot \zeta_j(q, \cdot) \text{ on } \partial \mathcal{S}(q), \quad \frac{\partial \Phi_j}{\partial n}(q, \cdot) = 0 \text{ on } \partial \Omega. \tag{3.96}$$

We can now define the added inertia

$$\mathcal{M}_a(q) := \int_{\partial \mathcal{S}(q)} \Phi(q, \cdot) \otimes \frac{\partial \Phi}{\partial n}(q, \cdot) ds = \left( \int_{\mathcal{F}(q)} \nabla \Phi_i \cdot \nabla \Phi_j dx \right)_{1 \leq i, j \leq 3}. \tag{3.97}$$

The added inertia matrix  $\mathcal{M}_a(q)$  is symmetric positive-semidefinite.

### 3.3.2 Proof of Munnier's Result: Theorem 3.28

The first step of the proof of Theorem 3.28 consists in a trade of the fluid pressure against the fluid velocity and its first order derivatives in the body's dynamics.

Indeed we start with the observation that Eqs. (3.91c) can be summarized in the variational form:

$$mh'' \cdot \ell^* + \mathcal{J}\theta'' r^* = \int_{\partial S(q)} \pi(r^*(x-h)^\perp + \ell^*) \cdot nds, \quad \forall p^* = (\ell^*, r^*) \in \mathbb{R}^3. \quad (3.98)$$

Let us associate with  $(q, p^*) \in \mathcal{Q} \times \mathbb{R}^3$ , with  $p^* = (p_1^*, p_2^*, p_3^*)$ , the potential vector field

$$u^* := \nabla(\Phi(q, \cdot) \cdot p^*) = \nabla\left(\sum_{j=1}^3 \Phi_j(q, \cdot) p_j^*\right), \quad (3.99)$$

which is defined on  $\mathcal{F}(q)$ . The pressure  $\pi$  can be recovered by means of Bernoulli's formula which is obtained by combining (3.91a) and (3.92), and which reads:

$$\nabla\pi = -\left(\frac{\partial u}{\partial t} + \frac{1}{2}\nabla(u^2)\right) \quad \text{in } \mathcal{F}(q). \quad (3.100)$$

According to Bernoulli's formula (3.100) and upon an integration by parts, identity (3.98) can be turned into:

$$mh'' \cdot \ell^* + \mathcal{J}\theta'' r^* = -\int_{\mathcal{F}(q)} \left(\frac{\partial u}{\partial t} + \frac{1}{2}\nabla(u^2)\right) \cdot u^* dx, \quad \forall p^* = (\ell^*, r^*) \in \mathbb{R}^3. \quad (3.101)$$

So far we have only used that the fluid velocity  $u$  is irrotational. Let us now use that it is potential and therefore reads as  $u = u_1$  with  $u_1$  as follows:

$$u_1(q, \cdot) := \nabla(\Phi(q, \cdot) \cdot q') = \nabla\left(\sum_{j=1}^3 \Phi_j(q, \cdot) q_j'\right), \quad (3.102)$$

where  $q \in \mathcal{Q}$ . For any  $q \in \mathcal{Q}$  this vector field  $u_1(q, \cdot)$  is the only solution to the div-curl type system in the doubly-connected domain  $\mathcal{F}(q)$ , constituted of (3.91b), (3.92), (3.91d), (3.91e), together with the prescription of zero circulation. Observe that besides the dependence with respect to  $\mathcal{S}_0$ , to  $\Omega$  and to the space variable,  $u_1$  depends on  $q$  and linearly on  $q'$ .

Then Theorem 3.28 will follow from the following lemma.

**Lemma 3.29** *For any smooth curve  $q(t)$  in  $\mathcal{Q}$  and every  $p^* = (\ell^*, r^*) \in \mathbb{R}^3$ , the following identity holds:*

$$\begin{aligned} mh'' \cdot \ell^* + \mathcal{J}\theta'' r^* + \int_{\mathcal{F}(q)} \left(\frac{\partial u_1}{\partial t} + \frac{1}{2}\nabla|u_1|^2\right) \cdot u^* dx \\ = (\mathcal{M}_g + \mathcal{M}_a(q))q'' \cdot p^* + \langle \Gamma_a(q), q', q' \rangle \cdot p^*, \end{aligned} \quad (3.103)$$

where  $u^*$  is given by (3.99),  $u_1$  is given by (3.102),  $\mathcal{M}_a(q)$  and  $\Gamma_a(q)$  are defined in (3.97) and Definition 3.27.

*Proof of Lemma 3.29* We start with observing that, under the assumptions of Lemma 3.29,

$$mh'' \cdot \ell^* + \mathcal{J}\theta''r^* = \mathcal{M}_g q'' \cdot p^*. \tag{3.104}$$

Now in order to deal with the last term of the left hand side of (3.103) we use a Lagrangian strategy. For any  $q$  in  $\mathcal{Q}$  and every  $p = (p_1, p_2, p_3)$  in  $\mathbb{R}^3$ , let us denote

$$\mathcal{E}_1(q, p) := \frac{1}{2} \int_{\mathcal{F}(q)} |\nabla(\Phi(q, \cdot) \cdot p)|^2 dx. \tag{3.105}$$

Thus  $\mathcal{E}_1(q, p)$  denotes of the kinetic energy of the potential part of the flow associated with a body at position  $q$  with velocity  $p$ . It follows from classical shape derivative theory that  $\mathcal{E}_1 \in C^\infty(\mathcal{Q} \times \mathbb{R}^3; [0, +\infty))$ .

**Lemma 3.30** *For any smooth curve  $t \mapsto q(t)$  in  $\mathcal{Q}$ , for every  $p^* \in \mathbb{R}^3$ , we have:*

$$\int_{\mathcal{F}(q)} \left( \frac{\partial u_1}{\partial t} + \frac{1}{2} \nabla |u_1|^2 \right) \cdot u^* dx = \mathcal{E}\mathcal{L} \tag{3.106}$$

where  $u_1$  is given by (3.128),  $u^*$  is given by (3.99) and  $\mathcal{E}\mathcal{L}$  denotes the time-dependent smooth real-valued function:

$$\mathcal{E}\mathcal{L} := \left( \frac{d}{dt} \left( \frac{\partial \mathcal{E}_1}{\partial p}(q(t), q'(t)) \right) - \frac{\partial \mathcal{E}_1}{\partial q}(q(t), q'(t)) \right) \cdot p^*. \tag{3.107}$$

The name of the function  $\mathcal{E}\mathcal{L}$  refers to Euler and Lagrange. For sake of simplicity below we will simply denote

$$\mathcal{E}\mathcal{L} = \left( \frac{d}{dt} \frac{\partial \mathcal{E}_1}{\partial p} - \frac{\partial \mathcal{E}_1}{\partial q} \right) \cdot p^*.$$

Let us also introduce a slight abuse of notations which simplifies the presentation of the proof of Lemma 3.30. For a smooth function  $I(q, p)$ , where  $(q, p)$  is running into  $\mathcal{Q} \times \mathbb{R}^3$ , and a smooth curve  $q(t)$  in  $\mathcal{Q}$  let us denote

$$\left( \frac{\partial}{\partial q} \frac{d}{dt} I(q, p) \right) (t) := \left( \frac{\partial}{\partial q} J \right) (q(t), q'(t), q''(t)),$$

where, for  $(q, p, r)$  in  $\mathcal{Q} \times \mathbb{R}^3 \times \mathbb{R}^3$ ,

$$J(q, p, r) = p \frac{\partial I}{\partial q}(q, p) + r \frac{\partial I}{\partial p}(q, p). \tag{3.108}$$

Observe in particular that

$$\frac{d}{dt}(I(q(t), q'(t))) = J(q(t), q'(t), q''(t)),$$

and

$$\frac{d}{dt} \left( \frac{\partial I}{\partial q}(q(t), q'(t)) \right) = \left( \frac{\partial}{\partial q} \frac{d}{dt} I(q, p) \right) (t). \quad (3.109)$$

Below, in such circumstances, it will be comfortable to write

$$\frac{\partial}{\partial q} [J(q(t), q'(t), q''(t))] \text{ instead of } \left( \frac{\partial J}{\partial q} \right) (q(t), q'(t), q''(t)),$$

and it will be understood that  $J$  is extended from  $(q(t), q'(t), q''(t))$  to general  $(q, p, r)$  by (3.108).

*Proof of Lemma 3.30* We start with computing the right hand side of (3.106). On the one hand the linearity of  $u_1$  with respect to  $p$  and then an integration by parts leads to:

$$\frac{\partial \mathcal{E}_1}{\partial p} \cdot p^* = \int_{\mathcal{F}(q)} u_1 \cdot u^* dx = \int_{\partial \mathcal{S}(q)} (\Phi \cdot p)(u^* \cdot n) ds.$$

Then, invoking Reynold's transport theorem, we get:

$$\frac{\partial \mathcal{E}_1}{\partial p} \cdot p^* = \frac{\partial}{\partial q} \left( \int_{\mathcal{F}(q)} (\Phi \cdot p) dx \right) \cdot p^* - \int_{\mathcal{F}(q)} \left( \frac{\partial \Phi}{\partial q} \cdot p \right) \cdot p^* dx. \quad (3.110)$$

On the other hand, again using Reynold's formula, we have:

$$\frac{\partial \mathcal{E}_1}{\partial q} \cdot p^* = \int_{\mathcal{F}(q)} \left( \frac{\partial u_1}{\partial q} \cdot p^* \right) \cdot u_1 dx + \frac{1}{2} \int_{\partial \mathcal{S}(q)} |u_1|^2 (u^* \cdot n) ds. \quad (3.111)$$

Differentiating (3.110) with respect to  $t$ , we obtain:

$$\frac{d}{dt} \frac{\partial \mathcal{E}_1}{\partial p} \cdot p^* = \frac{d}{dt} \frac{\partial}{\partial q} \left( \int_{\mathcal{F}(q)} (\Phi \cdot p) dx \right) \cdot p^* - \frac{d}{dt} \left( \int_{\mathcal{F}(q)} \left( \frac{\partial \Phi}{\partial q} \cdot p \right) \cdot p^* dx \right). \quad (3.112)$$

With the abuse of notations mentioned above we commute the derivatives involved in the first term of the right hand side, so that the identity (3.112) can be rewritten as follows:

$$\frac{d}{dt} \frac{\partial \mathcal{E}_1}{\partial p} \cdot p^* = \frac{\partial}{\partial q} \frac{d}{dt} \left( \int_{\mathcal{F}(q)} (\Phi \cdot p) dx \right) \cdot p^* - \frac{d}{dt} \left( \int_{\mathcal{F}(q)} \left( \frac{\partial \Phi}{\partial q} \cdot p \right) \cdot p^* dx \right). \quad (3.113)$$

Moreover, using again Reynold's formula, we have:

$$\frac{d}{dt} \left( \int_{\mathcal{F}(q)} (\Phi \cdot p) \, dx \right) = \int_{\mathcal{F}(q)} \partial_t(\Phi \cdot p) \, dx + \int_{\partial\mathcal{S}(q)} (\Phi \cdot p)(u_1 \cdot n) \, ds \quad (3.114)$$

$$= \int_{\mathcal{F}(q)} \partial_t(\Phi \cdot p) \, dx + 2\mathcal{E}_1(q, p), \quad (3.115)$$

by integration by parts.

We infer from (3.113) and (3.114), again with the abuse of notations mentioned above, that:

$$\mathcal{E}\mathcal{L} = \frac{\partial\mathcal{E}_1}{\partial q} + \frac{\partial}{\partial q} \left[ \int_{\mathcal{F}(q)} \partial_t(\Phi \cdot p) \, dx \right] \cdot p^* - \frac{d}{dt} \left( \int_{\mathcal{F}(q)} \left( \frac{\partial\Phi}{\partial q} \cdot p \right) \cdot p^* \, dx \right). \quad (3.116)$$

Thanks to Reynold's formula, we get for the second term of the right hand side

$$\frac{\partial}{\partial q} \left[ \int_{\mathcal{F}(q)} \partial_t(\Phi \cdot p) \, dx \right] \cdot p^* = \int_{\mathcal{F}(q)} \frac{\partial}{\partial q} (\partial_t(\Phi \cdot p)) \cdot p^* \, dx + \int_{\partial\mathcal{S}(q)} \partial_t(\Phi \cdot p)(u^* \cdot n) \, ds, \quad (3.117)$$

and for the last one:

$$\begin{aligned} \frac{d}{dt} \left( \int_{\mathcal{F}(q)} \left( \frac{\partial\Phi}{\partial q} \cdot p \right) \cdot p^* \, dx \right) &= \int_{\mathcal{F}(q)} \partial_t \left( \left( \frac{\partial\Phi}{\partial q} \cdot p \right) \cdot p^* \right) \, dx \\ &\quad + \int_{\partial\mathcal{S}(q)} \left( \left( \frac{\partial\Phi}{\partial q} \cdot p \right) \cdot p^* \right) (u_1 \cdot n) \, ds. \end{aligned} \quad (3.118)$$

Using again (3.109) for the first term and integrating by parts the second one, we obtain:

$$\begin{aligned} \frac{d}{dt} \left( \int_{\mathcal{F}(q)} \left( \frac{\partial\Phi}{\partial q} \cdot p \right) \cdot p^* \, dx \right) &= \int_{\mathcal{F}(q)} \frac{\partial}{\partial q} (\partial_t(\Phi \cdot p)) \cdot p^* \, dx \\ &\quad + \int_{\mathcal{F}(q)} \left( \frac{\partial u_1}{\partial q} \cdot p^* \right) \cdot u_1 \, dx. \end{aligned} \quad (3.119)$$

Plugging the expressions (3.111), (3.117) and (3.119) into (3.116) and simplifying, we end up with:

$$\mathcal{E}\mathcal{L} = \int_{\partial\mathcal{S}(q)} \left[ \partial_t(\Phi \cdot p) + \frac{1}{2}|u_1|^2 \right] (u^* \cdot n) \, ds.$$

Upon an integration by parts, we recover (3.106) and the proof is then completed.  $\square$

Now, we observe that  $\mathcal{E}_1(q, p)$ , as defined by (3.105), can be rewritten as:

$$\mathcal{E}_1(q, p) = \frac{1}{2} \mathcal{M}_a(q) p \cdot p, \quad (3.120)$$

where  $\mathcal{M}_a(q)$  is defined by (3.97). Indeed this allows us to prove the following result.

**Lemma 3.31** *For any smooth curve  $q(t)$  in  $\mathcal{Q}$ , for every  $p^* \in \mathbb{R}^3$ , we have:*

$$\mathcal{E}\mathcal{L} = \mathcal{M}_a(q) q'' \cdot p^* + \langle \Gamma_a(q), q', q' \rangle \cdot p^*. \quad (3.121)$$

*Proof of Lemma 3.31* Using (3.120) in the definition (3.107) of  $\mathcal{E}\mathcal{L}$  we have

$$\mathcal{E}\mathcal{L} = \mathcal{M}_a(q) q'' \cdot p^* + \left( (D\mathcal{M}_a(q) \cdot q') q' \right) \cdot p^* - \frac{1}{2} \left( (D\mathcal{M}_a(q) \cdot p^*) q' \right) \cdot q'.$$

Then

$$\mathcal{E}\mathcal{L} = \mathcal{M}_a q'' \cdot p^* + \sum (\mathcal{M}_a)_{ij}^k q'_k q'_j p_i^* - \frac{1}{2} \sum (\mathcal{M}_a)_{ij}^k q'_i q'_j p_k^*,$$

where the sums are over  $1 \leq i, j, k \leq 3$ . Let us recall the notation  $(\mathcal{M}_a)_{ij}^k(q)$  in (3.95). A symmetrization with respect to  $j$  and  $k$  of the second term and an exchange of  $i$  and  $k$  in the last sum of the right hand side above leads to the result.  $\square$

Then Lemma 3.29 straightforwardly results from the combination of (3.104), Lemmas 3.30 and 3.31.  $\square$

### 3.3.3 Reduction to an ODE in the General Case: Statement of Theorem 3.32

Now let us deal with the general case of a nonzero circulation  $\gamma$ . Next result, obtained in [8], extends Theorem 3.28 and establishes a reformulation of the system in terms of an ordinary differential equation in the general case of a circulation  $\gamma \in \mathbb{R}$ .

**Theorem 3.32** *Let be given the open regular connected and simply connected bounded cavity  $\Omega$ , the initial closed domain  $\mathcal{S}_0 \subset \Omega$  occupied by the body, the initial solid translation and rotation velocities  $(\ell_0, r_0)$  in  $\mathbb{R}^2 \times \mathbb{R}$ , the circulation  $\gamma$  in  $\mathbb{R}$ , and  $u_0$  the associated compatible initial fluid velocity according to Definition 3.5. There exists  $F$  in  $C^\infty(\mathcal{Q} \times \mathbb{R}^3; \mathbb{R}^3)$  depending only on  $\mathcal{S}_0$ ,  $\gamma$  and  $\Omega$ , and vanishing when  $\gamma = 0$ , such that, up to the first collision, System (3.91) is equivalent to the second order ODE:*

$$(\mathcal{M}_g + \mathcal{M}_a(q)) q'' + \langle \Gamma_a(q), q', q' \rangle = F(q, q'), \quad (3.122)$$



with Cauchy data  $q(0) = 0 \in \mathcal{Q}$ ,  $q'(0) = (\ell_0, r_0) \in \mathbb{R}^2 \times \mathbb{R}$ , where  $\mathcal{M}_a(q)$  and its associated  $a$ -connection  $\Gamma_a(q)$  are given by Theorem 3.28. For a solid position  $q \in \mathcal{Q}$  the fluid velocity  $u(q, \cdot)$  is uniquely determined as the solution of a div-curl type system in the doubly-connected domain  $\mathcal{F}(q)$ , constituted of (3.91b), (3.92), (3.91d), (3.91e), together with the prescription of the circulation  $\gamma$ .

The local-in-time existence and uniqueness of smooth solutions stated in Theorem 3.6 therefore simply follows from Theorem 3.32 and the Cauchy-Lipschitz theorem. That the life-time of such a smooth solution can only be limited by a collision will follow from an energy argument below, cf. Sect. 3.3.5.

Indeed we are going to provide a rather explicit definition of the force term  $F(q, q')$ . Let us first introduce a normalized stream function for the circulation term: for every  $q \in \mathcal{Q}$ , there exists a unique  $C(q)$  in<sup>7</sup>  $\mathbb{R}$  such that the unique solution  $\psi(q, \cdot)$  of the Dirichlet problem:

$$\Delta\psi(q, \cdot) = 0 \text{ in } \mathcal{F}(q) \quad \psi(q, \cdot) = C(q) \text{ on } \partial\mathcal{S}(q) \quad \psi(q, \cdot) = 0 \text{ on } \partial\Omega, \tag{3.123a}$$

satisfies

$$\int_{\partial\mathcal{S}(q)} \frac{\partial\psi}{\partial n}(q, \cdot) ds = -1. \tag{3.123b}$$

Observe that for any  $q \in \mathcal{Q}$ ,  $C(q) < 0$  and that  $C \in C^\infty(\mathcal{Q}; (-\infty, 0))$  and depends on  $\mathcal{S}_0$  and  $\Omega$ . Eventually, we define:

$$B(q) := \int_{\partial\mathcal{S}(q)} \left( \frac{\partial\psi}{\partial n} \left( \frac{\partial\Phi}{\partial n} \times \frac{\partial\Phi}{\partial \tau} \right) \right) (q, \cdot) ds, \tag{3.124}$$

$$E(q) := -\frac{1}{2} \int_{\partial\mathcal{S}(q)} \left( \left| \frac{\partial\psi}{\partial n} \right|^2 \frac{\partial\Phi}{\partial n} \right) (q, \cdot) ds, \tag{3.125}$$

and, for  $(q, p)$  in  $\mathcal{Q} \times \mathbb{R}^3$ , the force term

$$F(q, p) := \gamma^2 E(q) + \gamma p \times B(q). \tag{3.126}$$

The notations  $E$  and  $B$  are chosen on purpose to highlight the analogy with the Lorentz force acting on a charged particle moving under the influence of a couple of electromagnetic fields  $E$  and  $B$ .

---

<sup>7</sup>The function  $C(q)$  is actually the opposite of the inverse of the condenser capacity of  $\mathcal{S}(q)$  in  $\Omega$ .

### 3.3.4 Proof of Theorem 3.32

As mentioned above (3.101) only relies on the fact that the fluid velocity is irrotational and is therefore still granted. However the fluid velocity  $u(q, \cdot)$  now involves an extra term due to the non-vanishing circulation. Indeed, for any  $q \in \mathcal{Q}$ , one obtains, using (3.123) and (3.96), that the solution  $u(q, \cdot)$  to the div-curl type system in the doubly-connected domain  $\mathcal{F}(q)$ , constituted of (3.91b), (3.92), (3.91d), (3.91e), together with the prescription of circulation  $\gamma$  takes the form:

$$u(q, \cdot) = u_1(q, \cdot) + u_2(q, \cdot), \quad (3.127)$$

where  $u_1(q, \cdot)$  is given by (3.102) as in the potential case and the new contribution  $u_2(q, \cdot)$  is defined by

$$u_2(q, \cdot) := \gamma \nabla^\perp \psi(q, \cdot). \quad (3.128)$$

So besides the dependence with respect to  $\mathcal{S}_0$ , to  $\Omega$  and to the space variable,  $u_2$  depends on  $q$  and linearly on  $\gamma$ . Therefore plugging the decomposition (3.127) into (3.101) leads to

$$\begin{aligned} m\ell' \cdot \ell^* + \mathcal{J}r' r^* + \int_{\mathcal{F}(q)} \left( \frac{\partial u_1}{\partial t} + \frac{1}{2} \nabla |u_1|^2 \right) \cdot u^* dx &= - \int_{\mathcal{F}(q)} \left( \frac{1}{2} \nabla |u_2|^2 \right) \cdot u^* dx \\ &- \int_{\mathcal{F}(q)} \left( \frac{\partial u_2}{\partial t} + \frac{1}{2} \nabla (u_1 \cdot u_2) \right) \cdot u^* dx, \end{aligned} \quad (3.129)$$

for all  $p^* := (\ell^*, r^*) \in \mathbb{R}^3$ , with  $u^*$  given by (3.99).

By a simple integration by parts, one obtains that the first term in the right hand side above satisfies:

$$- \int_{\mathcal{F}(q)} \left( \frac{1}{2} \nabla |u_2|^2 \right) \cdot u^* dx = \gamma^2 E(q) \cdot p^*, \quad (3.130)$$

where  $E(q)$  defined in (3.125).

Then the reformulation of Eqs. (3.91g–h) mentioned in Theorem 3.32 will follow from (3.129), (3.130), Lemma 3.29 and from the following identity:

$$- \int_{\mathcal{F}(q)} \left( \frac{\partial u_2}{\partial t} + \nabla (u_1 \cdot u_2) \right) \cdot u^* dx = \gamma (q' \times B(q)) \cdot p^*, \quad (3.131)$$

where  $B(q)$  is defined in (3.124). We refer to [11] for the proof of (3.131).

### 3.3.5 The Role of the Energy

An important feature of the system (3.122) is that it is conservative. Let us denote for any  $(q, p)$  in  $\mathcal{Q} \times \mathbb{R}^3$ ,

$$\mathcal{E}(q, p) := \frac{1}{2}(\mathcal{M}_g + \mathcal{M}_a(q))p \cdot p - \frac{1}{2}\gamma^2 C(q), \quad (3.132)$$

with  $C(q)$  given by (3.123). Indeed one can prove that for any  $q \in \mathcal{Q}$ ,

$$E(q) = \frac{1}{2}DC(q), \quad (3.133)$$

where the notation  $DC(q)$  stands for the derivative of  $C(q)$  with respect to  $q$ , cf. Lemma 2.4 in [11] for a proof, so that the second term in the right-hand-side of (3.132) can be seen as a potential energy related to the first term in the right-hand-side of (3.126). Observe that  $\mathcal{E}(q, p)$  is the sum of two positive terms and that in addition to its dependence on  $q$  and  $p$ , the energy  $\mathcal{E}$  depends on  $\mathcal{S}_0, m, \mathcal{J}, \gamma$  and  $\Omega$ . Next result proves that  $\mathcal{E}(q, q')$  is indeed the natural total kinetic energy of the “fluid+solid” system.

**Proposition 3.33** *For any  $q = (h, \theta) \in C^\infty([0, T]; \mathcal{Q})$  satisfying (3.122), as far as there is no collision,*

$$\mathcal{E}(q, q') = \frac{1}{2} \int_{\mathcal{F}(q)} u(q, \cdot)^2 dx + \frac{1}{2}m(h')^2 + \frac{1}{2}\mathcal{J}(\theta')^2.$$

*Proof* First we have by integrations by parts that

$$\frac{1}{2} \int_{\mathcal{F}(q)} u^2 dx = -\frac{1}{2}\gamma^2 C(q) \text{ and } \int_{\mathcal{F}(q)} u_1 \cdot u_2 dx = 0.$$

Then we use (3.120) and the decomposition (3.127) to conclude.  $\square$

The following result is therefore very natural.

**Proposition 3.34** *For any  $q \in C^\infty([0, T]; \mathcal{Q})$  satisfying (3.122), as far as there is no collision,  $\mathcal{E}(q, q')$  is constant in time.*

*Proof* Let us give a proof of Proposition 3.34 which uses the ODE formulation (3.122). We start with the observation that the energy  $\mathcal{E}(q, q')$  as defined in (3.132) has for time derivative

$$(\mathcal{E}(q, q'))' = (\mathcal{M}_g + \mathcal{M}_a(q))q'' \cdot q' + \frac{1}{2}(D\mathcal{M}_a(q) \cdot q')q' \cdot q' - \frac{1}{2}\gamma^2 DC(q) \cdot q'. \quad (3.134)$$

Now, thanks to (3.122) and (3.126), we have

$$(\mathcal{M}_g + \mathcal{M}_a(q))q'' \cdot q' = -\langle \Gamma_a(q), q', q' \rangle \cdot q' + F(q, q') \cdot q', \quad (3.135)$$

and

$$F(q, q') \cdot q' = \gamma^2 E(q) \cdot q'. \quad (3.136)$$

We introduce the matrix

$$S_a(q, q') := \left( \sum_{1 \leq i \leq 3} (\Gamma_a)_{ij}^k(q) q'_i \right)_{1 \leq k, j \leq 3}, \quad (3.137)$$

so that

$$\langle \Gamma_a(q), q', q' \rangle = S_a(q, q') q'. \quad (3.138)$$

Combining (3.134)–(3.138) we obtain

$$(\mathcal{E}(q, q'))' = \gamma^2 (E(q) - \frac{1}{2} DC(q)) \cdot q' + \left( \frac{1}{2} D\mathcal{M}_a(q) \cdot q' - S_a(q, q') \right) q' \cdot q'.$$

The first term of the right hand side vanishes thanks to (3.133) and the proof of Proposition 3.34 then follows from the following result.

**Lemma 3.35** *For any  $(q, p) \in \mathcal{Q} \times \mathbb{R}^3$ , the matrix  $\frac{1}{2} D\mathcal{M}_a(q) \cdot p - S_a(q, p)$  is skew-symmetric.*

*Proof of Lemma 3.35* We start with the observation that  $D\mathcal{M}_a(q) \cdot p$  is the  $3 \times 3$  matrix containing the entries

$$\sum_{1 \leq k \leq 3} (\mathcal{M}_a)_{ij}^k(q) p_k, \text{ for } 1 \leq i, j \leq 3.$$

On the other hand, the  $3 \times 3$  matrix  $S_a(q, p)$  contains the entries

$$\frac{1}{2} \sum_{1 \leq k \leq 3} \left( (\mathcal{M}_a)_{ij}^k + (\mathcal{M}_a)_{i,k}^j - (\mathcal{M}_a)_{k,j}^i \right) (q) p_k,$$

for  $1 \leq i, j \leq 3$ . Therefore, the  $3 \times 3$  matrix  $D\mathcal{M}_a(q) \cdot p - S_a(q, p)$  contains the entries

$$c_{ij}(q, p) = -\frac{1}{2} \sum_{1 \leq k \leq 3} \left( (\mathcal{M}_a)_{i,k}^j - (\mathcal{M}_a)_{k,j}^i \right) (q) p_k,$$

for  $1 \leq i, j \leq 3$ . Using that the matrix  $\mathcal{M}_a(q)$  is symmetric, we get that  $c_{ij}(q, p) = -c_{ji}(q, p)$  for  $1 \leq i, j \leq 3$ , which ends the proof.  $\square$

This ends the proof of Proposition 3.34.<sup>8</sup>  $\square$

If we assume that the body stays at distance at least  $\delta > 0$  from the boundary we may infer from Proposition 3.34 a bound of the body velocity depending only on the data and on  $\delta$ . Indeed we have the following immediate corollary of Proposition 3.34 and of the regularity properties of the functions  $C(q)$  and  $\mathcal{M}_a(q)$ . We denote  $\mathcal{Q}_\delta := \{q \in \mathbb{R}^3 : d(S(q), \partial\Omega) > \delta\}$ .

**Corollary 3.36** *Let  $S_0 \subset \Omega$ ,  $p_0 \in \mathbb{R}^3$  and  $(\gamma, m, \mathcal{J}) \in \mathbb{R} \times (0, +\infty) \times (0, +\infty)$ ;  $\delta > 0$ ;  $q \in C^\infty([0, T]; \mathcal{Q}_\delta)$  satisfying (3.122) with the Cauchy data  $(q, q')(0) = (0, p_0)$ . Then there exists  $K > 0$  depending only on  $S_0, \Omega, p_0, \gamma, m, \mathcal{J}, \delta$  such that  $|q'|_{\mathbb{R}^3} \leq K$  on  $[0, T]$ .*

This entails in particular that the life-time of a smooth solution to (3.122) can only be limited by a collision and therefore completes the proof of Theorem 3.6.

### 3.3.6 Zero Radius Limit

Let us now turn our attention to the limit of the dynamics when the size of the solid goes to 0 that is considering an initial domain for the body of the form (3.5) with the inertia scaling described in Definition 3.1. This aims to extend the analysis performed in Sect. 3.2.6 to the case where the “fluid+solid” system occupies a bounded domain rather than the whole plane.

Below, we will use the following notation: for  $S_0 \subset \Omega$ ;  $p_0 = (\ell_0, r_0) \in \mathbb{R}^3$ ,  $(m, \mathcal{J}) \in (0, +\infty) \times (0, +\infty)$ ,  $\gamma$  in  $\mathbb{R}$  (resp. in  $\mathbb{R}^*$ ) in the case of a massive (respectively massless) particle, for every  $\varepsilon \in (0, 1]$  small enough to ensure that the set  $S_0^\varepsilon$  defined by (3.5) satisfies  $S_0^\varepsilon \subset \Omega$ , we denote  $(q^\varepsilon, T^\varepsilon)$  the maximal solution to (3.122) associated with the coefficients  $\mathcal{M}^\varepsilon$ ,  $\Gamma_a^\varepsilon$  and  $F^\varepsilon$  which are themselves associated with  $S_0^\varepsilon, m^\varepsilon, \mathcal{J}^\varepsilon$  and  $\gamma$  (as  $\mathcal{M}, \Gamma_a$  and  $F$  were associated with  $S_0, m, \mathcal{J}$  and  $\gamma$ ) where  $m^\varepsilon, \mathcal{J}^\varepsilon$  are given in Definition 3.1, and with the initial data  $(q^\varepsilon, (q^\varepsilon)')(0) = (0, p_0)$ .

**Theorem 3.37** *Let  $S_0 \subset \Omega$ ;  $p_0 = (\ell_0, r_0) \in \mathbb{R}^3$ ,  $(m, \mathcal{J}) \in (0, +\infty) \times (0, +\infty)$ ,  $\gamma$  in  $\mathbb{R}$  (resp. in  $\mathbb{R}^*$ ) in the case of a massive (respectively massless) particle. Let  $(h, T)$  be the maximal solution to (3.8) (resp.  $h$  be the global solution to (3.9)). Then, as  $\varepsilon \rightarrow 0$ ,  $\liminf T^\varepsilon \geq T$  (resp.  $T^\varepsilon \rightarrow +\infty$ ) and  $h^\varepsilon \rightharpoonup h$  in  $W^{2,\infty}([0, T']; \mathbb{R}^2)$  (resp. in  $W^{1,\infty}([0, T']; \mathbb{R}^2)$ ) weak- $\star$  for all  $T' \in (0, T)$  (resp. for all  $T' > 0$ ). Furthermore in the case a massive particle, one also has that  $\varepsilon\theta^\varepsilon \rightharpoonup 0$  in  $W^{2,\infty}([0, T']; \mathbb{R})$  weak- $\star$  for all  $T' \in (0, T)$ .*

<sup>8</sup>It is also possible to achieve an alternative proof of Proposition 3.34 thanks to the original PDE formulation of the “fluid+solid” system, relying on the equivalence between the ODE and PDE formulations obtained in Theorem 3.32 and on the reformulation of the energy obtained in Proposition 3.33.

In the statement above it is understood that  $q^\varepsilon$  was decomposed into  $q^\varepsilon = (h^\varepsilon, \theta^\varepsilon)$ . It follows from Theorem 3.32 that Theorem 3.37 implies Theorem 3.7.

Let us provide a scheme of proof of Theorem 3.37.

*Scheme of Proof of Theorem 3.37* Using that for the inertia regimes considered in Definition 3.1 the genuine inertia matrix scales as in (3.87), the equation for  $q^\varepsilon$  reads:

$$\left(\varepsilon^\alpha I_\varepsilon \mathcal{M}_g I_\varepsilon + \mathcal{M}_a^\varepsilon(q^\varepsilon)\right)(q^\varepsilon)'' + \langle \Gamma_a^\varepsilon(q^\varepsilon), (q^\varepsilon)', (q^\varepsilon)' \rangle = \gamma^2 E^\varepsilon(q^\varepsilon) + \gamma (q^\varepsilon)' \times B^\varepsilon(q^\varepsilon), \tag{3.139}$$

where the added inertia matrix  $\mathcal{M}_a^\varepsilon$ , the a-connection  $\Gamma_a^\varepsilon$  and the electric and magnetic type terms  $E^\varepsilon$  and  $B^\varepsilon$  are associated with the body of size  $\varepsilon$  as mentioned above. Here one crucial step in passing to the limit in (3.139) is to find some uniform bounds in  $\varepsilon$ . The energy is of course a natural candidate in order to get such estimates. In particular one may turn toward an appropriate modification of Corollary 3.36 in the zero radius limit. A difficulty is that the potential part of the energy (corresponding to the last term in (3.132)) diverges logarithmically as  $\varepsilon \rightarrow 0^+$ . However such a contribution can be discarded from the energy conservation since it does not depend on the solid position and velocity. Indeed an appropriate renormalization of the energy provides an uniform estimate of  $\varepsilon^{\min(1, \frac{\alpha}{2})} |(h^\varepsilon)', \varepsilon(\theta^\varepsilon)'|_{\mathbb{R}^3}$  at least till the solid stays away from the external boundary. Unfortunately in the massless case the coefficient  $\alpha$  satisfies  $\alpha > 0$  and the previous estimate is not sufficient.<sup>9</sup>

One then turns toward the search for an asymptotic normal form of (3.139) with the hope that more structure shows up in the zero radius limit and reveals another candidate in order to obtain some uniform bounds in  $\varepsilon$ . In order to do so we first establish some expansions in the limit  $\varepsilon \rightarrow 0$  of  $\mathcal{M}_a^\varepsilon$ ,  $\Gamma_a^\varepsilon$ ,  $E^\varepsilon$  and  $B^\varepsilon$ . These expansions are obtained by a multi-scale analysis of the Kirchhoff potentials and of the stream functions and repeated use of Lamb’s lemma, that is Lemma 3.25. More precisely these expansions involve two scales corresponding respectively to variations over length  $O(1)$  and  $O(\varepsilon)$  respectively on  $\partial\Omega$  and  $\partial S^\varepsilon(q)$ . The profiles appearing in these expansions are obtained by successive corrections, considering alternatively at their respective scales the body boundary from which the external boundary seems remote and the external boundary from which the body seems tiny, so that good approximations are given respectively by the case without external boundary and without the body. We refer to [11] for more details on this intricate process and sum up the results below. The leading term of the expansions of  $\mathcal{M}_a^\varepsilon$ ,  $\Gamma_a^\varepsilon$  and  $B^\varepsilon$  in the zero-radius limit are given, up to an appropriate scaling, by the terms obtained in the case where the rigid body is of size  $\varepsilon = 1$  and is immersed in a fluid filling the whole plane, that is in the case tackled in Theorem 3.12. On the

---

<sup>9</sup>Indeed the case where  $\alpha \geq 2$  is the most delicate and we will focus on it.

other hand the leading term of the expansion of  $E^\varepsilon$  in the zero-radius limit is given, up to an appropriate scaling, by the field

$$E_0(q) := - \left( \begin{array}{c} u_\Omega(h)^\perp \\ u_\Omega(h) \cdot R(\theta)\xi \end{array} \right), \text{ where } q = (h, \theta). \quad (3.140)$$

We recall that  $u_\Omega$  and  $\xi$  were defined respectively above (3.8) and in (3.34). Given  $\delta > 0$  and  $\varepsilon_0$  in  $(0, 1)$ , we define the open set of the shrinking body positions at distance  $\delta$  from the boundary for a radius of order  $\varepsilon$  with  $0 < \varepsilon < \varepsilon_0$ :

$$\mathcal{Q}_{\delta, \varepsilon_0} := \{(\varepsilon, q) \in (0, \varepsilon_0) \times \mathbb{R}^3 / d(\mathcal{S}^\varepsilon(q), \partial\Omega) > \delta\}.$$

**Proposition 3.38** *Let  $\delta > 0$ . There exists  $\varepsilon_0$  in  $(0, 1)$ ,  $\mathbf{E}_I(q)$  and  $\mathbf{B}_I(q)$  in  $L^\infty(\mathcal{Q}_\delta; \mathbb{R}^3)$ ,  $\mathcal{M}_r$  in  $L^\infty(\mathcal{Q}_{\delta, \varepsilon_0}; \mathbb{R}^{3 \times 3})$ ,  $\Gamma_r$  in  $L^\infty(\mathcal{Q}_{\delta, \varepsilon_0}; \mathcal{BL}(\mathbb{R}^3 \times \mathbb{R}^3; \mathbb{R}^3))$ , and  $E_r$  and  $B_r$  in  $L^\infty(\mathcal{Q}_{\delta, \varepsilon_0}; \mathbb{R}^3)$  such that, for all  $(\varepsilon, q)$  in  $\mathcal{Q}_{\delta, \varepsilon_0}$ , with  $q = (h, \theta)$ ,*

$$\mathcal{M}_a^\varepsilon(q) = \varepsilon^2 I_\varepsilon \left( \mathcal{M}_{a, \theta} + \varepsilon^2 \mathcal{M}_r(\varepsilon, q) \right) I_\varepsilon, \quad (3.141)$$

$$\langle \Gamma_a^\varepsilon(q), \cdot, \cdot \rangle = \varepsilon I_\varepsilon \left( \langle \Gamma_{a, \theta}, I_\varepsilon \cdot, I_\varepsilon \cdot \rangle + \varepsilon^2 \langle \Gamma_r(\varepsilon, q), I_\varepsilon \cdot, I_\varepsilon \cdot \rangle \right), \quad (3.142)$$

$$E^\varepsilon(q) = I_\varepsilon \left( \mathbf{E}_0(q) + \varepsilon \mathbf{E}_I(q) + \varepsilon^2 E_r(\varepsilon, q) \right), \quad (3.143)$$

$$B^\varepsilon(q) = \varepsilon I_\varepsilon^{-1} \left( B_\theta + \varepsilon \mathbf{B}_I(q) + \varepsilon^2 B_r(\varepsilon, q) \right). \quad (3.144)$$

We recall that  $\mathcal{M}_{a, \theta}$  and  $B_\theta$  are given by Theorem 3.12 as associated with the rigid body of size  $\varepsilon = 1$  and as if the body was immersed in a fluid filling the whole plane,  $\Gamma_{a, \theta}$  denotes the a-connection associated with  $\mathcal{M}_{a, \theta}$ ,  $I_\varepsilon$  is the diagonal matrix  $I_\varepsilon := \text{diag}(1, 1, \varepsilon)$  and let us avoid any confusion by highlighting that the  $\cdot$  in (3.142) stands for the application to any  $p$  in  $\mathbb{R}^3$  (which determines completely the bilinear symmetric mapping). Let us also recall that quite explicit expressions of  $\mathcal{M}_{a, \theta}$ ,  $B_\theta$  and  $\Gamma_{a, \theta}$  are given in Sect. 3.2.2.

Therefore, using (3.143), (3.144), (3.140) and (3.36), one obtains that the leading part of the expansion of the right hand side of (3.139) is

$$I_\varepsilon \left( \gamma^2 \mathbf{E}_0(q^\varepsilon) + \gamma (I_\varepsilon(q^\varepsilon))' \times B_{\theta^\varepsilon} \right) = I_\varepsilon \left( \gamma \hat{p}^\varepsilon \times B_{\theta^\varepsilon} \right), \quad (3.145)$$

for any  $\hat{p}^\varepsilon$  of the form

$$\hat{p}^\varepsilon = ((h^\varepsilon)' - \gamma u_\Omega(h^\varepsilon), \varepsilon(\theta^\varepsilon)')^t + \eta B_{\theta^\varepsilon}, \quad (3.146)$$

with  $\eta$  in  $\mathbb{R}$ .

**An Instructive Digression** The identities (3.145) and (3.146) remind a well-known modulation strategy used by Berkowitz and Gardner, cf. [1], in order the tackle the

zero-mass limit of the following dynamics of a light particle in a smooth electromagnetic field:

$$\varepsilon^2 q'' = E(q) + q' \times B(q) \text{ with the condition } E(q) \cdot B(q) = 0. \quad (3.147)$$

Here we have dropped the index  $\varepsilon$  of  $q$  for sake of clarity and we will assume that the fields  $E(q)$  and  $B(q)$  (which actually stand here for electric and magnetic fields) smoothly depend on its argument  $q$  but not on  $\varepsilon$  otherwise. The setting of [1] is slightly more general but the toy-system above will be sufficient for the exposition of the gain obtained by modulation in the analysis. The starting point is that a naive application of the Cauchy-Lipschitz theorem does only provide existence of a solution over a time which may vanish as  $\varepsilon$  converges to 0. The difficulty resides within the lack of sign or structure of the  $E(q)$  term which prevents from obtaining straightforwardly some uniform estimates by energy. To overcome this difficulty Berkowitz and Gardner introduced the modulated variable:

$$\tilde{p} = q' - u(q) \text{ where } u(q) \text{ satisfies } E(q) + u(q) \times B(q) = 0. \quad (3.148)$$

Observe that the existence for any  $q$  of such a vector  $u(q)$  is guaranteed by the condition  $E(q) \cdot B(q) = 0$  and that the set of such vectors is an one-dimensional affine space. Indeed in [1] Berkowitz and Gardner makes use of the following explicit field

$$u(q) := |B(q)|^{-2} E(q) \times B(q), \quad (3.149)$$

which does satisfy the condition in (3.148) and which turns to be the actual physical drift velocity for this system.

Using the chain-rule, one obtains  $\tilde{p}' = q'' - q' \cdot \nabla u(q)$ , and then, by using (3.147) and (3.148),

$$\varepsilon^2 \tilde{p}' = E(q) + q' \times B(q) - \varepsilon^2 q' \cdot \nabla u(q) = \tilde{p} \times B(q) - \varepsilon^2 (\tilde{p} + u(q)) \cdot \nabla u(q).$$

Therefore, one obtains the following gyroscopic normal form:

$$\tilde{p}' = \frac{1}{\varepsilon^2} \tilde{p} \times B(q) - (\tilde{p} + u(q)) \cdot \nabla u(q) \quad (3.150)$$

Now that the  $E(q)$  has been absorbed by the choice of the modulated variable, the only factor with a singular (i.e. negative) power of  $\varepsilon$  is in front of the  $B(q)$  term and this term disappears when taking the inner product of (3.150) with  $p$  in an energy-type estimate. Some Gronwall estimates on (3.150) and (3.148) then provide uniform bound of  $q$  and  $q'$ . In particular the second Gronwall estimate relies on the fact that the modulation is a term of lower order in term of time derivative with respect to  $q'$ .

Let us now go back to our search for an asymptotic normal form of (3.139) and let see how to extend the analysis performed above. We first observe that the drift



velocity (naively) computed as in (3.149) with  $E_0(q^\varepsilon)$  and  $B_{\theta^\varepsilon}$  instead of  $E(q)$  and  $B(q)$  corresponds to a nonzero  $\eta$  in (3.146). Still in the case of (3.145) one observes as we already did in the proof of Theorem 3.26 that the natural counterpart to  $(h^\varepsilon)'$  for what concerns the angular velocity is rather  $\varepsilon(\theta^\varepsilon)'$  than  $(\theta^\varepsilon)'$ . Moreover we will benefit from the fact that the contribution due to  $\varepsilon(\theta^\varepsilon)'$  in the first two coordinates of the result of the cross product in the right hand side of (3.145) provides the term (3.90) whose special structure somehow allows to gain one factor  $\varepsilon$ . It turns out that the leading part of the relevant drift velocity in order to pass to the limit in (3.139) is given by (3.146) with  $\eta = 0$ , that is by

$$\hat{p}^\varepsilon = ((h^\varepsilon)' - \gamma u_\Omega(h^\varepsilon), \varepsilon(\theta^\varepsilon)')^t. \tag{3.151}$$

Still the leading terms of the inertia matrix  $\varepsilon^\alpha I_\varepsilon \mathcal{M}_g I_\varepsilon + \mathcal{M}_a^\varepsilon(q^\varepsilon)$  in front of  $(q^\varepsilon)''$  in (3.139) is<sup>10</sup>  $I_\varepsilon(\varepsilon^\alpha \mathcal{M}_g + \varepsilon^2 \mathcal{M}_{a,\theta}) I_\varepsilon$ , and therefore, in order to cover the case where  $\alpha \geq 2$ , one has to investigate further the structure of the other terms of Eq. (3.139), and to hope that a recombination as nice as in (3.145) occurs at the next order. This is actually why we had expanded up to order  $\varepsilon^2$  in Proposition 3.38. One observes in particular from (3.142) that at order  $\varepsilon$  the a-connection  $\Gamma_a^\varepsilon$  comes into play. Indeed combining the previous expansions of  $\Gamma_a^\varepsilon$ ,  $E^\varepsilon$  and  $B^\varepsilon$  one obtains

$$\begin{aligned} & \gamma^2 E^\varepsilon(q^\varepsilon) + \gamma(q^\varepsilon)' \times B^\varepsilon(q^\varepsilon) - \langle \Gamma_a^\varepsilon(q^\varepsilon), (q^\varepsilon)', (q^\varepsilon)' \rangle \\ &= I_\varepsilon \left[ \gamma \hat{p}^\varepsilon \times B_{\theta^\varepsilon} \right. \\ & \left. + \varepsilon \left( \gamma^2 E_I(q^\varepsilon) + \gamma I_\varepsilon(q^\varepsilon)' \times B_I(q^\varepsilon) - \langle \Gamma_{a,\theta^\varepsilon}, I_\varepsilon(q^\varepsilon)', I_\varepsilon(q^\varepsilon)' \rangle \right) + O(\varepsilon^2) \right], \end{aligned} \tag{3.152}$$

Above and thereafter the notation  $O(\varepsilon^2)$  holds for a term of the form  $\varepsilon^2 F(\varepsilon, q^\varepsilon, \hat{p}^\varepsilon)$  where  $F$  is a vector field which is weakly nonlinear in the sense that there exists  $\delta > 0$ ,  $\varepsilon_0 \in (0, 1)$  and  $K > 0$  such that for any  $(\varepsilon, q, p)$  in  $\Omega_{\delta, \varepsilon_0} \times \mathbb{R}^3$ ,  $|F(\varepsilon, q, p)|_{\mathbb{R}^3} \leq K(1 + |p|_{\mathbb{R}^3} + \varepsilon |p|_{\mathbb{R}^3}^2)$ . Indeed the way (3.152) has to be understood is even more intricate because among the terms hidden in the  $O(\varepsilon^2)$  there is a term for which one obtains such an order only when performing a Gronwall estimate for an energy-type method. More precisely one term abusively included in the notation  $O(\varepsilon^2)$  in (3.152) is of the form  $O(\varepsilon)F(q^\varepsilon)$ , where  $F$  is a vector field in  $C^\infty(\mathbb{R} \times \Omega; \mathbb{R}^3)$  weakly gyroscopic in the sense that for any  $\delta > 0$  and  $\varepsilon_0 \in (0, 1)$  there exists  $K > 0$  depending on  $S_0$ ,  $\Omega$ ,  $\gamma$  and  $\delta$  such that for any smooth curve  $q(t) = (h(t), \theta(t))$  in  $\{x \in \Omega / d(x, \partial\Omega) > \delta\} \times \mathbb{R}$ , we have, for any  $t \geq 0$  and any  $\varepsilon \in (0, \varepsilon_0)$ ,  $|\int_0^t \tilde{p} \cdot F(q)| \leq \varepsilon K(1 + t + \int_0^t |\tilde{p}|_{\mathbb{R}^3}^2)$ , with  $\tilde{p} = (h' - \gamma u_\Omega(h), \varepsilon \theta')^t$ .

A striking and crucial phenomenon is that some subprincipal contributions (that is, of order  $\varepsilon$ ) of the right hand side of (3.152) can be gathered into an a-connection

---

<sup>10</sup>Observe that one recovers the same inertia for the leading terms ( for which the hierarchy depends on whether  $\alpha \geq 2$  or  $\alpha \leq 2$ ) than in Sect. 3.2.6 for the case where the “fluid+solid” system occupies the full plane, cf. (3.86).

term involving the bilinear mapping  $\Gamma_a^\varepsilon$  obtained in the case where the rigid body is of size  $\varepsilon = 1$  and is immersed in a fluid filling the whole plane, but applied to the modulated variable as follows<sup>11</sup>:

$$\begin{aligned} & \gamma^2 \mathbf{E}_I(q^\varepsilon) + \gamma I_\varepsilon(q^\varepsilon)' \times \mathbf{B}_I(q^\varepsilon) - \langle \Gamma_{a,\theta^\varepsilon}, I_\varepsilon(q^\varepsilon)', I_\varepsilon(q^\varepsilon)' \rangle \\ &= -\langle \Gamma_{a,\theta^\varepsilon}, \hat{p}^\varepsilon, \hat{p}^\varepsilon \rangle + \gamma(u_c(q^\varepsilon), 0)^t \times B_{\theta^\varepsilon} + O(\varepsilon), \end{aligned} \quad (3.153)$$

where  $\hat{p}^\varepsilon$  is given by (3.151),  $u_c$  is a smooth vector field on  $\mathcal{Q}$  with values in  $\mathbb{R}^2$  which depends on  $\Omega$  and  $\mathcal{S}_0$ . Indeed a quite explicit expression can be given by  $u_c := \nabla_h^\perp (D_h \psi_\Omega(h) \cdot R(\theta) \xi)$ , where  $D_h$  denotes the derivative with respect to  $h$ . We refer here again to [11] for a proof of (3.153); it relies on explicit computations of the profiles  $\mathbf{E}_I(q)$  and  $\mathbf{B}_I(q)$  thanks to geometric quantities and some tedious algebraic computations.

Next the second term in the right hand side of (3.153) can be absorbed by the principal term in the right hand side of (3.152) up to a modification of size  $\varepsilon$  of the arguments that is, thanks to the following second order modulation:

$$\tilde{p}_\varepsilon := (h'_\varepsilon - \gamma[u_\Omega(h_\varepsilon) + \varepsilon u_c(q_\varepsilon)], \varepsilon \vartheta'_\varepsilon)^t. \quad (3.154)$$

Observe also that, as long as the solid does not touch the boundary, the drift term in the velocity of the center of mass is bounded. Indeed one may easily prove that there exists  $\delta > 0$ ,  $\varepsilon_0$  in  $(0, 1)$  and  $K > 0$  such that for any  $(\varepsilon, q)$  in  $\mathcal{Q}_{\delta, \varepsilon_0}$  with  $q = (h, \theta)$ ,  $|u_\Omega(h) + \varepsilon u_c(q)|_{\mathbb{R}^3} \leq K$ .

Thus we deduce from (3.152) and (3.153) that

$$\begin{aligned} & \gamma^2 E^\varepsilon(q^\varepsilon) + \gamma(q^\varepsilon)' \times B^\varepsilon(q^\varepsilon) - \langle \Gamma_a^\varepsilon(q^\varepsilon), (q^\varepsilon)', (q^\varepsilon)' \rangle \\ &= I_\varepsilon \left[ \gamma \tilde{p}^\varepsilon \times B_{\theta^\varepsilon} - \varepsilon \langle \Gamma_{a,\theta^\varepsilon}, \tilde{p}^\varepsilon, \tilde{p}^\varepsilon \rangle + O(\varepsilon^2) \right], \end{aligned} \quad (3.155)$$

Using now (3.141) and a few further tedious manipulations Eq. (3.139) can now be recast into the following geodesic-gyroscopic normal form:

$$\left( \varepsilon^\alpha M_g + \varepsilon^2 M_{a,\theta_\varepsilon} \right) \tilde{p}'_\varepsilon + \varepsilon \langle \Gamma_{a,\theta_\varepsilon}, \tilde{p}_\varepsilon, \tilde{p}_\varepsilon \rangle = \gamma \tilde{p}^\varepsilon \times B_{\theta^\varepsilon} + O(\varepsilon^{\min(2,\alpha)}). \quad (3.156)$$

Observe how (3.156) is close to (3.88): the only two differences are the modulation of  $p^\varepsilon$  into  $\tilde{p}^\varepsilon$  and the remainder  $O(\varepsilon^{\min(2,\alpha)})$ , which actually suffers from the same abuse of notation than the term  $O(\varepsilon^2)$  described below (3.152). At least till the solid

---

<sup>11</sup>As for (3.145), this relation is algebraic, in the sense that it does not rely on the fact that  $q^\varepsilon$  satisfies (3.122).

stays away from the external boundary one may take advantage of this normal form to obtain an estimate of the modulated energy

$$\frac{1}{2} \left( \varepsilon^\alpha M_g + \varepsilon^2 M_{a,\theta_\varepsilon} \right) \tilde{p}_\varepsilon \cdot \tilde{p}_\varepsilon,$$

thanks to a Gronwall estimate. This provides uniform bounds of  $|((h^\varepsilon)', \varepsilon(\theta^\varepsilon)')|_{\mathbb{R}^3}$ . This estimate in turn allows to pass to the limit proceeding as in the proof of Theorem 3.26. The issue of a possible collision is then tackled in a bootstrapping argument thanks to the behavior of the limit systems.

More precisely we first prove that the lifetime  $T^\varepsilon$  of the solution  $q^\varepsilon$ , which can be only limited by a possible encounter between the solid and the boundary  $\partial\Omega$ , satisfies the following: there exist  $\varepsilon_0 > 0$ ,  $\underline{T} > 0$  and  $\underline{d} > 0$ , such that for any  $\varepsilon$  in  $(0, \varepsilon_0)$ , we have  $T^\varepsilon \geq \underline{T}$  and moreover on  $[0, \underline{T}]$ , one has  $(\varepsilon, q^\varepsilon) \in \Omega_{\underline{d}, \varepsilon_0}$ .

Then, using again the uniform estimates obtained thanks to the asymptotic geodesic-gyroscopic normal form (3.156) one establishes the desired convergence on any time interval during which we have a minimal distance between  $\mathcal{S}_\varepsilon(q)$  and  $\partial\Omega$ , uniform for small  $\varepsilon$ . This consists in passing to the weak limit, with the help of all a priori bounds, in the two first components of each term of (3.156). It finally only remains to extend the time interval on which the above convergences are valid to any time interval.  $\square$

### 3.4 Case of an Unbounded Flow with Vorticity

In this section we investigate the case of a rigid body immersed in an unbounded flow with vorticity.

#### 3.4.1 Statement of an Existence and Uniqueness Theorem à la Yudovich in the Body Frame

For the Cauchy problem it is more convenient to consider the body frame which does not depend on time, as we did in Sect. 3.2. We will therefore start back from Eqs. (3.38)–(3.39). In the sequel we will use an abuse of notation and still denote by  $\omega$  the vorticity in the body frame given by  $\omega(t, x) := \text{curl } v(t, x)$ . Taking the curl of Eq. (3.38) we get

$$\partial_t \omega + [(v - \ell - rx^\perp) \cdot \nabla] \omega = 0 \text{ for } x \in \mathcal{F}_0. \tag{3.157}$$

Due to the equation of vorticity (3.157) the following quantities are conserved as time proceeds, at least for smooth solutions: for any  $t > 0$ , for any  $p$  in  $[1, +\infty]$ ,

$$\|\omega(t, \cdot)\|_{L^p(\mathcal{F}_0)} = \|\omega_0\|_{L^p(\mathcal{F}_0)}. \tag{3.158}$$

In the case of a fluid alone, the conservation laws (3.158) allowed Yudovich, and DiPerna and Majda to construct some global-in-time solutions of the 2d Euler equations in the case of a velocity with finite local energy and  $L^p$  initial vorticity, with  $p > 1$ . In the case  $p = +\infty$  Yudovich also obtained a uniqueness result using in particular that the corresponding fluid velocity is in the space  $\mathcal{L}\mathcal{L}(\mathcal{F}_0)$  of log-Lipschitz  $\mathbb{R}^2$ -valued vector fields on  $\mathcal{F}_0$ , that is the set of functions  $f \in L^\infty(\mathcal{F}_0)$  such that

$$\|f\|_{\mathcal{L}\mathcal{L}(\mathcal{F}_0)} := \|f\|_{L^\infty(\mathcal{F}_0)} + \sup_{x \neq y} \frac{|f(x) - f(y)|}{|(x - y)(1 + \ln^- |x - y|)|} < +\infty. \quad (3.159)$$

These results can be adapted to the case where there is a rigid body. In these notes we will focus on a result of global in time existence and uniqueness similar to the celebrated result by Yudovich about a fluid alone.

Let us first give a global weak formulation of the problem by considering (for the solution as well as for test functions) a velocity field on the whole plane, with the constraint to be rigid on  $\mathcal{S}_0$ . We introduce the following space

$$\mathcal{H} := \left\{ \Psi \in L^2_{loc}(\mathbb{R}^2) \middle/ \operatorname{div} \Psi = 0 \text{ in } \mathbb{R}^2 \text{ and } D\Psi = 0 \text{ in } \mathcal{S}_0 \right\},$$

where  $D\Psi := \nabla\Psi + (\nabla\Psi)^T$ . It is classical that the space  $\mathcal{H}$  can be recast thanks to the property:

$$\exists (\ell_\Psi, r_\Psi) \in \mathbb{R}^2 \times \mathbb{R}, \forall x \in \mathcal{S}_0, \Psi(x) = \ell_\Psi + r_\Psi x^\perp. \quad (3.160)$$

More precisely,  $\mathcal{H} = \left\{ \Psi \in L^2_{loc}(\mathbb{R}^2) \middle/ \operatorname{div} \Psi = 0 \text{ in } \mathbb{R}^2 \text{ and satisfies (3.160)} \right\}$ , and the ordered pair  $(\ell_\Psi, r_\Psi)$  above is unique. Let us also introduce

$$\tilde{\mathcal{H}} := \left\{ \Psi \in \mathcal{H} \middle/ \Psi|_{\overline{\mathcal{F}_0}} \in C^1_c(\overline{\mathcal{F}_0}) \right\},$$

where  $\Psi|_{\overline{\mathcal{F}_0}}$  denotes the restriction of  $\Psi$  to the closure of the fluid domain. We also introduce for  $T > 0$ ,  $\tilde{\mathcal{H}}_T := C^1([0, T]; \tilde{\mathcal{H}})$ . When  $(\bar{u}, \bar{v}) \in \mathcal{H} \times \tilde{\mathcal{H}}$ , we denote by

$$\langle \bar{u}, \bar{v} \rangle := m \ell_u \cdot \ell_v + \mathcal{J} r_u r_v + \int_{\mathcal{F}_0} u \cdot v \, dx,$$

where we use the notations  $u$  and  $v$  for the restrictions of  $\bar{u}$  and  $\bar{v}$  to  $\overline{\mathcal{F}_0}$ . Our definition of a weak solution is the following.

**Definition 3.39 (Weak Solution)** Let us be given  $\bar{v}_0 \in \mathcal{H}$  and  $T > 0$ . We say that  $\bar{v} \in C([0, T]; \mathcal{H} - w)$  is a weak solution to (3.38)–(3.41) in  $[0, T]$  if for any test function  $\Psi \in \mathcal{H}_T$ ,

$$\begin{aligned} \langle \Psi(T, \cdot), \bar{v}(T, \cdot) \rangle - \langle \Psi(0, \cdot), \bar{v}_0 \rangle &= \int_0^T \left\langle \frac{\partial \Psi}{\partial t}, \bar{v} \right\rangle dt \\ &+ \int_0^T \int_{\mathcal{F}_0} v \cdot ((v - \ell_v - r_v x^\perp) \cdot \nabla) \Psi \, dx \, dt - \int_0^T \int_{\mathcal{F}_0} r_v v^\perp \cdot \Psi \, dx \, dt \\ &- \int_0^T m r_v \ell_v^\perp \cdot \ell_\Psi \, dt. \end{aligned} \tag{3.161}$$

We say that  $\bar{v} \in C([0, +\infty); \mathcal{H} - w)$  is a weak solution to (3.38)–(3.41) in  $[0, +\infty)$  if it satisfies (3.161) for all  $T > 0$ .

Definition 3.39 is legitimate since a classical solution to (3.38)–(3.41) in  $[0, T]$  is also a weak solution. This follows easily from an integration by parts in space which provides the identity on  $[0, T]$ :

$$\langle \partial_t \bar{v}, \Psi \rangle = \int_{\mathcal{F}_0} v \cdot ((v - \ell_v - r_v x^\perp) \cdot \nabla) \Psi \, dx - \int_{\mathcal{F}_0} r_v v^\perp \cdot \Psi \, dx - m r_v \ell_v^\perp \cdot \ell_\Psi, \tag{3.162}$$

and then from an integration by parts in time.

In the sequel we will often drop the index of  $\ell_v$  and  $r_v$  and we will therefore rather write  $\ell$  and  $r$ . We will equivalently say that  $(\ell, r, v)$  is a weak solution to (3.38)–(3.41).

One has the following result of existence of weak solutions for the above system, the initial position of the solid being given.

**Theorem 3.40** *For any  $\bar{v}_0 \in \mathcal{H}$  with the restriction of  $\text{curl}_0$  to  $\overline{\mathcal{F}_0}$  in  $L_c^\infty(\overline{\mathcal{F}_0})$ , there exists a unique weak solution  $\bar{v} \in C([0, +\infty); \mathcal{H} - w)$  to (3.38)–(3.41) in  $[0, +\infty)$ . Moreover  $(\ell, r)$  is in  $C^1(\mathbb{R}^+; \mathbb{R}^2 \times \mathbb{R})$ ,  $v$  is in  $L^\infty(\mathbb{R}^+; \mathcal{L}\mathcal{L}(\mathcal{F}_0))$  and  $\text{curl } v$  is in  $L^\infty(\mathbb{R}^+; L_c^\infty(\overline{\mathcal{F}_0}))$ .*

Going back to the original frame Theorem 3.40 implies Theorem 3.9. Regarding the initial data, let us observe that with any  $(\ell_0, r_0) \in \mathbb{R}^2 \times \mathbb{R}$ ,  $\omega_0 \in L_c^\infty(\overline{\mathcal{F}_0})$ , one may associate  $\bar{v}_0 \in \mathcal{H}$  by setting  $\bar{v}_0 = \ell_0 + r_0 x^\perp$  in  $\mathcal{S}_0$  and  $\bar{v}_0 = u_0$ , where  $u_0$  is the compatible initial velocity associated with  $\ell_0, r_0$  and  $\omega_0$  by Definition 3.8.

### 3.4.2 Proof of Theorem 3.40

In order to take into account the velocity contribution due to the vorticity we consider the Green’s function  $G(x, y)$  of  $\mathcal{F}_0$  with Dirichlet boundary conditions. We also introduce the function  $K(x, y) = \nabla^\perp G(x, y)$  known as the kernel of the

Biot-Savart operator  $K[\omega]$  which therefore acts on  $\omega \in L_c^\infty(\overline{\mathcal{F}_0})$  through the formula

$$K[\omega](x) = \int_{\mathcal{F}_0} K(x, y)\omega(y) dy.$$

It is classical that  $K[\omega]$  is in  $\mathcal{LL}(\mathcal{F}_0)$ , divergence-free, tangent to the boundary and satisfies  $\text{curl } K[\omega] = \omega$  and  $K[\omega](x) = \mathcal{O}(|x|^{-2})$  as  $x \rightarrow \infty$ , (so that it is square-integrable), and its circulation around  $\partial\mathcal{S}_0$  is given by  $\int_{\partial\mathcal{S}_0} K[\omega] \cdot \tau ds = -\int_{\mathcal{F}_0} \omega dx$ . Then, given  $\omega$  in  $L_c^\infty(\mathcal{F}_0)$ ,  $\ell$  in  $\mathbb{R}^2$ ,  $r$  and  $\gamma$  in  $\mathbb{R}$ , there is a unique solution  $v$  in  $\mathcal{LL}(\mathcal{F}_0)$  to the following system:

$$\begin{aligned} \text{div } v &= 0 \text{ and } \text{curl } v = \omega \quad \text{for } x \in \mathcal{F}_0, \\ v \cdot n &= (\ell + rx^\perp) \cdot n \quad \text{for } x \in \partial\mathcal{S}_0 \text{ and } \int_{\partial\mathcal{S}_0} v \cdot \tau ds = \gamma, \\ v &\longrightarrow 0 \quad \text{as } x \rightarrow \infty. \end{aligned}$$

Moreover  $v$  is given by

$$v = \tilde{v} + \beta H, \tag{3.163}$$

$$\text{with } \tilde{v} := K[\omega] + \ell_1 \nabla \Phi_1 + \ell_2 \nabla \Phi_2 + r \nabla \Phi_3 \text{ and } \beta := \gamma + \int_{\mathcal{F}_0} \omega dx.$$

We start with looking for some a priori estimates that is to some estimates satisfied by smooth solutions to (3.38)–(3.41). From Kelvin's theorem and the vorticity equation (3.157) we deduce, at least for smooth solutions, the estimates (3.158), the conservation of the total vorticity and

$$\gamma = \int_{\partial\mathcal{S}_0} v_0 \cdot \tau ds \quad \text{and} \quad \int_{\mathcal{F}_0} \omega(t, x) dx = \int_{\mathcal{F}_0} \omega_0(x) dx.$$

In particular it follows from these two conservation laws that the coefficient  $\beta$  in (3.163) is constant in time. Regarding the energy observe that  $\tilde{v}$  is in  $L^2(\mathcal{F}_0)$  whereas  $v$  is not<sup>12</sup> unless  $\beta = 0$ . Still we have the following result.

**Proposition 3.41** *There exists a constant  $C > 0$  (depending only on  $\mathcal{S}_0$ ,  $m$  and  $\mathcal{J}$ ) such that for any smooth solution  $(\ell, r, v)$  of the problem (3.38)–(3.41) on the time interval  $[0, T]$ , with compactly supported fluid vorticity, the energy-like quantity defined by:*

$$\tilde{\mathcal{E}}(t) := \frac{1}{2} \left( m|\ell(t)|^2 + \mathcal{J}r(t)^2 + \int_{\mathcal{F}_0} \tilde{v}(t, \cdot)^2 dx \right),$$

<sup>12</sup>It is interesting to compare the decomposition above with the one used in Sect. 3.2, cf. (3.54).

satisfies the inequality  $\tilde{\mathcal{E}}(t) \leq \tilde{\mathcal{E}}(0)e^{C|\beta|t}$ .

*Remark 3.42* In the case where  $\beta = 0$ , that is, when the solution is of finite energy, the energy is conserved.

*Proof* We start by recalling that a classical solution satisfies (3.162), and we use the decomposition (3.163) in the left hand side. One has for all  $t$ :

$$\tilde{v} = \mathcal{O}\left(\frac{1}{|x|^2}\right) \text{ and } \nabla \tilde{v} = \mathcal{O}\left(\frac{1}{|x|^3}\right) \text{ as } x \rightarrow \infty. \quad (3.164)$$

We use an integration by parts for the first term of the right hand side of (3.162) to get that for any test function  $\Psi \in \tilde{\mathcal{H}}_T$ ,

$$\begin{aligned} m \ell' \cdot \ell_\Psi + \mathcal{J}r' r_\Psi + \int_{\mathcal{F}_0} \partial_t \tilde{v} \cdot \Psi \, dx &= - \int_{\mathcal{F}_0} \Psi \cdot ((v - \ell - rx^\perp) \cdot \nabla) v \, dx \\ &\quad - \int_{\mathcal{F}_0} rv^\perp \cdot \Psi \, dx - mr \ell^\perp \cdot \ell_\Psi. \end{aligned}$$

Then, using a standard regular truncation process, we obtain that the previous identity is still valid for the test function  $\Psi$  defined by  $\Psi(t, x) = \tilde{v}(t, x)$  for  $(t, x)$  in  $[0, T] \times \mathcal{F}_0$  and  $\Psi(t, x) = \ell(t) + r(t)x^\perp$  for  $(t, x)$  in  $[0, T] \times S_0$ . Hence we get:

$$\begin{aligned} \tilde{\mathcal{E}}'(t) &= - \int_{\mathcal{F}_0} \tilde{v} \cdot ((v - \ell - rx^\perp) \cdot \nabla) v \, dx - \int_{\mathcal{F}_0} rv^\perp \cdot \tilde{v} \, dx \\ &= - \int_{\mathcal{F}_0} \tilde{v} \cdot ((v - \ell - rx^\perp) \cdot \nabla \tilde{v}) \, dx - \beta \int_{\mathcal{F}_0} \tilde{v} \cdot ((\tilde{v} \cdot \nabla)H) \, dx \\ &\quad + \beta \int_{\mathcal{F}_0} \tilde{v} \cdot ((\ell \cdot \nabla)H) \, dx - \beta r \int_{\mathcal{F}_0} \tilde{v} \cdot (H^\perp - (x^\perp \cdot \nabla)H) \, dx \\ &\quad - \beta^2 \int_{\mathcal{F}_0} \tilde{v} \cdot ((H \cdot \nabla)H) \, dx \\ &=: I_1 + I_2 + I_3 + I_4 + I_5. \end{aligned}$$

Integrating by parts we infer that  $I_1 = 0$ , since  $v - \ell - rx^\perp$  is a divergence free vector field, tangent to the boundary. Let us stress that there is no contribution at infinity because of the decay properties of the various fields involved, see (3.164).

On the other hand, using the smoothness and decay at infinity of  $H$ , we get that there exists  $C > 0$  depending only on  $\mathcal{F}_0$  such that

$$|I_2| + |I_3| + |I_4| \leq C|\beta| \left( \int_{\mathcal{F}_0} \tilde{v}^2 \, dx + |\ell|^2 + r^2 \right).$$

Let us now turn our attention to  $I_5$ . We first use that  $H$  being curl free, we have

$$\int_{\mathcal{F}_0} \tilde{v} \cdot ((H \cdot \nabla)H) dx = \frac{1}{2} \int_{\mathcal{F}_0} (\tilde{v} \cdot \nabla) |H|^2 dx,$$

and then an integration by parts and (3.40) to obtain

$$\begin{aligned} \int_{\mathcal{F}_0} \tilde{v} \cdot ((H \cdot \nabla)H) dx &= \frac{1}{2} \int_{\partial \mathcal{S}_0} (\tilde{v} \cdot n) |H|^2 ds \\ &= \frac{1}{2} \ell \cdot \int_{\partial \mathcal{S}_0} |H|^2 n ds + \frac{1}{2} r \int_{\partial \mathcal{S}_0} |H|^2 x^\perp \cdot n ds. \end{aligned}$$

We make use of Blasius' lemma and Cauchy's residue Theorem to obtain that  $I_5 = 0$ .

Collecting all these estimates it only remains to use Gronwall's lemma to conclude.  $\square$

Proposition 3.41 provides in particular some a priori estimates of the solid velocity. We aim now at finding an a priori bound of the body acceleration.

**Proposition 3.43** *There exists a constant  $C > 0$  depending only on  $\mathcal{S}_0$ ,  $m$ ,  $\mathcal{J}$ ,  $\beta$  and  $\tilde{\mathcal{E}}(0)$  such that any classical solution to (3.38)–(3.41) satisfies the estimate  $\|(\ell', r')\|_{L^\infty(0,T)} \leq C$ .*

*Proof* Again, after a regular truncation procedure, we can use (3.162) with, as test functions, the functions  $(\Psi_i)_{i=1,2,3}$  defined by  $\Psi_i = \nabla \Phi_i$  in  $\mathcal{F}_0$  and  $\Psi_i = e_i$ , for  $i = 1, 2$  and  $\Psi_3 = x^\perp$  in  $\mathcal{S}_0$ . We observe that the left hand side of (3.162) can be recast in terms of the acceleration of the body only thanks to the added mass phenomenon:

$$\begin{aligned} (\langle \partial_t \tilde{v}, \Psi_i \rangle)_{i=1,2,3} &= \mathcal{M}_g \begin{pmatrix} \ell \\ r \end{pmatrix}'(t) + \left( \int_{\mathcal{F}_0} \partial_t v \cdot \nabla \Phi_i dx \right)_{i=1,2,3} \\ &= (\mathcal{M}_g + \mathcal{M}_a) \begin{pmatrix} \ell \\ r \end{pmatrix}', \end{aligned}$$

using (3.52) (observe that the new contribution in the velocity due to the vorticity does not modify this identity). We recall that  $\mathcal{M}_g$  and  $\mathcal{M}_a$  were respectively given by (3.18) and (3.27). Therefore we infer from (3.162) that

$$\begin{aligned} (\mathcal{M}_g + \mathcal{M}_a) \begin{pmatrix} \ell \\ r \end{pmatrix}' &= \begin{pmatrix} -mr\ell^\perp \\ 0 \end{pmatrix} \\ &+ \left( \int_{\mathcal{F}_0} v \cdot [((v - \ell - rx^\perp) \cdot \nabla) \nabla \Phi_i] dx - \int_{\mathcal{F}_0} rv^\perp \cdot \nabla \Phi_i dx \right)_{i \in \{1,2,3\}}. \end{aligned} \tag{3.165}$$



It then suffices to use the decomposition (3.163), Proposition 3.41 and the decay properties of  $\nabla\Phi_i$  and  $H$  to obtain a bound of  $\ell'$  and  $r'$ .  $\square$

With these a priori estimates in hand there are several classical ways to infer the local in time existence of a weak solution to (3.38)–(3.41) as promised in the statement of Theorem 3.40. In order to produce directly weak solutions (without any knowledge regarding the existence of smooth solutions) one method is to apply the following Schauder’s fixed point theorem.

**Theorem 3.44** *Let  $E$  denotes a Banach space and let  $C$  be a nonempty closed convex set in  $E$ . Let  $F : C \mapsto C$  be a continuous map such that  $F(C) \subset K$ , where  $K$  is a compact subset of  $C$ . Then  $F$  has a fixed point in  $K$ .*

Theorem 3.44 is applied to an operator  $F$  which maps  $(\omega, \ell, r)$  to  $(\tilde{\omega}, \tilde{\ell}, \tilde{r})$  as follows:

$$\begin{aligned} \partial_t \tilde{\omega} + [(v - \ell - rx^\perp) \cdot \nabla] \tilde{\omega} &= 0 \text{ in } \mathcal{F}_0, \\ (\mathcal{M}_g + \mathcal{M}_a) \begin{pmatrix} \tilde{\ell} \\ \tilde{r} \end{pmatrix}' &= \left( \int_{\mathcal{F}_0} \left( v \cdot [((v - \ell - rx^\perp) \cdot \nabla) \nabla \Phi_i] - rv^\perp \cdot \nabla \Phi_i \right) dx \right)_{i \in \{1,2,3\}} \\ &\quad + \begin{pmatrix} -mr\ell^\perp \\ 0 \end{pmatrix}, \end{aligned}$$

where  $v$  is given by (3.163), with some appropriate sets  $C$  and  $K$  of functions  $(\omega, \ell, r)$  defined on a time interval  $(0, T)$  with  $T$  small enough. We thus observe that a fixed point of  $F$  verifies (3.157) and (3.165). Moreover the previous a priori bounds can be adapted to the system above and this allows to apply Schauder’s fixed point theorem. In particular the compactness for the  $(\ell, r)$ -part is given by an appropriate extension of Proposition 3.43 to weak solutions.

The global in time existence follows then from global a priori estimates in particular of the vorticity.

On the other hand the uniqueness part of Theorem 3.40 relies on Yudovich’s method for the case of a fluid alone. Suppose that we have two solutions  $(\ell_1, r_1, v_1)$  and  $(\ell_2, r_2, v_2)$  with the same initial data (observe that in this part of the proof the indices do not stand for the components). In particular, they share the same circulation  $\gamma$  and initial vorticity  $w_0$ . As a consequence, despite the fact that  $v_1$  and  $v_2$  are not necessarily in  $L^2(\mathcal{F}_0)$ , their difference  $v_1 - v_2$  does belong to  $L^\infty(0, T; L^2(\mathcal{F}_0))$  with<sup>13</sup>

$$v_1 - v_2 = \mathcal{O} \left( \frac{1}{|x|^2} \right) \text{ and } \nabla(v_1 - v_2) = \mathcal{O} \left( \frac{1}{|x|^3} \right) \text{ as } |x| \rightarrow +\infty. \quad (3.166)$$

Moreover  $\ell_1, \ell_2, r_1, r_2$  belong to  $W^{1,\infty}(0, T)$ . As a consequence, one can prove that  $\nabla q_1$  and  $\nabla q_2$  belong to  $L^\infty(0, T; L^2(\mathcal{F}_0))$ . Then defining  $\tilde{\ell} := \ell_1 - \ell_2, \tilde{r} := r_1 - r_2,$

---

<sup>13</sup>Recall that both  $v_1$  and  $v_2$  are harmonic for  $|x|$  large enough and converge to 0 at infinity.

$\check{v} := v_1 - v_2$  and  $\check{q} = q_1 - q_2$ , we deduce from (3.38) that

$$\frac{\partial \check{v}}{\partial t} + [(v_1 - \ell_1 - r_1 x^\perp) \cdot \nabla] \check{v} + [(\check{v} - \check{\ell} - \check{r} x^\perp) \cdot \nabla] v_2 + r_1 \check{v}^\perp + \check{r} v_2^\perp + \nabla \check{q} = 0.$$

We multiply by  $\check{v}$ , integrate over  $\mathcal{F}_0$  and integrate by parts (which is permitted by (3.166) and by the regularity of the pressure), and deduce:

$$\frac{1}{2} \frac{d}{dt} \|\check{v}\|_{L^2}^2 + \int_{\mathcal{F}_0} \check{v} \cdot [(\check{v} - \check{\ell} - \check{r} x^\perp) \cdot \nabla v_2] dx + \check{r} \int_{\mathcal{F}_0} \check{v} \cdot v_2^\perp dx + \int_{\partial \mathcal{F}_0} \check{q} \check{v} \cdot n = 0.$$

For what concerns the last term,

$$\begin{aligned} \int_{\partial \mathcal{F}_0} \check{q} \check{v} \cdot n &= \check{\ell} \cdot \int_{\partial \mathcal{F}_0} \check{q} n + \check{r} \int_{\partial \mathcal{F}_0} \check{q} x^\perp \cdot n \\ &= m \check{\ell} \cdot (\check{\ell}' + \check{r} \ell_1^\perp + r_2 \check{\ell}^\perp) + \mathcal{J} \check{r} \check{r}' \\ &= m \check{r} \check{\ell} \cdot \ell_1^\perp + m \check{\ell} \cdot \check{\ell}' + \mathcal{J} \check{r} \check{r}'. \end{aligned}$$

Using  $(x^\perp \cdot \nabla) v_2 = \nabla(x^\perp \cdot v_2) - v_2^\perp - x^\perp \omega_2$ , and an integration by parts, one has

$$\int_{\mathcal{F}_0} \check{v} \cdot [(x^\perp \cdot \nabla) v_2] dx = \int_{\mathcal{S}_0} (x^\perp \cdot v_2) [(\check{\ell} + \check{r} x^\perp) \cdot n] ds + \int_{\mathcal{F}_0} \check{v} \cdot (-v_2^\perp - x^\perp \omega_2) dx.$$

Hence using the boundedness of  $v_2$  and  $\omega_2$  in  $L^\infty(0, T; L^\infty(\mathcal{F}_0))$ , the boundedness of  $\ell^1$  and the one of  $\text{Supp}(\omega_2)$ , we arrive to

$$\frac{d}{dt} (\|\check{v}\|_{L^2}^2 + \|\check{\ell}\|^2 + \|\check{r}\|^2) \leq C \left( \|\check{v}\|_{L^2}^2 + \|\check{\ell}\|^2 + \|\check{r}\|^2 + \|\nabla v_2\|_{L^p} \|\check{v}^2\|_{L^{p'}} \right),$$

for  $p > 2$ . Here, the various constants  $C$  may depend on  $\mathcal{S}_0$  and on the solutions  $(\ell_1, r_1, v_1)$  and  $(\ell_2, r_2, v_2)$ , but not on  $p$ . Hence using elliptic regularity and interpolation, we obtain that for  $p$  large,

$$\begin{aligned} \frac{d}{dt} (\|\check{v}\|_{L^2}^2 + \|\check{\ell}\|^2 + \|\check{r}\|^2) &\leq C \left( \|\check{v}\|_{L^2}^2 + \|\check{\ell}\|^2 + \|\check{r}\|^2 \right) + \tilde{C}_p \|\check{v}^2\|_{L^{p'}} \\ &\leq C \left( \|\check{v}\|_{L^2}^2 + \|\check{\ell}\|^2 + \|\check{r}\|^2 \right) + \tilde{C}_p \|\check{v}\|_{L^2}^{\frac{2}{p}} \|\check{v}^2\|_{L^\infty}^{\frac{1}{p}}. \end{aligned}$$

For some constant  $K > 0$ , we have on  $[0, T]$ :  $\|\check{v}\|_{L^2}^2 + \|\check{\ell}\|^2 + \|\check{r}\|^2 \leq K$ , so for some  $C > 0$  one has in particular

$$\frac{d}{dt} (\|\check{v}\|_{L^2}^2 + \|\check{\ell}\|^2 + \|\check{r}\|^2) \leq C_p \left( \|\check{v}\|_{L^2}^2 + \|\check{\ell}\|^2 + \|\check{r}\|^2 \right)^{1/p'}.$$

Now the unique solution to  $y' = Ny^\delta$  and  $y(0) = \varepsilon > 0$  for  $\delta \in (0, 1)$  and  $N > 0$  is given by  $y(t) = \left[ (1 - \delta)Nt + \varepsilon^{1-\delta} \right]^{\frac{1}{1-\delta}}$ . Hence a comparison argument proves that  $\|\check{v}\|_{L^2}^2 + \|\check{\ell}\|^2 + \|\check{r}\|^2 \leq (Ct)^p$ . We conclude that  $\check{v} = 0$  for  $t < 1/C$  by letting  $p$  converge to  $+\infty$ .

### 3.4.3 Energy Conservation

Despite the energy-type bound obtained in Proposition 3.41 turned out to be sufficient in order to deal with the Cauchy problem, one may wonder if even in the case where  $\beta \neq 0$  (for which the kinetic fluid energy is infinite, see the discussion above Proposition 3.41) there is a renormalized energy which is exactly conserved at least for regular enough solutions to the problem (3.38)–(3.41). Another motivation is that the constant  $C$  which appears in Proposition 3.41 depends on the body geometry in such a way that the corresponding estimate is not uniform in the zero radius limit. One may hope that an exactly conserved quantity overcomes this lack of uniformity. For any  $p$  in  $\mathbb{R}^3$  and for any  $\omega \in L_c^\infty(\overline{\mathcal{F}_0})$  we define

$$\begin{aligned} \mathcal{E}(p, \omega) := & \frac{1}{2}p \cdot (\mathcal{M}_g + \mathcal{M}_a)p - \frac{1}{2} \int_{\mathcal{F}_0 \times \mathcal{F}_0} G_H(x, y) \omega(x) \omega(y) \, dx \, dy \\ & - \gamma \int_{\mathcal{F}_0} \omega(x) \Psi_H(x) \, dx, \end{aligned} \quad (3.167)$$

where  $\Psi_H$  is defined in Sect. 3.2.2 and  $G_H$  is the so-called hydrodynamic Green function defined by

$$G_H(x, y) := G(x, y) + \Psi_H(x) + \Psi_H(y), \quad (3.168)$$

where  $G$  is the standard Dirichlet Green's function defined at the beginning of Sect. 3.4.2. We recall that  $\mathcal{M}_g$  and  $\mathcal{M}_a$  were respectively given by (3.18) and (3.27). Observe that in the irrotational case where  $\omega$  is vanishing on  $\overline{\mathcal{F}_0}$  the energy  $\mathcal{E}(p, 0)$  is equal to the quantity (3.23) which was proved to be conserved in Proposition 3.14. Indeed the three terms in the right hand side of (3.167) can therefore be respectively interpreted as the kinetic energy of the rigid body with its total inertia included its genuine inertia and the added inertia due to the incompressible fluid around, the self-interaction energy of the fluid vorticity and the interaction between the fluid vorticity and the circulation around the body.

The following energy conservation property can therefore be interpreted as an extension of Proposition 3.14 to the rotational case.

**Proposition 3.45** *For any smooth solution  $(\ell, r, v)$  of the problem (3.38)–(3.41) with compactly supported vorticity, the quantity  $\mathcal{E}(\ell, r, \text{curl } v)$  is conserved along the motion.*

*Proof* We will proceed in two steps. We first give another form of (3.167). Let us prove that

$$\mathcal{E}(\ell, r, \text{curl } v) = \frac{1}{2}p \cdot \mathcal{M}_g p + \frac{1}{2} \int_{\mathcal{F}_0} (|\tilde{v}|^2 + 2\beta \tilde{v} \cdot H) dx, \quad (3.169)$$

with  $\tilde{v}$  and  $\beta$  given by the decomposition (3.163). Observe that the right hand side above can be obtained formally by expanding the natural total kinetic energy of the “fluid+solid” system  $\mathcal{E}_g(p) + \frac{1}{2} \int_{\mathcal{F}_0} |v(t, \cdot)|^2 dx$  thanks to the decomposition (3.163) and discarding the infinite term  $\frac{1}{2}\beta^2 \int_{\mathcal{F}_0} |H|^2 dx$  associated with the circulation around the body. Note in particular that  $\tilde{v}(x) = \mathcal{O}(1/|x|^2)$  as  $|x| \rightarrow +\infty$ , so that the last integral in the right hand side of (3.169) is well-defined. Let us highlight that a difference with the irrotational case discussed in Sect. 3.2.3 is that  $K[\omega]$  and  $H$  being not orthogonal in  $L^2(\mathcal{F}_0)$  there is a crossed term, given by the contribution of the last summand of the last term of (3.169), and which encompasses a dependence on  $\gamma$ , through  $\beta$ .

In order to simplify the proof of (3.169) we introduce a few notations. Let us denote  $\Psi(x) := \int_{\mathcal{F}_0} G(x, y)\omega(y)dy$  which is a stream function of  $K[\omega]$  vanishing on the boundary  $\mathcal{S}_0$ , so that  $K[\omega] = \nabla^\perp \Psi$ . Let us also denote  $\nabla \Phi := \ell_1 \nabla \Phi_1 + \ell_2 \nabla \Phi_2 + r \nabla \Phi_3$ , so that  $\tilde{v} = \nabla^\perp \Psi + \nabla \Phi$ . Then we compute

$$\int_{\mathcal{F}_0} |\tilde{v}|^2 dx = \int_{\mathcal{F}_0} \nabla^\perp \Psi \cdot \tilde{v} + \int_{\mathcal{F}_0} \nabla^\perp \Psi \cdot \nabla \Phi + \int_{\mathcal{F}_0} \nabla \Phi \cdot \nabla \Phi. \quad (3.170)$$

First, integrating by parts yields

$$\int_{\mathcal{F}_0} \nabla^\perp \Psi \cdot \tilde{v} = - \int_{\mathcal{F}_0 \times \mathcal{F}_0} G(x, y)\omega(x)\omega(y) dx dy, \quad (3.171)$$

$$\int_{\mathcal{F}_0} \nabla^\perp \Psi \cdot \nabla \Phi = 0 \text{ and } \int_{\mathcal{F}_0} \tilde{v} \cdot H = - \int_{\mathcal{F}_0} \omega(x)\Psi_H(x)dx. \quad (3.172)$$

There is no boundary terms since  $\Psi$  and  $\Psi_H$  vanish on the boundary  $\mathcal{S}_0$ , and  $\nabla \Phi$  and  $\tilde{v}$  decrease also like  $1/|x|^2$  at infinity.

Also, by definition, we have

$$\frac{1}{2} \int_{\mathcal{F}_0} \nabla \Phi \cdot \nabla \Phi = \frac{1}{2}p \cdot \mathcal{M}_a p. \quad (3.173)$$

Thus combining (3.170)–(3.173) we obtain that

$$\begin{aligned} \frac{1}{2} \int_{\mathcal{F}_0} (|\tilde{v}|^2 + 2\beta \tilde{v} \cdot H) dx &= \frac{1}{2} p \cdot \mathcal{M}_{ap} - \frac{1}{2} \int_{\mathcal{F}_0 \times \mathcal{F}_0} G(x, y) \omega(x) \omega(y) dx dy \\ &\quad - \beta \int_{\mathcal{F}_0} \omega(x) \Psi_H(x) dx. \end{aligned}$$

This entails (3.169) thanks to Fubini's theorem, (3.163) and (3.168).

Now by taking the time derivative of (3.169), using the definition of  $\mathcal{M}_g$  given in (3.18), (3.163) and that the coefficient  $\beta$  in (3.163) is constant in time, one obtains:

$$\frac{d}{dt} (\mathcal{E}(\ell, r, \text{curl } v)) = m\ell \cdot \ell'(t) + \mathcal{J}rr'(t) + \int_{\mathcal{F}_0} \partial_t v \cdot v. \quad (3.174)$$

Using now the fluid equation (3.38) one deduces from (3.174) that  $\frac{d}{dt} (\mathcal{E}(\ell, r, \text{curl } v)) = I_1 + I_2 + I_3$ , where where

$$\begin{aligned} I_1 &:= m\ell \cdot \ell'(t) + \mathcal{J}rr'(t) - \int_{\mathcal{F}_0} \nabla q \cdot v, \\ I_2 &:= - \int_{\mathcal{F}_0} (v - \ell) \cdot \nabla v \cdot v \text{ and } I_3 := -r \int_{\mathcal{F}_0} [v^\perp - (x^\perp \cdot \nabla)v] \cdot v. \end{aligned}$$

One easily justifies from the decay properties of  $H$  and  $\tilde{v}$  that each integral above is convergent. This allows to integrate by parts both  $I_1$  and  $I_2$ . Using the interface condition (3.40) and then Newton's equations for the body's dynamics, we obtain that  $I_1 = 0$ . For what concerns  $I_2$  we get that

$$I_2 = -\frac{1}{2} \int_{\partial S_0} |v|^2 (v - \ell) \cdot n.$$

For what concerns  $I_3$ , we consider  $R > 0$  large in order that  $S_0 \subset B(0, R)$ , and consider the same integral as  $I_3$ , over  $\mathcal{F}_0 \cap B(0, R)$ . Integrating by parts we obtain

$$\int_{\mathcal{F}_0 \cap B(0, R)} [v^\perp - (x^\perp \cdot \nabla)v] \cdot v = - \int_{\partial S_0} (x^\perp \cdot n) \frac{|v|^2}{2} - \int_{S(0, R)} (x^\perp \cdot n) \frac{|v|^2}{2},$$

where we denote by  $n$  also the unit outward normal on the circle  $S(0, R)$ . Of course  $x^\perp \cdot n = 0$  on  $S(0, R)$ , so letting  $R \rightarrow +\infty$ , we end up with

$$I_3 = \frac{1}{2} \int_{\partial S_0} (rx^\perp \cdot n) |v|^2.$$

Using (3.40) we deduce  $I_2 + I_3 = 0$ , so in total we get  $\frac{d}{dt}(\mathcal{E}(\ell, r, \text{curl } v)) = 0$ .  $\square$

One difficulty with the quantity  $\mathcal{E}$  is that both its form (3.167) and (3.169) are not the sum of positive terms. However one may extirpate some information from the conservation of  $\mathcal{E}$  thanks to the support of vorticity. The basic idea can be exhibited thanks to the following technical lemma, having in mind that the hydrodynamic Green function  $G_H(x, y)$  behaves like  $\frac{1}{2\pi} \ln |x - y|$  at infinity.

**Lemma 3.46** *Let  $f$  in  $L^1(\mathbb{R}^2) \cap L^\infty(\mathbb{R}^2)$ . We denote by  $\rho_f := \inf\{d > 1 / \text{Supp}(f) \subset B(0, d)\}$ . Then there exists  $C > 0$  such that or any  $y \in B(0, \rho_f)$ ,*

$$\int_{\mathbb{R}^2} \left| \ln |x - y| f(x) \right| dx \leq C \|f\|_{L^\infty} + \ln(2\rho_f) \|f\|_{L^1}.$$

*Proof* It is sufficient to decompose the integral depending on whether  $|x - y| \geq 1$  or not.  $\square$

As a consequence we have the following result.

**Corollary 3.47** *One has the following estimate for some positive constant  $C$  depending only on  $m, \mathcal{J}, \|\omega_0\|_{L^1 \cap L^\infty}, |\ell_0|, |r_0|, |\gamma|, \rho(0)$ , and the geometry:  $|\ell(t)| + |r(t)| \leq C[1 + \ln(\rho(t))]$ , where  $\rho(t) := \inf\{d > 1 / \text{Supp}(\omega(t, \cdot)) \subset B(0, d)\}$ .*

### 3.4.4 A Macroscopic Normal form Tailored for the Zero-Radius Limit

We define the set

$$\mathcal{B} := \cup_{q \in \mathbb{R}^3} \{q\} \times \mathbb{R}^3 \times \mathbb{R} \times L^\infty(\mathcal{F}(q); \mathbb{R}).$$

The following result is deduced, by going back to the original frame, from the existence and uniqueness result established in Sect. 3.4.2 for the div/curl type system satisfied by the velocity in the body frame.

**Proposition 3.48** *For any  $(q, p, \gamma, \omega)$  in  $\mathcal{B}$  with  $p = (\ell, r)$  in  $\mathbb{R}^2 \times \mathbb{R}$ , there exists a unique  $U(q, p, \gamma, \omega)$  in the space  $\mathcal{LL}(\mathcal{F}(q))$  such that*

$$\text{div } U(q, p, \gamma, \omega) = 0 \text{ and } \text{curl } U(q, p, \gamma, \omega) = \omega \text{ for } x \in \mathcal{F}(q),$$

$$U(q, p, \gamma, \omega) \cdot n = (\ell + rx^\perp) \cdot n \text{ for } x \in \partial\mathcal{S}(q) \text{ and } \int_{\partial\mathcal{S}(q)} U(q, p, \gamma, \omega) \cdot \tau ds = \gamma,$$

$$U(q, p, \gamma, \omega) \longrightarrow 0 \text{ as } x \rightarrow \infty.$$

In order to prepare the asymptotic analysis of the rigid body's dynamics in the zero radius limit, we first establish here an exact normal form of the Newton

equations for the solid motion for a fixed radius. It follows the analysis performed in Sect. 3.3 so that we will adopt here the real-analytic approach developed in [11] rather than the complex-analytic approach performed in [9]. This will simplify the study of the zero radius limit in the next subsection.

**Theorem 3.49** *There exists a mapping  $F$  in  $C(\mathcal{B}; \mathbb{R}^3)$  depending only on  $\gamma$  and  $S_0$  such that Eqs. (3.13)–(3.16) are equivalent to the following system:*

$$(\mathcal{M}_g + \mathcal{M}_{a,\theta}) q'' + \langle \Gamma_{a,\theta}, q', q' \rangle = F(q, q', \gamma, \omega), \quad (3.175)$$

$$\frac{\partial \omega}{\partial t} + \operatorname{div}(\omega U(q, q', \gamma, \omega)) = 0 \text{ for } x \in \mathcal{F}(q(t)), \quad (3.176)$$

where  $\mathcal{M}_{a,\theta}$  is given by Theorem 3.12 and  $\Gamma_{a,\theta}$  denotes the  $a$ -connection associated with  $\mathcal{M}_{a,\theta}$  by Definition 3.11.

Above it is understood that the equivalence concerns Yudovich type solutions.

One observes that the left hand side of (3.175) is the same than the one of (3.20). On the other hand the right hand side of (3.175) is more intricate. Indeed we are going to provide a rather explicit definition of the force term  $F$ . In order to do so we split, for  $(q, p, \gamma, \omega)$  in  $\mathcal{B}$ , the vector field  $U(q, p, \gamma, \omega)$  into

$$U(q, p, \gamma, \omega) = U_1(q, p) + U_2(q, \gamma, \omega), \quad (3.177)$$

where  $U_1(q, p)$  denotes the potential part that is the unique solution in the space  $\mathcal{LL}(\mathcal{F}(q))$  to the following system:

$$\operatorname{div} U_1(q, p) = 0 \text{ and } \operatorname{curl} U_1(q, p) = 0 \quad \text{for } x \in \mathcal{F}(q),$$

$$U_1(q, p) \cdot n = (\ell + r(x - h)^\perp) \cdot n \quad \text{for } x \in \partial\mathcal{S}(q) \text{ and } \int_{\partial\mathcal{S}(q)} U_1(q, p) \cdot \tau \, ds = 0,$$

$$U_1(q, p) \longrightarrow 0 \quad \text{as } x \rightarrow \infty,$$

where  $q = (h, \theta)$  and  $p = (\ell, r)$ , and  $U_2(q, \gamma, \omega)$  therefore denotes the unique solution in the space  $\mathcal{LL}(\mathcal{F}(q))$  to the following system:

$$\operatorname{div} U_2(q, \gamma, \omega) = 0 \text{ and } \operatorname{curl} U_2(q, \gamma, \omega) = \omega \quad \text{for } x \in \mathcal{F}(q),$$

$$U_2(q, \gamma, \omega) \cdot n = 0 \quad \text{for } x \in \partial\mathcal{S}(q) \text{ and } \int_{\partial\mathcal{S}(q)} U_2(q, \gamma, \omega) \cdot \tau \, ds = \gamma,$$

$$U_2(q, \gamma, \omega) \longrightarrow 0 \quad \text{as } x \rightarrow \infty.$$

Observe that the vector fields  $U_1(q, p)$  and  $U_2(q, \gamma, \omega)$  are respectively linear with respect to  $p$  and  $(\gamma, \omega)$  whereas their dependence on  $q$  is encoded into the change of variable (3.37) (since their counterpart in the body frame do not depend on  $q$ ).

Eventually, we define for  $(q, p, \gamma, \omega)$  in  $\mathcal{B}$ , three vector in  $\mathbb{R}^3$ , by

$$B(q, \gamma, \omega) := - \int_{\partial\mathcal{S}(q)} U_2(q, \gamma, \omega) \cdot \tau \left( (U_1(q, e_i) \cdot n)_i \times (U_1(q, e_i) \cdot \tau)_i \right) ds, \quad (3.178)$$

$$E(q, \gamma, \omega) := - \frac{1}{2} \left( \int_{\partial\mathcal{S}(q)} |U_2(q, \gamma, \omega)|^2 U_1(q, e_i) \cdot n ds \right)_i, \quad (3.179)$$

$$D(q, p, \gamma, \omega) := - \left( \int_{\mathcal{F}(q)} \omega U(q, p, \gamma, \omega)^\perp \cdot U_1(q, e_i) dx \right)_i, \quad (3.180)$$

where the index  $i$  runs over 1, 2, 3 and the  $e_i$  stands for the canonical basis of  $\mathbb{R}^3$ . We will prove Theorem 3.49 with the mapping  $F$  given, for  $(q, p, \gamma, \omega)$  in  $\mathcal{B}$ , by

$$F(q, p, \gamma, \omega) := \gamma^2 E(q, \gamma, \omega) + \gamma p \times B(q, \gamma, \omega) + D(q, p, \gamma, \omega). \quad (3.181)$$

Observe that the vector fields  $B(q, \gamma, \omega)$  and  $E(q, \gamma, \omega)$  above have the same form than the vector fields  $B(q)$  and  $E(q)$  used in Sect. 3.3, see (3.124) and (3.125) except that they also encompass a contribution due to the vorticity through the vector fields  $U_2$ . The last term in (3.181) is a direct contribution of the vorticity, in the sense that it intervenes explicitly inside an integral over the fluid domain. In particular this term may be nonzero even if  $\gamma = 0$  unlike the two first terms.

*Proof* First of all (3.176) simply recasts the transport of the fluid vorticity by the fluid velocity characterized by Proposition 3.48. The proof of Theorem 3.49 therefore reduces to prove the equivalence of Newton's equations for the solid motion with (3.175). In a perhaps surprising way it seems more convenient not to use the reformulation (3.38)–(3.39) of the system in the body frame. Instead we rather proceed as in Sect. 3.3 with a few modifications due to the fact that we now deal with a non-vanishing vorticity  $\omega = \text{curl } u$ . In particular one has to modify (3.100) into

$$\nabla \pi = - \left( \frac{\partial u}{\partial t} + \frac{1}{2} \nabla |u|^2 + \omega u^\perp \right) \quad \text{in } \mathcal{F}(q).$$

and therefore (3.101) becomes

$$\begin{aligned} mh'' \cdot \ell^* + \mathcal{J} \theta'' r^* &= - \int_{\mathcal{F}(q)} \left( \frac{\partial u}{\partial t} + \frac{1}{2} \nabla (u^2) \right) \cdot U_1(q, p^*) dx \\ &\quad - \int_{\mathcal{F}(q)} \omega u^\perp \cdot U_1(q, p^*) dx, \quad \text{for all } p^* = (\ell^*, r^*) \in \mathbb{R}^3. \end{aligned}$$



Then we use that  $u = U(q, q', \gamma, \omega) = U_1(q, q') + U_2(q, \gamma, \omega)$  to obtain, for all  $p^* := (\ell^*, r^*) \in \mathbb{R}^3$ ,

$$\begin{aligned}
 m\ell' \cdot \ell^* + \mathcal{J}r'r^* + \int_{\mathcal{F}(q)} \left( \frac{\partial U_1(q, q')}{\partial t} + \frac{1}{2} \nabla |U_1(q, q')|^2 \right) \cdot U_1(q, p^*) dx \\
 = - \int_{\mathcal{F}(q)} \left( \frac{1}{2} \nabla |U_2(q, \gamma, \omega)|^2 \right) \cdot U_1(q, p^*) dx \\
 - \int_{\mathcal{F}(q)} \left( \frac{\partial U_2(q, \gamma, \omega)}{\partial t} + \frac{1}{2} \nabla (U_1(q, q') \cdot U_2(q, \gamma, \omega)) \right) \cdot U_1(q, p^*) dx \\
 - \int_{\mathcal{F}(q)} \omega U(q, q', \gamma, \omega)^\perp \cdot U_1(q, p^*) dx. \tag{3.182}
 \end{aligned}$$

Using Theorem 3.12 in the case where  $\gamma = 0$  yields that the left hand side of (3.182) is equal to inner product of the left hand side of (3.175) with  $p^*$ . By integration by parts one obtains that the first term in the right hand side of (3.182) is equal to inner product of  $\gamma^2 E(q, \gamma, \omega)$  with  $p^*$ . By adapting the proof of (3.131) one proves that the second term in the right hand side of (3.182) is equal to inner product of  $\gamma q' \times B(q, \gamma, \omega)$  with  $p^*$ . It follows from the linearity of  $U_1(q, p)$  with respect to  $p$  that the last term of (3.182) is equal to inner product of  $D(q, q', \gamma, \omega)$  with  $p^*$ , and this concludes the proof of Theorem 3.49.  $\square$

### 3.4.5 Zero Radius Limit

We now investigate the zero radius limit and therefore assume that, for every  $\varepsilon \in (0, 1]$ , the solid domain occupies (3.5) where  $\mathcal{S}_0$  is a fixed simply connected smooth compact subset of  $\mathbb{R}^2$ . We consider  $p_0 = (\ell_0, r_0) \in \mathbb{R}^3$ ,  $m > 0$ ,  $\mathcal{J} > 0$ ,  $\gamma$  in  $\mathbb{R}$  (respectively in  $\mathbb{R}^*$ ) in the case of a massive (resp. massless) particle. Let  $\omega_0$  in  $L_c^\infty(\mathbb{R}^2 \setminus \{0\})$  Then for every  $\varepsilon \in (0, 1]$ , combining Theorems 3.9 and 3.49, we obtain that there exists a unique global solution  $(h^\varepsilon, \theta^\varepsilon, \omega^\varepsilon)$  with Yudovich regularity (in particular with bounded vorticity) to Eqs. (3.175)–(3.176) with some coefficients  $\mathcal{M}_g^\varepsilon$ ,  $\mathcal{M}_a^\varepsilon$ ,  $\Gamma_a^\varepsilon$  and  $F^\varepsilon$  associated with  $\mathcal{S}_0^\varepsilon$ ,  $m^\varepsilon$ ,  $\mathcal{J}^\varepsilon$  given in Definition 3.1 and  $\gamma$ , and with the initial data  $(q^\varepsilon, (q^\varepsilon)')(0) = (0, p_0)$  and  $\omega^\varepsilon|_{t=0} = \omega_0|_{\mathcal{F}_0^\varepsilon}$ . In the massless case with  $\alpha \geq 2$ , we will consider only here the case where  $\mathcal{S}_0$  is not a disk. As already mentioned in the fifth remark after Definition 3.1 the case where  $\mathcal{S}_0$  is a non-homogeneous disk requires a few adaptations and can be tackled as in [11] for the irrotational bounded case (whereas this case was actually omitted in [8, 9]). Our results then read as follows.

**Theorem 3.50** *Let be given a circulation  $\gamma$  in  $\mathbb{R}$  in the case of a massive particle and in  $\mathbb{R}^*$  in the case of a massless particle. Let be given  $(\ell_0, r_0) \in \mathbb{R}^3$ ,  $\omega_0$  in  $L_c^\infty(\mathbb{R}^2 \setminus \{0\})$ . For any  $\varepsilon \in (0, 1]$ , let us denote  $(h^\varepsilon, \theta^\varepsilon, \omega^\varepsilon)$  the solution to the system associated with  $\mathcal{S}_0^\varepsilon$ ,  $m^\varepsilon$ ,  $\mathcal{J}^\varepsilon$ ,  $\ell_0$ ,  $r_0$ ,  $\gamma$  and  $\omega_0|_{\mathcal{F}_0^\varepsilon}$  as above. Then in the zero radius*

limit  $\varepsilon \rightarrow 0$ , with the inertia scaling described in Definition 3.1, one has, in the case of a massive (respectively massless) particle, that for any  $T > 0$ , up to a subsequence (resp. for the whole sequence),  $h^\varepsilon$  converges to  $h$  weakly- $*$  in  $W^{2,\infty}(0, T; \mathbb{R}^2)$  (resp. in  $W^{1,\infty}(0, T; \mathbb{R}^2)$ ),  $\varepsilon\theta^\varepsilon$  converges to 0 weakly- $*$  in  $W^{2,\infty}(0, T; \mathbb{R})$   $\omega^\varepsilon$  (extended by 0 inside the solid) converges to  $\omega$  in  $C^0([0, T]; L^\infty(\mathbb{R}^2))$  – weak- $\star$ . Moreover one has (3.12) in  $[0, T] \times \mathbb{R}^2$ , respectively (3.10) in the massive limit and (3.11) in the massless limit, with the initial conditions  $\omega|_{t=0} = \omega_0$ ,  $h(0) = 0$ ,  $h'(0) = \ell_0$  (resp.  $\omega|_{t=0} = \omega_0$ ,  $h(0) = 0$ ).

*Remark 3.51* Note that the convergence of  $h^\varepsilon$  cannot be strong in  $W^{1,\infty}(0, T; \mathbb{R}^2)$  in general, as this would entail that

$$\ell_0 = \frac{1}{2\pi} \int_{\mathbb{R}^2} \frac{(h_0 - y)^\perp}{|h_0 - y|^2} \omega_0(y) dy.$$

Theorem 3.10 is a consequence of Theorem 3.50.

*Proof* We will proceed as in the proof of Theorem 3.37 with a few modifications. First using  $p^\varepsilon = ((h^\varepsilon)', \varepsilon(\theta^\varepsilon)')$  we obtain that the solid equations are of the form

$$\begin{aligned} & (\varepsilon^\alpha \mathcal{M}_g + \varepsilon^2 \mathcal{M}_{a,\theta^\varepsilon})(p^\varepsilon)' + \varepsilon \langle \Gamma_{a,\theta^\varepsilon}, p^\varepsilon, p^\varepsilon \rangle \tag{3.183} \\ & = \gamma^2 \tilde{E}^\varepsilon(q^\varepsilon, \gamma, \omega^\varepsilon) + \gamma p^\varepsilon \times \tilde{B}^\varepsilon(q^\varepsilon, \gamma, \omega^\varepsilon) + \tilde{D}^\varepsilon(q^\varepsilon, p^\varepsilon, \gamma, \omega^\varepsilon), \end{aligned}$$

where  $\tilde{E}^\varepsilon$ ,  $\tilde{B}^\varepsilon$  and  $\tilde{D}^\varepsilon$  are respectively deduced from  $E$ ,  $B$  and  $D$  defined in (3.178), (3.179) and (3.180) by some appropriate scalings. Here again the crucial issue is to obtain some bounds uniformly in  $\varepsilon$  in order to pass to the limit in (3.183). First we look for an appropriate modification of Corollary 3.47 in the zero radius limit thanks to an appropriate renormalization of the energy (3.167) as  $\varepsilon \rightarrow 0^+$  by discarding some terms which are logarithmically divergent in the limit but which do not bear any information on the state of the system.<sup>14</sup> This provides a uniform estimate of  $\varepsilon^{\min(1, \frac{\alpha}{2})} |(h^\varepsilon)', \varepsilon(\theta^\varepsilon)'|_{\mathbb{R}^3}$  at least till the vorticity is neither too far from the solid nor too close. Unfortunately in the massless case the coefficient  $\alpha$  satisfies  $\alpha > 0$  and the previous estimate is not sufficient. In order to get some improved estimates, we expand the coefficients in (3.183) as  $\varepsilon \rightarrow 0^+$  using in particular an irrotational approximation of the fluid velocity on the body’s boundary in order to use Lamb’s lemma. Some cancellations similar to (3.152) and (3.153) allow in particular to absorb the leading orders of the term  $\tilde{E}^\varepsilon$  into the leading part of the expansions of the terms involving  $\Gamma_{a,\theta^\varepsilon}$  and  $\tilde{B}^\varepsilon$  thanks to the following modulation of the velocity:

$$\tilde{\ell}^\varepsilon(t) := (h^\varepsilon)'(t) - K_{\mathbb{R}^2}[\omega^\varepsilon(t, \cdot)](h^\varepsilon) - \varepsilon \nabla K_{\mathbb{R}^2}[\omega^\varepsilon(t, \cdot)](h^\varepsilon) \cdot R(\theta^\varepsilon)\xi,$$

---

<sup>14</sup>Observe that the quantity (3.167) was already obtained from the natural total kinetic energy of the “fluid+solid” system by a renormalization at infinity. Here the renormalization rather tackles some undesired concentrations at the center of mass of the shrinking particle.

where  $\xi$  is the conformal center of  $\mathcal{S}_0$ , cf. (3.34). On the other hand the term  $\tilde{D}^\varepsilon$  turns out to be smaller at least till the vorticity stays supported at distance of order 1 of the solid. Next we introduce the notation  $\tilde{p}^\varepsilon := (\tilde{\ell}^\varepsilon, \varepsilon(\theta^\varepsilon)')$ . We thus obtain the following asymptotic normal form.

**Proposition 3.52** *Let us fix  $\rho > 0$ . There exists  $C > 0$  such that if for a given  $T > 0$  and an  $\varepsilon \in (0, 1)$  one has for all  $t \in [0, T]$ :*

$$d(h^\varepsilon(t), \text{Supp}(\omega^\varepsilon(t))) \geq 1/\rho \text{ and } \text{Supp}(\omega^\varepsilon(t)) \subset B(h^\varepsilon(t), \rho), \tag{3.184}$$

then there exist a function  $G = G(\varepsilon, t) : (0, 1) \times [0, T] \rightarrow \mathbb{R}^3$  satisfying

$$\left| \int_0^t \tilde{p}^\varepsilon(s) \cdot G(\varepsilon, s) ds \right| \leq \varepsilon C \left( 1 + t + \int_0^t |\tilde{p}^\varepsilon(s)|^2 ds \right), \tag{3.185}$$

and a function  $F = F(\varepsilon, t) : (0, 1) \times [0, T] \rightarrow \mathbb{R}^3$  satisfying

$$|F(\varepsilon, t)| \leq C (1 + |\tilde{p}^\varepsilon(t)| + \varepsilon |\tilde{p}^\varepsilon(t)|^2), \tag{3.186}$$

such that one has on  $[0, T]$ :

$$\begin{aligned} & (\varepsilon^\alpha \mathcal{M}_g + \varepsilon^2 \mathcal{M}_{a, \theta^\varepsilon})(\tilde{p}^\varepsilon)' + \varepsilon \langle \Gamma_{a, \theta^\varepsilon}, \tilde{p}^\varepsilon, \tilde{p}^\varepsilon \rangle \\ & = \gamma \tilde{p}^\varepsilon \times B_{\theta^\varepsilon} + \varepsilon \gamma G(\varepsilon, t) + \varepsilon^{\min(\alpha, 2)} F(\varepsilon, t). \end{aligned} \tag{3.187}$$

From this normal form, we deduce the following modulated energy estimates.

**Lemma 3.53** *Let  $\rho > 0$ . There exists  $C > 0$  such that if for a given  $T > 0$  and an  $\varepsilon \in (0, 1)$  one has that (3.184) is valid on  $[0, T]$ , then one has  $|(h^\varepsilon)'| + \varepsilon |(\theta^\varepsilon)'| \leq C$  on  $[0, T]$ .*

*Proof* Let  $\rho > 0$  and let  $C > 0$  be given by Proposition 3.52. Let  $T > 0$  and an  $\varepsilon \in (0, 1)$  one has that (3.184) is valid on  $[0, T]$ . Then according to Proposition 3.52 one has (3.187) on  $[0, T]$ . It is then sufficient to multiply (3.187) by  $\tilde{p}^\varepsilon$ , to deal with the right hand side as in Proposition 3.14, to use the assumption on the initial data and finally to apply two Gronwall type estimates<sup>15</sup> to conclude.  $\square$

Let us now tackle the passage to the limit. In a first time, we obtain the convergence stated in Theorem 3.50 on a small interval  $[0, T]$ , and only in a second time obtain this convergence on any time interval. We consider  $T^\varepsilon$  the supremum of the positive real number  $\tau$  for which one has for any  $t \in [0, \tau]$ ,  $d(h^\varepsilon(t), \text{Supp} \omega^\varepsilon(t)) > 1/(2\rho_T)$  and  $\text{Supp} \omega^\varepsilon(t) \subset B(h^\varepsilon(t), 2\rho_T)$ . For any  $\varepsilon > 0$  small enough such that  $d(\text{Supp} \omega_0, \mathcal{S}_0^\varepsilon) > 2\rho_T/3$ , we have of course  $T^\varepsilon > 0$ . Using Proposition 3.53, we deduce that there exists  $\varepsilon_0 > 0$  and  $\underline{T} > 0$  such that  $\inf_{\varepsilon \in (0, \varepsilon_0)} T^\varepsilon \geq \underline{T}$ .

---

<sup>15</sup>The second one being devoted to deduce some estimates for  $(h^\varepsilon)'$  from the ones on the modulated velocities.

Thanks to a compactness argument using these estimates, the uniqueness of the solutions in the limit and Proposition 3.52 this allows to prove the convergence claimed in Theorem 3.50 locally in time, that is  $h^\varepsilon$  converges to  $h$  weakly- $\star$  in  $W^{1,\infty}(0, \underline{T}; \mathbb{R}^2)$  and  $\omega^\varepsilon$  converges to  $\omega$  in  $C^0([0, \underline{T}]; L^\infty(\mathbb{R}^2) - \text{weak-}\star)$ . Finally we obtain the solid part of Theorem 3.50 by a sort of continuous induction argument. Moreover, with the previous uniform estimates, passing to the limit in the fluid equation is routine.  $\square$

**Acknowledgements** The author thanks the Agence Nationale de la Recherche, Project DYFI-COLTI, grant ANR-13-BS01-0003-01 and Project IFSMACS, grant ANR-15-CE40-0010 for their financial support.

## References

1. J. Berkowitz, C.S. Gardner, On the asymptotic series expansion of the motion of a charged particle in slowly varying fields. *Commun. Pure Appl. Math.* **12**, 501–512 (1959)
2. K.O. Friedrichs, *Special Topics in Fluid Dynamics* (Gordon and Breach, New York, 1966)
3. T. Gallay, Interaction of vortices in weakly viscous planar flows. *Arch. Ration. Mech. Anal.* **200**(2), 445–490 (2011)
4. O. Glass, F. Sueur, The movement of a solid in an incompressible perfect fluid as a geodesic flow. *Proc. Am. Math. Soc.* **140**(6), 2155–2168 (2012)
5. O. Glass, F. Sueur, On the motion of a rigid body in a two-dimensional irregular ideal flow. *SIAM J. Math. Anal.* **44**(5), 3101–3126 (2013)
6. O. Glass, F. Sueur, Low regularity solutions for the two-dimensional “rigid body + incompressible Euler” system. *Differ. Integr. Equ.* **27**(7–8), 625–642 (2014)
7. O. Glass, F. Sueur, Uniqueness results for weak solutions of two-dimensional fluid-solid systems. *Arch. Ration. Mech. Anal.* **218**(2), 907–944 (2015)
8. O. Glass, C. Lacave, F. Sueur, On the motion of a small body immersed in a two dimensional incompressible perfect fluid. *Bull. Soc. Math. France* **142**(3), 489–536 (2014)
9. O. Glass, C. Lacave, F. Sueur, On the motion of a small light body immersed in a two dimensional incompressible perfect fluid with vorticity. *Commun. Math. Phys.* **341**(3), 1015–1065 (2016)
10. O. Glass, C. Lacave, A. Munnier, F. Sueur, Dynamics of rigid bodies of various sizes and masses in a two dimensional incompressible perfect fluid (in preparation)
11. O. Glass, A. Munnier, F. Sueur, Point vortex dynamics as zero-radius limit of a of the motion of a rigid body in an irrotational fluid. <https://hal.inria.fr/hal-00950544/en>
12. H. Helmholtz, Über Integrale der hydrodynamischen Gleichungen, welche den Wirbelbewegungen entsprechen. *Crelles J.* **55**, 25 (1858). Translation in: On the integral of the hydrodynamical equations which express vortex motion. *Philos. Mag.* **33**, 485–513 (1867)
13. J. Houot, Analyse mathématique des mouvements des rigides dans un fluide parfait. Thèse de l’Université de Nancy 1, 2008
14. J. Houot, A. Munnier, On the motion and collisions of rigid bodies in an ideal fluid. *Asymptot. Anal.* **56**(3–4), 125–158 (2008)
15. D. Iftimie, M.C. Lopes Filho, H.J. Nussenzveig Lopes, Two dimensional incompressible ideal flow around a small obstacle. *Commun. Partial Differ. Equ.* **28**(1–2), 349–379 (2003)
16. G. Kirchhoff, *Vorlesungen über mathematische Physik, Mechanik* (Teuber, Leipzig, 1876)
17. C. Lacave, Two-dimensional incompressible ideal flow around a small curve. *Commun. Partial Differ. Equ.* **37**(4), 690–731 (2012)

18. C. Lacave, E. Miot, Uniqueness for the vortex-wave system when the vorticity is constant near the point vortex. *SIAM J. Math. Anal.* **41**(3), 1138–1163 (2009)
19. H. Lamb, *Hydrodynamics*. Reprint of the 1932 sixth edition (Cambridge University Press, Cambridge, 1993)
20. C.C. Lin, On the motion of vortices in two dimensions I. Existence of the Kirchhoff-Routh function. *Proc. Natl. Acad. Sci. U. S. A.* **27**, 570–575 (1941)
21. C.C. Lin, On the motion of vortices in two dimensions II. Some further investigations on the Kirchhoff-Routh function. *Proc. Natl. Acad. Sci. U. S. A.* **27**, 575–577 (1941)
22. M.C. Lopes Filho, Vortex dynamics in a two-dimensional domain with holes and the small obstacle limit. *SIAM J. Math. Anal.* **39**(2), 422–436 (2007)
23. C. Marchioro, M. Pulvirenti, *Mathematical Theory of Incompressible Nonviscous Fluids*. Applied Mathematical Sciences, vol. 96 (Springer, Berlin, 1994)
24. A. Munnier, Locomotion of deformable bodies in an ideal fluid: Newtonian versus Lagrangian formalisms. *J. Nonlinear Sci.* **19**, 665–715 (2009)
25. J. Ortega, L. Rosier, T. Takahashi, On the motion of a rigid body immersed in a bidimensional incompressible perfect fluid. *Ann. Inst. H. Poincaré Anal. Non Linéaire* **24**(1), 139–165 (2007)
26. H. Poincaré, *Théorie des Tourbillons* (George Carré, Paris, 1893)
27. E.J. Routh, Some applications of conjugate functions. *Proc. Lond. Math. Soc.* **12**, 73–89 (1881)
28. L. Sedov, *Two-Dimensional Problems of Hydrodynamics and Aerodynamics* (Moscow Izdatel Nauka 1, Moscow, 1980)
29. F. Sueur, On the motion of a rigid body in a two-dimensional ideal flow with vortex sheet initial data. *Ann. Inst. H. Poincaré Anal. Non Linéaire* **30**(3), 401–417 (2013)
30. W. Thomson (Lord Kelvin), *Mathematical and Physical Papers* (Cambridge University Press, Cambridge, 1910)
31. B. Turkington, On the evolution of a concentrated vortex in an ideal fluid. *Arch. Rational Mech. Anal.* **97**(1), 75–87 (1987)
32. V.I. Yudovich, Non-stationary flows of an ideal incompressible fluid. *Ž. Vyčisl. Mat. i Mat. Fiz.* **3**, 1032–1066 (1963) (in Russian). English translation in *USSR Comput. Math. Math. Phys.* **3**, 1407–1456 (1963)

# Chapter 4

## Stability of Permanent Rotations and Long-Time Behavior of Inertial Motions of a Rigid Body with an Interior Liquid-Filled Cavity

G.P. Galdi

**Abstract** A rigid body, with an interior cavity entirely filled with a Navier-Stokes liquid, moves in absence of external torques relative to the center of mass of the coupled system body-liquid (inertial motions). The only steady-state motions allowed are then those where the system, as a whole rigid body, rotates uniformly around one of the central axes of inertia (permanent rotations). Objective of this article is twofold. On the one hand, we provide sufficient conditions for the asymptotic, exponential stability of permanent rotations, as well as for their instability. On the other hand, we study the asymptotic behavior of the generic motion in the class of weak solutions and show that there exists a time  $t_0$  after that all such solutions must decay exponentially fast to a permanent rotation. This result provides a *full* and rigorous explanation of Zhukovsky's conjecture, and explains, likewise, other interesting phenomena that are observed in both lab and numerical experiments.

**Keywords** Center manifold • Liquid-filled cavity • Navier-Stokes • Rigid body • Stability

**MSC2010:** 35B35; 35B41; 35Q35; 74F10

### 4.1 Introduction

The problem of the motion of the coupled system constituted by a rigid body with an interior cavity that is entirely filled with a liquid has represented, over the centuries, one of the main focuses of theoretical and applied research. As a matter of fact, the first mathematical analysis of such a problem can be traced back to the pioneering

---

G.P. Galdi (✉)

Department of Mechanical Engineering and Materials Science, University of Pittsburgh, 607

Benedum Engineering Hall, Pittsburgh, PA 15621, USA

e-mail: [galdi@pitt.edu](mailto:galdi@pitt.edu)

work of Stokes concerning the motion of a rectangular box filled with an inviscid liquid [31, §13].

One of the main reasons why this topic received all along increasing attention is because it was rather immediately recognized that the dynamics of the rigid body can be substantially and drastically affected by the presence of the liquid, in several different and major aspects. In these regards, the finding of Lord Kelvin (W. Thomson) [33] can be considered a true cornerstone. Actually, it was well known from both a theoretical viewpoint—basically, by Lagrange [20, Part 2, §9] and Poisson [28]—and practical one—after the use of gyroscopes in navigation since the early 1740s—that uniform rotations occurring around either the shorter or the longer axis of a spheroid, in absence of external torques (*inertial motions*), are *both stable*. However, Kelvin’s experiment showed that if a thin-walled spheroidal gyroscope is filled up with water (“*liquid gyrostat*”), it would be stable when set in rotation around its shorter axis, whereas it would be unstable otherwise, no matter how large the magnitude of the initial angular velocity. Notice that the shorter axis is the one with respect to which the moment of inertia of the system is a maximum. The mathematical explanation of Kelvin’s experiment was the object of studies by several prominent mathematicians, including Poincaré [27]—who considered the more general case of an elastic container—and Basset [13], who analyzed the homogeneous vortex motion of a liquid in an ellipsoidal cavity. However, the outcome of these investigations provided only approximate or incomplete answers.

Another fundamental insight to the problem is due to N.Y. Zhukovsky. In his thorough analysis [34], Zhukovsky puts forward a completely unexpected property of the coupled system body-liquid,  $\mathcal{S}$ , in the case when the liquid filling the cavity is *viscous* and  $\mathcal{S}$  moves by inertial motion. More precisely, on the basis of a straightforward energy analysis, he envisages that the liquid should produce a substantial *stabilizing effect* on the motion of the body in a way that the terminal state should be one where  $\mathcal{S}$  moves as a single rigid body by uniform, rotational motion around one of the central axes of inertia [34, §38]. This dynamical behavior is entirely at odds with the one that the body might perform with an *empty* cavity, where the unsteady motion is much more complicated and, of course, far from reaching any steady-state configuration (e.g., [21, §4]). It must be emphasized, at this point, that Zhukovsky’s argument is altogether of heuristic nature and, therefore, lacks of sound mathematical rigor. As a result, even though the above property is often referred to (especially in the Russian literature, e.g., [25, p. 98], [4, p. 3]) as “Zhukovsky’s theorem”, it is more precise to call it, instead, “Zhukovsky’s conjecture.” However, despite the absence of a rigorous analysis, the use of interior cavities filled with liquid as dampers in rigid and elastic structures is a common procedure, adopted since the mid 1960s [5] in different branches of applied sciences, especially space technology (e.g., [3]) and civil engineering (e.g., [1]).

Coming to the mathematical analysis and interpretation of the phenomena described above and, more generally, the generic motion of a rigid body with a liquid-filled cavity, the classical literature includes a very large number of contributions. However, this body of work, probably also due to the strong influence of the seminal articles of Rumyantsev [30] and Chernousko [4] on the entire field, is

only seldom of rigorous nature, and mostly based on a simplified set of equations—that at times reduces to ordinary differential equations—and/or special shapes of the body and cavity. Since it would be hopeless to cite all the relevant literature, we refer the reader to the monographs [2, 4, 18, 19, 25] and the bibliography there cited.

Very recently, the present author, jointly with his associates, has started a systematic study of the motion of a rigid body with a liquid-filled cavity [6, 10–12, 23, 24]. In these papers, one main objective, among others, was to provide a mathematically rigorous explanation of Kelvin’s experiment and a likewise solid proof of Zhukovsky’s conjecture. The outcome of this effort has been remarkably successful [6] though, however, not entirely satisfactory. In fact, on the one hand, Kelvin’s experiment is only partially recovered. Actually, just in the case of systems such as prolate spheroids entirely filled with a liquid, in [6, Theorem 6(e)] it is shown, in particular, that permanent rotations around the longer axis are *unstable*, but not that those around the shorter axes are indeed *stable*, as demonstrated by Kelvin’s finding. On the other hand, in [6, Theorem 4] Zhukovsky’s conjecture is rigorously proved for all types of body-liquid systems, with the exception of those whose mass distribution is such that two central moments of inertia coincide and are strictly greater than the third one. This happens, for example, in cylindrically-shaped containers filled with liquid, when the radius of the base is shorter than the height (like in a soda can). Finally, the results presented in [6] are not able to explain another interesting phenomenon that both lab [14] and numerical [6, Sect. 9.1] experiments strongly suggest. More precisely, it is observed that after a finite interval of time, whose length mostly depends on the viscosity of the liquid and the size of the initial conditions, the coupled system almost abruptly reaches a uniform terminal state. In fact, both experiments indicate that once the viscosity of the liquid has reduced its motion “sufficiently close” to the (relative) rest, the rate of decay to the terminal state appears to be of exponential type.

The main goal of this article is to analyze in details the stability properties of uniform rotations (“*permanent rotations*”) and long-time behavior of motions of a rigid body with an interior cavity entirely filled with a viscous liquid around its center of mass  $G$ , in absence of external torques relative to  $G$  (“*inertial motions*”). In doing so, we shall, in particular, provide a positive answer to all problems left open in [6] and mentioned above. Besides  $C^2$ -smoothness of the cavity, we do not make any other assumption about its shape or the shape of the body.

Our approach is quite different than the one adopted in [6], which is based on (appropriately modified) tools borrowed from classical dynamical system theory. Instead, the method we use here relies upon a detailed study of the spectrum of the relevant linear operator,  $L$ , obtained by linearizing the full nonlinear operator around a given permanent rotation,  $\mathfrak{s}_0$ , of  $\mathcal{S}$ . As is well known, this rotation may only occur about an axis,  $\mathbf{e}$ , coinciding with one of the eigenvectors,  $\mathbf{e}_1$ ,  $\mathbf{e}_2$ , and  $\mathbf{e}_3$ , of the inertia tensor of  $\mathcal{S}$  relative to  $G$  (*central axes of inertia*). Let  $A$ ,  $B$ , and  $C$  denote, in the order, the associated eigenvalues (*central moments of inertia*), and for  $\lambda \in \{A, B, C\}$ , by  $\mathcal{S}(\lambda)$  the corresponding eigenspace. Without loss of generality, we take  $A \leq B \leq C$ . We then show (Lemma 4.3) that, for any given  $\mathfrak{s}_0$ , the spectrum  $\sigma(L)$  of  $L$  is purely discrete with eigenvalues clustering only at infinity. Furthermore,



0 is always an eigenvalue with algebraic multiplicity  $m = \dim(\mathcal{S}(\lambda)) \in \{1, 2, 3\}$ . This implies, in particular, the existence of a center manifold,  $\mathcal{C}$ , in our problem. However, we show (Proposition 4.6) that  $\mathcal{C}$  is “slow”, namely, 0 is the only point of  $\sigma(\mathbf{L})$  on the imaginary axis. In addition, we prove that 0 is semisimple and this allows us to characterize the sign of  $\operatorname{Re}[\sigma(\mathbf{L})] \setminus \{0\}$  in terms of the central moments  $A, B$ , and  $C$  and the direction  $\mathbf{e}$  (Proposition 4.6). We then employ this information along with a form of the “generalized linearization principle” [29] to show that if the uniform rotation  $\mathbf{S}_0$  occurs around an axis with maximum moment of inertia, then it is asymptotically *exponentially* stable; see Proposition 4.10 and Theorem 4.11. By this we mean that  $\mathbf{S}_0$  is stable in the sense of Lyapunov (in appropriate norms), and, moreover, every motion starting in a suitable neighborhood of  $\mathbf{S}_0$  will converge exponentially fast to a terminal state that is still a uniform rotation around  $\mathbf{e}$ ; see Definition 4.8. The latter, however, will in general be different from  $\mathbf{S}_0$ , due to the conservation of total angular momentum for  $\mathcal{S}$ ; see Remark 4.9. Conversely, we show that if  $\mathbf{S}_0$  occurs around an axis of minimum moment of inertia, then it is unstable (Proposition 4.10 and Theorem 4.11), and so furnishing, in particular, a full explanation of the outcome of Kelvin’s experiment; see Remark 4.12.

The spectral properties of  $\mathbf{L}$  mentioned earlier on also enable us to give a rigorous proof of the “abrupt” decay of the coupled system body-liquid to the terminal state of uniform rotation. In fact, also with the help of the results already established in [6], we prove that there is a time  $t_0 > 0$  after that all solutions possessing finite kinetic energy at time  $t = 0$  (*weak solutions*) must decay *exponentially fast* to their terminal state. This result provides a full proof of Zhukovsky’s conjecture; see Theorem 4.17. Finally, we investigate the question of around which central axis the terminal uniform rotation will take place (*attainability problem*). Again with the help of the results established in [6] we show that, for an open set of initial data, all corresponding weak solution after some time  $t_0 > 0$  will converge at an *exponential rate* to a rotation around the axis with respect to which the moment of inertia is a maximum; see Theorem 4.18. The norm in which this convergence is established is quite strong, since it involves first time derivatives and second spatial derivatives of the velocity field of the liquid, and angular velocity and acceleration of the body.

The plan of the paper is as follows. In Sect. 4.2 we give the mathematical formulation of inertial motions of a body with an interior cavity entirely filled with a Navier-Stokes liquid. We then show that the associated perturbation problem can be formulated as an abstract evolution equation in a suitable Hilbert space and show, by using a classical semigroup approach, that the initial-value problem possesses a unique smooth solution, at least locally in time. Section 4.2 is devoted to the study of the spectrum of the relevant linear operator  $\mathbf{L}$ , for which we show the properties reported earlier on. These results are then employed in the following Sect. 4.4 to show, on the one hand, that the local solution constructed in Sect. 4.2 can be made global in time for sufficiently “small” data, and, on the other hand, to provide sufficient conditions for the exponential stability and instability of permanent rotations. In Sect. 4.5 we investigate the long-time behavior of the generic motion and show that, under suitable assumptions on the central moments of inertia, any weak solution after some time  $t_0$  must converge exponentially fast to

a permanent rotation (Zhukovsky's conjecture). A crucial role in the proof is played by Lemma 4.15 that ensures that the velocity field of *any* weak solution must decay to 0, as times diverges, in higher-order spatial norms. The final Sect. 4.6 is dedicated to the problem of attainability of permanent rotations.

## 4.2 Formulation of the Problem and Local Existence Theory

The motion of the coupled system body-liquid,  $\mathcal{S}$ , is governed by the following set of equations (e.g., [6]):

$$\left. \begin{aligned} \mathbf{v}_t + \mathbf{v} \cdot \nabla \mathbf{v} + \dot{\boldsymbol{\omega}} \times \mathbf{x} + 2\boldsymbol{\omega} \times \mathbf{v} &= \nu \Delta \mathbf{v} - \nabla p \\ \operatorname{div} \mathbf{v} &= 0 \end{aligned} \right\} \text{ in } \mathcal{C} \times (0, \infty) \quad (4.1)$$

$$\mathbf{v}(x, t) = \mathbf{0} \text{ at } \partial \mathcal{C}$$

and

$$\dot{\mathbf{M}} + \boldsymbol{\omega} \times \mathbf{M} = \mathbf{0}, \quad \mathbf{M} := \mathbb{I} \cdot \boldsymbol{\omega} + \int_{\mathcal{C}} \mathbf{x} \times \mathbf{v}. \quad (4.2)$$

Here,  $\mathbf{v}$ ,  $\rho p$  (with  $\rho$  constant density of the liquid that, without loss of generality, will be taken to be 1 for simplicity) and  $\nu$  are velocity, (modified) pressure, and kinematic viscosity of the liquid,  $\boldsymbol{\omega}$  is the angular velocity of the body, and  $\mathcal{C}$  is the domain of  $\mathbb{R}^3$  occupied by the liquid. Throughout this paper we shall assume that  $\mathcal{C}$  is of class  $C^2$ . Moreover,  $\mathbb{I}$  denotes the inertia tensor of the coupled system  $\mathcal{S}$ . We finally notice that the vector function  $\mathbf{M}$  represents the total angular momentum of  $\mathcal{S}$ .

Equations (4.1)–(4.2) are written in a body-fixed frame,  $\mathcal{F}$  with the origin at the center of mass,  $G$ , of  $\mathcal{S}$ . We choose  $\mathcal{F} \equiv \{G, \mathbf{e}_i\}$  where  $\{\mathbf{e}_i\}$ , are eigenvectors of the inertia tensor  $\mathbb{I}$  (central axes of inertia). Moreover, we denote by  $A, B$ , and  $C$  the central moments of inertia, namely, the eigenvalues of  $\mathbb{I}$  corresponding to the eigenvectors  $\mathbf{e}_1, \mathbf{e}_2$ , and  $\mathbf{e}_3$ , respectively. Without loss of generality, we shall assume  $A \leq B \leq C$ .

For  $\lambda \in \{A, B, C\}$  we let  $\mathcal{S}(\lambda)$  be the eigenspace associated to  $\lambda$ . If we pick a unit vector  $\mathbf{e} \in \mathcal{S}(\lambda)$  it is immediately verified that

$$\mathbf{s}_0 = (\mathbf{v}_0 \equiv \mathbf{0}, \boldsymbol{\omega}_0 = \omega_0 \mathbf{e}), \quad \omega_0 \in \mathbb{R} - \{0\}, \quad (4.3)$$

is a (non-trivial) steady-state solution to (4.1)–(4.2) representing a *permanent rotation* performed by the coupled system as a single rigid body. In fact, permanent rotations are the only steady-state motions allowed for the coupled system  $\mathcal{S}$ , and, as is well known, can only occur around a central axis of inertia.

Even though of rather trivial proof, for the relevance acquired later on, we would like to single out the following result in the form of a lemma.

**Lemma 4.1** *Suppose  $\omega_0 \in \mathcal{S}(\lambda) - \{\mathbf{0}\}$ . Then,  $\omega \in \mathbb{R}^3$  is a solution to*

$$\omega_0 \times \mathbb{I} \cdot \omega + \omega \times \mathbb{I} \cdot \omega_0 = \mathbf{0}. \quad (4.4)$$

*if and only if  $\omega \in \mathcal{S}(\lambda)$ .*

*Proof* By assumption,

$$\mathbb{I} \cdot \omega_0 = \lambda \omega_0. \quad (4.5)$$

Now, if  $\omega \in \mathcal{S}(\lambda)$ , we also have

$$\mathbb{I} \cdot \omega = \lambda \omega.$$

so that, by (4.5),

$$\omega_0 \times \mathbb{I} \cdot \omega + \omega \times \mathbb{I} \cdot \omega_0 = \lambda (\omega_0 \times \omega + \omega \times \omega_0) = \mathbf{0}.$$

Conversely, from (4.4) and (4.5) we get

$$\mathbb{I} \cdot \omega - \lambda \omega = \sigma \omega_0 \quad \text{some } \sigma \in \mathbb{R}.$$

Dot-multiplying both sides of this equation by  $\omega_0$  and using the symmetry of  $\mathbb{I}$  along with (4.5), we deduce  $\sigma |\omega_0|^2 = 0$ , which is possible if and only if  $\sigma = 0$ . □

One of our main objectives is to determine necessary and sufficient conditions for the stability of the steady-state solution (4.3), in a sense made precise later on in Definition 4.8. To this end, denoting by  $(v, p, \omega_0 + \omega)$  a generic solution to (4.1)–(4.2) with  $\omega_0 \in \mathcal{S}(\lambda)$ , we deduce that the “perturbation”  $(v, p, \omega)$  must satisfy the following system

$$\left. \begin{aligned} v_t + \dot{\omega} \times x + 2\omega_0 \times v - \nu \Delta v - \nabla p &= -2\omega \times v - v \cdot \nabla v \\ \operatorname{div} v &= 0 \end{aligned} \right\} \text{ in } \mathcal{C} \times (0, \infty)$$

$$v(x, t) = \mathbf{0} \quad \text{at } \partial\Omega \quad (4.6)$$

and

$$\mathbb{I} \cdot \dot{\omega} - \mathbb{I} \cdot \dot{a} + \omega_0 \times \mathbb{I} \cdot \omega + \omega \times \mathbb{I} \cdot \omega_0 - \omega_0 \times \mathbb{I} \cdot a = -\omega \times \mathbb{I} \cdot \omega + \omega \times \mathbb{I} \cdot a, \quad (4.7)$$

where

$$a := -\mathbb{I}^{-1} \cdot \int_{\mathcal{C}} x \times v. \quad (4.8)$$

We shall now rewrite (4.6)–(4.7) in a suitable abstract form. To this end, we introduce the Hilbert space<sup>1</sup>

$$H := L^2_\sigma(C) \oplus \mathbb{R}^3 = \{ \mathbf{u} = (\mathbf{v}, \boldsymbol{\omega})^\top : \mathbf{v} \in L^2_\sigma(C), \boldsymbol{\omega} \in \mathbb{R}^3 \},$$

where

$$L^2_\sigma(C) = \{ \mathbf{v} \in L^2(\Omega) : \operatorname{div} \mathbf{v} = 0 \text{ in } C, \text{ and } \mathbf{v} \cdot \mathbf{n}|_{\partial C} = 0 \},$$

and  $\mathbf{n}$  is the unit exterior normal on  $\partial C$ . The scalar product of two elements  $\mathbf{u}_i = (\mathbf{v}_i, \boldsymbol{\omega}_i)^\top, i = 1, 2$ , in  $H$  is defined by

$$\langle \mathbf{u}_1, \mathbf{u}_2 \rangle := \int_C \mathbf{v}_1 \cdot \mathbf{v}_2 \, dC + \boldsymbol{\omega}_1 \cdot \boldsymbol{\omega}_2,$$

with associated norm

$$\| \mathbf{u} \| := \langle \mathbf{u}, \mathbf{u} \rangle^{\frac{1}{2}}.$$

We next define the following operators

$$\begin{aligned} \mathbf{I} : \mathbf{u} \in H &\mapsto \mathbf{I}\mathbf{u} := \left( \mathbf{v} + \mathbf{P}(\boldsymbol{\omega} \times \mathbf{x}), \mathbb{I} \cdot (\boldsymbol{\omega} - \mathbf{a}) \right)^\top \in H, \\ \mathbf{A} : \mathbf{u} \in D(\mathbf{A}) &:= [W^{2,2}(C) \cap W_0^{1,2}(C) \cap L^2_\sigma(C)] \oplus \mathbb{R}^3 \subset H \\ &\qquad \qquad \qquad \mapsto \mathbf{A}\mathbf{u} := (-\nu \mathbf{P} \Delta \mathbf{v}, \boldsymbol{\omega})^\top \in H, \\ \mathbf{B} : \mathbf{u} \in H &\mapsto \mathbf{B}\mathbf{u} := \left( 2\mathbf{P}(\boldsymbol{\omega}_0 \times \mathbf{v}), \boldsymbol{\omega}_0 \times \mathbb{I} \cdot \boldsymbol{\omega} + \boldsymbol{\omega} \times \mathbb{I} \cdot \boldsymbol{\omega}_0 - \boldsymbol{\omega}_0 \times \mathbb{I} \cdot \mathbf{a} - \boldsymbol{\omega} \right)^\top \in H \\ \mathbf{N} : \mathbf{u} \in D(\mathbf{A}) \subset H &\mapsto \mathbf{N}\mathbf{u} := \left( -2\mathbf{P}(\boldsymbol{\omega} \times \mathbf{v}) - \mathbf{P}(\mathbf{v} \cdot \nabla \mathbf{v}), -\boldsymbol{\omega} \times \mathbb{I} \cdot (\boldsymbol{\omega} - \mathbf{a}) \right)^\top \in H \end{aligned} \tag{4.9}$$

where  $\mathbf{P}$  is the Helmholtz projection from  $L^2(C)$  onto  $L^2_\sigma(C)$ . As a consequence, the system of equations (4.6)–(4.7) can be formally written as the following evolution equation in the Hilbert space  $H$

$$\frac{d}{dt} \mathbf{I}\mathbf{u} + \mathbf{A}\mathbf{u} + \mathbf{B}\mathbf{u} = \mathbf{N}\mathbf{u}. \tag{4.10}$$

We shall now state some important properties of the above operators. In the first place, we observe that, by well known results on the Stokes operator,  $\mathbf{A}_0 := -\nu \mathbf{P} \Delta$ , with

$$D(\mathbf{A}_0) = W^{2,2}(C) \cap W_0^{1,2}(C) \cap L^2_\sigma(C),$$

---

<sup>1</sup>The notation used in this article is quite standard; see e.g. [7].

it follows that  $\mathbf{A}$  is selfadjoint, positive and with compact inverse. For  $\alpha \in (0, 1)$ , its fractional powers are given by

$$\mathbf{A}^\alpha \mathbf{u} := (\mathbf{A}_0^\alpha \mathbf{v}, \boldsymbol{\omega})^\top, \quad \mathbf{A}^{-\alpha} := (\mathbf{A}^{-1})^\alpha.$$

Moreover, the operator  $\mathbf{B}$  is, obviously, linear and bounded. Furthermore, in [18, §6.2.3] it is shown that the bounded operator  $\mathbf{I}$  is positive and invertible. In addition, it is easy to check that  $\mathbf{I}$  is symmetric, namely,

$$\langle \mathbf{I} \mathbf{u}_1, \mathbf{u}_2 \rangle = \langle \mathbf{u}_1, \mathbf{I} \mathbf{u}_2 \rangle, \quad \mathbf{u}_1, \mathbf{u}_2 \in H,$$

so that  $\mathbf{I}$  is also selfadjoint. Finally, by using classical embedding theorems, one can easily check that  $\mathbf{N}$  is well defined. As a result, setting

$$\mathbf{A} := \mathbf{I}^{-1} \mathbf{A}, \quad \mathbf{B} := \mathbf{I}^{-1} \mathbf{B}, \quad \mathbf{N} := \mathbf{I}^{-1} \mathbf{N}. \tag{4.11}$$

Equation (4.10) is equivalent to the following one

$$\frac{d\mathbf{u}}{dt} + \mathbf{A}\mathbf{u} + \mathbf{B}\mathbf{u} = \mathbf{N}\mathbf{u} \text{ in } H. \tag{4.12}$$

From the properties of  $\mathbf{I}$  and  $\mathbf{A}$ , it readily follows that the operator  $\mathbf{A}$ , with  $D(\mathbf{A}) = D(\mathbf{A})$ , is sectorial [13, Definition 1.3.1] and has a purely discrete, positive spectrum.

By employing classical methods, it is now rather straightforward to prove local in time existence and uniqueness of “strict” solutions to (4.12), corresponding to appropriate initial data. More precisely, we have the following

**Lemma 4.2** *Let  $\beta \in [\frac{4}{3}, 1)$ , and  $\mathbf{u}_0 \in D(\mathbf{A}^\beta)$ . Then, there exists  $t^* \in (0, \infty]$  and a unique function  $\mathbf{u} = \mathbf{u}(t)$  defined for all  $t \in [0, t_1]$ ,  $t_1 < t^*$ , such that*

$$\mathbf{u} \in C([0, t_1]; D(\mathbf{A}^\beta)) \cap C((0, t_1]; D(\mathbf{A})) \cap C^1((0, t_1]; H),$$

*solving (4.12) (or, equivalently, (4.10)) for all  $t \in (0, t_1]$ , with  $\mathbf{u}(0) = \mathbf{u}_0$ . Moreover, if  $t^* < \infty$ , then  $\|\mathbf{A}^\alpha \mathbf{u}(t)\| \rightarrow \infty$  as  $t \rightarrow t^*$ .*

*Proof* The proof is quite standard (see, e.g., [17, Lemma 5.1] and [26, Theorem 3.1 in Chap. 6]) and we shall only sketch it here. Observing that  $\mathbf{A}$ , being sectorial, is the generator of the analytic semigroup  $e^{-\mathbf{A}t}$ , we begin to consider the following integral equation

$$\mathbf{w}(t) = e^{-\mathbf{A}t} \mathbf{w}_0 + \int_0^t \mathbf{A}^\beta e^{-\mathbf{A}(t-s)} \mathbf{G}(\mathbf{w}) ds, \quad \mathbf{G}(\mathbf{w}) := -\mathbf{B}(\mathbf{A}^{-\beta} \mathbf{w}) + \mathbf{N}(\mathbf{A}^{-\beta} \mathbf{w}). \tag{4.13}$$

with  $\mathbf{w}_0 = \mathbf{A}^\beta \mathbf{u}_0$ . By a classical result [16, Lemma 3] it follows that

$$\|\mathbf{P}(\mathbf{v}_1 \cdot \nabla \mathbf{v}_1 - \mathbf{v}_2 \cdot \nabla \mathbf{v}_2)\|_2 \leq c_1 (\|\mathbf{A}_0^\beta \mathbf{v}_1\|_2 + \|\mathbf{A}_0^\beta \mathbf{v}_2\|_2) \|\mathbf{A}_0^\beta (\mathbf{v}_1 - \mathbf{v}_2)\|_2. \tag{4.14}$$

Also, since  $I^{-1}$  is bounded, we have (Heinz inequality),

$$\|A^\alpha \mathbf{u}\| \leq c_2 \|A^\alpha \mathbf{u}\| \leq c_3 \|A^\alpha \mathbf{u}\|, \quad \alpha \in [0, 1]. \tag{4.15}$$

From these two properties, we then easily show that

$$\|G(\mathbf{w}_1) - G(\mathbf{w}_2)\| \leq c_4 \|\mathbf{w}_1 - \mathbf{w}_2\|, \quad \text{all } \mathbf{w}_1, \mathbf{w}_2 \in H \text{ in a neighborhood of } \mathbf{w} = \mathbf{0}. \tag{4.16}$$

It then follows (e.g., [26, pp. 196–197]) that (4.13) has one and only one solution  $\mathbf{w} = \mathbf{w}(t)$ ,  $t \in [0, t^*]$  for some  $t^* > 0$ , with  $\mathbf{w} \in C([0, t_1]; H)$ , all  $t_1 \in (0, t^*)$ . As a result, the field  $\mathbf{u} := A^{-\beta} \mathbf{w}$  is in  $C([0, t_1]; D(A^\beta))$  and is a mild solution to (4.12), namely,

$$\mathbf{u}(t) = e^{-\mathbf{A}t} \mathbf{u}_0 + \int_0^t e^{-\mathbf{A}(t-s)} [-\mathbf{B}\mathbf{u} + \mathbf{N}\mathbf{u}] ds. \tag{4.17}$$

However, again by standard arguments (e.g., [26, p. 198]), from (4.17) one shows that, in fact,  $\mathbf{u} \in C^1((0, t_1]; H) \cap C^1((0, t_1]; D(A))$ , so that  $\mathbf{u}$  is a “strict” solution to (4.12) and is unique. Finally, it is clear that the above procedure can be extended to provide a solution beyond any time  $\tau \in [t_1, t^*)$  if  $\|A^\beta \mathbf{u}(\tau)\| < \infty$ , whereas, if  $t^* < \infty$ , it will fail if and only if  $\lim_{t \rightarrow t^*} \|A^\beta \mathbf{u}(t)\| = \infty$ . □

### 4.3 The Spectrum of the Linearized Operator

Let

$$\mathbf{L} := \mathbf{A} + \mathbf{B}, \quad D(\mathbf{L}) = D(\mathbf{A}) \equiv D(\mathbf{A}). \tag{4.18}$$

The spectral properties of the operator  $\mathbf{L}$  will play a primary role in establishing stability of the steady-state motion (4.3) and the long-time behavior of solutions to the nonlinear problem (4.12) [or, equivalently, (4.10)]. To this end, we begin to show the following preliminary result.

**Lemma 4.3** *The spectrum,  $\sigma(\mathbf{L})$ , of  $\mathbf{L}$  consists of eigenvalues of finite multiplicity that can cluster only at infinity. Moreover, 0 is an eigenvalue with corresponding eigenspace*

$$\mathbf{N}[\mathbf{L}] = \{\mathbf{u}^{(0)} \in H : \mathbf{u}^{(0)} = (\mathbf{v} \equiv \mathbf{0}, \boldsymbol{\omega}^{(0)})^\top, \text{ for some } \boldsymbol{\omega}^{(0)} \in \mathcal{S}(\lambda)\},$$

and

$$\dim(\mathbf{N}[\mathbf{L}]) = \dim(\mathcal{S}(\lambda)) = m, \quad 1 \leq m \leq 3. \tag{4.19}$$

In addition, the range of  $\mathbf{L}$ ,  $\mathbf{R}[\mathbf{L}]$ , is closed and the following decomposition holds,

$$H = \mathbf{N}[\mathbf{L}] \oplus \mathbf{R}[\mathbf{L}], \tag{4.20}$$

namely, 0 is a semisimple eigenvalue.

*Proof* Since  $\mathbf{B}$  is bounded and  $\mathbf{A}$  is positive definite, all  $\zeta \in \mathbb{R}$  with  $\zeta$  sufficiently negative are in the resolvent set of  $\mathbf{L}$ . For one of these values of  $\zeta$  and for a given  $\mathbf{g} \in H$ , consider the equation

$$\mathbf{L}u - \zeta u = \mathbf{g}. \tag{4.21}$$

Taking into account that ( $\bar{\cdot}$  := complex conjugate)

$$\langle \mathbf{A}u, \bar{u} \rangle = \nu \|\nabla v\|_2^2 + |\omega|^2, \quad c_1 \|u\|^2 \geq \langle \mathbf{L}u, \bar{u} \rangle \geq c_0 \|u\|^2,$$

by first applying the operator  $\mathbf{I}$  to both sides of (4.21) and then taking the scalar product with  $\bar{u}$ , it follows that

$$\nu \|\nabla v\|_2^2 + |\omega|^2 - c_0(\zeta + \|\mathbf{B}\|)\|u\|^2 \leq c_1 \|\mathbf{g}\| \|u\|.$$

From the latter expression, by means of the Poincaré inequality, we easily show that, for  $\zeta < -\|\mathbf{B}\|$ ,

$$\|v\|_{1,2} + |\omega| \leq c_2 \|\mathbf{g}\|$$

which, in turn, by the compact embedding  $W^{1,2}(\mathcal{C}) \subset L^2(\mathcal{C})$ , implies that  $\mathbf{L}$  has a compact resolvent. The first part of the lemma is then a consequence of [15, Theorem 6.29]. To show the second part, we observe that, taking into account (4.9), (4.11) and (4.18), the equation

$$\mathbf{L}u = \mathbf{0}$$

is equivalent to the system

$$\begin{aligned} -\nu \Delta v + 2\omega_0 \times v &= -\nabla p, \quad \operatorname{div} v = 0, \quad \text{in } \mathcal{C}; \quad v = \mathbf{0} \text{ at } \partial\mathcal{C} \\ \omega_0 \times \mathbb{I} \cdot \omega + \omega \times \mathbb{I} \cdot \omega_0 - \omega_0 \times \mathbb{I} \cdot a &= 0 \end{aligned}$$

for some  $p \in W^{1,2}(\mathcal{C})$ . Dot-multiplying both sides of the first equation by  $v$  and integrating by parts over  $\mathcal{C}$ , with the help of the second and third equation we show  $\|\nabla v\|_2 = 0$ , which furnishes  $v \equiv \mathbf{0}$ . Replacing this information back into the last equation, we get

$$\omega_0 \times \mathbb{I} \cdot \omega + \omega \times \mathbb{I} \cdot \omega_0 = \mathbf{0},$$

which, by Lemma 4.1, furnishes  $\omega \in \mathcal{S}(\lambda)$ . Therefore, an eigenvector  $\mathbf{u}^{(0)}$  associated to the eigenvalue 0 must be of the form  $\mathbf{u}^{(0)} = (\mathbf{v} \equiv \mathbf{0}, \omega^{(0)})^\top$ , with  $\omega^{(0)} \in \mathcal{S}(\lambda)$ . This property also implies (4.19). We next show that  $\mathbf{L}$  is an (unbounded) Fredholm operator of index 0. Actually, since  $D(\mathbf{A})$  is, obviously, dense in  $H$ , the same property holds for  $D(\mathbf{L})$ . Moreover, by well-known results concerning the Stokes operator, we have  $\mathbf{N}[\mathbf{A}] = \{\mathbf{0}\}$  and  $\mathbf{R}[\mathbf{A}] = H$ , so that  $\text{ind}(\mathbf{A}) = 0$ . It is easy to see that  $\mathbf{B}$  is  $\mathbf{A}$ -compact, namely, if  $\{\mathbf{u}_n\}$  is a sequence such that

$$\|\mathbf{u}_n\| + \|\mathbf{A}\mathbf{u}_n\| \leq C$$

with  $C$  independent of  $n$ , there is  $\mathbf{u} \in H$  such that

$$\lim_{n \rightarrow \infty} \|\mathbf{B}\mathbf{u}_n - \mathbf{B}\mathbf{u}\| = 0.$$

This property is an elementary consequence of the classical inequality (e.g. [8, Theorem IV.6.1])

$$\|\mathbf{A}_0 \mathbf{v}\|_2 \leq 3^{\frac{1}{2}} \|\mathbf{v}\|_{2,2} \leq \gamma \|\mathbf{A}_0 \mathbf{v}\|_2, \quad \gamma = \gamma(C) > 0, \tag{4.22}$$

the compact embedding  $W^{2,2} \subset L^2$ , and the definition of  $\mathbf{B}$  given in (4.9)<sub>3</sub>. Therefore,  $\mathbf{A} + \mathbf{B}$  is Fredholm of index 0. Since  $\mathbf{I}^{-1}$  is a homeomorphism, by the product property, we find that also  $\mathbf{L}$  is Fredholm of index 0. Now, assume  $\dim \mathcal{S}(\lambda) = 1$ . By what we have already shown,  $\dim(\mathbf{N}[\mathbf{L}]) = 1$  as well, which, by the Fredholm property of  $\mathbf{L}$ , implies  $\text{codim}(\mathbf{R}[\mathbf{L}]) = 1$ . Let us prove that

$$\mathbf{R}[\mathbf{L}] \cap \mathbf{N}[\mathbf{L}] = \{\mathbf{0}\}. \tag{4.23}$$

In fact, suppose there is  $\mathbf{u}^{(0)} = (\mathbf{0}, \omega^{(0)})^\top \in \mathbf{N}[\mathbf{L}]$  such that

$$\mathbf{L}\mathbf{u} = \mathbf{u}^{(0)},$$

or, equivalently,

$$(\mathbf{A} + \mathbf{B})\mathbf{u} = \mathbf{I}\mathbf{u}^{(0)}.$$

Recalling (4.9), this equation can be rewritten as follows

$$\begin{aligned} -\nu \Delta \mathbf{v} + 2\omega_0 \times \mathbf{v} &= -\nabla p + \omega^{(0)} \times \mathbf{x}, \quad \text{div } \mathbf{v} = 0, \quad \text{in } \mathcal{C}; \quad \mathbf{v} = \mathbf{0} \text{ at } \partial \mathcal{C} \\ \omega_0 \times \mathbb{I} \cdot \boldsymbol{\omega} + \boldsymbol{\omega} \times \mathbb{I} \cdot \boldsymbol{\omega}_0 - \boldsymbol{\omega}_0 \times \mathbb{I} \cdot \mathbf{a} &= \mathbb{I} \cdot \boldsymbol{\omega}^{(0)}. \end{aligned} \tag{4.24}$$



Taking into account that  $\mathbb{I} \cdot \boldsymbol{\omega}_0 = \lambda \boldsymbol{\omega}_0$  and that, by assumption,  $\boldsymbol{\omega}^{(0)} = \alpha \boldsymbol{\omega}_0$ ,  $\alpha \in \mathbb{R}$ , from (4.24) we get, in particular,

$$\boldsymbol{\omega}_0 \times (\mathbb{I} \cdot \boldsymbol{\omega} - \lambda \boldsymbol{\omega} - \mathbb{I} \cdot \boldsymbol{a}) = \lambda \alpha \boldsymbol{\omega}_0,$$

which implies  $\boldsymbol{\omega}^{(0)} = \mathbf{0}$ , namely,  $\boldsymbol{u}^{(0)} = \mathbf{0}$ , and as a result we conclude (4.23). Likewise, if  $\dim(\mathcal{S}(\lambda)) \equiv \dim(\mathbf{N}[\mathbf{L}]) = 3$ , we have  $(\mathbb{I})_{ij} = \lambda \delta_{ij}$ , so that the last equation in (4.24) furnishes

$$\boldsymbol{\omega}^{(0)} \cdot \boldsymbol{a} = 0. \quad (4.25)$$

On the other side, by dot-multiplying both sides of the first equation in (4.24) by  $\boldsymbol{v}$ , integrating by parts over  $\mathcal{C}$ , and recalling (4.8), we show

$$\boldsymbol{v} \|\nabla \boldsymbol{v}\|_2^2 = \boldsymbol{\omega}^{(0)} \cdot \boldsymbol{a}$$

which in view of (4.25) implies  $\boldsymbol{v} \equiv \mathbf{0}$ . Replacing this information into (4.24)<sub>1</sub> entails

$$\boldsymbol{\omega}^{(0)} \times \boldsymbol{x} = \nabla p, \quad (4.26)$$

so that, by operating with curl on both sides, we conclude, also in this case,  $\boldsymbol{u}^{(0)} = \mathbf{0}$  and the validity of (4.23). Let us, finally, consider the case  $m = 2$ . In this regard, we begin to notice that from (4.24)<sub>4</sub> it follows  $\boldsymbol{\omega}_0 \cdot \boldsymbol{\omega}^{(0)} = 0$ . To fix the ideas, we assume  $\lambda \equiv A = B (< C)$ , the case  $B = C (> A)$  being treated in an entirely similar way. Thus, taking (for instance)

$$\boldsymbol{\omega}_0 = \omega_0 \boldsymbol{e}_1, \quad \boldsymbol{\omega}^{(0)} = \omega^{(0)} \boldsymbol{e}_2, \quad (4.27)$$

Eq. (4.24)<sub>4</sub> becomes

$$\boldsymbol{\omega}_0 \times [(C - A)\boldsymbol{\omega}] = \boldsymbol{\omega}_0 \times \mathbb{I} \cdot \boldsymbol{a} + A \boldsymbol{\omega}^{(0)} := \boldsymbol{F},$$

where  $\boldsymbol{\omega} = \omega \boldsymbol{e}_3$ . Since  $\boldsymbol{F} \cdot \boldsymbol{\omega}_0 = 0$ , this equation is solvable for  $\boldsymbol{\omega}$  and we get

$$\boldsymbol{\omega} = \frac{\boldsymbol{F} \times \boldsymbol{\omega}_0}{\omega_0^2 (C - A)}. \quad (4.28)$$

Observing that

$$\boldsymbol{F} \times \boldsymbol{\omega}_0 = \omega_0^2 \mathbb{I} \cdot \boldsymbol{a} - (\boldsymbol{\omega}_0 \cdot \mathbb{I} \cdot \boldsymbol{a}) \boldsymbol{\omega}_0 + A \boldsymbol{\omega}^{(0)} \times \boldsymbol{\omega}_0,$$

from (4.27) and (4.28) we deduce that the condition  $\boldsymbol{\omega} \cdot \boldsymbol{\omega}^{(0)} = 0$  implies

$$\boldsymbol{\omega}^{(0)} \cdot \mathbb{I} \cdot \boldsymbol{a} = 0. \quad (4.29)$$

However, if we dot-multiply both sides of (4.24)<sub>1</sub> by  $\mathbf{v}$ , integrate by parts over  $\mathcal{C}$  and use (4.24)<sub>2,3</sub> and (4.8), we get

$$\|\nabla \mathbf{v}\|_2^2 = \boldsymbol{\omega}^{(0)} \cdot \mathbb{I} \cdot \mathbf{a},$$

which, combined with (4.29) furnishes  $\mathbf{v} \equiv \mathbf{0}$ . Replacing the latter in (4.24)<sub>1</sub> entails again (4.26) that, as shown previously, implies  $\boldsymbol{\omega}^{(0)} = \mathbf{0}$  and the proof of (4.23) is completed. Now, since  $\text{codim}(\mathbf{R}[\mathbf{L}]) = m$ , there exists at least one  $S \subset H$  such that  $H = S \oplus \mathbf{R}[\mathbf{L}]$ , with  $S \cap \mathbf{R}[\mathbf{L}] = \{\mathbf{0}\}$ . However,  $\dim(S) = \dim(\mathbf{N}[\mathbf{L}]) = m$  and (4.23) holds, so that we may take  $S = \mathbf{N}[\mathbf{L}]$ , as claimed.  $\square$

Let  $\mathcal{Q}$  and  $\mathcal{P}$  be the spectral projections according to the spectral sets

$$\sigma_0(\mathbf{L}) := \{0\}, \quad \sigma_1(\mathbf{L}) := \sigma(\mathbf{L}) \setminus \sigma_0(\mathbf{L}),$$

which are well defined in view of Lemma 4.3. Thus, setting

$$H_0 := \mathcal{Q}(H), \quad H_1 := \mathcal{P}(H), \quad (4.30)$$

we have the following decomposition

$$H = H_0 \oplus H_1 \quad (4.31)$$

that completely reduces  $\mathbf{L}$  into  $\mathbf{L} = \mathbf{L}_0 \oplus \mathbf{L}_1$  with

$$\mathbf{L}_0 := \mathcal{Q}\mathbf{L} = \mathbf{L}\mathcal{Q}, \quad \mathbf{L}_1 := \mathcal{P}\mathbf{L} = \mathbf{L}\mathcal{P}, \quad (4.32)$$

and  $\sigma(\mathbf{L}_0) \equiv \sigma_0(\mathbf{L})$ ,  $\sigma(\mathbf{L}_1) \equiv \sigma_1(\mathbf{L})$  (e.g., [32, Theorems 5.7-A,B]).

A fundamental issue in the proof of the nonlinear results that we shall present later on, is the identification of the subspace  $H_0$  with  $\mathbf{N}[\mathbf{L}]$ . In general, this is not true and we only have  $\mathbf{N}[\mathbf{L}] \subseteq H_0$ , whereas  $\mathbf{R}[\mathbf{L}] \supseteq H_1$ . However, if (and only if) the decomposition (4.20) holds, then this property is valid and the above subspaces coincide (e.g. [22, Proposition A.2.2]). Thus, Lemma 4.3 implies the next one.

**Lemma 4.4** *The following characterization holds*

$$H_0 = \mathbf{N}[\mathbf{L}], \quad H_1 = \mathbf{R}[\mathbf{L}].$$

*Remark 4.5* It is worth noticing that one can show that the ortho-complement of  $\mathbf{N}[\mathbf{L}]$  does *not* coincide with  $\mathbf{R}[\mathbf{L}]$ . Therefore, under the assumption of Lemma 4.4, the decomposition (4.31) is not orthogonal.

The next result provides a complete characterization of the distribution of the eigenvalues of  $\mathbf{L}_1$  in terms of the central moments of inertia of  $\mathcal{S}$  and of the axis where the permanent rotation occurs.

**Proposition 4.6** *Let  $\mathbf{s}_0$  be given by (4.3). Then,*

$$\sigma_1(\mathbf{L}) \cap \{i\mathbb{R}\} = \emptyset. \tag{4.33}$$

*Moreover, we have*

$$\operatorname{Re}[\sigma_1(\mathbf{L})] \subset (0, \infty). \tag{4.34}$$

*whenever at least one of the following conditions holds.*

- (i)  $A = B = C$ , arbitrary  $\mathbf{e}$ ;
- (ii)  $A \leq B < C$ ,  $\mathbf{e} \equiv \mathbf{e}_3$ ;
- (iii)  $A < B = C$ ,  $\mathbf{e} = \gamma_1 \mathbf{e}_2 + \gamma_2 \mathbf{e}_3$ , with  $\boldsymbol{\gamma} \equiv (\gamma_1, \gamma_2) \in S^1$ .

*Conversely, if any of the following conditions are met*

- (iv)  $A < B \leq C$ ,  $\mathbf{e} \equiv \mathbf{e}_1$ ;
- (v)  $A < B < C$ ,  $\mathbf{e} \equiv \mathbf{e}_2$ ;
- (vi)  $A = B < C$ ,  $\mathbf{e} \equiv \gamma_1 \mathbf{e}_1 + \gamma_2 \mathbf{e}_2$  with  $\boldsymbol{\gamma} = (\gamma_1, \gamma_2) \in S^1$ .

*Then*

$$\operatorname{Re}[\sigma_1(\mathbf{L})] \cap (-\infty, 0) \neq \emptyset. \tag{4.35}$$

*Proof* Consider the linear problem

$$\frac{d\mathbf{u}}{dt} + \mathbf{L}\mathbf{u} = \mathbf{0}, \quad \mathbf{u}(0) = \mathbf{u}_0 \in H. \tag{4.36}$$

We begin to notice that, being a bounded perturbation of the operator  $\mathbf{A}$ , the operator  $\mathbf{L}$  is the generator of an analytic semigroup (e.g., [26, Theorem 2.1 in Chap. 3]). As a consequence, the solution to (4.36) is unique and smooth for all  $t \in (0, \infty)$ . In particular, the map

$$\mathbf{u}_0 \mapsto \mathbf{u}(t; \mathbf{u}_0)$$

with  $\mathbf{u}(\cdot; \mathbf{u}_0)$  solution to (4.36) corresponding to the initial data  $\mathbf{u}_0$ , defines a dynamical system in  $H$ . Now, the abstract equation (4.36) is equivalent to the following system

$$\left. \begin{aligned} \mathbf{v}_t + \dot{\boldsymbol{\omega}} \times \mathbf{x} + 2\boldsymbol{\omega}_0 \times \mathbf{v} - \nu \Delta \mathbf{v} - \nabla p &= \mathbf{0} \\ \operatorname{div} \mathbf{v} &= 0 \end{aligned} \right\} \text{ in } \mathcal{C} \times (0, \infty), \tag{4.37}$$

$$\mathbf{v}(x, t) = \mathbf{0} \text{ at } \partial\Omega,$$

$$\mathbb{I} \cdot (\dot{\boldsymbol{\omega}} - \dot{\mathbf{a}}) + \boldsymbol{\omega}_0 \times \mathbb{I} \cdot \boldsymbol{\omega} + \boldsymbol{\omega} \times \mathbb{I} \cdot \boldsymbol{\omega}_0 - \boldsymbol{\omega}_0 \times \mathbb{I} \cdot \mathbf{a} = \mathbf{0},$$

where, we recall,  $\mathbf{a}$  is defined in (4.8). Next, for a given vector  $\mathbf{h} \in \mathbb{R}^3$ , we write  $\mathbf{h} = \mathbf{h}_\perp + \mathbf{h}_\parallel$ , where  $\mathbf{h}_\parallel = h_\parallel \mathbf{e}$ , and  $\mathbf{h}_\perp \cdot \mathbf{e} = 0$ . Clearly,  $\mathbf{h}_\perp \in \mathcal{S}(\lambda)^\perp$  if and only if  $\dim \mathcal{S}(\lambda) = 1$ . Since

$$\boldsymbol{\omega}_0 \times \mathbb{I} \cdot \boldsymbol{\omega}_\parallel + \boldsymbol{\omega}_\parallel \times \mathbb{I} \cdot \boldsymbol{\omega}_0 = \mathbf{0},$$

from (4.37)<sub>4</sub>, we deduce

$$\begin{aligned} \mathbb{I} \cdot (\dot{\boldsymbol{\omega}}_\perp - \dot{\mathbf{a}}_\perp) + \boldsymbol{\omega}_0 \times \mathbb{I} \cdot \boldsymbol{\omega}_\perp + \boldsymbol{\omega}_\perp \times \mathbb{I} \cdot \boldsymbol{\omega}_0 - \boldsymbol{\omega}_0 \times \mathbb{I} \cdot \mathbf{a}_\perp &= \mathbf{0} \\ \dot{\boldsymbol{\omega}}_\parallel &= \dot{\mathbf{a}}_\parallel. \end{aligned} \quad (4.38)$$

Setting  $\boldsymbol{\omega}_* := \boldsymbol{\omega}_\perp - \mathbf{a}_\perp$  and taking into account (4.38)<sub>2</sub> we can then rewrite (4.37) in the following equivalent way:

$$\begin{aligned} \left. \begin{aligned} \mathbf{v}_t + \dot{\mathbf{a}} \times \mathbf{x} + \dot{\boldsymbol{\omega}}_* \times \mathbf{x} + 2\boldsymbol{\omega}_0 \times \mathbf{v} - \nu \Delta \mathbf{v} - \nabla p &= \mathbf{0} \\ \operatorname{div} \mathbf{v} &= 0 \end{aligned} \right\} \text{ in } \mathcal{C} \times (0, \infty), \\ \mathbf{v}(x, t) &= \mathbf{0} \text{ at } \partial\Omega, \\ \mathbb{I} \cdot \dot{\boldsymbol{\omega}}_* + \boldsymbol{\omega}_0 \times \mathbb{I} \cdot \boldsymbol{\omega}_* + (\boldsymbol{\omega}_* + \mathbf{a}_\perp) \times \mathbb{I} \cdot \boldsymbol{\omega}_0 &= \mathbf{0}, \\ \dot{\boldsymbol{\omega}}_\parallel &= \dot{\mathbf{a}}_\parallel. \end{aligned} \quad (4.39)$$

If we dot-multiply (4.39)<sub>1</sub> by  $\mathbf{v}$ , integrate by parts over  $\mathcal{C}$  and take into account (4.39)<sub>2,3</sub>, we obtain

$$\frac{dE}{dt} + \nu \|\nabla \mathbf{v}\|_2^2 = \dot{\boldsymbol{\omega}}_* \cdot \mathbb{I} \cdot \mathbf{a}_\perp, \quad (4.40)$$

where

$$E := \frac{1}{2} (\|\mathbf{v}\|_2^2 - \mathbf{a} \cdot \mathbb{I} \cdot \mathbf{a}). \quad (4.41)$$

Due to [19, §§ 7.23, 7.2.4], we know that there is  $c_0 \in (0, 1)$  such that

$$c_0 \|\mathbf{v}\|_2^2 \leq 2E \leq \|\mathbf{v}\|_2^2. \quad (4.42)$$

We next dot-multiply (4.39)<sub>4</sub> one time by  $\boldsymbol{\omega}_*$  and a second time by  $\mathbf{a}_\perp$  to get

$$\begin{aligned} \boldsymbol{\omega}_* \cdot \mathbb{I} \cdot \dot{\boldsymbol{\omega}}_* + \boldsymbol{\omega}_0 \times \mathbb{I} \cdot \boldsymbol{\omega}_* \cdot \boldsymbol{\omega}_* + (\boldsymbol{\omega}_* + \mathbf{a}_\perp) \times \mathbb{I} \cdot \boldsymbol{\omega}_0 \cdot \boldsymbol{\omega}_* &= \mathbf{0} \\ \dot{\boldsymbol{\omega}}_* \cdot \mathbb{I} \cdot \mathbf{a}_\perp + \boldsymbol{\omega}_0 \times \mathbb{I} \cdot \boldsymbol{\omega}_* \cdot \mathbf{a}_\perp + (\boldsymbol{\omega}_* + \mathbf{a}_\perp) \times \mathbb{I} \cdot \boldsymbol{\omega}_0 \cdot \mathbf{a}_\perp &= \mathbf{0}, \end{aligned}$$

from which we show

$$\dot{\boldsymbol{\omega}}_* \cdot \mathbb{I} \cdot \mathbf{a}_\perp = -\boldsymbol{\omega}_* \cdot \mathbb{I} \cdot \dot{\boldsymbol{\omega}}_* - \boldsymbol{\omega}_0 \times \mathbb{I} \cdot \boldsymbol{\omega}_* \cdot (\boldsymbol{\omega}_* + \mathbf{a}_\perp).$$

Replacing the latter into (4.40) produces

$$\frac{d}{dt} \left( E + \frac{1}{2} \boldsymbol{\omega}_* \cdot \mathbb{I} \cdot \boldsymbol{\omega}_* \right) + \nu \|\nabla \mathbf{v}\|_2^2 = -\boldsymbol{\omega}_0 \times \mathbb{I} \cdot \boldsymbol{\omega}_* \cdot (\boldsymbol{\omega}_* + \mathbf{a}_\perp). \quad (4.43)$$

On the other hand, if we dot-multiply both sides of (4.39)<sub>4</sub> by  $\mathbb{I} \cdot \boldsymbol{\omega}_*$  and recall that  $\mathbb{I} \cdot \boldsymbol{\omega}_0 = \lambda \boldsymbol{\omega}_0$ , for some  $\lambda \in \{A, B, C\}$ , we show

$$\frac{1}{2} \frac{d}{dt} (\mathbb{I} \cdot \boldsymbol{\omega}_*)^2 = -\lambda \boldsymbol{\omega}_0 \times \mathbb{I} \cdot (\boldsymbol{\omega}_* + \mathbf{a}_\perp).$$

The latter, in conjunction with (4.43) allows us to conclude

$$\frac{d}{dt} \left( 2E + \boldsymbol{\omega}_* \cdot \mathbb{I} \cdot \boldsymbol{\omega}_* - \frac{1}{\lambda} (\mathbb{I} \cdot \boldsymbol{\omega}_*)^2 \right) + 2\nu \|\nabla \mathbf{v}\|_2^2 = 0. \quad (4.44)$$

This equation is the fundamental tool in our proof. In fact, let us begin to show (4.33). Assuming the contrary would imply that (4.36) has (at least) one non-trivial, smooth solution  $\mathbf{u} = (\mathbf{v}, \boldsymbol{\omega})^\top$  such that

$$\mathbf{u}(T) = \mathbf{u}(0), \quad \int_0^T \mathbf{u}(t) = 0, \quad \text{some } T > 0. \quad (4.45)$$

Integrating both sides of (4.44) over  $[0, T]$  and using (4.45) would then produce

$$\int_0^T \|\nabla \mathbf{v}(t)\|_2^2 = 0,$$

namely,

$$\mathbf{v} \equiv \mathbf{0} \quad \text{in } [0, T]. \quad (4.46)$$

If we replace this information back in (4.39), we get, in particular,

$$\dot{\boldsymbol{\omega}}_* \times \mathbf{x} = \nabla p, \quad \mathbb{I} \cdot \dot{\boldsymbol{\omega}}_* + \boldsymbol{\omega}_0 \times \mathbb{I} \cdot \boldsymbol{\omega}_* + \boldsymbol{\omega}_* \times \mathbb{I} \cdot \boldsymbol{\omega}_0 = \mathbf{0}. \quad (4.47)$$

Operating with curl on both sides of the first of these equations we deduce  $\boldsymbol{\omega}_* = \text{const.}$ . This condition combined with (4.45), (4.46) and (4.39)<sub>5</sub> implies  $\boldsymbol{\omega}(t) \equiv \mathbf{0}$ , so that the latter and, again, (4.46) provide that there is no non-trivial solution  $\mathbf{u}$  to (4.36) satisfying (4.45), and (4.33) is thus established. With the help of this result and Lemma 4.3 we then infer that  $\sigma_1(\mathbf{L})$  must satisfy either (4.34) or (4.35). We next prove the second property stated in the proposition. To this end, we observe that if (4.34) is not true, then there exists at least one solution to (4.36) that becomes unbounded in  $H$  as  $t \rightarrow \infty$ . Thus, in order to show our stability claim it is sufficient to show that, under any of the assumptions (i)–(iii), all solutions to (4.36) are

bounded. In turn, in view of (4.39)<sub>5</sub>, this amounts to show that there is a constant  $M > 0$ , depending on the data, such that

$$\|\mathbf{v}(t)\|_2 + |\boldsymbol{\omega}_\perp(t)| \leq M, \quad \text{all } t \geq 0. \quad (4.48)$$

Set

$$G := \boldsymbol{\omega}_* \cdot \mathbb{I} \cdot \boldsymbol{\omega}_* - \frac{1}{\lambda} (\mathbb{I} \cdot \boldsymbol{\omega}_*)^2$$

and consider the three different cases (i)–(iii) stated in the proposition. If  $A = B = C$ , we get  $G = 0$ , so that from (4.42), (4.44) and Poincaré inequality, we deduce

$$\frac{dE}{dt} \leq -\sigma E, \quad \sigma = \text{const.} > 0$$

that in turn, again by (4.42), implies that  $\|\mathbf{v}(t)\|_2$  is uniformly bounded in time. Since in this case  $\boldsymbol{\omega}_\perp = \mathbf{0}$ , (4.48) is proved, and, with it, the proposition in case (i). In case (ii), we get

$$G = A\omega_{*1}^2 + B\omega_{*2}^2 - \frac{1}{C}(A^2\omega_{*1}^2 + B^2\omega_{*2}^2) = \alpha\omega_{*1}^2 + \beta\omega_{*2}^2,$$

where

$$\alpha := \frac{1}{C}A(C - A), \quad \beta := \frac{1}{C}B(C - B) > 0.$$

So, under the given assumptions,  $G$  is a positive definite quadratic form in the components of  $\boldsymbol{\omega}_*$ . This property along with (4.42) and (4.44) implies that there exists a constant  $M > 0$  such that

$$\|\mathbf{v}(t)\|_2^2 + |\boldsymbol{\omega}_*(t)|^2 \leq M, \quad \text{all } t \geq 0,$$

which proves condition (4.48). We next consider the case (iii). Without loss of generality (we can always rotate  $\mathbf{e}_2$  and  $\mathbf{e}_3$  appropriately) we take  $\mathbf{e} \equiv \mathbf{e}_3$ . We thus deduce

$$G = A\omega_{*1}^2 + B\omega_{*2}^2 - \frac{1}{B}(A^2\omega_{*1}^2 + B^2\omega_{*2}^2) = \frac{A}{B}(B - A)\omega_{*1}^2,$$

which with the help of (4.42) and (4.44) entails, for some constant  $M > 0$ ,

$$\|\mathbf{v}(t)\|_2 + |\omega_1(t)| \leq M, \quad \text{all } t \geq 0. \quad (4.49)$$

However, taking the projection of (4.36) along the subspace  $H_0$  and recalling Lemma 4.4, we also obtain  $\omega_2(t) = \text{const.}$ , so that (4.48) follows from the latter

and (4.49). Finally, we prove the last claim in the proposition. If (4.35) were not true, then all solutions to (4.36) must be uniformly bounded in time, so that, in particular, they must satisfy (4.48). We shall then show that, in such a case, the following relation holds

$$2\nu \int_0^\infty \|\nabla \mathbf{v}(s)\|_2^2 ds = 2E(0) + G(0). \quad (4.50)$$

To this end, by integrating both sides of (4.44) and using (4.48) we deduce that

$$\int_0^\infty \|\nabla \mathbf{v}(t)\|_2^2 dt < \infty,$$

which, by Poincaré inequality, entails

$$\int_0^\infty \|\mathbf{v}(t)\|_2^2 dt \leq M. \quad (4.51)$$

Now, (4.48) along with (4.39)<sub>4</sub>, furnishes

$$|\dot{\omega}_*(t)| \leq M_1 \quad \text{all } t > 0,$$

for another constant  $M_1 > 0$ . Replacing this information on the right-hand side of (4.40) and using (4.42) and Schwarz and Poincaré inequalities, we show

$$\frac{dE}{dt} + c_1 E \leq c_2 E^{\frac{1}{2}},$$

which, by a generalized form of Gronwall's lemma [11, Lemma 2.1] and (4.42), (4.51) implies

$$\lim_{t \rightarrow \infty} \|\mathbf{v}(t)\|_2 = 0. \quad (4.52)$$

From (4.39)<sub>5</sub>, (4.48) and (4.52) we infer that the orbits generated by the solutions to (4.36) through any initial data  $\mathbf{u}_0$  are compact and, therefore, the  $\omega$ -limit set is not empty and, in particular, invariant. By (4.52),  $\mathbf{v} \equiv \mathbf{0}$  on this set so that by taking the curl of both sides of (4.39)<sub>1</sub> (with  $\mathbf{v} \equiv \mathbf{0}$ ) we derive  $\omega_* = \bar{\omega} = \text{const.}$ , which once replaced in (4.39)<sub>4</sub> entails that  $\bar{\omega}$  must satisfy

$$\omega_0 \times \mathbb{I} \cdot \bar{\omega} + \bar{\omega} \times \mathbb{I} \cdot \omega_0 = \mathbf{0}.$$

From Lemma 4.1 and the latter we thus deduce

$$\bar{\omega} \in \mathcal{S}(\lambda). \quad (4.53)$$

At this point, let us first discuss the cases (iv) and (v) stated in the proposition. Then, in both situations,  $\bar{\omega}$  must also belong to  $\mathcal{S}(\lambda)^\perp$ , which produces  $\bar{\omega} = \mathbf{0}$ . Therefore, by definition of  $\omega$ -limit set, we conclude

$$\lim_{t \rightarrow \infty} |\omega_*(t)| = 0. \tag{4.54}$$

If we now integrate both sides of (4.44) from 0 to  $t$  and then let  $t \rightarrow \infty$ , with the help of (4.52), (4.42) and (4.54) we show (4.50). Now, assume condition (iv). In that case, we have  $\omega_* = \omega_{*2}e_2 + \omega_{*3}e_3$ . Therefore

$$G = \frac{B}{A}(A - B) \omega_{*2}^2 + \frac{C}{A}(A - C) \omega_{*3}^2 \tag{4.55}$$

Thus, from (4.55) and (4.50), we deduce

$$0 \leq 2E(0) + \frac{B}{A}(A - B) \omega_{*2}^2(0) + \frac{C}{A}(A - C) \omega_{*3}^2(0)$$

which, in view of the assumptions on  $A, B$ , and  $C$  cannot be true if we pick initial data such that

$$2E(0) < \frac{B}{A}(B - A) \omega_{*2}^2(0) + \frac{C}{A}(C - A) \omega_{*3}^2(0).$$

Thus, (4.35) is established. Likewise, in the case (v), we have

$$G = \frac{A}{B}(B - A) \omega_{*1}^2 + \frac{C}{B}(B - C) \omega_{*3}^2,$$

and, arguing as before, from (4.50) we deduce

$$0 \leq 2E(0) + \frac{A}{B}(B - A) \omega_{*1}^2(0) + \frac{C}{B}(B - C) \omega_{*3}^2(0),$$

which cannot hold if we choose (for example)

$$2E(0) < \frac{C}{B}(C - B) \omega_{*3}^2(0), \quad \omega_{*1}(0) = 0.$$

We now turn to the case (vi), and begin to show that also in this case (4.50) holds. To this end, without loss of generality (it is enough to rotate  $e_1$  and  $e_2$  appropriately) we assume  $e = e_1$ . Therefore, we have

$$G = A\omega_{*2}^2 + C\omega_{*3}^2 - \frac{1}{A}(A^2\omega_{*2}^2 + C^2\omega_{*3}^2) = \frac{C}{A}(A - C)\omega_{*3}^2. \tag{4.56}$$



On the other hand, from (4.53) we deduce  $\overline{\omega}_3 = 0$ , which gives

$$\lim_{t \rightarrow \infty} \omega_{*3}(t) = 0. \quad (4.57)$$

Thus, integrating both sides of (4.44) from 0 to  $t$ , letting  $t \rightarrow \infty$ , and using (4.56) and (4.57) we establish (4.50) also in the case (vi). As a consequence, from (4.50) we obtain a contradiction if we choose initial data such that

$$E(0) < \frac{C}{A}(C - A)\omega_{*3}^2(0).$$

The proof of the proposition is completed. □

*Remark 4.7* In physical terms, Proposition 4.6 may be restated by saying that a permanent rotation is “linearly stable” if and only if it occurs around an axis of maximum moment of inertia. This is in total agreement with Kelvin’s experiment.

#### 4.4 Global Existence and Stability of Permanent Rotations: A Full Explanation of Kelvin’s Experiment

The main objective of this section is to use the results established in the previous one, to prove necessary and sufficient conditions for the stability of the permanent rotation (4.3). To this purpose, we give the following definition.

**Definition 4.8** The permanent rotation  $\mathbf{s}_0$  in (4.3) is called *stable* if for any  $\varepsilon > 0$  there is  $\delta = \delta(\varepsilon) > 0$  such that

$$\|\mathbf{A}^\beta \mathbf{u}_0\| < \delta \implies \sup_{t \geq 0} \|\mathbf{A}^\beta \mathbf{u}(t)\| < \varepsilon$$

for some  $\beta \in [0, 1]$  and all solutions  $\mathbf{u} = \mathbf{u}(t)$  to (4.10) with  $\mathbf{u}(0) = \mathbf{u}_0$ . Also,  $\mathbf{s}_0$  is called *unstable* if it is not stable. Furthermore,  $\mathbf{s}_0$  is *asymptotically stable*, if it is stable and there exist  $\rho_0 > 0$  such that

$$\|\mathbf{A}^\beta \mathbf{u}_0\| < \rho_0 \implies \lim_{t \rightarrow \infty} \|\mathbf{A}^\beta \mathbf{u}(t) - \mathbf{u}^{(0)}\| = 0,$$

for some  $\mathbf{u}^{(0)} = (\mathbf{0}, \boldsymbol{\omega}^{(0)})^\top \in H$  with  $\boldsymbol{\omega}^{(0)} \in \mathcal{S}(\lambda)$ . Finally,  $\mathbf{s}_0$  is *exponentially stable* if it is asymptotically stable and there are constants  $C, \kappa > 0$  such that

$$\|\mathbf{A}^\beta \mathbf{u}(t) - \mathbf{u}^{(0)}\| \leq C \|\mathbf{A}^\beta \mathbf{u}(0)\| e^{-\kappa t}, \quad \text{all } t \geq 0.$$

*Remark 4.9* Because of conservation of total angular momentum for  $\mathcal{S}$ , in the asymptotic stability definition, we cannot expect  $\mathbf{u}^{(0)} = \mathbf{0}$ , due to the fact that  $\mathfrak{S}_0$  in (4.3) is non-trivial. As a matter of fact,  $\mathbf{u}^{(0)} = \mathbf{0}$  if and only if the initial data  $\mathbf{u}_0 := (\mathbf{v}(0), \boldsymbol{\omega}(0))^\top$  satisfy [6, Remark 5]

$$\mathbb{I} \cdot (\boldsymbol{\omega}(0) + \boldsymbol{\omega}_0) + \int_C \mathbf{x} \times \mathbf{v}(0) = \mathbf{0},$$

a non-generic condition that is physically irrelevant.

The next result provides a suitable “linearization principle” for the equation (4.10).

**Proposition 4.10** *Let  $\mathfrak{S}_0$  be given by (4.3). The following stability properties are valid.*

(a) *If (4.34) holds, then there exists  $\gamma_0 > 0$  such that if for some  $\beta \in [\frac{3}{4}, 1)$*

$$\|A^\beta \mathbf{u}_0\| < \gamma_0,$$

*the unique solution  $\mathbf{u}$  to (4.12) [or, equivalently, (4.10)] constructed in Lemma 4.2 exists for all  $t > 0$  (namely, we can take  $t^* = \infty$ ). Moreover,  $\mathfrak{S}_0$  is exponentially stable.*

(b) *Conversely, if (4.35) holds then  $\mathfrak{S}_0$  is unstable.*

*Proof* In view of Lemma 4.4, for any  $\mathbf{u} := (\mathbf{v}, \boldsymbol{\omega})^\top \in H$ , the spectral projections  $\mathcal{Q}, \mathcal{P}$  satisfy

$$\mathcal{Q}\mathbf{u} := \mathbf{u}^{(0)} \equiv (\mathbf{0}, \boldsymbol{\omega}^{(0)})^\top \in \mathbf{N}[\mathbf{L}] \equiv H_0, \quad \mathcal{P}\mathbf{u} := \mathbf{u}^{(1)} \equiv (\mathbf{v}, \boldsymbol{\omega}^{(1)})^\top \in \mathbf{R}[\mathbf{L}] \equiv H_1.$$

Applying  $\mathcal{Q}$  and  $\mathcal{P}$  on both sides of (4.12) and taking into account (4.32) we easily show

$$\begin{aligned} \frac{d\mathbf{u}^{(1)}}{dt} + \mathbf{L}_1 \mathbf{u}^{(1)} &= \mathcal{P}\mathbf{I}^{-1} \mathbf{M}(\mathbf{u}^{(1)}, \mathbf{u}^{(0)}) \\ \frac{d\mathbf{u}^{(0)}}{dt} + \mathbf{L}_0 \mathbf{u}^{(0)} &= \mathcal{Q}\mathbf{I}^{-1} \mathbf{M}(\mathbf{u}^{(1)}, \mathbf{u}^{(0)}), \end{aligned}$$

where

$$\mathbf{M}(\mathbf{u}^{(1)}, \mathbf{u}^{(0)}) := \mathbf{N}(\mathbf{u}^{(1)} + \mathbf{u}^{(0)}). \quad (4.58)$$

Moreover, observing that  $L_0 \mathbf{u}^{(0)} = \mathbf{0}$ , the previous equations simplify to the following ones

$$\begin{aligned} \frac{d\mathbf{u}^{(1)}}{dt} + L_1 \mathbf{u}^{(1)} &= \mathcal{P}I^{-1} \mathbf{M}(\mathbf{u}^{(1)}, \mathbf{u}^{(0)}) \\ \frac{d\mathbf{u}^{(0)}}{dt} &= \mathcal{Q}I^{-1} \mathbf{M}(\mathbf{u}^{(1)}, \mathbf{u}^{(0)}). \end{aligned} \quad (4.59)$$

In view of Lemma 4.3 we know that (4.59) has one and only one solution—in the class specified there—in the time interval  $[0, t^*)$ , which can be extended to a global solution provided we show the existence of  $\rho > 0$  such that

$$\sup_{t \in [0, t^*)} \|\mathbf{A}^\beta \mathbf{u}(t)\| \leq \rho. \quad (4.60)$$

In this regard, we begin to observe that since the operator  $L$  is the generator of an analytic semigroup in  $H$ , so is  $L_1$  in  $H_1$ . Thus, for all  $t \in [0, t^*)$  from (4.59)<sub>1</sub> we have

$$\mathbf{u}^{(1)}(t) = e^{-L_1 t} \mathbf{u}_0^{(1)} + \int_0^t e^{-L_1(t-s)} [\mathcal{P}I^{-1} \mathbf{M}(\mathbf{u}^{(1)}(s), \mathbf{u}^{(0)}(s))] ds. \quad (4.61)$$

Also, by assumption and Lemma 4.3, there is  $\gamma > 0$  such that

$$\operatorname{Re}[\sigma(L_1)] > \gamma > 0, \quad (4.62)$$

which implies that the fractional powers  $L_1^\alpha$ ,  $\alpha \in (0, 1)$ , are well defined in  $H_1$ . Thus, setting

$$\mathbf{w} := e^{bt} L_1^\beta \mathbf{u}^{(1)}, \quad 0 < b < \gamma,$$

from (4.61) we get

$$\mathbf{w}(t) = e^{bt} e^{-L_1 t} L_1^\beta \mathbf{u}_0^{(1)} + \int_0^t e^{bt} L_1^\beta e^{-L_1(t-s)} [\mathcal{P}I^{-1} \mathbf{M}(e^{-bs} L_1^{-\beta} \mathbf{w}(s), \mathbf{u}^{(0)}(s))] ds. \quad (4.63)$$

We now make the obvious but *crucial* observation that

$$\boldsymbol{\omega}^{(0)} \times \mathbb{I} \cdot \boldsymbol{\omega}^{(0)} = \mathbf{0}.$$

So, from (4.58) and (4.9)<sub>4</sub>, we obtain

$$\begin{aligned} \mathbf{M}(\mathbf{u}^{(1)}, \mathbf{u}^{(0)}) &= \left( -\mathcal{P} [2(\boldsymbol{\omega}^{(1)} + \boldsymbol{\omega}^{(0)}) \times \mathbf{v} + \mathbf{v} \cdot \nabla \mathbf{v}], \right. \\ &\quad \left. -\boldsymbol{\omega}^{(1)} \times \mathbb{I} \cdot (\boldsymbol{\omega}^{(0)} + \boldsymbol{\omega}^{(1)}) - \boldsymbol{\omega}^{(0)} \times \mathbb{I} \cdot \boldsymbol{\omega}^{(1)} + (\boldsymbol{\omega}^{(0)} + \boldsymbol{\omega}^{(1)}) \times \mathbb{I} \cdot \mathbf{a} \right)^\top. \end{aligned} \quad (4.64)$$

With the help of (4.14), we show

$$\begin{aligned} \|\mathbf{M}(\mathbf{u}^{(1)}, \mathbf{u}^{(0)})\| &\leq c [ (|\boldsymbol{\omega}^{(1)}| + |\boldsymbol{\omega}^{(0)}|)(\|\mathbf{v}\|_2 + |\boldsymbol{\omega}^{(1)}|) + \|\mathbf{A}_0^\beta \mathbf{v}\|^2 ] \\ &\leq c [ (\|\mathbf{u}^{(1)}\| + \|\mathbf{u}^{(0)}\|)\|\mathbf{u}^{(1)}\| + \|\widehat{\mathbf{A}}^\beta \mathbf{u}^{(1)}\|^2 ], \end{aligned} \tag{4.65}$$

where  $\widehat{\mathbf{T}}$  denotes the restriction of the operator  $\mathbf{T}$  to  $H_1$ . Since  $\mathbf{B}$  is a bounded operator, from the definition (4.18) we have (e.g. [13, Theorem 1.4.6])

$$\|\widehat{\mathbf{A}}^\alpha \mathbf{u}\| \leq c_1 \|\mathbf{L}_1^\alpha \mathbf{u}\| \leq c_2 \|\widehat{\mathbf{A}}^\alpha \mathbf{u}\|, \quad \alpha \in [0, 1],$$

which, by (4.15), implies

$$\|\widehat{\mathbf{A}}^\alpha \mathbf{u}\| \leq c_1 \|\mathbf{L}_1^\alpha \mathbf{u}\| \leq c_2 \|\widehat{\mathbf{A}}^\alpha \mathbf{u}\|, \quad \alpha \in [0, 1]. \tag{4.66}$$

Consequently, from (4.65) and the latter we derive

$$\|\mathcal{P}\mathbf{I}^{-1}\mathbf{M}(e^{-bs}\mathbf{L}_1^{-\beta}\mathbf{w}(s), \mathbf{u}^{(0)}(s))\| \leq c_3 e^{-bs} [ (\|\mathbf{w}\| + \|\mathbf{u}^{(0)}\|)\|\mathbf{w}\| + \|\mathbf{w}\|^2 ]. \tag{4.67}$$

Next, observing that, in  $H_1$ , it is  $\|\mathbf{L}_1^\alpha e^{-L_1 t}\| \leq C_\alpha t^{-\alpha} e^{-\gamma t}$ ,  $\alpha \in [0, 1]$ , from (4.63), and (4.67) we deduce

$$\begin{aligned} \|\mathbf{w}(t)\| &\leq C_0 e^{-(\gamma-b)t} \|\mathbf{L}_1^\beta \mathbf{u}_0^{(1)}\| \\ &\quad + c_3 \int_0^t \frac{e^{-(\gamma-b)(t-s)}}{(t-s)^\beta} [ (\|\mathbf{w}(s)\| + \|\mathbf{u}^{(0)}(s)\|)\|\mathbf{w}(s)\| + \|\mathbf{w}(s)\|^2 ]. \end{aligned} \tag{4.68}$$

From Lemma 4.2 we know that the pair  $(\mathbf{w}, \mathbf{u}^{(0)})$  is continuous with values in  $H$ , and so for any given  $\rho > 0$  there exists an interval of time  $[0, \tau]$ ,  $\tau < t^*$ , such that

$$\sup_{t \in [0, \tau]} (\|\mathbf{w}(t)\| + \|\mathbf{u}^{(0)}(t)\|) < \rho, \tag{4.69}$$

provided  $\|\mathbf{w}(0)\| + \|\mathbf{u}^{(0)}(0)\| < \frac{1}{2}\rho$  (say). Thus, observing that

$$\int_0^t \frac{e^{-(\gamma-b)(t-s)}}{(t-s)^\beta} ds \leq \int_0^\infty \frac{e^{-(\gamma-b)t}}{t^\beta} dt := c_0 < \infty$$

from (4.68) we get

$$(1 - c_3 c_0 \rho)\|\mathbf{w}(t)\| \leq \|\mathbf{L}_1^\beta \mathbf{u}_0^{(1)}\|, \quad t \in [0, \tau]. \tag{4.70}$$

We now go back to (4.59)<sub>2</sub>, which, with the help of (4.65), furnishes

$$\|\mathbf{u}^{(0)}(t)\| \leq \|\mathbf{u}^{(0)}(0)\| + c_4 \int_0^t [(\|\mathbf{u}^{(1)}(s)\| + \|\mathbf{u}^{(0)}(s)\|)\|\mathbf{u}^{(1)}(s)\| + \|\widehat{\mathbf{A}}^\beta \mathbf{u}^{(1)}(s)\|^2] ds.$$

Thus, if we restrict to  $t \in [0, \tau]$ , choose  $\rho = 1/(2c_3c_0)$  and use (4.66), (4.69) and (4.70), the preceding inequality furnishes

$$\begin{aligned} \|\mathbf{u}^{(0)}(t)\| &\leq \|\mathbf{u}^{(0)}(0)\| + c_5 \int_0^t \|\mathbf{A}^\beta \mathbf{u}(s)\| ds \leq \|\mathbf{u}^{(0)}(0)\| + c_6 \int_0^t e^{-bs} \|\mathbf{w}(s)\| ds \\ &\leq c_7 \|\mathbf{A}^\beta \mathbf{u}_0\|, \quad t \in [0, \tau]. \end{aligned} \tag{4.71}$$

Combining (4.70) with (4.71) and again recalling (4.66), we conclude in particular

$$\|\mathbf{A}^\beta \mathbf{u}(t)\| \leq c_8 \|\mathbf{A}^\beta \mathbf{u}_0\|, \tag{4.72}$$

for all  $t \in [0, \tau]$ , namely, for as long as  $\|\mathbf{A}^\beta \mathbf{u}(t)\| < \rho$ . However, by (4.72) and a standard argument one can show that if we choose  $\|\mathbf{A}^\beta \mathbf{u}_0\|$  sufficiently small,  $\mathbf{A}^\beta \mathbf{u}(t)$  will never reach the boundary of the ball of radius  $\rho$ , implying that (4.72) must hold for all  $t > 0$ . The proof of global existence is thus completed. Obviously, from (4.72) (valid now for all  $t \geq 0$ ), it also follows that  $\mathbf{S}_0$  is stable, in the sense of Definition 4.8. We shall now show the asymptotic behavior. From what we have just proved, under the stated condition on the data and with the above choice of  $\rho$ , from (4.70) and (4.66) we find

$$\|\widehat{\mathbf{A}}^\beta \mathbf{u}^{(1)}(t)\| \leq c_9 e^{-bt} \|\widehat{\mathbf{A}}^\beta \mathbf{u}^{(1)}(0)\|, \quad \text{all } t > 0. \tag{4.73}$$

Moreover, integrating (4.59)<sub>2</sub> between arbitrary  $t_1, t_2 > 0$  using (4.73) and reasoning in a way similar to what we did to obtain (4.71) we infer

$$\|\mathbf{u}^{(0)}(t_1) - \mathbf{u}^{(0)}(t_2)\| \leq c_{10} \int_{t_1}^{t_2} \|\widehat{\mathbf{A}}^\beta \mathbf{u}^{(1)}(s)\| ds \leq c_{11} \|\widehat{\mathbf{A}}^\beta \mathbf{u}^{(1)}(0)\| \int_{t_1}^{t_2} e^{-bs} ds, \tag{4.74}$$

from which we deduce that there exists  $\bar{\mathbf{u}}^{(0)} \in \mathcal{S}(\lambda)$  such that

$$\lim_{t \rightarrow \infty} \|\mathbf{u}^{(0)}(t) - \bar{\mathbf{u}}^{(0)}\| = 0.$$

Plugging this information back into (4.74) with  $t_2 = \infty, t_1 = t$  we infer

$$\|\mathbf{u}^{(0)}(t) - \bar{\mathbf{u}}^{(0)}\| \leq c_{12} \|\widehat{\mathbf{A}}^\beta \mathbf{u}^{(1)}(0)\| e^{-bt},$$

which, once combined with (4.73), proves the exponential rate of decay. It remains to show the instability statement. To this end we observe that, in view of the properties of the spectrum and the estimate of the nonlinearity showed in (4.14),

it is easy to check that all conditions of [13, Theorem 5.1.3] are satisfied, so that our statement follows from that theorem. The proof of the proposition is thus accomplished.  $\square$

Combining the results of Propositions 4.6 and 4.10 we may conclude with the following result that furnishes necessary and sufficient conditions for the stability of permanent rotations.

**Theorem 4.11** *Let  $\lambda \in \{A, B, C\}$ , and let  $\mathbf{S}_0$  be the permanent rotation (4.3) with  $\boldsymbol{\omega}_0 \in \mathcal{S}(\lambda) - \{\mathbf{0}\}$ . Then, if any of the conditions (i)–(iii) in Proposition 4.6 is satisfied,  $\mathbf{S}_0$  is stable. Moreover, there exists  $\gamma_0 > 0$  such that if for some  $\beta \in [\frac{3}{4}, 1)$*

$$\|\mathbf{A}^\beta \mathbf{u}_0\| < \gamma_0,$$

*then there is  $\mathbf{u}^{(0)} \equiv (\mathbf{0}, \boldsymbol{\omega}^{(0)})$ ,  $\boldsymbol{\omega}^{(0)} \in \mathcal{S}(\lambda)$ , such that all solutions to the perturbation equation (4.10) corresponding to such initial data satisfy*

$$\|\mathbf{A}^\beta \mathbf{u}(t) - \mathbf{u}^{(0)}\| \leq C \|\mathbf{A}^\beta \mathbf{u}_0\| e^{-\kappa t}, \quad \text{all } t \geq 0,$$

*for some constants  $C, \kappa > 0$ . Conversely, if any of the conditions (iv)–(vi) in Proposition 4.6 holds, the permanent rotation  $\mathbf{S}_0$  is unstable.*

*Remark 4.12* The result of Theorem 4.11 provides, in particular, a sharp and rigorous explanation of Lord Kelvin’s experiment, mentioned in the introductory section. Actually, this experiment shows that rotations occurring around the shorter axis (= maximum moment of inertia) of a prolate spheroid filled with water are stable, while those around the other central axes are unstable. As a matter of fact, our result implies a much more general phenomenon, namely, that *whatever the shape of the body and cavity, the only stable rotations* are those occurring along the axis with respect to which the moment of inertia is a maximum, all others being unstable.

## 4.5 Asymptotic Behavior for Large Data: A Full Proof of Zhukovsky Conjecture

In view of Theorem 4.11 we may deduce that under any of the assumptions (i)–(ii) stated in Proposition 4.6 all solutions to (4.1)–(4.2) that belong to a suitable function class and with initial data “sufficiently close” to a permanent rotation (4.6) in the eigenspace  $\mathcal{S}(\lambda)$  must converge exponentially fast to (another) permanent rotation that lies in the same eigenspace. Objective of this section is to show that, in fact, the same conclusion holds in the more general class of *weak* solutions to (4.1)–(4.2) and for data that not only are less regular, but also not necessarily “close” to a permanent rotation. These results provide, in particular, a positive answer to an important question that was left open in [6], thus providing a completely affirmative answer to the *Zhukovsky conjecture* mentioned in the introduction.

We begin to recall the definition of weak solution.

**Definition 4.13** A pair  $(\mathbf{v}, \boldsymbol{\omega})$  is a *weak solution* to (4.1)–(4.2) if it satisfies the following properties

- (i)  $\mathbf{v} \in C_w([0, \infty); L^2_\sigma(\mathcal{C})) \cap L^\infty(0, \infty; L^2_\sigma(\mathcal{C})) \cap L^2(0, \infty; W^{1,2}_0(\mathcal{C}))$ ;
- (ii)  $\boldsymbol{\omega} \in C([0, \infty))$ ,  $(\boldsymbol{\omega} - \mathbf{a}) \in W^{1,\infty}((0, \infty))$ ;
- (iii) Strong energy inequality:

$$\mathcal{E}(t) + \nu \int_s^t \|\nabla \mathbf{v}(\tau)\|_2^2 \leq \mathcal{E}(s)$$

for  $s = 0$ , for a.a.  $s > 0$  and all  $t \geq s$ , where

$$\mathcal{E} := \frac{1}{2} (\|\mathbf{v}\|_2^2 + \boldsymbol{\omega} \cdot \mathbb{I} \cdot \boldsymbol{\omega} - 2\mathbf{a} \cdot \mathbb{I} \cdot \boldsymbol{\omega}) ,$$

and, we recall,  $\mathbf{a}$  is defined in (4.8);

- (iv)  $(\mathbf{v}, \boldsymbol{\omega})$  obey (4.1)–(4.2) in the sense of distribution .

*Remark 4.14* Employing the important property that  $\mathcal{E}$  is positive definite in the variables  $(\mathbf{v}, \boldsymbol{\omega})$ , one can show [23, §3.2] that the class,  $\mathcal{C}_w$ , of weak solutions is not empty. Moreover, any  $(\mathbf{v}, \boldsymbol{\omega}) \in \mathcal{C}_w$  is unique in the class of those  $(\mathbf{w}, \boldsymbol{\varpi}) \in \mathcal{C}_w$  such that  $\mathbf{w} \in L^q(0, \tau; L^r(\mathcal{C}))$ ,  $3r^{-1} + 2q^{-1} = 1$  [23, §3.4].

We need the following preliminary result.

**Lemma 4.15** *Let  $(\mathbf{v}, \boldsymbol{\omega})$  be a weak solution to the problem (4.1)–(4.2) corresponding to data  $(\mathbf{v}_0, \boldsymbol{\omega}_0) \in L^2_\sigma(\mathcal{C}) \times \mathbb{R}^3$ . Then, there exists  $t_0 > 0$  such that for all  $t > t_0$  the solution becomes regular and, in particular, satisfies the following conditions,*

$$\begin{aligned} \mathbf{v} &\in W^{1,\infty}(t_0, \infty; L^2_\sigma(\mathcal{C})) \cap C([t_0, \infty); W^{1,2}_0(\mathcal{C})) \cap L^\infty([t_0, \infty); W^{2,2}(\mathcal{C})) , \\ \boldsymbol{\omega} &\in C^1([t_0, \infty); \mathbb{R}^3) . \end{aligned} \tag{4.75}$$

Moreover,

$$\lim_{t \rightarrow \infty} \|A_0^\alpha \mathbf{v}(t)\|_2 = 0 , \text{ for all } \alpha \in [0, 1) . \tag{4.76}$$

*Proof* Setting

$$\boldsymbol{\omega}_\infty := \boldsymbol{\omega} - \mathbf{a} , \tag{4.77}$$

we have that the governing equations (4.1)–(4.2) can be rewritten as follows

$$\left. \begin{aligned} \mathbf{v}_t + \mathbf{v} \cdot \nabla \mathbf{v} + (\dot{\boldsymbol{\omega}}_\infty + \dot{\mathbf{a}}) \times \mathbf{x} + 2(\boldsymbol{\omega}_\infty + \mathbf{a}) \times \mathbf{v} &= \nu \Delta \mathbf{v} - \nabla p \\ \operatorname{div} \mathbf{v} &= 0 \end{aligned} \right\} \text{ in } \mathcal{C} \times (0, \infty)$$

$$\mathbf{v}(x, t) = \mathbf{0} \text{ at } \partial\Omega \tag{4.78}$$

and

$$\mathbb{I} \cdot \dot{\boldsymbol{\omega}}_\infty + (\boldsymbol{\omega}_\infty + \mathbf{a}) \times \mathbb{I} \cdot \boldsymbol{\omega}_\infty = \mathbf{0}. \tag{4.79}$$

From [6, Proposition 1] we know already that, for any given weak solution  $(\mathbf{v}, \boldsymbol{\omega}_\infty)$  to (4.78)–(4.79) there is  $t_0 > 0$  such that for all  $t \geq t_0$  the solution becomes strong. Precisely, for all  $T > 0$ :

$$\begin{aligned} \mathbf{v} &\in C([t_0, \infty); W_0^{1,2}(\mathcal{C})) \cap L^2(t_0, t_0 + T; W^{2,2}(\mathcal{C})), \\ \mathbf{v}_t &\in L^2(t_0, t_0 + T; L^2(\mathcal{C})), \quad \boldsymbol{\omega}_\infty \in C^1([t_0, \infty); \mathbb{R}^3), \end{aligned} \tag{4.80}$$

and there exists  $p \in L^2(t_0, t_0 + T; W^{1,2}(\mathcal{C}))$ , such that  $(\mathbf{v}, p, \boldsymbol{\omega}_\infty)$  satisfy (4.78)–(4.79), a.e. in  $\mathcal{C} \times (0, \infty)$ . Finally,

$$\lim_{t \rightarrow \infty} \|\mathbf{v}(t)\|_{1,2} = 0. \tag{4.81}$$

In view of (4.80)<sub>1</sub>, and (4.81) we deduce that for any  $\eta > 0$  there exists some time  $t' \geq t_0$  such that the  $W^{2,2}$ -norm of  $\mathbf{v}$  is finite at  $t'$ , while the  $W^{1,2}$ -norm is less than  $\eta$  for all  $t \geq t'$ . Without loss of generality, we may take  $t' = t_0$  and shall thus suppose

$$\|\mathbf{v}(t_0)\|_{2,2} < \infty, \quad \|\mathbf{v}(t)\|_{1,2} < \eta, \quad \text{for all } t \geq t_0. \tag{4.82}$$

Our next goal is to construct a solution to (4.78)–(4.79) for  $t \geq t_0$ , corresponding to the initial data  $(\mathbf{v}(t_0), \boldsymbol{\omega}_\infty(t_0))$ . It will be achieved by an argument analogous to that presented in [9, Theorem 4.1]. To this end, we will prove some basic a priori estimates for solutions to (4.78)–(4.79). Taking the time-derivative of both sides of (4.78), then dot-multiplying the resulting equation by  $\mathbf{v}_t$  and integrating by parts over  $\mathcal{C}$ , we get (formally)

$$\frac{1}{2} \frac{d}{dt} (\|\mathbf{v}_t\|_2^2 - \dot{\mathbf{a}} \cdot \mathbb{I} \cdot \dot{\mathbf{a}}) + \nu \|\nabla \mathbf{v}_t\|_2^2 = -(\mathbf{v}_t \cdot \nabla \mathbf{v}, \mathbf{v}_t) + \ddot{\boldsymbol{\omega}}_\infty \cdot \mathbb{I} \cdot \dot{\mathbf{a}} - 2((\dot{\boldsymbol{\omega}}_\infty + \dot{\mathbf{a}}) \times \mathbf{v}, \mathbf{v}_t). \tag{4.83}$$

Moreover, from [6] we know that  $(\mathbf{v}, \boldsymbol{\omega}_\infty)$  satisfy the energy balance equation (energy equality)

$$\frac{1}{2} \frac{d}{dt} (\|\mathbf{v}\|_2^2 - \mathbf{a} \cdot \mathbb{I} \cdot \mathbf{a} + \boldsymbol{\omega}_\infty \cdot \mathbb{I} \cdot \boldsymbol{\omega}_\infty) + \nu \|\nabla \mathbf{v}\|_2^2 = 0. \tag{4.84}$$

From (4.79) it follows that

$$|\dot{\boldsymbol{\omega}}_\infty| \leq c_1 (|\boldsymbol{\omega}_\infty|^2 + \|\mathbf{v}\|_2^2), \tag{4.85}$$



so that

$$|2((\dot{\boldsymbol{\omega}}_\infty + \dot{\boldsymbol{a}}) \times \boldsymbol{v}, \boldsymbol{v}_t)| \leq c_1 [(|\boldsymbol{\omega}_\infty|^2 + \|\boldsymbol{v}\|_2^2) \|\boldsymbol{v}_t\|_2 + \|\boldsymbol{v}\|_2 \|\boldsymbol{v}_t\|_2^2]. \quad (4.86)$$

Furthermore, taking the time-derivative of both sides of (4.79) and dot-multiplying the resulting equation by  $\dot{\boldsymbol{a}}$  produces

$$\ddot{\boldsymbol{\omega}}_\infty \cdot \mathbb{I} \cdot \dot{\boldsymbol{a}} = -\dot{\boldsymbol{\omega}}_\infty \times \mathbb{I} \cdot \boldsymbol{\omega}_\infty \cdot \dot{\boldsymbol{a}} - (\boldsymbol{\omega}_\infty + \boldsymbol{a}) \times \mathbb{I} \cdot \dot{\boldsymbol{\omega}}_\infty \cdot \dot{\boldsymbol{a}}.$$

Therefore, employing (4.85) we show

$$|\ddot{\boldsymbol{\omega}}_\infty \cdot \mathbb{I} \cdot \dot{\boldsymbol{a}}| \leq c_2 [(|\boldsymbol{\omega}_\infty|^2 + \|\boldsymbol{v}\|_2^2)(|\boldsymbol{\omega}_\infty| + \|\boldsymbol{v}\|_2) \|\boldsymbol{v}_t\|_2]. \quad (4.87)$$

Now, from (4.84) we obtain rather simply

$$\|\boldsymbol{v}(t)\|_2 + |\boldsymbol{\omega}_\infty(t)| \leq D, \quad (4.88)$$

where  $D$ , here and in the following, denotes a constant depending only on the initial data. Using (4.88) and (4.86) we then deduce

$$|2((\dot{\boldsymbol{\omega}}_\infty + \dot{\boldsymbol{a}}) \times \boldsymbol{v}, \boldsymbol{v}_t)| \leq c_3(1 + \|\boldsymbol{v}\|_2 \|\boldsymbol{v}_t\|_2^2) \quad (4.89)$$

with  $c_3$  depending on  $D$ . Furthermore, employing in (4.87) the bound (4.88) and the Cauchy-Schwarz inequality, we show for arbitrary  $\varepsilon > 0$

$$|\ddot{\boldsymbol{\omega}}_\infty \cdot \mathbb{I} \cdot \dot{\boldsymbol{a}}| \leq c_4 + \varepsilon \|\boldsymbol{v}_t\|_2^2 \quad (4.90)$$

with  $c_4$  depending on  $D, \varepsilon$ . Furthermore, by Cauchy-Schwarz inequality and Sobolev embedding theorem, it follows that

$$|(\boldsymbol{v}_t \cdot \nabla \boldsymbol{v}, \boldsymbol{v}_t)| \leq \|\boldsymbol{v}_t\|_4^2 \|\nabla \boldsymbol{v}\|_2 \leq \|\nabla \boldsymbol{v}_t\|_2^{\frac{3}{2}} \|\boldsymbol{v}_t\|_2^{\frac{1}{2}} \|\nabla \boldsymbol{v}\|_2 \leq \varepsilon \|\nabla \boldsymbol{v}_t\|_2^2 + c_5 \|\boldsymbol{v}_t\|_2^2 \|\nabla \boldsymbol{v}\|_2^4. \quad (4.91)$$

whereas, by (4.84), (4.85) and (4.88), we also show

$$\|\nabla \boldsymbol{v}\|_2^2 \leq c_4(\|\boldsymbol{v}_t\|_2 + 1). \quad (4.92)$$

As a result, combining (4.83), (4.89)–(4.92), and by choosing  $\varepsilon = \nu/2$  in (4.91), we infer

$$\frac{d}{dt} (\|\boldsymbol{v}_t\|_2^2 - \dot{\boldsymbol{a}} \cdot \mathbb{I} \cdot \dot{\boldsymbol{a}}) + \nu \|\nabla \boldsymbol{v}_t\|_2^2 \leq c_5(1 + \|\boldsymbol{v}_t\|_2^4). \quad (4.93)$$

If we now set

$$E_1 := \frac{1}{2} (\|\boldsymbol{v}_t\|_2^2 - \dot{\boldsymbol{a}} \cdot \mathbb{I} \cdot \dot{\boldsymbol{a}})$$

from (4.40) we deduce

$$c_0 \|\mathbf{v}_t\|_2^2 \leq 2E_1 \leq \|\mathbf{v}_t\|_2^2. \tag{4.94}$$

Thus (4.93) furnishes, in particular,

$$\frac{d}{dt} E_1 \leq c_6 (1 + E_1)^4.$$

Integrating this inequality and taking into account (4.94), we easily show that there exists

$$\tau \geq c_7 / (\|\mathbf{v}_t(t_0)\|_2 + 1)^3, \tag{4.95}$$

and continuous functions  $H_i, i = 1, 2$ , in  $[t_0, t_0 + \tau)$  such that

$$\|\mathbf{v}_t(t)\|_2 \leq H_1(t), \quad \int_{t_0}^t \|\nabla \mathbf{v}_s(s)\|_2^2 \leq H_2(t) \quad t \in [t_0, t_0 + \tau). \tag{4.96}$$

Using (4.78)<sub>1</sub> and proceeding exactly as in [9, Theorem 4.1] we can prove that

$$\|\mathbf{v}_t(t_0)\|_2 \leq c_8 [\mathbf{P}(\|\mathbf{v}(t_0)\|_{2,2}) + 1] \tag{4.97}$$

where  $\mathbf{P}(r)$  is a polynomial in  $r$  with  $\mathbf{P}(0) = 0$ . Thus, in view of (4.82) and (4.95), this implies, on the one hand, that  $\|\mathbf{v}_t(t_0)\|_2$  is well defined and, on the other hand the following estimate on  $\tau$

$$\tau \geq c / (\mathbf{P}(\|\mathbf{v}(t_0)\|_{2,2}) + 1)^3. \tag{4.98}$$

Estimates (4.96) along with (4.92) allow us to establish by the classical Faedo-Galerkin method the existence of a solution  $(\tilde{\mathbf{v}}, \tilde{\boldsymbol{\omega}})$  to (4.78)–(4.79) in the time interval  $[t_0, t_0 + \tau)$  with the following properties valid for all  $t_1 \in (0, \tau)$

$$\begin{aligned} \tilde{\mathbf{v}} &\in W^{1,\infty}([t_0, t_1]); L^2(\mathcal{C}) \cap L^\infty(t_0, t_1; W^{1,2}(\mathcal{C})), \\ \tilde{\mathbf{v}}_t &\in L^2(t_0, t_1; W^{1,2}(\mathcal{C})), \quad \tilde{\boldsymbol{\omega}}_\infty \in C^1([t_0, t_1]; \mathbb{R}^3); \end{aligned}$$

for details, see [23, Chap. 4]. By the uniqueness result recalled in Remark 4.14, we must have  $(\tilde{\mathbf{v}}, \tilde{\boldsymbol{\omega}}) = (\mathbf{v}, \boldsymbol{\omega})$  in  $[t_0, t_0 + \tau)$ . Using (4.98) and arguing in a way entirely analogous to [9, Theorem 4.1], one can then show that either  $\tau = \infty$ , or else  $\|\mathbf{v}(t)\|_{2,2}$  becomes unbounded in a (left) neighborhood of  $\tau$ . In view of (4.22), the above is equivalent to say that  $\|A_0 \mathbf{v}(t)\|_2$  becomes unbounded. We shall prove that

$$\sup_{t \in [t_0, t_0 + \tau)} \|A_0 \mathbf{v}(t)\|_{2,2} \leq M < \infty, \tag{4.99}$$

and thus conclude  $\tau = \infty$ . To secure (4.99), we go back to (4.83) and employ the estimates (4.89)–(4.91) on its right-hand side. We thus obtain

$$\frac{d}{dt}E_1 + \nu \|\nabla \mathbf{v}_t\|_2^2 \leq c_9 + \varepsilon \|\mathbf{v}_t\|_{1,2}^2 + c_{10} (\|\mathbf{v}\|_2^2 + \|\nabla \mathbf{v}\|_2^4) \|\mathbf{v}_t\|_2^2$$

Observing that, by Poincaré inequality and (4.94),

$$\|\nabla \mathbf{v}_t\|_2^2 \geq c_{11} \|\mathbf{v}_t\|_2^2 \geq 2c_{11}E_1, \quad (4.100)$$

we may take  $\varepsilon$  sufficiently small to obtain

$$\frac{d}{dt}E_1 + c_{12}E_1 \leq c_9 + 2c_{10} (\|\mathbf{v}\|_2^2 + \|\nabla \mathbf{v}\|_2^4)E_1$$

However, by (4.82),  $\eta$  can be chosen in such a way that

$$2c_{10} (\|\mathbf{v}\|_2^2 + \|\nabla \mathbf{v}\|_2^4) < \frac{1}{2}c_{12},$$

so that the preceding inequality becomes

$$\frac{d}{dt}E_1 + c_{13}E_1 \leq c_9$$

Integrating this differential equation between  $t_0$  and  $t < \tau$ , and taking into account (4.97), (4.82) we show

$$\|\mathbf{v}_t(t)\|_2 \leq D, \quad t \in [t_0, \tau). \quad (4.101)$$

Next, dot-multiplying both sides of (4.78) by  $P\Delta \mathbf{v}$  and using Schwarz inequality, we also show

$$\begin{aligned} \|\mathbf{A}_0 \mathbf{v}(t)\|_2 &\leq c_{14} [\|\mathbf{v}_t(t)\|_2 + (|\dot{\boldsymbol{\omega}}_\infty(t)| + \|\mathbf{v}(t)\|_2) \|\mathbf{v}(t)\|_2 \\ &\quad + |\dot{\boldsymbol{\omega}}_\infty(t)| + \|\mathbf{v}(t) \cdot \nabla \mathbf{v}(t)\|_2]. \end{aligned} \quad (4.102)$$

The following inequality is well known (e.g., [9, Eq. (3.22)])

$$\|\mathbf{v} \cdot \nabla \mathbf{v}\|_2 \leq c_{14} \|\nabla \mathbf{v}\|_2^3 + \varepsilon \|\mathbf{A}_0 \mathbf{v}\|_2$$

with arbitrary  $\varepsilon > 0$  and  $c_{14} \rightarrow \infty$  as  $\varepsilon \rightarrow 0$ . Thus, using the latter with  $\varepsilon = 1/(2c_{14})$  into (4.102) delivers

$$\|\mathbf{A}_0 \mathbf{v}(t)\|_2 \leq 2c_{14} [\|\mathbf{v}_t(t)\|_2 + (|\dot{\boldsymbol{\omega}}_\infty(t)| + \|\mathbf{v}(t)\|_2) \|\mathbf{v}(t)\|_2 + |\dot{\boldsymbol{\omega}}_\infty(t)| + \|\nabla \mathbf{v}(t)\|_2^3], \quad (4.103)$$

which, by virtue of (4.82), (4.85), (4.88), and (4.101) allows us to show (4.99). As a result, (4.99) holds with  $\tau = \infty$ , namely

$$\sup_{t \geq t_0} \|A_0 v(t)\|_2 \leq M. \tag{4.104}$$

This property, in conjunction with (4.80) and (4.101), shows that  $(v, \omega)$  is in the class (4.75). Finally, we recall the well-known inequality (e.g., [13, p. 28])

$$\|A_0^\alpha v(t)\|_2 \leq \|A_0 v(t)\|_2^\alpha \|v(t)\|_2^{1-\alpha}, \quad \alpha \in [0, 1]$$

which, with the help of (4.81) and (4.104) implies (4.76). The proof is completed. □

*Remark 4.16* We wish to observe that, by using arguments similar to those employed in the proof of the previous lemma, one can show that the weak solution possesses regularity properties, in the time variable, even stronger than that stated in (4.75)<sub>1</sub>. More precisely, one can show  $v \in W^{k,2}((t_0, T); W^{2,2}(C))$ , for all  $k \geq 1$  and  $T > 0$  (e.g., [7, Lemma 5.5]).

We are now in a position to prove the main result of this section that gives a complete and positive answer to Zhukovsky's conjecture.

**Theorem 4.17** *Let  $\mathfrak{s} := (v, \omega)$  be a weak solution to (4.1)–(4.2) corresponding to initial data  $(v(0), \omega(0)) \in L^2_\sigma(C) \times \mathbb{R}^3$ . Then, there exists  $t_0 = t_0(\mathfrak{s})$  such that, for all  $t \geq t_0$ ,  $\mathfrak{s}$  becomes smooth and, precisely, lies in the function class defined by (4.78). Moreover,*

$$\lim_{t \rightarrow \infty} \|A_0^\alpha v(t)\|_2 = 0, \tag{4.105}$$

for all  $\alpha \in [0, 1)$ , and there exists  $\bar{\omega} \in \mathbb{R}^3$  such that

$$\lim_{t \rightarrow \infty} |\omega(t) - \bar{\omega}| = 0. \tag{4.106}$$

the rate of decay in both (4.105) and (4.106) being exponential.

*Proof* The first part of the theorem that includes (4.105), has been proved in Lemma 4.15. Concerning the property related to (4.106), in [6, Theorem 4] it is shown that it is always true with  $\bar{\omega} = \mathbf{0}$  in the (physically irrelevant) case that the initial total angular momentum  $M(0)$  vanishes [see (4.2)]. If, however,  $M(0) \neq \mathbf{0}$  (which necessarily implies  $\bar{\omega} \neq \mathbf{0}$ ), in [6, loc.cit.] the above property is secured only when either  $A \leq B < C$  or  $A = B = C$ . Thus, the case  $A < B = C$  is left open. In fact, in such circumstance it is only shown that either, for some  $\bar{\omega} \in \mathbb{R}$ ,

$$\lim_{t \rightarrow \infty} |\omega(t) - \bar{\omega}e_1| = 0,$$

in which case (4.106) is proved, or else

$$\lim_{t \rightarrow \infty} \text{dist}(\boldsymbol{\omega}(t), \mathcal{S}(\lambda)) = 0, \quad (4.107)$$

with  $\lambda \equiv B = C$ . Therefore, in the occurrence of (4.107), we cannot assert the validity of (4.106). However, with the help of Theorem 4.11 we will now show that also in the case (4.107) there must be  $\bar{\boldsymbol{\omega}} (\neq \mathbf{0})$  for which (4.106) holds. Actually, from (4.107) it follows that we can find  $\boldsymbol{\omega}_0 \in \mathcal{S}(\lambda)$ ,  $\boldsymbol{\omega}_0 \neq \mathbf{0}$ , and an unbounded sequence of times  $\{t_n\}$  such that

$$\lim_{n \rightarrow \infty} |\boldsymbol{\omega}(t_n) - \boldsymbol{\omega}_0| = 0.$$

In view of the latter and (4.105), there is  $\tau_0 \geq t_0$  such that

$$\|A_0^\beta \mathbf{v}(\tau_0)\|_2 + |\boldsymbol{\omega}(\tau_0) - \boldsymbol{\omega}_0| < \gamma_0,$$

where  $\beta$  and  $\gamma_0$  are the constants introduced in Theorem 4.11. Because of the uniqueness property (see Remark 4.14), our weak solution will then coincide with the solution of that theorem. In particular, since the assumption  $A < B = C$  is exactly case (ii) of Proposition 4.6, from Theorem 4.11 we conclude the existence of  $\bar{\boldsymbol{\omega}} \in \mathcal{S}(\lambda)$  for which (4.106) holds. The exponential decay rate, in all cases, is ensured by (4.105), (4.106) and Theorem 4.11. The proof is completed.  $\square$

## 4.6 Attainability of Permanent Rotations

One of the significant questions posed by Theorem 4.17 concerns around which central axis the terminal permanent rotation will occur. Notice that this problem is further reinforced by the fact that, since we are dealing with *weak* solutions for which uniqueness is *not* known, it may happen, in principle, that two solutions corresponding to the *same* initial data may converge, eventually, to permanent rotations occurring around two *different* central axes.

The above question has been analyzed in some detail in [6, Sect. 8], where it is shown for an open set of “large” data that, provided  $A \leq B < C$ , the terminal permanent rotation,  $r_0$ , will take place around the  $\mathbf{e}_3$ -axis, namely, the axis with maximum moment of inertia. However, this result leaves open two important aspects. In the first place, it does not allow us to draw an analogous conclusion if  $A < B = C$ , that is,  $r_0$  will occur around an axis spanned by  $\{\mathbf{e}_2, \mathbf{e}_3\}$ , as somehow expected on the basis of Theorem 4.17. Moreover, it does not provide any rate of decay. In this regard, both lab [14] and numerical [6, Sect. 9.1] experiments show that, after a transient interval of time, whose length depends (inversely) on the kinematic viscosity coefficient, the motion of the coupled system almost abruptly converges to a permanent rotation.

Objective of this section is to fill these two gaps. In particular, we shall show that when the (relative) velocity of the liquid becomes “sufficiently small” and the angular velocity of the body is “sufficiently close” to that of the corresponding terminal permanent rotation, both quantities must decay exponentially fast to their respective limits, which thus also explains the “abrupt” convergence mentioned before.

**Theorem 4.18** *Let  $(\mathbf{v}, \boldsymbol{\omega})$  be a weak solution in the sense of Definition 4.8, corresponding to data  $(\mathbf{v}_0, \boldsymbol{\omega}_0)$ , and let  $E = E(t)$  the functional defined in (4.41). The following properties hold.<sup>2</sup>*

(a) *If  $A = B < C$ , assume*

$$E(0) \leq \frac{(C - A) C}{2A} \omega_{03}^2(0),$$

*whereas, if  $A < B < C$ , assume*

$$\begin{aligned} E(0) + \frac{A}{2B}(B - A)\omega_{01}^2(0) &\leq \frac{C}{2B}(C - B)\omega_{03}^2(0), \\ E(0) &\leq \frac{B}{2A}(B - A)\omega_{02}^2(0) + \frac{C}{2A}(C - A)\omega_{03}^2(0). \end{aligned}$$

*Then, there exists  $\bar{\boldsymbol{\omega}} \in \mathcal{S}(C) - \{\mathbf{0}\}$  such that*

$$\lim_{t \rightarrow \infty} (\|A_0^\alpha \mathbf{v}(t)\|_2 + |\boldsymbol{\omega}(t) - \bar{\boldsymbol{\omega}}|) = 0, \quad \text{all } \alpha \in [0, 1). \tag{4.108}$$

(b) *If  $A < B = C$ , assume*

$$E(0) \leq \frac{B(B - A)}{2A}(\omega_{02}^2(0) + \omega_{03}^2(0)). \tag{4.109}$$

*Then, (4.108) holds for some  $\bar{\boldsymbol{\omega}} \in \mathcal{S}(B) (\equiv \mathcal{S}(C)) - \{\mathbf{0}\}$ .*

(c) *Under the assumptions stated in (a) and (b), there exist positive constants  $t_0, C$  and  $\gamma$ , depending at most on  $\nu, C, A, B, C$  and  $(\mathbf{v}_0, \boldsymbol{\omega}_0)$ , such that*

$$\|\mathbf{v}_t(t)\|_2 + \|\mathbf{v}(t)\|_{2,2} + |\dot{\boldsymbol{\omega}}(t)| + |\boldsymbol{\omega}(t) - \bar{\boldsymbol{\omega}}| \leq C e^{-\gamma t}, \quad \text{for all } t \geq t_0.$$

*Proof* We begin to prove the statement in (a). Under the given assumptions on the initial data, in [6, Theorem 5] it is shown that

$$\lim_{t \rightarrow \infty} |\boldsymbol{\omega}(t) - \bar{\boldsymbol{\omega}}| = 0.$$

---

<sup>2</sup>We assume  $\mathbf{M}(0) \neq \mathbf{0}$ , otherwise the motion of the coupled system is physically irrelevant; see Remark 4.9.

The claim then follows from Lemma 4.15. In [6, Theorem 5] it has also proved that if (4.109) holds, necessarily

$$\lim_{t \rightarrow \infty} |\omega_1(t)| = 0.$$

As a result, by Theorem 4.17 we deduce that  $\omega(t)$  must converge, as  $t \rightarrow \infty$ , to some  $\bar{\omega} \in \mathcal{S}(B) (\equiv \mathcal{S}(C))$ , which proves the statement in (b). We shall next show (c). From Theorem 4.11 we already know, in particular, that

$$\|\mathbf{v}(t)\|_{1,2} + |\omega(t) - \bar{\omega}| \leq C e^{-\kappa t}, \quad \text{for all } t \geq t_0, \quad (4.110)$$

where, here and in what follows,  $C$  denotes a generic constant whose value may change from line to line, that depends, at most, on  $\nu, \mathcal{C}$ , the central moments of inertia of the coupled system body-liquid and the initial data. Observing that  $\bar{\omega} \times \mathbb{I} \cdot \bar{\omega} = \mathbf{0}$ , from (4.79) we have

$$\mathbb{I} \cdot \dot{\omega}_\infty = -(\mathbf{w} + \mathbf{a}) \times \mathbb{I} \cdot \omega_\infty - \bar{\omega} \times \mathbb{I} \cdot \mathbf{w}, \quad (4.111)$$

with  $\mathbf{w} := \omega_\infty - \bar{\omega}$ . Therefore, from (4.88), (4.110), and (4.88) we conclude

$$|\dot{\omega}_\infty(t)| \leq C e^{-\kappa t}, \quad t \geq t_0. \quad (4.112)$$

By Schwarz inequality, (4.110) and (4.112), we show

$$\begin{aligned} |2((\dot{\omega}_\infty + \dot{\mathbf{a}}) \times \mathbf{v}, \mathbf{v}_t)| &\leq 2|\dot{\omega}_\infty| \|\mathbf{v}\|_2 \|\mathbf{v}_t\|_2 + C \|\mathbf{v}\|_2 \|\mathbf{v}_t\|_2^2 \\ &\leq |\dot{\omega}_\infty|^2 \|\mathbf{v}\|_2 + C \|\mathbf{v}\|_2 \|\mathbf{v}_t\|_2^2 \\ &\leq C e^{-\kappa t} (1 + \|\mathbf{v}_t\|_2^2). \end{aligned} \quad (4.113)$$

Moreover, taking the time-derivative of both sides of (4.111) and dot-multiplying the resulting equation by  $\dot{\mathbf{a}}$ , we get

$$\dot{\omega}_\infty \cdot \mathbb{I} \cdot \dot{\mathbf{a}} = -\dot{\mathbf{w}} \times \mathbb{I} \cdot \omega_\infty \cdot \dot{\mathbf{a}} - (\mathbf{w} + \mathbf{a}) \times \mathbb{I} \cdot \dot{\omega}_\infty \cdot \dot{\mathbf{a}} - \bar{\omega} \times \mathbb{I} \cdot \dot{\omega}_\infty \cdot \dot{\mathbf{a}}.$$

Thus, employing in this relation Cauchy-Schwarz inequality along with (4.110) and (4.112) we obtain

$$|\dot{\omega}_\infty \cdot \mathbb{I} \cdot \dot{\mathbf{a}}| \leq C e^{-\kappa t} (1 + \|\mathbf{v}_t\|_2^2). \quad (4.114)$$

We next observe that, in view of Theorem 4.11 and Lemma 4.15, the generic weak solution becomes smooth for sufficiently large  $t$  (see also Remark 4.16). Therefore, in particular, (4.83) holds for all such instant of times. Now, the latter in conjunction

with (4.91) (with  $\varepsilon = \nu/2$ ), (4.110), (4.113) and (4.114), entails that the weak solution satisfies, for all large  $t$ , the following inequality

$$\frac{d}{dt}(\|\mathbf{v}_t\|_2^2 - \dot{\mathbf{a}} \cdot \mathbb{I} \cdot \dot{\mathbf{a}}) + \nu \|\nabla \mathbf{v}_t\|_2^2 \leq C e^{-\kappa t} (1 + \|\mathbf{v}_t\|_2^2).$$

By Poincaré inequality and (4.94), this relation allows us to conclude that for all  $t > \kappa^{-1} \ln(2C/\nu) := \tau$ , we must have

$$\frac{d}{dt} E_1 + \gamma E_1 \leq C e^{-\kappa t}, \quad (4.115)$$

for suitable constant  $\gamma = \gamma(\nu, \Omega) > 0$ . Notice that, without loss of generality, we can assume  $\gamma < \kappa$ , because if (4.115) holds for some  $\gamma$ , it continues to hold for  $\gamma_1 < \gamma$ . If we integrate (4.115) from  $\tau$  to  $t > \tau$ , we show

$$E_1(t) \leq E_1(\tau) e^{-\gamma t} + C e^{-\gamma t} \int_{\tau}^t e^{-(\kappa-\gamma)s} ds, \quad t \geq \tau$$

from which, with the help of (4.94) and observing that  $\kappa > \gamma$ , we deduce

$$\|\mathbf{v}_t(t)\|_2^2 \leq C e^{-\gamma t} \quad (4.116)$$

If we now consider inequality (4.103) and estimate its right-hand side with the help of (4.110), (4.112) and (4.116), we arrive at

$$\|\mathbf{A}_0 \mathbf{v}(t)\|_2 \leq C e^{-\gamma t},$$

which by (4.22) allows us to conclude

$$\|\mathbf{v}(t)\|_{2,2} \leq C e^{-\gamma t}.$$

The statement in part (c) then follows from the latter, (4.111), (4.112), (4.116), and the theorem is completely proved.  $\square$

**Acknowledgements** Work partially supported by NSF grant DMS-1614011. I would like to thank Professor Jan Prüss and Mr. Jan A. Wein for inspiring conversations.

## References

1. A.M. Aly, Proposed robust tuned mass damper for response mitigation in buildings exposed to multidirectional wind. *Struct. Des. Tall Special Build.* (2012). doi:10.1002/tal.1068
2. A.B. Basset, On the steady motion and stability of liquid contained in an ellipsoidal vessel. *Q. J. Math.* **45**, 223–238 (1914)



3. P.G. Bhuta, L.R. Koval, A viscous ring damper for a freely precessing satellite. *Int. J. Mech. Sci.* **8**, 5–21 (1966)
4. F.L. Chernousko, Motion of a rigid body with cavities containing a viscous fluid (1968). NASA Technical Translations, Moscow (1972)
5. R.M. Cooper, Dynamics of liquids in moving containers. *ARS J.* **30**, 725–729 (1960)
6. K. Disser, G.P. Galdi, G. Mazzone, P. Zunino, Inertial motions of a rigid body with a cavity filled with a viscous liquid. *Arch. Ration. Mech. Anal.* **221**, 487–526 (2016)
7. G.P. Galdi, An introduction to the Navier-Stokes initial-boundary value problem, in *Fundamental Directions in Mathematical Fluid Mechanics*. Advances in Mathematical Fluid Mechanics (Birkhäuser, Basel, 2000), pp. 1–70
8. G.P. Galdi, *An Introduction to the Mathematical Theory of the Navier-Stokes Equations. Steady-State Problems*, 2nd edn. Springer Monographs in Mathematics (Springer, New York, 2011)
9. G.P. Galdi, G. Mazzone, On the motion of a pendulum with a cavity entirely filled with a viscous liquid, in *Recent Progress in the Theory of the Euler and Navier–Stokes Equations*. London Mathematical Society Lecture Note Series, vol. 430 (Cambridge University Press, Cambridge, 2016), pp. 37–56
10. G.P. Galdi, G. Mazzone, P. Zunino, Inertial motions of a rigid body with a cavity filled with a viscous liquid. *C. R. Mec.* **341**, 760–765 (2013)
11. G.P. Galdi, G. Mazzone, P. Zunino, Inertial motions of a rigid body with a cavity filled with a viscous liquid (2014). arXiv:1405.6596
12. G.P. Galdi, G. Mazzone, M. Mohebbi, On the motion of a liquid-filled rigid body subject to a time-periodic torque, in *Recent Developments of Mathematical Fluid Mechanics*. Advances in Mathematical Fluid Mechanics (Birkhäuser/Springer, Basel/New York, 2016), pp. 233–255
13. D. Henry, *Geometric Theory of Semilinear Parabolic Equations*. Lecture Notes in Mathematics, vol. 840 (Springer, Berlin, 1981)
14. P. Jacob, G. Weiss, [www.youtube.com/watch?v=wXID\\_yPbla8](http://www.youtube.com/watch?v=wXID_yPbla8)
15. T. Kato, *Perturbation Theory of Linear Operators*. Classics in Mathematics (Springer, Berlin, 1995)
16. T. Kato, H. Fujita, On the nonstationary Navier-Stokes system. *Rend. Sem. Mat. Univ. Padova.* **32**, 243–360 (1962)
17. K. Kirchgssner, H. Kielhöfer, Stability and bifurcation in fluid dynamics. *Rocky Mt. J. Math.* **3**, 275–318 (1973)
18. N.D. Kopachevsky, S.G. Krein, *Operator Approach to Linear Problems of Hydrodynamics, Volume 1: Nonself-Adjoint Problems for an Ideal Fluid* (Birkhäuser Verlag, Basel, 2001)
19. N.D. Kopachevsky, S.G. Krein, *Operator Approach to Linear Problems of Hydrodynamics, Volume 2: Nonself-Adjoint Problems for Viscous Fluids* (Birkhäuser Verlag, Basel, 2003)
20. J.L. Lagrange, *Mécanique Analytique* (Veuve Desaint, Paris, 1788)
21. E. Leimanis, *The General Problem of the Motion of Coupled Rigid Bodies About a Fixed Point* (Springer, Berlin, 1965)
22. A. Lunardi, *Analytic Semigroups and Optimal Regularity in Parabolic Problems*. Progress in Nonlinear Differential Equations and Their Applications, vol. 16 (Birkhäuser Verlag, Basel, 1995)
23. G. Mazzone, A mathematical analysis of the motion of a rigid body with a cavity containing a Newtonian fluid. PhD thesis, Department of Mathematics, Università del Salento, 2012
24. G. Mazzone, On the dynamics of a rigid body with cavities completely filled by a viscous liquid. Ph.D. thesis, University of Pittsburgh, 2016
25. N.N. Moiseyev, V.V. Rumyantsev, *Dynamic Stability of Bodies Containing Fluid* (Springer, New York, 1968)
26. A. Pazy, *Semigroups of Linear Operators and Applications to Partial Differential Equations*. Applied Mathematical Sciences, vol. 44 (Springer, New York, 1983)
27. M.H. Poincaré, Sur la precession des corps deformables. *Bull. Astron.* **27**, 321–356 (1910)
28. S.D. Poisson, Sur un cas particulier du mouvement de rotation des corps pesans. *J. Ecole Polyt.* **16**, 247–262 (1813)

29. J. Prüss, G. Simonett, R. Zacher, On convergence of solutions to equilibria for quasilinear parabolic problems. *J. Differ. Equ.* **246**, 3902–3931 (2009)
30. V.V. Rumyantsev, Stability of motion of solid bodies with liquid-filled cavities by Lyapunov's methods, in *Advances in Applied Mechanics*, vol. 8 (Academic, New York, 1964), pp. 183–232
31. G.G. Stokes, On some cases of fluid motion. *Trans. Camb. Philos. Soc.* **8**, 105–156 (1849)
32. A.E. Taylor, *Introduction to Functional Analysis* (Wiley, New York/Chapman & Hall Ltd., London, 1958)
33. W. Thomson, (Lord Kelvin), On an experimental illustration of minimum energy. *Nature.* **23**, 69–70 (1880)
34. N.Y. Zhukovsky, On the motion of a rigid body with cavities filled with a homogeneous liquid drop. *Zh. Fiz.-Khim. Obs. physics part*, **17**, 81–113, 145–199, 231–280 (1885) [Reprinted in his *Selected Works*, **1** (Gostekhizdat, Moscow, 1948), pp. 31–152]

# Chapter 5

## Dissipative Particle Dynamics: Foundation, Evolution, Implementation, and Applications

Z. Li, X. Bian, X. Li, M. Deng, Y.-H. Tang, B. Caswell, and G.E. Karniadakis

**Abstract** Dissipative particle dynamics (DPD) is a particle-based Lagrangian method for simulating dynamic and rheological properties of simple and complex fluids at mesoscopic length and time scales. In this chapter, we present the DPD technique, beginning from its original ad hoc formulation and subsequent theoretical developments. Next, we introduce various extensions of the DPD method that can model non-isothermal processes, diffusion-reaction systems, and ionic fluids. We also present a brief review of programming algorithms for constructing efficient DPD simulation codes as well as existing software packages. Finally, we demonstrate the effectiveness of DPD to solve particle-fluid problems, which may not be tractable by continuum or atomistic approaches.

**Keywords** Coarse-Graining • Computational biology • Fluctuating hydrodynamics • Fluid mechanics • Lagrangian approach • Mesoscopic method • Multiscale simulation • Particle-based method • Soft matter • Stochastic simulation • Thermostat

**MSC2010:** 76Z05, 76V05, 74F10, 80A32, 92C35, 74F25, 80A30, 92C45, 92C40

### 5.1 Introduction

In many applications to soft matter and biological systems, despite of the sustained fast growth of computing power during the past few decades, it is still computationally prohibitive or impractical to simulate dynamics for long temporal scales and large spatial scales with brute-force atomistic simulations [82]. The reason is that the atomistic approaches are limited by the number of atoms/molecules that can be

---

Z. Li • X. Bian • X. Li • M. Deng • Y.-H. Tang • G.E. Karniadakis (✉)  
Division of Applied Mathematics, Brown University, Box F, Providence, RI 02912, USA  
e-mail: [george\\_karniadakis@brown.edu](mailto:george_karniadakis@brown.edu)

B. Caswell  
School of Engineering, Brown University, Providence, RI 02912, USA

included in the simulation, typically  $10^4 - 10^8$  corresponding to a length-scale on the order of tens of nanometers, and the maximum time step in atomistic simulations is limited by the smallest oscillation period of the fastest atomic motions in a molecule, which is typically several femtoseconds ( $10^{-15}$  s). However, if only mesoscopic structures of molecules or their collective behavior are of practical interest, it may be unnecessary to explicitly take into account all of the atomistic details of materials [110]. To this end, the mesoscopic approach drastically simplifies the atomistic dynamics by eliminating fast degrees of freedom while preserving the behavior of slow entities, and provides an economical simulation path to capture the correct dynamics of complex fluids on larger spatial and temporal scales beyond the capability of conventional atomistic simulations [78]. In recent years, with increasing attention to the research of soft matter and biophysics, mesoscopic modeling has become a rapidly expanding methodology [98] with applications to material science [81, 95], polymer physics [40, 59, 70], rheology of complex fluids [10, 88] and computational biology [55, 56, 93].

Dissipative particle dynamics (DPD) is currently one of the most popular mesoscopic methods [71]. In DPD, a single coarse-grained (CG) particle represents an entire cluster of molecules, with unresolved degrees of freedom approximated by stochastic dynamics [61, 64]. Similar to the molecular dynamics (MD) method, a DPD system consists of many interacting particles with their dynamics computed by time integration of Newton's equation of motion. However, in contrast to MD, DPD has soft interaction potentials allowing for larger integration time steps. As a bottom-up mesoscopic approach, the DPD method smoothly bridges the gap between the microscopic and macroscopic worlds. On the one hand, DPD has its roots in microscopic dynamics as its governing equations can be rigorously derived from the microscopic dynamics by applying the Mori-Zwanzig projection operator [61]. On the other hand, the framework of DPD can be derived from the fluctuating Navier-Stokes equation [25]. The interactions between DPD particles are pairwise so that the total momentum of the DPD system is strictly conserved. By using the Fokker-Planck equation and applying the Mori projection operator, Español [22] and Marsh et al. [77] showed that the hydrodynamic equations of a DPD system recover the continuity and Navier-Stokes equations. Therefore, the DPD method can be considered as a particle-based Lagrangian representation of the continuity and momentum equations at the mesoscopic level.

In this chapter, we will revisit the theory, algorithms and applications of the DPD method. In Sect. 5.2 we consider its theoretical formulation. Beginning with the statistical mechanics behind the DPD method, both bottom-up and top-down derivations of its governing equations as well as the parameterizations will be presented. Next, in Sect. 5.3 we review several extensions of DPD that have been developed in recent years for tackling the challenges in diverse multi-physics applications beyond the capability of the classical DPD method. In Sect. 5.4 we introduce some useful algorithms for computer implementation of DPD simulations. Finally, we present some selected applications in Sect. 5.5 and end with a brief summary in Sect. 5.6.

## 5.2 Theoretical Formulation and Parameterization

The DPD method was invented intuitively by Kolemman and Hoggerbruggee [39, 44] to study hydrodynamic phenomena at the mesoscale. In the original formulation, DPD has only two types of pairwise forces: dissipative and random forces. Later on Español and Warren [26] further introduced the pairwise conservative force. Meanwhile they also derived the stochastic differential equations (SDE) as the equation of motion (EoM) for the particles. This is a fundamental step putting DPD on a firm physical ground, where the equilibrium invariant distribution of a DPD system is the canonical ensemble of Gibbs if the fluctuation-dissipation theorem (FDT) is satisfied by the DPD inputs. In Sect. 5.2.1, we will introduce the detailed derivations of the FDT for DPD systems.

Furthermore, we describe the projection technique (the Mori projection) in the first part of Sect. 5.2.2, which establishes the correspondence between DPD parameters and thermodynamic properties and transport coefficients of the fluids from the continuum point of view. This is indicated as route A in Fig. 5.1. To connect DPD with a continuum description, one may also interpret DPD as a Lagrangian discretization of the Landau-Lifshitz-Navier-Stokes equation. In this case, it is named as Smoothed DPD or SDPD for brevity. This will be explained in detail in the second part of Sect. 5.2.2, which corresponds to route B in Fig. 5.1. We may further apply the method of BBGKY (Bogoliubov-Born-Green-Kirkwood-Yvon) hierarchy to obtain a kinetic equation for the single particle distribution and then solve it to recover the Navier-Stokes' transport coefficients, as will be explained in Sect. 5.2.3. This corresponds also to the route A in Fig. 5.1. Another simpler alternative to predict the transport coefficients of DPD is by assuming the continuum limit within the cut off radius and take a continuum integral of the DPD parameters as indicated also as the route A in Fig. 5.1. The continuum integral approach together with parameterization of thermodynamic properties (compressibility) are both explained in Sect. 5.2.4. Finally, in Sect. 5.2.5, we revisit some representative work on the fundamental basis for coarse-graining the underlying system of molecular dynamics, including again the projection technique. This time it is the Zwanzig projection instead of the Mori projection. This corresponds to route C in Fig. 5.1.

### 5.2.1 Fokker-Planck Equation and Fluctuation-Dissipation Theorem

Rather than the *discrete* form from the original DPD paper [39], Español and Warren [26] formulated an EoM for DPD particles as *continuous* stochastic differential equations (SDE)

$$\begin{aligned}\dot{\mathbf{r}}_i &= \dot{\mathbf{p}}_i/m, \\ \dot{\mathbf{p}}_i &= \mathbf{F}_i = \sum_{j \neq i} \mathbf{F}_{ij} = \sum_{j \neq i} (\mathbf{F}_{ij}^C + \mathbf{F}_{ij}^D + \mathbf{F}_{ij}^R),\end{aligned}\tag{5.1}$$

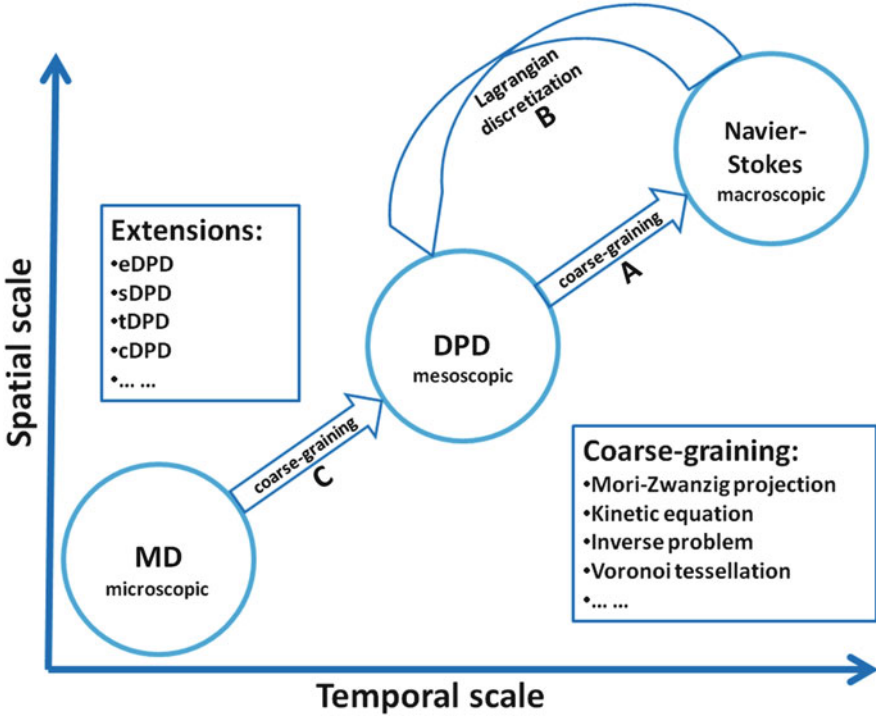


Fig. 5.1 Sketch of the current developments of the dissipative particle dynamics (DPD) method

where  $\mathbf{r}_i$  and  $\mathbf{p}_i$  are the position and momentum of particle  $i$ . Particle index  $i$  ranges from 1 to the total number of particles  $N$ . The mass  $m$  for each particle is taken an identical constant. For Galilean invariance, the forces are postulated to depend only on relative position  $\mathbf{r}_{ij} = \mathbf{r}_i - \mathbf{r}_j$  and relative velocity  $\mathbf{v}_{ij} = \mathbf{v}_i - \mathbf{v}_j$  of two particles. To preserve linear momentum, forces are antisymmetric and satisfy Newton’s third law, that is,  $\mathbf{F}_{ij} = -\mathbf{F}_{ji}$ . To preserve angular momentum, forces between two particles always lie along the line of centers  $\mathbf{e}_{ij} = \mathbf{r}_{ij}/r_{ij}$ . Therefore, the three types of forces are expressed as [26, 35]

$$\begin{aligned}
 \mathbf{F}_{ij}^C &= a w_C(r_{ij}) \mathbf{e}_{ij}, \\
 \mathbf{F}_{ij}^D &= -\gamma w_D(r_{ij}) (\mathbf{e}_{ij} \cdot \mathbf{v}_{ij}) \mathbf{e}_{ij}, \\
 \mathbf{F}_{ij}^R &= \sigma w_R(r_{ij}) \xi_{ij} \mathbf{e}_{ij},
 \end{aligned}
 \tag{5.2}$$

in which  $a$ ,  $\gamma$  and  $\sigma$  are the strengths of individual forces. Weighting functions  $w_C$ ,  $w_D$ , and  $w_R$  are isotropic and depend only on the relative distance  $r_{ij} = |\mathbf{r}_{ij}|$  of two

particles.  $\xi_{ij} = \xi_{ji}$  is a Gaussian white noise with

$$\begin{aligned} \langle \xi_{ij}(t) \rangle &= 0, \\ \langle \xi_{ij}(t)\xi_{kl}(t') \rangle &= (\delta_{ik}\delta_{jl} + \delta_{il}\delta_{jk}) \delta(t - t'), \end{aligned} \quad (5.3)$$

where  $\delta_{ij}$  is the Kronecker delta and  $\delta(t - t')$  is the Dirac delta function [26]. If we replace the forces in Eq. (5.1) by Eq. (5.2), we can write the Langevin equations in a mathematically well-defined form of SDE

$$\begin{aligned} d\mathbf{r}_i &= \frac{\mathbf{p}_i}{m_i} dt, \\ d\mathbf{p}_i &= \left( \sum_{j \neq i} \mathbf{F}_{ij}^C + \sum_{j \neq i} \mathbf{F}_{ij}^D \right) dt + \sum_{j \neq i} \sigma w^R(r_{ij}) \mathbf{e}_{ij} dW_{ij}, \end{aligned} \quad (5.4)$$

where  $dW_{ij} = dW_{ji}$  are independent increments of the Wiener process and the Itô calculus rule is assumed. Therefore,

$$dW_{ij}dW_{kl} = (\delta_{ik}\delta_{jl} + \delta_{il}\delta_{jk}) dt. \quad (5.5)$$

In continuum mechanics [46], we know that the conservation law can be expressed as the continuity equation in the differential form as

$$\frac{\partial f(\mathbf{x}, t)}{\partial t} + \nabla \cdot [\dot{\mathbf{x}}f(\mathbf{x}, t)] = 0, \quad (5.6)$$

which states that in an infinitesimal volume the rate of change of density (e.g., mass density, momentum density, ...) is balanced by the divergence of the corresponding flux. In phase space the relevant coordinate becomes  $6N$  dimensional as  $\mathbf{x} = (r_1, r_2, \dots, r_{3N}, p_1, p_2, \dots, p_{3N})$ . Accordingly, the velocity in phase space is then  $\dot{\mathbf{x}} = (\dot{r}_1, \dot{r}_2, \dots, \dot{r}_{3N}, \dot{p}_1, \dot{p}_2, \dots, \dot{p}_{3N})$ , and so  $f(\mathbf{x}, t)$  is the *probability density function* (PDF) in phase space [32]. Now we may substitute the derivatives in SDE of Eq. (5.4) into Eq. (5.6). By applying the gradient operator  $\nabla$  applied on  $6N$  dimensions, that is,  $\partial/\partial r_i$  and  $\partial/\partial p_i$ , and after some algebraic manipulations, we obtain the Fokker-Planck equation (FPE) as [26]

$$\frac{\partial f(\mathbf{x}, t)}{\partial t} = \mathcal{L}f(\mathbf{x}, t) = \mathcal{L}_C f(\mathbf{x}, t) + \mathcal{L}_D f(\mathbf{x}, t) + \mathcal{L}_R f(\mathbf{x}, t), \quad (5.7)$$

where the Fokker-Planck operator  $\mathcal{L}$  decomposes into three operators  $\mathcal{L}_C$ ,  $\mathcal{L}_D$  and  $\mathcal{L}_R$ . The individual operators are defined as follows

$$\begin{aligned}\mathcal{L}_C &\equiv - \left( \sum_i \frac{\mathbf{p}_i}{m} \cdot \frac{\partial}{\partial \mathbf{r}_i} + \sum_{ij} \mathbf{F}_{ij}^C \cdot \frac{\partial}{\partial \mathbf{p}_i} \right), \\ \mathcal{L}_D &\equiv \sum'_{ij} \mathbf{e}_{ij} \cdot \frac{\partial}{\partial \mathbf{p}_i} [\gamma w_D(r_{ij}) (\mathbf{e}_{ij} \cdot \mathbf{v}_{ij})], \\ \mathcal{L}_R &\equiv \sum'_{ij} \mathbf{e}_{ij} \cdot \frac{\partial}{\partial \mathbf{p}_i} \left[ \frac{\sigma^2}{2} w_R^2(r_{ij}) \mathbf{e}_{ij} \cdot \left( \frac{\partial}{\partial \mathbf{p}_i} - \frac{\partial}{\partial \mathbf{p}_j} \right) \right],\end{aligned}\tag{5.8}$$

where  $\sum' \equiv \sum \sum$  with  $i \neq j$ . The FPE for the DPD system is an extension of the Kramers equation for the Langevin equation of a single particle under an external potential. The FPE is also an extension of the Liouville's equation for the Hamiltonian system of many particles.

We note that the evolution of PDF in the FPE is already averaged so that no random variable appears in Eq.(5.8). The operator  $\mathcal{L}_C$  is the classical Liouville operator for a Hamiltonian system interacting with conservative forces  $\mathbf{F}^C$  alone, where  $\mathbf{F}^C$  is simply the negative gradient of a potential. For a conservative system of particles, it can be shown that the divergence of the PDF is zero, that is, the PDF is *incompressible* and divergence of velocity in Eq. (5.6) is zero. However, due to the dissipative and random forces  $\mathbf{F}^D$  and  $\mathbf{F}^R$  in DPD, the PDF is generally compressible and these effects are taken into account by the operators  $\mathcal{L}_D$  and  $\mathcal{L}_R$ . We wish to find the steady state solution of Eq. (5.7) for  $\partial f / \partial t = 0$ , and in particular, the solution is expected to be the Gibbs canonical ensemble:

$$f^{eq}(\mathbf{x}) = \frac{1}{Z} \exp[-\beta H(\mathbf{x})].\tag{5.9}$$

Here  $\beta = (k_B T)^{-1}$  and the Hamiltonian is the sum of the potential energy and kinetic energy of the system, that is,  $H = V(\mathbf{r}) + \sum_i \frac{p_i^2}{2m_i}$ . The negative gradient of the potential  $V$  gives rise to the conservative force  $\mathbf{F}^C$ . The partition function  $Z$  is there for normalization and is not particularly relevant in this context. Since the canonical ensemble is the equilibrium solution for a conservative system, it is straightforward to obtain  $\mathcal{L}_C f^{eq} = 0$ . Furthermore,  $\mathcal{L}_D f^{eq} + \mathcal{L}_R f^{eq} = 0$  can also be satisfied by postulating two relations as

$$\begin{aligned}w_D(r) &= [w_R(r)]^2, \\ \sigma^2 &= 2\gamma k_B T.\end{aligned}\tag{5.10}$$

This is the celebrated fluctuation-dissipation theorem first derived by Español and Warren [26], which is of fundamental importance for a DPD system. With the FDT



as a constraint on the input model parameters, the canonical ensemble of the DPD system is warranted in the *continuum* limit, i.e.,  $dt \rightarrow 0$ .

Another operator  $\tilde{\mathcal{L}}$  related to the Fokker-Planck operator proves to be important later and we shall also briefly introduce it. Given an arbitrary function of phase space coordinates, that is,  $a(\mathbf{x})$ , we can write down its differential as

$$\begin{aligned}
 da &= \sum_i \left( \frac{\partial a}{\partial \mathbf{r}_i} \cdot d\mathbf{r}_i + \frac{\partial a}{\partial \mathbf{p}_i} \cdot d\mathbf{p}_i \right) \\
 &+ \frac{1}{2} \sum_{ij} \left( \frac{\partial^2 a}{\partial \mathbf{r}_i \partial \mathbf{r}_j} d\mathbf{r}_i d\mathbf{r}_j + \frac{\partial^2 a}{\partial \mathbf{r}_i \partial \mathbf{p}_j} d\mathbf{r}_i d\mathbf{p}_j + \frac{\partial^2 a}{\partial \mathbf{p}_i \partial \mathbf{p}_j} d\mathbf{p}_i d\mathbf{p}_j \right) \\
 &+ \mathcal{O}(dt^{3/2}) \\
 &= \tilde{\mathcal{L}}adt + \sum'_{ij} \sigma w_R(r_{ij}) \mathbf{e}_{ij} \frac{\partial a}{\partial \mathbf{p}_i} dW_{ij} + \mathcal{O}(dt^{3/2}),
 \end{aligned} \tag{5.11}$$

where  $\tilde{\mathcal{L}}$  is defined as

$$\begin{aligned}
 \tilde{\mathcal{L}} &\equiv \left( \sum_i \frac{\mathbf{p}_i}{m} \frac{\partial}{\partial \mathbf{r}_i} + \sum'_{ij} \mathbf{F}_{ij}^C \frac{\partial}{\partial \mathbf{p}_i} \right) \\
 &+ \sum'_{ij} \gamma w_D(r_{ij}) \left[ -(\mathbf{e}_{ij} \cdot \mathbf{v}_{ij}) \mathbf{e}_{ij} \cdot \frac{\partial}{\partial \mathbf{p}_i} \right] \\
 &+ \sum'_{ij} \frac{\sigma^2}{2} w_R^2(r_{ij}) \mathbf{e}_{ij} \cdot \left( \frac{\partial}{\partial \mathbf{p}_i} - \frac{\partial}{\partial \mathbf{p}_j} \right).
 \end{aligned} \tag{5.12}$$

The SDE of Eq.(5.4) and the Itô calculus rule in Eq.(5.5) were applied to derive Eqs. (5.11) and (5.12). We will need  $\tilde{\mathcal{L}}$  to compute the time derivatives of hydrodynamic variables due to the property of Eq. (5.11)

$$\frac{d\langle a \rangle}{dt} = \langle \tilde{\mathcal{L}}a \rangle, \tag{5.13}$$

in which “ $\langle \rangle$ ” means ensemble average. It is also noteworthy that DPD satisfies the *detailed balance*

$$\mathcal{L}^{feq} a = f^{eq} \tilde{\mathcal{L}}^\epsilon a, \tag{5.14}$$

where operator  $\tilde{\mathcal{L}}^\epsilon$  is defined by reversing the sign of velocities in  $\tilde{\mathcal{L}}$ .

For practical purposes, besides the FDT in Eq. (5.10) on the input parameters, we did not specify the actual values of  $a$ ,  $\gamma$  and  $\sigma$ , nor did we talk about the functional forms of  $w_C$ ,  $w_R$  and  $w_D$ . These discussions are presented in Sects. 5.2.4 and 5.2.5.

In the following section we shall discuss how these input parameters determine the hydrodynamic properties of a DPD system.

### 5.2.2 Bottom-Up and Top-Down Derivations

Since a DPD system respects Galilean invariance, it only allows for isotropic interactions while preserving conservations of mass and momentum. The equation to be expected to govern on a large spatial-temporal scale is the continuum Navier-Stokes system. This intuitive argument can be put on firm ground by applying the projection operator techniques of Zwanzig and Mori [80, 112, 113]. The projection formalism not only yields the hydrodynamic equations for a DPD system, but also establishes an explicit correspondence between the sound speed and viscosities of the Navier-Stokes and the model parameters of DPD. To this end, the *time-independent* projection operator of Mori [80] was generalized by Español [22] for the non-Hamiltonian system of DPD to derive a linear generalized Langevin equation, from which he obtained the linearized hydrodynamic equations.

We shall revisit a few key steps of the derivations [22]; more details on the technical aspects may be found in [33, 80, 113]. To start with a simplest example, we present the essential idea of projection upon a two dimensional system, that is, two coupled ordinary different equations (ODE).

#### Projection in a Nutshell

Given a system of two ODEs as follows [113]

$$\frac{dp}{dt} = A_{11}p + A_{12}q, \quad (5.15a)$$

$$\frac{dq}{dt} = A_{21}p + A_{22}q. \quad (5.15b)$$

Suppose that our interest is on  $p$ , not  $q$ . Then, by solving Eq. (5.15b) for  $q$  we have

$$q(t) = e^{A_{22}t}q(0) + \int_0^t e^{A_{22}(t-\tau)}A_{21}p(\tau)d\tau. \quad (5.16)$$

Inserting Eq. (5.16) back into Eq. (5.15a), we have

$$\begin{aligned} \frac{dp}{dt} &= A_{11}p + A_{12} \int_0^t e^{A_{22}(t-\tau)}A_{21}p(\tau)d\tau + A_{12}e^{A_{22}t}q(0) \\ &= A_{11}p + \int_0^t K(t-\tau)p(\tau)d\tau + R(t), \end{aligned} \quad (5.17)$$

which has the form of the generalized Langevin equation (GLE). Furthermore, the memory kernel and noise terms are defined as

$$\begin{aligned} K(t) &= A_{12}e^{A_{22}t}A_{21}, \\ R(t) &= A_{12}e^{A_{22}t}q(0). \end{aligned} \quad (5.18)$$

If we are not interested in a specific initial condition  $q(0)$ , but only in an ensemble of  $q(0)$ , which has certain statistical distribution, it makes sense to name  $R(t)$  as the noise term. In general, given a set of  $N$  variables and we are only interested in a subset of them or a set of functions of the  $N$  variables, after projection or substitution we are left with equations for the dynamics of a few relevant variables. However, the eliminated variables leave their footprints within the memory kernel and random term.

Next we shall introduce the linear projection adopted by Mori and introduce the concepts of relevant variables and relevant probability density. Subsequently, we apply the Mori formalism to obtain the hydrodynamic equations of DPD. This corresponds to the route A in Fig. 5.1.

### The Mori Formalism

First we introduce a scalar product between two functions of phase space coordinates,

$$(\phi, \psi) \equiv \int f^{eq}(\mathbf{x})\phi(\mathbf{x})\psi(\mathbf{x})d\mathbf{x} \equiv \text{tr}[f^{eq}\phi\psi]. \quad (5.19)$$

The technique of projection operators, requires the identification of variables  $A_i(\mathbf{x}, t)$  relevant to the macroscopic properties of the system, and subscript  $i$  is a free index. In our case, the  $A_i$  are hydrodynamic variables to be defined later, with zero equilibrium averages. A *relevant ensemble* has the following form,

$$\bar{f}(\mathbf{x}, t) = \frac{1}{Z} \exp[-\beta H + \beta \lambda_i(t)A_i(\mathbf{x}, t)], \quad (5.20)$$

where the Einstein convention is assumed on the repeated index  $i$ . The thermodynamic parameters  $\lambda_i$  are functions of time to be selected in such a way that the average of  $A_i$  performed with the relevant ensemble agrees with the average performed with the original ensemble from the solution of the FPE of Eq. (5.7). Mathematically, this means that the time-dependent average is

$$\langle A_i(t) \rangle = \text{tr}[f(t)A_i(t)] = \text{tr}[\bar{f}(t)A_i(t)], \quad (5.21)$$

where the  $\mathbf{x}$  arguments are omitted for brevity. We further assume that the system is not far from equilibrium, which implies a *linear response* in Eq. (5.20). This allows

us to keep the first two terms of a Taylor expansion,

$$\bar{f}(\mathbf{x}, t) = \frac{1}{Z} \exp[-\beta H] \exp[\beta \lambda_i(t) A_i(\mathbf{x})] \approx f^{eq}(\mathbf{x}) [1 + \beta \lambda_i(t) A_i(\mathbf{x})]. \quad (5.22)$$

The linear departures from equilibrium of the two ensembles are defined by,

$$\begin{aligned} f(\mathbf{x}, t) &= f^{eq}(\mathbf{x}) [1 + \Psi(\mathbf{x}, t)], \\ \bar{f}(\mathbf{x}, t) &= f^{eq}(\mathbf{x}) [1 + \bar{\Psi}(\mathbf{x}, t)], \end{aligned} \quad (5.23)$$

where the  $\Psi(\mathbf{x}, t)$  is constructed in accord with Eq. (5.20) as,

$$\bar{\Psi}(\mathbf{x}, t) = \beta \lambda_i(t) A_i(\mathbf{x}, t). \quad (5.24)$$

From Eq. (5.21) we can now calculate the average either by use of the original ensemble as

$$\begin{aligned} \langle A_i(t) \rangle &= tr [f(\mathbf{x}, t) A_i] = \int f(\mathbf{x}, t) A_i(\mathbf{x}, t) d\mathbf{x} \\ &= \int f^{eq}(\mathbf{x}) [1 + \Psi(\mathbf{x}, t)] A_i(\mathbf{x}, t) d\mathbf{x} \\ &= \int f^{eq} \Psi(\mathbf{x}, t) A_i(\mathbf{x}, t) d\mathbf{x} \\ &= (A_i, \Psi), \end{aligned} \quad (5.25)$$

or by use of the relevant ensemble as

$$\begin{aligned} \langle A_i(t) \rangle &= tr [\bar{f}(\mathbf{x}, t) A_i] = \int \bar{f}(\mathbf{x}, t) A_i(\mathbf{x}, t) d\mathbf{x} \\ &= \int f^{eq}(\mathbf{x}) [1 + \bar{\Psi}(\mathbf{x}, t)] A_i(\mathbf{x}, t) d\mathbf{x} \\ &= \int f^{eq} \bar{\Psi}(\mathbf{x}, t) A_i(\mathbf{x}, t) d\mathbf{x} \\ &= (A_i, \bar{\Psi}), \end{aligned} \quad (5.26)$$

where in both Eqs. (5.25) and (5.26) the equilibrium averages vanish,

$$\int f^{eq}(\mathbf{x}) A_i(\mathbf{x}, t) d\mathbf{x} = 0,$$

and the scalar product definition Eq. (5.19) has been used. Therefore,

$$\begin{aligned}
 \langle A_i(t) \rangle &= (A_i, \Psi) = (A_i, \bar{\Psi}) = \int f^{eq} \bar{\Psi}(\mathbf{x}, t) A_i(\mathbf{x}, t) d\mathbf{x} \\
 &= \int f^{eq} \beta \lambda_j(t) A_j(\mathbf{x}, t) A_i(\mathbf{x}, t) d\mathbf{x} \\
 &= \beta \lambda_j(t) \int f^{eq} A_j(\mathbf{x}, t) A_i(\mathbf{x}, t) d\mathbf{x} \\
 &= \beta \lambda_j(t) (A_i, A_j),
 \end{aligned} \tag{5.27}$$

where the definitions of the scalar product and the departure from equilibrium of the relevant ensemble, Eqs. (5.19), (5.24) respectively, are employed. Finally, we have

$$\begin{aligned}
 \beta \lambda_j(t) &= (A_i, A_j)^{-1} \langle A_i(t) \rangle = (A_i, A_j)^{-1} (A_i, \Psi), \\
 \bar{\Psi}(\mathbf{x}, t) &= \beta \lambda_j(t) A_i = A_i (A_i, A_j)^{-1} (A_i, \Psi) \equiv \mathcal{P} \Psi(\mathbf{x}, t),
 \end{aligned} \tag{5.28}$$

here  $\mathcal{P}$  is a *projection operator* that extracts the relevant part of the original ensemble. Accordingly,  $\mathcal{Q} \Psi(\mathbf{x}, t) \equiv (1 - \mathcal{P}) \Psi(\mathbf{x}, t)$  is the irrelevant part.

From the FPE in Eq. (5.7), we have

$$\begin{aligned}
 \frac{\partial f(\mathbf{x}, t)}{\partial t} &= \mathcal{L} f(\mathbf{x}, t), \\
 \frac{\partial \{f^{eq}(\mathbf{x}) [1 + \Psi(\mathbf{x}, t)]\}}{\partial t} &= \mathcal{L} \{f^{eq}(\mathbf{x}) [1 + \Psi(\mathbf{x}, t)]\}, \\
 \frac{\partial [f^{eq} \Psi(\mathbf{x}, t)]}{\partial t} &= \mathcal{L} f^{eq} \Psi(\mathbf{x}, t), \\
 f^{eq} \frac{\partial \Psi(\mathbf{x}, t)}{\partial t} &= f^{eq} \tilde{\mathcal{L}}^\epsilon \Psi(\mathbf{x}, t), \\
 \frac{\partial \Psi(\mathbf{x}, t)}{\partial t} &= \tilde{\mathcal{L}}^\epsilon \Psi(\mathbf{x}, t),
 \end{aligned} \tag{5.29}$$

where detailed balance in Eq. (5.14) is employed. The formal solution to Eq. (5.29) is

$$\Psi(\mathbf{x}, t) = \exp(\tilde{\mathcal{L}}^\epsilon t) \Psi(\mathbf{x}, 0), \tag{5.30}$$

in which the operator  $\exp(\tilde{\mathcal{L}}^\epsilon t)$  is defined in terms of its Taylor expansion. However, if we first solve Eq. (5.29) for the irrelevant part  $\mathcal{Q} \Psi(\mathbf{x}, t)$ , and then substitute its solution back into the system to obtain the relevant part, we then get

$$\frac{\partial \bar{\Psi}(\mathbf{x}, t)}{\partial t} = \mathcal{P} \tilde{\mathcal{L}}^\epsilon \bar{\Psi}(\mathbf{x}, t) + \int_0^t d\tau \mathcal{P} \tilde{\mathcal{L}}^\epsilon \exp[\mathcal{Q} \tilde{\mathcal{L}}^\epsilon (t - \tau)] \mathcal{Q} \tilde{\mathcal{L}}^\epsilon \bar{\Psi}(\mathbf{x}, \tau). \tag{5.31}$$

Also from Eq. (5.29), we obtain an evolution equation for the relevant variables as

$$\begin{aligned} \frac{d\langle A_i(\mathbf{x}, t) \rangle}{dt} &= (\tilde{\mathcal{L}}A_i, \bar{\Psi}) + \int_0^t d\tau (\exp[\tilde{\mathcal{L}}\mathcal{Q}\{t - \tau\}] \tilde{\mathcal{L}}A_i, \mathcal{Q}\tilde{\mathcal{L}}^\epsilon A_j) \beta\lambda_j(\tau), \end{aligned} \quad (5.32)$$

which is exact. However, in practice Eq. (5.32) is difficult to apply so that one often tries to further simplify the complex memory kernel by searching for proper relevant variables. With a clear time separation between the memory kernel (fast) and the relevant variables (slow) the Markovian approximation can be invoked so that the equation reads

$$\frac{d\langle A_i(\mathbf{x}, t) \rangle}{dt} = (\tilde{\mathcal{L}}A_i, \bar{\Psi}) + \left\{ \int_0^t d\tau (\exp[\tilde{\mathcal{L}}\mathcal{Q}\tau] \tilde{\mathcal{L}}A_i, \mathcal{Q}\tilde{\mathcal{L}}^\epsilon A_j) \right\} \beta\lambda_j(t). \quad (5.33)$$

Furthermore, it is also extremely difficult to generate the projected dynamics, and in practice, one often approximates the projected dynamics with the real dynamics as  $\exp(\tilde{\mathcal{L}}\mathcal{Q}\tau) \approx \exp(\tilde{\mathcal{L}}\tau)$ , which can be justified only a posteriori.

## Hydrodynamics

If we apply Dirac's  $\delta$  function to define the relevant variables as those which appear in Navier-Stokes (NS) equations, we have

$$\begin{aligned} \delta\rho(\mathbf{r}, t) &= \sum_i m\delta[\mathbf{r} - \mathbf{r}_i(t)] - \rho_0, \\ \mathbf{g}(\mathbf{r}, t) &= \sum_i \mathbf{p}_i\delta[\mathbf{r} - \mathbf{r}_i(t)], \end{aligned} \quad (5.34)$$

here  $\rho_0$  is the equilibrium density so that both the averages of  $\delta\rho_{\mathbf{r}}$  and  $\mathbf{g}_{\mathbf{r}}$  vanish at equilibrium. Since the energy was not defined as a relevant variable which would appear in the Fourier equations, the classical DPD applies only to isothermal fluids and their flows, in which the energy varies instantaneously and can not be taken as a slow relevant variable.

On following through with the Mori projection introduced previously on these relevant variables, the equation of continuity takes the form

$$\frac{\partial\delta\rho(\mathbf{r}, t)}{\partial t} = -\frac{\partial}{\partial\mathbf{r}} \cdot \mathbf{g}(\mathbf{r}, t), \quad (5.35)$$

and the momentum equations is [22]

$$\begin{aligned} \frac{\partial \mathbf{g}(\mathbf{r}, t)}{\partial t} &= (\bar{\Psi}, \tilde{\mathcal{L}} \mathbf{g}(\mathbf{r}, t)) \\ &+ \int_0^t d\tau \int_V d\mathbf{r}' (\exp[\tilde{\mathcal{L}} \mathcal{Q}(t - \tau)] \tilde{\mathcal{L}} \mathbf{g}(\mathbf{r}, t), \mathcal{Q} \tilde{\mathcal{L}}^e \mathbf{g}(\mathbf{r}', t)) \beta \mathbf{v}(\mathbf{r}', t), \end{aligned} \quad (5.36)$$

where  $V$  is the special volume and  $\mathbf{v}(\mathbf{r}, t)$  is the velocity field. The momentum equation can then be cast into the form of

$$\frac{\partial \mathbf{g}(\mathbf{r}, t)}{\partial t} = -c_s^2 \nabla \delta \rho(\mathbf{r}, t) + \eta \nabla^2 \mathbf{v}(\mathbf{r}, t) + \left( \zeta - \frac{2\eta}{3} \right) \nabla \nabla \cdot \mathbf{v}(\mathbf{r}, t), \quad (5.37)$$

in which the isothermal sound speed  $c_s = \partial p / \partial \rho|_T$  and it is only determined by  $\mathbf{F}_{ij}^C$  [22]. With the super-indices  $C$  and  $D$  to denote the contributions of conservative and dissipative forces respectively the shear viscosity  $\eta = \eta^C + \eta^D$  and bulk viscosity  $\zeta = \zeta^C + \zeta^D$ . Each term is further defined as

$$\begin{aligned} \eta^C &= \beta \int_0^\infty \frac{1}{V} \left[ \sum_{\mu\nu}^C(\tau), \mathcal{Q} \sum_{\mu\nu}^C \right] d\tau, \\ \left( \zeta^C - \frac{2}{3} \eta^C \right) &= \beta \int_0^\infty \frac{1}{V} \left[ \sum_{\mu\mu}^C(\tau), \mathcal{Q} \sum_{\mu\mu}^C \right] d\tau, \\ \eta^D &= \beta \int_0^\infty \frac{1}{V} \left[ \sum_{\mu\nu}^D(\tau), \mathcal{Q} \sum_{\mu\nu}^D \right] d\tau, \\ \left( \zeta^D - \frac{2}{3} \eta^D \right) &= \beta \int_0^\infty \frac{1}{V} \left[ \sum_{\mu\mu}^D(\tau), \mathcal{Q} \sum_{\mu\mu}^D \right] d\tau. \end{aligned} \quad (5.38)$$

In these summations  $\mu \neq \nu$  with no summation on repeated indices. Moreover, the stress tensor contributions are given as

$$\begin{aligned} \sum^C &= \sum_i \frac{\mathbf{p}_i}{m} \mathbf{p}_i + \sum_{ij} (\mathbf{r}_i - \mathbf{r}_j) \mathbf{F}_{ij}^C, \\ \sum^D &= \sum_{ij} (\mathbf{r}_i - \mathbf{r}_j) \mathbf{F}_{ij}^D, \end{aligned} \quad (5.39)$$

which follows the identification of the conservative and the dissipative force contributions to the shear and the bulk viscosities respectively.

Such formal derivations via the Mori projection on the SDE of the DPD system provide further insight and support for understanding why DPD satisfies the hydrodynamic equations at large spatial-temporal scales. However, in practice it is not possible to quantify a priori the sound speed and viscosities of a DPD system from the given input parameters without actually running DPD simulations.

## Fluctuating Hydrodynamics

To circumvent the difficulty of specifying a priori the equation of state and the transport coefficients of classical DPD, an alternative approach is smooth particle hydrodynamics (SPH) which begins with the Lagrangian discretization of Navier-Stokes or in general Landau-Lifshitz-Navier-Stokes (LLNS) equations [25]. Given the governing differential equations of NS in Lagrangian form

$$\frac{d\rho}{dt} = -\rho\nabla\cdot\mathbf{v}, \quad (5.40a)$$

$$\rho\frac{d\mathbf{v}}{dt} = -\nabla P + \eta\nabla^2\mathbf{v} + \left(\zeta + \frac{\eta}{3}\right)\nabla\nabla\cdot\mathbf{v}, \quad (5.40b)$$

where  $d/dt$  is the substantial derivative (or material derivative), which describes how quantities such as, density field  $\rho(\mathbf{r}, t)$ , and velocity field  $\mathbf{v}(\mathbf{r}, t)$ , evolve with time along the trajectory of a point particle  $\mathbf{r}$  at time  $t$ . Intensive variables, such as the pressure field  $P = P^{eq}[\rho(\mathbf{r}, t)]$ , are determined by an equation of state under the local equilibrium assumption. For simplicity the shear (dynamic) and bulk viscosities  $\eta, \zeta$  are taken as input constants.

The NS equations are discretized by following the methodology of SPH [79]. An arbitrary function  $A(\mathbf{r})$  can be formulated in an integral form by convolution with the Dirac  $\delta$  function as

$$A(\mathbf{r}) = \int A(\mathbf{r}')\delta(\mathbf{r}' - \mathbf{r})d\mathbf{r}'. \quad (5.41)$$

The essence of SPH consists of two steps to evaluate Eq.(5.41): first a *kernel approximation* to replace the Dirac  $\delta(r)$  function, and second a *particle summation* to approximate the integration. In the end, an arbitrary function  $A(\mathbf{r})$  is expressed in terms of values at a set of  $N$  discrete disordered points—the SPH particles.

In SPH, a normalized smoothing function  $W(\mathbf{r}' - \mathbf{r}, h)$  is used as the *kernel* with  $h$  as its *smoothing length* such that in the limit  $h \rightarrow 0$   $W(\mathbf{r}' - \mathbf{r}, h)$  tends to the Dirac  $\delta$  function,

$$\int W(\mathbf{r}' - \mathbf{r}, h)d\mathbf{r} = 1, \quad \lim_{h \rightarrow 0} W(\mathbf{r}' - \mathbf{r}, h) = \delta(\mathbf{r}' - \mathbf{r}). \quad (5.42)$$



Note that  $W(\mathbf{r}' - \mathbf{r}, h)$  is bell-shaped and radially-symmetric. Therefore, it can be written as a function of a scalar variable:  $W(\mathbf{r}' - \mathbf{r}, h) \equiv W(|\mathbf{r}' - \mathbf{r}|, h) \equiv \frac{1}{h^D} w(s)$ , where  $D$  is the dimension of the problem and  $s = |\mathbf{r}' - \mathbf{r}|/h = r/h$ . Here we shall not specify any kernel and for practical flow problems different kernels may have different properties. Equations (5.40a) and (5.40b) require the gradient of the kernel function derived from,

$$\nabla W(\mathbf{r}' - \mathbf{r}, h) = -(\mathbf{r}' - \mathbf{r})G(|\mathbf{r}' - \mathbf{r}|, h), \quad (5.43)$$

with  $G \geq 0$ , the physical meaning of  $G$  will be clarified below.

The volume  $\mathcal{V}_i$  is defined as the inverse of the number density  $d_i$ , which, in turn, is related to mass  $m_i$  and mass density  $\rho_i$  as

$$\frac{1}{\mathcal{V}_i} = d_i = \frac{\rho_i}{m_i} = \sum_j W(|\mathbf{r}_i - \mathbf{r}_j|) = \sum_j W_{ij}. \quad (5.44)$$

Recall the hydrodynamic Eqs. (5.40a) and (5.40b), which can now be given in their discrete forms as

$$\dot{\rho}_i = -\rho_i (\nabla \cdot \mathbf{v})_i, \quad (5.45a)$$

$$m_i \dot{\mathbf{v}}_i = -\frac{(\nabla P)_i}{d_i} + \frac{\eta (\nabla^2 \mathbf{v})_i}{d_i} + \frac{\eta (\nabla \nabla \cdot \mathbf{v})_i}{3d_i}, \quad (5.45b)$$

where any quantity associated with particle  $i$  is denoted with a sub-index  $i$  and “ $\dot{\phantom{x}}$ ” is an abbreviation for the total (Lagrangian) time derivative.

According to Eqs. (5.44) and (5.45a), we have the following equivalent continuity equations

$$\begin{aligned} \dot{\rho}_i &= -\rho_i (\nabla \cdot \mathbf{v})_i \\ \iff \dot{d}_i &= -d_i (\nabla \cdot \mathbf{v})_i \\ \iff \dot{\mathcal{V}}_i &= \mathcal{V}_i (\nabla \cdot \mathbf{v})_i. \end{aligned} \quad (5.46)$$

In the Lagrangian description, each particle moves according to

$$\dot{\mathbf{r}}_i = \mathbf{v}_i. \quad (5.47)$$

Therefore, the time derivative of Eq. (5.44) is given as

$$\dot{d}_i = \sum_j \dot{W}(|\mathbf{r}_i - \mathbf{r}_j|) = \sum_j [\nabla W(|\mathbf{r}_i - \mathbf{r}_j|) \cdot (\mathbf{v}_i - \mathbf{v}_j)]. \quad (5.48)$$

If we define notations

$$\begin{aligned}\mathbf{r}_{ij} &= \mathbf{r}_i - \mathbf{r}_j, \\ \mathbf{v}_{ij} &= \mathbf{v}_i - \mathbf{v}_j, \\ -G_{ij}\mathbf{r}_{ij} &= \nabla W_{ij} = \nabla W(|\mathbf{r}_i - \mathbf{r}_j|),\end{aligned}\tag{5.49}$$

then Eq. (5.48) becomes

$$\dot{d}_i = \sum_j (G_{ij}\mathbf{r}_{ij} \cdot \mathbf{v}_{ij}).\tag{5.50}$$

By comparing Eq. (5.50) with Eq. (5.46), we get a SPH representation for the divergence operator of velocity

$$(\nabla \cdot \mathbf{v})_i = \frac{1}{d_i} \sum_j (G_{ij}\mathbf{r}_{ij} \cdot \mathbf{v}_{ij}).\tag{5.51}$$

The extensive variables of the system are as follows,

$$\begin{aligned}M &= \sum_i m_i, \\ E &= \sum_i \left( \frac{m\mathbf{v}_i^2}{2} + E_i \right),\end{aligned}\tag{5.52}$$

where the total mass  $M$  is a sum of the individual masses. The total energy  $E$  is sum of the individual kinetic energy  $m\mathbf{v}_i^2/2$  and internal energy  $E_i$  of each particle  $i$ .

Each particle  $i$  has the same constant mass  $m_i = m$ ; hence conservation of total mass is  $\dot{M} = 0$ .  $E_i$  is a prescribed function of the particle's own mass  $m_i$ , and volume  $\mathcal{V}_i$

$$E_i = E^{eq}(m_i, \mathcal{V}_i).\tag{5.53}$$

Its time derivative is given by

$$\dot{E}_i = \frac{\partial E^{eq}}{\partial m_i} \dot{m}_i + \frac{\partial E^{eq}}{\partial \mathcal{V}_i} \dot{\mathcal{V}}_i.\tag{5.54}$$

The thermodynamics equation of state [14] yields the pressure as

$$P_i = -\frac{\partial E^{eq}}{\partial \mathcal{V}_i}.\tag{5.55}$$

Therefore, Eq. (5.54) with constant  $m_i$  becomes

$$\dot{E}_i = -P_i \dot{\mathcal{V}}_i. \quad (5.56)$$

As required by the first and second laws of thermodynamics, the SPH representation of an isolated system must satisfy

$$\dot{E} = \sum_i (m \mathbf{v}_i \cdot \mathbf{v}_i + \dot{E}_i) = 0, \quad (5.57a)$$

$$\dot{S} = \sum_i \dot{S}_i \geq 0. \quad (5.57b)$$

- *Reversible dynamics*: Suppose we deal with an inviscid Euler flow with  $\eta = 0$  and  $\kappa = 0$ , we have

$$\begin{aligned} \dot{E} &= \sum_i (m \dot{\mathbf{v}}_i \cdot \mathbf{v}_i + \dot{E}_i) \quad \text{with Eqs. (5.45b) and (5.56)} \\ &= \sum_i \left[ -\frac{(\nabla P)_i}{d_i} \cdot \mathbf{v}_i - P_i \dot{\mathcal{V}}_i \right] \quad \text{with Eq. (5.46)} \\ &= \sum_i \left[ -\frac{(\nabla P)_i}{d_i} \cdot \mathbf{v}_i - \frac{P_i}{d_i} (\nabla \cdot \mathbf{v})_i \right] \\ &= 0, \end{aligned} \quad (5.58)$$

which is required by Eq. (5.57a). This leads to

$$\begin{aligned} &\sum_i \left[ -\frac{(\nabla P)_i}{d_i} \cdot \mathbf{v}_i \right] \\ &= \sum_i \left[ \frac{P_i}{d_i} (\nabla \cdot \mathbf{v})_i \right] \quad \text{with Eq. (5.51)} \\ &= \sum_i \left[ \frac{P_i}{d_i^2} \sum_j (G_{ij} \mathbf{r}_{ij} \cdot \mathbf{v}_{ij}) \right] \\ &= \sum_i \left[ \frac{P_i}{d_i^2} \sum_j (G_{ij} \mathbf{r}_{ij} \cdot \mathbf{v}_i) \right] - \sum_i \left[ \frac{P_i}{d_i^2} \sum_j (G_{ij} \mathbf{r}_{ij} \cdot \mathbf{v}_j) \right] \\ &= \sum_i \left[ \frac{P_i}{d_i^2} \sum_j (G_{ij} \mathbf{r}_{ij} \cdot \mathbf{v}_i) \right] + \sum_j \left[ \frac{P_j}{d_j^2} \sum_i (G_{ij} \mathbf{r}_{ij} \cdot \mathbf{v}_i) \right] \\ &= \sum_i \sum_j \left[ \left( \frac{P_i}{d_i^2} + \frac{P_j}{d_j^2} \right) G_{ij} \mathbf{r}_{ij} \cdot \mathbf{v}_i \right]. \end{aligned} \quad (5.59)$$

Therefore, a physically faithful SPH representation of pressure gradient operator is proposed as

$$\frac{(\nabla P)_i}{d_i} = \sum_i \left[ \left( \frac{P_i}{d_i^2} + \frac{P_j}{d_j^2} \right) G_{ij} \mathbf{r}_{ij} \right]. \quad (5.60)$$

Hence, in the SPH representation, a pairwise conservative force from pressure gradient can be written as

$$\mathbf{F}_{ij}^C = \left( \frac{P_i}{d_i^2} + \frac{P_j}{d_j^2} \right) G_{ij} \mathbf{r}_{ij}. \quad (5.61)$$

In summary, by the density definition in Eq. (5.44) and the position evolution of the Lagrangian description in Eq. (5.47), we get a divergence operator of SPH for velocity in Eq. (5.51) so that continuity equation is accounted for. The velocity divergence operator Eq. (5.51) generates a pressure gradient operator Eq. (5.60) which ensures the total energy of an inviscid fluid to be constant. Further note that using a variational approach, it can be shown that Eqs. (5.44) and (5.60) are also variationally consistent [12].

- *Irreversible dynamics*: Using the kernel approximation, we have the following identity [25]

$$\begin{aligned} & \int d\mathbf{r}' [A(\mathbf{r}') - A(\mathbf{r})] G(|\mathbf{r}' - \mathbf{r}|) \left[ 5 \frac{(\mathbf{r}' - \mathbf{r})^\alpha (\mathbf{r}' - \mathbf{r})^\beta}{(\mathbf{r}' - \mathbf{r})^2} - \delta^{\alpha\beta} \right] \\ &= \nabla^\alpha \nabla^\beta A(\mathbf{r}) + \mathcal{O}(\nabla^4 A h^2), \end{aligned} \quad (5.62)$$

where we have assumed that  $A(\mathbf{r})$  is sufficiently smooth on the scale of  $h$ . Taking the trace of Eq. (5.62) leads to

$$2 \int d\mathbf{r}' [A(\mathbf{r}') - A(\mathbf{r})] G(|\mathbf{r}' - \mathbf{r}|) = \nabla \cdot \nabla A(\mathbf{r}) + \mathcal{O}(\nabla^4 A h^2). \quad (5.63)$$

Note that

$$\int d\mathbf{r}' \rightarrow \sum_j \mathcal{V}_j = \sum_j \frac{1}{d_j}. \quad (5.64)$$

The second derivatives in SPH are discretized as

$$\begin{aligned} \frac{(\nabla^2 \mathbf{v})_i}{d_i} &= -2 \sum_j \left( \frac{G_{ij}}{d_i d_j} \mathbf{v}_{ij} \right), \\ \frac{(\nabla \nabla \cdot \mathbf{v})_i}{d_i} &= - \sum_j \left[ \frac{G_{ij}}{d_i d_j} (5 \mathbf{e}_{ij} \cdot \mathbf{v}_{ij} \mathbf{e}_{ij} - \mathbf{v}_{ij}) \right], \end{aligned} \quad (5.65)$$

where we have introduced the notation

$$\mathbf{e}_{ij} = \frac{\mathbf{r}_i - \mathbf{r}_j}{|\mathbf{r}_i - \mathbf{r}_j|} = \frac{\mathbf{r}_{ij}}{r_{ij}}. \quad (5.66)$$

Finally, the pairwise dissipative force is

$$\mathbf{F}_{ij}^D = - \left( \frac{5\eta}{3} - \zeta \right) \frac{G_{ij}}{d_i d_j} \mathbf{v}_{ij} - 5 \left( \zeta + \frac{\eta}{3} \right) \frac{G_{ij}}{d_i d_j} (\mathbf{e}_{ij} \cdot \mathbf{v}_{ij} \mathbf{e}_{ij}). \quad (5.67)$$

One may go ahead and apply the SPH methodology to discretize the random stress part of LLNS, but it is difficult to impose thermodynamic consistency by this route. Although the original stochastic partial differential equation (SPDE) of LLNS is thermodynamically consistent, a separate discretization of the viscous and random stresses does not guarantee the same consistency at the discrete level. This inconsistency is avoided by the creation directly at the discrete level of a random force  $\mathbf{F}_{ij}^R$  consistent with  $\mathbf{F}_{ij}^D$ , as was first done by Español and Revenga [25]. One could also extend the continuous FPE introduced in Sect. 5.2.1 to a discrete version, and so derive a consistent form of  $\mathbf{F}_{ij}^R$ . An elegant alternative is to apply the GENERIC (general equation for the nonequilibrium reversible-irreversible coupling) [84] method, which imposes thermodynamic consistency on any discrete mesoscopic model without the need to involve derivations in phase space directly. Consequently, in GENERIC, all operations and constraints are simply algebraic. Without further derivations, we shall simply provide the pairwise random force as

$$\mathbf{F}_{ij}^R = \sum_j \left( A_{ij} d\overline{\overline{\mathbf{W}}}_{ij} + \frac{B_{ij}}{3} \text{tr}[d\mathbf{W}_{ij}] \right) \cdot \mathbf{e}_{ij}, \quad (5.68)$$

where  $d\mathbf{W}_{ij}$  is matrix of independent increments of the Wiener process,  $d\overline{\overline{\mathbf{W}}}_{ij}$  is the symmetric part of it, and  $d\overline{\overline{\overline{\mathbf{W}}}}_{ij}$  is the traceless symmetric part of it. They are given explicitly by

$$\begin{aligned} d\overline{\overline{\mathbf{W}}}_{ij} &= (d\mathbf{W}_{ij} + d\mathbf{W}_{ij}^T) / 2, \\ d\overline{\overline{\overline{\mathbf{W}}}}_{ij} &= d\overline{\overline{\mathbf{W}}}_{ij} - \text{tr}[d\mathbf{W}_{ij}] \mathbf{I} / 3, \\ \text{tr}[d\mathbf{W}_{ij}] &= \sum_{\alpha} d\mathbf{W}^{\alpha\alpha}. \end{aligned} \quad (5.69)$$

Furthermore, the magnitude of noise is given as

$$\begin{aligned} A_{ij} &= \left[ 4k_B T \left( \frac{5\eta}{3} - \zeta \right) \frac{G_{ij}}{d_i d_j} \right]^{1/2}, \\ B_{ij} &= \left[ 4k_B T \left( \frac{5\eta}{3} + 8\zeta \right) \frac{G_{ij}}{d_i d_j} \right]^{1/2}. \end{aligned} \quad (5.70)$$

From the SPH discretization of the Navier-Stokes equation and the introduction of the random force corresponding to the fluctuating hydrodynamic equations known as LLNS [46], we get a version of DPD named SDPD. In contrast to the DPD method, the equation of state and transport coefficients are explicitly specified a priori in SDPD. This may avoid some of the difficulties associated with the original DPD mentioned above. This also corresponds to the top-down view of DPD, or the route B on Fig. 5.1. However, from this version of DPD, one cannot expect more than the continuum behavior of the system. Whereas in the original DPD designed by coarse-graining or parameterization, small scale behavior is expected to arise that corresponds to some underlying physical process.

### 5.2.3 Transport Coefficients from Kinetic Theory

Besides the Mori projection, we may also formulate the transport coefficients of DPD by deriving its kinetic equations. This also corresponds to the route A in Fig. 5.1. Let us introduce the  $\mu$ -space density, single-particle and pair distribution functions as [76, 77]

$$\begin{aligned}\hat{f}(\mathbf{x}, t) &= \sum_i \delta(\mathbf{x} - \mathbf{x}_i), \\ f^s(\mathbf{x}, t) &= \left\langle \sum_i \delta(\mathbf{x} - \mathbf{x}_i) \right\rangle = \langle \hat{f}(\mathbf{x}, t) \rangle, \\ f^2(\mathbf{x}, \mathbf{x}', t) &= \left\langle \sum_{i,j} \delta(\mathbf{x} - \mathbf{x}_i) \delta(\mathbf{x}' - \mathbf{x}_j) \right\rangle.\end{aligned}\tag{5.71}$$

We apply Eqs. (5.11)–(5.71) and neglect the conservative force (corresponding to the high  $\gamma$  limit), we get

$$\begin{aligned}\frac{\partial f^s(\mathbf{x}, t)}{\partial t} &= -\nabla \cdot \left\langle \sum_i \mathbf{v}_i \delta(\mathbf{x} - \mathbf{x}_i) \right\rangle \\ &+ \gamma \frac{\partial}{\partial \mathbf{v}} \cdot \left\langle \sum_{i,j} \delta(\mathbf{x} - \mathbf{x}_i) w^D(r_{ij}) (\mathbf{e}_{ij} \cdot \mathbf{v}_{ij}) \mathbf{e}_{ij} \right\rangle \\ &+ \frac{\sigma^2}{2} \frac{\partial^2}{\partial \mathbf{v} \partial \mathbf{v}} : \left\langle \sum_{i,j} \delta(\mathbf{x} - \mathbf{x}_i) w^D(r_{ij}) \mathbf{e}_{ij} \mathbf{e}_{ij} \right\rangle,\end{aligned}\tag{5.72}$$

where the contraction “ $\cdot$ ” of tensors is defined as  $A:B = \sum_{ij} A_{ij}B_{ji}$  and  $\nabla = \partial/\partial\mathbf{r}$ . We perform the integrals over all variables except  $\mathbf{x}_i$  and  $\mathbf{x}_j$ ,

$$\begin{aligned} & \frac{\partial f^s(\mathbf{x}, t)}{\partial t} + \mathbf{v} \cdot f^s(\mathbf{x}, t) \\ &= \gamma \int d\mathbf{v}' \int d\mathbf{R} \hat{\mathbf{R}} \hat{\mathbf{R}} w^D(\hat{\mathbf{R}}) : \left\{ \frac{\partial}{\partial \mathbf{v}} (\mathbf{v} - \mathbf{v}') + \frac{\sigma^2}{2\gamma} \frac{\partial^2}{\partial \mathbf{v} \partial \mathbf{v}} \right\} f^2(\mathbf{x}, \mathbf{x}', t), \end{aligned} \quad (5.73)$$

where  $\mathbf{x} = (\mathbf{r}, \mathbf{v})$ ,  $\mathbf{x}' = (\mathbf{r}', \mathbf{v}')$ ,  $\mathbf{R} = \mathbf{r} - \mathbf{r}'$  and  $\hat{\mathbf{R}} = \mathbf{R}/|\mathbf{R}|$ . This is the first equation of the BBGKY (Bogoliubov-Born-Green-Kirkwood-Yvon) hierarchy [37]. Note that the difference here is we apply the Fokker-Planck operator for a dissipative system instead of the Louville operator for a Hamiltonian system. If we assume molecular chaos to be

$$f^2(\mathbf{x}, \mathbf{x}', t) \approx f^s(\mathbf{x}, t) f^s(\mathbf{x}', t), \quad (5.74)$$

then we arrive at a nonlinear integro-partial differential equation,

$$\begin{aligned} & \frac{\partial f^s(\mathbf{x}, t)}{\partial t} + \mathbf{v} \cdot f^s(\mathbf{x}, t) \\ &= \gamma \int d\mathbf{v}' \int d\mathbf{R} \hat{\mathbf{R}} \hat{\mathbf{R}} w^D(\hat{\mathbf{R}}) f(\mathbf{r}', \mathbf{v}', t) : \left\{ \frac{\partial}{\partial \mathbf{v}} (\mathbf{v} - \mathbf{v}') + \frac{\sigma^2}{2\gamma} \frac{\partial^2}{\partial \mathbf{v} \partial \mathbf{v}} \right\} f(\mathbf{r}, \mathbf{v}, t). \end{aligned} \quad (5.75)$$

Following the Chapman-Enskog method, we solve Eq. (5.75) as a power series in a small parameter  $\mu$  on the hydrodynamic scale, i.e.,  $f = f_0 + \mu f_1 + \dots$ ; then, we define a mean free time as  $t_0 = 1/(\gamma n r_c)$ , where  $n$  is the number density of a DPD system, and define a mean thermal velocity as  $v_0 = \sqrt{k_B T/m}$ . Hence, the small parameter is  $\mu = t_0 v_0 \nabla$ , essentially  $\sim 1/\gamma$  in the high friction limit. The first two terms  $f_0$  and  $f_1$  suffice to estimate the Navier-Stokes transport coefficients as follows,

$$\eta_K = \frac{dk_B T}{2[w]\gamma}, \quad \zeta_K = \frac{k_B T}{\gamma[w]}, \quad (5.76)$$

where subscript “K” denotes the kinetic contributions. From the contribution of the dissipative force we have

$$\eta_D = \frac{m\gamma n^2 [r_c^2 w g_0]}{2d(d+2)}, \quad \zeta_D = \frac{m\gamma n^2 [r_c^2 w g_0]}{2d^2}, \quad (5.77)$$

where the square brackets mean a spatial integral as  $[\dots] = \int \dots d\mathbf{r}$ .

### 5.2.4 Parameterization

The parameterization of input parameters for a particular DPD simulation falls generally into two approaches: one approach is to solve an inverse problem and the other approach is to directly coarse-grain from an underlying MD system. The first approach generally initiates a loop of processes involving trial simulations and tuning input parameters until the desired properties are simulated by the DPD system. Although not accurately, the kinetic equations (neglecting conservative force) from the last section indeed provide a guideline of tuning the DPD parameters. We may also apply the kinetic equations further here to provide a guideline for selecting the finite time step  $\Delta t$  of DPD. This part largely follows the methodologies introduced in [75]. Furthermore, we shall also present the continuum integral approximation [35], which provides an alternative reference to tune the input parameters. Nevertheless, with either the kinetic equations or the continuum integral approximation, one may need a few trial simulations to solve the inverse problem. This can be done systematically by applying the Bayesian framework, but this topic is beyond the scope of this chapter.

The direct or forward way of coarse-graining will be presented in Sect. 5.2.5.

#### Timestep for a Constant Temperature and Noise Level

In Sect. 5.2.1, we learnt that, at  $\Delta t \rightarrow 0$ , the temperature is well defined if the input parameters of DPD satisfy the FDT given by Eq. (5.10). Here we try to find out how the finite time step  $\Delta t$  affects the temperature, since one advantage of DPD is the use of a larger time step than that of MD.

We define the one-particle distribution function for DPD as

$$f^{(1)}(\mathbf{x}, t) = \sum_i \int d\mathbf{x} \delta(\mathbf{r} - \mathbf{r}_i(t)) \delta(\mathbf{p} - \mathbf{p}_i(t)) f(\mathbf{x}, t), \quad (5.78)$$

where  $f(\mathbf{x}, t)$  is the distribution function in the  $6N$  phase-space introduced above. For simplicity, if we ignore the conservative force in DPD as is in the original form introduced by Hoogerbrugge and Koelman [39], the equilibrium distribution is the Gibbs distribution for the momentum

$$f^{eq}(\mathbf{p}) = \frac{1}{Z} \exp\left(-\beta \sum_i \frac{\mathbf{p}_i^2}{2m}\right). \quad (5.79)$$

In a simulation with a discrete time step  $\Delta t$ , the changes in position and momentum for particle  $i$  are  $\Delta \mathbf{r}_i(t)$  and  $\Delta \mathbf{p}_i(t)$ , then the change in  $f^{(1)}(\mathbf{x}, t)$  from



$t$  to  $t + \Delta t$  is

$$\begin{aligned}
 \Delta f^{(1)}(t) &= f^{(1)}(\mathbf{x}, t + \Delta t) - f^{(1)}(\mathbf{x}, t) \\
 &= \sum_i \int d\mathbf{x} [\delta(\mathbf{r} - \mathbf{r}_i - \Delta \mathbf{r}_i) \delta(\mathbf{p} - \mathbf{p}_i - \Delta \mathbf{p}_i) - \delta(\mathbf{r} - \mathbf{r}_i) \delta(\mathbf{p} - \mathbf{p}_i)] f(\mathbf{x}),
 \end{aligned} \tag{5.80}$$

where  $t$  is suppressed in the last expression to save space. We can expand the terms under the integral of Eq. (5.80) by Taylor series. Keeping only up to second partial derivatives, we can have an expression for the differential  $\Delta f^{(1)}$ . The first moment of  $\Delta f^{(1)}$  is

$$\begin{aligned}
 \Delta \int d\mathbf{p} \int d\mathbf{r} f^{(1)} \mathbf{p} &= \int d\mathbf{p} \int d\mathbf{r} \left( \sum_i \int d\mathbf{x} f^{eq} \delta(\mathbf{r} - \mathbf{r}_i) \delta(\mathbf{p} - \mathbf{p}_i) \Delta \mathbf{p}_i \right) \\
 &= 0,
 \end{aligned} \tag{5.81}$$

which follows from the momentum conservation of DPD. The second moment of  $\Delta f^{(1)}$  is

$$\begin{aligned}
 \Delta \int d\mathbf{p} \int d\mathbf{r} f^{(1)} \mathbf{p}^2 &= -2\gamma \Delta t k_B T n [w_D] + \sigma^2 \Delta t [w_R^2] + \frac{k_B T \gamma^2 \Delta t^2}{m} \left\{ 2n [w_D^2] + \frac{n^2 [w_D]^2}{d} \right\},
 \end{aligned} \tag{5.82}$$

where  $d$  is the number of space dimensions and the square brackets denote the integral

$$[w(\mathbf{r})] = \int d\mathbf{r} w(\mathbf{r}). \tag{5.83}$$

To have an invariant one-particle distribution, Eq. (5.82) must be zero, therefore,

$$mk_B T = \frac{A_3}{A_1(2 - A_1 n \Delta t) - A_2 \Delta t}, \tag{5.84}$$

where

$$A_1 = \frac{\gamma}{md} [w_D], \quad A_2 = \frac{2\gamma^2}{m^2 d} [w_D^2], \quad A_3 = \frac{\sigma^2}{d} [w_R^2]. \tag{5.85}$$

For the distribution function in Eq. (5.79), higher moments are related to lower ones as

$$\int d\mathbf{p} f^{(1)} p^{n+2} \propto \int d\mathbf{p} f^{(1)} p^n, \quad (5.86)$$

and so if the first and second moments remain constant then all moments are constant.

We shall briefly discuss the implications of Eq. (5.85) as follows [75].

- For a special case of Eq. (5.85) with  $\Delta t = 0$ , we then have  $mk_B T = A_3/(2A_1)$ . This recovers Eq. (5.10), which was obtained from the equilibrium solutions of Fokker-Planck equation correspond to the SDE of DPD.
- For a given set of input parameters of DPD ( $\gamma, \sigma, w_D, w_R, n$ ), the measured temperature of the system will increase as the time step becomes larger. Furthermore,  $1/(k_B T)$  is a linearly monotonic function of  $\Delta t$ . For example, one way to measure the equilibrium temperature is to calculate the averaged kinetic energy of the particles. Then, from the equipartition theorem one obtains temperature as

$$k_B T = \langle \mathbf{v}^2 \rangle / 3. \quad (5.87)$$

- For a given set of input parameters, if  $\Delta t > \Delta t_c$ , the denominator of Eq. 5.85 becomes negative and the system will become unstable, where

$$\Delta t_c = (2A_1)/(nA_1^2 + A_2). \quad (5.88)$$

- Once a value of  $\Delta t$  is selected, the density can not exceed a critical density

$$n_c = (2A_1 - A_2 \Delta t)/(A_1^2 \Delta t), \quad (5.89)$$

for a stable simulation.

- The choice of larger  $\gamma$  (and  $\sigma$ ) will amplify the effects of a finite  $\Delta t$ .

The analysis above ignored the conservative force for the simplification of the equilibrium solution of  $f^{eq}(\mathbf{x})$ . To select a proper  $\Delta t$  for a practical simulation with conservative force, one may draw similar conclusions by running actual trial simulations and measure the temperature by Eq. (5.87). Depending on the level of the artificial temperature increase we are willing to accept in the simulation we can then pick the appropriate  $\Delta t$ .

In our experience with random number generation, there is no statistical difference between using uniform-distributed and Gaussian-distributed random numbers. In practice the uniform distribution is preferred for the random forces, as it is computationally less expensive. From Eq. (5.85), it is also clear that the temperature increases as the noise level as  $\sigma^2$ . But the value of  $\sigma$  does not change the range of  $\Delta t$  over which the system is stable. However, with higher  $\sigma$ ,  $\gamma$  is larger due to

the FDT (5.10) and this accelerates the process of a DPD system changing from a deviated temperature  $k_B T'$  to the target temperature  $k_B T$ .

### Repulsive Parameter in the Conservative Force

For modeling a correct thermodynamic state of a liquid, a DPD system must have the correct fluctuations, which are determined by the compressibility of the liquid [37]. Therefore, the repulsive force parameter  $a$  in Eq. (5.2) is selected to recover the compressibility of realistic fluids [35]. By applying the virial theorem, we obtain the pressure of a DPD system as

$$\begin{aligned}
 p &= \rho k_B T + \frac{1}{3V} \left\langle \sum_{i < j} (\mathbf{r}_i - \mathbf{r}_j) \cdot \mathbf{f}_i \right\rangle \\
 &= \rho k_B T + \frac{1}{3V} \left\langle \sum_{i < j} (\mathbf{r}_i - \mathbf{r}_j) \cdot \mathbf{F}_{ij}^c \right\rangle \\
 &= \rho k_B T + \frac{2\pi}{3} \rho^2 \int_0^{r_c} r f(r) g(r) r^2 dr,
 \end{aligned} \tag{5.90}$$

where  $g(r)$  is the radial distribution function of DPD particles,  $\rho$  the number density of DPD particles and  $r_c$  the cutoff radius beyond which  $f(r)$  vanishes. For a wide range of parameters, the pressure can be approximated for high densities ( $\rho > 2$ ) as

$$p = \rho k_B T + \alpha a \rho^2 (\alpha = 0.101 \pm 0.001). \tag{5.91}$$

The compressibility of a DPD fluid is computed by  $\kappa_c^{-1} = (\partial p / \partial \rho)_T / k_B T$ . To match the compressibility of a DPD fluid to that of a realistic fluid, the dimensionless compressibility is defined by

$$\kappa_c^{-1} = \frac{[L]^3}{\rho k_B T \beta_T}, \tag{5.92}$$

where  $\beta_T$  is the isothermal compressibility of the fluid of interest and  $[L]$  the length scale and  $\rho$  the number of DPD particles in a volume of  $[L]^3$ . For example, the liquid water at 300 K has a thermal energy of  $k_B T = 4.142 \times 10^{-21} \text{ kg m}^2 \text{ s}^{-2}$  and a compressibility of  $\beta_T = 4.503 \times 10^{-10} \text{ m}^2 / \text{kg}$ . Let  $\rho = 3$  be the number density of a DPD system where one DPD particle represents a water molecule, a length scale  $[L] = 0.448 \text{ nm}$  is determined so that the DPD system matches the number density of water molecule. Substituting these values into Eq. (5.92) gives  $\kappa_c^{-1} = 16.0$ . Therefore, the repulsive force parameter is  $a = k_B T (\kappa_c^{-1} - 1.0) / 2\alpha \rho \approx 75.0 k_B T / \rho$  with  $\alpha = 0.101 \pm 0.001$  for liquid water [35]. It is worth notable that the expression  $a = 75.0 k_B T / \rho$  is obtained based on a choice of  $[L] = 0.448 \text{ nm}$ . Whenever the

coarse-graining level or the length scale  $[L]$  is changed,  $a_{ij}$  should be modified accordingly to recover the correct compressibility of the fluid. Otherwise, the value of  $\kappa_c^{-1}$  will be underestimated, and hence the DPD fluid's sound speed will be lower than expected.

### Dissipative Coefficient

We consider a fluid undergoing uniform linear flow  $v_\alpha = e_{\alpha\beta} r_\beta$ . From the Irving-Kirkwood formula [41], we know that the stress has contributions from both a kinetic part due to particle transfer across streamlines and a dynamic part due to inter-particle forces. We first consider the second part due to forces. In particular, the one arising from the dissipative force is

$$\sigma_{\alpha\beta} = \frac{1}{V} \left\langle \sum_{i>j} r_{ij\alpha} \mathbf{F}_{ij\beta}^D \right\rangle, \quad (5.93)$$

where the expression for  $\mathbf{F}_{ij}^D$  is given in Eq. (5.2). If we assume a uniform density without a particular structure for the particles, that is,  $g(r) = 1$ , we can then replace the summation by an integral as

$$\sigma_{\alpha\beta} = \frac{2\pi\gamma\rho^2}{15} \int_0^\infty dr r^4 \gamma w_D(r) [e_{\alpha\beta} + e_{\beta\alpha} + \delta_{\beta\alpha} e_{\gamma\gamma}]. \quad (5.94)$$

Therefore, the viscosity due to dissipative contribution is

$$\eta^D = \frac{2\pi\gamma\rho^2}{15} \int_0^\infty dr r^4 w_D(r). \quad (5.95)$$

For any specific weight function  $w_D(r)$  chosen, the viscosity can be calculated in a straightforward way.

Next we derive the kinetic contribution to viscosity due to the diffusion of the particles. The Langevin equation for a single particle without conservative forces reads as,

$$\frac{d\mathbf{v}_i}{dt} = \sum_{j \neq i} \mathbf{F}_{ij}^D + \sum_{j \neq i} \mathbf{F}_{ij}^R. \quad (5.96)$$

Since the friction force is linear in the velocity difference, we may write

$$\frac{d\mathbf{v}_i}{dt} + \frac{\mathbf{v}_i}{\tau} = \mathbf{F}^R, \quad (5.97)$$

where

$$\frac{1}{\tau} = \sum_{j \neq i} \gamma w_D(r_{ij}) \frac{\hat{\mathbf{r}}_{ij} \cdot \hat{\mathbf{r}}_{ij}}{3}, \quad \mathbf{F}^R = \sum_{j \neq i} \sigma w_R(r_{ij}) \theta_{ij} \hat{\mathbf{r}}_{ij}. \quad (5.98)$$

We further replace the sum by integral and get

$$\begin{aligned} \frac{1}{\tau} &= \frac{4\pi\gamma\rho}{3} \int_0^\infty dr r^2 w_D(r), \\ \langle \mathbf{F}^R \rangle &= 0, \\ \langle \mathbf{F}^R(t) \cdot \mathbf{F}^R(t') \rangle &= 4\pi\sigma^2\rho \int_0^\infty dr r^2 [w_R(r)] \delta(t - t'). \end{aligned} \quad (5.99)$$

We can solve the Langevin equation Eq. (5.96) straightforwardly to obtain the time correlation of velocity as

$$\langle \mathbf{v}_i(0) \cdot \mathbf{v}_i(t) \rangle = 3k_B T \exp(-t/\tau). \quad (5.100)$$

Thereafter, the diffusion coefficient is obtained as

$$D = \frac{1}{3} \int_0^\infty dt \langle \mathbf{v}_i(0) \cdot \mathbf{v}_i(t) \rangle = \tau k_B T. \quad (5.101)$$

According to the kinetic theory, the viscosity contribution due to the particle diffusion reads

$$\eta^K = \rho \langle \mathbf{v}^2 \rangle \tau / 3. \quad (5.102)$$

The total viscosity is simply the sum of  $\eta^D$  and  $\eta^K$ . Therefore, given Eqs. (5.95) and (5.102), one may estimate the input parameters to achieve a desired viscosity of a DPD system.

## 5.2.5 The Zwanzig Formalism for Coarse-Graining

We have applied the Mori formalism in Sect. 5.2.2 to get the linear GLE or the linearized hydrodynamic equations, where the correspondence between thermodynamic response and transport coefficients of the NS equations and DPD parameters are established. Here we introduce another projection adopted by Zwanzig [38, 43, 50, 61, 112, 113], from which a non-linear GLE is obtained. It can be shown that Zwanzig's approach is more general and in fact Mori's approach is an approximation to Zwanzig's near equilibrium [33].

We shall introduce the microdynamics described by a Hamiltonian, which has Gibbsian statistics. Furthermore, we derive two equivalent ways of projection. Firstly, we work on the relevant density adopted by Zwanzig [111]. Secondly, we work on the relevant variables directly [38].

## Microdynamics

Given  $N$  particles (atoms or molecules) of a Hamiltonian system, a phase space point is defined as  $\mathbf{Z}(t) = [Z_1(t), \dots, Z_{6N}(t)] = [\mathbf{r}_1(t), \dots, \mathbf{r}_N(t), \mathbf{p}_1(t), \dots, \mathbf{p}_N(t)]$  where  $\mathbf{r}_i$  and  $\mathbf{p}_i$  are the position and momentum of  $i$ th particle in three dimensions. The dynamics of  $N$  atoms is governed by Hamilton's equations of motion

$$\dot{\mathbf{r}}_i = \frac{\partial \mathcal{H}}{\partial \mathbf{p}_i}, \quad \dot{\mathbf{p}}_i = -\frac{\partial \mathcal{H}}{\partial \mathbf{r}_i}, \quad (5.103)$$

where  $\mathcal{H}$  is the Hamiltonian of the system defined as the sum of kinetic energy and potential energy of the particles

$$\mathcal{H}(\mathbf{r}_1, \dots, \mathbf{r}_N, \mathbf{p}_1, \dots, \mathbf{p}_N) = K(\mathbf{p}_1, \dots, \mathbf{p}_N) + V(\mathbf{r}_1, \dots, \mathbf{r}_N), \quad (5.104)$$

where  $K = \sum_i^N \frac{\mathbf{p}_i^2}{2m}$  with  $m$  as the particle mass, and  $V$  is yet to be specified. In particular, given the initial condition  $\mathbf{Z}(0) = \mathbf{z}$ , the evolution of dynamics for  $\mathbf{Z}(t)$  is determined.

Generally, we are not interested in  $\mathbf{Z}(t)$  *per se*, but in a set of  $M$  functions defined on the phase space  $\mathbf{A}(\mathbf{Z}(t)) \equiv [A_1(\mathbf{Z}(t)), \dots, A_M(\mathbf{Z}(t))] \equiv \mathbf{a}(t, \mathbf{z})$ , where  $\mathbf{a}$  is introduced to indicate the explicit dependence on initial condition  $\mathbf{z}$ . The evolution of dynamics of  $\mathbf{a}$  is

$$\frac{\partial \mathbf{a}(t, \mathbf{z})}{\partial t} = \mathcal{L}\mathbf{a}(t, \mathbf{z}), \quad (5.105)$$

in which  $\mathcal{L}$  is the Liouville operator defined in Sect. 5.2.2, and it was referred to as  $\mathcal{L}_C$  in the context of a dissipative system. Here we simply omit the subscript  $C$  without ambiguity. The formal solution to Eq. (5.105) is

$$\mathbf{a}(t, \mathbf{z}) = \exp\{t\mathcal{L}\}\mathbf{a}(0, \mathbf{z}) = \exp\{t\mathcal{L}\}\mathbf{A}(\mathbf{z}), \quad (5.106)$$

where the exponential operator is defined via its Taylor expansions. Inserting Eq. (5.106) into Eq. (5.105) we get

$$\frac{\partial \mathbf{a}(t, \mathbf{z})}{\partial t} = \mathcal{L}\mathbf{a}(t, \mathbf{z}) = \mathcal{L} \exp\{t\mathcal{L}\}\mathbf{A}(\mathbf{z}) = \exp\{t\mathcal{L}\}\mathcal{L}\mathbf{A}(\mathbf{z}), \quad (5.107)$$

where  $\mathcal{L}$  and  $\exp\{t\mathcal{L}\}$  commute.

We have also the Liouville equation for the PDF of particle microdynamics as

$$i \frac{\partial f(t)}{\partial t} = \mathcal{L}cf(t), \quad (5.108)$$

which has the formal solution as  $f(t) = \exp(-i\mathcal{L}t)$ . Note that the PDF here describes the microdynamics of a Hamiltonian system, in contrast to the PDF for the dissipative system of DPD particles in Sect. 5.2.1.

### The Zwanzig Formalism: Relevant Density

We introduce an operator  $\mathcal{P}$  [111], which is used to divide an ensemble density  $f(t)$  into a relevant part  $f_1(t) = \mathcal{P}f(t)$  and an irrelevant part  $f_2(t) = (1 - \mathcal{P})f(t)$ ,

$$f(t) = f_1(t) + f_2(t). \quad (5.109)$$

Here  $\mathcal{P}$  is a linear operator and time-independent so that  $\mathcal{P}$  and  $\partial/\partial t$  commute. Therefore, the Liouville's equation can be decomposed into a pair of equations

$$\begin{aligned} \mathcal{P}[i(\partial f/\partial t)] &= i(\partial f_1/\partial t) = \mathcal{P}L(f_1 + f_2), \\ (1 - \mathcal{P})[i(\partial f/\partial t)] &= i(\partial f_2/\partial t) = (1 - \mathcal{P})L(f_1 + f_2). \end{aligned} \quad (5.110)$$

The second equation is a first-order inhomogeneous equation and can be solved in terms of  $f_2(0)$  and  $f_1(t)$  in a straightforward manner [113] to obtain:

$$\begin{aligned} f_2(t) &= \exp[-it(1 - \mathcal{P})\mathcal{L}]f_2(0) \\ &\quad - i \int_0^t ds \exp[-is(1 - \mathcal{P})\mathcal{L}] (1 - \mathcal{P})\mathcal{L}f_1(t - s). \end{aligned} \quad (5.111)$$

Substitute  $f_2(t)$  into the first equation we get

$$\begin{aligned} i \frac{\partial f_1(t)}{\partial t} &= \mathcal{P}L f_1(t) \\ &\quad - i \int_0^t ds \mathcal{P}L \exp[-is(1 - \mathcal{P})\mathcal{L}] (1 - \mathcal{P})\mathcal{L}f_1(t - s) \\ &\quad + \mathcal{P}L \exp[-it(1 - \mathcal{P})\mathcal{L}]f_2(0), \end{aligned} \quad (5.112)$$

which is the evolution equation for the relevant density.

### The Zwanzig Formalism: Relevant Variable

More specifically, if we are interested in the statistical properties of  $A(\mathbf{a}(t, \mathbf{z})) \equiv A(\mathbf{Z}(t))$ , with initial condition  $\mathbf{Z}(0) = \mathbf{z}$  satisfying  $\mathbf{A}(\mathbf{z}) = \boldsymbol{\alpha}$ . That is, the

initial condition of  $\mathbf{z}$  is distributed according to the equilibrium density  $f^{eq}(\mathbf{z})$ , such as  $f^{eq}(\mathbf{z}) = \Omega_0^{-1} \delta(\mathcal{H}(\mathbf{z}) - E)$  in the microcanonical ensemble and  $\Omega_0$  is the normalization factor, and meanwhile  $f^{eq}(\mathbf{z})$  is conditional on the initial condition  $\mathbf{A}(\mathbf{z}) = \boldsymbol{\alpha}$ . Zwanzig's approach allows us to write an exact integro-differential equation with random coefficients and when the equation is solved with different realizations, the ensemble of  $\mathbf{A}(\mathbf{Z}(\mathbf{t}))$  is generated.

We introduce a conditional expectation operator  $\mathcal{P}_\alpha$ , whose action to an arbitrary phase-space function  $F(\mathbf{z})$  at  $\mathbf{A}(\mathbf{z}) = \boldsymbol{\alpha}$  gives the conditional equilibrium expectation of  $F(\mathbf{z})$  as [38]

$$\mathcal{P}_\alpha F(\mathbf{z}) = \frac{1}{\Omega(\boldsymbol{\alpha})} \int F(\mathbf{z}) f^{eq}(\mathbf{z}) \delta(\mathbf{A}(\mathbf{z}) - \boldsymbol{\alpha}) d\mathbf{z}, \quad (5.113)$$

where the probability density of  $\mathbf{A}(\mathbf{z})$  is defined as

$$\Omega(\boldsymbol{\alpha}) = \int f^{eq}(\mathbf{z}) \delta(\mathbf{A}(\mathbf{z}) - \boldsymbol{\alpha}) d\mathbf{z}. \quad (5.114)$$

Let  $\mathcal{Q}_{\mathbf{A}(\mathbf{z})} = 1 - \mathcal{P}_{\mathbf{A}(\mathbf{z})}$  and insert 1 into Eq. (5.107) we get

$$\frac{\partial \mathbf{a}(t, \mathbf{z})}{\partial t} = \exp\{t\mathcal{L}\} \mathcal{L} \mathbf{A}(\mathbf{z}) = \exp\{t\mathcal{L}\} \mathcal{P}_{\mathbf{A}(\mathbf{z})} \mathcal{L} \mathbf{A} + \exp\{t\mathcal{L}\} \mathcal{Q}_{\mathbf{A}(\mathbf{z})} \mathcal{L} \mathbf{A}. \quad (5.115)$$

Recall the Duhamel-Dyson identity as already applied in Sect. 5.2.2

$$\exp\{t\mathcal{L}\} = \exp\{t\mathcal{Q}_{\mathbf{A}(\mathbf{z})}\mathcal{L}\} + \int_0^t ds \exp\{(t-s)\mathcal{L}\} \mathcal{P}_{\mathbf{A}(\mathbf{z})} \mathcal{L} \exp\{s\mathcal{Q}_{\mathbf{A}(\mathbf{z})}\mathcal{L}\}, \quad (5.116)$$

which can be verified by differentiation [33, 113]. If we apply Eq. (5.116) to replace the second term in Eq. (5.115), we get

$$\frac{\partial \mathbf{a}(t, \mathbf{z})}{\partial t} = \exp\{t\mathcal{L}\} \mathcal{P}_{\mathbf{A}(\mathbf{z})} \mathcal{L} \mathbf{A} + \int_0^t ds \exp\{(t-s)\mathcal{L}\} \mathcal{P}_{\mathbf{A}(\mathbf{z})} \mathcal{L} \tilde{\mathbf{R}}(s, \cdot) + \tilde{\mathbf{R}}(t, \mathbf{z}), \quad (5.117)$$

with

$$\tilde{\mathbf{R}}(t, \mathbf{z}) = \exp\{t\mathcal{Q}_{\mathbf{A}(\mathbf{z})}\mathcal{L}\} \mathcal{L} \mathbf{A} = \mathcal{Q}_{\mathbf{A}} \exp\{t\mathcal{Q}_{\mathbf{A}(\mathbf{z})}\mathcal{L}\} \mathcal{L} \mathbf{A}. \quad (5.118)$$

Equation (5.117) is the evolution equation for relevant variables. Lei et al. [50] have applied it to derive a set of equations of motion for mesoscopic particles, each of which represents a cluster of constrained MD particles. The resultant equation of motion has the same form as DPD. Hijón et al. [38] and Li et al. [61] also applied the Mori-Zwanzig formalism to coarse-grain a system of homogeneous star polymer melts, where each DPD particle represents the center of mass of



individual star polymer. In the context of coarse-graining, the parameters such as  $a$ ,  $\gamma$  ( $\sigma$ ) and weighting functions  $w_C$ ,  $w_D$  ( $w_R$ ) for DPD depend on the properties of the underlying MD system at a specific state point performed. Typically, we have numerical values for DPD input parameters obtained from the MD values.

### 5.3 Extensions of Dissipative Particle Dynamics

The classical DPD model was initially proposed as a minimal working version for mesoscopic simulation of fluids. It only considers the momentum equation governing the evolution of flow field, which precludes the classical DPD method from modeling some specific problems, e.g., liquid-vapor coexistence in one-component multiphase fluid systems, heat flow in non-isothermal systems and diffusion-reaction process in biological systems. To this end, several extensions of the DPD method have been developed in recent years for tackling the challenges in diverse applications involving multiple physical fields (i.e., flow field, thermal field and concentration field), which are beyond the capability of classical DPD model.

In this section, we will introduce some of them, including the many-body DPD (mDPD) model for multiphase flows [85], the energy-conserving DPD (eDPD) model for non-isothermal systems [6, 23] and the transport DPD (tDPD) model for advection-diffusion-reaction processes [66], as shown by the ‘‘DPD Alphabet’’ in Fig. 5.2. The eDPD model is the first extension of DPD proposed by Avalos et al. [6]

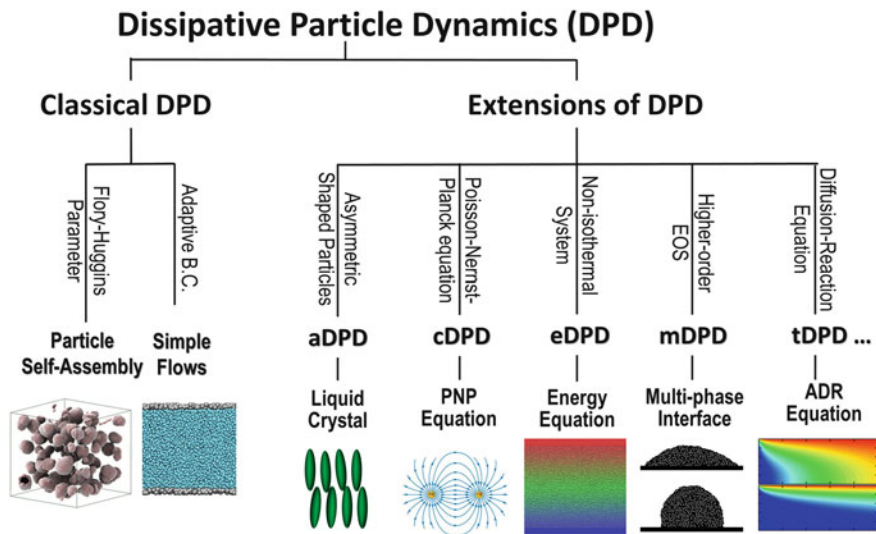


Fig. 5.2 State of the art of the DPD method (‘‘DPD Alphabet’’), in which the classical DPD model is widely used for studying hydrodynamics of isothermal fluid systems while various extensions of DPD have been developed for modeling different phenomena in multiphysics applications

and Español [23] independently in 1997, the mDPD model is another extension of DPD initialized by Pagonabarraga and Frenkel [85] in 2001 and subsequently specified by Warren [106] in 2003, and the tDPD model was developed by Li et al. [66] in 2015.

### 5.3.1 Energy-Conserving DPD (eDPD) for Non-Isothermal Systems

The dissipative force or force of friction between DPD particles reduces their velocity difference and thus dissipates the thermal kinetic energy of the system, while the random force generates a stochastic force on each DPD particle that inputs kinetic energy into the system. In the classical DPD model, the dissipative and random forces together satisfy the fluctuation-dissipation theorem and so act as a thermostat to maintain the system at a constant temperature [26]. The evolution equation for the macroscopic energy density in a DPD system does not have the form of a local conservation equation [77], but contains source and sink terms corresponding to the random and dissipative forces, respectively, and hence the total energy of the system is not conserved [6]. As a result, the classical DPD method is limited to isothermal systems and can neither sustain temperature gradients nor can it model heat transfer [23].

To extend the isothermal DPD equations to modeling heat transport in non-isothermal fluid systems, energy conservation is satisfied in DPD by introducing the internal energy as an additional property of the system [23, 96]. Therefore, an energy-conserving DPD model was developed and is known in the literature as eDPD [62, 95]. As in classical DPD, each eDPD particle is considered to be coarse-grained representation of a group of molecules rather than individual atoms. The time evolution of an eDPD particle  $i$  with mass  $m_i$  is governed by the conservation of momentum and energy, which is described by the following set of equations [23, 62]:

$$m_i \frac{d^2 \mathbf{r}_i}{dt^2} = m_i \frac{d\mathbf{v}_i}{dt} = \mathbf{F}_i = \sum_{i \neq j} (\mathbf{F}_{ij}^C + \mathbf{F}_{ij}^D + \mathbf{F}_{ij}^R), \quad (5.119a)$$

$$C_v \frac{dT_i}{dt} = q_i = \sum_{i \neq j} (q_{ij}^C + q_{ij}^V + q_{ij}^R), \quad (5.119b)$$

where  $t$ ,  $\mathbf{r}_i$ ,  $\mathbf{v}_i$  and  $\mathbf{F}_i$  denote time, and position, velocity, force vectors, respectively,  $T_i$  the temperature,  $C_v$  the thermal capacity of eDPD particles and  $q_i$  the heat flux between particles. The summation of forces is carried out over all other particles within a cutoff radius  $r_c$ , beyond which the forces are considered to be zero.

The three components of  $\mathbf{F}_i$ , including the conservative force  $\mathbf{F}_{ij}^C$ , dissipative force  $\mathbf{F}_{ij}^D$  and random forces  $\mathbf{F}_{ij}^R$ , are given by Eq. (5.2) [35]. For an eDPD system

in local thermodynamic equilibrium, a Fokker-Planck equation, mathematically identical to the stochastic equations of Eqs. (5.119a) and (5.119b), can now be derived [23]. The solution of the FPE gives the relationship between the dissipative force and random force, which requires  $\sigma_{ij}^2 = 4\gamma_{ij}k_B T_i T_j / (T_i + T_j)$  and  $w_D(r) = w_R^2(r)$ . The key aspect of eDPD is that the temperature  $T_i$  is defined on each particle, and the fluctuation-dissipation theorem is applied locally based on the particle temperature  $T_i$  rather than the thermodynamic temperature of the system. As a result, eDPD allows temperature gradients and can be used in non-isothermal problems, where thermal transport plays a critical role.

The heat fluxes between particles accounting for the thermal conduction  $q^C$ , viscous heating  $q^V$ , and random heat flux  $q^R$  are given by Qiao and He [95] and Li et al. [62]:

$$\begin{aligned} q_i^C &= \sum_{j \neq i} k_{ij} w_{CT}(r_{ij}) (T_i^{-1} - T_j^{-1}), \\ q_i^V &= \frac{1}{2C_v} \sum_{j \neq i} \left\{ w_D(r_{ij}) \left[ \gamma_{ij} (\mathbf{e}_{ij} \mathbf{v}_{ij})^2 - \sigma_{ij}^2 / m_i \right] - \sigma_{ij} w_R(r_{ij}) \mathbf{e}_{ij} \mathbf{v}_{ij} \zeta_{ij} \right\}, \\ q_i^R &= \sum_{j \neq i} \beta_{ij} w_{RT}(r_{ij}) \xi_{ij}^e, \end{aligned} \quad (5.120)$$

where the expression of thermal conduction  $q^C$  contains  $T^{-1}$  rather than  $T$  because the thermodynamic quantity conjugated to the internal energy is the inverse of the temperature rather than the temperature itself [35]. The parameters  $k_{ij}$  and  $\beta_{ij}$  determine the strength of the thermal conduction and the random heat flux, respectively. In particular,  $k_{ij}$  plays the role of a thermal conductivity given as  $k_{ij} = C_v^2 \kappa (T_i + T_j)^2 / 4k_B$  in which  $\kappa$  is interpreted as a mesoscale heat friction coefficient [95, 96], and  $\beta_{ij}^2 = 2k_B k_{ij}$ . The weight functions  $w_{CT}(r)$  and  $w_{RT}(r)$  in Eq. (5.120) are given as  $w_{CT}(r) = w_{RT}^2(r) = (1 - r/r_{ct})^{s_T}$  in which  $s_T$  is the exponent of the weight functions and  $r_{ct}$  is a cutoff radius for heat fluxes. The case of  $s_T = 2.0$  corresponds to the typical quadratic weighting function [35].

For an eDPD particle, the characteristic scale of the kinetic energy related to its momentum is  $k_B T$ , while the characteristic scale of the internal energy related to its temperature is  $C_v T$ . To convert the kinetic energy into the internal energy, we need a scaling factor  $k_B T / C_v T$ . Therefore, the viscous heating  $q_i^V$  given by Eq. (5.120) has a factor  $1/C_v$  when the kinetic energy  $k_B T$  has been rescaled into the unit. Also, the factor 2 in the denominator means that the heat generated by non-conservative interactions is distributed evenly to both particles of a pair. By performing practical eDPD simulations, Li et al. [62] verified the energy conservation of the eDPD system.

The transport properties including diffusivity and viscosity of the eDPD fluid are output properties instead of input parameters. Groot and Warren [35] and Marsh et al. [77] have investigated the expressions of the diffusivity and the viscosity

in terms of DPD parameters. With the interaction between particles described by Eq. (5.2), they are given by Groot and Warren [35] and Marsh et al. [77]

$$\begin{aligned} D &= k_B T \left( \frac{4\pi\gamma\rho}{3} \int_0^\infty r^2 g(r) w_D(r) dr \right)^{-1}, \\ \nu &= \frac{D}{2} + \frac{2\pi\gamma\rho}{15} \int_0^\infty r^4 g(r) w_D(r) dr, \end{aligned} \quad (5.121)$$

where  $g(r)$  is the radial distribution function of DPD particles. A rough analytical prediction of the diffusivity and the kinematic viscosity can be obtained by assuming  $g(r) = 1.0$  corresponding to ideal gases [35]. Substituting  $w_D(r) = w_R^2(r) = (1 - r/r_c)^s$  into Eq. (5.121), the diffusivity and kinematic viscosity of the eDPD fluid can be approximated by:

$$\begin{aligned} D &= \frac{3k_B T (s+1)(s+2)(s+3)}{8\pi\gamma\rho r_c^3}, \\ \nu &= \frac{3k_B T (s+1)(s+2)(s+3)}{16\pi\gamma\rho r_c^3} + \frac{16\pi\gamma\rho r_c^5}{5(s+1)(s+2)(s+3)(s+4)(s+5)}. \end{aligned} \quad (5.122)$$

Equation (5.122) indicates that both the diffusivity  $D$  and the kinematic viscosity  $\nu$  of the eDPD fluid increase with the increase of temperature when other variables in Eq. (5.122) are kept constant. However, for most of the simple liquids such as water, ethanol and glycerin, the diffusivity increases but the kinematic viscosity decreases with increasing temperature. In order to simulate the flow dynamics of such liquids, at least one of the parameters  $\rho$ ,  $r_c$ ,  $\gamma$  and  $s$  should be function of temperature so that the eDPD model can reproduce the correct dynamic behavior of non-isothermal fluid systems. After studying the sensitivity of  $D$  and  $\nu$ , the exponent of the weighting function  $s$  is defined as a function of temperature for modeling the temperature-dependent diffusion and viscosity of eDPD fluids. For details on choosing the function for  $s$ , readers are referred to [52, 62].

In addition, if the variation of fluid density with temperature is also considered, a temperature-dependent conservative coefficient  $a(T)$  is required to capture the effect of temperature on the fluid density. More specifically, let both the fluid density  $\rho(T)$  and compressibility  $\kappa_c^{-1}(T)$  be functions of temperature obtainable from experimental data. The temperature-dependent conservative coefficient is determined by  $a(T) = k_B T (\kappa_c^{-1}(T) - 1) / 2\alpha\rho(T)$  in which  $\alpha = 0.101 \pm 0.001$ . For example, the density of a DPD fluid with constant  $a$  is invariant with respect to temperature, while  $a(T) = 75k_B T / \rho$  yield a linear dependence of density on temperature [62].

Similar to the diffusivity and the kinematic viscosity, the thermal conductivity is also an output property. For an eDPD system whose transport of energy is dominated by the dissipative interactions of Eq. (5.120), the macroscopic thermal conductivity

$\lambda$  can be calculated by Mackie et al. [74]:

$$\lambda = \frac{2\pi}{3} \frac{\rho^2}{T^2} \int_0^{r_c} r^4 k w_{CT}(r) g(r) dr, \quad (5.123)$$

where  $k = C_v^2 \kappa T^2 / k_B$  and  $w_{CT}(r)$  the weight function used in Eq. (5.120). Given  $w_{CT}(r) = (1 - r/r_c)^{s_T}$  an analytical estimate for the thermal conductivity  $\lambda$  can be obtained by assuming the radial pair distribution function  $g(r) = 1.0$  corresponding to ideal gases, and it is given as:

$$\lambda = \frac{16\pi\rho^2\kappa C_v^2 r_c^5}{k_B(s_T + 1)(s_T + 2)(s_T + 3)(s_T + 4)(s_T + 5)}. \quad (5.124)$$

In particular, when the typical quadratic weight function  $(1 - r/r_c)^2$  is employed for  $w_{CT}(r)$  with  $s_T = 2.0$ , then Eq. (5.124) becomes

$$\lambda = \frac{2\pi\rho^2}{315k_B} \kappa C_v^2 r_c^5. \quad (5.125)$$

The definition of the Prandtl number is  $\text{Pr} = \rho\nu C_v / \lambda$ , which is a temperature-dependent dimensionless number and its value can be obtained from available experimental data. After replacing  $\lambda$  by  $\text{Pr}$  in Eq. (5.125), we have a formula for determining the mesoscale heat friction  $\kappa$  for the eDPD system given by:

$$\kappa = \frac{315k_B\nu}{2\pi\rho C_v r_c^5} \frac{1}{\text{Pr}}, \quad (5.126)$$

where  $\nu$  is the kinematic viscosity which can be roughly approximated by Eq. (5.121) or given by the computed kinematic viscosity. The expression of Eq. (5.126) is obtained from the typical quadratic weight function  $w_{CT}(r) = (1 - r/r_c)^2$  and a similar formula can be derived from Eq. (5.123) when a different weight function is employed.

By including the energy equation in the DPD framework, the eDPD method has been successfully used in diverse applications involving thermal fields. For example, Li et al. [62] considered the coupling of the flow and the thermal fields, where an eDPD simulation of a Poiseuille flow confined between a hot wall and a cold wall was performed. Since the hotter fluid is less viscous than the colder fluid, the variation of the viscosity perpendicular to the flow direction leads to an asymmetric velocity profile. As a result, the peak of the velocity profile shifts to the hotter side, as shown in Fig. 5.3a. Li et al. [65] also applied the eDPD method to modeling of thermoresponsive polymers. Because of the energy conservation in eDPD, they demonstrated that eDPD simulations are able to correctly capture not only the transient behavior of polymer precipitation from solvent induced by temperature changes, as shown in Fig. 5.3b, but also the energy variation associated with the phase transition process. Moreover, natural convection in microchannels [1]

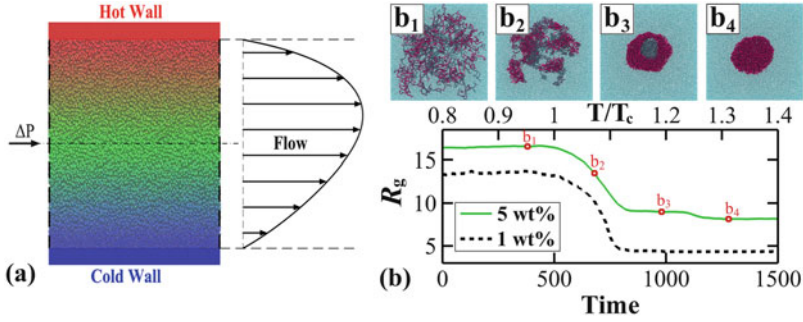


**Fig. 5.3** (a) An eDPD simulation [62] of the Poiseuille flow combined with the heat conduction between a cold wall  $T_C$  and a hot wall  $T_H$ . (b) eDPD modeling of thermoresponsive microgels [65]. Lines show the evolution of gyration radius  $R_g$  and (b1–b4) show cross sections of their transient microstructure corresponding to the changes of  $R_g$  during heating. Images (b) is adapted with permissions from [65]

and in eccentric annulus [15], thermal conduction of nanofluids [95] and doubly thermoresponsive self-assemblies [102], to name but a few, have been also studied using eDPD simulations.

### 5.3.2 Many-Body DPD (mDPD) for Multiphase Flows

The conservative force between particles  $i$  and  $j$  is given as  $\mathbf{F}_{ij}^C = aw_c(r_{ij})\mathbf{e}_{ij}$  in the classical DPD model, where  $a$  is a repulsive force parameter and  $w_c(r_{ij})$  is a soft and unspecific weight function. A common choice of the weight function is  $w_c(r_{ij}) = 1 - r_{ij}/r_c$  for  $r_{ij} \leq r_c$  and vanishes beyond the cutoff radius  $r_c$ . For a single-component DPD fluid with a purely repulsive conservative force, the equation of state (EOS) of the system can be computed by Groot and Warren [35]

$$\begin{aligned}
 p &= \rho k_B T + \frac{1}{3V} \left\langle \sum_{j>i} (\mathbf{r}_i - \mathbf{r}_j) \cdot \mathbf{F}_{ij}^C \right\rangle \\
 &= \rho k_B T + a\rho^2 \cdot \frac{2\pi}{3} \int_0^\infty w_c(r)g(r)r^3 dr,
 \end{aligned} \tag{5.127}$$

where  $g(r)$  is the RDF, and  $\rho$  is the number density of DPD particles. The first term in the EOS is an ideal gas term, and the second term is the excess pressure. In the mean-field theory, Eq. (5.127) can be simplified by employing the RDF of the idea gas  $g(r) = 1$ ,

$$p = \rho k_B T + \alpha_{MF} a \rho^2, \tag{5.128}$$

where  $\alpha_{\text{MF}} = \frac{2\pi}{3} \int_0^\infty w_c(r) r^3 dr$ . Given a weighting function  $w_c(r) = 1 - r/r_c$  with a cutoff radius  $r_c = 1$ , we arrive at  $\alpha_{\text{MF}} = \pi/30$ . The realistic EOS of a DPD fluid can be computed by performing a series of DPD simulations at various densities. The computed EOS of DPD fluids is in the form of  $p \approx \rho k_B T + \alpha a \rho^2$  with a coefficient  $\alpha = 0.101 \pm 0.001$  very close to the mean-field prediction  $\alpha_{\text{MF}} = \pi/30 = 0.1047$ , which is perfectly quadratic in the density [35]. This monotonic function of EOS does not have a van der Waals loop and excludes the possibility of modeling phenomena involving vapor-liquid coexistence and free-surfaces of single-component fluids. To this end, Pagonabarraga and Frenkel [85] defined the free energy  $\psi$  of an inhomogeneous system with density  $\rho(\mathbf{r})$  as  $\psi = \int \rho(\mathbf{r}) \varphi(\rho(\mathbf{r})) d\mathbf{r}$ , where  $\varphi(\rho)$  is the local free energy per particle associated to the local configuration of particles rather than a mechanical potential energy. If the free energy determines the relevant energy for a given configuration of DPD particles, then the force acting on each particle can be derived as the variation of such energy when the corresponding particle is displaced. However, the ideal contribution to the free energy of the system has already been accounted for by the dissipative and random forces. Therefore, only the excess free energy is involved in the conservative interaction between DPD particles. Let  $\psi_{\text{ex}}(\rho)$  be the excess component of the total free energy  $\psi(\rho)$ , the conservative force acting on a particle  $i$  is written as  $\mathbf{F}_i = -\frac{\partial}{\partial \mathbf{r}_i} \sum_j \psi_{\text{ex}}(\rho_j) = \sum_j \mathbf{F}_{ij}$ . Then, the conservative force between a pair of particles  $i$  and  $j$  depends not only on their relative positions, but also on their local densities. This defines the many-body DPD (mDPD) model [106].

Let  $\phi(\rho)$  be an unspecified function of density, the density-dependent conservative force is written as,

$$\mathbf{F}_{ij}^{\text{C}} = \frac{1}{2} [\phi(\rho_i) + \phi(\rho_j)] w_c(r_{ij}) \mathbf{e}_{ij}, \quad (5.129)$$

for a one-component fluid. The local density  $\rho_i$  of a particle  $i$  is taken to be the instantaneously weighted average  $\rho_i = \sum_{i \neq j} w_\rho(r_{ij})$  with a weight function  $w_\rho(r_{ij}) = 15(1 - r_{ij}/r_c)^2 / (2\pi r_c^3)$ , which is normalized so that  $\int_0^\infty d^3 \mathbf{r} w_\rho(r) = 1$ . It is obvious that if  $\phi(\rho) \equiv a$ , the method with Eq. (5.129) reduces exactly to the classical DPD model. By the mean-field theory, the modified force law of Eq. (5.129) should give an EOS

$$p_{\text{MF}} = \rho k_B T + \alpha_{\text{MF}} \phi(\rho) \rho^2, \quad (5.130)$$

where  $\alpha_{\text{MF}} = \pi/30$  for the standard choice of  $w_c(r)$ . Since  $\phi(\rho)$  is an unspecified function of density, in principle, an arbitrary dependence of EOS on density can be recovered. However, having a van der Waals loop in the EOS is not sufficient to stabilize the vapor-liquid interface. Pagonabarraga and Frenkel [85] discussed that a simple many-body DPD model with a single interaction range may not yield a stable interface. To simulate the vapor-liquid coexistence with mDPD, one must also give consideration to the ranges of interactions. In the approach developed by Warren [106], the density-dependent conservative force is introduced empirically

with a different cut-off radius  $r_d$ , and can be written as,

$$\mathbf{F}_{ij}^C = Aw_c(r_{ij})\mathbf{e}_{ij} + B(\rho_i + \rho_j)w_d(r_{ij})\mathbf{e}_{ij}, \tag{5.131}$$

where the first term with a negative coefficient  $A < 0$  stands for an attractive force within an interaction range  $r_c$ , and the second term with  $B > 0$  is the density-dependent repulsive force within an interaction range  $r_d$ . Then, the mean-field EOS is

$$p_{\text{MF}} = \rho k_B T + \alpha_{\text{MF}}(A\rho^2 + 2Br_d^4\rho^3). \tag{5.132}$$

Thus, given  $A < 0$  and  $B > 0$ , this EOS has the potential to contain a van der Waals loop for modeling vapor-liquid coexistence.

Using numerical experiments, Warren [106] explored a wider parameter space for the mDPD model with the conservative force given by Eq. (5.131). By defining a function  $\Phi = (p - \rho k_B T - \alpha A \rho^2 - 2\alpha B r_d^4 \rho^3) / B r_d^4$ , the data of the mDPD fluids collapse onto a straight line, as shown in Fig. 5.4a. The computed EOS can be fitted by

$$p = \rho k_B T + \alpha A \rho^2 + 2\alpha B r_d^4 (\rho^3 - c\rho^2 + d), \tag{5.133}$$

where  $\alpha = 0.101 \pm 0.001$ ,  $c = 4.16 \pm 0.02$ , and  $d = 18 \pm 1$ . Let  $\rho_V$  and  $\rho_L$  be vapor and liquid coexistence densities, respectively, then a phase separation can be observed in a range of densities  $\rho_V < \rho < \rho_L$ . In principle, integration of the EOS gives the free-energy density from which predictions can be made about  $\rho_V$  and

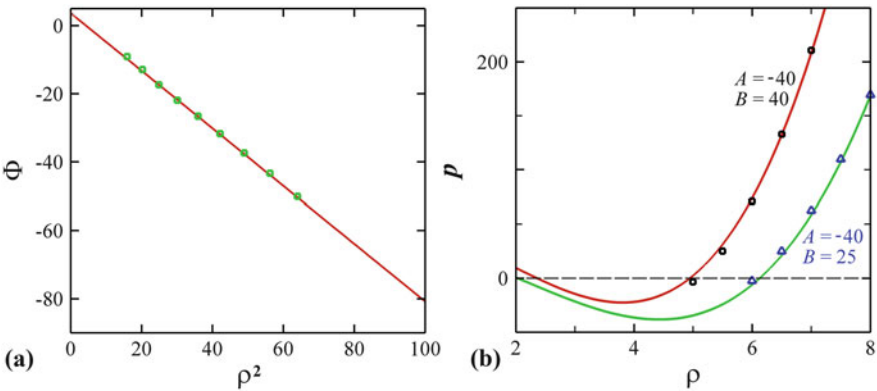


**Fig. 5.4** (a) Data collapse of pressure against density for  $\rho_L < \rho \leq 8, A = -40 \sim -20, B = 25$  or  $40, k_B T = r_c = 1, r_d = 0.75$ . The ordinate is the function  $\Phi = (p - \rho k_B T - \alpha A \rho^2 - 2\alpha B r_d^4 \rho^3) / B r_d^4$ . The straight line is a fit to data given by Eq. (5.133). (b) Pressure as a function of density for the two selected parameter sets  $A = -40, B = 40$  or  $25, r_d = 0.75, k_B T = r_c = 1.0$ . The lines are the predictions of the fitted EOS in the form of Eq. (5.133). Data are from [106]



$\rho_L$ . Unfortunately, the EOS must deviate from the above fitted form of Eq. (5.133) for  $\rho \ll 1$ . Therefore, the vapor phase is inadequately characterized. If the case  $\rho_L \geq 1$  in coexistence with a very dilute vapor is of practical interest, it would be easier to use the EOS to predict the point where the pressure vanishes as an estimate of the coexisting liquid phase density, i.e.,  $p(\rho_L) = 0$ . Using this, the numerical experiments performed by Warren [106] obtained the liquid densities of the order  $\rho_L \sim 5$  for  $-A \sim B \sim 30$ . Figure 5.4b plots the computed EOS of two DPD fluids with parameters  $A = -40, B = 40$  or  $25, r_d = 0.75, k_B T = r_c = 1.0$ . The two parameter sets are distinguished by the different values of the liquid densities, i.e.,  $\rho_L = 5.08 \pm 0.01$  for  $B = 40$  and  $\rho_L = 6.05 \pm 0.01$  for  $B = 25$ , as indicated in Fig. 5.4b by  $p(\rho_L) = 0$ . The coexisting vapor density  $\rho_L \ll 1$ , so these parameters are suitable for free-surface simulations.

Ever since its inception, the mDPD model has been applied to simulations of various wetting phenomena and multiphase flows. For example, Arienti et al. [5] investigated the performance of the mDPD model at vapor/liquid and liquid/solid interfaces and simulated the dynamics of droplets entering an inverted Y-shaped fracture junction, as shown in Fig. 5.5a. Li et al. [60] performed mDPD simulations of the manipulation of a liquid droplet on solid surfaces driven by a linear gradient of wettability. They explored the internal three-dimensional velocity field with transverse flow in a moving droplet, as shown in Fig. 5.5b. Li et al. [58] also studied droplet oscillations in AC electrowetting using mDPD simulations. Wang and Chen [105] used mDPD to simulate droplets sliding across micropillars and investigated how the pillars with different intrinsic wettability influence the movement of droplets, as shown in Fig. 5.5c, which describes the evolution of the advancing and receding contact angle with time as well as five snapshots of the droplet sliding across multiple micropillars.

The essential concept of the mDPD model is to construct a density-dependent conservative force, which yields EOS with a van der Waals loop for modeling vapor-liquid coexistence. In the strategy proposed by Warren, an empirical expression of the conservative force is first introduced, and then the mDPD model is calibrated to determine the true EOS and thermodynamic properties of the mDPD fluid. Alternatively, following the original formulations of mDPD proposed by Pagonabarraga and Frenkel [85], Tiwari and Abraham [103] used an opposite strategy to construct the conservative force for the mDPD model. They started from a van der Waals equation of state and formulated the conservative force in the context of the mean-field theory.

Using the mean-field approximation for intermolecular attraction, the free energy per particle is given by

$$\psi = \int_{r>\sigma} u_{\text{att}}(r)\rho(\mathbf{r})d\mathbf{r}, \quad (5.134)$$

where  $u_{\text{att}}(r)$  is the attractive component of the interaction potential,  $r$  the separation distance of particles and  $\sigma$  the diameter of particles for excluded volume. Expanding  $\rho(\mathbf{r})$  in Eq. (5.134) about  $\mathbf{r}$  and assuming that the gradient of  $\rho$  is small, only the even

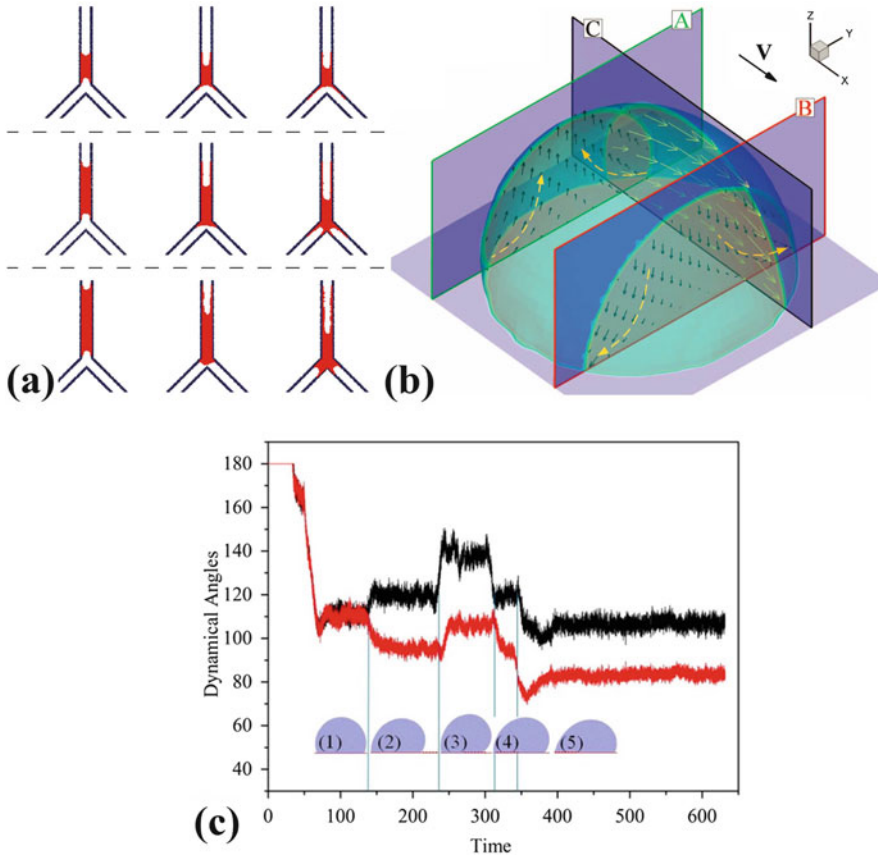


**Fig. 5.5** (a) mDPD simulations of droplets with different sizes entering an inverted Y-shaped fracture junction. (b) Three-dimensional velocity field inside a moving droplet, where the vector  $\mathbf{V}$  denotes the direction of movement. (c) Advancing and receding contact angle evolution versus time for a droplet sliding over pillars. Images (a), (b) and (c) are adapted with permissions from [5, 60, 105]

derivatives of density survive and the leading two terms are

$$\psi = -\mu\rho - \kappa\nabla^2\rho, \tag{5.135}$$

in which  $\mu = -\int_{r>\sigma} u_{\text{att}}(r)d\mathbf{r}$  and  $\kappa = -\frac{1}{6}\int_{r>\sigma} r^2u_{\text{att}}(r)d\mathbf{r}$ . The parameters  $\mu$  and  $\kappa$  arise due to the long-range attractive forces and give rise to the weak attraction and surface tension, respectively, between the mDPD particles at the coarse-grained level. Then, the form of the conservative force  $\mathbf{F}^C$ , which gives rise to phase segregation and surface tension in a liquid-vapor system, is given by

$$\mathbf{F}^C = -\nabla\psi_{\text{ex}} + \mathbf{F}^S, \tag{5.136}$$

with  $\psi_{\text{ex}}$  being the excess part of the free energy  $\psi$ .  $\mathbf{F}^S = \kappa \nabla \nabla^2 \rho$  represents the surface tension component that comes from the second term in Eq. (5.135). Here, only the contribution from the excess part is considered in the conservative force because the ideal part has already been considered through the random and dissipative forces. If the EOS of the mDPD fluids is described by the van der Waals equation of state, then

$$p = \frac{\rho k_B T}{1 - b\rho} - a\rho^2, \quad (5.137)$$

where  $a$  and  $b$  are the parameters for the EOS. More specifically, the parameter  $a$  accounts for the long-range attractive behavior, while the parameter  $b$  is responsible for excluded volume effects. Then, the free energy  $\psi$  of particles can be derived from Eq. (5.137) by  $p = -\partial\psi/\partial v$  where  $p$  is the pressure and  $v = \rho^{-1}$  the specific volume,

$$\psi = \psi_{\text{ex}} + k_B T \ln \rho = -k_B T \ln(1 - b\rho) - a\rho + k_B T \ln \rho, \quad (5.138)$$

where the first term is responsible for repulsion between the particles, the second term originates from the attractive part of interaction potential, and the last term is the ideal gas part. Substituting the excess free energy  $\psi_{\text{ex}}$  into Eq. (5.136), we obtain

$$\mathbf{F}^C = -\nabla [k_B T \ln(1 - b\rho) + a\rho] + \kappa \nabla \nabla^2 \rho. \quad (5.139)$$

It is clear that the conservative force in the form of Eq. (5.139) is also density-dependent. For mDPD system consisting of discrete particles, the density in the vicinity of a particle  $i$  is computed as a weighted average of contributions from its neighbors, i.e.,  $\rho_i = \sum_j w_\rho(r_{ij})$ , where the weighting function  $w_\rho(r_{ij})$  can be the widely used smoothing kernels in the smoothed particle hydrodynamics (SPH) method [79]. For example, the Lucy kernel reads

$$w_\rho(r, r_c) = \begin{cases} \frac{105}{16\pi r_c^3} \left(1 + \frac{3r}{r_c}\right) \left(1 - \frac{r}{r_c}\right)^3, & r \leq r_c \\ 0, & r > r_c \end{cases} \quad (5.140)$$

Let  $w_\rho^{(1)}(r)$  and  $w_\rho^{(3)}(r)$  be the first and third derivatives of the weight function of Eq. (5.140) with respect to the particle separation  $r$ . Then, the conservative force for a pair of particles  $i$  and  $j$  takes the final form

$$\mathbf{F}_{ij}^C = \left\{ -\left( \frac{bk_B T}{1 - b\rho_i} + \frac{bk_B T}{1 - b\rho_j} - 2a \right) w_\rho^{(1)}(r_{ij}) + \kappa w_\rho^{(3)}(r_{ij}) \right\} \mathbf{e}_{ij}. \quad (5.141)$$

With parameters  $a = 3.012 \times 10^{-3}$ ,  $b = 2.5 \times 10^{-2}$ ,  $k_B T = 2.1 \times 10^{-2}$  and  $r_c = 1.11$  in DPD units, Tiwari and Abraham [103] successfully validated the mDPD model with the two-dimensional Young–Laplace equation  $\Delta p = p_{\text{in}} - p_{\text{out}} = \sigma_{\text{lv}}/R$  where

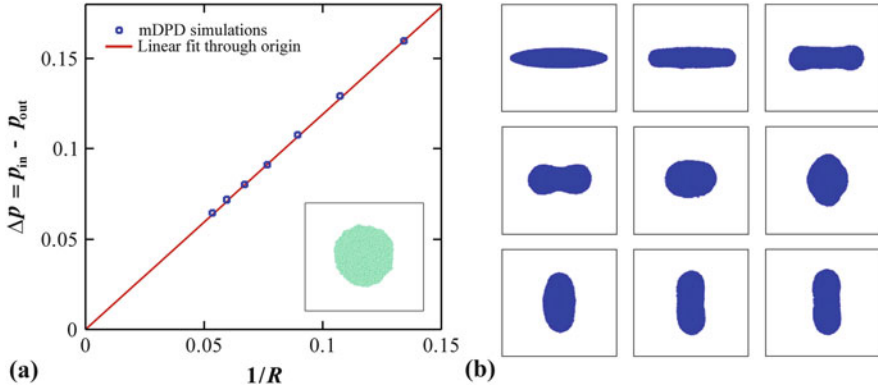


**Fig. 5.6** (a) Validation of the mDPD model with the two-dimensional Young–Laplace equation  $\Delta p = p_{in} - p_{out} = \sigma_{lv}/R$ . The *inset* shows the setup of mDPD simulations for a two-dimensional droplet in a periodic box. (b) Snapshots of large-amplitude oscillations of liquid cylinder with an initial aspect ratio of 5. (a) and (b) are adapted with permission from [103]

$\sigma_{lv}$  is the liquid–vapor interfacial tension and  $R$  the equilibrium radius of the droplet, as shown in Fig. 5.6a, and simulated large-amplitude oscillations of liquid cylinders, as shown in Fig. 5.6b.

Surface tension is one of the most important fluid properties relevant to the liquid–vapor coexistence. Although the magnitude of surface tension is determined by the interactions between mDPD particles, it is an output property of the mDPD system rather than an input parameter. The exact value of the surface tension needs to be computed from mDPD simulations. Several methods can be applied to compute the surface tension of a mDPD fluid. The first one is to compute the pressure difference between the inside and the outside of a droplet for various radii. According to the Young–Laplace equation, i.e.,  $\Delta p = p_{in} - p_{out} = 2\sigma_{lv}/R$  for three-dimensional droplets, the surface tension  $\sigma_{lv}$  is determined by the slope of the line  $\Delta p \sim R^{-1}$ , as shown in Fig. 5.6a. The second one is the pendant drop method, which is also widely used in experimental tensiometers. To set up the pendant droplet in mDPD simulations, a vertical cylindrical column of fluid at a density close to the equilibrium liquid density is equilibrated. A “support” needs to be constructed by “freezing” particles at the top of the column as a solid wall. By applying a gravitational body force onto each mDPD particle, the liquid forms a pendant droplet after the system reaches equilibrium. Then, a numerical fit of the theoretical drop shape to the shape obtained by mDPD simulations eventually yields the surface tension [106]. The third method is the easiest one that only needs a thin liquid film in a periodic computational box. The surface tension is computed from the standard mechanical definition of the pressure tensor using the Irving–Kirkwood

expression,

$$\sigma_{lv} = \int \left[ p_{zz} - \frac{1}{2}(p_{xx} + p_{yy}) \right] dz, \quad (5.142)$$

where  $p_{xx}$ ,  $p_{yy}$  and  $p_{zz}$  are the three diagonal components of the pressure tensor, with  $x$  and  $y$  parallel to the planar interface and  $z$  normal to it. More practically, let  $\Lambda$  be the surface area of the planar surface of the liquid film, then the surface tension is computed by

$$\sigma_{lv} = \left\langle \frac{1}{2\Lambda} \sum_{i \neq j} \left[ \mathbf{r}_{ij,x} \mathbf{F}_{ij,x} - \frac{1}{2}(\mathbf{r}_{ij,y} \mathbf{F}_{ij,y} + \mathbf{r}_{ij,z} \mathbf{F}_{ij,z}) \right] \right\rangle, \quad (5.143)$$

where the factor 2 in the denominator accounts for the fact that the liquid film has two interfaces,  $\mathbf{r}_{ij,\beta}$  and  $\mathbf{F}_{ij,\beta}$  are the  $\beta$ -component ( $\beta$  is  $x, y$  or  $z$ ) of  $\mathbf{r}_{ij}$  and  $\mathbf{F}_{ij}$ , respectively.

In the last decade, the mDPD model proposed by Warren [106] has been more widely used in diverse applications than Tiwari's mDPD model [103]. The reason may lie in the convenience of Warren's approach in modeling solid-liquid interfacial tensions. More specifically, Warren employed empirical expressions of the conservative force in Eq. (5.131), where the coefficients  $A$  and  $B$  can be defined as species-dependent parameters. For instance, let  $A_{ll}$  and  $B_{ll}$  be the coefficients for liquid-liquid interaction while  $A_{sl}$  and  $B_{sl}$  for solid-liquid interaction, the solid-liquid interfacial tension can be easily changed just by varying  $A_{sl}$  and  $B_{sl}$ , which generates various wetting phenomena of droplets on solid substrates. However, Tiwari's mDPD model starts from the van der Waals equation of state, which does not easily model solid-liquid interfaces. Moreover, the van der Waals model describes vapor-liquid equilibrium over very limited ranges of temperature. The famous loops provide only a qualitative representation of the two-phase boundary in PVT space. Therefore, Warren's approach has been successfully applied to various wetting problems involving solid-liquid interfacial tensions, while Tiwari's approach has been only applied to fluids in periodic boxes.

### 5.3.3 Transport DPD (tDPD) for Advection-Diffusion-Reaction

The classical DPD system has only equations governing the evolution of density and velocity fields but no evolution equations for describing the concentration field, which precludes the classical DPD method from modeling diffusion-reaction processes, i.e., two of the most fundamental processes in biological systems [21]. More specifically, proteins in an aqueous solution diffuse in a living cell due to Brownian motion, and some collisions of appropriate proteins may lead to chemical reactions. Moreover, most biological functions depend highly on the concentrations

of specific proteins, ions or other biochemical factors [4], whose transports at the cellular and subcellular levels are crucial to corresponding biological processes in living systems. Therefore, it is important to include the advection-diffusion-reaction (ADR) equation in the DPD model when diffusion and reactions are involved. To this end, Li et al. [66] developed a transport dissipative particle dynamics model named tDPD for mesoscopic problems involving ADR processes.

Similar to classical DPD method, in tDPD each particle is associated with extra variables for carrying concentrations in addition to other quantities such as position and momentum. The transport of concentration is modeled by a Fickian flux and a random flux between tDPD particles. More specifically, the time evolution of a tDPD particle  $i$  with unit mass  $m_i \equiv 1$  is governed by the conservation of momentum and concentration, which is described by the following set of equations

$$\begin{aligned} \frac{d^2 \mathbf{r}_i}{dt^2} &= \frac{d\mathbf{v}_i}{dt} = \mathbf{F}_i = \sum_{i \neq j} (\mathbf{F}_{ij}^C + \mathbf{F}_{ij}^D + \mathbf{F}_{ij}^R) + \mathbf{F}_i^{ext}, \\ \frac{dC_i}{dt} &= Q_i = \sum_{i \neq j} (Q_{ij}^D + Q_{ij}^R) + Q_i^S, \end{aligned} \quad (5.144)$$

where  $t$ ,  $\mathbf{r}_i$ ,  $\mathbf{v}_i$  and  $\mathbf{F}_i$  denote time, and position, velocity, force vectors, respectively.  $\mathbf{F}_i^{ext}$  is the force on particle  $i$  from an external force field. Just as in the standard DPD model, the pairwise interaction between tDPD particles  $i$  and  $j$  consists of the conservative force  $\mathbf{F}_{ij}^C = a_{ij}w_C(r_{ij})\mathbf{e}_{ij}$ , dissipative force  $\mathbf{F}_{ij}^D = -\gamma_{ij}w_D(r_{ij})(\mathbf{e}_{ij} \cdot \mathbf{v}_{ij})\mathbf{e}_{ij}$  and random force  $\mathbf{F}_{ij}^R = \sigma_{ij}w_R(r_{ij})\xi_{ij}\mathbf{e}_{ij}$ .  $C_i$  represents the concentration of one species defined as the number of a chemical species carried by a tDPD particle  $i$  and  $Q_i$  the corresponding concentration flux. The total concentration flux on a particle  $i$  accounts for the Fickian flux  $Q_{ij}^D$ , the random flux  $Q_{ij}^R$  and a source term  $Q_{ij}^S$  due to chemical reactions. Since tDPD particles have unit mass, this definition of concentration is equivalent to the concentration in terms of chemical species per unit mass. Then, the volume concentration, i.e. chemical species per unit volume, is  $\rho C_i$  where  $\rho$  is the number density of tDPD particles. We note that  $C_i$  can be a vector  $\mathbf{C}_i$  containing  $N$  components i.e.  $\{C_1, C_2, \dots, C_N\}_i$  when  $N$  chemical species are considered.

The driving force for diffusion of each species is the gradient of chemical potential  $Q = -DC\nabla\mu/RT$  in which  $D$  is the diffusion coefficient,  $R$  the universal gas constant,  $T$  the absolute temperature and  $\mu$  the chemical potential given by  $\mu = \mu_0 + RT \ln C$  for dilute solutions [83]. By substituting the chemical potential into the expression of driving force, we find that the diffusion driving force is proportional to the concentration gradient  $\nabla C$ , which corresponds to a concentration difference between two neighboring tDPD particles. It follows that the Fickian flux

$Q_{ij}^D$  and random flux  $Q_{ij}^R$  in the tDPD model are given by

$$Q_{ij}^D = -\kappa_{ij}w_{DC}(r_{ij})(C_i - C_j), \quad (5.145a)$$

$$Q_{ij}^R = \epsilon_{ij}w_{RC}(r_{ij})\xi_{ij}, \quad (5.145b)$$

where  $\kappa_{ij}$  and  $\epsilon_{ij}$  determine the strength of the Fickian and random fluxes, and  $\xi_{ij}$  is the Gaussian white noise [26].  $w_{DC}(r)$  and  $w_{RC}(r)$  are weight functions with a cutoff radius  $r_{cc}$ . The Fickian friction parameter  $\kappa$  plays the analogous role for concentration differences between tDPD particles as  $\gamma$  does for momentum. In general, the concentration friction  $\kappa$  is a  $N \times N$  matrix when the interdiffusivities of  $N$  different chemical species are involved. However, considering  $N$  chemical species in dilute solution and neglecting the interdiffusivities of different species, the system is then reduced to a set of uncoupled diffusion equations with independent diffusivities between species, and hence  $\kappa$  becomes a diagonal matrix [8].

By applying the local-equilibrium assumption to the tDPD system, the random term  $Q_{ij}^R$  is related to the dissipative term  $Q_{ij}^D$  by satisfying the fluctuation-dissipation theorem [66, 83]

$$\epsilon_{ij}^2 = m_s^2 \kappa_{ij} \rho (C_i + C_j), \quad w_{DC}(r_{ij}) = w_{RC}^2(r_{ij}), \quad (5.146)$$

where  $m_s$  the mass of a single solute molecule,  $C_i$  and  $C_j$  are the concentrations on particle  $i$  and  $j$ , respectively. For detailed derivations for obtaining Eq. (5.146), readers are referred to [66]. In general, the mass of a single solute molecule  $m_s$  is much smaller than the mass of a tDPD particle  $m$ , which is chosen as mass unit. Consequently, the magnitude of  $\epsilon$  is small at  $m_s \ll m$ , which indicates that the contribution of the random flux  $Q_{ij}^R$  to the total diffusion coefficient  $D$  is negligible unless  $m_s$  becomes comparable to  $m$  in nanoscale systems.

The macroscopic properties including viscosity and diffusivity of a tDPD system are output properties rather than input parameters. Since the stochastic forces on tDPD particles yield random movements, the effective diffusion coefficient  $D$  is the result of contributions from the random diffusion  $D^\xi$  and the Fickian diffusion  $D^F$ . In general, the random contribution  $D^\xi$  is a combined result of the random movements of tDPD particles and random flux  $Q_{ij}^R$  in Eq. (5.145b). However, the variance of random flux  $Q_{ij}^R$  has a small prefactor  $m_s^2$  as given by Eq. (5.146). In practical applications, the contribution of the random flux  $Q_{ij}^R$  to  $D^\xi$  is negligible, which has been confirmed by Kordilla et al. [45] Thus, in the mathematical derivations in this section, we consider that  $D^\xi$  is due to the random movements of tDPD particles. In particular, for a tDPD system in thermal equilibrium, the diffusion coefficient  $D^\xi$  induced by the random movements of tDPD particles can be calculated by Groot and Warren [35]

$$D^\xi = \frac{3k_B T}{4\pi \gamma \rho \cdot \int_0^{r_c} r^2 w_D(r) g(r) dr}, \quad (5.147)$$

where  $r_c$  is the cutoff radius for forces. Also, the macroscopic diffusion coefficient  $D^F$  due to the Fickian flux can be computed by Mackie et al. [74]

$$D^F = \frac{2\pi\kappa\rho}{3} \int_0^{r_{cc}} r^4 w_{DC}(r) g(r) dr, \quad (5.148)$$

in which  $\kappa$  is the Fickian friction coefficient and  $r_{cc}$  is the cutoff radius for concentration flux. Let  $w_D(r) = (1 - r/r_c)^{s_1}$  and  $w_{DC}(r) = (1 - r/r_{cc})^{s_2}$  be the weight functions of the dissipative force  $\mathbf{F}_{ij}^D$  and of the Fickian flux  $\mathbf{Q}_{ij}^D$ , respectively. When the radial distribution function of ideal gas  $g(r) = 1.0$  is employed, both  $D^\xi$  and  $D^F$  can be evaluated analytically

$$\begin{aligned} D &= D^\xi + D^F \\ &= \frac{3k_B T (s_1 + 1)(s_1 + 2)(s_1 + 3)}{8\pi\gamma\rho r_c^3} \\ &\quad + \frac{16\pi\kappa\rho r_{cc}^5}{(s_2 + 1)(s_2 + 2)(s_2 + 3)(s_2 + 4)(s_2 + 5)}, \end{aligned} \quad (5.149)$$

where  $s_1$  and  $s_2$  are the exponents of  $w_D(r)$  and  $w_{DC}(r)$ . Equation (5.149) provides a relationship between the macroscopic effective diffusion coefficient  $D$  (which can be experimentally measured) and parameters in the tDPD model. Equation (5.149) indicates that the effective diffusion coefficient  $D$  is a linear function of the parameter  $\kappa$ , and the minimum value of the effective diffusion coefficient  $D_{\min} = D^\xi$  is obtained at  $\kappa = 0$ . Since the radial distribution function  $g(r) = 1$  corresponding to the ideal gas is used, Eq. (5.149) provides a rough prediction of the effective diffusion coefficient  $D$ . The accurate value of  $D$  can only be obtained by computations in tDPD simulations.

Li et al. [66] proposed a numerical diffusivity benchmark to compute the accurate value of  $D$  of tDPD systems, which shares the same strategy of reverse Poiseuille flow as a numerical viscometer [7] and computation of the thermal conductivity in eDPD [62]. For a tDPD fluid with constant diffusion coefficient, the ADR equation is given by  $dC/dt = D\nabla^2 C + Q^S$  where  $D$  is the diffusion coefficient and  $Q^S$  a source term. For steady state problems, the ADR equation is simplified to  $D\nabla^2 C = -Q^S$ , which is the same as the governing equation of Poiseuille flow driven by a body force  $\nu\nabla^2 \mathbf{V} = -g$ . To obtain the accurate value of the effective diffusion coefficient, one needs to perform a tDPD simulation in a computational domain with periodic boundary conditions. Let  $z = 0$  be a plane subdividing the fluid system into two equal domains in  $z$ -direction. A small concentration source  $+Q^S$  is applied in the domain of  $z > 0$  while a concentration sink with same magnitude  $-Q^S$  is applied in the other domain  $z < 0$ , as shown in Fig. 5.7a. Because of the periodic boundary conditions, the concentration of the tDPD fluid is constrained to be invariable at the plane  $z = 0$ . When the diffusion coefficient  $D$  is constant, the steady state solution



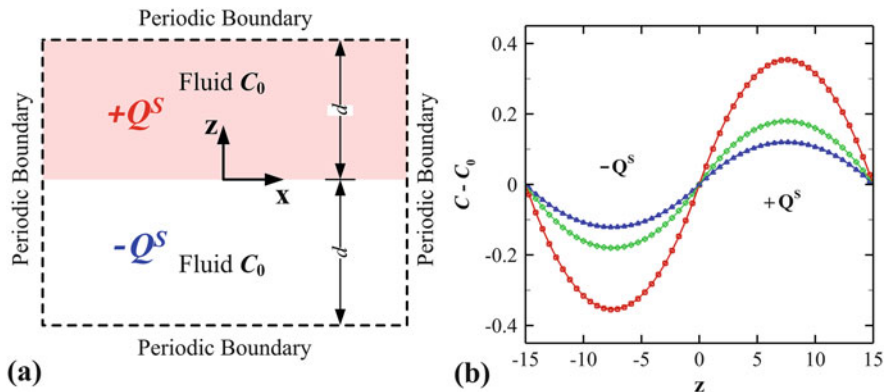


**Fig. 5.7** (a) Schematic geometry for the numerical diffusivity meter using fully periodic boundary conditions. (b) Concentration profiles obtained by running tDPD simulations for different Fickian friction coefficients  $\kappa$ . (b) is adapted with permission from [66]

of the concentration profile is given by

$$C(z) = \frac{Q^S z}{2D} (d - |z|) + C_0, \quad (5.150)$$

where  $Q^S$  is the source term,  $C_0$  the initial concentration of the tDPD system, and  $d$  the half length of the computational domain in  $z$ -direction. The concentration profiles can be easily obtained by running the tDPD simulation to the steady state. Figure 5.7b shows the concentration profiles obtained from tDPD simulations for different Fickian friction coefficients  $\kappa$ , in which the lines are the best-fitting parabolas for each case. Then, the effective diffusion coefficient can be determined by fitting the concentration profile with the analytical solution given by Eq. (5.150). It is obvious that the effective diffusion coefficient  $D$  can be significantly changed by varying the Fickian friction coefficient  $\kappa$ .

Boundary conditions are crucial for the investigation of diffusion-reaction processes in wall-bounded systems. Usually, defining stationary particles to represent solid objects is a common treatment in classical DPD simulations [108]. However, those solid walls made up by discrete frozen particles induce unwanted temperature and density fluctuations in the vicinity of the walls [90]. Alternatively, Li et al. [66] used effective boundary fluxes to impose Dirichlet and Neumann boundary conditions for concentration in the tDPD systems.

### Dirichlet Boundary Condition

Since the fluid particles do not penetrate into wall boundaries, the random movements of fluid particles do not have any contributions to the boundary concentration

flux. Therefore, the effective boundary concentration flux is induced only by the Fickian flux. For a fluid particle  $i$  in the vicinity of a wall boundary, the effective Fickian concentration flux on particle  $i$  from the wall can be calculated [66] by

$$\begin{aligned}
 Q_{D,i}^W(h) &= 2\pi\rho \int_{z=h}^{r_{cc}} \int_{x=0}^{\sqrt{r_{cc}^2-z^2}} Q^D(r)g(r)xdxdz \\
 &= 2\pi\rho \int_{z=h}^{r_{cc}} \int_{x=0}^{\sqrt{r_{cc}^2-z^2}} -\kappa \cdot w_{DC}(r) \cdot \frac{z}{h}(C_i - C_w) \cdot g(r)xdxdz \\
 &= 2\pi\rho\kappa (C_w - C_i) \cdot \varphi(h),
 \end{aligned} \tag{5.151}$$

where  $C_i$  is the concentration of particle  $i$ ,  $C_w$  the expected concentration at the wall surface, and  $h$  the distance of the particle  $i$  away from the wall surface. Here,  $\varphi(h)$  is a function of  $h$ , which is defined as

$$\varphi(h) = \int_{z=h}^{r_{cc}} \int_{x=0}^{\sqrt{r_{cc}^2-z^2}} w_{DC}(r)g(r)\frac{zx}{h} \cdot dx \cdot dz. \tag{5.152}$$

Equation (5.151) reveals that the boundary concentration flux is determined by the concentration difference between particle  $i$  and the wall, and also their distance. Given a radial distribution function  $g(r)$  and the weight function  $w_{DC}(r)$ , the function  $\varphi(h)$  can be evaluated through Eq. (5.152). As the distance  $h$  approaches to zero, the magnitude of  $\varphi(h)$  goes to infinity. In practical tDPD simulations, a truncation of  $\varphi(h)$  at small distances can be used to stabilize the simulation, i.e., setting  $\varphi(h < 0.01r_{cc}) = \varphi(0.01r_{cc})$ .

## Neumann Boundary Condition

To consider the effective flux along the normal direction of wall surface, we integrate the effect of concentration flux from the wall boundary and define a distance dependent function given by

$$\Phi(h) = \int_{z=h}^{r_{cc}} \int_{x=0}^{\sqrt{r_{cc}^2-z^2}} w_{DC}(r)g(r)\frac{zx}{r}dxdz. \tag{5.153}$$

The normalized  $\Phi(h)$  is defined as  $\bar{\Phi}(h) = \Phi(h) / \int_0^{r_{cc}} \Phi(x)dx$ . Then, the integral of  $\bar{\Phi}(h)$  is equal to one. Using the computed  $g(r)$  and the expression of  $w_{DC}(r)$ , the function  $\bar{\Phi}(h)$  can be obtained through Eq. (5.153). To impose a Neumann boundary condition  $dC/dn = \Lambda$  at a wall boundary, it is equivalent to applying a concentration flux  $Q^W = D\Lambda$  across the boundary. In practice, the flux  $Q^W$  is distributed onto the fluid particles in the vicinity of the wall weighted by  $\bar{\Phi}(h)$ . Let  $\rho$  be the number density of the fluid particles, the volume concentration is  $\rho C$

because the concentration  $C$  in tDPD is defined as the number of a chemical species per particle. Then, any fluid particle  $i$  close to the wall receives a concentration flux from the wall boundary given by

$$Q_i^W(h) = D\Lambda\rho \cdot \bar{\Phi}(h). \tag{5.154}$$

One-dimensional test cases have been performed in [66] to check the effectiveness and the accuracy of using the effective boundary fluxes for implementation of the Dirichlet and Neumann boundary conditions. Figure 5.8(a1) illustrates the initial condition  $C(x, 0) = 0$  and the boundary conditions for the test case of the Dirichlet boundary condition. By solving a one-dimensional diffusion equation  $dC/dt = D\nabla^2 C$  with boundary conditions of  $C(0, t) = 0$  and  $C(L_x, t) = C_0$ , an analytical solution for the transient concentration profile can be obtained [66]

$$C(x, t) = \frac{C_0 x}{L_x} + \sum_{n=1}^{\infty} \frac{2C_0}{n\pi} (-1)^n \sin(\beta_n x) \exp(-D\beta_n^2 t), \tag{5.155}$$

where  $\beta_n = n\pi/L_x$  with  $L_x$  being the length of the computational domain in the  $x$ -direction,  $D$  the diffusion coefficient. Figure 5.8(b1) shows a comparison between the concentration profiles obtained using tDPD and theoretical solution Eq.(5.155) at several times including the steady state solution. The results are in good agreement, which validates the effective boundary flux of Eq.(5.151) for imposing the correct Dirichlet boundary condition in the tDPD simulation.

Figure 5.8(a2) shows a similar setup as the previous test case but different wall boundary conditions for the Neumann boundary condition. Considering a

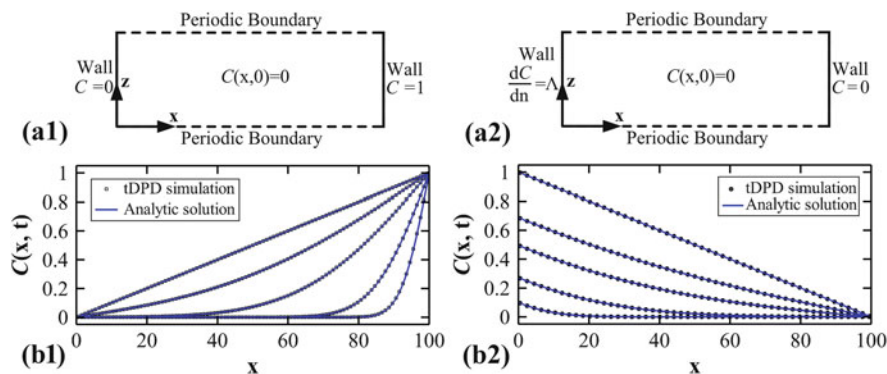


**Fig. 5.8** Initial condition and boundary conditions for the one-dimensional diffusion with (a1) the Dirichlet boundary condition and (a2) the Neumann boundary condition. The corresponding transient concentration profiles and comparison with theoretical solutions are shown in (b1) and (b2). These plots are adapted with permission from [66]

concentration flux at the left wall  $x = 0$ , we apply the a Neumann boundary condition  $dC/dn = \Lambda$  at  $x = 0$ . Also, the right wall at  $x = L_x$  has a fixed concentration  $C(100, t) = 0$ . By solving a one-dimensional diffusion equation  $dC/dt = D\nabla^2 C$  with boundary conditions of  $dC(0, t)/dx = \Lambda$  and  $C(L_x, t) = 0$ , we have the theoretical solution for the transient concentration profile given by Li et al. [66]

$$C(x, t) = \Lambda(x - L_x) + \frac{4\Lambda}{L_x} \sum_{n=1, \text{odd}}^{\infty} \beta_n^{-2} \sin^2\left(\frac{n\pi}{4}\right) \cos(\beta_n x) \exp(-D\beta_n^2 t), \quad (5.156)$$

where  $\beta_n = n\pi/(2L_x)$  with  $L_x$  being the length of the computational domain in the  $x$ -direction,  $D$  the diffusion coefficient. Figure 5.8(b2) compares the transient concentration profiles obtained using tDPD with the theoretical solution Eq. (5.156). The excellent agreement between the tDPD results and the theoretical solution confirms the validity of the effective boundary flux of Eq. (5.154) for imposing the correct Neumann boundary condition.

The particle-based tDPD method satisfies the conservation of concentration automatically and provides an economical way to solve ADR equations with a large number of species. It has been reported [66] that the tDPD solution of a 25-species coagulation model is only twice as computationally expensive as the conventional DPD simulation of hydrodynamics alone, unlike the continuum model requiring more than 20 Poisson/Helmholtz solvers making the computational cost over ten times higher than the Navier-Stokes solver. This low additional cost for solving ADR equations indicates the promising potential of tDPD in biological applications involving multiple biochemical species at the mesoscale.

### 5.3.4 Other Extensions

In addition to eDPD, mDPD and tDPD models, there are some other extensions of DPD developed for different purposes. Examples include:

1. Fluid particle model (FPM): It is a generalization of the classical DPD method developed by Español [24]. FPM considers both linear and angular momenta of the particles and includes both central and noncentral forces between particles, while the classical DPD method considers only linear momentum and includes only central forces. By introducing torques and angular velocities of the particles, both linear and angular momenta of FPM are conserved.
2. Single-particle DPD model: It is based on FPM with modified colloid-solvent pairwise potentials [86]. In this model, each spherical colloidal particle can be represented by a single FPM particle rather than a cluster of particles. As a result,

it shows high computational efficiency in studying the dynamical and rheological properties of colloidal suspensions in simple fluid solvents.

3. Anisotropic single-particle DPD model (aDPD): It is a further development of the single-particle DPD model [20]. By introducing a shape matrix indicating the particle size and shape, aDPD formulates the conservative and dissipative interactions between anisotropic DPD particles using a linear mapping from the original single-particle DPD model of isotropic spherical particles, while the random forces are properly formulated by satisfying the fluctuation-dissipation theorem. Consequently, aDPD enables the DPD method to efficiently model the colloidal ellipsoids under the effect of thermal fluctuation. Examples include the orientation-dependent diffusion of an anisotropic particle, and the isotropic-nematic transition in an ellipsoidal suspension induced by the changes of volume fraction or the aspect ratio of ellipsoid particles.
4. Charged DPD model (cDPD): It was developed by Deng et al. [19] based on tDPD for simulating mesoscopic electrokinetic phenomena governed by the stochastic Poisson-Nernst-Planck and the Navier-Stokes equations. By introducing extra degrees of freedom for the ionic concentration and the electrostatic potential associated with each DPD particle, cDPD models the diffusion of ionic species driven by the ionic concentration gradient, electrostatic potential gradient and thermal fluctuations through pairwise fluxes between DPD particles, while the electrostatic potential is obtained by solving the Poisson equation on the moving DPD particles iteratively at each time-step. Since both the fluctuations of momentum and ionic concentration are systematically included in cDPD without any grid-based algorithms, it is a flexible and powerful method in studying complex fluids with electrostatic interactions at the micro- and nano-scales.
5. Smoothed DPD (SDPD) model: It is a top-down approach [25] developed from smoothed particle hydrodynamics (SPH). SDPD starts from continuum equations while other DPD models are bottom-up approaches starting from microscopic dynamics. As a matter of fact, SDPD is a Lagrangian discrete model for simulating Navier-Stokes hydrodynamics that includes thermal fluctuations consistently. Unlike these bottom-up DPD methods, the parameters in the governing equations of SDPD have clear physical meanings. Its inputs are the viscosity, equation of state, temperature and other parameters required by the fluctuating Navier-Stokes equations. However, since the constitutive equations and macroscale properties of the system must be given as inputs, SDPD works well with simple fluids but loses its effectiveness in modeling complex fluids and materials, which may not have a known constitutive equation.

Motivated by tackling different challenges in the mesoscopic modeling, the various extensions of DPD have been developed and constitute the “DPD Alphabet”, as shown in Fig. 5.2. These new developed DPD models dramatically extend the capability of the DPD simulations beyond the classical DPD, which makes DPD a more promising mesoscopic method for diverse applications.

## 5.4 Computer Implementation

A DPD program shares the structure with an atomistic molecular dynamics simulator, and iterates over a time stepping loop consists of four stages: force evaluation, position/velocity update, parallel communication, and data collection.

### 5.4.1 Pairwise Search

Due to the short-range nature of the DPD pairwise force, the evaluation is usually assisted with the use of a spatial searching algorithm, which loops over all pairs of particles that are within the cutoff distance  $r_c$ . One of the classical approaches used by the most DPD software, as well as many other existing MD software, is to use a Verlet list, which is essentially a table storing the indices of particles within a given distance  $r_v$  for each particle in the system.  $r_v$  is usually chosen to be slightly larger than  $r_c$  such that the list does not need to be updated for every time step. As a trade-off the list will contain some extra particles which are not within  $r_c$ .

The Verlet list can be constructed naively by a  $O(N^2)$  pairwise search, but more efficiently with the help of a cell list. The cell list algorithm makes use of a uniform lattice to partition the system into many nearly-cubic cells, and stores the indices of the particles that are located within each cell. The cells are numbered consecutively along the axes, allowing the index of cell that each particle belongs to be determined by simply dividing the particle's coordinate by the length of the cells and then flooring to the nearest integer.

Given a system of  $N$  particles occupying a volume of  $L_x \times L_y \times L_z$ , a Verlet list can be constructed from a cell list using  $O(N)$  time and storage by looping over each particle, first finding the cell that the particle belongs to, and then comparing against other particles in this cell as well as particles in all 26 immediate neighboring cells. The cell list itself takes  $O(L_x L_y L_z + N)$  storage and  $O(N)$  time to construct as shown by Algorithm 1. Alternatively, the cell list can be used directly for computing the pairwise force [97] and may delivery better performance on massively parallel processors where memory bandwidth is more precious than computing power.

### 5.4.2 Force Computation

The conservative force is usually defined directly using a weight function, or through the differentiation of a potential function. The computation of the conservative force is relatively straightforward because it only affects static properties such as radial distribution function and compressibility. In fact, several splitting integration schemes evaluate the dissipative and random force separately from the conservative force.

**Algorithm 1** The cell list algorithm

---

```

Method RectilinearCelllist( Np: integer,
                          ncell: integer[3],
                          cell_size: integer[3],
                          coord: real[N][3] )
Ncell      = ncell[0] * ncell[1] * ncell[2]
bin_size   = zeros[Ncell] # O(L^3) space
local_seq  = integer[N]   # O(N)   space
cid        = integer[N]   # O(N)   space

# Get cell id and cell-local index for each particle
# Count cell size
for i = 0:N
  # operator ./: element-wise division
  cell_xyz = floor( coord[i] ./ cell_size )
  cid[i] = cell_xyz[0] + cell_xyz[1] * ncell[0] + cell_xyz[2] * ncell[1] *
           ncell[2]
  local_seq[i] = bin_size[ cid[i] ]
  ++bin_size[ cid[i] ]

# O(N) prefix sum for the starting index of each cell
bin_start = zeros[Ncell] # O(L^3) space
for i = 1:Ncell
  bin_start[i] = bin_start[i-1] + bin_size[i-1]

# Scatter particle indices into corresponding cell
cell_list = integer[N] # O(N) space
for i = 0:N
  cell_list[ bin_start[ cid[i] ] + local_seq[i] ] = i

return cell_list, bin_start

```

---

The dissipative force is usually evaluated together with the random force, due to the common arithmetics for computing the weight function as dictated by the fluctuation-dissipative theorem. However, the most prevalent and convenient approach is to still evaluate the dissipative and random force alongside the conservative force, because this saves the work for the pairwise searching, a dominant workload in DPD simulations.

It is a common practice in molecular dynamics simulation to omit the pairwise interactions between particles that are connected by bonds. For example, in the CHARMM force field the pairwise interaction between atoms separated by less than three bonds are not computed, because the interaction is assumed to be already considered by the bonded potential. The same principle could be applied to DPD, but a careful consideration must be made on whether to also exclude the dissipative and random terms. The decision to include the dissipative and random force can be justified by noting that the conservative bonded force may only serve the role of the DPD conservative force. The friction and random effects thus are still needed between particles that are bonded, but may be based on different weight functions or coefficients.

The random force in DPD need to be handled carefully for distributed-memory parallelization, which is usually done with a domain decomposition scheme that divides the simulation box into non-overlapping subregions. The force on particles within each subregion can be computed locally on each processor. The force between subregions can be computed with the help of *ghost* particles, which are the local images of remote particles from neighboring processors that are within the cutoff of each subregion. A *forward* communication is responsible for the exchange of the ghost particles. A *backward* communication process is necessary if we are to take advantage of the Newton's 3rd law of action and reaction, which is widely used in serial DPD programs to speed up the force computation. The extra communication stages may actually compromise parallel efficiency on massively parallel clusters due to the overhead for sending and synchronizing over the messages. The computation for pairwise interactions across subregions can be duplicated in order to eliminate the *backward* communication stage. This overhead does not incur network communication and should be negligible as long as the area-to-volume ratio of the subregion remains reasonably large. However, the random term need to be handled carefully in this case because the reproduction of the same random number between the a pair of particles spanning two processors is necessary to ensure momentum conservation. This is usually handled by using a stateless random number generator that crunches in situ a global random variable, which changes over time steps but remains the same across all processors within a time step, with some per-particle signature that is persistent on each particle [2, 89, 101]. As long as the same signature is presented, the same random number can be recovered for each of the particles on two different processors. A common choice for the signature is the *id* of the particle. Alternatively, the signature may be computed from a blend of the highly volatile bits of the particles' degrees of freedom such as position and velocity, which serves as a source of entropy.

### 5.4.3 Numerical Optimization

In [26], the random numbers between pairs of particles are assumed to be delta-correlated, symmetric Gaussian *i.i.d.* random variables with zero mean and unit variance. However, the generation of Gaussian random numbers is less straightforward and more expensive, despite the existence of highly efficient algorithms such as the Box-Muller method. The non-compact nature of the Gaussian distribution makes it possible for extremely large forces to occur regardless of magnitude. This can cause numerical instability in practice and hence requires treatment such as re-generation or truncation. However, due to the law of large numbers, any random variable with the same mean and variance could lead to the same stochastic differential equation for DPD and thus can lead to the same invariant distribution indistinguishable from that driven by a Gaussian term. This observation liberates us to use much cheaper random number generators, e.g. one that generates numbers uniformly distributed on  $[-\sqrt{3}, \sqrt{3}]$ . Other possibilities include the arcsin



distribution on  $[-\sqrt{2}, \sqrt{2})$ , which can be generated using the logistic map with only floating point operations. This fits better to the architectural characteristics of general purpose graphics processing units with less integer arithmetic throughput.

An effective approach to achieve high Schmidt number in DPD simulation is to increase the power  $s$  of the dissipative weight function  $w_D(r_{ij}) = (1 - r_{ij}/r_c)^s$  in Eq. (5.2). If the power is non-integral, a general transcendental function that evaluates the result of  $w^s$  is needed. This function is among one of the slowest math functions in every programming language, because it has to be evaluated as  $w^s = e^{s \cdot \ln w}$  using the identity  $x = e^{\ln x}$ , and in turn involves the evaluation of the natural logarithm and exponential function. In order to conform to the IEEE floating point standard, a generic implementation of the functions as provided in most programming languages has to deal with the full range of inputs as well as possible exceptions, which triggers instruction branching and reduced CPU efficiency. The process, however, can be sped up by exploiting the limited range of the weight function and the power. The possibility that the base or the exponent being 0 can be precluded by the cutoff testing prior to the function call; it is also unlikely that the base or the exponent would be NaN or Inf unless there are serious problems in the underlying physics of the model. As such, both the logarithm and exponential component of the power function can be implemented using a Chebyshev polynomial expansion with accuracy up to the last digit of the floating point number [101].

#### 5.4.4 Time Integration

The velocity Verlet (VV) algorithm is the most commonly used algorithm for integrating DPD systems due to their symplecticity, numerical stability, and ease of implementation. It integrates position using half-step values of velocity. The form most frequently used in molecular dynamics simulations is:

$$\begin{aligned}
 v(t + \frac{\Delta t}{2}) &= v(t) + \frac{\Delta t}{2} \cdot a(t), \\
 r(t + \Delta t) &= r(t) + \Delta t \cdot v(t + \frac{\Delta t}{2}), \\
 a(t + \Delta t) &= F(r(t + \Delta t)), \\
 v(t + \Delta t) &= v(t + \frac{\Delta t}{2}) + \frac{\Delta t}{2} \cdot a(t + \Delta t).
 \end{aligned}
 \tag{5.157}$$

However, due to the dependence of the dissipative force on particle velocity, the scheme in DPD is of the form:

$$\begin{aligned}
 v(t + \frac{\Delta t}{2}) &= v(t) + \frac{\Delta t}{2} \cdot a(t), \\
 r(t + \Delta t) &= r(t) + \Delta t \cdot v(t + \frac{\Delta t}{2}), \\
 a(t + \Delta t) &= F\left[r(t + \Delta t), v(t + \frac{\Delta t}{2})\right], \\
 v(t + \Delta t) &= v(t + \frac{\Delta t}{2}) + \frac{\Delta t}{2} \cdot a(t + \Delta t).
 \end{aligned}
 \tag{5.158}$$

There is a temporal misalignment between the position and velocity used for the force. As such, the modified velocity Verlet algorithm aims to improve the stability of the integrator by using an extrapolated version of the velocity for the force evaluation [35]:

$$\begin{aligned}
 v(t + \frac{\Delta t}{2}) &= v(t) + \frac{\Delta t}{2} \cdot a(t), \\
 r(t + \Delta t) &= r(t) + \Delta t \cdot v(t + \frac{\Delta t}{2}), \\
 a(t + \Delta t) &= F\left[r(t + \Delta t), v(t) + \lambda \cdot \Delta t \cdot a(t)\right], \\
 v(t + \Delta t) &= v(t + \frac{\Delta t}{2}) + \frac{\Delta t}{2} \cdot a(t + \Delta t),
 \end{aligned}
 \tag{5.159}$$

where  $\lambda \in [0, 1]$  is a parameter that depends on the specific choice of DPD parameter, and need to be tuned case-by-case. There also exist more advanced time integrators that are based on iterative or splitting techniques, such as DPD-VV [9], Shardlow splitting scheme [99], the pairwise Noose-Hoover-Langevin method [53], and the pairwise adaptive Langevin method [54].

## 5.5 Applications

The DPD method was invented more than two decades ago for simulating complex fluids at the mesoscale [39]. Ever since its inception, DPD modeling has found a wide spectrum of applications including simple fluids hydrodynamics, polymer solutions and melts, biological membranes, colloidal suspensions and blood flow [34, 72]. This section will briefly introduce a few examples of DPD applications.

### 5.5.1 *Single-Phase Fluid Flow*

DPD provides the correct hydrodynamic behavior of fluids at the mesoscale, which is of fundamental importance for particles in flow and colloidal/polymer suspensions. In the following, we briefly introduce the implementation of boundary conditions for wall-bounded flows in DPD, and present two examples of single-phase fluid flow.

#### **No-Slip Boundary Condition in DPD**

In fluid dynamics, the tangential component of the fluid velocity at the solid boundary is always equal to that of the solid boundary, thus, the no-slip boundary condition is usually used in modeling of wall-bounded flows. When one performs DPD simulation of Couette flow or Poiseuille flow in a microchannel or microtube, the soft repulsion between two particles cannot prevent fluid particles from penetrating solid boundaries, and thus extra effort is required to impose the no-slip boundary condition.

To impose a wall boundary condition in DPD, layers of particles at the solid walls are usually frozen (velocity of these particles are set to zero) to model solid walls. To prevent the penetration of fluid particles into the solid walls, a proper reflection, such as bounce-back reflection, specular reflection, or Maxwellian reflection, at the fluid-solid interface are usually implemented. In order to enforce the no-slip boundary condition at the fluid–solid interface, the DPD repulsive forces from wall particles are adjusted appropriately according to the wall density  $n_w$  [90],

$$F^W = a_e (0.0303n_w^2 + 0.5617n_w - 0.8536). \quad (5.160)$$

In this implementation, the average force acting on the DPD particles from the solid wall in the near-wall region is equal to the average force from the fluid.

In addition, interaction of liquids with solid walls causes layering of the fluid, which is responsible for the large density fluctuations near the wall. These fluctuations are physical and thus desirable in simulations, but they may be erroneous in some other simulations; for example, spurious density fluctuations have been observed in particle systems such as stochastic rotational dynamics, MD and DPD simulations. Thus, one needs to control the density fluctuations in wall-bounded DPD systems.

An adaptive boundary condition (ABC) [91] has been developed and applied to fluid particles in the vicinity of the walls in order to control fluid density fluctuations near the solid walls. In the ABC method, the magnitude of the adaptive force,  $F^W(i_b)$ , depends on the distance of the fluid particles to the solid walls and is updated simultaneously during the simulations according to the estimated density

fluctuations,

$$F_{\text{new}}^W(i_b) = F_{\text{old}}^W(i_b) + C_W \left( \frac{\sum_{i=i_a}^{i_b} \rho_s(i)}{\sum_{i=i_a}^{i_b} \rho_d(i)} - 1 \right), \quad (5.161)$$

where  $C_W$  is a weighting factor.

The no-slip boundary condition in shear flow can also be implemented by numerical periodicity, such as the use of Lees–Edwards boundary conditions [47]. Instead of including physical wall boundary, Lees and Edwards [47] proposed a simple and ingenious modification to the standard periodic boundary condition for particle-based simulations of shear flow. In particular, particles are considered as being embedded in a fluid which has a constant velocity gradient to maintain the system under a shear stress in a steady state. Once a particle leaves the simulation box in the direction parallel to the velocity gradient, it will be reintroduced into the box from the opposite boundary with a displacement and a velocity shift in the flow direction. Although the Lees–Edwards boundary conditions have been successfully used in many MD and DPD simulations [3, 87], it can only be applied to fluid systems in steady states with constant shear rates.

### Couette Flow

In fluid dynamics, Couette flow is a simple shear flow of a viscous fluid between two parallel walls, one of which is moving relative to the other. The constitutive relation for Couette flow can be expressed as,

$$\tau_{yx} = -\mu \frac{du}{dy}, \quad (5.162)$$

where  $\tau_{yx}$  is the shear stress, and  $du/dy$  is the velocity gradient in the  $y$  direction, and  $\mu$  the dynamic viscosity. In DPD, the friction between the fluid and the moving wall particles causes the fluid to shear. Figure 5.9a shows the simulation results of transient development to the steady-state Couette flow. The DPD results agree well with the analytical solution for different times. A notable aspect of this simple shear flow is that the shear stress is constant throughout the flow domain. Thus, Couette flow is frequently used to measure the viscosity of a fluid.

### Poiseuille Flow

Poiseuille flow is a steady viscous fluid flow driven by an effective pressure gradient established between the two ends of a long duct, usually a pipe, of uniform circular cross-section. For a fluid flow through a pipe of radius  $R$  and length  $L$ , in the presence of a uniform pressure gradient  $\Delta P/L$ , the velocity of the fluid at a specified

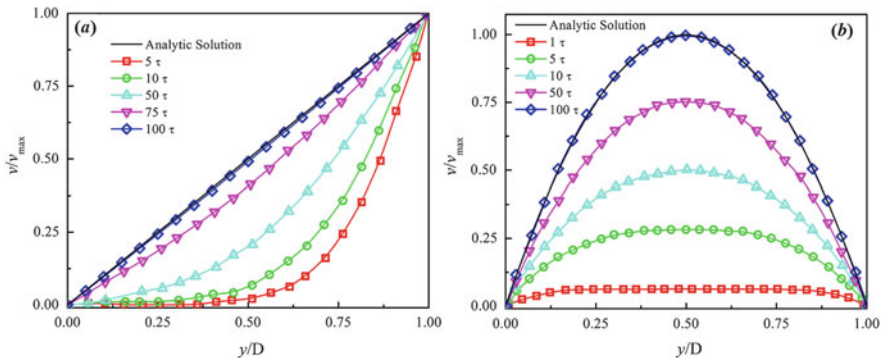


**Fig. 5.9** Time evolution of the velocity profiles in (a) Couette and (b) Poiseuille flows, in which  $\tau$  denotes the DPD time unit

distance  $r$  from the center of the pipe,  $v(r)$ , is given by,

$$v(r) = \frac{\Delta P}{4L\eta}(R^2 - r^2), \quad (5.163)$$

in which  $\eta$  is the fluid viscosity. In DPD, Poiseuille flow can be obtained by applying a body force to the DPD fluid. Figure 5.9b shows the simulation results of development of Poiseuille flow. The fluid velocity in a pipe changes from zero at the wall surface because of the no-slip condition to a maximum  $v_{max}$  at the pipe center.

In DPD modeling of Poiseuille flow, it is also worth to mention the periodic (or reverse) Poiseuille flow method developed by Backer et al. [7], which is also commonly used to estimate the viscosity of the DPD fluid. The method produces counter-flowing Poiseuille flows by uniform body forces in opposite directions along two-halves of a computational domain. The absence of density artifacts makes this method useful for studying the bulk Poiseuille flow.

## 5.5.2 Blood Flow

Blood is a complex fluid exhibiting intriguing dynamic and its rheology depends on the flowrate and volume fraction of suspending particles especially the red blood cells (RBCs). In recent years, particle-based RBC models have attracted increasing attention in multiscale modeling of blood flows. In particle-based approaches, the motion of particles is flow governed by the interactions between discrete particles. Early attempts focused on simulating blood flow with RBC being an elastic particle, whose inner skeleton is represented by a rectangular lattice connected by elastic springs. More recently, DPD was employed in a systematic coarse-grained

procedure for modeling RBCs [92], which served as a basis of a general multiscale RBC (MS-RBC) model that included membrane viscosity and external/internal fluid viscosity contrast [28]. In the MS-RBC model, the membrane of RBC is represented by a two-dimensional triangulated network with a collection of DPD particles, while constraints on the area and volume conservation of RBC are imposed to mimic the area-preserving lipid bilayer and the incompressible interior fluid. Specifically, the elastic part of bond is represented by

$$V_s = \sum_{j \in 1 \dots N_s} \left[ \frac{k_B T l_m (3x_j^2 - 2x_j^3)}{4p(1-x_j)} + \frac{k_p}{(n-1)l_j^{n-1}} \right], \quad (5.164)$$

where  $l_j$  is the length of the spring  $j$ ,  $l_m$  is the maximum spring extension,  $x_j = l_j/l_m$ ,  $p$  is the persistence length,  $k_B T$  is the energy unit,  $k_p$  is the spring constant, and  $n$  is a specified exponent. The membrane viscosity is imposed by introducing a viscous force on each spring. The bending resistance of the RBC membrane is modeled by

$$V_b = \sum_{j \in 1 \dots N_s} k_b [1 - \cos(\theta_j - \theta_0)], \quad (5.165)$$

in which  $k_b$  is the bending constant,  $\theta_j$  is the instantaneous angle between two adjacent triangles having the common edge  $j$ , and  $\theta_0$  is the spontaneous angle. In addition, the RBC model includes the area and volume conservation constraints, which mimic the area-incompressibility of the lipid bilayer and the incompressibility of the interior fluid, respectively. The corresponding energy is given by

$$V_{a+v} = \sum_{j \in 1 \dots N_t} \frac{k_d (A_j - A_0)^2}{2A_0} + \frac{k_a (A - A_0^{tot})^2}{2A_0^{tot}} + \frac{k_v (V - V_0^{tot})^2}{2V_0^{tot}}, \quad (5.166)$$

where  $N_t$  is the number of triangles in the membrane network,  $A_0$  is the triangle area, and  $k_d$ ,  $k_a$  and  $k_v$  are the local area, global area and volume constraint coefficients, respectively. The terms  $A_0^{tot}$  and  $V_0^{tot}$  are the specified total area and volume, respectively.

The MS-RBC model is multiscale, as the RBC can be represented on the spectrin level, where each spring in the network corresponds to a single spectrin tetramer with the equilibrium distance between two neighboring actin connections of  $\sim 75$  nm. On the other hand, for more efficient computation, the RBC network can also be highly coarse-grained with the equilibrium spring lengths of up to  $500 \sim 600$  nm. The RBC membrane interacts with the fluid particles through DPD forces, and the temperature of the system is controlled through the DPD thermostat. The internal and external fluids are modelled by collections of free DPD particles and their separation is enforced by bounce-back reflections of these particles at the RBC membrane surface. The MS-RBC has been successfully applied in RBC simulations, such as RBC dynamics in Poiseuille flow [28], RBC thermal fluctuations [29] and RBCs in diseases like malaria [31] and sickle cell disease [49, 68].

## Modeling Blood Flow in Health

DPD simulations have proven effective in modeling the collective dynamics and microrheology of RBCs in shear flow. The simulations for shear flow can accurately predict the dependence of blood viscosity on shear rate, see Fig. 5.10a. A novel feature is the inclusion of attractive cell–cell interactions which allows to investigate cell aggregation and formation of rouleaux. Simulations in larger tubes with diameters ranging from 10 to 40  $\mu\text{m}$  successfully reproduced several hemodynamic phenomena, including cell migration towards the flow centerline, cell-free layer near the wall and blunt velocity profile [51]. Recently, more complex geometries have been considered, e.g. the blood flow in a bifurcating microfluidic channel or complex arterial network [57, 73]. The results quantify the effect of branch location and bifurcation angle variation on blood-plasma separation, which is agreement with experiment.

An important characteristic of the dynamics of an individual RBC in shear flow is the tank-treading frequency. Simulations with continuum models suggest that the membrane viscosity needs to be accounted for in order to agree with the experiments. Indeed, the MS-RBC model with membrane viscosity captures this effect [28]. More recently, the simulations with a two-component RBC model have been demonstrated to capture the observed dependency between TT frequency and shear rate for RBCs with different degrees of confinement [63]: it follows a linear relationship for a narrow channel but a nonlinear one for a wide channel. The simulations also probed the apparent bilayer–cytoskeleton slip for a defective membrane in hereditary spherocytosis and elliptocytosis.

## Modeling Blood Flow in Malaria

Malaria is one of the most prevalent human infections worldwide. In malaria, RBCs are hosts of Plasmodium parasites which change the cell biomechanical properties. Progression through the parasite development from ring to trophozoite then to schizont stages leads to *Pf*-RBCs loss of their deformability with a relative membrane stiffening more than tenfold in comparison to healthy ones. Moreover, at the final stage (schizont) of the parasite development, the *Pf*-RBCs often show near-spherical shapes due to the formation of intracellular parasitophorous vacuoles, which further impaires cell deformability. These changes can greatly affect the dynamic and rheological properties of *Pf*-RBCs, alter blood flow and may even cause occlusions of small capillaries. Quantifying cell deformability for various stages of *Pf*-RBCs is significant. Recent efforts have been directed towards this end. For example, Bow et al. [13] employed a MS-RBC model to study the biomechanical properties of *Pf*-RBCs. They investigated a progressive stiffening of *Pf*-RBCs with parasite growth. Ye et al. [109] simulated the flow dynamics of *Pf*-RBCs in shear flow. They found that malaria parasites can perturb blood flow, causing *Pf*-RBCs move towards blood vessel wall and adhere to the subendothelial surface. Recently, Chang et al. [16] developed a two-step multiscale framework

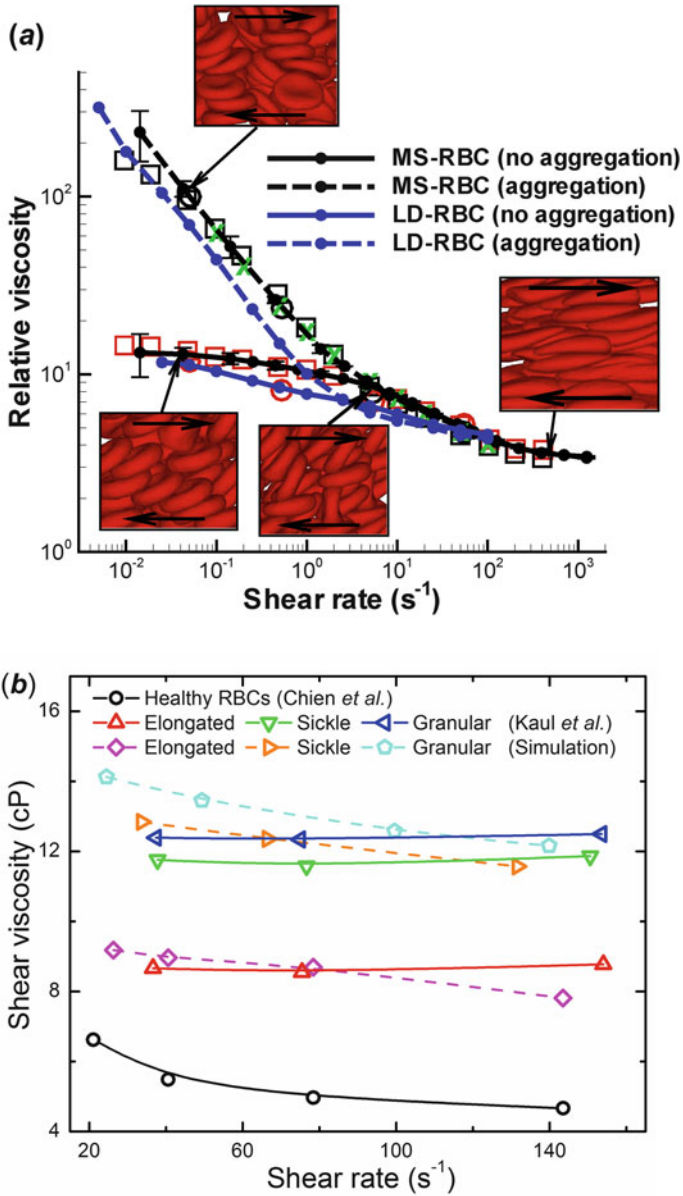


**Fig. 5.10** Predicting human blood viscosity in-silico. **(a)** Shear viscosity of normal blood as a function of shear rate; Adapted from [30]. **(b)** Shear viscosity of sickle cell suspension with different cell morphology at different shear rate. Adapted from [68]



for RBC modeling. Using this two-step multiscale framework, they predicted the altered biomechanical properties of RBCs associated with their pathophysiological states, including malaria. They investigated the influence of the nanoscale knob density on RBC deformability and found a decrease in elongation index for *Pf*-RBCs at trophozoite and schizont stages with the increase of knob density, indicating that the nanoscale knobs, being rigid, contribute to cell membrane stiffness.

### Modeling Blood Flow in Sickle Cell Anemia (SCA)

SCA is a genetic blood disorder exhibiting heterogeneous cell morphology and abnormal rheology under hypoxic conditions [17, 42]. In sickle cell disease, mechanically fragile but rather stiff RBCs contribute to impaired blood flow and other pathophysiological aspects of the disease. When the flow of blood is relatively slow, cellular reactions occur that lead to adhesion of sickle RBCs to vascular endothelium, resulting in vaso-occlusion and consequent clinical manifestations such as organ damage, pain, and even death. Using the same DPD-based RBC model, Li et al. [68] performed simulations of blood flow in sickle cell disease. The simulation results confirmed the previous experimental measurements that the sickle cell blood exhibit different levels of viscosity for different cell morphologies (Fig. 5.10b): the granular RBC suspension is the most viscous, while the shear viscosity of sickle RBC suspensions containing elongated RBCs shows a dramatic decrease. Moreover, it is known that the origin of SCA can be traced to a common molecular basis, but individual patients with SCA have a highly variable clinical phenotype. For these reasons, Li et al. [68] have recently developed a predictive patient-specific model of SCA. Through the simulations they were able to reveal the role of approved drugs like hydroxyurea on the blood viscosity, which has remained a mystery for a long time.

DPD-based RBC models have also been used to quantify the adhesive properties of sickle RBCs and probe vaso-occlusion phenomena in SCA (Fig. 5.11) [49]. Given the same “adhesive potential”, their results validate the hypothesis that heterogeneous cell adhesive dynamics is mainly due to the different cell rigidities and peculiar cell morphologies (Fig. 5.11a) [48]. They also quantified the specific physiological conditions triggering the vaso-occlusion crisis. Under physiological conditions, their simulations show that the interplay of deformable SS2 cells and ISCs can potentially trigger full blood occlusion. In addition, they also employed a DPD-based white blood cell (WBC) model to probe its effect to blood vaso-occlusion. They found that the blood flow undergoes slow down due to the WBC recruitment and the moderate sickle RBC–WBC interaction leads to multiple sickle RBC trapped on the WBCs and the full occlusion (Fig. 5.11b).

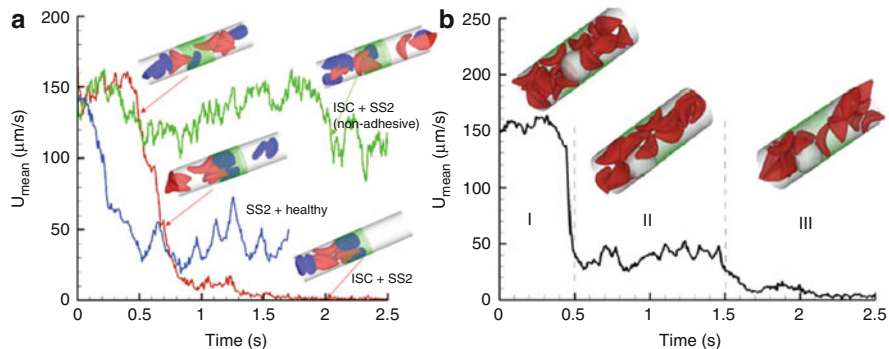


**Fig. 5.11** Vaso-occlusion in post-capillaries. **(a)** Instantaneous mean velocity of blood flow in a cylindrical tube of  $D = 10 \mu\text{m}$  infused with different sickle RBC suspensions. The *red curve* represents the resultant velocity infused with SS2 and ISC cell groups. The *inset plots* represent the instantaneous snapshots where SS2 cells adhere to vessel wall, consequently trapping the ISCs and resulting in cell blockage. The *green curve* represents the blood velocity infused with SS2 and ISC cell groups, where adhesive interaction is only applied to the ISC group. The *inset plot* represents a snapshot where transient adhesion is established between ISC and the tube wall. Steady flow is recovered due to the detachment of the cell from the tube wall. The *blue curve* represents the instantaneous velocity of blood flow infused with SS2 and healthy cell groups. Blood flow exhibits a slow down but not a full occlusion. **(b)** Effect of WBCs: instantaneous mean velocity of the blood flow in a tube of  $D = 13.4 \mu\text{m}$ . The *inset snapshots* represent blood cells in free motion, WBC adhesion and blood occlusion states. Reproduced from [49], by permission

### 5.5.3 Dynamics of Polymers in Shear Flow

A polymer is a large molecule composed of many repeated subunits bonded together. The dynamics of a polymer in shear flow is of central importance in biomolecular engineering, materials science, and medicine. Therefore, it is not surprising that the polymer behavior in shear flow has become a subject of intensive experimental, theoretical, and computational studies.

Through the DPD approach, a polymer can be represented by linking collections of DPD particles into chains with appropriate forces arising from different combinations of the following types [100]:

- *Harmonic spring model*: It is one of the most popular polymer models. In the spring model, the consecutive particles in the polymer chain are connected by harmonic springs,

$$F_{ij}^S = k_S(1 - r_{ij}/r_0), \quad (5.167)$$

with  $k_S$  being the spring constant, and  $r_0$  the equilibrium bond length.

- *Wormlike chain (WLC) model*: It is a continuous model used to characterize the behavior of a semi-flexible polymer.

$$F_{ij}^{WLC} = -\frac{k_B T}{4\lambda_P} \left[ \left( 1 - \frac{r_{ij}}{L_{SP}} \right)^{-2} + \frac{4r_{ij}}{L_{SP}} - 1 \right], \quad (5.168)$$

where  $\lambda_P$  is an effective persistence length, and  $L_{SP}$  is the maximum length of the spring.

- *Finitely extensible nonlinear elastic (FENE) model*: It simplifies the chain of monomers by connecting a sequence of beads with nonlinear springs, which can capture the finite extensibility of a polymer chain. For the FENE chain, the force on particle  $i$  due to particle  $j$  is,

$$F_{ij}^{FENE} = -\frac{Hr_{ij}}{1 - (r_{ij}/r_{max}^2)}, \quad (5.169)$$

in which  $H$  is the spring constant, and  $r_{max}$  is the maximum length of the spring.

- *Lennard-Jones chain (LJC) model*: The force for each pair of particles is given by a truncated Lennard-Jones potential,

$$U_{LJ} = 4\epsilon \left[ \left( \frac{L}{r_{ij}} \right)^{12} - \left( \frac{L}{r_{ij}} \right)^6 + \frac{1}{4} \right], \quad (5.170)$$

where  $\epsilon$  is the depth of the potential well, and  $L$  is the finite distance at which the inter-particle potential is zero.

Industrial and biological applications based on the dynamics of polymer in microfluidic and nanofluidic channels are ubiquitous in past decades. Recent works have focused on the dynamics and flow behaviors of polymers in fluidic channels. Such studies deepen our understanding of the detailed conformational changes of polymers inside the fluidic channels. Dynamic simulation and modeling help in predicting how polymers will behave in fluidic flows and channels. For example, Wijmans and Smit [107] simulate tethered polymers in shear flow using DPD. They found that the polymer chains are able to stretch in the flow direction with respect to the shear rate. Symeonidis and Karniadakis [100] employed DPD to study the  $\lambda$ -phage DNA under shear flow. They presented comparison of WLC models under shear with experimental results and demonstrated the correct static scaling laws for the radius of gyration. Fan et al. [27] simulated the dynamics of macromolecular solutions in shear flow. They found that the velocity profiles of FENE polymer chain suspensions can be fitted using the power-law model.

Dynamics of the translocation of polymers through a narrow channel or a narrow pore is significant in the understanding of several chemical and biological processes such as the transport of protein through membrane channels, motion of DNA and RNA across narrow pores, and infection of virus into the cell nucleus. Therefore, the translocation dynamics of polymer in shear flow have received increasing

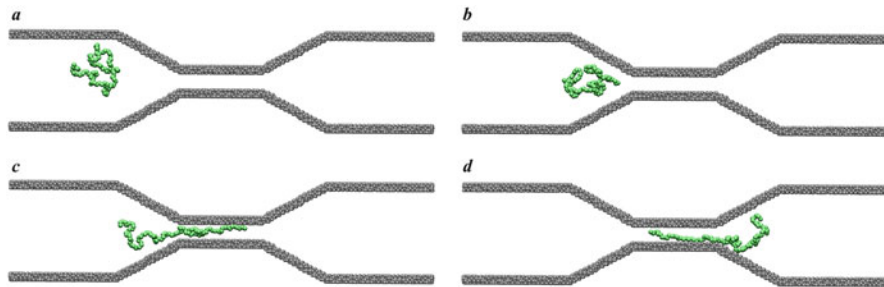


**Fig. 5.12** Translocation event produced by a polymer molecule passing through the fluidic channel in single-file conformations in the simulation at (a)  $t = 110$ , (b)  $t = 160$ , (c)  $t = 180$ , and (d)  $t = 220$ . Adapted with permission from [36]

attention in past decades. In the process of polymer translocation through a narrow channel, the number of available configurations of polymer molecules decreases, resulting in an effective entropy barrier for polymer molecules. Therefore, an external driving force such as an external electric field, chemical potential gradient, or a direct pulling force, is needed to overcome this entropy barrier and hasten the translocation. In DPD, an applied pressure gradient, which generates a fluid flow in narrow channel, can drive polymer chains through the narrow channel.

The DPD simulation provides a reliable approach to investigate the conformational changes and dynamic behaviors of polymers in the translocation processes. For example, Guo et al. [36] employed DPD to simulate the dynamics of flow-induced translocation of polymers through a fluidic channel. They found that there are three stages in the translocation process of linear polymer molecule (Fig. 5.12): (1) drift diffusion; (2) capture; and (3) translocation. These simulations can help in clearly understanding the detailed conformational, dynamical, and transport properties of polymer molecules and the events taking place inside the fluidic channels during the process of the polymer translocation.

## 5.6 Concluding Remarks

Dissipative particle dynamics, as a coarse-grained molecular dynamics method that can be rigorously derived through the Mori-Zwanzig formalism, has been demonstrated to be a powerful and flexible mesoscopic method for simulating the mesoscopic dynamics of complex fluids and various mesoscopic phenomena in soft matter systems. In the past decade, the classical DPD method and its extensions have already been applied successfully to a wide range of problems occurring at the mesoscale. However, there still remain many open questions both in the foundation of DPD and in its applications.

An open question of DPD's foundation is the theoretical derivation of mesoscopic principle from molecular dynamics simulations of unbonded atoms. Unlike bonded atoms in polymers and proteins, unbonded atoms does not move as a group and cannot be packed into a coarse-grained entity. Consequently, the coarse-grained representation of unbonded atoms does not have clear physical definition. Although constraints can be applied to enforce unbonded atoms to move as a group in molecular dynamics simulations for coarse-graining [50, 94], these constraints significantly change the dynamical behavior of the unbonded atoms; hence, these constrained molecular dynamics systems can no longer represent the correct solvents. Therefore, the theoretical derivation of mesoscopic principles for unconstrained and unbonded solvents is an open question.

Another interesting relevant problem of DPD is that memory effects should be included in mesoscopic modeling when the Markovian property breaks down. The classical DPD model was constructed with Gaussian white noise, which assumes that the typical time scales of resolved dynamics and unresolved dynamics are well-separated. However, at small coarse-grained levels, it is expected that the time scale of unresolved dynamics is comparable with that of resolved dynamics, where the correlation of random force cannot simply be replaced by the Dirac delta function. Then, we need to consider non-Markovian dynamics by including memory effects. So far there have been several attempts to include non-Markovian memory into mesoscopic modeling, such as introduction of additional internal variables [104], computing a time-convolution for friction directly [64], using a set of fictitious particles [18], or coupling to the Ornstein-Uhlenbeck process [69].

Finally, DPD application to diverse practical problems requires the development of fast time-evolution algorithms for large-scale simulations and useful boundary methods for modeling biological systems. To this end, many attempts have been made to enhance the capability of DPD simulations. Examples include the open source GPU-accelerated DPD simulators [11, 101] for large-scale simulations, the efficient time-integrators allowing for larger time steps [53, 54], an inflow/outflow boundary method for blood flows [73] and a local detection boundary method for arbitrarily complex geometries [67].

## References

1. E. Abu-Nada, Natural convection heat transfer simulation using energy conservative dissipative particle dynamics. *Phys. Rev. E* **81**(5), 056704 (2010)
2. Y. Afshar, F. Schmid, A. Pishevar, S. Worley, Exploiting seeding of random number generators for efficient domain decomposition parallelization of dissipative particle dynamics. *Comput. Phys. Commun.* **184**(4), 1119–1128 (2013)
3. M.P. Allen, D.J. Tildesley, *Computer Simulation of Liquids* (Clarendon Press, Oxford, 1989)
4. M. Anand, K. Rajagopal, K.R. Rajagopal, A model incorporating some of the mechanical and biochemical factors underlying clot formation and dissolution in flowing blood. *J. Theor. Med.* **5**(3–4), 183–218 (2003)

5. M. Arienti, W.X. Pan, X.Y. Li, G. Karniadakis, Many-body dissipative particle dynamics simulation of liquid/vapor and liquid/solid interactions. *J. Chem. Phys.* **134**(20), 204114 (2011)
6. J.B. Avalos, A.D. Mackie, Dissipative particle dynamics with energy conservation. *Europhys. Lett.* **40**(2), 141–146 (1997)
7. J.A Backer, C.P Lowe, H.C.J Hoefsloot, P.D Iedema, Poiseuille flow to measure the viscosity of particle model fluids. *J. Chem. Phys.* **122**(15), 154503 (2005)
8. R.W. Balluffi, S.M. Allen, W.C. Carter, *Kinetics of Materials* (Wiley, Hoboken, 2005)
9. G. Besold, I. Vattulainen, M. Karttunen, J.M. Polson, Towards better integrators for dissipative particle dynamics simulations. *Phys. Rev. E* **62**(6), R7611–R7614 (2000)
10. X. Bian, S. Litvinov, R. Qian, M. Ellero, N.A. Adams, Multiscale modeling of particle in suspension with smoothed dissipative particle dynamics. *Phys. Fluids* **24**(1), 012002 (2012)
11. A.L. Blumers, Y.-H. Tang, Z. Li, X.J. Li, G.E. Karniadakis, GPU-accelerated red blood cells simulations with transport dissipative particle dynamics. *Comput. Phys. Commun.* **217**, 171–179 (2017)
12. J. Bonet, T.S.L. Lok, Variational and momentum preservation aspects of smooth particle hydrodynamic formulations. *Comput. Methods Appl. Mech. Eng.* **180**(1–2), 97–115 (1999)
13. H. Bow, I.V. Pivkin, M. Diez-Silva, S.J. Goldfless, M. Dao, J.C. Niles, S. Suresh, J. Han, A microfabricated deformability-based flow cytometer with application to malaria. *Lab Chip* **11**, 1065–1073 (2011)
14. H.B. Callen, *Thermodynamics and An Introduction to Thermostatistics* (Wiley, New York, 1985)
15. Z.H. Cao, K. Luo, H.L. Yi, H.P. Tan, Energy conservative dissipative particle dynamics simulation of natural convection in eccentric annulus. *Int. J. Heat Mass Transf.* **65**, 409–422 (2013)
16. H.-Y. Chang, X.J. Li, H. Li, G.E. Karniadakis, MD/DPD multiscale framework for predicting morphology and stresses of red blood cells in health and disease. *PLOS Comput. Biol.* **10**, e1005173 (2016)
17. S. Chien, S. Usami, J.F. Bertles, Abnormal rheology of oxygenated blood in sickle cell anemia. *J. Clin. Invest.* **49**, 623–634 (1970)
18. A. Davtyan, J.F. Dama, G.A. Voth, H.C. Andersen, Dynamic force matching: a method for constructing dynamical coarse-grained models with realistic time dependence. *J. Chem. Phys.* **142**(15), 154104 (2015)
19. M.G. Deng, Z. Li, O. Borodin, G.E. Karniadakis, cDPD: a new dissipative particle dynamics method for modeling electrokinetic phenomena at the mesoscale. *J. Chem. Phys.* **145**(14), 144109 (2016)
20. M.G. Deng, W.X. Pan, G.E. Karniadakis, Anisotropic single-particle dissipative particle dynamics model. *J. Comput. Phys.* **336**, 481–491 (2017)
21. R. Erban, S.J. Chapman, Reactive boundary conditions for stochastic simulations of reaction-diffusion processes. *Phys. Biol.* **4**(1), 16–28 (2007)
22. P. Español, Hydrodynamics from dissipative particle dynamics. *Phys. Rev. E* **52**(2), 1734–1742 (1995)
23. P. Español, Dissipative particle dynamics with energy conservation. *Europhys. Lett.* **40**(6), 631–636 (1997)
24. P. Español, Fluid particle model. *Phys. Rev. E* **57**(3), 2930–2948 (1998)
25. P. Español, M. Revenga, Smoothed dissipative particle dynamics. *Phys. Rev. E* **67**, 026705 (2003)
26. P. Español, P. Warren, Statistical mechanics of dissipative particle dynamics. *Europhys. Lett.* **30**(4), 191–196 (1995)
27. X.J. Fan, N. Phan-Thien, N.T. Yong, X.H. Wu, D. Xu, Microchannel flow of a macromolecular suspension. *Phys. Fluids* **15**(1), 11–21 (2003)
28. D.A. Fedosov, B. Caswell, G.E. Karniadakis, A multiscale red blood cell model with accurate mechanics, rheology, and dynamics. *Biophys. J.* **98**(10), 2215–2225 (2010)

29. D.A. Fedosov, H. Lei, B. Caswell, S. Suresh, G.E. Karniadakis, Multiscale modeling of red blood cell mechanics and blood flow in malaria. *PLoS Comput. Biol.* **7**, e1002270 (2011)
30. D.A. Fedosov, W.X. Pan, B. Caswell, G. Gompper, G.E. Karniadakis, Predicting human blood viscosity in silico. *Proc. Natl. Acad. Sci. USA* **108**(29), 11772–11777 (2011)
31. D.A. Fedosov, B. Caswell, S. Suresh, G.E. Karniadakis, Quantifying the biophysical characteristics of *Plasmodium-falciparum*-parasitized red blood cells in microcirculation. *Proc. Natl. Acad. Sci. USA* **108**, 35–39 (2011)
32. C. Gardiner, *Handbook of Stochastic Methods: For Physics, Chemistry and the Natural Sciences*, 3rd edn. (Springer, New York, 2004)
33. H. Grabert, *Projection Operator Techniques in Nonequilibrium Statistical Mechanics*, vol. 95 (Springer, Berlin/Heidelberg, 1982)
34. R.D. Groot, *Applications of Dissipative Particle Dynamics*. Lecture Notes in Physics, chapter 1, vol. 640 (Springer, Berlin/Heidelberg, 2004), pp. 5–38
35. R.D. Groot, P.B. Warren, Dissipative particle dynamics: bridging the gap between atomistic and mesoscopic simulation. *J. Chem. Phys.* **107**(11), 4423–4435 (1997)
36. J.Y. Guo, X.J. Li, Y. Liu, H.J. Liang, Flow-induced translocation of polymers through a fluidic channel: a dissipative particle dynamics simulation study. *J. Chem. Phys.* **134**(13), 134906 (2011)
37. J.-P. Hansen, I.R. McDonald, *Theory of Simple Liquids, Fourth Edition: With Applications to Soft Matter* (Academic, Amsterdam, 2013)
38. C. Hijón, P. Español, E. Vanden-Eijnden, R. Delgado-Buscalioni, Mori–Zwanzig formalism as a practical computational tool. *Faraday Discuss.* **144**, 301–322 (2010)
39. P.J. Hoogerbrugge, J.M.V.A. Koelman, Simulating microscopic hydrodynamic phenomena with dissipative particle dynamics. *Europhys. Lett.* **19**(3), 155–160 (1992)
40. M.X. Huang, Z.Q. Li, H.X. Guo, The effect of janus nanospheres on the phase separation of immiscible polymer blends via dissipative particle dynamics simulations. *Soft Matter* **8**(25), 6834–6845 (2012)
41. J.H. Irving, J.G. Kirkwood, The statistical mechanical theory of transport processes. IV. The equations of hydrodynamics. *J. Chem. Phys.* **18**(6), 817–829 (1950)
42. D.K. Kaul, H. Xue, Rate of deoxygenation and rheologic behavior of blood in sickle cell anemia. *Blood* **77**, 1353–1361 (1991)
43. T. Kinjo, S.A. Hyodo, Equation of motion for coarse-grained simulation based on microscopic description. *Phys. Rev. E* **75**(5), 051109 (2007)
44. J.M.V.A. Koelman, P.J. Hoogerbrugge, Dynamic simulations of hard-sphere suspensions under steady shear. *Europhys. Lett.* **21**(3), 363–368 (1993)
45. J. Kordilla, W.X. Pan, A. Tartakovsky, Smoothed particle hydrodynamics model for Landau-Lifshitz-Navier-Stokes and advection-diffusion equations. *J. Chem. Phys.* **141**, 224112 (2014)
46. L.D. Landau, E.M. Lifshitz, *Fluid Mechanics (Volume 6 of A Course of Theoretical Physics)* (Pergamon Press, New York, 1959)
47. A.W. Lees, S.F. Edwards, The computer study of transport processes under extreme conditions. *J. Phys. C: Solid State Phys.* **5**(15), 1921–1929 (1972)
48. H. Lei, G.E. Karniadakis, Quantifying the rheological and hemodynamic characteristics of sickle cell anemia. *Biophys. J.* **102**, 185–194 (2012)
49. H. Lei, G.E. Karniadakis, Probing vasoocclusion phenomena in sickle cell anemia via mesoscopic simulations. *Proc. Natl. Acad. Sci. USA* **110**(28), 11326–11330 (2013)
50. H. Lei, B. Caswell, G.E. Karniadakis, Direct construction of mesoscopic models from microscopic simulations. *Phys. Rev. E* **81**(2), 026704 (2010)
51. H. Lei, D.A. Fedosov, B. Caswell, G.E. Karniadakis, Blood flow in small tubes: quantifying the transition to the non-continuum regime. *J. Fluid Mech.* **722**, 214–239 (2013)
52. H. Lei, X. Yang, Z. Li, G.E. Karniadakis, Systematic parameter inference in stochastic mesoscopic modeling. *J. Comput. Phys.* **330**, 571–593 (2017)
53. B. Leimkuhler, X.C. Shang, On the numerical treatment of dissipative particle dynamics and related systems. *J. Comput. Phys.* **280**, 72–95 (2015)

54. B. Leimkuhler, X.C. Shang, Pairwise adaptive thermostats for improved accuracy and stability in dissipative particle dynamics. *J. Comput. Phys.* **324**, 174–193 (2016)
55. H. Li, G. Lykotrafitis, A coarse-grain molecular dynamics model for sickle hemoglobin fibers. *J. Mech. Behav. Biomed.* **4**(2), 162–173 (2011)
56. H. Li, G. Lykotrafitis, Two-component coarse-grained molecular-dynamics model for the human erythrocyte membrane. *Biophys. J.* **102**(1), 75–84 (2012)
57. X.J. Li, A.S. Popel, G.E. Karniadakis, Blood-plasma separation in Y-shaped bifurcating microfluidic channels: a dissipative particle dynamics simulation study. *Phys. Biol.* **9**(2), 026010 (2012)
58. Z. Li, Z. W. Zhou, G.H. Hu, Dissipative particle dynamics simulation of droplet oscillations in AC electrowetting. *J. Adhes. Sci. Technol.* **26**(12–17), 1883–1895 (2012)
59. H. Li, V. Ha, G. Lykotrafitis, Modeling sickle hemoglobin fibers as one chain of coarse-grained particles. *J. Biomech.* **45**(11), 1947–1951 (2012)
60. Z. Li, G.H. Hu, Z.L. Wang, Y.B. Ma, Z.W. Zhou, Three dimensional flow structures in a moving droplet on substrate: a dissipative particle dynamics study. *Phys. Fluids* **25**(7), 072103 (2013)
61. Z. Li, X. Bian, B. Caswell, G.E. Karniadakis, Construction of dissipative particle dynamics models for complex fluids via the Mori–Zwanzig formulation. *Soft Matter* **10**(43), 8659–8672 (2014)
62. Z. Li, Y.-H. Tang, H. Lei, B. Caswell, G.E. Karniadakis, Energy-conserving dissipative particle dynamics with temperature-dependent properties. *J. Comput. Phys.* **265**, 113–127 (2014)
63. X.J. Li, Z.L. Peng, H. Lei, M. Dao, G.E. Karniadakis, Probing red blood cell mechanics, rheology and dynamics with a two-component multiscale model. *Phil. Trans. R. Soc. A* **372**, 20130389 (2014)
64. Z. Li, X. Bian, X.T. Li, G.E. Karniadakis, Incorporation of memory effects in coarse-grained modeling via the Mori–Zwanzig formalism. *J. Chem. Phys.* **143**(24), 243128 (2015)
65. Z. Li, Y.-H. Tang, X.J. Li, G.E. Karniadakis, Mesoscale modeling of phase transition dynamics of thermoresponsive polymers. *Chem. Commun.* **51**(55), 11038–11040 (2015)
66. Z. Li, A. Yazdani, A. Tartakovsky, G.E. Karniadakis, Transport dissipative particle dynamics model for mesoscopic advection-diffusion-reaction problems. *J. Chem. Phys.* **143**(1), 014101 (2015)
67. Z. Li, X. Bian, Y.-H. Tang, G.E. Karniadakis, A dissipative particle dynamics method for arbitrarily complex geometries. arXiv preprint arXiv:1612.08761 (2016)
68. X.J. Li, E. Du, H. Lei, Y.-H. Tang, M. Dao, S. Suresh, G.E. Karniadakis, Patient-specific blood rheology in sickle-cell anaemia. *Interface Focus* **6**(1), 20150065 (2016)
69. Z. Li, H.S. Lee, E. Darve, G.E. Karniadakis, Computing the non-Markovian coarse-grained interactions derived from the Mori–Zwanzig formalism in molecular systems: application to polymer melts. *J. Chem. Phys.* **146**(1), 014104 (2017)
70. M. Lissal, J.K. Brennan, Alignment of lamellar diblock copolymer phases under shear: insight from dissipative particle dynamics simulations. *Langmuir* **23**(9), 4809–4818 (2007)
71. M.B. Liu, G.R. Liu, L.W. Zhou, J.Z. Chang, Dissipative particle dynamics (DPD): an overview and recent developments. *Arch. Comput. Meth. Eng.* **22**(4), 529–556 (2015)
72. Z.Y. Lu, Y.M. Wang, *An Introduction to Dissipative Particle Dynamics*. Methods in Molecular Biology, chap. 24, vol. 924 (Humana Press, New York, 2013), pp. 617–633
73. K. Lykov, X.J. Li, H. Lei, I.V. Pivkin, G.E. Karniadakis, Inflow/outflow boundary conditions for particle-based blood flow simulations: application to arterial bifurcations and trees. *PLoS Comput. Biol.* **11**(8), e1004410 (2015)
74. A.D. Mackie, J.B. Avalos, V. Navas, Dissipative particle dynamics with energy conservation: modelling of heat flow. *Phys. Chem. Chem. Phys.* **1**(9), 2039–2049 (1999)
75. C.A. Marsh, J.M. Yeomans, Dissipative particle dynamics: the equilibrium for finite time steps. *Europhys. Lett.* **37**(8), 511–516 (1997)
76. C.A. Marsh, G. Backx, M.H. Ernst, Fokker-Planck-Boltzmann equation for dissipative particle dynamics. *Europhys. Lett.* **38**(6), 411–415 (1997)



77. C.A. Marsh, G. Backx, M.H. Ernst, Static and dynamic properties of dissipative particle dynamics. *Phys. Rev. E* **56**(2), 1676–1691 (1997)
78. Z.G. Mills, W.B. Mao, A. Alexeev, Mesoscale modeling: solving complex flows in biology and biotechnology. *Trends Biotechnol.* **31**(7), 426–434 (2013)
79. J.J. Monaghan, Smoothed particle hydrodynamics. *Rep. Prog. Phys.* **68**(8), 1703–1759 (2005)
80. H. Mori, Transport, collective motion, and Brownian motion. *Prog. Theor. Phys.* **33**(3), 423–455 (1965)
81. S.V. Nikolov, H. Shum, A.C. Balazs, A. Alexeev, Computational design of microscopic swimmers and capsules: from directed motion to collective behavior. *Curr. Opin. Colloid Interface Sci.* **21**, 44–56 (2016)
82. W.G. Noid, Perspective: coarse-grained models for biomolecular systems. *J. Chem. Phys.* **139**, 090901 (2013)
83. J.M. Ortiz de Zárate, J.V. Sengers, *Hydrodynamic Fluctuations in Fluids and Fluid Mixtures* (Elsevier, Amsterdam, 2006)
84. H.C. Öttinger, *Beyond Equilibrium Thermodynamics* (Wiley-Interscience, New York, 2005)
85. I. Pagonabarraga, D. Frenkel, Dissipative particle dynamics for interacting systems. *J. Chem. Phys.* **115**(11), 5015–5026 (2001)
86. W.X. Pan, I.V. Pivkin, G.E. Karniadakis, Single-particle hydrodynamics in DPD: a new formulation. *Europhys. Lett.* **84**(1), 10012 (2008)
87. D.Y. Pan, J.X. Hu, X.M. Shao, Lees-Edwards boundary condition for simulation of polymer suspension with dissipative particle dynamics method. *Mol. Simul.* **42**(4), 328–336 (2016)
88. N. Phan-Thien, N. Mai-Duy, B.C. Khoo, A spring model for suspended particles in dissipative particle dynamics. *J. Rheol.* **58**(4), 839–867 (2014)
89. C.L. Phillips, J.A. Anderson, S.C. Glotzer, Pseudo-random number generation for Brownian dynamics and dissipative particle dynamics simulations on GPU devices. *J. Comput. Phys.* **230**(19), 7191–7201 (2011)
90. I.V. Pivkin, G.E. Karniadakis, A new method to impose no-slip boundary conditions in dissipative particle dynamics. *J. Comput. Phys.* **207**(1), 114–128 (2005)
91. I.V. Pivkin, G.E. Karniadakis, Controlling density fluctuations in wall-bounded dissipative particle dynamics systems. *Phys. Rev. Lett.* **96**, 206001 (2006)
92. I.V. Pivkin, G.E. Karniadakis, Accurate coarse-grained modeling of red blood cells. *Phys. Rev. Lett.* **101**, 118105 (2008)
93. I.V. Pivkin, Z. Peng, G.E. Karniadakis, P.A. Buffet, M. Dao, S. Suresh, Biomechanics of red blood cells in human spleen and consequences for physiology and disease. *Proc. Natl. Acad. Sci. USA* **113**(28), 7804–7809 (2016)
94. M. Praprotnik, L.D. Site, K. Kremer, Adaptive resolution scheme for efficient hybrid atomistic-mesoscale molecular dynamics simulations of dense liquids. *Phys. Rev. E* **73**, 066701 (2006)
95. R. Qiao, P. He, Simulation of heat conduction in nanocomposite using energy-conserving dissipative particle dynamics. *Mol. Simul.* **33**(8), 677–683 (2007)
96. M. Ripoll, P. Español, M.H. Ernst, Dissipative particle dynamics with energy conservation: heat conduction. *Int. J. Mod. Phys. C* **9**(8), 1329–1338 (1998)
97. D. Rossinelli, Y.-H. Tang, K. Lykov, D. Alexeev, M. Bernaschi, P. Hadjidoukas, M. Bisson, W. Joubert, C. Conti, G. Karniadakis, M. Fatica, I. Pivkin, P. Koumoutsakos, The in-silico lab-on-a-chip: petascale and high-throughput simulations of microfluidics at cell resolution, in *Proceedings of the International Conference for High Performance Computing, Networking, Storage and Analysis, SC '15* (Association for Computing Machinery, New York, 2015), pp. 2:1–2:12
98. M.G. Saunders, G.A. Voth, Coarse-graining methods for computational biology. *Annu. Rev. Biophys.* **42**, 73–93 (2013)
99. T. Shardlow, Splitting for dissipative particle dynamics. *SIAM J. Sci. Comput.* **24**(4), 1267–1282 (2003)

100. V. Symeonidis, G.E. Karniadakis, B. Caswell, Dissipative particle dynamics simulations of polymer chains: scaling laws and shearing response compared to dna experiments. *Phys. Rev. Lett.* **95**, 076001 (2005)
101. Y.-H. Tang, G.E. Karniadakis, Accelerating dissipative particle dynamics simulations on GPUs: algorithms, numerics and applications. *Comput. Phys. Commun.* **185**(11), 2809–2822 (2014)
102. Y.-H. Tang, Z. Li, X.J. Li, M.G. Deng, G.E. Karniadakis, Non-equilibrium dynamics of vesicles and micelles by self-assembly of block copolymers with double thermoresponsivity. *Macromolecules* **49**(7), 2895–2903 (2016)
103. A. Tiwari, J. Abraham, Dissipative particle dynamics model for two-phase flows. *Phys. Rev. E* **74**, 056701 (2006)
104. A. Vázquez-Quesada, M. Ellero, P. Español, Smoothed particle hydrodynamic model for viscoelastic fluids with thermal fluctuations. *Phys. Rev. E* **79**, 056707 (2009)
105. Y.X. Wang, S. Chen, Numerical study on droplet sliding across micropillars. *Langmuir* **31**(16), 4673–4677 (2015)
106. P.B. Warren, Vapor-liquid coexistence in many-body dissipative particle dynamics. *Phys. Rev. E* **68**, 066702 (2003)
107. C.M. Wijmans, B. Smit, Simulating tethered polymer layers in shear flow with the dissipative particle dynamics technique. *Macromolecules* **35**(18), 7138–7148 (2002)
108. S.M. Willemsen, H.C.J. Hoefsloot, P.D. Iedema, No-slip boundary condition in dissipative particle dynamics. *Int. J. Mod. Phys. C* **11**(5), 881–890 (2000)
109. T. Ye, N. Phan-Thien, B. Khoo, C.T. Lim, Numerical modelling of a healthy/malaria-infected erythrocyte in shear flow using dissipative particle dynamics method. *J. Appl. Phys.* **115**(22), 224701 (2014)
110. S. Yip, M.P. Short, Multiscale materials modelling at the mesoscale. *Nat. Mater.* **12**(9), 774–777 (2013)
111. R. Zwanzig, Ensemble method in the theory of irreversibility. *J. Chem. Phys.* **33**(5), 1338–1341 (1960)
112. R. Zwanzig, Memory effects in irreversible thermodynamics. *Phys. Rev.* **124**(4), 983–992 (1961)
113. R. Zwanzig, *Nonequilibrium Statistical Mechanics*, vol. 54 (Oxford University Press, Oxford, 2001)

# Chapter 6

## Numerical Methods for Dispersed Multiphase Flows

M. Sommerfeld

**Abstract** This article gives an overview of numerical methods for the calculation of dispersed multi-phase flows. At the beginning, a brief introduction is given on the different flow regimes observed for multi-phase flows in general. Then a characterisation and classification of dispersed multi-phase flows is introduced based on inter-particle spacing and volume fraction. As an introduction to the subject, the numerical methods used for single-phase flows are briefly described based on the turbulent scales being resolved by the numerical grid. Since even dispersed multi-phase flows are extremely complex, the hierarchy of the different numerical methods is highlighted ranging from macro-scale numerical simulations for an entire industrial process down to micro-scale simulations required for analysing particle scale phenomena. Due to constraints in computational power and storage availability, macro-scale simulations can only be done with a limited grid resolution and the assumption of particles being treated as point-masses. Consequently, all transport phenomena occurring on scales smaller than the grid cell and on the scale of the particle have to be considered through additional closures and models. Therefore, essential elements in this multi-scale problem are direct numerical simulations that fully resolve the particles and the flow around them. The different methods for such resolved simulations are briefly described. The major part of this article is focused on the modelling of dispersed multi-phase flows relying on the point-particle assumption. The multi-fluid method or Euler/Euler model is briefly described in order to demark its applicability and limitations. The hybrid Euler/Lagrange approach based on tracking a large number of point particles and its different variants are introduced in more detail, emphasising the two-way coupling approaches for unsteady flows. The importance of accurately modelling particle-scale phenomena is highlighted and an estimate for the significance of particle-wall and inter-particle collisions is given. Finally, three application examples are introduced, emphasising the potential of Euler/Lagrange simulations. For a particle-laden swirling flow the semi-unsteady approach is used for analysing unsteady particle roping phenomena. The simulations of particle

---

M. Sommerfeld (✉)

Institut für Verfahrenstechnik, Otto-von-Guericke Universität (OvGU) Magdeburg,  
Zeppelinstraße 1, 06130 Halle (Saale), Germany  
e-mail: [martin.sommerfeld@ovgu.de](mailto:martin.sommerfeld@ovgu.de)

suspension in a stirred vessel highlight the importance of inter-particle collisions even at relatively low volume fractions up to 5%. Finally, it is demonstrated that the Euler/Lagrange approach may also be used to study an industrial filtration process where it allows the prediction of particle deposits and filter cake formation. In this respect extensions are possible which provide more information on the internal filter cake structure.

**Keywords** Application examples • Characterisation of multi-phase flows • Dispersed multi-phase flows • DNS • Euler/Euler method • Euler/Lagrange approach • Filter cake formation • Fluid particles • Four-way coupling • Horizontal blade filter • Inter-particle collisions • LES • Modelling dispersed flows • Modelling particle-scale phenomena • Multi-scale effects • Numerical methods • Particle deposition • Particle dispersion in stirred vessel • Point-particle approximation • RANS • Resolved particle-scale simulations • Rigid particles • Two-way coupling • Turbulence modelling • Unsteady swirling flow • Wall collisions

**MSC2010:** 76F25, 76F65, 76T10, 76T15, 76T20, 82C22, 97R20, 82C80, 70S05

## 6.1 Introduction to Multi-Phase Flows

The simultaneous presence of several different phases in external or internal flows consisting of combinations of gas, liquid and solid is found in daily life, environment and numerous industrial processes. These types of flows are termed multi-phase flows, which may exist in different forms depending on the respective phase distribution. Examples are gas-liquid transportation, crude oil recovery, spray cans, sediment transport in rivers, pollutant transport in the atmosphere, cloud formation, fuel injection in engines, bubble column reactors, mixing vessels and spray driers for food processing, to name only a few. This demonstrates the huge importance of multi-phase flows, which might occur even more frequently than single-phase flows. Because of the interactions between the different phases, such flows are rather complicated and very difficult to describe theoretically. For the design and optimisation of such multi-phase systems, a detailed understanding of the interfacial transport phenomena is essential. For single-phase flows, computational fluid dynamics (CFD) already has a long history and nowadays is standard in the developments for aeronautical and automotive industries using different commercially available CFD-tools. Due to the complex physics involved in multi-phase flow, the application of CFD in this area is rather young (probably 30–40 years). The different methods applied for the numerical calculation of multi-phase flows are summarised below. This chapter is devoted first to the classification of multi-phase flows and their characterisation by integral properties in order to provide an idea of their complexity.

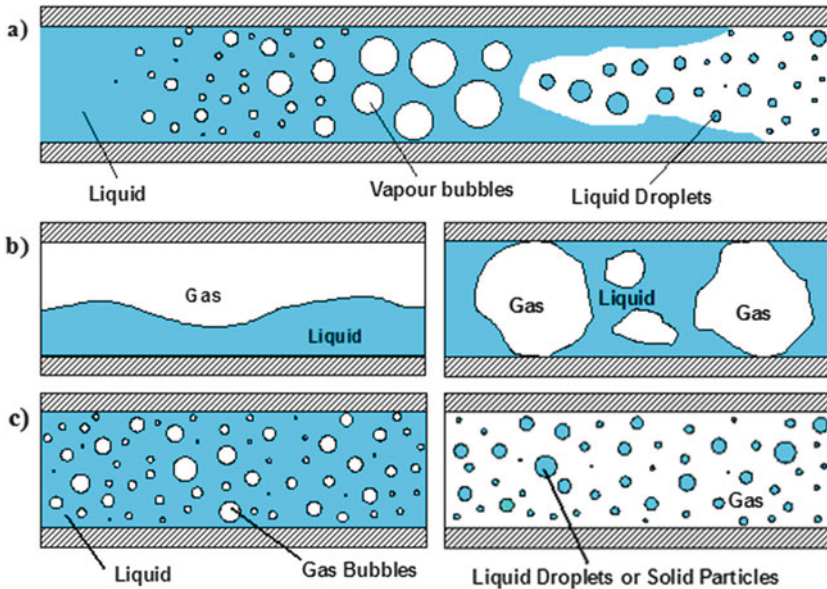


**Fig. 6.1** Different regimes of two-phase flows, (a) transient two-phase flow with transition from liquid to vapour flow, (b) separated or segregated two-phase flow with large regions of gas, (c) dispersed two-phase flow with gas bubbles (or liquid droplets) dispersed in a liquid or solid particles or droplets dispersed in gas

Multi-phase flows may be encountered in various forms in industrial practice and technology depending on the involved phases (Fig. 6.1). These are, exemplarily, transitional flows with development from pure liquid to a vapour flow as a result of external heating (e.g. heat pipe), separated or segregated flows (i.e. stratified flows, slug flows, or annular flows), and dispersed two-phase flows where one phase is present in the form of particles, droplets, or bubbles dispersed in a continuous carrier phase (i.e. gas or liquid). Note that in the following the term particles will be often used also for droplets and bubbles. In all these different types of multi-phase flows, different interfacial transport mechanisms are relevant. Consequently, the application of different numerical approaches is required. Transient multi-phase flows may be found in steam generators of boilers, where the heat addition results in nucleation and the formation of dispersed vapour bubbles, which further grow in size and will coalesce, yielding larger vapour slugs and eventually a pure vapour flow is established. Further evaporation results in annular two-phase flow with small droplets being dispersed in the core region of the pipe. Stratified and slug flows are for example found in transportation pipes for crude oil recovery or other liquids, where the observed flow regime depends of course on the superficial velocities and also on the orientation of the pipelines, e.g. horizontal, vertical or inclined (see for example [44]). This kind of gas liquid flows may also be highly unsteady.

**Table 6.1** Summary of two-phase flow systems and important industrial and technical processes

Continuous-dispersed phase	Industrial and technical application
Gas-solid flows	Pneumatic conveying, particle separation in cyclones and filters, fluidised beds
Liquid-solid flows	Hydraulic conveying, liquid-solid separation, particle dispersion in stirred vessels
Gas-droplet flows	Spray drying, spray cooling, spray painting, spray scrubbers
Liquid-droplet flows	Mixing of immiscible liquids, liquid-liquid extraction
Liquid-gas flows	Bubble columns, aeration of sewage water, flotation

Dispersed two-phase flows are encountered in numerous technical and industrial processes, as for example in particle technology (i.e. production and transportation of solid particles), chemical engineering, and biotechnology. Dispersed two-phase flows may be classified in terms of the different phases being present as summarised in Table 6.1 together with some of the most important industrial processes.

Additionally, numerous processes may involve more than one dispersed phase (i.e. multi-phase flows), as for example in a spray scrubber where droplets and solid particles are dispersed in a gas flow and the aim is collecting the particles by the droplets through collisions. Another example is a bubble column reactor with catalyst particles.

In dispersed two-phase flows the transport of the particles by the fluid phase and their response is essential. Depending on the concentration of particles this transport will be affected by fluid dynamic interactions, collisions and other phenomena as for example coalescence of droplets or bubbles and agglomeration of particles. These issues will be discussed below, focusing on dispersed two-phase flows only.

## 6.2 Characterisation of Dispersed Multi-Phase Flows

For the characterisation of dispersed two-phase flows different integral properties are used, which are briefly summarised below (see for example [17]). The volume fraction of the dispersed phase is the volume occupied by particles, droplets or bubbles in a unit volume. Hence, this property is given by:

$$\alpha_p = \frac{\sum_i N_i V_{P_i}}{V} \quad (6.1)$$

where  $N_i$  is the number of all particles in the size fraction  $i$ , having the particle volume  $V_{P_i} = \pi D_{P_i}^3/6$ . The particle diameter  $D_{P_i}$  in this context is the volume equivalent diameter of a sphere in case non-spherical particles are considered. Note that several volume fractions may be defined depending on the number of dispersed phases. Since the sum of the volume fraction of the dispersed phases and the

continuous phase is unity, the continuous phase volume fraction is:

$$\alpha_F = 1 - \sum_n \alpha_{p,n} \quad (6.2)$$

The bulk density or mass concentration of the dispersed phase is the mass of particles per unit volume and hence given by:

$$\sigma_p = c_p = \frac{m_{p,tot}}{V} = \alpha_p \rho_p \quad (6.3)$$

where  $\rho_p$  is the particle density, i.e. particle weight divided by its volume. Here one has to distinguish between particle density  $\rho_p$  and particle material density  $\rho_s$  (index  $s$  for solid) which is of course different for porous particles (i.e.  $\rho_p < \rho_s$ ). Correspondingly, the bulk density of the continuous phase is:

$$\sigma_F = (1 - \alpha_p) \rho_F \quad (6.4)$$

The sum of both bulk densities is called mixture density:

$$\rho_m = \sigma_F + \sigma_p = (1 - \alpha_p) \rho_F + \alpha_p \rho_p \quad (6.5)$$

Often the particle concentration is also expressed by the number of particles per unit volume, as for example in clean-room technology:

$$n_p = \frac{N_p}{V} \quad (6.6)$$

Especially in gas-solid flows for example in pneumatic conveying the mass loading is frequently used, which is defined as the total mass flux of the dispersed phase to that of the fluid phase:

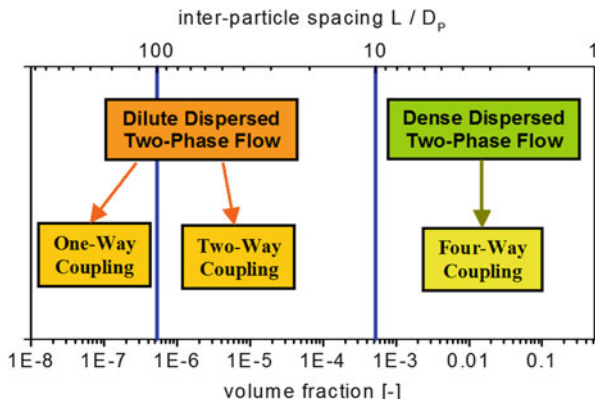
$$\eta = \frac{\dot{m}_p}{\dot{m}_F} = \frac{\alpha_p \rho_p U_p}{(1 - \alpha_p) \rho_F U_F}, \quad (6.7)$$

where  $\dot{m}_p$  is the dispersed phase mass flow rate and  $\dot{m}_F$  the continuous mass flow rate, both in [kg/s]. The velocities for particles  $U_p$  and fluid  $U_F$  are averaged velocities in a considered cross-section. The mass fraction is the mass of one component divided by the total mass of the system.

The mass flux is defined as the mass of particles flowing through a unit area per unit time. It should be noted that the mass flux is a vector quantity (i.e. a mass flux can be defined for each velocity direction) which therefore also can be defined as a local property.

The proximity of particles in a two-phase flow system may be estimated from the inter-particle spacing, which can be easily determined for regular arrangements of the particles. For a cubic arrangement, the inter-particle spacing, i.e. the distance

**Fig. 6.2** Regimes of dispersed two-phase flows as a function of particle volume fraction and inter-particle spacing for a regular cubic arrangement of particles and coupling regimes



between the centres of particles, is obtained from the definition of the volume fraction [119]:

$$\frac{L}{D_p} = \left( \frac{\pi}{6\alpha_p} \right)^{1/3} \tag{6.8}$$

The result is depicted in Fig. 6.2 by comparing inter-particle spacing and dispersed phase volume fraction. For a volume fraction of 1% the spacing is 3.74 diameters and for 10% only 1.74. Hence, for such high volume fractions the particles cannot be treated to move isolated, since fluid dynamic interactions become of importance. In many practical fluid-particle systems however, the particle volume fraction is much lower. Consider for example a gas-solid flow (particle density  $\rho_p = 2500 \text{ kg/m}^3$ , gas density of  $\rho_f = 1.18 \text{ kg/m}^3$ ) with a mass loading of one (i.e.  $\eta = 1$ ) and assume no slip between the phases, then the volume fraction is about 0.05% (i.e.  $\alpha_p = 5 \times 10^{-4}$ ). This results in an inter-particle spacing of about 10 particle diameters; hence, under such a condition a fluid dynamic interaction may be neglected. In industrial bubble columns the gas volume fraction can have values of 40% or even more. This yields an inter-bubble spacing of 1.1 bubble diameters and will in such a highly turbulent flow result in a large collision rate and hence bubble coalescence will occur.

Elghobashi [28] suggested a classification of dispersed two-phase flows concerning the importance of interaction mechanisms and turbulence modulation (dissipation or enhancement by the particles). Generally, one may distinguish between dilute and dense two-phase flows as mentioned above (Fig. 6.2) and shown in Fig. 6.3. A two-phase system may be regarded as dilute for volume fractions up to  $\alpha_p = 5 \times 10^{-4}$  (i.e.  $L/D_p \approx 10$ ). In this regime, the influence of the particle phase on the fluid flow may be however only neglected for  $\alpha_p < 5 \times 10^{-7}$  (i.e.  $L/D_p \approx 100$ ). This regime is termed one-way coupling where the particles are transported by the flow, but have no remarkable influence on the flow (i.e. mean flow and turbulence). For higher volume fractions the influence of the particles on the fluid flow, which



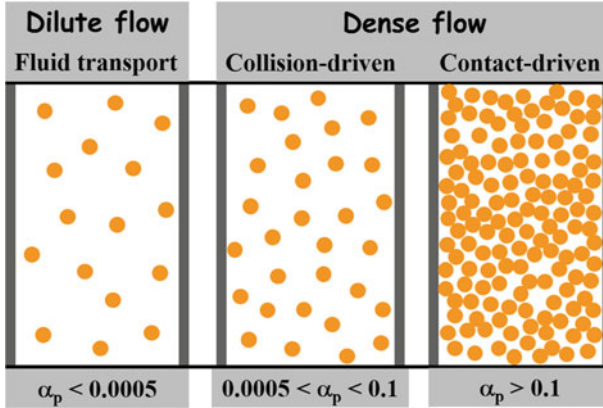


**Fig. 6.3** Regimes of dispersed two-phase flows in terms of transport phenomena; *left*: dilute flow dominated by fluid-dynamic transport of particles, inter-particle spacing larger than 10 (see Fig. 6.2); *middle*: dense flow regime dominated by inter-particle collision with inter-particle spacing between 2 and 10; *right*: dense flow regime that is particle contact dominated with averaged inter-particle spacing less than 2

is often referred to as two-way coupling, needs to be accounted for. In the dilute regime, fluid dynamic forces and possibly existing external forces dominate the transport of particles in a flow (see Fig. 6.3 left). Thereupon, interactions between particles (i.e. collisions and fluid dynamic interactions between particles) become of importance in the dense regime (i.e. for  $\alpha_p > 5 \times 10^{-4}$ ,  $L/D_p \approx 10$ ). Hence, this regime is characterised by the so-called four-way coupling, which comprises fluid-dynamic interactions and collisions between the particles (Fig. 6.3 middle). Three-way coupling is only associated with fluid-dynamic interactions between particles (Chap. 13 in [15]). Such a mode however may be difficult to observe since relative particle motion always is associated with collisions. With further increasing solid volume fraction the importance of interactions among particles is becoming more and more dominant in comparison to the fluid dynamic transport. Eventually, the contact-dominated regime is reached at very high volume fractions, i.e.  $\alpha_p > 0.1$  [17]. It should be noted that also contact dominated flows with solid particles are referred to as dispersed two-phase flows as for example occurring in dense fluidised beds. The maximum attainable particle volume fraction of systems with mono-sized spherical particles is depending on their packing structure, i.e. cubic packing:  $\alpha_p = 0.524$ ; hexagonal packing  $\alpha_p = 0.605$ , tetragonal packing  $\alpha_p = 0.698$  and rhombohedral packing  $\alpha_p = 0.74$ .

The particle velocity or momentum response time is very important for characterising the capability of particles to follow sudden velocity changes in fluid flows, occurring for example in flows with curvature, large scale vortex structures [124] or turbulent eddies. In order to derive the particle response time the equation of motion

(Newton's law of motion) is used by only considering the drag force:

$$m_p \frac{du_p}{dt} = \frac{\rho_F \pi}{2} D_p^2 C_D |u_F - u_p| (u_F - u_p) \quad (6.9)$$

where  $m_p$ ,  $u_p$  and  $D_p$  are the particle properties, mass, velocity and diameter,  $\rho_F$  and  $u_F$  are fluid density and velocity. The drag coefficient  $C_D$  in dependence of the particle Reynolds number, defined as the ratio of inertial force to viscous force ( $\mu_F$  is the dynamic viscosity),

$$Re_p = \frac{\rho_F D_p (u_F - u_p)}{\mu_F} \quad (6.10)$$

is obtained by the correlation of Schiller and Naumann [90], which fits the experimental data up to a particle Reynolds number of  $Re_p = 1000$  reasonably well:

$$C_D = \frac{24}{Re_p} (1 + 0.15 Re_p^{0.687}) = \frac{24}{Re_p} f_D \quad (6.11)$$

In the Newton regime between  $1000 < Re_p < 2.5 \times 10^5$  the drag coefficient is almost constant with  $C_D \approx 0.44$ .

Dividing by the particle mass and introducing the particle Reynolds number gives:

$$\frac{du_p}{dt} = \frac{18 \mu_F C_D Re_p}{\rho_p D_p^2 24} (u_F - u_p) \quad (6.12)$$

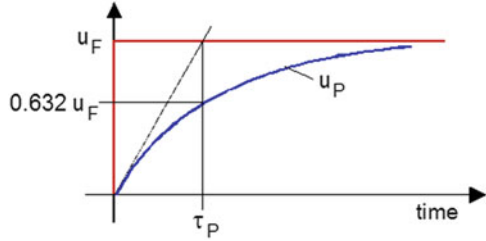
The term  $C_D Re_p / 24$  corresponds to the non-linear term in the drag coefficient  $f_D$  (Eq. (6.11)) and the first term of Eq. (6.12) has the dimension of a reciprocal time, the particle response time:

$$\tau_p = \frac{\rho_p D_p^2}{18 \mu_F f_D} \quad (6.13)$$

This time scale shall be mainly used for particle-laden gas flows where the particle to fluid density is rather high. In other situations as for example liquid flows with solid particles, droplets or bubbles where the fluid to particle density ratio is much smaller the particle response time scale has to be extended with an added mass term and one obtains:

$$\tau_B = \frac{(\rho_B + 0.5 \rho_F) D_B^2}{18 \mu_F f_D} \quad (6.14)$$

**Fig. 6.4** Graphical illustration of the particle response time, a sudden fluid velocity jump of  $u_F$  accelerates the particle until the fluid velocity is reached



Hence, the equation of motion becomes:

$$\frac{du_p}{dt} = \frac{1}{\tau_p}(u_F - u_p) \quad (6.15)$$

The solution of this equation for a simplified case, namely a jump of the fluid velocity from zero to  $u_F$  and an initial particle velocity of zero is:

$$u_p = u_F \left( 1 - \exp\left(-\frac{t}{\tau_p}\right) \right) \quad (6.16)$$

From this equation, it is obvious that  $\tau_p$  is the time required for a particle, released with zero velocity into a flow with  $u_F$ , to reach 63.2% of the flow velocity as illustrated in Fig. 6.4.

In the Stokes-regime  $Re_p < 1$ , where  $f_D$  is unity, the response time for solid particles in air becomes:

$$\tau_p = \frac{\rho_p D_p^2}{18\mu} \quad (6.17)$$

The Stokes number is the ratio of the particle response time to a characteristic time scale of the flow or a system time scale and characterises the particle response behaviour:

$$St = \frac{\tau_p}{\tau_f} \quad (6.18)$$

Considering particle motion in a turbulence field the fluid flow time scale corresponds to the time scale of the energetic eddies, i.e. the integral time scale of turbulence,  $T_L \approx k/\varepsilon$  (where  $k$  is the turbulent kinetic energy and  $\varepsilon$  its dissipation rate). In the case of particle motion in large scale vortices (occurring for example in a shear layer) the eddy passage time across a fixed point in space is the relevant fluid time scale [124]. Here it was shown that particles with  $St < 1$  follow the vortex structure very well and are almost homogeneously distributed. On the other hand, very inertial particles,  $St \gg 1$ , are not able to respond to the fluid flow and

pass almost straight through the vortices. Particles with  $St \approx 1$  accumulate near the edges of the vortices due to increasing importance of inertial effects. For particles with  $St \approx 1$  the effect of particle accumulation (or preferential concentration) in regions of low vorticity and high strain rates of turbulent flows was observed (see for example [31, 120]).

### 6.3 Numerical Approaches for Single-Phase Flows

The numerical calculation of single-phase flows may be broadly separated into three classes depending on their spatial resolution as illustrated in Fig. 6.5. An introduction to these methods may be found in [35] together with details about discretisation schemes and solution procedures. The first approach, Direct Numerical Simulations (DNS) should resolve all relevant flow scales down to the Kolmogorov-scales (i.e. the dissipation scales). Consequently, the numerical grid should be smaller than this scale to ensure a proper resolution. This however implies that the size of the computational domain is limited due to the restricted number of

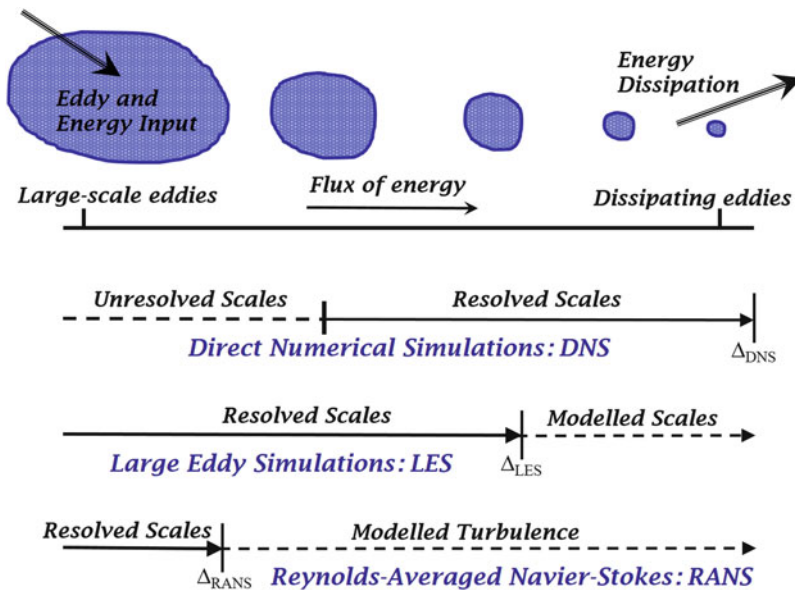


**Fig. 6.5** Numerical methods (CFD) for turbulent single-phase flows indicating the respective resolution of eddies and turbulence; the spectrum of eddies ranges from the system induced large scales down to the Kolmogorov scales; direct numerical simulations (DNS) resolving the small turbulent scales up to the large scales in the order of the domain size; large eddy simulations (LES) resolving all scales up to the dissipation length scale (filter size); calculations based on Reynolds-averaged Navier-Stokes (RANS) equations resolving only large-scale structures, small scales are described by turbulence models (introduced by Bakker [3])

numerical control volumes that can be handled by today's computers. Consequently, DNS is not able to resolve the entire spectrum of vortex scales or wave numbers and hence there is a cut-off at larger scales. Moreover, the ratio of macro-scale vortices to the Kolmogorov-scale is proportional to  $Re^{3/4}$ . As a result, also the flow Reynolds number which may be considered in DNS has a limitation; typically the maximum is between 5000 and 10,000. Therefore, the application of DNS is limited to simple flow conditions, such as, homogeneous isotropic turbulence, shear flows and channel or pipe flows. Nevertheless, DNS is very helpful in analysing and understanding basic phenomena in turbulence research.

The second class of numerical methods, which is rapidly growing in importance, are Large Eddy Simulations (LES) where the filtered Navier-Stokes equations are solved (Fig. 6.5). Hence, the numerical grid may be much coarser compared to DNS, however, requiring a sub-grid-scale (SGS) turbulence model. With such a coarse grid also processes with larger dimensions can be simulated which may be even very close to industrial or technical scale. Hence, the vortex spectrum is fully resolved except for the dissipation regime (i.e. Kolmogorov-scale). These unresolved scales (SGS) are however close to being isotropic and therefore require only quite simple turbulence modelling (see for example [37, 62]).

The third class of numerical methods is based on the Reynolds-averaged Navier-Stokes (RANS) equations combined with an appropriate turbulence model. A number of turbulence models have been developed in the past [133] with a variety of derivatives and improvements. Most of them are based on the solution of additional transport equations such as the well-known two-equation  $k - \varepsilon$  and  $k - \omega$  turbulence models, as well as the full Reynold-stress turbulence model. A turbulence model is based on the integration of the entire energy spectrum. The  $k - \varepsilon$  model solves additional transport equations for the turbulent kinetic energy  $k$  and its dissipation rate  $\varepsilon$  which is related to the Kolmogorov scale. These values provide the turbulent viscosity that is introduced in the transport equations. In the Reynolds stress model 7 additional transport equations have to be solved, making this method more complex and sometimes it is difficult to obtain converged results. However, such an approach is suggested for complex anisotropic flows, such as swirling flows in combustors or cyclones or flows with recirculations and separations.

## 6.4 Hierarchy of Numerical Methods for Multi-Phase Flows

From the introduction the complexity of multi-phase flows became obvious. Therefore, it is also not possible to use only one kind of numerical method that allows a complete numerical prediction of industrial processes. Whether separated or dispersed multi-phase flows (Fig. 6.1) are considered, requires different numerical approaches and the consideration of various physical phenomena. Naturally, also a mix of separated and dispersed two-phase flow may occur due to the entrainment of fine droplets from the liquid as typical for annular flows. In addition, the liquid

fraction in separated flows may include droplets, bubbles or solid particles as for example in oil and gas recovery. For a numerical calculation of such rather complex and mostly time-dependent multi-phase flows, different methods need to be combined. The most complex type of multi-phase flow is the transient multi-phase flow (Fig. 6.1a) which goes from pure liquid to pure vapour for example, with different multi-phase flow states in-between calling for different numerical methods. On the other hand, more simple one-dimensional methods may be used for large-scale technical equipment, supported by numerous correlations and closures as for example needed for long pipelines in oil and gas transportation (see for example [50, 51, 73]). For the numerical calculation of separated and slug-type multi-phase flow one may use a two-fluid approach including an appropriate treatment of the interfaces wherefore different numerical methods may be used. These will be described briefly below in the frame of particle-scale simulations.

For dispersed flows of industrial scale including bubbles or droplets, an interface resolving simulation is, even with today's computational power, not possible. Therefore, these kind of two- or multi-phase flows in a technical or industrial scale are calculated numerically by treating the dispersed phase elements as point-particles or point-masses using appropriate correlations for describing their fluid dynamic transport as for example drag or lift coefficients. In most technical cases, the particle Reynolds number is larger than unity so that a theoretical derivation of such correlations is not possible and therefore experimental based correlations are mostly used [17, 102]. In addition a large number of other particle-scale phenomena influence dispersed two-phase flows, such as inter-particle collisions, agglomeration, wall collisions, coalescence and break-up of bubbles and droplets, to name only a few. In a point-particle approach, all these elementary processes need additional modelling and closures. This is the most important task in the development of macro-scale numerical methods for industrial and technical processes.

Therewith one strikes the so-called "multi-scale phenomenon" which is especially important for multi-phase flows (Fig. 6.6). Industrial-scale processes can only be simulated with a limited number of grids and dispersed particles, even if treated as point-masses. This is illustrated in Fig. 6.6(left) for an industrial-scale fluidised bed simulated by a two-fluid approach [82]. Using a too coarse mesh, which however yields a reasonable computational time, the fine-scale structures of particle clustering during their transport through the riser cannot be resolved. This can only be achieved with a very fine mesh, which consequently results in unrealistically high computational time and storage requirements. Therefore, a sub-grid-scale drift velocity model was developed to allow for coarser meshes [49, 83]. This shows that all phenomena on scales smaller than the numerical grid require modelling which is first of all turbulence modelling for the fluid flow using RANS or LES methods, briefly summarized above. Such models however need extensions to account for two-way coupling. The modelling of particle scale phenomena was previously mainly based on detailed experiments, for example collisions of droplets. However, due to the increasing computational power, more and more fully resolved DNS methods (i.e. resolving particles or bubbles and

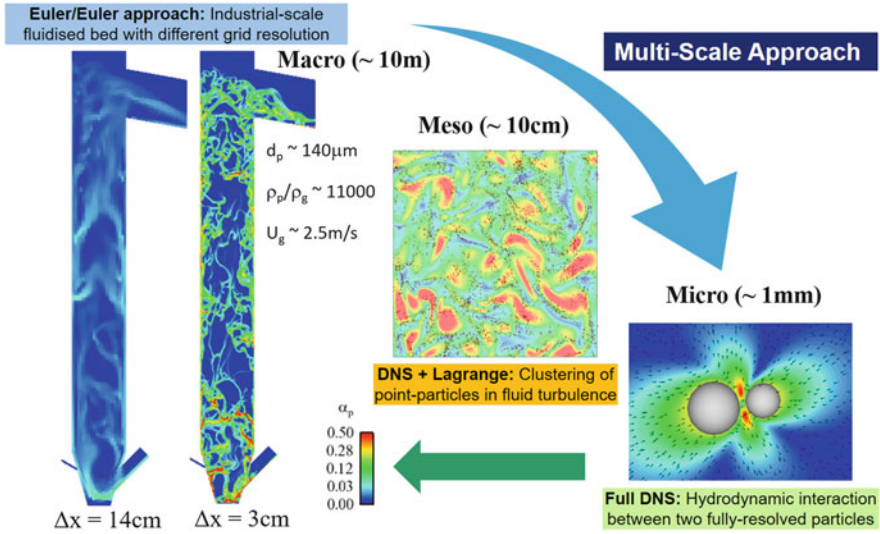


**Fig. 6.6** Illustration of multiscale approach for the numerical calculation of dispersed two-phase flows; *left*: industrial-scale fluidised bed simulation by a two-fluid approach with different grid resolution (see e.g. [82, 83]), *middle*: analysis of particle segregation and accumulation in homogeneous isotropic turbulence accounting for inter-particle collisions using LBM [31]; *right*: hydrodynamic interaction between colliding solid particles simulated by the LBM in the frame of agglomeration studies [30, 32]

droplets by the numerical grid including the flow around them) are being used for evaluating models to be applied for point-particle approximations. Such simulations may be termed micro-scale simulations as shown in Fig. 6.6(right). Here the hydrodynamic interaction between colliding solid particles was simulated by the Lattice-Boltzmann method (LBM) in the frame of agglomeration studies [30, 32]. In the middle of Fig. 6.6 meso-scale simulations are shown, again conducted by LBM, but considering particles as point masses [31]. Here different measures were used for characterising particle segregation in homogeneous isotropic turbulence, accounting for inter-particle collisions. In this category fall for example DNS and LES considering point-particles for analysing particle clustering or particle transport in channels or pipes. In the case of DNS such simulations can be conducted for simple geometries up to flow Reynolds numbers of about 5000 to 10,000. LES of course allows for considering much more complex multi-phase flows due to the coarser grid resolution compared to DNS, but the dispersed phase is still treated by the point-particle approximation (see for example reviews Dhotre et al. [24] for bubbly flows and by Kuerten [55] for particle-laden flows).

## 6.5 Particle-Scale Simulation Methods

As mentioned above, fully resolved simulations, which are feasible for a small group of particles, may considerably support modelling particle-scale phenomena needed for macro-scale simulations. The requirements for such kind of resolved simulations first depend on the type of particles considered. Resolved simulations for rigid solid particles (as illustrated in Fig. 6.6 right) do not need any special treatment of the interface and just require a no-slip wall boundary condition on the surface. Special interpolation methods are often needed if the particle moves across a fixed Eulerian grid or one may also use adaptive grids that follow the resolved particles. A special type of method is the immersed boundary method, which is computationally very efficient. Here the no-slip boundary condition is not explicitly enforced, but mimicked through a source term distribution in the region of the particle. The second class of particles are those with non-rigid interface and internal flows, namely droplets or bubbles. Here the major problem is resolving the state jumps across the interface accurately. Mostly the flow inside and outside the particle is calculated with a one-field formulation with appropriate boundary or jump conditions at the interface.

### 6.5.1 Resolved Rigid Particles

Numerical simulations of the flow around resolved rigid particles, which are either stationary in space or immersed in a certain flow system require that a no-slip condition at the particle surface is fulfilled. For such kind of simulations, referred to as PR-DNS (particle-resolved DNS) several numerical approaches may be used (see for example [72, 125]). Finite element methods with body-fitted numerical grids require a re-generation of the grid each time-step as the particles are moving through the flow (see e.g. [48]). Such an approach is numerically very costly and therefore limited to systems with only a few particles or even only feasible for two-dimensional simulations (Fig. 6.7a). However, there exists a broad range of different methods which are based on a structured Eulerian grid for calculating the fluid flow. With respect to treating the particle these methods may be classified in the following way:

- Methods using an overlay grid attached to the particles and a structured base-grid for the flow simulations. These methods requires interpolation of the flow field between both grids.
- Methods using a structured grid for the flow simulation and enforcing the no-slip condition on the particle surface by introducing some kind of force field distribution in the region of the particle object. All these methods may be grouped under the term “fictitious domain methods” each using different approaches for emulating the presence of the particles and enforcing the no-slip condition on the surface.



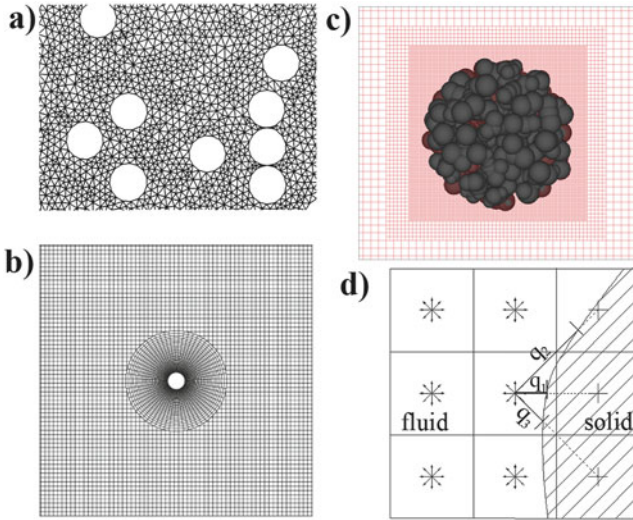


**Fig. 6.7** Illustration of the different methods for conducting fully resolved particle simulations; (a) finite element methods with body-fitted numerical grid [48]; (b) overlay grid fitted to the surface of a particle [9]; (c) grid refinement around an agglomerate for LBM; (d) curved wall boundary condition in the bounce-back method for LBM simulations [26]

- The Lattice-Boltzmann method (LBM) normally uses a regular base-grid and embedded solid bodies or particles are considered as being rigid with a bounce-back boundary condition on the surface.

An overlay grid may perfectly fit the surface of a particle (Fig. 6.7b), but the results between base-grid and particle grid have to be interpolated (see [9, 130]). Such a method is suitable for a few fixed particles which might even have a complex geometry (e.g. non-spherical particles or agglomerates), but becomes more difficult to handle if these particles move and may interact and collide.

In the fictitious domain method a field of Lagrange multipliers is applied over the particle volume so that the no-slip boundary condition is enforced on the particle surface (see [40]). This approach allows handling many particles and also collisions between them. At that time, they considered for example the two-dimensional sedimentation of 6400 particles and the fluidization of 1204 particles in a small domain having the thickness of the particle diameter.

The force coupling method allows the coupling between resolved particles and fluid flow by adding a finite and localized (in the region of the particle) forcing to the Navier-Stokes equations as a spatially distributed source term [12, 70]. The particles are tracked in a Lagrangian way based on the interaction force between fluid and particle and any external forces being relevant. Therefore, such a method does not need a numerical grid fitted to the surface of the particle and the two-phase system may be simulated on a regular grid.

The immersed boundary method (IBM), which goes probably back to the work of Peskin [84], is also an approximate method to account for the presence of any stationary or moving object in fluid flows using a regular Cartesian grid. The no-slip boundary condition on the surface of the object is realized by introducing a localized force field, which appears in the fluid momentum equation as a source term distribution. The immersed boundary method is nowadays very popular in any flow system with fluid-solid boundaries, moving or stationary. Therefore, it has numerous applications summarized for example by Mittal and Iaccarino [76]. This method was adapted for allowing simulations for a large number of resolved solid particles (in the order of 1000) by Uhlmann [127]. Also forces acting on non-spherical particles may be obtained by this method [136]. The big advantage of the IBM is its conceptually simple structure which is easy to implement and numerically quite efficient. Like all the other fictitious domain methods, a flow field is also produced inside rigid objects.

A very powerful method, which also allows simulations of resolved particles moving in a flow, is the Lattice-Boltzmann method (LBM). Here not the Navier-Stokes equations are solved, but the Lattice-Boltzmann equation describing the change of state of a fluid through a probability distribution function. This approach is numerically very efficient and easy to parallelise however has limitation in the maximum flow Mach number to be considered since an incompressible flow is considered. Normally, this method uses an equidistant regular grid for discretising flow domain and particles. However, also a local grid refinement in several steps may be used to improve spatial resolution [25, 36] as illustrated in Fig. 6.7c. The LBM has been applied to numerous problems in particle-laden flows and for studying the flow around non-spherical particles [46] and agglomerates [25, 26], because of its numerical efficiency and good spatial resolution. The interaction of a flow with imbedded objects is realised by using a bounce-back boundary condition on the real surface of the particle (Fig. 6.7d) by applying an extrapolation method [43]. Consequently, the fluid dynamic forces acting on complex aggregate structures are directly obtained through the bounce-back boundary condition of the LBM simulations.

Also moving particles in turbulent [38] and laminar flows [32] have been studied by LBM. Here the resolved particles move across a regular Eulerian grid through the forces and moments acting on the particles. Hence, fluid nodes in front of the particle are switched to solid nodes and solid nodes behind the particle to fluid nodes by an extrapolation approach. In the work of Ernst et al. [33] the agglomeration of resolved sedimenting particles and the evolving structures were analysed and in the second study additionally agglomeration in a shear flow was considered [32], emphasising the effect of hydrodynamic interaction on agglomeration. Naturally, there will be a problem if the gap between contacting particles becomes smaller than the mesh size. Therefore, some nodes inside contacting particles were switched to fluid nodes using the equilibrium distribution function together with the known particle velocity. In these agglomeration studies contacting particles were assumed to stick together; however, one also may account for interaction forces between contacting resolved

particles, for example by a square well potential as done by Derksen [22] for the analysis of resolved particle agglomeration in homogeneous isotropic turbulence. Here also the LBM was used in combination with the immersed boundary method to mimic the presence of solid particles.

### 6.5.2 Resolved Particles with Fluid Interfaces

With such kind of methods, the motion of deformable droplets or bubbles may be studied in order to derive for example correlations for the fluid dynamic forces acting on these particles under certain flow conditions or in a swarm. Moreover, the direct interaction and collision of droplets or bubbles, which may result in coalescence, is an important issue for providing appropriate modelling approaches. For the numerical treatment of deformable fluid interfaces between two immiscible fluids two classes of approaches are being used, namely [135]:

- surface methods or interface tracking methods,
- volume methods or interface capturing methods.

Both methods are mostly used in connection with a one-fluid formulation of the Navier-Stokes equations including a source term at the interface in order to account for the surface tension force [85]. Additionally, differential equations have to be solved (also across the interface) for the change of fluid density and viscosity. For an interface tracking method, the interface is marked with particles or an interface grid and advected according to the local fluid velocity [128]. Interface tracking methods are very accurate regarding the conservation of the interface structure and sharpness, but cannot easily handle topological changes of the grid which are for example needed to analyse coalescence.

The volume methods do not explicitly track the interface but it is reconstructed from the solution of an indicator function  $f$ :

$$\frac{\partial f}{\partial t} + \vec{u} \cdot \nabla f = 0 \quad (6.19)$$

In the well-known VOF (volume of fluid) method the indicator function may be understood as the volume fraction of one phase. Hence, across an interface it varies between zero to one and the interface is assumed to be located for example at 0.5. One of the outstanding advantages of VOF is that it is mass conserving and allows for topological changes occurring for example during bubble break-up and coalescence. The latter however implies that coalescence always occurs if bubbles come close together. A major challenge of the VOF is the required geometrical reconstruction of the interface in order to ensure a smooth topology of the interface. There are several options for interface reconstruction as summarised by Rudman [87], which define the interface location within a grid for example to be parallel

or oblique to the mesh. The initial approach was using a Simple Line Interface Calculation (SLIC) where the interface is parallel to the grid line for each of the advection steps. More advanced and still used today is the PLIC (Piecewise Linear Interface Construction) method (see e.g. [135]).

Another volume tracking method is the Level set Method (LSM) where also a similar marker function (called level-set function) is solved (as in VOF) however with the conditions  $\varphi > 1$  fluid 1 and  $\varphi < 1$  fluid 2, so that the interface is located at  $\varphi = 0$ . Consequently, the level set function basically defines the distance to the interface and is advected by:

$$\frac{\partial \varphi}{\partial t} + \bar{u} \cdot \nabla \varphi = 0 \quad (6.20)$$

The LSM does not require any geometrical reconstruction of the interface and the transition from one fluid to the other occurs smoothly over several cells [85]. Also interface normal vector and interface curvature are obtained accurately which is important for the determination of the surface tension force. However, in order to avoid overshoots in the gradient of the level-set function near the interface a re-initialisation of the level-set function is required. Consequently, the LSM is very robust and rather simple to realise, but faces the problem of being not mass conservative [85]. Therefore, the level-set approach is very often coupled with other methods such as VOF and ghost fluid method [13, 23, 75].

## 6.6 Modelling of Dispersed Multi-Phase Flows

For the numerical computation of technically relevant turbulent multi-phase flow systems two approaches are commonly applied, namely, the two-fluid or Euler/Euler approach and the Euler/Lagrange method [17, 71, 119]. Note that here the focus is only on dispersed multi- or two-phase flows as defined above. Hence, both methods have to be regarded as being complementary and have the same important limitation, namely the particles must be much smaller than the grid dimensions. Otherwise, the point-particle assumption is violated. Both methods rely on the Reynolds-averaged conservation equations (often referred to as RANS: Reynolds-averaged Navier-Stokes equations) in connection with an appropriate turbulence model to close the set of equations. For most of the technical applications, the standard  $k - \varepsilon$  or  $k - \omega$  turbulence models are used because they are very economic and yield good convergence rate. Especially for strongly anisotropic turbulent flows (e.g. channel or pipe flows and swirling flows), also multiple-scale  $k - \varepsilon$  turbulence models and different formulations of Reynolds-stress models are developed for two-phase flow computations [93]. In recent years also the application of LES is extended towards simulations of industrial scale processes using the filtered Navier-Stokes equations and an appropriate sub-grid-scale turbulence model which however may be much simpler as turbulence on this scale is more close to isotropic [37, 62].

In order to account for the interaction between phases, i.e. momentum exchange and heat as well as mass transfer, the conservation equations of the continuous phase have to be extended by appropriate source/sink terms resulting from the dispersed phase. This coupling method is referred to as two-way coupling (Fig. 6.2).

In the two-fluid approach, both phases are considered as interacting continua. Hence, properties such as the mass of particles per unit volume are considered as a continuous property and the particle velocity is the averaged velocity over an averaging volume (i.e. the control volume or computational cell). Also the interfacial transfer of mass, momentum, or energy requires averaging over the control volumes. Especially in turbulent flows, the closures for the dispersed phase Reynolds-stresses (or kinetic stresses) and the fluid-particle correlation terms are associated with more or less sophisticated modelling approaches (see e.g. [86, 93]). The consideration of a particle size distribution requires the solution of a set of basic equations for each size class to be considered. Hence the computational effort increases with the number of size classes. Another possibility of accounting for a particle size distribution is the coupling with a population balance which can account for particle enlargement (coalescence and agglomeration) and destruction (see e.g. [10, 53]). The two-fluid method is however preferable for dense dispersed two-phase flows, as for example found in fluidised beds [4, 122] or in bubble columns [137]. As one may expect, there exists a vast number of publications related to the development of the two-fluid approach. Some of the key earlier work is mentioned here. Enwald et al. [29] published an early review on developments of Eulerian models for predicting fluidisation processes. Also van Wachem et al. [129] did a comparison of several CFD models for dense gas-solid flows. Pioneering developments were also done in the group of Simonin at IMFT (Institute de Mécanique des Fluides de Toulouse) who presented the continuum modelling of turbulent reactive particulate flows based on the probability density function kinetic equation [5, 93]. Also the pioneering works of Gidaspow [39] and Ding and Gidaspow [27] on modelling granular flows should be emphasised.

The efforts in improving two fluid models especially for fluidisation of solids and bubbly flows have even further increased until today because of the big advantages in simulating industrial processes at full scale at reasonable computational cost. Regarding the simulation of fluidised beds at industrial scale still the problem of required grid resolution and modelling of a subgrid-scale drift velocity is an important issue [49, 83, 91]. Moreover, inter-particle collisions and wall collisions need to be modelled properly [34] and not to forget the old problem of appropriate swarm drag forces which account in an averaged way for fluid dynamic interactions between particles [69], which is called three-way coupling [15]. For calculating bubbly flows by the Euler/Euler approach recent efforts focus on correct modelling of interfacial forces, such as drag, lift and wall forces [54, 132] as well as mass transfer, coalescence and break-up [65, 134].

The hybrid Euler/Lagrange approach is only applicable to dispersed two-phase flows and is based on a coupled computation of fluid flow and particle phase. The term dispersed implies that all regimes shown in Fig. 6.3 can be calculated by a

Lagrangian method. There is no physical limitation on the volume fraction (as very often stated in the literature) as long as all physical phenomena are reproduced correctly, as for example particle collisions in the dense regime or multi-particle contacts in the contact dominated regime. The dispersed phase is modelled by tracking a large number of representative point-particles through the flow field by solving the equations of motion accounting for all relevant forces acting on the particles. Local average properties such as dispersed phase density or velocity are obtained by ensemble and time averaging for each control volume in the computational domain. An essential advantage of this method is that the discrete nature of the dispersed phase particles is accounted for. Moreover, physical effects influencing the particle motion, such as particle-turbulence interaction, particle-wall collisions, and collisions between particles including coalescence or agglomeration can be modelled on the basis of first physical principles (e.g. [42, 96]). Additionally, a particle size distribution may be easily considered by randomly drawing the size of the injected particles from a given distribution function [94].

Essential for a reliable application of both methods is an appropriate modelling of relevant physical mechanisms affecting the particle motion, as summarised above. In some cases the physical phenomena are far too complex for allowing a derivation of the models from basic principles of physics (e.g. impact of droplets on a wall or coalescence of bubbles). Therefore, detailed experiments or fully resolved direct numerical simulations (DNS) are often required to analyse the considered phenomenon and to derive appropriate empirical or semi-empirical models. In order to validate the models, the results of the numerical predictions need to be compared with bench mark test cases (i.e. validation) featuring the considered phenomenon (see for example [101, 103, 104]).

### ***6.6.1 Two-Fluid or Euler/Euler Approach***

As briefly summarised above, the two-fluid approach (mostly referred to as Euler/Euler method) relies on the assumption of interpenetrating continua. This implies that a control volume is shared by both phases according to the respective volume fractions. The conservation equations for the mean properties of both phases are derived by applying certain averaging approaches. Depending on the multi-phase system considered different averaging methods are being used [17]. The resulting conservation equations for both phases have a similar structure and include the interfacial exchange terms (coupling between the phases or two-way coupling) for mass, momentum and heat. For closing the set of equations different closure assumptions may be used, which again depend on the multi-phase system considered. For dispersed multi-phase flows two concepts are possible; the mixture or homogeneous approach and the two- or multi-fluid method. In the mixture model, the conservation equations for the mixture are solved implying that no interfacial transfer terms appear in these equations. The mixture model can be further divided

into the homogeneous mixture model where both phases share the same velocity and a model where a relative or slip velocity is considered using algebraic slip formulations [131, 140]. Both mixture approaches are however only applicable for systems with small particles where the mass loading is small or in bubbly flows with very low volume fraction.

Besides that, a “full” two-fluid approach has to be chosen where a set of conservation equations for each phase has to be solved accounting for the coupling through pressure and interfacial exchange. In case turbulent multi-phase flows are considered there are two options. Transport equations for turbulence are only solved for the carrier phase and the fluctuating motion of the dispersed phase is linked to the continuous phase turbulence through analytic correlations. In the second case, also transport equations for the dispersed phase fluctuating motion (kinetic stresses) are solved including additional closures for the turbulent transport of the dispersed phase [93].

As an example, the two-fluid approach where the dispersed phase fluctuating motion is linked to fluid turbulence will be briefly described [92]. It should be emphasised that this approach is only applicable to dispersed two-phase flows as defined above. Restricting to a two-phase flow without heat and mass transfer between the phases one obtains for the continuity equations of both phases:

$$\begin{aligned}\frac{\partial \sigma_F}{\partial t} + \frac{\partial}{\partial x_i} (\sigma_F \bar{u}_i) &= 0 \\ \frac{\partial \sigma_p}{\partial t} + \frac{\partial}{\partial x_i} (\sigma_p \bar{u}_{pi}) &= 0\end{aligned}\quad (6.21)$$

here  $\bar{u}_i$  and  $\bar{u}_{pi}$  are the mean velocity components of fluid and dispersed phase and  $\sigma_F$  and  $\sigma_p$  are the mean mixture densities of both phases as defined by Eq. (6.22). Both properties can be expressed in terms of the dispersed phase volume fraction:

$$\begin{aligned}\sigma_F &= \alpha_F \rho_F = (1 - \alpha_p) \rho_F \\ \sigma_p &= \alpha_p \rho_p\end{aligned}\quad (6.22)$$

The momentum equations for both phases including the interfacial exchange through the fluid dynamic forces acting on the particles are:

$$\sigma_F \frac{\partial \bar{u}_i}{\partial t} + \sigma_F \bar{u}_j \frac{\partial \bar{u}_i}{\partial x_j} = -\alpha_F \frac{\partial \bar{p}}{\partial x_i} - \mu_{eff} \frac{\partial^2 \bar{u}_i}{\partial x_j \partial x_j} - \frac{\partial}{\partial x_j} (\sigma_F \bar{u}'_i \bar{u}'_j) + \sigma_F g_i - \sigma_p \frac{\overline{F_{p,i}}}{m_p}\quad (6.23)$$

$$\sigma_p \frac{\partial \bar{u}_{p,i}}{\partial t} + \sigma_p \bar{u}_{p,j} \frac{\partial \bar{u}_{p,i}}{\partial x_j} = -\alpha_p \frac{\partial \bar{p}}{\partial x_i} - \frac{\partial}{\partial x_j} (\sigma_p \bar{u}'_{p,i} \bar{u}'_{p,j}) + \sigma_p g_i + \sigma_p \frac{\overline{F_{p,i}}}{m_p}\quad (6.24)$$

The interfacial force to be considered depends on the type of two-phase flow system (i.e. gas-solid, liquid-gas or liquid-liquid) and the ratio of fluid to particle density

[17, 119]. When considering gas-solid flows with reasonably small particles, the dominating interfacial force is the drag force:

$$\overline{F_{p,i}} = \frac{18\mu_f f_D}{\rho_p D_p^2} m_p \{(\overline{u_i} - \overline{u_{p,i}}) + V_{p,i}\} \quad (6.25)$$

It should be noted that here transverse lift forces due to shear flow and particle rotation [102] are neglected. The term  $(\overline{u_i} - \overline{u_{p,i}})$  is the slip velocity between the phases. The drift velocity  $V_{p,i}$  accounts for the transport of the particles by turbulence (often referred to as turbulent dispersion) and may be expressed in terms of a binary turbulent diffusion tensor and the gradient of the volume fractions of both phases:

$$V_{p,i} = -D_{p,ij} \left[ \frac{1}{\alpha_p} \frac{\partial \alpha_p}{\partial x_j} - \frac{1}{\alpha_f} \frac{\partial \alpha_f}{\partial x_j} \right] \quad (6.26)$$

The binary diffusion tensor for the dispersed phase depends on numerous properties, such as particle size and turbulence structure. Using a semi-empirical analysis the diffusion tensor is expressed in terms of the correlation between fluid and particle fluctuations and a fluid-particle characteristic turbulent time scale:

$$D_{p,ij} = \overline{\tau_{fp} u'_{f,i} u'_{p,j}} \quad (6.27)$$

The time scale  $\tau_{fp}$  of fluid turbulence viewed by a particle along its trajectory can be related to the integral time scale of turbulence  $T_L$  computed along the trajectory. This time scale is affected mainly by the relative drift between particle and fluid caused by external forces. It may be split in two components parallel and perpendicular to the mean relative velocity [18]:

$$\tau_{fp}^{\parallel} = \frac{T_L}{\sqrt{1 + C_\beta \xi_r^2}} \quad \tau_{fp}^{\perp} = \frac{T_L}{\sqrt{1 + 4C_\beta \xi_r^2}} \quad (6.28)$$

$$\xi_r = \frac{|u_{rel}|}{\sqrt{\frac{2}{3}k}} \quad C_\beta = 0.45 \quad (6.29)$$

For the simple situation of homogeneous isotropic turbulence, an assumption which is often made in turbulence, the kinetic stresses of the dispersed phase (or the fluctuating energy of the dispersed phase) can be related to the Reynolds stresses of the carrier phase through a response function  $\eta_r$ . This function depends on the ratio of fluid turbulent integral time scale viewed by the particle to the particle response or relaxation time  $\tau_p$  (see Eq. (6.13)). The latter defines the time the particle would



need to follow any sudden change of fluid velocity.

$$\overline{u'_{p,i}u'_{p,j}} = \overline{u'_{F,i}u'_{F,j}} \left\{ \frac{\eta_r}{1 + \eta_r} \right\} \quad \eta_r = \frac{\tau_{fp}}{\tau_p} \quad (6.30)$$

In a similar way the correlation between particle and fluid fluctuation components can be related to the Reynolds stresses.

$$\overline{u'_{F,i}u'_{p,j}} = 2\overline{u'_{F,i}u'_{F,j}} \left\{ \frac{\eta_r}{1 + \eta_r} \right\} \quad (6.31)$$

This model was also evaluated for particle dispersion in a turbulent shear layer by Horender and Hardalupas [47]. For more details the reader is referred to the literature cited above and the work of Simonin [92, 93].

## 6.6.2 Hybrid Euler/Lagrange Approach

The hybrid Euler/Lagrange approach is only applicable to dispersed two-phase flows and accounts for the discrete nature of individual particles being tracked through the flow field based on the relevant forces. First the flow field is calculated on the basis of the Reynolds-averaged conservation equations in connection with an appropriate turbulence model if necessary. The dispersed phase is modelled by tracking a large number of particles through the beforehand computed flow field in solving the equations of motion accounting for all relevant forces acting on the particles [102] and heat as well as mass transfer if required [17, 115, 119]. Generally, the particles are considered as point-particles, i.e. the finite dimension of the particles is not considered and the flow around individual particles is not resolved. An essential consequence of this approach is that the particles need to be considerably smaller than the dimensions of the numerical grid or control volume.

Physically, there is no limitation in the maximum particle volume fraction to be considered, as long as all relevant elementary processes are accounted for. Hence, applications of this method range from the dilute to the dense regime (see Fig. 6.3), as for example in fluidised beds. However, there are some different forms of the Lagrangian particle tracking methods suggesting a classification as summarised in Fig. 6.8. For dilute two-phase flows normally the classical Lagrangian approach considering parcels is adopted (Fig. 6.8 left), whereas in the dense regime both the discrete particle method or DPM (e.g. [63, 64]) as well as the DEM (discrete element method) are being applied (e.g. [138]). Both methods, DPM and DEM, rely on tracking all real particles in the system, wherefore the system size is limited. The difference between these two methods is the treatment of inter-particle collisions (see e.g. [21]). In DPM a hard sphere collision model is used (Fig. 6.8 middle), which is more realistic, however, imposes strong limitations on the tracking time

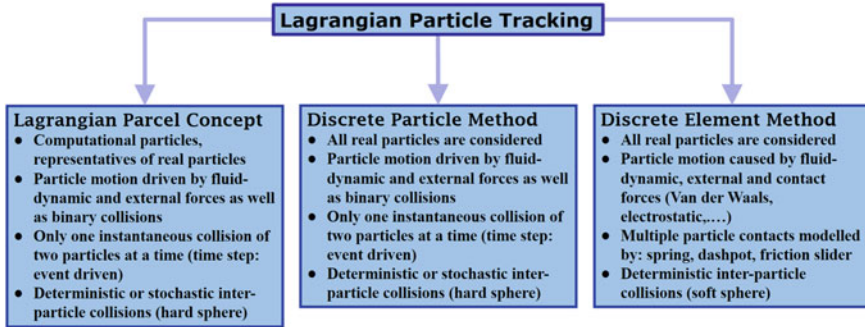


**Fig. 6.8** Illustration of the classification of Lagrangian particle tracking methods. *LPC* Lagrangian parcel concept, *DPM* discrete particle method, *DEM* discrete particle method

step in order to guarantee only binary collisions. Therefore, this kind of method is also called event driven. Binary collisions only last for a very small time period and are described by the impulse equations in connection with Coulombs law of friction, so that the only model parameters are normal restitution ratio and friction coefficient. On the other hand in the DEM (Fig. 6.8 right) multiple and overlapping particle contacts (called soft-sphere collisions) are allowed, often modelled by a “spring, dashpot and friction slider element” according to Tsuji et al. [126] and the pioneering work of Cundall and Strack [19]. This approach uses constant time steps (time-driven) which have to be properly chosen as it determines the possible overlap. In this method naturally all real particles need to be tracked. Still today, the computers determine the available storage and available computational time, whereby the number of the considered particles and the equipment size has strong limits; considering larger facilities also requires larger particles to be used, as the particle number is limited. Due to the modelling of multiple contacts DEM of course allows the consideration of much denser systems than DPM.

In the case of fine particles, for example in a spray, the tracking of all real particles in the system is even today computationally not affordable. Therefore, in the classical Lagrangian approach the parcel concept (LPC, Fig. 6.8 left) is utilised, where the computational particles mostly called *parcels* represent a certain number of real particles with the same properties (i.e. size, velocity and temperature). This procedure also ensures that the correct particle mass flux into the system is realised. In stationary flows a sequential or simultaneous tracking of the parcels may be adopted, while in unsteady flows all parcels need to be tracked simultaneously on the same time level. Local average properties such as dispersed phase concentration, number density and velocities are obtained by ensemble averaging for each control volume in the computational domain, coupled with time averaging in a stationary flow. For three-dimensional flows, statistically reliable results for each computational cell require the tracking of typically between 100,000 and 1,000,000 parcels, depending on the considered flow geometry.

Essential for the hybrid Euler/Lagrange approach is the coupling between the phases. For very low particle phase volume fraction (let's say below  $10^{-6}$ ) a one-way coupled calculation is sufficient, implying that the particles are tracked only once through the previously calculated and fully converged flow field (see Fig. 6.2) and their properties are sampled. For higher volume fractions the influence of the particle phase on the flow field and turbulence properties has to be taken into account (i.e. so called two-way coupling). The associated computational approach was first introduced by Crowe et al. [16] and was called "Particle-Source-In-Cell" method. Here, particles are tracked in the flow field predicted by the flow-solver and the particle phase properties as well as the source terms in each computational cell of the flow domain are sampled. The source terms are sampled for kinetic interaction (i.e. for the momentum equations and the transport equations for the turbulence properties) as well as for heat and mass transfer across the phase boundaries, if required. A converged solution of the coupled system is obtained by successive computation of flow field (Eulerian) and particle phase (Lagrangian). Normally an under-relaxation procedure is required for the source terms in order to avoid divergence and instabilities [52, 57]. The number of coupling iterations depends on the degree of coupling between the phases (i.e. particle concentration) and the under-relaxation factor. However, convergence problems may still be encountered for very dense two-phase systems. The term four-way coupling is used when in connection with two-way coupling also inter-particle collisions and fluid-dynamic interaction upon collision are taken into account, which is necessary for particle volume fractions larger than about  $10^{-3}$  (see Fig. 6.2). Hence, the particle phase properties are not only influenced by the modified flow field, but also by the alteration of the particle phase properties through inter-particle collisions.

The Euler/Lagrange approach described here is based on the three-dimensional Reynolds-averaged conservation equations in connection with the well-established  $k - \varepsilon$  turbulence model [61]. Although this turbulence model has some limitations in its applicability, it allows however an efficient solution to most engineering problems. The general form of the conservation equations for an incompressible, unsteady and three-dimensional flow with dispersed phase heat and mass transfer [115] is given by:

$$\frac{\partial}{\partial t}(\rho\phi) + \frac{\partial}{\partial x_i}(\rho U_i\phi) = \frac{\partial}{\partial x_i} \left( \Gamma_\phi \frac{\partial \phi}{\partial x_i} \right) + S_\phi + S_{\phi,P,m} + S_{\phi,P,ev} \quad (6.32)$$

The continuity equation results with  $\phi = 1$  and the momentum equations with  $\phi = U_i$  where  $U_i$  ( $i \in [1, 2, 3]$ ) are the three velocity components. The fluid temperature equation is obtained with  $\phi = T$  and also different species conservation equations may be considered (e.g. gas phase and vapour phase). The conservation equations for the turbulent kinetic energy  $k$  and the dissipation rate  $\varepsilon$  are obtained with  $\phi = k$  and  $\phi = \varepsilon$ , respectively. The diffusion coefficients for all the conservation equations are given in Table 6.2 together with the fluid phase source terms  $S_\phi$ .

**Table 6.2** Summary of the variables,  $\phi$ , the fluid source terms,  $S_\phi$ , and the effective transport tensor,  $\Gamma_\phi$ , in Eq. (6.32) and constants of the  $k - \varepsilon$  turbulence model

$\phi$	$S_\phi$	$\Gamma_\phi$
1	–	–
$U_i$	$\frac{\partial}{\partial x_i} \left( \Gamma_{U_i} \frac{\partial U_i}{\partial x_i} \right) - \frac{\partial p}{\partial x_i} + \rho g_i$	$\mu + \mu_t$
$T$	0	$\frac{\mu}{Pr} + \frac{\mu_t}{Pr_t}$
$Y_k$	0	$\frac{\mu}{Sc} + \frac{\mu_t}{Sc_t}$
$k$	$G_k - \rho \varepsilon$	$\mu + \frac{\mu_t}{\sigma_k}$
$\varepsilon$	$\frac{\varepsilon}{k} (C_1 G_k - C_2 \rho \varepsilon)$	$\mu + \frac{\mu_t}{\sigma_\varepsilon}$

$$G_k = \mu_t \left( \frac{\partial U_i}{\partial x_j} + \frac{\partial U_j}{\partial x_i} \right) \frac{\partial U_i}{\partial x_j}, \quad \mu_t = C_\mu \rho \frac{k}{\varepsilon}$$

$$C_\mu = 0.09; \quad C_1 = 1.44; \quad C_2 = 1.92; \quad \sigma_k = 1.0; \quad \sigma_\varepsilon = 1.3$$

**Table 6.3** Summary of particle phase source terms for the different fluid flow conservation equations (middle column: interfacial momentum and heat transfer; right column: interfacial mass transfer)

$\phi$	$S_{\phi,P,m}$	$S_{\phi,P,ev}$
1	0	$\sum_k \frac{N_k \dot{m}_{k,ev}}{V_{CV}}$
$U_i$	$\sum_k \frac{\dot{m}_k N_k}{V_{CV}} \left[ (u_{k,i}^{t+\Delta t} - u_{k,i}^t) - g_i \left( 1 - \frac{\rho_f}{\rho_p} \right) \Delta t \right]$	$\sum_k \frac{N_k \dot{m}_{k,ev} u_{ki}}{V_{CV}}$
$T$	$-\sum_k \frac{N_k}{V_{CV}} (H_{Lat} \dot{m}_k + \dot{Q}_L)$	$\sum_k \frac{N_k \dot{m}_{k,ev}}{V_{CV}} C_{pL}(T_k) T_k$
$Y_1$	0	0
$Y_2$	0	$\sum_k \frac{N_k \dot{m}_{k,ev}}{V_{CV}}$
$k$	$\sum_i \left( \overline{U_i S_{U_i,P,m}} - \overline{U_i} \overline{S_{U_i,P,m}} \right)$	$\overline{U_i S_{U_i,P,ev}} - \overline{U_i} \overline{S_{U_i,P,ev}} + \frac{1}{2} \left( \overline{U_i U_i S_{\rho,P,ev}} - \overline{U_i U_i} \overline{S_{\rho,P,ev}} \right)$
$\varepsilon$	$C_3 \frac{\varepsilon}{k} S_{k,P,m}$	$C_3 \frac{\varepsilon}{k} S_{k,P,ev}$

For evaporation:  $u_a, v_a, w_a = u_k, v_k, w_k$

For condensation:  $u_a, v_a, w_a = u, v, w$

$Y_1$ : air;  $Y_2$ : water

The particle phase source terms  $S_{\phi,P,m}$  account for the effect of the particles on mean flow and turbulence due to interfacial momentum transfer and  $S_{\phi,P,ev}$  is the transfer caused by particle/droplet evaporation or condensation. The source terms for the dispersed phase are summarised in Table 6.3 for the different flow variables. The middle column provides the source terms due to interfacial momentum and heat transfer and the right column those resulting from droplet evaporation, i.e. mass transfer [115, 119]. In this case, two gaseous species are considered, e.g. air and water vapour. It should be noted that momentum transfer due to evaporation occurs with the particle velocity and in the case of condensation the instantaneous fluid velocity seen by the particle has to be used. The summation of the source terms has to be performed along all particle trajectories (index  $k$ ) passing through a considered

control volume. The gathering procedure for obtaining these source terms from the particle trajectory calculations will be described below in more detail.

In the Lagrangian approach the trajectories of the parcels moving through the flow field are calculated by solving ordinary differential equations for the parcel location, and the linear and angular velocity components. The change of particle linear velocity components is obtained by considering all relevant forces acting on the particle which depends on the flow system considered [102, 119]. The change of the angular velocity along the particle trajectory results from the viscous interaction with the fluid (i.e. the torque). Hence, the equations of motion for the particles in vector form are given by:

$$\frac{d\vec{x}_p}{dt} = \vec{u}_p \quad (6.33)$$

$$m_p \frac{d\vec{u}_p}{dt} = \sum \vec{F}_n \quad (6.34)$$

$$I_p \frac{d\vec{\omega}_p}{dt} = \vec{T} \quad (6.35)$$

where  $m_p = (\pi/6)\rho_p D_p^3$  is the particle mass and  $I_p = 0.1m_p D_p^2$  is its moment of inertia for a sphere. The different forces acting on the particle are fluid dynamic forces and external forces; e.g. gravity, buoyancy and electrical forces. The fluid dynamic forces acting on the particle surface are drag, added mass, pressure force, Basset force and transverse lift forces due to shear and particle rotation. In technical applications the particle Reynolds number is mostly larger than unity so that appropriate correlations for the resistance coefficients (e.g. drag and lift coefficients) have to be used. A summary of the forces and the resistance coefficients as well as their relevance depending on the two-phase flow system considered, i.e. gas-solid, liquid-solid, sprays and bubbly flows, is provided by Sommerfeld et al. [119] and Sommerfeld [102].

The consideration of the rotational motion of particles is especially of importance in case of wall bounded flows where wall collisions induce high angular velocity or it is modified due to wall collisions. Also in cases with strong changes in fluid vorticity the particle angular velocity should be considered, where the viscous torque of course will reduce the angular slip. In the non-equilibrium situation (i.e. high angular slip) the slip-rotation lift force or often called Magnus force should be considered [96]. It should be emphasised here, that the different forces and the torque (Eqs. (6.34) and (6.35)) include the instantaneous fluid velocity seen (or experienced) by the particles. In case LES or RANS are used for the calculation of the fluid velocity field these instantaneous fluid velocities are not available, only the Reynolds averaged velocities or the filtered velocities. Therefore, the respective fluid fluctuating velocities have to be generated from the turbulent kinetic energy or from the sub-grid-scale turbulence. The respective models should describe the effect

of turbulence on particle motion (turbulent dispersion of particles) and should also respect the crossing trajectory effect induced by external forces [119].

The generation of the instantaneous fluid velocity along the particle trajectory can be based on several stochastic approaches, as for example the simple “eddy-lifetime model” [41], the single-step correlated model based on the Langevin equation [74, 116, 139] or the multi-step correlated model [6]. The principles of these methods were summarised for example by Gouesbet and Berlemont [42] and Crowe [15]. Essential for all these schemes is the estimation of the relevant time and length scales of turbulence, which is not a simple task in complex anisotropic flows. A thorough comparison and validation of a modified eddy-lifetime and the single-step Langevin model was conducted by Sommerfeld [96]. A brief summary of the above-mentioned models is also provided in [119]. Also in the frame of LES for particle-laden flows the developed sub-grid-scale turbulent transport model was based on the single-step Langevin model [67].

If dispersed multi-phase flows with heat and mass transfer between the phases are considered two additional partial differential equations for the change of particle diameter and temperature have to be solved (see e.g. [88]):

$$\frac{dD_p}{dt} = -\frac{\dot{m}_{ev}}{\pi\rho_L D_p^2} \quad (6.36)$$

$$\frac{dT_p}{dt} = \frac{6\dot{Q}_L}{\pi\rho_L C_{pL} D_p^3} \quad (6.37)$$

In order to calculate the particle evaporation process a model for the determination of the evaporation rate  $\dot{m}_{ev}$  and the heat flux  $\dot{Q}_L$  is needed. For the determination of the limiting gas-side heat and mass transfer a number of assumptions need to be made, such as spherical symmetry, and film thickness around the droplet based on film theory [2, 119]. There are mainly two approaches regarding the temperature distribution inside the droplet; namely the infinite conductivity model assuming constant temperature inside the droplet and the finite thermal conductivity model (see e.g. [89]) which numerically resolves the temperature distribution inside the droplet.

The time step for the particle tracking calculation should be automatically adjusted along the trajectory by considering all local relevant time scales which also are changing throughout the flow field:

- the time required for a particle to cross a control volume  $t_{cv}$ ,
- the particle response time  $\tau_p$ ,
- the integral time scale of turbulence  $T_L$ ,
- the average time between binary particle collisions  $\tau_c$ .

The limitation of the time step by the inter-particle collision time scale is required in order to insure that only binary collisions may occur during a Lagrangian tracking time step. Hence, the time step  $\Delta t$  must be a fraction of the minimum of these time

scales for accurate calculations, for example 20%:

$$\Delta t = 0.2 \cdot \min(t_{CV}, \tau_p, T_L, \tau_c). \quad (6.38)$$

In order to account for the influence of the particle phase on the fluid flow a consecutive solution of the Eulerian and Lagrangian part is required. The calculation starts with the solution of the fluid flow by not accounting for the source terms of the dispersed phase. After having reached a certain degree of convergence for the single phase flow (inner fluid iterations), the particle trajectories are calculated and the particle phase properties (i.e. concentration and particle velocities) as well as the source terms are sampled for each control volume. In case a particle size distribution is considered, also the local particle size distributions and the size-velocity correlations should be determined. A detailed description of possible two-way coupling procedures is given below.

### 6.6.3 Euler/Lagrange Coupling Approaches

Because of the hybrid nature of the Euler/Lagrange approach (i.e. continuum assumption for the carrier phase and discrete particle method for the dispersed phase) special attention has to be taken in the two-way coupling approach. This means from the particle tracking in the beforehand calculated flow field the particle phase properties and the source terms for the continuous phase equations have to be evaluated by statistical averaging. Depending on the requirements for the temporal resolution of the flow and the coupling between both phases, different approaches may be used.

For *stationary flows*, only the terminal coupled solution of the two-phase system at  $t \rightarrow \infty$  is of interest. Therefore, particle tracking may be done simultaneously or sequentially (i.e. one particle after the other) for a sufficiently large number of parcels. The solution procedure is illustrated in Fig. 6.9 [57, 119] and may be summarised as follows:

- Solve the fluid flow without particles until convergence is reached.
- Track a large number of parcels for a sufficient statistical averaging of particle properties and source terms in all computational cells.
- In this calculation mode, source term evaluation is based on temporal and ensemble averaging (see Fig. 6.10a).
- The momentum coupling is determined based on the change of particle velocity within a numerical cell, subtracting however external forces. Thereby, the influence of all forces considered to act on the particle is accounted for. This approach is numerically much more efficient compared to the summation of all fluid dynamic forces acting on all particles (see below).
- Under-relaxation of source terms is suggested for smoothly approaching a converged solution of the coupled system [52, 57]

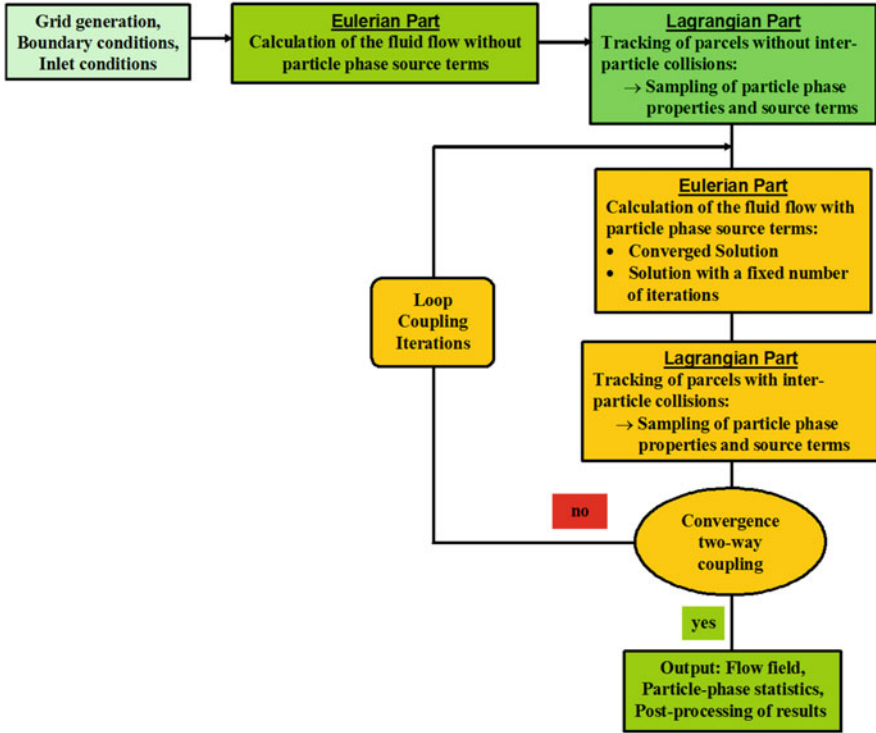


**Fig. 6.9** Flow chart of coupling iteration procedure for the hybrid Euler/Lagrange approach in the case of stationary flows

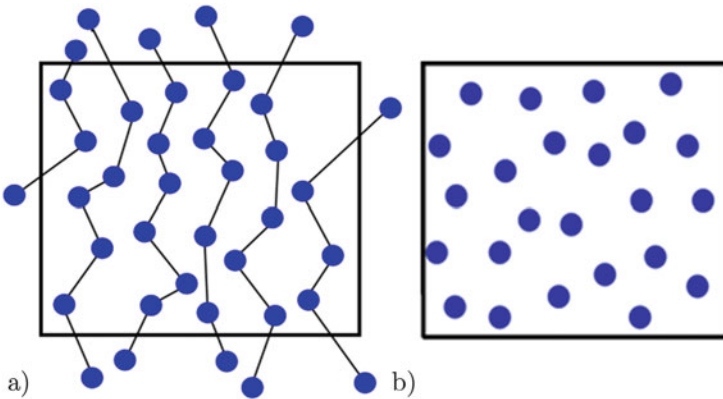


**Fig. 6.10** Illustration of the averaging procedure for different two-way coupling methods; (a) steady-state approach with temporal and ensemble averaging or semi-unsteady approach; (b) full unsteady calculations based on instantaneous fluid dynamic forces on all particles in a numerical cell



- Re-calculate the flow field with the new source terms being obtained from Eq. (6.42) with a pre-set under-relaxation factor. The under-relaxation factor depends on the degree of coupling between the phases (e.g. particle concentration).
- Recalculate the Lagrangian part since the flow field has changed and perform averaging.
- This sequential calculation of Euler and Lagrange program modules has to be repeated until the coupled system is converged. This should preferably be decided based on the evolution of some fluid property in the computational domain (see [57, 96]).

Consequently, the momentum source terms are determined by [52]:

$$\overline{S_{U_i,p}} = -\frac{1}{V_{cv} \Delta t_{ref}} \sum_{k=1}^{k_{tot}} m_k N_k \sum_{n=1}^{n_s} \left\{ (u_{p,k,i}^{t+\Delta t} - u_{p,k,i}^t) - g_i \left( 1 - \frac{\rho_F}{\rho_p} \right) \Delta t \right\} \quad (6.39)$$

In this equation the sum over  $n$  implies a time-space averaging along the particle trajectory and the sum over all parcels  $k_{tot}$  passing the considered control volume is an ensemble averaging. Therefore, to obtain statistically reliable source terms a sufficient number of parcels need to pass the control volumes. The source terms in the conservation equation of the turbulent kinetic energy  $k$  are obtained from the Reynolds-averaging procedure:

$$S_{k,p} = \sum_{i=1}^3 \overline{u_i S_{U_i,p}} - \overline{u_i} \overline{S_{U_i,p}} \quad (6.40)$$

The source term in the  $\varepsilon$ -equation is modelled following in the following way:

$$S_{\varepsilon,p} = C_{\varepsilon,3} \frac{\varepsilon}{k} S_{k,p} \quad (6.41)$$

As demonstrated by Squires and Eaton [121] the constant  $C_{\varepsilon,3}$  is not universal, but depends on the particle response time and concentration. For many situations a value of  $C_{\varepsilon,3} = 1.1$  may be used.

Thereafter, the continuous phase is re-calculated by accounting for the particle phase source terms (Fig. 6.9). In order to avoid convergence problems, an under-relaxation procedure should be applied using the following equation [52]:

$$S_{\phi,p}^{new} = (1 - \gamma) S_{\phi,p}^{old} + \gamma S_{\phi,p}^{samp} \quad (6.42)$$

where  $S_{\phi,p}^{new}$  are the source terms used to calculate the new flow field,  $S_{\phi,p}^{old}$  are the source terms used in the previous Eulerian calculation and  $S_{\phi,p}^{samp}$  are the new source terms sampled in the Lagrangian calculation.

The under-relaxation factor depends on the degree of coupling (i.e. on the particle concentration and their size) and is selected accordingly in the range between zero and one (see for example: [52, 57]). After a certain number of Eulerian iterations

or after a certain degree of convergence is reached for the fluid flow, the particle tracking is performed again since the flow field has changed due to the two-way coupling (i.e. the influence of the particles on the flow field). With the sampled new source terms the continuous phase is solved again and so forth until convergence is reached for the coupled system (Fig. 6.9). The overall convergence is decided based on the evolution of a certain reference value (see [52]), as for example the fluid velocity at a monitoring location.

In the numerical calculations of a horizontal particle-laden pipe flow Lain and Sommerfeld [57] demonstrated the convergence behaviour of a four-way coupled simulation. The residuals showed strong peaks after each introduction of the under-relaxed source terms and then decayed again. This behaviour was maintained throughout the simulation until convergence was reached. However, profiles of the fluid properties showed a continuous approach towards the converged solution which was reached after 27 coupling iterations.

The next coupling mode should be used if the temporal evolution of the flow field needs to be fully resolved. For such *unsteady multi-phase flows*, the timescales of flow and particle tracking are in the same range, namely  $\Delta t_E \approx \Delta t_L$ . This solution procedure applies mainly for DNS and implies that Eulerian and Lagrangian modules are sequentially solved with the same time steps. The minimum of all relevant time scales should be selected here. The special features of this solution approach are:

- All particles or parcels need to be tracked simultaneously.
- The averaging of particle phase properties and the source terms is based on all parcels residing in the computational cells at one instant of time (Fig. 6.10b).
- This requires a very large number of particles to be tracked for obtaining reliable particle phase properties and source terms.
- Moreover, the momentum source terms need to be determined from the instantaneous values of all fluid dynamic forces acting on the particles within a cell (Fig. 6.10b).
- Under-relaxation is not suitable for the full-unsteady approach.

Additionally, there are many unsteady situations where the required Eulerian time step  $\Delta t_E$  is much larger than the expected Lagrangian time steps  $\Delta t_L$ . However by using a common time step, this will be very often dictated by the particle response time. A typical Eulerian time step for URANS or LES simulations may be found between  $\Delta t_E = [10^{-4} \text{ s}, 10^{-2} \text{ s}]$  and Lagrangian time steps may lay in the range  $\Delta t_L = [10^{-8} \text{ s}, 10^{-3} \text{ s}]$ , depending on the type of particle considered. Especially for very small particles, their response time is rather low and hence limiting the Lagrangian time step. For such a situation a so-called *semi-unsteady approach* may be used which was probably first introduced by Sommerfeld et al. [117] and has the following features:

- The flow field is calculated with  $\Delta t_E$  starting from a certain initial condition. Here  $\Delta t_E$  determines the temporal resolution of the flow field and may be pre-determined.

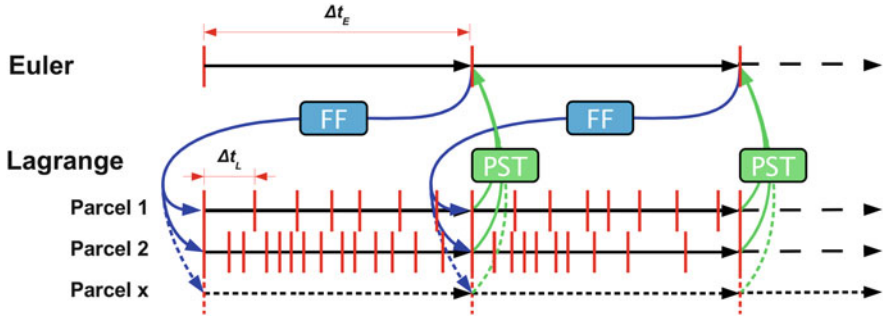


**Fig. 6.11** Illustration of the time-lines for a semi-unsteady Euler/Lagrange simulation [66, 68] with  $\Delta t_E > \Delta t_L$  (At the end of the Eulerian calculation the “frozen” flow field (FF) is used for particle tracking; the particle-phase source terms are coupled back to the fluid flow for the next Eulerian simulation steps (PST))

- Then simultaneous particle tracking is conducted in this “frozen” flow field until the actual time level of the flow is reached for all particles. The particle tracking time step is dynamically adapted for each particle according to the locally relevant time scales (see Eq.(6.38)). During each Eulerian time step, several thousands of computational particles are randomly injected.
- Now the particle phase source terms and the particle properties are averaged over the time sequence  $\Delta t_E$  and additionally ensemble averaging is done (see Fig. 6.10a), similar to the steady-state approach.
- Under-relaxation of source terms shall not be applied in this situation.
- The new source terms are introduced into the fluid flow equations which are then solved for the next Eulerian time step.

This semi-unsteady approach is illustrated in Fig. 6.11, where the upper line shows the fluid timeline and the lower one the particle tracking timeline for several particles exemplarily. This approach is numerically very efficient compared to a full unsteady simulation, since mostly the particle time scales are very small and hence would dictate the Eulerian time step. Such a method was proposed by Sommerfeld et al. [117] for URANS simulations of a locally aerated bubble column and later on used by Lipowsky and Sommerfeld [67] for simulating small particle separation in a gas cyclone.

### 6.6.4 Modelling of Particle-Scale Processes

For the above introduced point-particle approaches all sub-grid-scale and particle-scale phenomena need additional models. The observed particle-scale phenomena are first depending on the type of particles considered, i.e. solid particles, droplets or bubbles. Consequently, processes such as particle motion dynamics (i.e. oscil-

lations), particle-wall collisions and inter-particle collisions need more or less complicated models. Considering for example wall collisions for solid particles, they will be mostly rebound with a change of state (i.e. translational and rotational velocity). They however also might be depositing on the walls due to adhesion forces or even be fragmented. If droplets are considered, then they may be rebound, deposited or splashed [77]. Bubbles will probably only deform, lose momentum and change their direction of motion. Inter-particle collisions of solids result in rebound, but may also yield agglomeration if there exist strong enough adhesion forces. Considering liquid particles (i.e. droplets or bubbles), a collision might result in a number of different outcomes, such as bouncing, coalescence or separation with satellite formation. In the case of liquid particles one also may observe break-up due to the action of shear flows.

This brief survey shows that the modelling of particle-scale phenomena is quite extensive and may be very important for the development of a multi-phase flow process. If possible, the developed models should be based on first principles of physics and theoretical derivations in order to be generally applicable. This however, is not always possible if the particle-scale process is too complex such as droplet wall collisions. In such a case models are being derived from experiments and integrated in the computations in the form of empirical correlations [78]. Therefore, sometimes very extensive experiments are needed for model derivation as for example in the case of droplet collisions where a large parameter space determines the outcome of such collisions (see for example [107]). Indeed, particle-resolved simulations are becoming more and more important in today's model development, but they also require enormous computational resources and sometimes also sophisticated numerical approaches [11]. In the following it is tried to provide an estimate under which conditions particle-wall and inter-particle collisions are important and have to be modelled appropriately.

*Particle-wall collisions* become of importance in confined flows, such as pneumatic conveying or particle separation in cyclones. In pneumatic conveying, for example, the momentum loss of particles caused by an inelastic wall impact is associated with a required re-acceleration of the particles by the fluid after rebound. Hence, momentum is extracted from the fluid phase for this acceleration causing the additional pressure loss. This pressure loss depends on the average wall collision frequency or mean free path between subsequent particle-wall collisions. The wall collision frequency is mainly determined by the following parameters:

- particle mass loading,
- dimensions of the confinement, e.g. pipe diameter in pneumatic conveying,
- particle response time or response distance,
- conveying velocity and turbulence intensity,
- particle shape and wall roughness,
- combination of particle and wall material.

A simple estimate of the importance of particle-wall collisions may be based on the ratio of the particle response distance  $\lambda_p$  to the dimension of the confinement, e.g. the diameter of the pipe  $D$ . The particle response distance can be estimated from the

following equation:

$$\lambda_p = \frac{\rho_p D_p^2}{18\mu_f f_D} w_t \quad (6.43)$$

where  $w_t$  is the terminal velocity of the particles. For the case  $\lambda_p > D$  (the particle response distance is larger than the dimension of the confinement), the particles are not able to respond to the flow before they collide with the opposite wall, hence their motion is dominated by wall collisions. In addition to the above mentioned effects the wall collision process may be affected by hydrodynamic interaction between particle and wall which eventually causes a deceleration of the particle before impact. This effect however is only of importance for viscous fluids and hence small particle Reynolds numbers. Other effects relevant for solid particle wall collisions are the wall roughness structure [95, 106] and a possible adhesion and deposition of the particles. Numerous simulations have been done in the past on pneumatic conveying in pipe systems, emphasising the huge importance of wall roughness and the proper modelling by a statistical approach [56, 58, 98, 108, 109].

In the following the importance of *inter-particle collisions* in turbulent fluid-particle flows is discussed. The inter-particle collision probability depends mainly on the particle concentration, the particle size, and the fluctuating motion of the particles. A classification of particle-laden flows in terms of the importance of inter-particle collisions and the boundary between dilute and dense systems may be based on the ratio of particle response time  $\tau_p$  to the averaged time between collisions  $\tau_c$  [14]. In dilute two-phase flows the particle motion will be mainly governed by fluid dynamic transport effects, i.e. drag force, lift forces, and turbulence. On the other hand dense flows are characterised by high collision frequencies between particles and hence their motion is dominantly influenced by inter-particle collisions. Fluid dynamic transport effects are of minor importance. Therefore, the two regimes are characterised by the following time scale ratios:

$$\text{dilute two-phase flow:} \quad \tau_p < \tau_c \quad \implies \quad \frac{\tau_p}{\tau_c} < 1 \quad (6.44)$$

$$\text{dense two-phase flow:} \quad \tau_p > \tau_c \quad \implies \quad \frac{\tau_p}{\tau_c} > 1 \quad (6.45)$$

This implies that in dense two-phase flows the time between particle-particle collisions is smaller than the particle response time, whereby the particles are not able to completely respond to the fluid flow between successive collisions. This regime may occur when either very large particles at a low number density are present in the flow or in the case of small particles when the number density is large. In dilute two-phase flows collisions between particles may also occur and influence the particle motion to a certain degree, but the time between successive inter-particle collisions is larger than the particle response time, whereby the fluid dynamic transport of the particles is the dominant transport effect.

In the following section an estimate of the boundary between the two regimes will be given for turbulent particle-laden flows by introducing some simplifications. The average time between successive inter-particle collisions results from the average collision frequency:

$$\tau_c = \frac{1}{f_c} \quad (6.46)$$

The collision frequency of one particle (i.e.  $n_i = 1$ ) with diameter  $D_i$  and instantaneous velocity  $u_i$  with all other particle classes (i.e.  $N_{class}$ ) with diameter  $D_j$  and velocity  $u_j$  can be calculated according to kinetic theory of gases from:

$$f_c = \frac{N_{ij}}{n_i} = \sum_{j=1}^{N_{class}} \frac{\pi}{4} (D_i + D_j)^2 |\vec{u}_i - \vec{u}_j| n_j \quad (6.47)$$

The main assumptions associated with the use of Eq. (6.14) are the following:

- The particle number concentration is small enough that the occurrence of binary collisions prevails.
- On the other hand, the particle number concentration must be large enough to allow a statistical treatment.
- The velocities of the colliding particles are not correlated, for example due to turbulence.

An analytic solution of Eq. (6.47) is only possible for relatively simple cases. For the estimation of the collision frequency, the derivation of Abrahamson [1] is followed, yielding a collision rate solely determined by turbulence. Furthermore, a mono-disperse particle phase is considered, whereby the mean fluctuating velocity is a constant. Hence the collision frequency is obtained as a function of the particle diameter,  $D_p$ , the total particle number concentration  $n_p$  and the mean fluctuating velocity of the particles  $\sigma_p$ :

$$f_c = 4\pi^{1/2} n_p D_p^2 \sigma_p \quad (6.48)$$

Introducing the volume fraction of the particles,  $\alpha_p = (\pi/6) D_p^3 n_p$ , one obtains after some re-arrangements:

$$f_c = \frac{24}{\pi^{1/2}} \frac{\alpha_p \sigma_p}{D_p} \quad (6.49)$$

or, similarly, the collision frequency can be expressed as a function of the mass loading  $\eta = \dot{m}_p / \dot{m}_F$ , which is often used to characterise gas-solid flows:

$$f_c = \frac{24}{\pi^{1/2}} \frac{\rho_F}{\rho_p} \frac{\eta \sigma_p}{D_p} \quad (6.50)$$

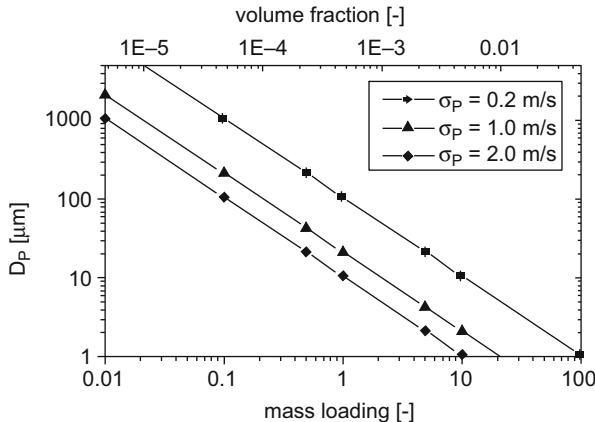


**Fig. 6.12** Regimes of dilute (left of the curves) and dense (right of the curves) gas-solid flows in dependence of mass loading (and volume fraction) and particle diameter for different particle velocity fluctuations  $\sigma_p$  ( $\rho_F = 1.15 \text{ kg/m}^3$ ,  $\rho_p = 2500 \text{ kg/m}^3$ ,  $\mu_F = 18.4 \times 10^{-6} \text{ kg/(m s)}$ ); the dilute regime is left of the curves and the dense regime in the right

By introducing the collision frequency and the Stokesian particle response time into Eqs. (6.49) and (6.50), the limiting particle diameter for a dilute two-phase flow can be determined as a function of volume fraction or mass loading, respectively:

$$D_p < \frac{3}{4} \pi^{1/2} \frac{\mu_F}{\alpha_p \rho_p \sigma_p} \tag{6.51}$$

$$D_p < \frac{3}{4} \pi^{1/2} \frac{\mu_F}{\alpha_p \rho_p \sigma_p} \tag{6.52}$$

Considering a gas-solid flow with the properties ( $\rho_F = 1.15 \text{ kg/m}^3$ ,  $\rho_p = 2500 \text{ kg/m}^3$ ,  $\mu_F = 18.4 \times 10^{-6} \text{ kg/(m s)}$ ) the limiting particle diameter which separates dilute and dense two-phase flow is calculated as a function of volume fraction and mass loading with the particle velocity fluctuation as a parameter. The result is given in Fig. 6.12 where the dilute two phase flow domain is on the left of the individual lines and the dense flow regime is on the right hand side. With increasing particle diameter associated with higher particle inertia (larger  $\tau_p$ ), the range of dilute flow is shifted towards lower volume fractions and mass loading. With increasing velocity fluctuation of the particles the boundary line between dilute and dense two-phase flow is shifted to the left, i.e. to smaller mass loading of the dispersed phase. From Eq. (6.48) it is obvious that the collision frequency increases with the velocity fluctuation of the particles.

Modelling of inter-particle collisions in the frame of the Euler/Lagrange method for the numerical calculation of two-phase flows has been based mainly on two approaches, a direct deterministic simulation and a stochastic model based on concepts of the kinetic theory of gases. The most straight forward approach to

account for inter-particle collisions is the deterministic simulation approach. This requires that all the particles (or in most cases parcels which represent a number of real particles with the same properties) are tracked simultaneously through the flow field. Thereby, the occurrence of collisions between any pair of particles can be judged based on their positions and relative motion during one time step [31]. Once a collision occurs, the change in translational and angular particle velocities can be determined by solving the impulse equations together with Coulombs law of friction. This approach is however very time consuming, since at each time step it requires to search for a possible collision partner among the surrounding particles (see for example [123]). If  $N_p$  parcels are transported in the computational domain then  $N_p(N_p - 1)/2$  examinations of particle pairs are needed for finding collision partners. For that reason, collision partner search is only done within a computational control volume whereby however collisions from particles at the rim of this control volume with particles in one of the neighbouring cells may be missed. Consequently, such an approach would yield collision results which are depending on grid size, which is of course not acceptable. Therefore, mostly independent collision search volumes are defined (i.e. different from the numerical grid used for flow calculations) which reduce the error of grid dependence.

In order to avoid this problem and for having a numerically more efficient algorithm for collision detection the stochastic inter-particle collision model was developed going back to the work of Sommerfeld and Zivkovic [114] and Oesterle and Petitjean [81]. Here a collision partner is not searched, but generated from the local population of particles being represented by size and velocity distributions as well as their correlations. This approach therefore requires information on the particle phase properties in each control volume of the computational domain. The correlation of the velocities of colliding particles is respected in the fictitious particle generation. This stochastic inter-particle collision model is described in detail by Sommerfeld [99], including a thorough validation. Extensions of the stochastic collision model have been done for spray droplets [88], bubbly flows [118] and the agglomeration of fine particles where also the impact efficiency was accounted for [45, 113].

## 6.7 Application Examples of Euler/Lagrange Approach

As a result of the special features of the Euler/Lagrange approach in considering the discrete nature of the dispersed phase numerous technical and fundamental applications were realised in the past. Three application examples will be introduced below. Besides that, a number of other applications were considered, such as a detailed simulation of pneumatic conveying in channels and pipes including the effect of wall roughness and inter-particle collisions [56–58, 109]. A detailed validation based on experiments was conducted in all these studies. Recently, in the same pipe configuration the erosion of the pipe bend was modelled and analysed with respect to the influence of particle mass loading and coupling effects [110].



Also spraying systems are an ideal problem for the application of the Euler/Lagrange approach. In early times several experimental test cases were provided for validation of spray computations [97, 98] including evaporating sprays (with different operational conditions, see [115]), spray interaction with a turbulent flow analysing the effect of droplet collisions [88] and spray interaction with a solid cone modelling droplet-wall impacts [78]. Another important application of spray flows was electrostatic powder coating where the particle behaviour strongly affects the powder deposit layer thickness [7].

Moreover, bubbly flows are an important field of application for the Euler/Lagrange approach. Since normally bubbles are rather large, turbulence production through bubble wakes is an important phenomenon to be modelled. Such a Lagrangian wake turbulence model was developed by Lain et al. [59] and validated against measurements. Another important issue is bubble coalescence whereby the bubble size distribution is modified. A Lagrangian stochastic coalescence model based on the film drainage approach was developed and validated [118].

A very interesting technical process are three-phase bubble columns where the hydrodynamics is strongly affected by the interaction between bubbles and solid particles. This interaction causes the bubble rise to be hindered and the solid particles to be drafted upward. In comparison to measurements, the numerical results showed that bubble/particle interaction is very important in correctly predicting the solids volume fraction along the column. The two models considered, namely bubble/particle collisions using the stochastic model and an Eulerian drafting/hindering model through drag coefficient modifications showed basically the same result [8].

Also in the pharmaceutical field the application of the Euler/Lagrange approach has a huge potential in optimising production processes and dosage devices such as inhalers [112].

In the following three examples are described, each having certain features, such as, unsteady swirling flow with dust rope formation, particle dispersion in stirred vessel emphasizing the importance of inter-particle collisions and liquid solid flow with particle deposition and filter cake formation.

### ***6.7.1 Unsteady Swirling Flow***

This study examines the behaviour of a particle-laden swirling flow through a sudden pipe expansion. This kind of flow is relevant for a number of industrial processes, as for example for pulverised coal burners. It was observed that due to the establishment of the flow recirculation in front of the injection pipe (or burner mouth) a central recirculation region develops [111] which is responsible for the highly unsteady nature of such flows. Consequently, dust ropes (regions of high particle concentration) will develop, that rotate downward with the flow. The numerical prediction of such effects, and possibly the prediction of the characteristic frequencies of oscillations or rope behaviour, needs an unsteady approach, which

was therefore developed in the frame of the Euler/Lagrange approach using a Reynolds-stress turbulence closure [67]. The main problem for such a transient calculation lies in the very different timescales required for Eulerian and Lagrangian calculations. Consequently, here multiple Lagrangian time steps were used in one Eulerian time step (here referred to semi-unsteady method). A fully unsteady simulation on the other hand would lead to large computational times.

The present study concerns a swirling two-phase flow through a pipe expansion, where the gas particle mixture is injected through the central jet and the swirling air stream enters through the annulus. This geometry of the test section resembles a typical swirl burner with two concentric inlets, as shown in Fig. 6.13 which was already used previously [111]. The non-swirling flow laden with particles enters through the central pipe with an inner diameter of 36 mm and the clean annular swirling inflow has an inner diameter of  $W = 40$  mm and the outer diameter is  $1.6 \cdot W = 64$  mm. The diameter of the test section is 200 mm and the considered length is 500 mm. Two flow conditions were considered with different mean velocities and swirl numbers as listed in Table 6.4. This configuration produces very complex flow

**Fig. 6.13** Configuration of the pipe expansion geometry with details of inlet for particle-laden jet and annular swirling flow with dimensions ( $W = 40$  mm)

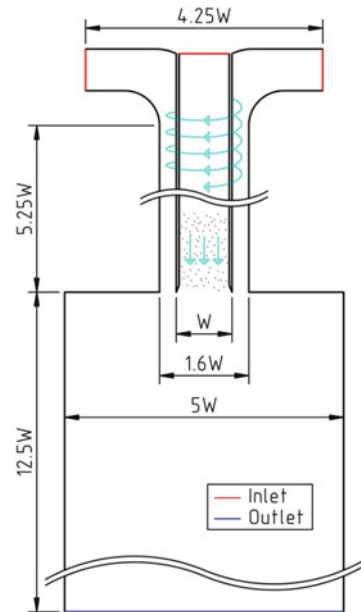


**Table 6.4** Flow conditions at the injection into the swirl chamber for the two considered cases with different swirl number  $S$

Condition	Axial mean velocity in central pipe [m/s]	Axial mean velocity in annulus inlet [m/s]	Swirl number $S$ with test section diameter [-]	Particle mass fraction at inlet [kg/kg]
C1 (case 1)	4.5	10.0	0.76	0.19
C2 (case 2)	7.8	18.2	2.01	0.04

fields with a central recirculation zone in front of the entrance. This recirculation zone moves towards the inlet with increasing swirl intensity. The carrier phase is air at a pressure of  $p = 10^5$  Pa, a density of  $\rho_f = 1.2$  kg/m<sup>3</sup> and a dynamic viscosity of  $\mu = 18 \times 10^{-6}$  Pa s. The particle phase consists of spherical glass beads with a density of  $\rho_p = 2950$  kg/m<sup>3</sup> and a size spectrum between 5 and 70  $\mu$ m having a mean of  $d_{p,m} = 45$   $\mu$ m. During each Eulerian time step several thousands of parcels were injected with randomly selected initial location and velocity from the pre-defined PDFs.

The numerical computations of the swirling flows through the pipe expansion were conducted according to the domain shown in Fig. 6.13, which was discretised by 234.660 control volumes. The computational domain includes the inlet geometry so that for the annular swirling flow radial and tangential velocities were specified as plug flows and for the central jet the mean axial velocities were specified for gas and particles initially without slip (see Table 6.4). Hence, in the calculations the flow developed through the inlet geometry and then entered the test section. The calculated inlet profiles reasonably matched the measurements.

The averaged quasi-steady-state flow structure developing in the pipe expansion is illustrated in Figs. 6.14, 6.15, and 6.16 comparing the low (left) and high (right) swirl case in each of the figures. For the low swirl number a closed central recirculation is observed shown in Fig. 6.14 (please note that negative velocities are

**Fig. 6.14** Averaged quasi-steady airflow field, here *stream-wise velocity*, with two different swirl numbers: left part  $S = 0.76$ , right part  $S = 2.01$  (vertical coordinate  $z$  in [m], radial coordinate  $y$  in [m])

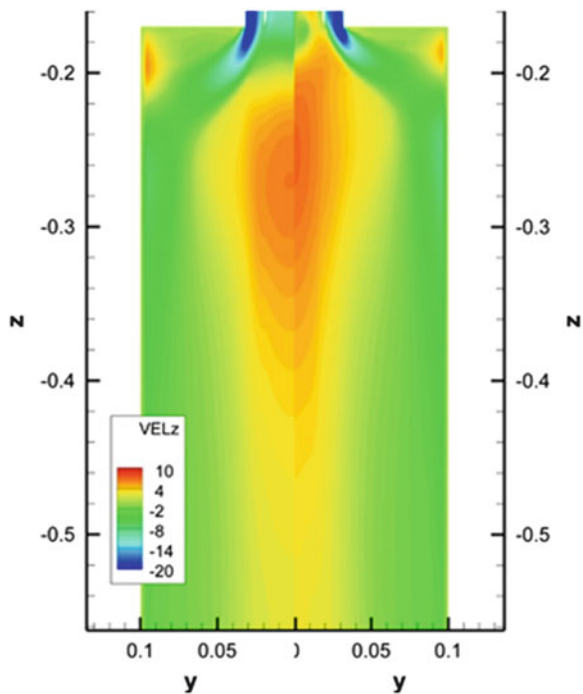
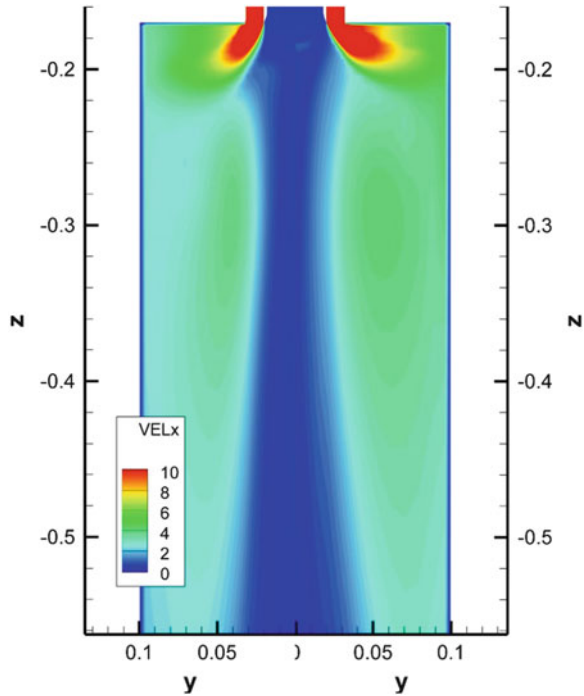


**Fig. 6.15** Averaged quasi-steady airflow field, here *tangential velocity*, with two different swirl numbers: left part  $S = 0.76$ , right part  $S = 2.01$  (see Table 6.4), (vertical coordinate  $z$  in [m], radial coordinate  $y$  in [m])



downward and positive values upward). When drastically increasing the tangential velocity at the injection (see Table 6.4 and Fig. 6.15) the flow expands much stronger and hence the central recirculation is shifted upward (Fig. 6.14). Thereby, the recirculation also extends further downstream until the outlet. The higher swirl and hence higher flow velocities at the injection also drastically increase the turbulent kinetic energy for  $S = 2.01$  as shown in Fig. 6.16.

The main interest in the present study was related to the highly unsteady behaviour of the particle phase in such swirling flows and whether the unsteady simulations capture the experimentally observed rope formation, which moves spirally downward the test section. The simulated temporal evolution of the particle concentration distribution within inlet and test section is shown in Fig. 6.17 at low swirl for three instants of time. From these results the typical particle rope formation may be identified which is rotating and moves spirally downward. It should be noted that this result was obtained without triggering any instabilities at the inlet. Naturally, also the underlying gas flow was continuously fluctuating, which is expected from such a swirling flow. When looking at the case with very high swirl, such a nice rope formation at the top end of the recirculation region is not observed

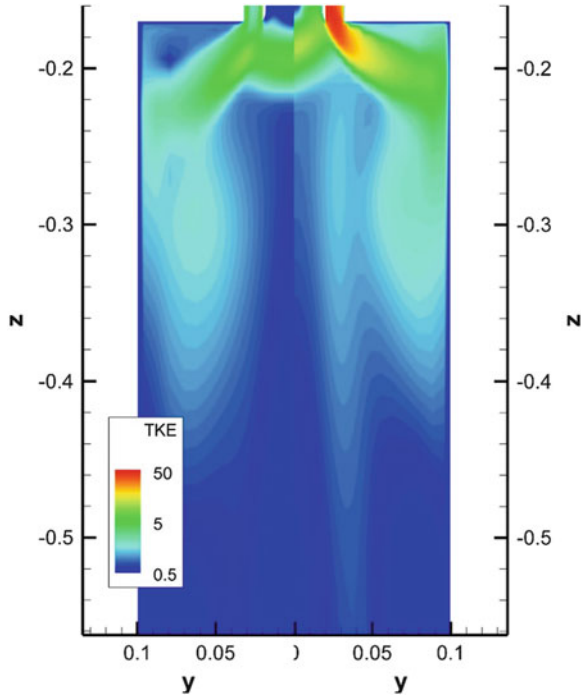


**Fig. 6.16** Averaged quasi-steady airflow field, here *turbulent kinetic energy*, with two different swirl numbers: left part  $S = 0.76$ , right part  $S = 2.01$  (see Table 6.4) (vertical coordinate  $z$  in [m], radial coordinate  $y$  in [m])

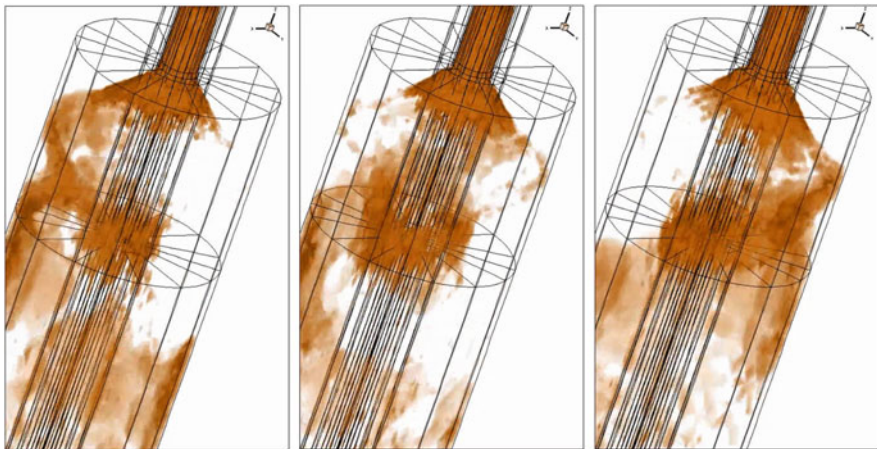


**Fig. 6.17** Temporal evolution of particle concentration for Case 1 with swirl number  $S = 0.76$  at three arbitrary instants of time (the colour represents iso-levels of the particle concentration)

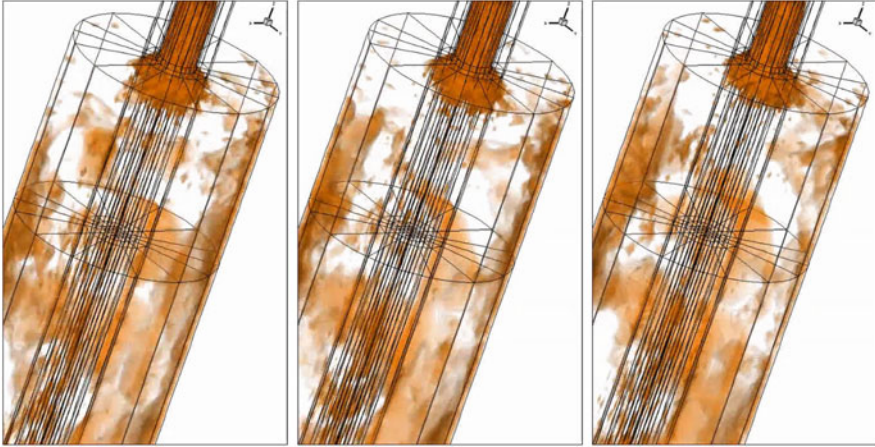


**Fig. 6.18** Temporal evolution of particle concentration for Case 2 with swirl number  $S = 2.01$  at three arbitrary instants of time (the colour represents iso-levels of the particle concentration)

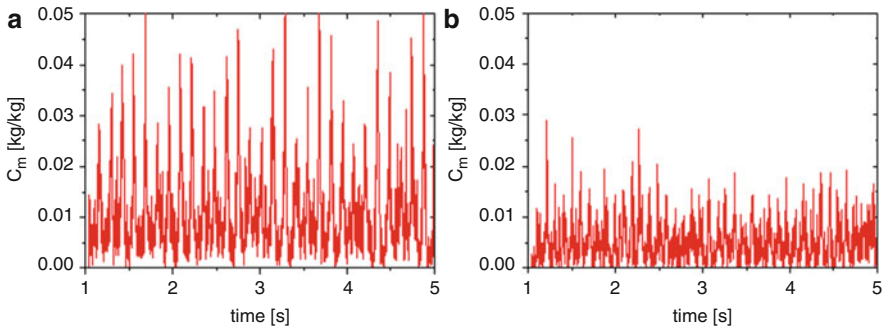


**Fig. 6.19** Simulated temporal development of particle mass fraction at a near-wall location, 300 mm downstream the inlet and 4 mm away from the wall; (a) Case 1 with swirl number  $S = 0.76$ ; (b) Case 2 with swirl number  $S = 2.01$

(Fig. 6.18). Rather, the particle concentration is more random, but still regions of concentrated lumps of particles exist (Fig. 6.18). For quantifying the fluctuations in particle concentration or mass fraction, a location 300 mm downstream of the inlet and 3 mm away from the wall was selected where these values were recorded over time. The result is shown in Fig. 6.19 for both swirl numbers. It is obvious, that the low swirl yields very high particle concentration fluctuations with distinct low frequency oscillations but also having rather strong high frequency fluctuations. On the other hand, high swirl, as already mentioned, shows concentrations that are more random distributed with much lower fluctuations. These recordings do also not show such a nice regular distribution as for the low swirl case. From these concentration signals a FFT (Fast-Fourier-Transformation) was made to identify the characteristic frequencies (see Fig. 6.20). For the low swirl a number of peaks may be identified,

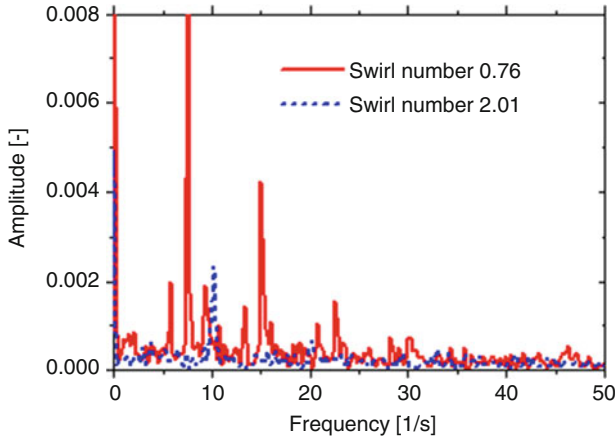


**Fig. 6.20** FFT of the temporal development of calculated particle mass fraction at a near-wall location, 300 mm downstream the inlet and 4 mm away from the wall for both swirl numbers (see Fig. 6.19)

however, the strongest one is observed at 7.5 Hz followed by another one at 15 Hz. As to be expected from the concentration signal, high swirl results in a noisier FFT amplitude with only one recognisable peak at 10 Hz (Fig. 6.20). This higher frequency at large swirl of course results from the larger tangential velocity in this case. Although the experiments visually showed the rope formation, the measured particle concentration signal was much noisier and the resulting FFTs did not show comparable peaks. Nevertheless, the presented scheme for semi-unsteady flows is applicable in many unsteady two-phase flows and allows for numerically efficient simulations.

### 6.7.2 Particle Dispersion in Stirred Vessel

In the following, computations for a stirred vessel (diameter 400 mm) with curved bottom, four baffles and a pitched blade impeller with six blades will be introduced (Fig. 6.21). The three-dimensional Reynolds-averaged conservation equations were solved in connection with the standard  $k - \varepsilon$  turbulence model [61]. The set of conservation equations was solved using a finite-volume discretisation scheme with collocated grid arrangement, which implies the solution of the integral form of the conservation equations. As a solver for the fluid flow the code FASTEST-3D was used, which is based on non-orthogonal block-structured grids with block-wise free topology. The diffusive terms are discretised by central differences, while a hybrid scheme combining upwind- and central differencing is used for the convective terms ( $\gamma_{CD}$  indicated the percentage of central differencing). It was found that a high degree of central differencing (blending factor  $\gamma_{CD} = 0.95$ ) is required to yield a good agreement with measurements [105].



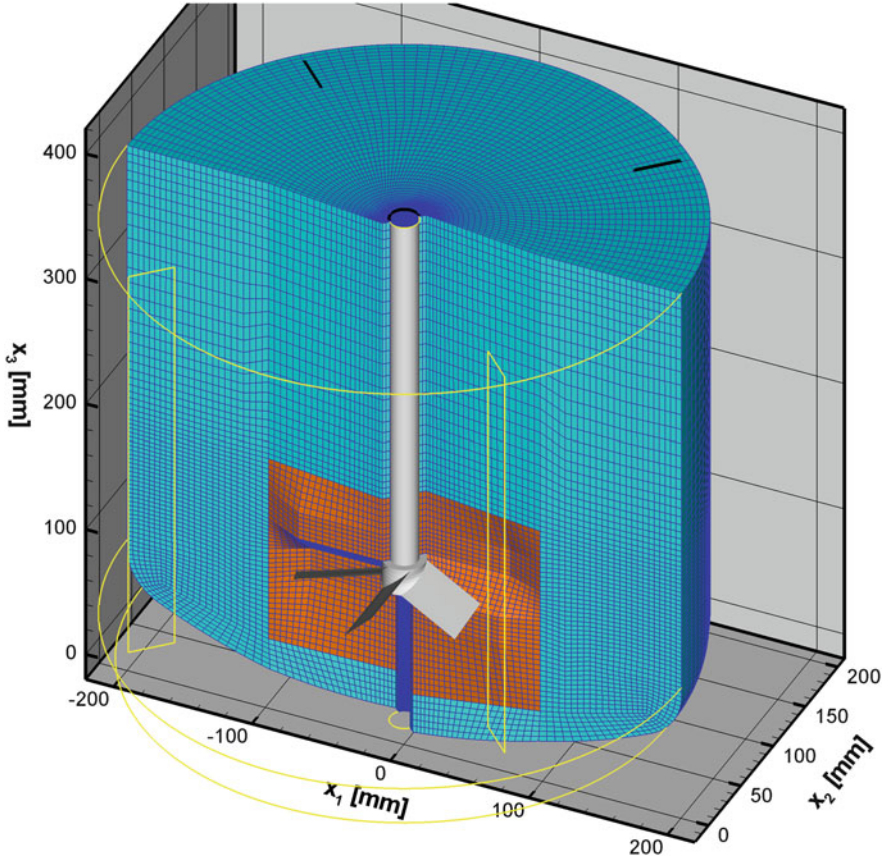


**Fig. 6.21** Geometry and numerical grid of the 400 mm stirred vessel with curved bottom applying the multiple frame of reference (MFR) method with full discretisation of impeller and baffles (the orange area was calculated in the rotating frame of reference)

In order to resolve both, the geometry of the impeller and the baffled tank, the multiple frame of reference (MFR) method was used. For simplicity the blades and baffles are considered to be infinitesimal thin. Due to the symmetry of the stirred vessel a  $180^\circ$  segment was considered by applying periodic boundary conditions in the circumferential direction (Fig. 6.21). At the walls of vessel, baffles and stirrer appropriate wall boundary conditions are specified for all variables. The free surface was treated as a plane wall, since also in the experiments the surface was covered with a thin lid. For analysing the effect of grid resolution on the results, three different meshes with 30,636 (G1), 245,088 (G2) and 1,960,704 (G3) control volumes were considered in the computations. The rotating domain around the impeller extended from  $0 < r < 116$  mm in the radial direction and in the range  $30 \text{ mm} < x < 180$  mm for the vertical direction. This selection ensured almost stationary flow conditions at the outer border of this region, a prerequisite of the



MFR-technique. The vessel was filled with water (density:  $\rho_F = 1000 \text{ kg/m}^3$ , dynamic viscosity:  $\mu_F = 10^{-3} \text{ Pa s}$ ) up to a level of 400 mm.

The effect of grid size and number of control volumes on the numerically calculated fluid properties, especially turbulent kinetic energy and its dissipation rate was already discussed before [105]. Moreover, it was shown that the determination of the Newton number should be done by integrating pressure and shear stress distribution over impeller and shaft and not by using the average dissipation rate throughout the vessel. Nevertheless, an accurate determination of the Newton number requires a huge number of cells for discretising the vessel correctly.

Here the emphasis relates to analysing the importance of inter-particle collisions on the dispersion of solid particles in the stirred vessel for still moderate overall particle volume fraction of up to 5%. These calculations were conducted based on the Euler/Lagrange approach using full two-way coupling for momentum exchange and turbulence modification using appropriate under-relaxation (see [20]). The particle phase simulations were conducted for the two coarser grids, namely G1 and G2. These relatively coarse grids were a compromise between achievable spatial resolution and computational time requirements for particle tracking. A finer grid resolution requires of course much more parcels to be tracked for obtaining the same statistical accuracy of particle properties and source terms. The particle phase was simulated by tracking for each coupling iteration 20,000 parcels simultaneously over a time period of 10 s. Hence, sufficient averaging of particle properties and source terms is guaranteed through a long averaging time period.

Particle motion was calculated using all relevant forces, such as drag, added mass, gravity/buoyancy, transverse lift forces due to shear and rotation [100], as well as centrifugal and Coriolis force in the rotating domain. Particle turbulent dispersion was modelled using a Langevin approach [116]. In addition, inter-particle collisions were considered through the stochastic approach [99], since they have a drastic effect on the particle concentration distribution already for relatively low overall solids volume fractions as will be demonstrated below. In the calculations spherical, mono-sized glass beads with diameters of 100, 200 and 500  $\mu\text{m}$  and a solids density of 2.5  $\text{g/cm}^3$  were used. The volume fraction of solids was varied between 1 and 3%.

A typical result for an impeller speed of 300 1/min is shown in Fig. 6.22 comparing vertical planes midway between two baffles for the calculated normalised fluid velocity modulus and typical trajectories of 200  $\mu\text{m}$  particles where the colour coding represents the normalised magnitude of particle velocity. The particles of this size, which follow the toroidal vortex flow very well, are accelerated downward by the impeller, turn around at the bottom and are lifted upward with the flow against gravity almost completely and reach the surface. Then they move downwards again towards the impeller supported by their gravity. The lifting of the particles from the bottom towards the surface against gravity is responsible for the additional power consumption in mixing of suspensions. Interestingly, some particles also circulate in the counter-rotating stagnation point vortex underneath the impeller.

Essential in the application of the hybrid Euler/Lagrange approach with two-way coupling is the decision about when a converged solution of the coupled system is

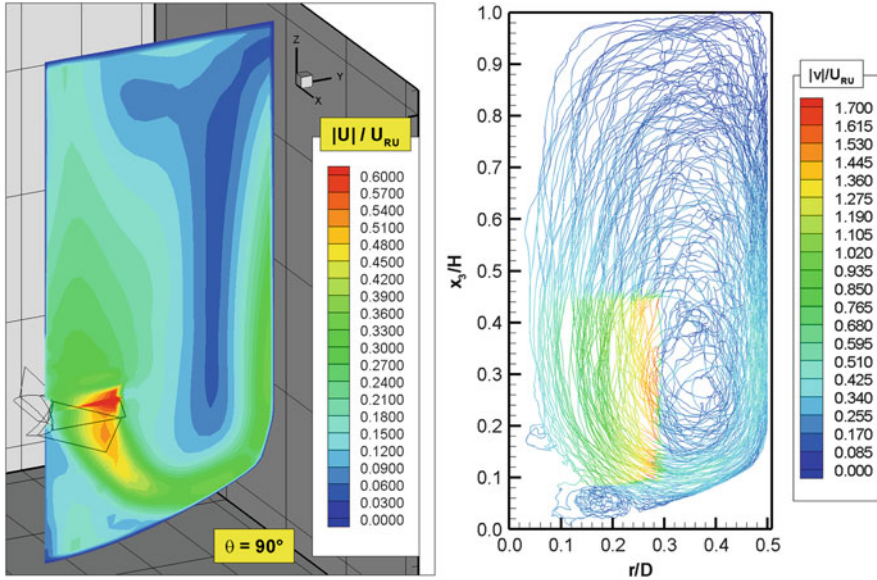


**Fig. 6.22** Illustration of calculated flow field (*left*: modulus of fluid velocity normalised by the impeller tip speed) and particle trajectories (*right*: trajectories colour coded with the normalised modulus of particle velocity) in vertical planes between baffles:  $\theta = 90^\circ$  ( $\gamma_{CD} = 0.95$ ,  $n = 300$  1/min, particle diameter  $200 \mu\text{m}$ , mean volume fraction 1%)

attained. In single-phase flow the residuals of the different fluid properties are normally used to find the required inner fluid iterations for reaching the converged state. For coupled Euler/Lagrange calculations these residuals are uninformative, as they continuously fluctuate [57], wherefore fluid properties at characteristic locations should be used instead. The normalised residuals for the vertical component of the fluid velocity and the turbulent kinetic energy demonstrate this behaviour (Fig. 6.23) for  $D_p = 100 \mu\text{m}$  and  $\varphi_p = 0.01$ . In the two-phase calculations, the number of inner fluid iterations was fixed with 1000, regardless of the values of the residuals. Initially, the residuals rapidly decrease down to values of  $10^{-3}$  to  $10^{-4}$ , as one would expect. However, when particle-phase source terms are introduced, also with under-relaxation the residuals jump up again. This fluctuation is maintained up to the end of the calculation with 160 Euler/Lagrange couplings. Only the lower bounds of the residuals may be somehow used to judge convergence and they oscillate around  $10^{-4}$ . For particle dispersion in stirred vessels, the mixing quality, which is for example the local particle volume fraction, should eventually approach a quasi-steady-state value. Therefore, the averaged particle volume fraction in the upper part of the vessel (here between  $0.85 < x_3/H < 0.9$ ) was used to decide convergence. In this region, stirrer-induced fluctuations are rather small. This spatially averaged and normalised volume fraction is shown in Fig. 6.24 together with the standard deviation. Please note that here  $D_p = 200 \mu\text{m}$  and  $\varphi_p = 0.02$  are considered.

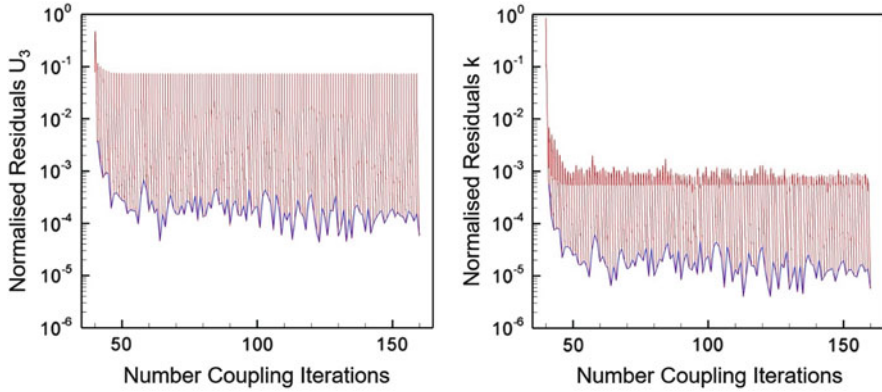


**Fig. 6.23** Development of the residuals for vertical fluid velocity component (*left*) and turbulent kinetic energy (*right*) in dependence of the number of coupling iterations including the behaviour during the inner fluid iterations; *blue line* indicates the lower bound of residuals ( $n = 300$  1/min,  $D_p = 100$   $\mu\text{m}$ , mean volume fraction and  $\varphi_p = 0.01$ )

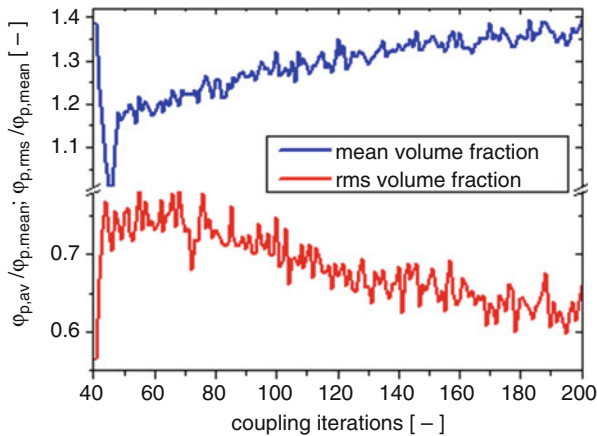


**Fig. 6.24** Development of averaged and normalised particle volume fraction in the vessel between  $0.85 < x_3/H < 0.9$  and associated normalised standard deviation in dependence of the number of coupling iterations ( $n = 300$  1/min,  $D_p = 200$   $\mu\text{m}$ , mean volume fraction and  $\varphi_p = 0.02$ )

In the upper part of the vessel, the particle volume fraction increases with some fluctuations towards a quasi-steady-state value which is reached only after about 200 coupling iterations. On the other hand, the standard deviation decreases as a result of a lower spread of particle volume fraction with increasing coupling iterations, implying an improvement of mixing quality.

The dispersion of particles with different diameter is illustrated in Fig. 6.25 for calculations with inter-particle collisions and for a rate of revolution of 300 1/min. It is obvious, that the small 100  $\mu\text{m}$  particles are almost homogeneously distributed throughout the vessel; only in the core of the toroidal vortex the particle volume

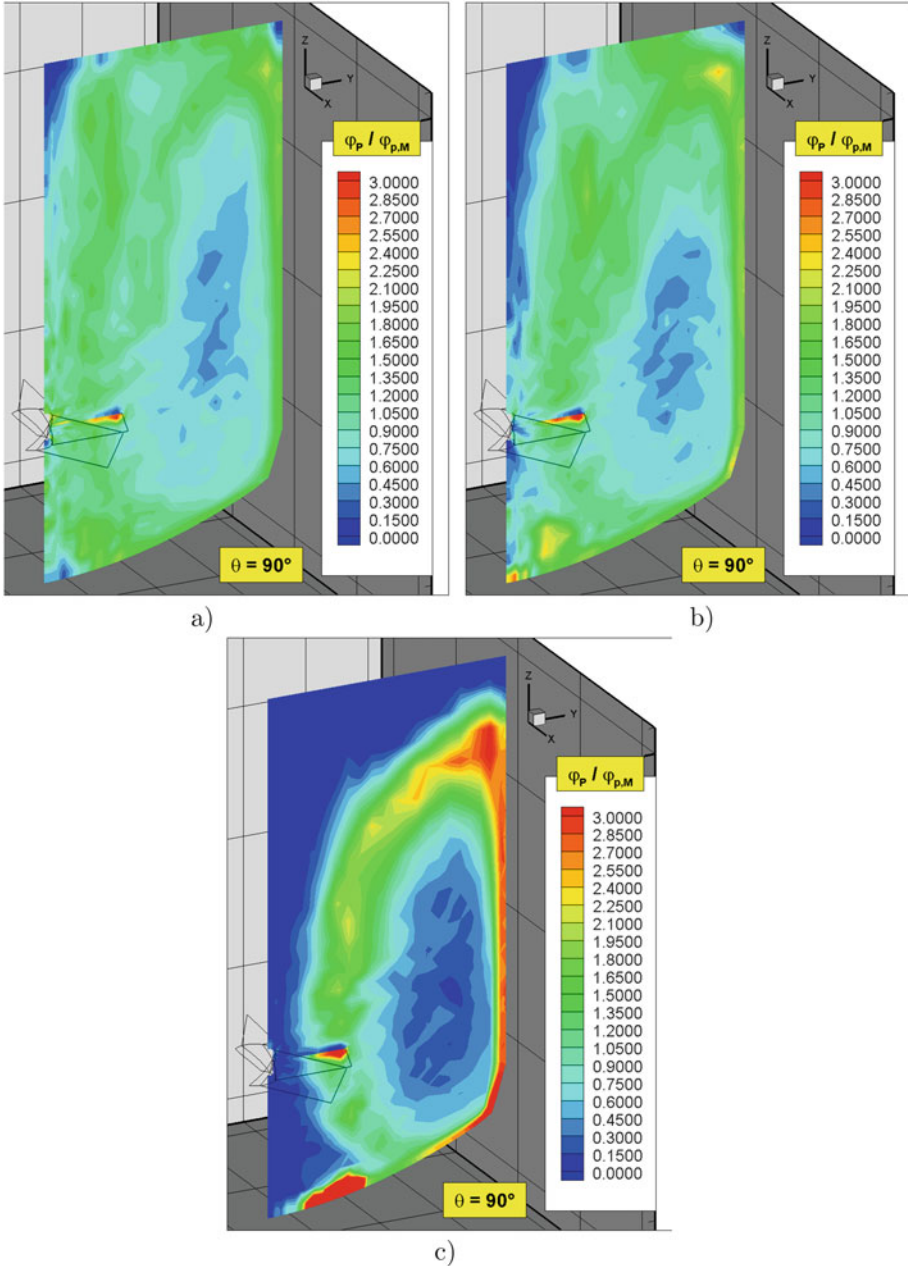


**Fig. 6.25** Comparison of numerically calculated distributions of normalised particle volume fraction (mean volume fraction 1%) for different particle sizes accounting for inter-particle collisions; (a) 100  $\mu\text{m}$ , (b) 200  $\mu\text{m}$ , (c) 500  $\mu\text{m}$  (vertical plane between two baffles:  $\theta = 90^\circ$ ,  $n = 300 \text{ 1/min}$ )

fraction is lower since the particles are centrifuged out of the vortex core. With increasing particle size, a continuous reduction of the particle volume fraction in the vortex core is observed due to their increasing inertia and the associated centrifuging effect. The largest particles considered (i.e.  $500\ \mu\text{m}$ ) are not anymore completely suspended and a large particle free region develops near the surface and in the core of the vessel. This implies that the power input is not sufficient to completely lift-up the particles and centrifugal effects are responsible for the very low particle concentration in the core of the vessel, as well as the core of the toroidal vortex. Because of that, the particles also accumulate near the outer wall of the vessel. Also near the bottom a region of high volume fraction develops which is close to the stagnation region between the large toroidal vortex and the contour-rotating vortex underneath the impeller (see Fig. 6.22).

The main objective of the present study was related to analysing the importance of inter-particle collisions on particle mixing characteristics in stirred vessels. This influence is especially visible for the particle volume fraction distributions that are shown in Fig. 6.26 for vertical planes through the vessel and in Fig. 6.27 for two horizontal planes; one in the plane of the impeller and the other one close to the surface. The particle size is  $200\ \mu\text{m}$  and their average volume fraction 2%, hence inter-particle collisions should be pronounced. Without inter-particle collisions a remarkable accumulation of particles is observed in the recirculation region

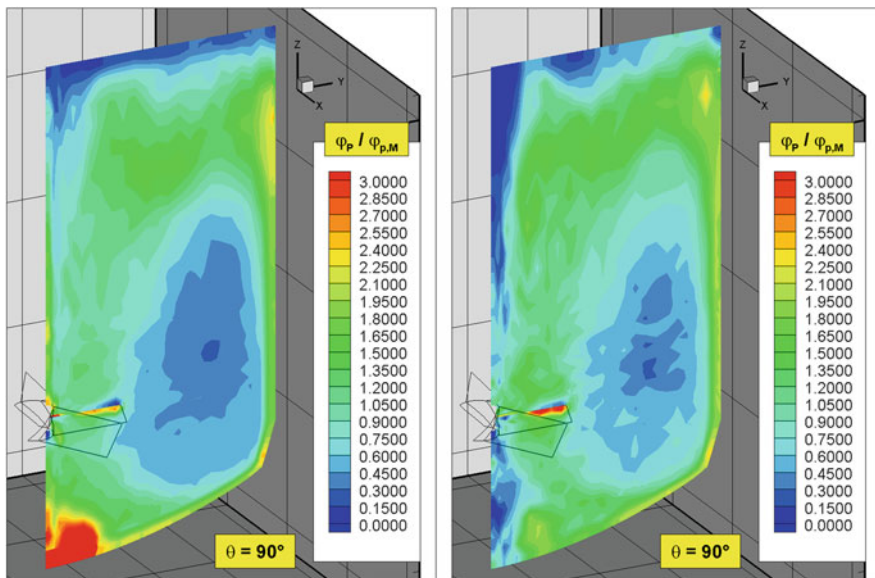


**Fig. 6.26** Comparison of numerically calculated distributions of normalised particle volume fraction in vertical planes (mean volume fraction 2%) for  $200\ \mu\text{m}$  particles, comparing simulations without (*left*) and with (*right*) inter-particle collisions (vertical plane between two baffles:  $\theta = 90^\circ$ ,  $n = 300\ \text{1/min}$ , grid spacing in vertical direction  $100\ \text{mm}$  see also Fig. 6.21)



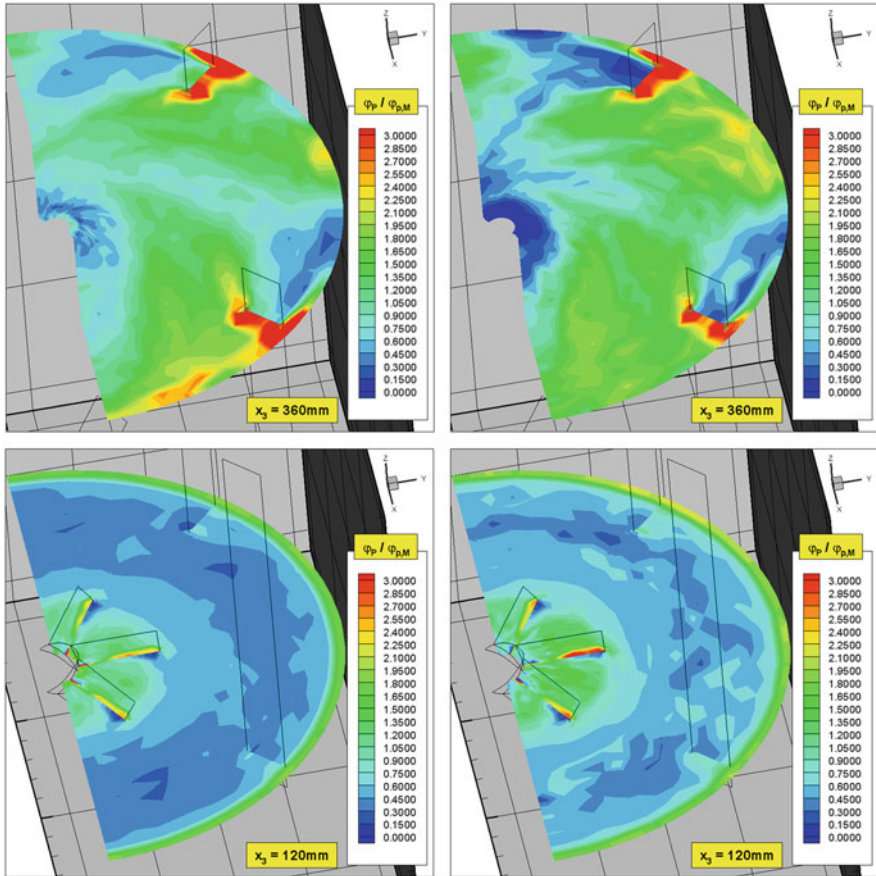


**Fig. 6.27** Comparison of numerically calculated cross-sectional profiles of normalised particle-phase volume fraction (mean volume fraction 2%), in the plane of the impeller ( $x_3 = 120$  mm) and near the surface ( $x_3 = 360$  mm) for  $200 \mu\text{m}$  particles, comparing simulations without (*left*) and with (*right*) inter-particle collisions ( $n = 300$  1/min)

underneath the impeller. Here inter-particle collisions occur with a high probability due to the large relative velocity between particles; here are particles moving around in the recirculation zone and additionally the impeller pumps particles downward. Also near the outer vessel wall inter-particle collisions modify the concentration field; the high particle concentration at the end of the bottom part is reduced and the high concentration region about 100 mm from the surface is shifted upwards.

From the cross-sectional contour plots (Fig. 6.27) it is found that the particle volume fraction behind the impeller blades slightly increases due to inter-particle collisions. Please note that the impeller rotates counter-clockwise. In the region outside the impeller, the particle volume fraction becomes more diffuse due to collisions between particles. The high particle concentration regions appearing in

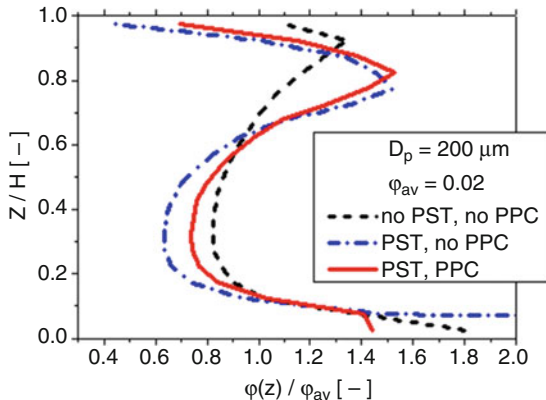


**Fig. 6.28** Numerically calculated vertical profiles of the cross-sectional averaged volume fraction normalised by the total mean particle volume fraction, comparing calculations without source terms and without inter-particle collisions (no PST, no PPC), with source terms and without inter-particle collisions (PST, no PPC) and with source terms and inter-particle collisions (PST, PPC) at higher mean particle volume fraction ( $\varphi_{av} = 0.02$ ,  $n = 300$  1/min)

front of the baffles in the upper region of the vessel are only marginally modified, here particles are trapped and cannot be “kicked” out by inter-particle collisions as the main flow is directed towards the baffles. Consequently, particles moving along with the flow towards the baffles collide with particles circulating in the stagnation region and hinder their re-dispersion into the main flow. This effect is similar to the observation in a pipe bend, where the developing rope is also more concentrated with inter-particle collisions [109].

A quantitative comparison of the effect of two-way coupling and inter-particle collisions on vertical profiles of particle concentration is provided in Figs. 6.28 and 6.29. Here the normalised particle volume fraction averaged in the cross-sectional planes is plotted versus the normalised height. Vertical profiles for the  $200\ \mu\text{m}$  particles at a mean volume fraction of 2% are compared for different simulation conditions (Fig. 6.28). Without the influence of the particles on the flow and neglecting inter-particle collisions, the particles are relatively homogeneously distributed throughout the vessel with the typical minimum at the impeller location (i.e.  $z/H \approx 0.3$ ). In this region the particle velocities are highest due to the acceleration by the impeller yielding the lowest residences here and consequently the lowest volume fractions (Fig. 6.28). However, the particles are completely lifted up to the surface and show some higher volume fraction near the bottom. Now when considering two-way coupling the particles have to be carried by the flow, especially when being lifted upward, which of course requires additional energy or power input. Since however power input is identical (i.e. same impeller speed), the particles cannot be lifted up to the same height due to gravity and the volume fraction maximum now appears at  $z/H \approx 0.72$  (Fig. 6.28). In the impeller region the two-way coupled results show the lowest volume fraction (i.e. about 60% of the

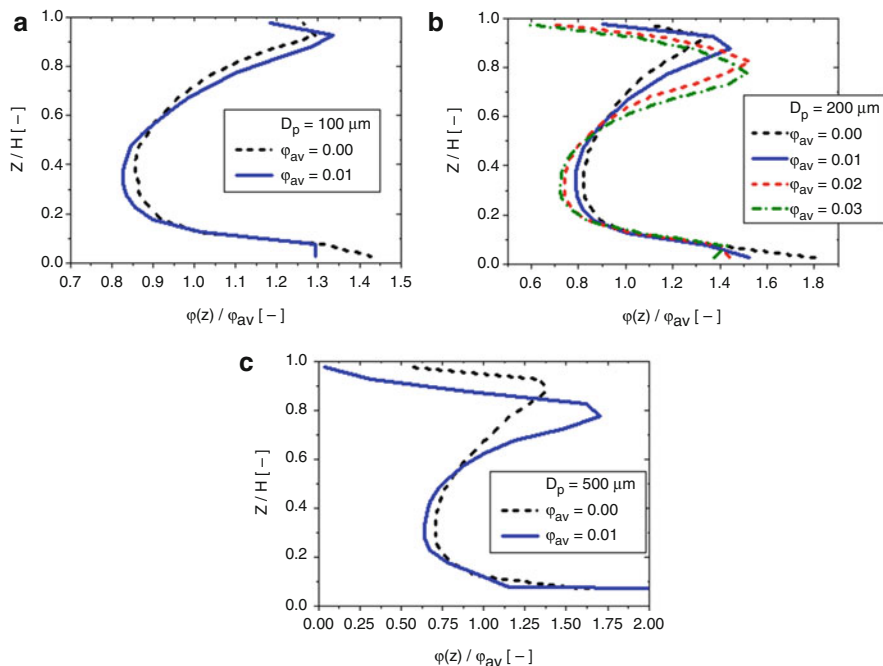


**Fig. 6.29** Numerically calculated vertical profiles of the cross-sectional averaged volume fraction normalised by the total mean particle volume fraction for different particle sizes, comparing calculations without source terms and inter-particle collisions ( $\varphi_{av} = 0.00$ ) with those with two-way coupling and inter-particle collisions at different mean particle volume fraction ( $n = 300$  l/min); (a)  $D_p = 100 \mu\text{m}$ , (b)  $D_p = 200 \mu\text{m}$ , (c)  $D_p = 500 \mu\text{m}$

mean value) since gravity of the particles acts downward, accelerating the liquid flow in this region. Thereby the residence time is further reduced and so the volume fraction. Near the bottom a very high volume fraction is found since the particles damp flow velocity and cannot be lifted upward. In the third case with two-way coupling and inter-particle collisions the high particle concentration near the bottom is further reduced (see also Fig. 6.26) as the particles are re-entrained into the flow by collisions. This improves particle dispersion in the vessel flow and also increases volume fraction in the impeller region. Finally the particles are slightly better lifted upward when accounting for inter-particle collisions (Fig. 6.28).

In Fig. 6.29 the vertical profiles of particle volume fraction for the three considered particle sizes are provided. The results shown for  $\varphi_{av} = 0.00$  represent calculations without two-way coupling as well as neglecting inter-particle collisions and the others are calculations including both effects at different solid volume fractions. In accordance with Fig. 6.25, the dispersion of  $500 \mu\text{m}$  particles is very poor even at this low mean volume fraction ( $\varphi_{av} = 0.01$ ) and accounting for inter-particle collisions (Fig. 6.29c). The power required is not sufficient to completely disperse the particles when respecting their influence on the fluid flow. A much



better dispersion is of course achieved for the smallest particles ( $100\ \mu\text{m}$ ) and the difference between calculations neglecting two-way coupling and inter-particle collisions and those accounting for both effects is marginal (Fig. 6.29a). Near the bottom however particle accumulation is avoided by inter-particle collisions. For the  $200\ \mu\text{m}$  particles the vertical profiles of normalized particle volume fraction are shown for several mean volume fractions (Fig. 6.29b). This result shows that with increasing mean volume fraction particles are more poorly dispersed and lifted for the same rate of revolution due to the limited power available. However, again near the bottom concentration is reduced due to inter-particle collisions, which of course occur more frequent with increasing mean volume fraction.

Another important issue in the prediction of particle suspension in stirred vessels is the resulting Newton number in dependence of particle size and average volume fraction. First the two-way coupling behaviour of the combined Euler/Lagrange calculations is illustrated including inter-particle collision effects. Here the Newton number obtained from the averaged dissipation rate normalised with the respective single phase values is plotted over the number of coupling iterations for different average particle volume fractions (Fig. 6.30a). In this case the  $200\ \mu\text{m}$ -particles are considered. Hence, the results indicate the percentage of additional power required for dispersing the particles. The result reveals that all the calculations for the different particle volume fractions converge towards a limiting value, illustrating that the normalised Newton number increases with volume fraction as expected. However, the number of coupling iteration increases with average volume fraction from about 100 for  $\varphi_{av} = 0.01$  to more than 200 for  $\varphi_{av} = 0.03$ . This is of course associated with an increase of computational time, which is a disadvantage of the Euler/Lagrange approach. On the other hand however, this method allows a much more refined modelling of all the relevant elementary processes affecting the particle motion, such as inter-particle collisions.

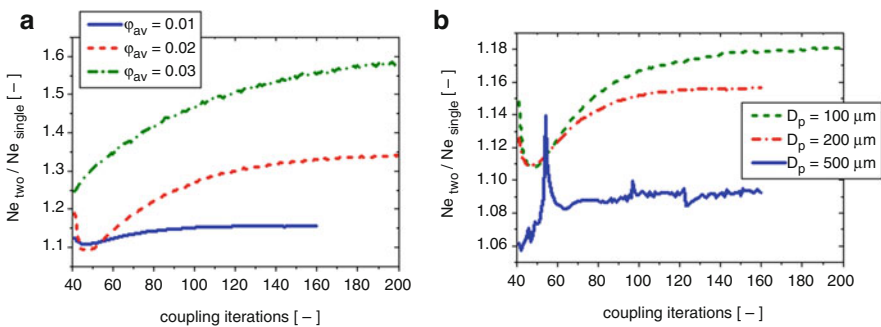


**Fig. 6.30** Two-phase Newton number calculated from the averaged dissipation rate normalised by the single-phase Newton number as a function of coupling iterations; (a) with the mean particle volume fraction as a parameter ( $D_p = 200\ \mu\text{m}$ ,  $n = 300\ \text{l/min}$ ); (b) with the particle diameter as a parameter ( $\varphi_{av} = 1\%$ ,  $n = 300\ \text{l/min}$ )

In Fig. 6.30b the normalised Newton number as a function of coupling iterations is shown for different particle diameters at an average volume fraction of  $\varphi_{av} = 1\%$ . Again, all computations approach a limiting value indicating that convergence is reached in all cases. Interestingly the number of required coupling iterations increases with a reduction of particle size. Moreover, the Newton number is reduced when the particle size increases. Both effects can be explained by the observation that with increasing particle size the quality of dispersion is reduced (see Fig. 6.25). This implies that less particle mass is circulated with the bulk of the flow, requiring less power consumption.

A realistic calculation of aerated stirred vessels becomes even more sophisticated since the bubble size distribution needs to be considered along with the effects of bubble break-up and coalescence. Bubble volume fraction and mean diameters within a vessel agitated by a Rushton turbine were calculated by Lane et al. [60] using a two-fluid approach. For this purpose an additional transport equation for the bubble number density was solved accounting for convective and turbulent transport of the bubbles as well as bubble coalescence and break-up. The coalescence rate was calculated using the collision rate of kinetic theory of gases and assuming the relative velocity between bubbles upon collision being identical to that of the liquid for the inertial subrange of turbulence. The bubble break-up rate was determined on the basis of a critical Weber number and the interaction frequency of bubbles with turbulent eddies. It should be emphasised that this approach can only predict a local bubble mean diameter, but not a bubble size distribution as observed in an experiment. Unfortunately, the computations were not compared with experiments, whereby no judgement on the quality of the computations can be made here.

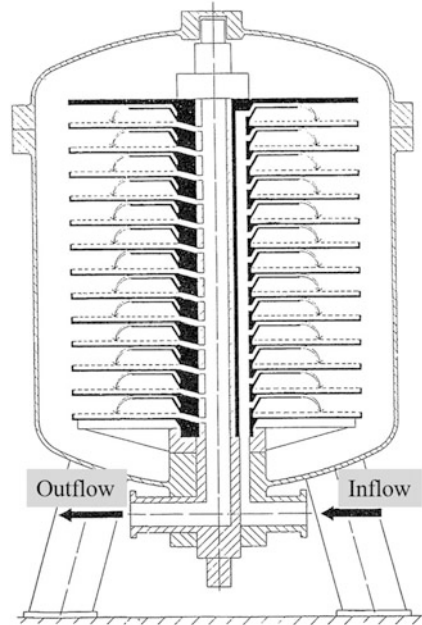
Also the Euler/Lagrange approach was already extended for the calculation of aerated stirred vessels, however, restricting to the phenomenon of bubble break-up [79]. Although the agreement of computed and measured bubble Sauter diameter distribution within the vessel was not yet satisfactorily, the potential of the Euler/Lagrange approach in considering bubble coalescence and break-up was demonstrated.

For more reliable and satisfactory computations of two-phase flows in stirred vessels, however, both approaches (i.e. two-fluid and Euler/Lagrange) need considerable further developments regarding the modelling of the essential two-phase elementary processes in stirred vessels. Until today, especially droplet and bubble coalescence constitute a huge modelling challenge when starting with first principles, since also the molecular scale is relevant due to the very thin fluid films developing between collision partners.

### 6.7.3 Application: Horizontal Blade Filter

Clarifying a liquid by pre-coat blade filters is an important process in the beverage industry. Such a process requires that a homogeneous bed of pre-coat particles, for example using fine kieselguhr particles, is produced on a coarse filter medium or

**Fig. 6.31** Illustration of the entire horizontal pre-coat filter with 13 blade filter elements, inflow of the suspension and outflow of the filtrate, principle of Schenk Filterbau [80]



sieve. Then, during the actual filtration process an actual filter layer already exists, which effectively removes the turbidity of the beverage, for example the yeast in a beer. The principle of this filtration process is a deep bed filtration in the initial stage followed by a cake filtration period. Essential for an effective filtration is a homogeneous thickness of the pre-coat layer. In the present study a stack of revolvable blade filters is considered (Fig. 6.31) which is mounted in a large filter vessel. Through a central pipe the beverage is introduced into the filter system and distributed homogeneously to all the blade filter elements. The inflow for each filter element is realised by a small annular slit underneath the upper filter blade (Fig. 6.32). Then the liquid flows outward across the circular blade filter elements and continuously moves downward through the filter medium to the filtrate outlet that is realised by a central pipe system, which is also used to fix all the circular filter blades. During the pre-coat period a suspension consisting of water and the kieselguhr particles is pumped through the filter apparatus to form the pre-coat layer homogeneously in the radial direction on all filter blades. As one may expect this is not an easy task due to the radial expansion of the flow and the involved pressure drops. However, a homogeneous pre-coat layer is essential for an effective filtration of beverages.

Computational fluid dynamics (CFD) is an effective way to analyse and optimise the pre-coat process, especially with regard to the homogeneity of the pre-coat layer. For that purpose the Euler/Lagrange approach was used to perform time-dependent simulations. As the flow may be turbulent in the inner region of the filter element, the standard  $k - \varepsilon$  turbulence model was used. The momentum equations of the fluid

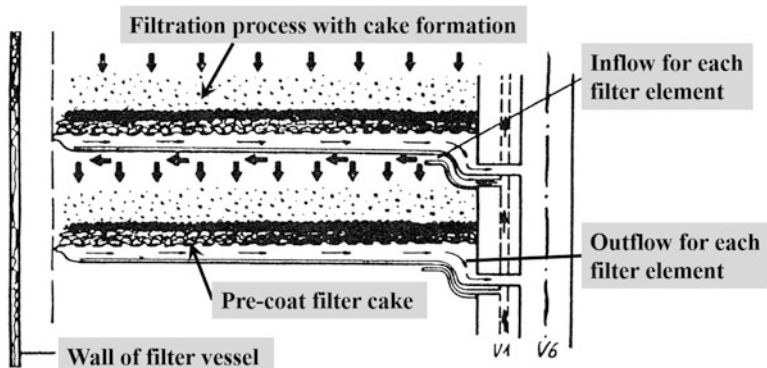


**Fig. 6.32** Details of the flow across one filter blade during the filtration process with inflow and outflow gaps, the filter cake consists of the pre-coat and the turbidity

phase were extended by source terms resulting from the coarse filter medium and the temporarily developing pre-coat layer thickness based on Darcy's law. Since, except for the filter cake, particle concentration was very low, two-way coupling could be neglected without error. Naturally, not the entire filter apparatus was numerically calculated, but only one filter element. Therefore, the problem could be treated to be two-dimensional and axisymmetric. A large number of particles were tracked after each Eulerian time interval  $\Delta t_E$  by accounting for drag, gravity and buoyancy. Although the density ratio  $\rho_p/\rho_w$  is not very large ( $\rho_p = 2400 \text{ kg/m}^3$  and  $\rho_w = 1000 \text{ kg/m}^3$ ) all other forces such as added mass, pressure term and Basset force were neglected and also all transverse lift forces were not considered. The time step of particle tracking was adapted according to the local limiting time scales such as particle response time and integral time scale of turbulence [119]. All particles reaching the initial filter sieve plane are assumed to deposit and the locally accumulated particle mass is summarised for determining the filter loading and the cake thickness that is used to determine the cake resistance source term in the momentum equation of normal fluid velocity component. Since the cake resistance was not known for the kieselguhr particles, these values were obtained by a simple measurement in dependence of cake thickness and the undisturbed through flow velocity.

The numerical grid used for two-dimensional axisymmetric calculations is shown in Fig. 6.33, together with details of the inlet and outlet geometry. The whole domain was discretised by 6898 control volumes separated in 5 blocks (block-structured grid). This grid resolution was found to be sufficient for calculating the features of the flow correctly. The filter sieve was located at  $x = 0.034 \text{ m}$  and was assumed to have a thickness of zero, extending from  $r = 0.169 \text{ m}$  to  $r = 0.724 \text{ m}$ . The inflow to the filter element is considered to be an annular gap with a height of  $h = 0.9 \text{ mm}$  being located at  $r = 0.206 \text{ m}$  (Fig. 6.33b). The inflow was assumed to have a parabolic profile with a mean velocity of  $0.57 \text{ m/s}$ . Thereby, the inflow Reynolds

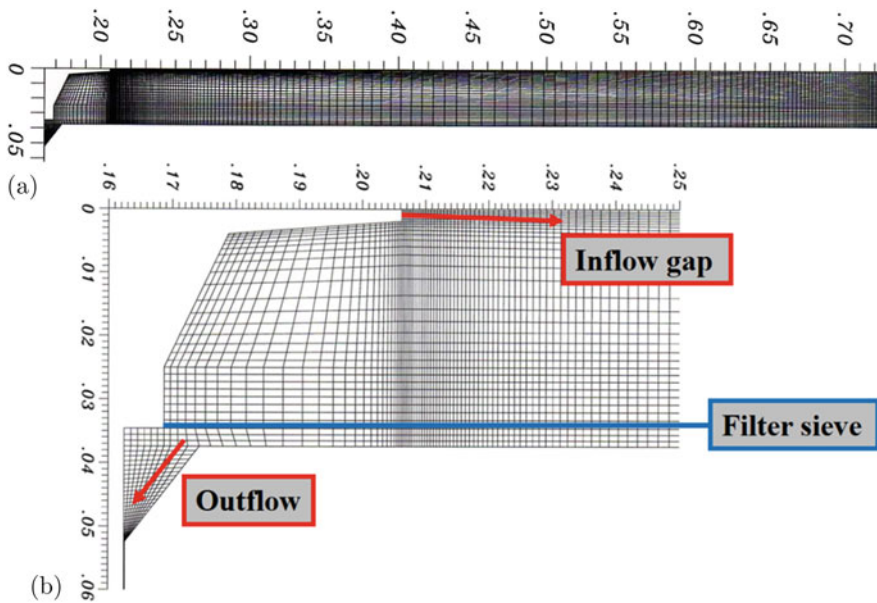


**Fig. 6.33** Two-dimensional numerical grid for one filter element with 6898 control volumes (a) and details of the discretised inflow geometry (b) indicating also the filter sieve (all dimensions in [m])

number is 500, with  $\rho_w = 998 \text{ kg/m}^3$  and  $\mu = 1.0 \times 10^{-3} \text{ Pa s}$ . The outflow was also discretised by an annular gap at the inner side of the filter element (i.e.  $r = 0.163 \text{ m}$ ) ranging from  $0.035 \text{ m} < x < 0.052 \text{ m}$  (Fig. 6.33b). The opening of the filter element towards the filter vessel (Figs. 6.32 and 6.33) was considered to be closed by a wall, since also in practice there exist only low velocities since the vessel is completely filled with stagnant liquid. As mentioned before, the pre-coat medium are fine kieselguhr particles having a size distribution ranging up to about  $128 \mu\text{m}$ . The number mean diameter is only  $0.60 \mu\text{m}$  and the mass mean diameter is  $35 \mu\text{m}$ . For particle injection at the inlet, the number based particle size distribution was of course used.

The time-dependent simulations were conducted in the following way. The conservation equations of the fluid flow were solved with an Eulerian time step of  $0.1 \text{ s}$ . At the beginning only the fluid flow was calculated for  $20 \text{ s}$  to establish a quasi-stationary starting solution. Then the starting time was set to zero and 45 computational particles (or parcels) were injected randomly in space and time at each Eulerian time step with the local fluid velocity. The particle mass flow rate was set to  $\dot{m}_k = 5.557 \times 10^{-3} \text{ kg/s}$  which is the same value as in real process conditions. During each Eulerian time step, the particles experience of course a frozen flow field. The entire pre-coat time of the filter and particle injection was  $420 \text{ s}$ . Thereafter, the simulations were continued for another  $500 \text{ s}$  so that all particles could deposit on the filter medium or filter cake. The temporal change of

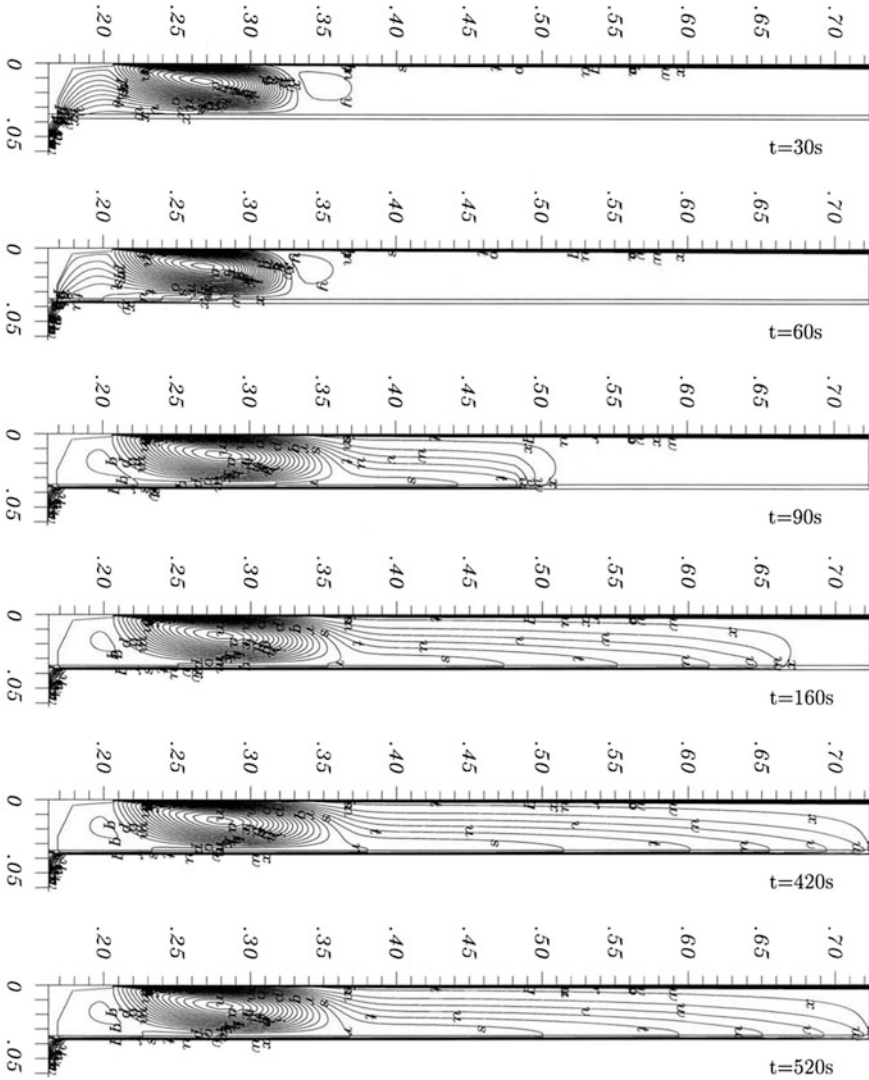


**Fig. 6.34** Temporal evolution of the streamlines in a blade filter element as a result of the continuous deposition of the pre-coat particles ( $t = 420$  s is the end of particle injection), (axis scale in [m], the small letters indicate the values of the stream-functions)

the flow field of course only results from the increasing pressure drop across newly deposited particles.

For understanding the particle behaviour during this simulation period, streamlines and instantaneous particle positions with their velocity vectors (due to the scale not always visible) are analysed (Figs. 6.34 and 6.35). Initially a clear short-cut of the flow is visible where the fluid coming out of the inlet gap turns around and

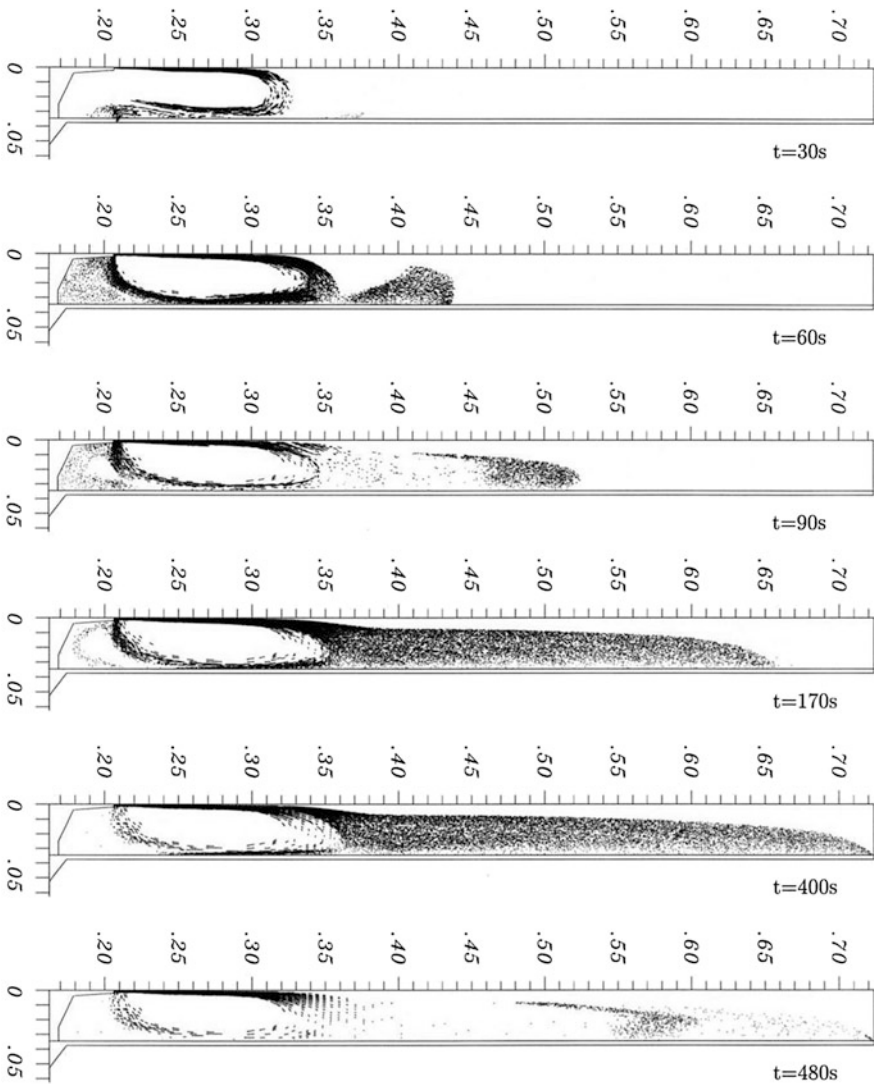


**Fig. 6.35** Temporal evolution of particle positions (shown with their velocity vectors) in a blade filter (at  $t = 420$  s particle injection is terminated), (axis scale in [m])

goes immediately to the outflow because this is the path with the lowest resistance. Thereby also a large recirculation region is initiated. Naturally, the particles follow this flow reversal and begin to deposit in the inner part of the filter medium. Quite large fractions of particles also circulate with the flow recirculation for some time before they deposit. Due to centrifuging, no particles are found in the core of this recirculation region. The growing filter cake in this region of course raises the



pressure drop whereby the flow is forced to move more radially outward until it goes through the filter medium. Consequently, also the particles are transported further in the radial direction and deposit at a larger radius (see Fig. 6.35). Hence, the continuous growth of the deposition in radial direction forces the flow to go further outward before it can pass through the filter medium. In Fig. 6.34 the radial movement of the point of flow return is clearly visible coupled of course with the particle transport (Fig. 6.35). Interestingly, only one large circulation region develops in the inner part of the filter element, which is quite stable. Also in a later stage, no other circulation region develops in the outer blade filter area. However, underneath the inlet gap, very close to the exit, a small counter rotating recirculation develops which also carries particles.

With these simulations, it is also possible to analyse the temporal evolution of the filter loading by the pre-coat particles (Fig. 6.36). The filter loading (also proportional to the filter cake thickness of the pre-coat if a porosity of the filter cake is assumed) of course grows continuously in time from the inside to the outside. Hence, the final pre-coat thickness decreases from the inside to the outside showing characteristic peaks caused by the developing flow structure. The location of the highest filter loading is just in the first part of the inner circulation at about

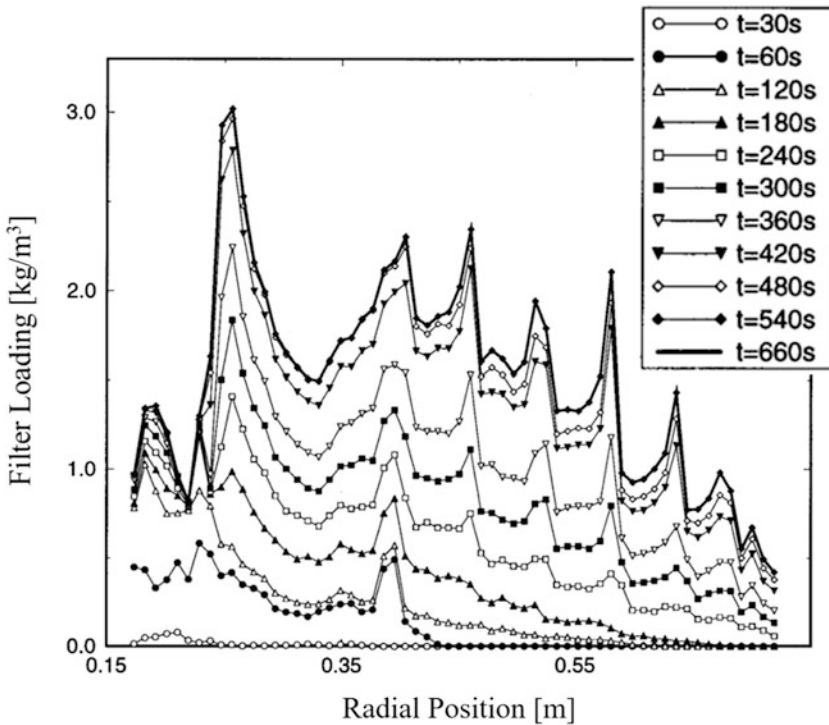


Fig. 6.36 Temporal evolution of the filter loading during the pre-coating of a blade filter element



$r = 0.25$  m and the subsequent minimum is found at its end where a stagnation region develops. As the particles easily follow the flow the particles spread out before the stagnation point (see Fig. 6.35,  $t = 170$  s). From about  $r = 0.40$  m regular peaks of the filter loading are visible which have a separation of about 55 mm again induced by the flow structure, being however not visible in the streamlines (Fig. 6.34).

In conclusion, the pre-coating of the filter medium is not very homogeneous whereby the filtration efficiency for the product liquid or suspension also will not be constant across the filter blade. In addition, it was found that a size separation takes place; in the outer filter region smaller particles are deposited; whereby the pre-coat filter cake structure and hence filtration efficiency will be affected. Naturally, the Lagrangian particle tracking approach may be further extended to account for more details in particle deposition modelling, as for example the relevant adhesion forces and the development of filter cake structure (see for example [26]).

## 6.8 Conclusions and Outlook

This article gives an overview of numerical methods for the calculation of dispersed multi-phase flows. After an introduction to the characteristic features of multi-phase flows, the numerical methods to be used for the different scales of multi-phase processes are introduced. The numerical calculation of large-scale industrial processes requires numerous assumptions regarding particle-scale phenomena and processes occurring on sub-grid scales since the number of control volumes for discretising the process is limited. Only then such large systems can be numerically simulated within an affordable and acceptable computational time. Hence, the dispersed phase particles need to be considered as point-masses in both the Euler/Euler and Euler/Lagrange approach. All transport phenomena not resolved by the numerical grid need additional models or closures. Besides detailed experiments also particle-resolved simulations may support such model development. The available particle-resolved simulation methods were briefly summarized.

Following that the concepts of modelling approaches for macro-scale simulations of dispersed multi-phase flows are introduced, namely the two-fluid (or Euler/Euler) and the Euler/Lagrange method. Based on the particle volume fraction or inter-particle spacing, different flow regimes may be identified in dispersed multi-phase flows, requiring other coupling strategies of fluid and particle phase. The main focus of this article is related to the hybrid Euler/Lagrange approach. Details are provided especially regarding the two-way coupling procedure for steady and unsteady flows. Very often, an efficient solution of unsteady dispersed multi-phase flows can be realized through the semi-unsteady approach using different temporal discretization (i.e. time steps) for the Eulerian and Lagrangian calculations. An essential feature of the Euler/Lagrange approach is the consideration of the discrete nature of the particle phase, allowing a much more detailed modelling of all relevant particle-scale phenomena, such as for example particle-wall and inter-particle collisions.

Estimates for the importance of these two phenomena are provided. Moreover, the Lagrangian approach can easily handle particle size distributions that exist as an inlet condition for the particle phase or are produced during the process under consideration through agglomeration or coalescence.

Finally three application examples are introduced which highlight the special features of the Euler/Lagrange approach; an unsteady swirling flow with dust rope formation, particle dispersion in a stirred vessel emphasizing the importance of inter-particle collisions and a liquid-solid filtration process where information on the structure of filter cake formation is obtained.

In the multi-phase community, there is an ever continuing discussion of the pros and cons of the Euler/Euler and Euler/Lagrange approaches. On a first glance, the two-fluid approach seems to be numerically much more efficient and therefore provides a quick answer to any engineering problem at hand. Very often however, this is at the cost of neglecting essential transport processes and phenomena such as particle size distributions or other of the above mentioned particle-scale processes. The two-fluid method may be extended to consider a spectrum of particle sizes, called multi-fluid approach, but this will dramatically increase computational time since for each size class a set of conservation equations has to be solved. Processes like agglomeration and coalescence may be effectively modelled by population balances, which however apply very often only empirical information.

In this respect the Euler/Lagrange approach has huge advantages since particle-scale phenomena can be modelled in a more descriptive way on the basis of first principles of physics. Hence, particle-scale phenomena are resolved in a much more accurate way compared to the multi-fluid approach including the respective closures. In addition, since computational power still continues to grow, the Euler/Lagrange approach may be extended with more and more sophisticated particle-scale phenomena such as for example the prediction of agglomerate structure [113]. In addition particle-resolved simulations will increase in importance, not only for supporting model and closure development, but also to simulate larger systems than only a hand full of particles.

## References

1. J. Abrahamson, Collision rates of small particles in a vigorously turbulent fluid. *Chem. Eng. Sci.* **30**, 1371–1379 (1975)
2. B. Abramzon, W. Sirignano, Droplet vaporization model for spray combustion calculations. *Int. J. Heat Mass Transf.* **32**, 1605–1618 (1989)
3. A. Bakker, Applied computational fluid dynamics: Lecture 10: Turbulence models (2002). <http://www.bakker.org>
4. G. Balzer, O. Simonin, Extension of Eulerian gas-solid flow modelling to dense fluidised bed prediction. in *Proceedings of the 5th International Symposium on Refined Flow Modelling and Turbulence Measurements* (1993)
5. G. Balzer, A. Boelle, O. Simonin, Eulerian gas-solid flow modelling of dense fluidized bed. *Fluidization* **8**, 1125–1134 (1995)

6. A. Berlemont, P. Desjonqueres, G. Gouesbet, Particle Lagrangian simulation in turbulent flows. *Int. J. Multiphase Flow* **16**, 19–34 (1990)
7. C.-U. Böttner, M. Sommerfeld, Numerical calculation of electrostatic powder painting using the Euler/Lagrange approach. *Powder Technol.* **125**, 206–216 (2002)
8. E. Bourloutski, M. Sommerfeld, Euler/Lagrange calculations of gas-liquid-solid-flows in bubble columns with phase interaction, in *Bubbly Flows: Analysis, Modelling and Calculation*, ed. by M. Sommerfeld (Springer, Berlin, 2004), pp. 243–259
9. T.M. Burton, J.K. Eaton, Fully resolved simulations of particle-turbulence interaction. *J. Fluid Mech.* **545**, 67–111 (2005)
10. P. Chen, M.P. Duduković, J. Sanyal, Three-dimensional simulation of bubble column flows with bubble coalescence and breakup. *AIChE J.* **51**, 696–712 (2005)
11. X.Y. Chen, Ch. Focke, H. Marschall, D. Bothe, Investigation of elementary processes of non-newtonian droplets inside spray processes by means of direct numerical simulation, in *Process-Spray* (Springer, Cham, 2016)
12. E. Climent, M.R. Maxey, The force coupling method: a flexible approach for the simulation of particulate flows. *Theoretical Methods for Micro Scale Viscous Flows* (Transworld Research Network, Trivandrum, 2009), pp. 173–193
13. J. Cousin, A. Berlemont, T. Ménard, S. Grout, Primary breakup simulation of a liquid jet discharged by a low-pressure compound nozzle. *Comput. Fluids* **63**, 165–173 (2012)
14. C.T. Crowe, On the relative importance of particle-particle collisions in gas-particle flows, in *Proceedings of the Conference on Gas Borne Particles*, Paper 78/81 (1981), pp. 135–137
15. C.T. Crowe (ed.), *Multiphase Flow Handbook* (CRC Press/Taylor & Francis Group, Boca Raton, 2006)
16. C.T. Crowe, M.P. Sharma, D.E. Stock, The particle-source-in-cell (psi-cell) model for gas-droplet flows. *J. Fluids Eng.* **99**, 325–332 (1977)
17. C.T. Crowe, J.D. Schwarzkopf, M. Sommerfeld, Y. Tsuji, *Multiphase Flows with Droplets and Particles*, 2nd edn. (CRC Press/Taylor & Francis Group, Boca Raton, 2012)
18. G.T. Csanady, Turbulent diffusion of heavy particles in the atmosphere. *Atmos. Sci.* **20**, 201–208 (1963)
19. P.A. Cundall, O.D.L. Strack, A discrete numerical model for granular assemblies. *Geotechnique* **29**, 47–65 (1979)
20. S. Decker, *Zur Berechnung von gerührten Suspensionen mit dem Euler-Lagrange-Verfahren*. Dissertation Martin-Luther-Universität Halle-Wittenberg, Fachbereich Ingenieurwissenschaften (2005)
21. N.G. Deen, M. Van Sint Annaland, M.A. Van der Hoef, J.A.M. Kuipers, Review of discrete particle modeling of fluidized beds. *Chem. Eng. Sci.* **62**, 28–44 (2007)
22. J.J. Derksen, Direct numerical simulations of aggregation of monosized spherical particles in homogeneous isotropic turbulence. *AIChE J.* **58**, 2589–2600 (2012)
23. O. Desjardins, V. Moureau, H. Pitsch, An accurate conservative level set/ghost fluid method for simulating turbulent atomization. *J. Comput. Phys.* **227**, 8395–8416 (2008)
24. M.T. Dhotre, N.G. Deen, B. Niceno, Z. Khan, J.B. Joshi, Large eddy simulation for dispersed bubbly flows: a review. *Int. J. Chem. Eng.* **2013**, Article ID 343276 (2013)
25. M. Dietzel, M. Sommerfeld, Numerical calculation of flow resistance for agglomerates with different morphology by the lattice-Boltzmann method. *Powder Technol.* **250**, 122–137 (2013)
26. M. Dietzel, M. Ernst, M. Sommerfeld, Application of the lattice-Boltzmann method for particle-laden flows: point-particles and fully resolved particles. *Flow Turbul. Combust.* **97**, 539–570 (2016)
27. J. Ding, D. Gidaspow, A bubbling fluidization model using kinetic theory of granular flow. *AIChE J.* **36**, 523–538 (1990)
28. S. Elghobashi, On predicting particle-laden turbulent flows. *Appl. Sci. Res.* **52**, 309–329 (1994)

29. H. Enwald, E. Peirano, A.-E. Almstedt, Eulerian two-phase flow theory applied to fluidisation. *Int. J. Multiphase Flow*, Suppl. **22**, 21–66 (1996)
30. M. Ernst, Analyse des Clustering-, Kollisions- und Agglomerationsverhalten von Partikeln in laminaren und turbulenten Strömungen, Dissertation Zentrum für Ingenieurwissenschaften, Martin-Luther-Universität Halle-Wittenberg (2016)
31. M. Ernst, M. Sommerfeld, On the volume fraction effects on inertial colliding particles in homogeneous isotropic turbulence. *J. Fluids Eng. Trans. ASME* **134**, 031302 (2012)
32. M. Ernst, M. Sommerfeld, Resolved numerical simulation of particle agglomeration, in *Colloid Process Engineering, Proceedings of Topical problems of Fluid Mechanics 2014* (Springer, Cham, 2015), pp. 45–71
33. M. Ernst, M. Dietzel, M. Sommerfeld, A lattice Boltzmann method for simulating transport and agglomeration of resolved particles. *Acta Mech.* **224**, 2425–2449 (2013)
34. P. Fede, O. Simonin, A. Ingram, 3D numerical simulation of a lab-scale pressurized dense fluidized bed focussing on the effect of the particle-particle restitution coefficient and particle-wall boundary conditions. *Chem. Eng. Sci.* **142**, 215–235 (2016)
35. J.H. Ferziger, M. Peric, *Computational Methods for Fluid Dynamics*, 3rd edn. (Springer, Berlin, 2002)
36. O. Filippova, D. Hänel, Grid refinement for lattice-BGK models. *J. Comput. Phys.* **147**, 219–228 (1998)
37. J. Fröhlich, *Large Eddy Simulation turbulenter Strömungen* (Teubner Verlag, Wiesbaden, 2006)
38. H. Gao, H. Li, L.-P. Wang, Lattice Boltzmann simulation of turbulent flow laden with finite-size particles. *Comput. Math. Appl.* **65**, 194–210 (2013)
39. D. Gidaspow, *Multiphase Flow and Fluidization-Continuum and Kinetic Theory Descriptions* (Academic, Boston, 1994)
40. R. Glowinski, T.W. Pan, T.I. Hesla, D.D. Joseph, J. Périaux, A fictitious domain approach to the direct numerical simulation of incompressible viscous flow past moving rigid bodies: application to particulate flow. *J. Comput. Phys.* **169**, 363–426 (2001)
41. A.D. Gosman, I.E. Ioannides, Aspects of computer simulation of liquid-fueled combustors. Aerospace Science Meeting, Paper No. AIAA-81-0323 (1981)
42. G. Gouesbet, A. Berlemont, Eulerian and Lagrangian approaches for predicting the behaviour of discrete particles in turbulent flows. *Prog. Energy Combust. Sci.* **25**, 133–159 (1999)
43. Z. Guo, C. Zheng, B. Shi, An extrapolation method for boundary conditions in lattice Boltzmann method. *Phys. Fluids* **14**, 2007–2010 (2002)
44. T.J. Hanratty, *Physics of Gas-Liquid Flows* (Cambridge University Press, Cambridge, 2013)
45. C.A. Ho, M. Sommerfeld, Modelling of micro-particle agglomeration in turbulent flow. *Chem. Eng. Sci.* **57**, 3073–3084 (2002)
46. A. Hölzer, M. Sommerfeld, Lattice Boltzmann simulations to determine drag, lift and torque acting on non-spherical particles. *Comput. Fluids* **38**, 572–589 (2009)
47. S. Horender, Y. Hardalupas, Turbulent particle mass flux in a two-phase shear flow. *Powder Technol.* **192**, 203–216 (2009)
48. H.H. Hu, N.A. Patankar, M.Y. Zhu, Direct numerical simulations of fluid-solid systems using the arbitrary Lagrangian-Eulerian technique. *J. Comput. Phys.* **169**, 427–462 (2001)
49. Y. Igci, A.T. Andrews IV, S. Sundaresan, S. Pannala, T. O'Brian, Filtered two-fluid models for fluidized gas-particle suspensions. *AIChE J.* **54**, 1431–1448 (2008)
50. R. Issa, Simulation of intermittent flow in multiphase oil and gas pipelines, in *Seventh International Conference on CFD in the Minerals and Process Industries*, CSIRO, Melbourne, Australia, 9–11 December 2009 (2013)
51. T.K. Kjeldby, R. Henkes, O.J. Nydal, Slug tracking simulation of severe slugging experiments. *Int. J. Mech. Aerospace Ind. Mechatron. Manuf. Eng.* **5**, 1156–1161 (2011)
52. G. Kohnen, M. Rügner, M. Sommerfeld, Convergence behaviour for numerical calculations by the Euler/Lagrange method for strongly coupled phases, in *Numerical Methods in Multiphase Flows 1994*, FED-vol. 185, ed. by C.T. Crowe et al. (ASME, New York, 1994)

53. E. Krepper, Th. Frank, D. Lucas, H.M. Prasser, Ph.J. Zwart, Inhomogeneous MUSIG model-a population balance approach for polydispersed bubbly flows, in *Proceedings of The 12th Int. Topical Meeting on Nuclear Reactor Thermal Hydraulics (NURETH-12)*, 30 September - 4 October 2007, Pittsburgh, Pennsylvania, Log No. 60 (2007)
54. S. Kriebitzsch, R. Rzehak, Baseline model for bubbly flows: simulation of monodisperse flow in pipes of different diameters. *Comput. Fluid Dyn.* **1**, 1–28 (2016)
55. J.G.M. Kuerten, Point-particle DNS and LES of particle-laden turbulent flow - a state-of-the-art review. *Flow Turbul. Combust.* **97**, 689–713 (2016)
56. S. Lain, M. Sommerfeld, Euler/Lagrange computations of pneumatic conveying in a horizontal channel with different wall roughness. *Powder Technol.* **184**, 76–88 (2008)
57. S. Lain, M. Sommerfeld, Numerical calculation of pneumatic conveying in horizontal channels and pipes: Detailed analysis of conveying behaviour. *Int. J. Multiphase Flow* **39**, 105–120 (2012)
58. S. Lain, M. Sommerfeld, Characterisation of pneumatic conveying systems using the Euler/Lagrange approach. *Powder Technol.* **235**, 764–782 (2013)
59. S. Lain, D. Bröder, M. Sommerfeld, M.F. Göz, Modelling hydrodynamics and turbulence in a bubble column using the Euler-Lagrange procedure. *Int. J. Multiphase Flow* **28**, 1381–1407 (2002)
60. G.L. Lane, M.P. Schwarz, G.M. Evans, Predicting gas-liquid flow in a mechanically stirred tank. *Appl. Math. Model.* **26**, 223–235 (2002)
61. B.E. Launder, D.B. Spalding, The numerical computation of turbulent flows. *Comput. Methods Appl. Mech. Eng.* **3**, 269–289 (1974)
62. M. Lesieur, O. Metais, P. Comte, *Large Eddy Simulations of Turbulence* (Cambridge University Press, Cambridge, 2005)
63. J. Li, J.A.M. Kuipers, Gas-particle interactions in dense gas-fluidized beds. *Chem. Eng. Sci.* **58**, 711–718 (2003)
64. J. Li, J.A.M. Kuipers, Effect of competition between particle-particle and gas-particle interactions on flow patterns in dense gas-fluidized bed. *Chem. Eng. Sci.* **62**, 3429–3442 (2007)
65. Y. Liao, R. Rzehak, D. Lucas, E. Krepper, Baseline closure model for dispersed bubbly flow: bubble coalescence and breakup. *Chem. Eng. Sci.* **122**, 336–349 (2015)
66. J. Lipowsky, Zur instationären Euler/Lagrange-Simulation partikelbeladener Drallströmungen, Dissertation, Zentrum Für Ingenieurwissenschaften, Martin-Luther-Universität Halle-Wittenberg (2013)
67. J. Lipowsky, M. Sommerfeld, Time dependent simulation of a swirling two-phase flow using an anisotropic turbulent dispersion model, in *Proceedings of the ASME Fluids Engineering Summer Conference, Houston, Texas* (2005)
68. J. Lipowsky, M. Sommerfeld, LES-simulation of the formation of particle strands in swirling flows using an unsteady Euler-Lagrange approach, in *Proceedings of the 6th International Conference on Multiphase Flow, ICMF2007* (2007)
69. C. Loha, H. Chattopadhyay, P.K. Chatterjee, Assessment of drag models in simulating bubbling fluidized bed hydrodynamics. *Chem. Eng. Sci.* **75**, 400–407 (2012)
70. S. Lomholt, M.R. Maxey, Force-coupling method for particulate two-phase flow: stokes flow. *J. Comput. Phys.* **184**, 381–405 (2003)
71. E. Loth, Numerical approaches for motion of dispersed particles, droplets and bubbles. *Prog. Energy Combust. Sci.* **26**, 161–223 (2000)
72. K. Luo, J. Tan, Z. Wang, J. Fan, Particle-resolved direct numerical simulation of gas-solid dynamics in experimental fluidized beds. *AIChE J.* **62**, 1917–1932 (2016)
73. M.V. Lurie, E. Sinaiski, *Modeling of Oil Product and Gas Pipeline Transportation* (Wiley-VCH, Weinheim, 2008)
74. J.M. MacInnes, F.V. Braco, Stochastic particle dispersion and the tracer particle limit. *Phys. Fluids A* **4**, 2809–2824 (1992)
75. T. Ménard, S. Tanguy, A. Berlemont, Coupling level set/vof/ghost fluid methods: Validation and application to 3d simulation of the primary break-up of a liquid jet. *Int. J. Multiphase Flow* **33**, 510–524 (2007)

76. R. Mittal, G. Iaccarino, Immersed boundary methods. *Annu. Rev. Fluid Mech.* **37**, 239–261 (2005)
77. Chr. Mundo, M. Sommerfeld, C. Tropea, Droplet-wall collisions: experimental studies of the deformation and breakup process. *Int. J. Multiphase Flow* **21**, 151–173 (1995)
78. Chr. Mundo, M. Sommerfeld, C. Tropea, On the modelling of liquid sprays impinging on surfaces. *Atomization Sprays* **8**, 625–652 (1998)
79. A.F. Nassar, G. Zivkovic, B. Genenger, F. Durst, PDA measurements and numerical simulation of turbulent two-phase flow in stirred vessels, in *Bubbly Flows: Analysis, Modelling and Calculation*, ed. by M. Sommerfeld (Springer, Berlin, 2004), pp. 337–352
80. D. Oechsle, W. Baur, Praxiserfahrungen mit einem neuen Horizontalfilter. *Brauwelt*, Jahrg. **129**, 2176–2180 (1989)
81. B. Oesterlé, A. Petitjean, Simulation of particle-to-particle interactions in gas-solid flows. *Int. J. Multiphase Flow* **19**, 199–211 (1993)
82. A. Ozel, P. Fede, O. Simonin, Development of filtered Euler-Euler two-phase model for circulating fluidized bed: high resolution simulation, formulation and a priori analyses. *Int. J. Multiphase Flow* **55**, 43–63 (2013)
83. J.-F. Parmentier, O. Simonin, A functional subgrid drift velocity model for filtered drag prediction in dense fluidized bed. *AIChE J.* **58**, 1084–1098 (2012)
84. C.S. Peskin, The fluid dynamics of heart valves: experimental, theoretical, and computational methods. *Annu. Rev. Fluid Mech.* **14**, 235–259 (1982)
85. A. Prosperetti, G. Tryggvason, *Computational Methods for Multiphase Flow* (Cambridge University Press, Cambridge, 2009)
86. M.A. Rizk, S.E. Elghobashi, A two-equation turbulence model for dispersed dilute confined two-phase flow. *Int. J. Multiphase Flow* **15**, 119–133 (1989)
87. M. Rudman, Volume-tracking methods for interfacial flow calculations. *Int. J. Numer. Methods Fluids* **24**, 671–691 (1997)
88. M. Rüger, S. Hohmann, M. Sommerfeld, G. Kohnen, Euler/Lagrange calculations of turbulent sprays: the effect of droplet collisions and coalescence. *Atomization Sprays* **10**, 47–81 (2000)
89. S. Sazhin, Modelling of heating, evaporation and ignition of fuel droplets: combined analytical, asymptotic and numerical analysis. *J. Phys. Conf. Ser.* **22**, 174–193 (2005)
90. L. Schiller, A. Naumann, Über die grundlegende Berechnung bei der Schwerkraftaufbereitung. *Ver. Dtsch. Ing.* **44**, 318–320 (1933)
91. S. Schneiderbauer, S. Pirker, A coarse-grained two-fluid model for gas-solid fluidized beds. *J. Comput. Multiphase Flows* **6**, 29–47 (2014)
92. O. Simonin, Prediction of the dispersed phase turbulence in particle laden jet, in *Gas-Solid Flows*, ed. by D.E. Stock et al. ASME-JSME Fluids Engineering Conference, FED-vol. 121 (ASME, New York, 1991), pp. 197–206
93. O. Simonin, Statistical and continuum modelling of turbulent reactive particulate flows. Part I: Theoretical derivation of dispersed phase Eulerian modelling from probability density function kinetic equation. *Theoretical and Experimental Modelling of Particulate Flow*. VKI Lecture Series 2000-06 (von Karman Institute for Fluid Dynamics, Brussels, 2000)
94. M. Sommerfeld, Particle dispersion in turbulent flow: the effect of particle size distribution. *Part. Part. Syst. Charact.* **7**, 209–220 (1990)
95. M. Sommerfeld, Modelling of particle/wall collisions in confined gas-particle flows. *Int. J. Multiphase Flow* **18**, 905–926 (1992)
96. M. Sommerfeld, *Modellierung und numerische Berechnung von partikelbeladenen turbulenten Strömungen mit Hilfe des Euler/Lagrange-Verfahrens*. Habilitationsschrift, Universität Erlangen-Nürnberg (Shaker Verlag, Aachen, 1996)
97. M. Sommerfeld, Modelling and numerical calculation of turbulent gas-solid flows with the Euler/Lagrange approach. *KONA (Powder and Particle)*, No. 16 (1998), pp. 194–206
98. Sommerfeld, M.: Analysis of isothermal and evaporating sprays using phase-Doppler anemometry and numerical calculations. *Int. J. Heat Fluid Flow* **19**, 173–186 (1998)
99. M. Sommerfeld, Validation of a stochastic Lagrangian modelling approach for inter-particle collisions in homogeneous isotropic turbulence. *Int. J. Multiphase Flows* **27**, 1828–1858 (2001)

100. M. Sommerfeld, Bewegung fester Partikel in Gasen und Flüssigkeiten, in *VDI-Wärmeatlas*, 9. Auflage, Kapitel Lca 1–9 (Springer, Berlin, 2002)
101. M. Sommerfeld (ed.), in *Proceedings of the 11th Workshop on Two-Phase Flow Predictions (CD-Rom)*, Merseburg, April 2005, Fachbereich Ingenieurwissenschaften, University of Halle (2005)
102. M. Sommerfeld, Particle motion in fluids, in *VDI-Buch: VDI Heat Atlas*, Part 11 (Springer, Berlin, 2010), pp. 1181–1196
103. M. Sommerfeld (ed.), in *Proceedings of the 12th Workshop on Two-Phase Flow Predictions (CD-Rom)*, Merseburg, März 2010, Zentrum für Ingenieurwissenschaften, Martin-Luther-Universität Halle-Wittenberg (2010)
104. M. Sommerfeld, Report on the 13th Workshop on Two-Phase Flow Predictions. ERCOFTAC Bulletin, No. 95 (2013)
105. M. Sommerfeld, S. Decker, State of the art and future trends in CFD simulation of stirred vessel hydrodynamics. *Chem. Eng. Technol.* **27**, 215–224 (2004)
106. M. Sommerfeld, N. Huber, Experimental analysis and modelling of particle-wall collisions. *Int. J. Multiphase Flow* **25**, 1457–1489 (1999)
107. M. Sommerfeld, M. Kuschel, Modelling droplet collision outcomes for different substances and viscosities. *Exp. Fluids* **57**, 187 (2016)
108. M. Sommerfeld, S. Lain, From elementary processes to the numerical prediction of industrial particle-laden flows. *Multiph. Sci. Technol.* **21**, 123–140 (2009)
109. M. Sommerfeld, S. Lain, Parameters influencing dilute-phase pneumatic conveying through pipe systems: a computational study by the Euler/Lagrange approach. *Can. J. Chem. Eng.* **93**, 1–17 (2015)
110. M. Sommerfeld, S. Lain, Euler/Lagrange methods. in *Multiphase Flow Handbook*, 2nd edn. (CRC Press, Boca Raton, 2017)
111. M. Sommerfeld, H.-H. Qiu, Characterization of particle laden, confined swirling flows by phase-doppler anemometry and numerical calculation. *Int. J. Multiphase Flow* **9**, 1093–1127 (1993)
112. M. Sommerfeld, S. Schmalfuß, Numerical analysis of carrier particle motion in dry powder inhaler. *ASME J. Fluid Eng.* **138**, 041308-1 to 041308-12 (2016)
113. M. Sommerfeld, S. Stübing, A novel Lagrangian agglomerate structure model. *Powder Technol.* **319**, 34–52 (2017)
114. M. Sommerfeld, G. Zivkovic, Recent advances in the numerical simulation of pneumatic conveying through pipe systems. in *Computational Methods in Applied Science* (Elsevier, Amsterdam, 1992)
115. M. Sommerfeld, G. Kohnen, H.-H. Qiu, Spray evaporation in turbulent flow: numerical calculations and detailed experiments by phase-doppler anemometry. *Rev. Inst. Fr. Pétrol.* **48**, 677–695 (1993)
116. M. Sommerfeld, G. Kohnen, M. Rüger, Some open questions and inconsistencies of Lagrangian particle dispersion models, in *Ninth Symposium on Turbulent Shear Flows, Kyoto Japan* (1993)
117. M. Sommerfeld, S. Decker, G. Kohnen, Time-dependent calculation of bubble columns based on the time-averaged Navier-Stokes equations with turbulence model, in *Proceedings of the Japanese-German Symposium on Multi-Phase Flow, Tokyo, Japan* (1997), pp. 323–334
118. M. Sommerfeld, E. Bourloutski, D. Bröder, Euler/Lagrange calculations of bubbly flows with consideration of bubble coalescence. *Can. J. Chem. Eng.* **81**, 508–518 (2003)
119. M. Sommerfeld, B. van Wachem, R. Oliemans, Best practice guidelines for computational fluid dynamics of dispersed multiphase flows, in *ERCOFTAC: European Research Community on Flow, Turbulence and Combustion*, Brussels (2008)
120. K.D. Squires, J.K. Eaton, Preferential concentration of particles by turbulence. *Phys. Fluids A* **3**, 1169–1178 (1991)
121. K.D. Squires, J.K. Eaton, Effect of selective modification of turbulence on two-equation models for particle-laden turbulent flows. *Trans. ASME, J. Fluids Eng.* **116**, 778–784 (1994)

122. S. Sundaresan, Modeling the hydrodynamics of multiphase flow reactors: Current status and challenges. *AIChE J.* **46**, 1102–1105 (2000)
123. T. Tanaka, Y. Tsuji, Numerical simulation of gas-solid two-phase flow in a vertical pipe: on the effect of inter-particle collision. In *Gas-Solid Flows* (ASME, New York, 1991)
124. L. Tang, F. Wen, Y. Yang C.T. Crowe, J.N. Chung, T.R. Troutt, Self-organizing particle dispersion mechanism in free shear flows. *Phys. Fluids* **A4**, 2244–2251 (1992)
125. S. Tenneti, S. Subramaniam, Particle-resolved direct numerical simulation for gas-solid flow model development. *Annu. Rev. Fluid Mech.* **46**, 199–230 (2014)
126. Y. Tsuji, T. Kawaguchi, T. Tanaka, Discrete particle simulation of two-dimensional fluidized bed. *Powder Technol.* **77**, 79–87 (1993)
127. M. Uhlmann, An immersed boundary method with direct forcing for simulation of particulate flows. *J. Comput. Phys.* **209**, 448–476 (2005)
128. S. Unverdi, G. Tryggvason, Front-tracking method for viscous, incompressible, multi-fluid flows. *J. Comput. Phys.* **100**, 25–37 (1992)
129. B.G.M. Van Wachem, J.C. Schouten, C.M. Van den Bleek, R. Krishna, J.L. Sinclair, Comparative analysis of CFD models of dense gas-solid systems. *AIChE J.* **47**, 1035–1051 (2001)
130. A.W. Vreman, Particle-resolved direct numerical simulation of homogeneous isotropic turbulence modified by small fixed spheres. *J. Fluid Mech.* **796**, 40–85 (2016)
131. G.B. Wallis, *One-Dimensional Two-Phase Flow*, 2nd edn. (McGraw Hill, New York, 1979)
132. Q.G. Wang, W. Yao, Computation and validation of the interphase force models for bubbly flow. *Int. J. Heat Mass Transf.* **98**, 799–813 (2016)
133. D.C. Wilcox, *Turbulence Modelling for CFD*, 3rd edn. (DCW Industries, La Cañada Flintridge, 2006)
134. G.H. Yeoh, J.Y. Tu, Numerical modelling of bubbly flows with and without heat and mass transfer. *Appl. Math. Modell.* **30**, 1067–1095 (2005)
135. G.H. Yeoh, J.Y. Tu, *Computational Techniques for Multi-Phase Flows* (Elsevier, Amsterdam, 2010)
136. M. Zastawny, G. Mallouppas, F. Zhao, B. van Wachem, Derivation of drag and lift force and torque coefficients for non-spherical particles in flows. *Int. J. Multiphase Flow* **39**, 227–239 (2012)
137. D.H. Zhang, N.G. Deen, J.A.M. Kuipers, Euler-Euler modelling of flow, mass transfer, and chemical reaction in a bubble column. *Ind. Eng. Chem. Res.* **48**, 47–57 (2009)
138. W. Zhong, Y.Q. Xiong, Z.L. Yuan, M.Y. Zhang, Dem simulation of gas-solid flow behaviours in spout-fluid bed. *Chem. Eng. Sci.* **61**, 1571–1584 (2006)
139. Q. Zhou, M.A. Leschziner, A time-correlated stochastic model for particle dispersion in anisotropic turbulence, in *8th Symposium on Turbulent Shear Flows, TU Munich*, vol. 1 (1991), p. 1031
140. N. Zuber, J. Findlay, Average volumetric concentration in two-phase systems. *Trans. ASME J. Heat Transf.* **87**, 453–468 (1965)



# Chapter 7

## Path Instabilities of Axisymmetric Bodies Falling or Rising Under the Action of Gravity and Hydrodynamic Forces in a Newtonian Fluid

J. Dušek

**Abstract** The chapter deals with the effect of instabilities on the paths of sedimenting or rising bodies in Newtonian fluids. To separate the effect of shape, we focus on axisymmetric objects. Spheres, discs, oblate spheroids and flat cylinders are all expected to follow vertical trajectories with axisymmetry axis aligned with the trajectory. This is, indeed, the case, however, this regime remains stable only if viscous effects are sufficiently strong. The loss of stability of the vertical regime leads to a large variety of trajectories depending on the details of shape, namely their flatness (expressed by aspect ratio for cylinders or spheroids), their inertia and viscous effects (expressed by some equivalent of Reynolds number). Defined in this manner, the problem is basically that of axisymmetry breaking.

Since a significant part of dynamics is expected to arise in the wake, we first focus on axisymmetry breaking of wakes of fixed axisymmetric bodies, the sphere being considered as a prototypical case. We show that the scenario is dominated by two bifurcations following systematically, with increasing Reynolds number, in the order of the regular one as primary and a Hopf one as secondary. The weakly non-linear analysis points out the relevance of Fourier azimuthal decomposition serving as an optimal numerical tool for all presented simulations. Next, the free body degrees of freedom are accounted for. The interplay of the regular and Hopf bifurcations still dominates, however, the scenario is significantly different for spheres and flat objects. The presented parametric study shows that trajectories of spheres become very rapidly chaotic. As an example of flat object, nominally infinitely thin disc is investigated. In this case the Hopf bifurcation is the primary one. The scenario is remarkable by strong subcritical effects due to the significant role of inertia of the combined motion of the solid and of the surrounding fluid.

**Keywords** Direct numerical simulations • Discs • Parametric study • Path instabilities • Spheres • Solid-fluid interaction

---

J. Dušek (✉)

Institut ICube, équipe Mécanique des Fluides, 2, rue Boussingault, 67000 Strasbourg, France  
e-mail: [dusek@unistra.fr](mailto:dusek@unistra.fr)

**MSC2010:** 35Q30, 76D05, 76D25, 76E09, 76E30, 76M22

## 7.1 Introduction

The understanding of the motion of a single body driven by gravity and buoyancy in a quiescent fluid is fundamental for all problems involving a free motion of particles in laminar and turbulent flows. Intuitively, a sphere or a flat axisymmetric body (disc, flat cylinder or an oblate spheroid) is expected to fall vertically with its axis also oriented vertically. To predict its terminal velocity, the knowledge of the drag is sufficient. This simple picture considerably changes with the onset of instabilities in the solid–fluid system in which the 6 degrees of motion of the solid body interact with the surrounding fluid. As soon as instabilities set in, many counter-intuitive phenomena appear not only in a system of a single particle in quiescent fluid but also in the particle interaction with turbulent flow and in multi-particle systems.

To evidence non vertical trajectories of discs, there is no need of sophisticated experiments. Figure 7.1 shows the behavior of a plastic shopping cart token dropped in water. Similarly, in a laboratory set up, we registered [13, 14] trajectories of buoyant spherical polypropylene balls of about 2.5 mm of diameter freely rising in water. As seen in Fig. 7.2, non-vertical trajectories were observed.

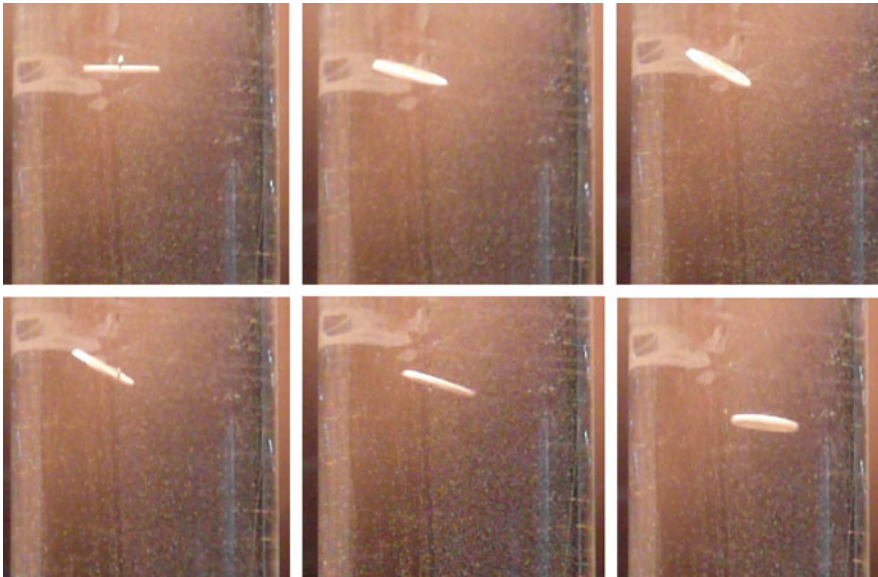


**Fig. 7.1** Six snapshots of a half period of the zig-zagging motion of a plastic disc falling in water

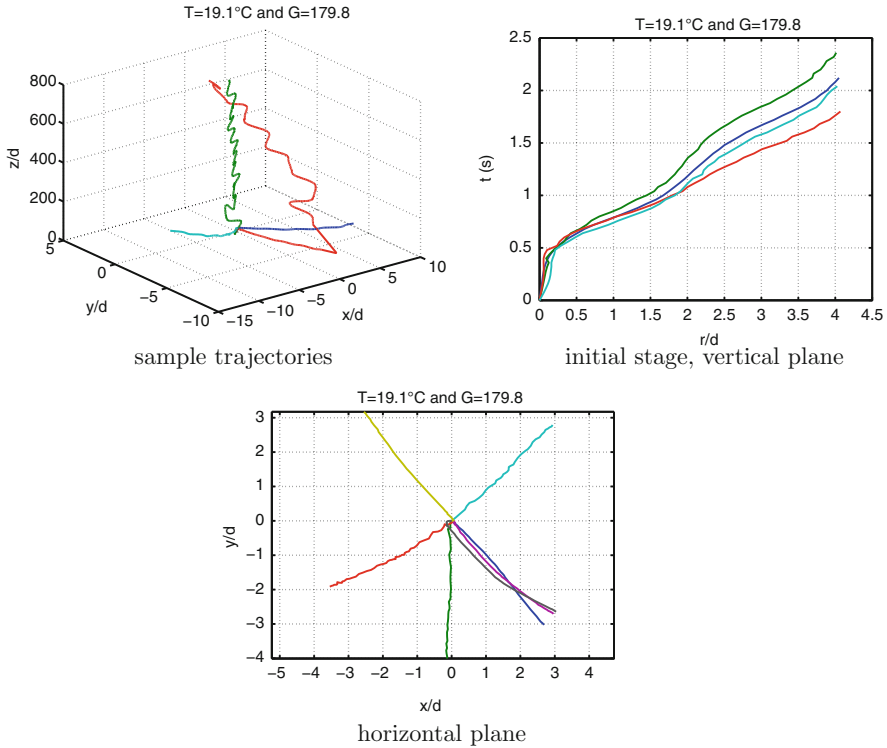


**Fig. 7.2** Example of non vertical trajectories of spheres rising in water (The temperature of water was used to control the viscosity and thus the Galileo number)

It easily seen that the vertical motion is closely linked to the axisymmetry of the surrounding flow. The loss of stability of the axisymmetric flow (axisymmetry breaking) generates a lift force responsible for a horizontal drift of the body. In what follows, we shall see that, in general, the fluid and the solid body degrees of freedom interact to determine the onset and the aspect of the symmetry breaking. Since the same phenomenon also concerns wakes of fixed objects, we shall start by explaining the loss of axisymmetry of the wake of a fixed bodies. In systems coupling the motion of the fluid with the motion a body driven by gravity and buoyancy, the instabilities result in changes of the form of the trajectories. They are therefore called “path instabilities” although the fluid strongly participates in their mechanism. An exhaustive understanding of various possibilities how axisymmetry breaks in such systems can be obtained by a simple theory describing the interplay of two bifurcations. Specific scenarios will then be illustrated using direct numerical simulations in the case of ideally spherical bodies, and ideally flat discs. The motion of flat cylinders and oblate spheroids of intermediate aspect ratio is not the topic of this chapter but, as indicated by available results, the presented extreme cases of a sphere and infinitely flat disc are helpful in its understanding.

## 7.2 Wake of Fixed Bodies

### 7.2.1 Loss of Axisymmetry in Wakes

Assuming a sphere placed in a uniform flow of a Newtonian fluid of density  $\rho$  and kinematic viscosity  $\nu$  (or an arbitrary axisymmetric body with its axis aligned with the flow direction), it is possible to define a system of cylindrical coordinates as depicted in Fig. 7.3. It is usual to use the imposed scales to define the inflow velocity  $U_\infty$  as velocity scale, and the diameter of the body cross section  $d$  as a length scale. Expressing, further the pressure in units defined as  $\rho U_\infty^2$  we arrive at the following non-dimensional form of Navier-Stokes equations

$$\nabla \cdot \mathbf{v} = 0, \tag{7.1}$$

$$\frac{\partial \mathbf{v}}{\partial t} + [\mathbf{v} \cdot \nabla] \mathbf{v} + \nabla p - \frac{1}{Re} \nabla^2 \mathbf{v} = 0. \tag{7.2}$$

in which the viscosity is replaced by the Reynolds number  $Re = U_\infty d / \nu$ , the single physical parameter of the problem.  $\mathbf{v}$  stands for the flow velocity (w.r.t. the body) and  $p$  for the pressure. The ‘no-slip’ condition at the solid body surface amounts to the Dirichlet boundary condition  $\mathbf{v} = 0$ .

Introducing cylindrical coordinates, Eqs. (7.1) and (7.2) can be written in more detail as system of four equations for three cylindrical velocity components  $u, v, w$ ,

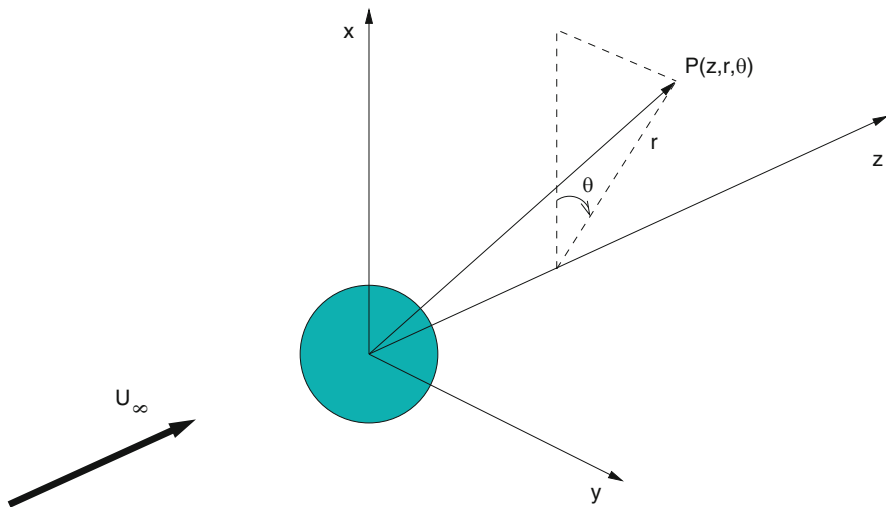


**Fig. 7.3** Schematic view of a configuration (flow past a sphere) presenting an axisymmetric solution for the flow.  $U_\infty$ —uniform inflow velocity (defining the symmetry axis)  $0z$ ,  $z$ —projection onto the axis,  $r$  distance from the axis,  $\theta$ —azimuthal angle

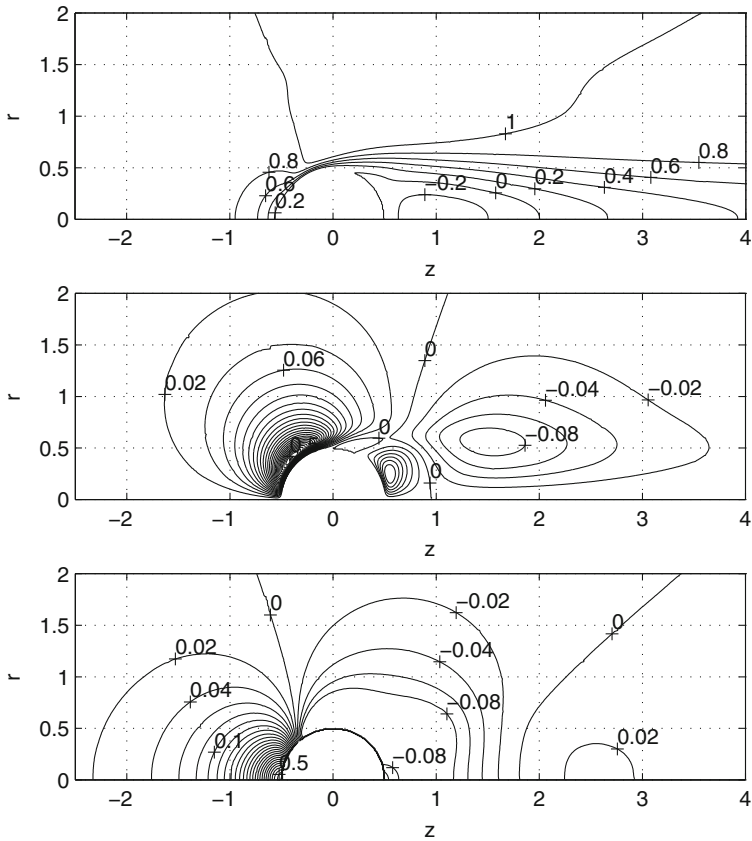


**Fig. 7.4** Axisymmetric flow past a fixed sphere at  $Re = 215$ . *Top*: axial velocity, *middle*: radial velocity, *bottom*: pressure. See [9]

where  $u, v, w$  stand, respectively, for the axial, radial and azimuthal velocity components, and the pressure  $p$ . All involved fields are functions of  $z, r$  and  $\theta$ . Obviously, due to the axisymmetry of configuration an axisymmetric solution (solution independent of  $\theta$ ) exists whatever the Reynolds number value. Assuming further that the body does not rotate, the azimuthal velocity of such solution is zero (non swirling axisymmetric flow). Figure 7.4 shows the axisymmetric solution for  $Re = 215$ .

The stability of the axisymmetric solution is a very important issue. Though, mathematically, the axisymmetric solution exists whatever the Reynolds number, only a stable solution will be observed in the reality due to the ambient noise. The stability issue is about the decay of disturbances. There are situations where the amplitude of the disturbances is of importance (see the cases of multiple stability), the most fundamental question consists, however, in testing the stability with respect to infinitely small perturbations. The assumption of infinitesimality of perturbations leads to a linear problem.

### 7.2.2 Linear Stability Analysis of an Axisymmetric Flow

The linear stability analysis consists in investigating the unsteady and non axisymmetric solutions of the form

$$\mathbf{v} = \mathbf{V} + \mathbf{v}'; \quad \mathbf{v}' = \mathbf{v}'(z, r, \theta, t) \quad (7.3)$$

$$p = P + p'; \quad p' = p'(z, r, \theta, t) \quad (7.4)$$

where  $\mathbf{V} = (U(z, r), V(z, r), 0)$  and  $P(z, r)$  stand for the (known) axisymmetric (non swirling) solution and the perturbations  $\mathbf{v}'$  are assumed small enough for all non-linear terms to be neglected. The so obtained linear problem reduces to the eigenvalue problem

$$\begin{aligned} \lambda \Phi + \mathcal{L}[\mathbf{V}]\Phi + \text{grad}\Pi &= 0, \\ \text{div}\Phi &= 0. \end{aligned} \quad (7.5)$$

predicting the exponential behavior of the projection of the perturbation onto the eigen-subspace associated to the eigenvalue  $\lambda$

$$\text{Proj}_\lambda(\mathbf{v}') = \alpha e^{\lambda t} \Phi + c.c. \quad (7.6)$$

$$\text{Proj}_\lambda(p') = \alpha e^{\lambda t} \Pi + c.c. \quad (7.7)$$

where “*c.c.*” stands for complex conjugate and  $\Phi$  and  $\Pi$  are the velocity and pressure components of the eigenfunction associated to  $\lambda$ .  $\mathcal{L}[\mathbf{V}]$  stands for the linearized Navier-Stokes operator. The most convenient way how to handle a 3D flow field in cylindrical coordinates consists in replacing the radial and azimuthal components by complex fields [18]  $v'_\pm = v' \pm iw'$  (with the redundancy  $\overline{v'_-} = v'_+$ ). The assumption of axisymmetry amounts to the commutation

$$\mathcal{L}[\mathbf{V}] \frac{\partial}{\partial \theta} = \frac{\partial}{\partial \theta} \mathcal{L}[\mathbf{V}] \quad (7.8)$$

allowing us to project the eigenvalue problem (7.5) onto separate sub-spaces associated to azimuthal wavenumber  $m = 0, \pm 1, \pm 2, \dots$ . The eigenfunctions are thus expressed as

$$\Phi(z, r, \theta) = \phi_m(z, r) e^{-im\theta} \quad (7.9)$$

$$\Pi(z, r, \theta) = \pi_m(z, r) e^{-im\theta} \quad (7.10)$$

where  $\phi_m(z, r)$  is written in the representation of [18]. The projection of the eigenvalue problem onto the  $m$ -subspace becomes

$$\begin{aligned} \lambda_m \phi_m + \Lambda_m[\mathbf{V}]\phi_m + \nabla_m \pi_m &= 0 \\ \nabla_m^\dagger \phi_m &= 0 \end{aligned} \quad (7.11)$$

where

$$\nabla_m = \left( \frac{\partial}{\partial z}, \frac{\partial}{\partial r} - \frac{m}{r}, \frac{\partial}{\partial r} + \frac{m}{r} \right)^T, \tag{7.12}$$

$$\nabla_m^\dagger = \left[ \frac{\partial}{\partial z}, \quad \frac{1}{2} \left( \frac{1}{r} \frac{\partial}{\partial r} r + \frac{m}{r} \right), \quad \frac{1}{2} \left( \frac{1}{r} \frac{\partial}{\partial r} r - \frac{m}{r} \right) \right] \tag{7.13}$$

and

$$\Lambda_m[\mathbf{V}] = \left( V_z \frac{\partial}{\partial z} + V_r \frac{\partial}{\partial r} \right) \mathbf{1} + \begin{bmatrix} \frac{\partial V_z}{\partial z} - \nu \nabla_{m^2}^2 & \frac{1}{2} \frac{\partial V_z}{\partial r} & \frac{1}{2} \frac{\partial V_z}{\partial r} \\ \frac{\partial V_r}{\partial z} & \frac{1}{2} \left( \frac{\partial V_r}{\partial r} + \frac{V_r}{r} \right) - \nu \nabla_{(m+1)^2}^2 & \frac{1}{2} \left( \frac{\partial V_r}{\partial r} - \frac{V_r}{r} \right) \\ \frac{\partial V_r}{\partial z} & \frac{1}{2} \left( \frac{\partial V_r}{\partial r} - \frac{V_r}{r} \right) & \frac{1}{2} \left( \frac{\partial V_r}{\partial r} + \frac{V_r}{r} \right) - \nu \nabla_{(m-1)^2}^2 \end{bmatrix} \tag{7.14}$$

with

$$\nabla_{m^2}^2 = \frac{\partial^2}{\partial z^2} + \frac{1}{r} \frac{\partial}{\partial r} \left( r \frac{\partial}{\partial r} \right) - \frac{m^2}{r^2} \tag{7.15}$$

and  $\nu = 1/Re$ . It appears that the obtained equations are invariant with respect to change of the sign of  $m$  (i.e., physically, with respect to the sign of helicity of perturbations) which means that the eigenvalues  $\lambda_m$  in Eq. (7.14) depend only on the absolute value of  $m$  ( $\lambda_m = \lambda_{|m|}$ ).

The results of the eigenvalue problems in individual azimuthal subspaces must be summed up by seeking globally the least stable eigenvalue that will cross from the left to right complex half-plane. The following table sums up all four possibilities:

	$m = 0$	$m \neq 0$
$\text{Imag}(\lambda_m) = 0$	Steady and axisymmetric	Steady, non-axisymmetric
$\text{Imag}(\lambda_m) \neq 0$	Unsteady axisymmetric	Unsteady non-axisymmetric

If the least stable eigenvalue is real and becomes positive, the bifurcation is commonly called regular, a bifurcation at which a complex eigen-pair crosses the imaginary axis is a Hopf bifurcation. In wakes (as well as for path instabilities) the least stable azimuthal subspace is always  $m > 0$ , mostly  $m = 1$ . However, axisymmetry breaking in  $m > 1$  sub-spaces was also evidenced. It was in the wake of a heated in the ‘assisting flow’ configuration—see Fig. 7.5. Since the problem (7.2) depends only on the Reynolds number, the ‘onset’ of the bifurcation is meant in terms of increasing Reynolds number. For sufficiently low Reynolds

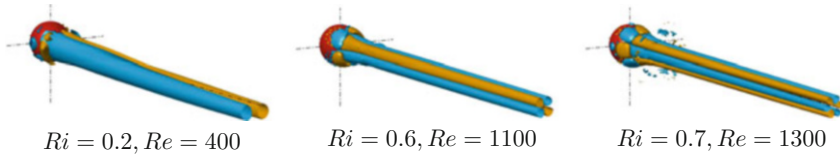


**Fig. 7.5** Steady non axisymmetric flow in the wake of a heated sphere in the configuration of ‘assisting flow’. In assisting flow, the flow comes from below, i.e. the convection assists the flow. (In the picture, the vertical axis is placed horizontally.) Nondimensional Richardson and Prandtl numbers are defined as  $Ri = \frac{\beta g(T_s - T_\infty)d}{U_\infty^2}$  and  $Pr = \frac{\nu}{\kappa} = 0.72$ . Boussinesq forcing term:  $\beta(T - T_\infty)\mathbf{g}$ . For more details, see [15]

**Table 7.1** Examples of primary bifurcation thresholds of wakes

Body	$Re_{crit}$
Sphere	212
Thin disc	117
Cylinder $d/h = 3$	160

numbers (sufficiently viscous flows) the axisymmetric solution is stable. There exists an upper limit of stability, expressed in terms of the critical Reynolds number  $Re_{crit}$ , at which the least stable eigenvalue becomes unstable (its real part becomes positive). Since other bifurcations usually follow, this first bifurcation is called primary. The primary bifurcation of unheated axisymmetric solids is always regular and in the  $m = 1$  subspace. However the critical Reynolds number (threshold of the bifurcation) depends relatively strongly on the body shape. Three examples are given in Table 7.1.

### 7.2.3 Weakly Non-linear Theory

The linear stability analysis shows that the axisymmetric state becomes unstable but does not provide any information on the new state to which the system settles after the onset of the bifurcation. For this purpose, non-linear effects must be considered. The weakly non-linear theory has also an important implication on the choice of the numerical method to be used for direct numerical simulations of 3D flows arising from axisymmetry breaking.

The linear theory of the previous sub-section showed that the eigenfunctions (7.9), (7.10) correspond to terms of azimuthal Fourier expansion. A general three-dimensional flow-field can be written as a Fourier series

$$\begin{aligned}
 \mathbf{v}(z, r, \theta; t) &= \sum_{m=-\infty}^{\infty} \mathbf{v}_m(z, r; t) e^{-im\theta}; & \mathbf{v}_{-m} &= \overline{\mathbf{v}_m} \\
 p(z, r, \theta; t) &= \sum_{m=-\infty}^{\infty} p_m(z, r; t) e^{-im\theta}; & p_{-m} &= \overline{p_m}.
 \end{aligned}
 \tag{7.16}$$



An axisymmetric flow has only one term ( $m = 0$ ). For cold wakes, the leading mode of the perturbation is  $\mathbf{v}_1(z, r; t)$ , i.e. the projection onto the  $m = 1$  azimuthal subspace. Using the spectral basis of eigenfunctions, we can characterize the instability by stating that the projections onto all eigen-subspaces decay exponentially except that onto the subspace associated to the unstable eigenvalue. After a sufficient time, any small perturbation becomes expressed by only two (independent) terms of expansion (7.16) corresponding to  $m = 0, \pm 1$  and, as long as the linear approximation holds, the term  $\mathbf{v}_1(z, r; t)$  is proportional to the eigenfunction  $\phi_{1,\lambda}$ , associated to the unstable eigenvalue  $\lambda$ . Since the linear theory predicts an exponential growth of this term, the linear approximation will become inaccurate at some moment and  $\mathbf{v}_1(z, r; t)$  will have projections onto the stable eigen-subspaces of the  $m = 1$  azimuthal subspace corresponding to other eigenvalues of the operator (7.14). To define an instability amplitude  $A(t)$  we shall use the projection onto the unstable subspace:

$$Proj_{\phi_{1,\lambda}} \mathbf{v}_1(z, r; t) = A(t) \phi_{1,\lambda} \tag{7.17}$$

Separating the perturbation from the axisymmetric base flow, assuming all terms of the Fourier expansion (7.16) to be analytical functions of  $A(t)$ , inserting into the full Navier-Stokes equations and comparing terms of the same order of  $A$  we can show that

$$\mathbf{v}_m \sim A^{|m|}, \tag{7.18}$$

i.e. that the convergence of the series is exponential (in terms of  $m$ ) and is especially fast close to the bifurcation threshold. The lowest order non-linear model of the dynamics is obtained by truncating at the third order of the bifurcation amplitude. If the bifurcation is of Hopf type, we get the well known Landau model. Considering the case of regular bifurcation common for unheated wakes and many free falling/rising axisymmetric bodies, the eigenvalue  $\lambda$  is real and the associated eigenfunction  $\phi_{1,\lambda}$  can also be defined as real. This results in a Landau model for a regular bifurcation having the form:

$$\frac{dA}{dt} = \lambda A - C|A|^2 A, \quad Im(\lambda) = 0 \tag{7.19}$$

where the constant  $C$  is real, whereas the amplitude  $A$  is complex. Equation (7.19) is clearly invariant with respect to rotations in the complex plane. Assuming the bifurcation to be supercritical (i.e.  $C > 0$ ), the asymptotic solution is  $\sqrt{\lambda/C} e^{i\alpha}$  the phase  $\alpha$  being arbitrary and determined by the initial condition. Similarly as for a standard Hopf bifurcation, Fig. 7.6 represents the corresponding bifurcation diagram. In contrast with the Hopf bifurcation, the circle does not represent a loop but a set of asymptotic points in the complex plane to which the solution can settle depending on initial perturbation as indicated by the two dash-dotted lines given as two examples. To understand the implication of this result on the asymptotic state

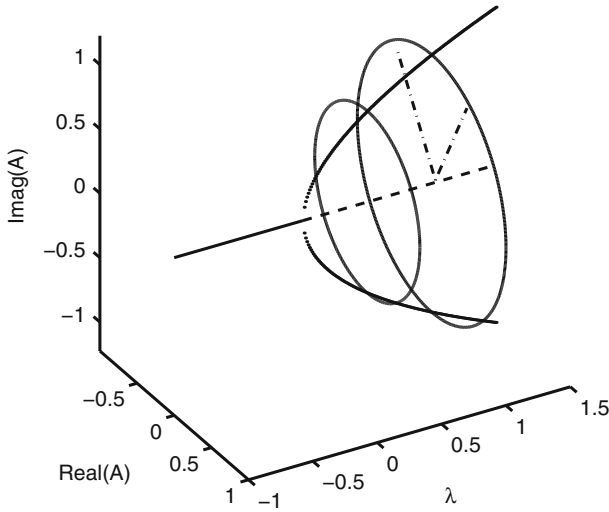


**Fig. 7.6** Bifurcation diagram of a regular bifurcation

of the non-axisymmetric perturbation, let us insert it into Eq. (7.16). Considering, say, only the axial velocity component we get:

$$u_1(z, r, \theta; t) = A\phi_{1,\lambda,z}e^{-i\theta} + c.c. = 2\sqrt{\lambda/C}\phi_{1,\lambda,z}(z, r) \cos(\theta - \alpha) \quad (7.20)$$

where  $\phi_{1,\lambda,z}(z, r)$  stands for the axial components of the eigenfunction  $\phi_{1,\lambda}$ . Equation (7.20) shows that the perturbation has a symmetry plane  $\theta = \alpha$ . The theoretical implication of the weakly non-linear theory can be summed up by stating that a supercritical regular bifurcation leads to a new steady state which has a planar symmetry with respect to an arbitrarily oriented plane containing the symmetry axis.

The practical implication consists in the fast convergence of the azimuthal Fourier expansion. The numerical implementation using the azimuthal Fourier decomposition was used (see [1, 9]) for direct numerical simulation of the wake of a sphere and was generalized for configurations involving freely moving axisymmetric bodies that will be discussed later on. The principle of the method can be understood from Fig. 7.7. The computational domain is assumed to be a cylinder, the sphere being placed at the cylinder axis. The so obtained configuration remains axisymmetric and a truncated Fourier expansion can be used to express the flow field. Each Fourier coefficient is function of only two variables  $z$  and  $r$  and be discretized on an arbitrary 2D mesh. We systematically use spectral elements for their accuracy and flexibility allowing a local refinement. All differential operations are applied to Fourier components (in spectral space). For simulations where the truncation was very short, the non-linear terms could be computed as convolutions

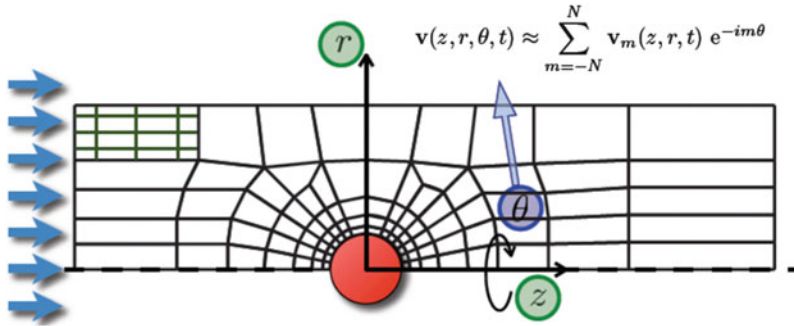


**Fig. 7.7** Spectral element decomposition of the axial-radial plane of a cylindrical domain around a sphere placed in a uniform flow, combined with Fourier expansion in the azimuthal direction

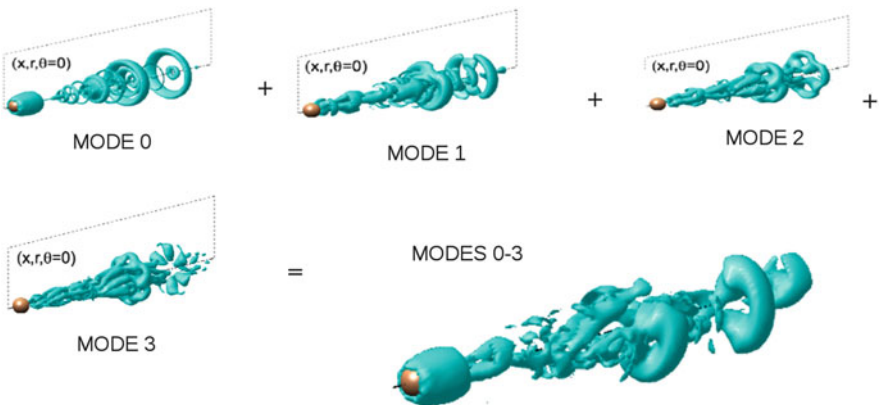


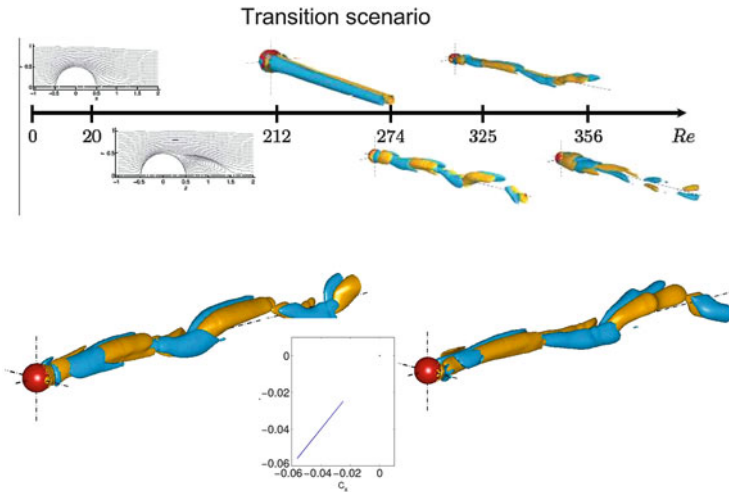
**Fig. 7.8** Pressure field in sphere wake represented by iso-surface corresponding to a negative pressure value at  $Re = 400$ . The contributions of modes 0–3 are represented separately. The last figure shows the resulting field

directly in the spectral space [9], otherwise the standard switching between spectral and physical space using a discrete (fast) Fourier transformation is used. The differential operations performed in the spectral space allow us to handle easily the symmetry axis using the complex coordinates [18] reducing all singularities at the axis to removable ones. The efficiency of this spectra–spectral element approach is illustrated in Fig. 7.8 where the pressure in the chaotic sphere wake at  $Re = 400$  is represented in terms of pressure iso-surfaces. The relatively complicated flow structures are actually well reproduced by truncating the Fourier series as low as at mode  $m = 3$  which is given by the fact that the fine structures arise rather in the  $z, r$  plane than in the azimuthal direction.

### 7.2.4 Some Examples of Bifurcation Scenarios in Wakes

Direct numerical simulations make it possible to investigate relatively easily the sequence of bifurcations preceding the onset of chaos (see e.g. [1]). It has become usual to include axisymmetric stages of attached and detached flow in the description of the transition scenario, but the primary bifurcation is the most important milestone. We have already seen that in all unheated flows it results in a steady non-axisymmetric flow having an arbitrarily selected symmetry plane. The primary bifurcation is followed by a secondary bifurcation of Hopf type. It can be said that the transition scenario is dominated by a real eigenvalue and a complex eigen-pair. In unheated wakes of fixed objects the first eigenvalue to become unstable is always real. However, in general the order can be inverted. An interesting illustration is the opposing flow past a heated sphere [15]. The same holds also for flat freely moving bodies. The discussion of the theoretical implication of the interplay between a real eigenvalue and a complex eigen-pair dominating a transition scenario will be done in the framework of the description path instabilities.

Figure 7.9 sums up the scenario in the wake of a fixed sphere. The streamlines in the first two figures show an attached axisymmetric flow below  $Re = 20$  and an onset of recirculation above  $Re = 20$ . The threshold of the primary bifurcation has already been mentioned ( $Re = 212$ ). The steady non-axisymmetric flow can



31

Fig. 7.9 Transition scenario in a fixed sphere wake

be very well represented by the axial vorticity. A plot of vorticity iso-surfaces at opposite levels of vorticity evidences two characteristic counter-rotating vortices easily observable also in experiments using dye injection. The secondary, Hopf bifurcation, sets in at  $Re = 274$ . It brings about a loss of stationarity. The symmetry plane of the flow remains, however, conserved. The vorticity is now shed periodically with alternating sign. The non axisymmetry of the flow results in a non zero lift, the vector of which lies in the symmetry plane. When the periodic oscillation sets in, the lift oscillates, its projection describing a segment marking the intersection of the symmetry plane with the flow cross-section. The two enlarged figures of the periodic wake show the up and down dissymmetry resulting in a non zero mean lift. Above  $Re = 300$ , the periodicity gives way to quasi-periodicity due to a secondary Hopf bifurcation. The new frequency is about 3.5 times smaller and can be observed as beatings. The symmetry plane resists also to this second Hopf bifurcation. In the interval between  $Re = 325$  and  $356$ , an increasingly complicated time behavior of a still planar symmetric flow could be observed. The dynamics seems to undergo additional subharmonic transitions witnessing of the progressive loss of correlation in vortex shedding. At the end of this process (with increasing Reynolds number), the flow eventually loses its planar symmetry and becomes completely three-dimensional which results in the lift describing a chaotic path in the cross-section plane. It is well known that the classical bifurcation theory of low dimensional dynamical systems defines chaos solely on the basis of the time behavior using the notions of Lyapunov exponents and Hausdorff dimension to characterize the stretching and folding. These theoretical characteristics are already difficult to quantify for as simple models as the Lorenz or Rössler ones and are, of course, inapplicable to results of direct numerical simulations of 3D flows. For this reason, we consider as chaotic all flows having lost all obvious periodicity and symmetry. This definition is certainly not mathematically rigorous but remains practically applicable provided sufficiently long simulations are available.

It not necessary to investigate the latest stages of transition to chaos to evidence a different scenario if very flat cylinders, very flat oblate spheroids or, in extreme case, an ideal infinitely thin disc are considered. As shown in the upper Fig. 7.10 for an oblate spheroid of aspect ratio  $d/(2a) = 6$ ,  $d$  being the diameter and  $a$  the half axis, (see also [3]), the secondary (Hopf) bifurcation does not conserve the symmetry of the flow at its onset. Instead of shedding alternate vortices as it is the case for the sphere, the wake twists periodically which results in a lift oscillating perpendicularly to the symmetry plane selected at the primary instability. As the Reynolds number increases the twisting transforms progressively to vortex shedding but in a plane perpendicular to that selected at the primary bifurcation. The plot of the lift shows that the lift oscillates perpendicularly to its mean deviation visible in the upper figure and that the mean value of the lift is zero. This is visible on the wake as an up/down symmetry of the vortex shedding.

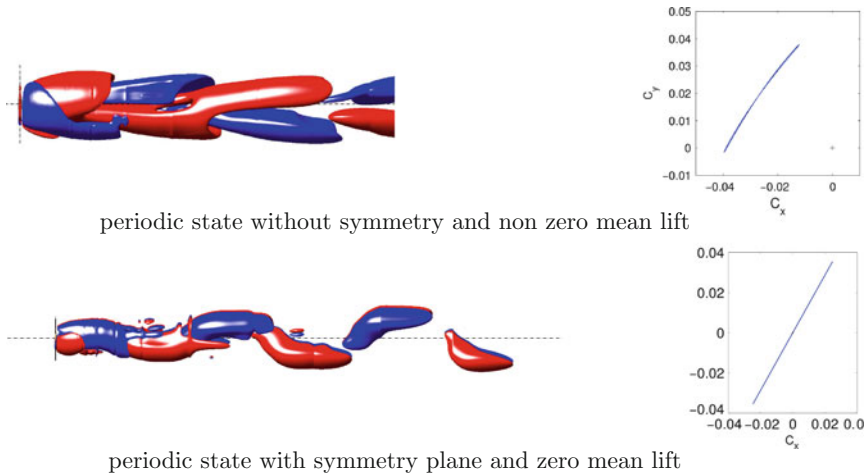


**Fig. 7.10** Unsteady periodic wake of an oblate spheroid of aspect ratio 6 represented in terms of axial vorticity. *Upper two figures:  $Re = 145$ , lower two figures:  $Re = 183$ .* Small figures on the *right*: paths of the lift vector

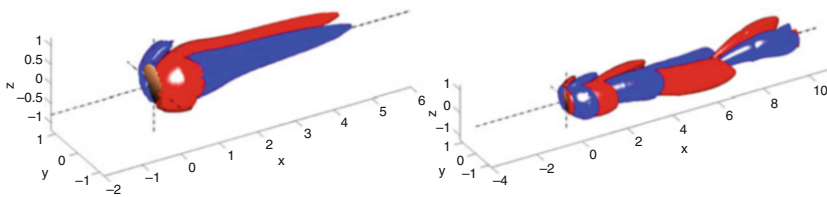


**Fig. 7.11** Disc with symmetry axis inclined by  $4^\circ$  with respect to the flow direction. *Left figure:  $Re = 120$ , steady flow. Right figure:  $Re = 140$ , periodic flow*

It is interesting to note that experiments aiming to evidence this scenario failed. A joint experimental and numerical work [5] provided the explanation showing that even a very small imperfection in the axisymmetry of the experimental setup makes a disc wake recover the scenario of a sphere. Of course, the axisymmetry breaking corresponds, strictly speaking, to an imperfect bifurcation without exact threshold but the effect of strong amplification of the steady vorticity threads remains observable. The symmetry plane is imposed by the setup. The vortex shedding conserves this symmetry plane and is asymmetric resulting in a significant non-zero mean lift. Figure 7.11 illustrates that a relatively small inclination is sufficient to switch to the sphere-like scenario in the wake of a disc. The paper [5] shows that this effect arises starting with a  $2^\circ$  inclination. In an experimental setup, it is not only difficult to assure a perfectly perpendicular position of the disc but already the disc holding itself perturbs the axisymmetry of the flow.

The last mentioned example shows that the agreement between numerical simulations and experimental is very often difficult to obtain.

## 7.3 Path Instabilities of Free Axisymmetric Bodies

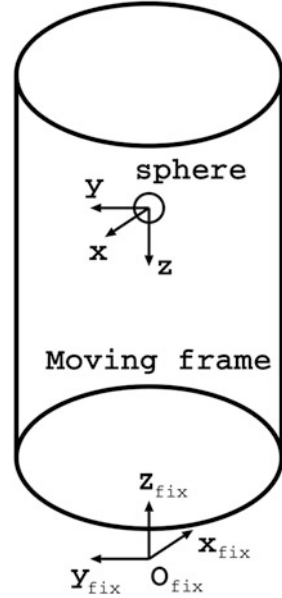
### 7.3.1 Problem Formulation for a Homogeneous Spherical Body

The problem of motion of a single sphere moving in an unconfined quiescent Newtonian fluid under the action of gravity and buoyancy is the best suited for the generalization of the spectral–spectra-element method [9] described in the previous section. The idea of the simulation consists in accompanying the sphere with a vertical cylindrical domain. If the motion remains vertical, the fixed wake and the free-body configurations are equivalent, the only difference consisting in the choice of reference frame for the velocity field and the necessity to couple the flow velocity with the balance of the drag and the resultant of the weight and buoyancy. With decreasing viscous effects, the Reynolds number will increase. A somewhat simplified and not totally accurate conclusion consists in expecting that, when the Reynolds number reaches the critical value of 212 evidenced in the fixed body wake, the axisymmetric solution will lose its stability giving way to a steady non-axisymmetric flow field. The loss of axisymmetry of the flow will result in a lift making the sphere drift in the horizontal direction. At the same time, the difference in the shear on opposite sides of the intersection of the sphere surface with the symmetry plane of the flow will drive a rotation. Neither of these two effects necessitates a modification of the geometry of the computational domain since the latter can be translated in any direction and, due to the sphericity of the body, any rotation can be accounted for merely by the boundary condition at the body surface without modifying the domain geometry. The schematic view of the configuration is thus basically identical to Fig. 7.3. Only the question of the reference frame and of the boundary conditions at sphere surface is to be raised (see also [14]). Figure 7.12 can be considered as referring to a rising sphere but, to account for a falling one, it is sufficient to turn it upside down. The velocity field will be referred to a fixed frame. This has the advantage of avoiding inertial acceleration terms arising in the non inertial moving frame. The motion of the computational domain is accounted for as moving mesh. The formulation of the problem requires to write both the flow and solid body motion equations.

The non-dimensionalization (choice of units) of flow equations follows the same lines as in Sect. 7.2.1. The basic difference consists in the absence of predefined velocity scale. Assuming the ambient fluid to be homogeneous of constant density  $\rho$ , the hydrostatic pressure gradient will be extracted from the equations by introducing the buoyancy force in the solid motion equations. As the result, a characteristic acceleration can be defined as

$$g_{eff} = \left| \frac{\rho_s}{\rho} - 1 \right| g \quad (7.21)$$

**Fig. 7.12** Schematic view of the configuration involving a free sphere. The  $O_{fix}z_{fix}$  axis of the fixed (laboratory) frame is vertical and points in the direction in which the sphere is driven by gravity and buoyancy. The  $Oxyz$  frame translates with the sphere center and the vertical  $Oz$  axis points in the direction of the wake



where  $\rho_s$  is the solid body density. The acceleration scale can be used to define a velocity scale as

$$U = \sqrt{\left| \frac{\rho_s}{\rho} - 1 \right| gd}. \quad (7.22)$$

Given the velocity scale  $U$ , the non-dimensionalization of the flow equations is the same as in Sect. 7.2.1 and results in equations

$$\frac{\partial \mathbf{v}}{\partial t} + [(\mathbf{v} - \mathbf{u}) \cdot \nabla] \mathbf{v} = -\nabla p + \frac{1}{G} \nabla^2 \mathbf{v} \quad (7.23)$$

$$\nabla \cdot \mathbf{v} = 0, \quad (7.24)$$

differing from Eqs. (7.1), (7.2) only in two points. (1) The advective terms account for the velocity of the mesh which is uniform and equal to translation velocity of the sphere denoted  $\mathbf{u}$ . (2) The Reynolds number, the inverse of which represented the non-dimensional viscosity in Eq. (7.2), is replaced by the Galileo number

$$G = \frac{\sqrt{\left| \frac{\rho_s}{\rho} - 1 \right| gd^3}}{\nu} \quad (7.25)$$

where  $\nu$  stands, again, for the fluid kinematic viscosity. The advantage of this choice is that the so defined Galileo number remains close to the Reynolds number based



on the terminal velocity  $u_\infty$  of the sphere. Indeed, considering the balance between the drag and the force driving the motion we get

$$\frac{\pi}{6}d^3|\rho_s - \rho|g = C_d \frac{\pi}{8}d^2 \rho u_\infty^2, \quad (7.26)$$

where  $C_d$  is the drag coefficient, which results in the relation

$$Re_\infty = \frac{u_\infty d}{\nu} = \sqrt{\frac{4}{3C_d}} G. \quad (7.27)$$

Knowing that, in the regimes we are interested in, the drag coefficient varies between 1 and 0.5, the factor multiplying the Galileo number, which is actually equal to the non-dimensional value of the terminal velocity, will not exceed 1.6.

Unlike in Fig. 7.7, the flow velocity is zero far from the body in the present formulation. That is, the inflow boundary condition is now a zero velocity. The motion of the sphere is accounted for by a Dirichlet boundary condition at the sphere surface

$$\mathbf{v}|_S = \mathbf{u} + \Omega \times \mathbf{r}_S \quad (7.28)$$

where  $\Omega$  is the angular velocity vector of the sphere rotation and  $\mathbf{r}_S$  is the position vector at the sphere surface.

The boundary condition at the sphere surface couples the flow equation with solid body motion equations

$$\frac{\rho_s}{\rho} \frac{d\mathbf{u}}{dt} = \frac{6}{\pi} \mathbf{F}_{fl}(\mathbf{v}, p) - \mathbf{i}; \quad \mathbf{F}_{fl} = \int_S \boldsymbol{\tau} \cdot \mathbf{n} dS \quad (7.29)$$

$$\frac{\rho_s}{\rho} \frac{d\Omega}{dt} = \frac{60}{\pi} \mathbf{M}_{fl}(\mathbf{v}, p); \quad \mathbf{M}_{fl} = \int_S \mathbf{r}_S \times \boldsymbol{\tau} \cdot \mathbf{n} dS \quad (7.30)$$

$$\boldsymbol{\tau} = -p\mathbf{1} + \frac{1}{G} (\nabla\mathbf{v} + \nabla\mathbf{v}^T) \quad (7.31)$$

where  $\mathbf{i} = (1, 0, 0)^T$  stands for the driving acceleration term. As indicated in Eqs. (7.29)–(7.31), the hydrodynamic force and torque are computed by integrating the pressure and the viscous shear over the sphere surface.

The spatial discretization of the flow equations has been described in Sect. 7.2.3. An additional difficulty arises in implementing a time discretization applicable to all density ratios  $\rho_s/\rho$  including very small ones corresponding to light ascending spheres. It is easily seen that, in the extreme case of  $\rho_s = 0$ , Eqs. (7.29), (7.30) reduce to constraints imposed to the current flow field, which makes the use of explicit treatment impossible. The difficulty can be partly avoided by introducing the added mass (equal to 0.5 times the mass of the displaced fluid), however the added mass effect accounts only for pressure and not viscous effects which are about of the same order in the considered regimes. An accurate implicit treatment is described in [12].

### 7.3.2 Primary Path Instability of a Sphere

The problem of a freely moving sphere summed up by Eqs. (7.29)–(7.31) depends on two parameters defined as the Galileo number and the solid fluid density ratio. The full parametric study of the transition scenario thus involves variation of both parameters. In particular, the thresholds of the bifurcations expressed as critical Galileo numbers is to be expected to depend on the density ratio.

In [13] the onset of the primary instability was investigated with special focus on light spheres of density smaller than one. Given that the axisymmetric base flow is steady, the Reynolds number is well defined by the constant terminal velocity and the found threshold can be expressed in terms of both the Galileo and the Reynolds number. In agreement with expectations, the primary instability was found to be regular (as well as that of a fixed sphere wake). Its threshold lies, however, slightly below that of the fixed sphere wake:  $Re_{crit} = 205$  ( $G_{crit} = 156$ ) instead of 212. There is an easy argument explaining why the critical Reynolds number is different. The formal structure of the linear stability problem can be represented as

$$\lambda \mathbf{Y} = \mathbf{M} \mathbf{Y} \quad (7.32)$$

$$\mathbf{Y} \equiv \begin{bmatrix} \mathbf{v}' \\ \mathbf{Z} \end{bmatrix}, \quad \mathbf{M} \equiv \begin{bmatrix} \mathbf{K} & \mathbf{H} \\ \mathbf{B} & \mathbf{0} \end{bmatrix}. \quad (7.33)$$

where  $\mathbf{v}'$  stands for the solenoidal flow perturbation ( $\nabla \cdot \mathbf{v}' = 0$ ),  $\mathbf{Z} \equiv (\mathbf{u}, \boldsymbol{\Omega})^T$  for the 6 degrees of freedom of the solid body and  $\mathbf{K}$  for the linearized Navier-Stokes operator (projected onto the subspace of solenoidal flow fields). The additional degrees of freedom modify the eigenvalue problem. Since the new system has a larger number of degrees of freedom, it can be expected to become more easily unstable. This intuitive expectation is confirmed in the present case of a spherical body, however a mathematical proof has been given (see [7]) that the free body degrees of freedom can have both a destabilizing and stabilizing effect on the regular bifurcation. The stabilizing effect was found for flat cylinders. This was also confirmed by direct numerical simulation in [4]. In the paper [13], the critical Reynolds number of 205 was erroneously interpolated with the value of 212 obtained in the fixed sphere wake and considered to apply to spheres of very large density ratio. This conjecture is, however, false since, if the bifurcation is regular, the density ratio does not influence this threshold as was noted in [7] and is obvious from Eqs. (7.29), (7.30) in which the time-derivative on LHS vanishes. As expected, the loss of axisymmetry of the flow results, initially in a lift. However, since the asymptotic state is steady, the velocity of the sphere is constant and thus no resultant force acts on free body. I.e., the non axisymmetry of the flow is compensated by the horizontal motion of the sphere letting the lift vanish. The sphere follows a straight oblique trajectory. The regime is called steady oblique. At the onset of the secondary bifurcation the horizontal velocity attains about 10% of the vertical one, i.e. the angle of the trajectory with respect to vertical direction is about  $6^\circ$ . This inclination

is easily observable experimentally since, because of the stability of the regime, the straight trajectories can be very long and the horizontal drift very significant.

The secondary bifurcation is of Hopf type and the flow past the sphere presents similar features as those described in Sect. 7.2.4, i.e., the symmetry plane is conserved and vortex shedding with planar symmetry sets in. However, the unsteadiness makes the effects of the density ratio very significant. As the Galileo number increases, a large variety of trajectories is observed necessitating some classification. The latter can be provided by theoretical considerations based on a third order weakly non linear theory involving a real eigenvalue and a complex eigen-pair.

### 7.3.3 *Weakly Non-linear Theory of the Interplay of a Regular and a Hopf Bifurcation*

When a secondary bifurcation sets in, the non-linear effects may have already so strongly modified the base flow of the primary bifurcation that the linear analysis of the primary base flow is of no value. This is the case, e.g., of the infinite cylinder for which the primary (Hopf) bifurcation sets in at  $Re = 46$ . This arising periodic oscillating regime is linearly stable until  $Re = 188.5$  at which no new frequency appears but the spatial structure of the wake becomes three-dimensional. Given the large difference of the flow at  $Re = 46$  and at  $Re = 188.5$ , the onset of three-dimensionality can not be predicted by a linear analysis of steady wake. This not the case for the sphere and other axisymmetric bodies. The secondary Hopf bifurcation of the sphere wake was predicted for the first time in [17] using a linear analysis of the axisymmetric wake by evidencing a complex eigen-pair following the leading real eigenvalue in crossing the imaginary axis. The prediction of the secondary instability threshold of [17]  $Re_{crit} = 277.5$  which is quite close to the exact value (of about 273) accounting for the fact that the base flow of the secondary bifurcation is no longer axisymmetric. This leads to the conclusion that the non-linear effects remain limited and that description of both bifurcations can be well approximated within a common weakly non-linear approximation. For light spheres, the secondary instability threshold is still closer to the primary one. While the critical Galileo number of the primary (regular) bifurcation) is 156, the secondary (Hopf) bifurcation sets in as early as for  $G = 167$  for an infinitely light ( $\rho_s/\rho = 0$ ) sphere.

Instead of assuming that the linear unstable perturbation is proportional to a single eigenfunction as in Eq. (7.17), we consider that both a real eigenvalue  $\lambda$  and a complex eigen-pair  $\gamma \pm i\omega$  become unstable almost simultaneously so that the perturbation is driven by the three eigenvalues. In Eq. (7.17), the subscript 1 referred to the azimuthal subspace  $m = 1$ . The considerations are based on the assumption that both eigenvalues  $\lambda$  and  $\mu$  have been obtained in the same sub-space. Since for the path instabilities the subspace is always  $m = 1$ , we drop this subscript in what follows. The velocity field is no longer a full characteristic of the state. In

Eq. (7.33) we made it clear that the state is characterized, in addition, by six velocity components. The perturbation is thus fully expressed by the array  $Y$  depending on three bifurcation amplitudes  $A, B_{\pm}$ :

$$Y = A(t)\chi_r + B_+(t)\chi_+ + B_-(t)\chi_- \quad (7.34)$$

where  $\chi_r$  is associated to the real eigenvalue  $\lambda$  and  $\chi_{\pm}$  are associated to the complex eigen-pair  $\gamma \pm \omega$ . To understand the dynamics, it is not necessary to use the full information of the  $Y$  array. Instead, the representation of the two horizontal components of the translational velocity of the sphere, conveys a sufficient idea. To keep a scalar representation, a complex velocity  $u_+ = u_x + iu_y$  will be used. (This choice is actually in line with the formalism [18] used in the code.) Normalizing the eigenfunctions so that their  $u_+$  velocity component be equal to 1, Eq. (7.34) reduces to

$$u_+ = u_x + iu_y = A(t) + B_+(t) + B_-(t), \quad (7.35)$$

i.e. the complex horizontal velocity is directly the sum of instability amplitudes. Recalling the arbitrariness of the selection of the symmetry plane at the regular bifurcation, we can consider, without loss of generality, that the amplitude  $A(t)$  is real. A third order weakly non-linear model describing the dynamics can be found in e.g. in [6] or in [16]. (For a more fundamental mathematical background see [10].) The details go beyond the scope of this presentation, moreover, some frequently observed regimes would require a higher order model to be entirely explained. For these reasons we present only a non exhaustive list of possible stable states expressed in terms of amplitudes (7.35).

- $B_+ = B_- = 0, A \rightarrow A_{\infty}: u_x = \text{const.}$ : steady oblique regime
- $A \rightarrow A_{\infty}, B_+ \rightarrow B_{\infty}e^{i\omega_{\infty}t}, B_- = \overline{B_+}$ : oblique oscillating planar regime
- $A_{\infty} = 0, B_+ \rightarrow B_{\infty}e^{i\omega_{\infty}t}, B_- = \overline{B_+}$ : planar oscillating trajectory, vertical in the average (zig-zagging regime)
- $A_{\infty} = 0, B_+ \rightarrow B_{\infty}e^{i\omega_{\infty}t}, B_- = 0$  (or the same with opposite helicity) purely helical regime with positive or negative helicity
- $A_{\infty} = 0, |B_+| \neq |B_-|$ : a general case of states with non zero helicity. A third order weakly non-linear model is insufficient to model such states, however, usually, higher order effects are present so that such states are relatively frequent.

Another purpose of Eq. (7.35) is to emphasize the interest of the path of the complex velocity  $u_+$  in the complex plane for the classification of the trajectories.

## 7.4 Transition Scenario of a Free Sphere

In this and the following sections we comment the results of direct numerical simulations for spheres, discs and oblate spheroids. The purpose of the investigations is to provide an exhaustive information on the regimes the dynamics of freely moving

solid bodies can undergo in the transition from steady vertical fall or rise to a fully chaotic motion as viscous effects decrease.

The transition scenario of a falling or rising sphere was first investigated in [14]. In view of the interest of this prototypical configuration for benchmarking of multi-particle codes as well as of later experimental results [11, 20], a more accurate investigation focusing also on the problem of characterization of chaotic regimes was published in [21].

As shown in Sect. 7.3.1 an exhaustive information can be obtained by investigating the trajectories and flow regimes in the two parameter space of the solid/fluid density and Galileo number. The up-to-date information [21] is summed up in the state diagram of Fig. 7.13.

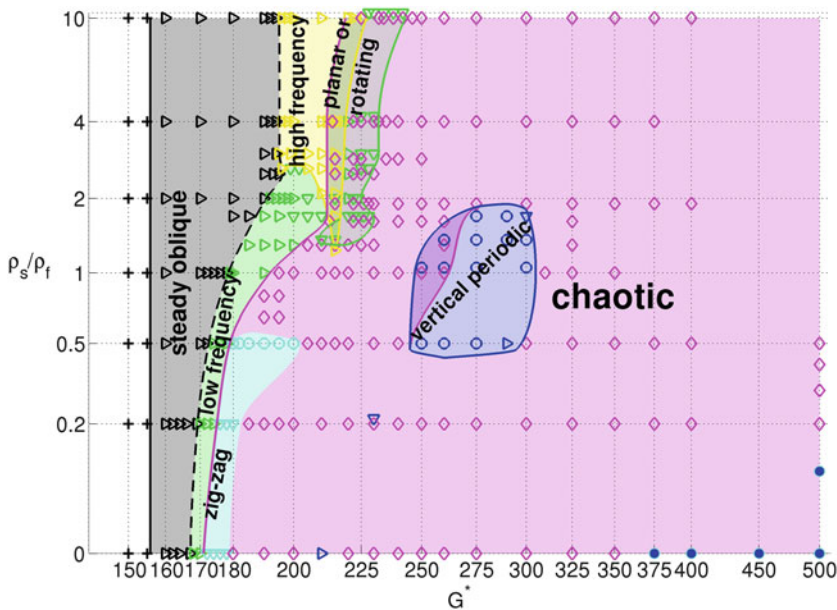


**Fig. 7.13** State diagram in the  $G - \rho_s/\rho_f$  parameter space. Thresholds of bifurcations are represented by lines, different colors represent regimes indicated in the figure. Overlapping areas mean bi-stability. The overlapping of the chaotic area with zones of high and low frequency oblique oscillating regimes (labeled as “planar or rotating”) is an area of bi-stability of states with fixed and slowly rotating symmetry axis. The symbols represent the simulated trajectories (in cases of coexistence of two or three regimes the symbols are artificially shifted). Meaning of symbols. Plus: vertical regime, black right pointing triangle: steady oblique, green right pointing triangle: low frequency oblique oscillating, green down pointing triangle: low frequency quasi-periodic oblique oscillating, yellow right pointing triangle: high frequency oblique oscillating, cyan open circle: perfect or slightly oblique zig-zag, cyan down pointing triangle: intermittent zig-zag, blue open circle: vertical oscillating planar, blue down pointing triangle: vertical quasi-periodic, blue right pointing triangle: periodic planar slightly inclined, blue filled circle: helical, pink diamond: chaotic (or rotating plane in the bi-stability domain)

### 7.4.1 Early Stages

The first two bifurcating states arising due the first two instabilities can be considered as early stages of the transition. In Fig. 7.13 the primary instability is recognized as the leftmost vertical line separating the vertical and steady oblique states. As has already been explained, the primary bifurcation being regular, the threshold must be independent of the density ratio. In [21], the critical Galileo number was found to be 155.8. The secondary bifurcation follows relatively close to the primary one. It is a Hopf bifurcation giving rise to the already discussed oblique oscillating regime. Both the primary and secondary bifurcations are supercritical. The horizontal complex velocity describes a segment of straight line passing through the origin but the segment is centered off the origin. As the result, the trajectory remains planar, the mean horizontal velocity is non zero (yielding a mean horizontal drift) and the oscillations are very accurately periodic. The most remarkable feature of the secondary bifurcation is its dependence on the density ratio. Its characteristics are given in Table 7.2 reproduced from [21]. It is seen that the critical Galileo number significantly increases for density ratios increasing from 0 to 2.5, whereas starting from  $\rho_s/\rho = 2.5$  the threshold is practically constant. This difference is related to the fact that actually two different Hopf bifurcations set in. Below  $\rho_s/\rho = 2.5$  the resulting frequency is about 2.3–2.6 times smaller than above. At the secondary bifurcation threshold, the separation between both frequencies is quite accurately at 2.5 as can be seen from the table showing that at this density ratio both frequencies were evidenced. The state diagram (Fig. 7.13) shows, however, that the high frequency state can be found at as low a density ratio as 1.3 at a higher Galileo number (215).

The physical reason of the two different frequencies can be understood from Figs. 7.14 and 7.15. Figure 7.14a represents the stream-wise vorticity in the wake of a sphere of density ratio 3 and Galileo number 199 in terms of iso-surfaces of

**Table 7.2** Critical Galileo number  $G_{crit}$ , horizontal velocity  $u_h$ , vertical velocity  $u_z$ , angular velocity of rotation  $\omega_h$  and frequency  $f$  at the onset of oblique oscillating regime

$\rho_s/\rho$	$G_{crit}$	$u_h$	$u_z$	$\omega_h$	$f$
0	167.18	0.0969	1.3355	0.0149	0.0701
0.2	169.23	0.1031	1.3388	0.0151	0.0667
0.5	172.52	0.1108	1.3443	0.0150	0.0644
1	178.55	0.1224	1.3544	0.0139	0.0672
1.3	182.5	0.1275	1.3622	0.0129	0.0677
1.7	187.35	0.1327	1.3704	0.0112	0.0711
2	190.69	0.1356	1.3763	0.0099	0.0729
2.5	196.08	0.1387	1.3859	0.0077	0.076/0.175 <sup>a</sup>
3	195.19	0.1383	1.3843	0.0081	0.1741
4	195.18	0.1383	1.3842	0.0081	0.1751
10	195.06	0.1384	1.3838	0.0082	0.1771

<sup>a</sup>For the density ratio of 2.5 both frequencies are present even at the threshold of unsteadiness

**Fig. 7.14** (a) High frequency (fluid) mode ( $G = 199, \rho_s/\rho = 3$ , stream-wise vorticity levels:  $\pm 0.15$ ). (b) Fixed sphere wake (frozen translation velocity of a), no rotation,  $Re = 277.9$ , same vorticity levels:  $\pm 0.15$  as in a. (c) Low frequency (solid) mode ( $G = 196, \rho_s/\rho = 2$ , vorticity levels:  $\pm 0.05$ )

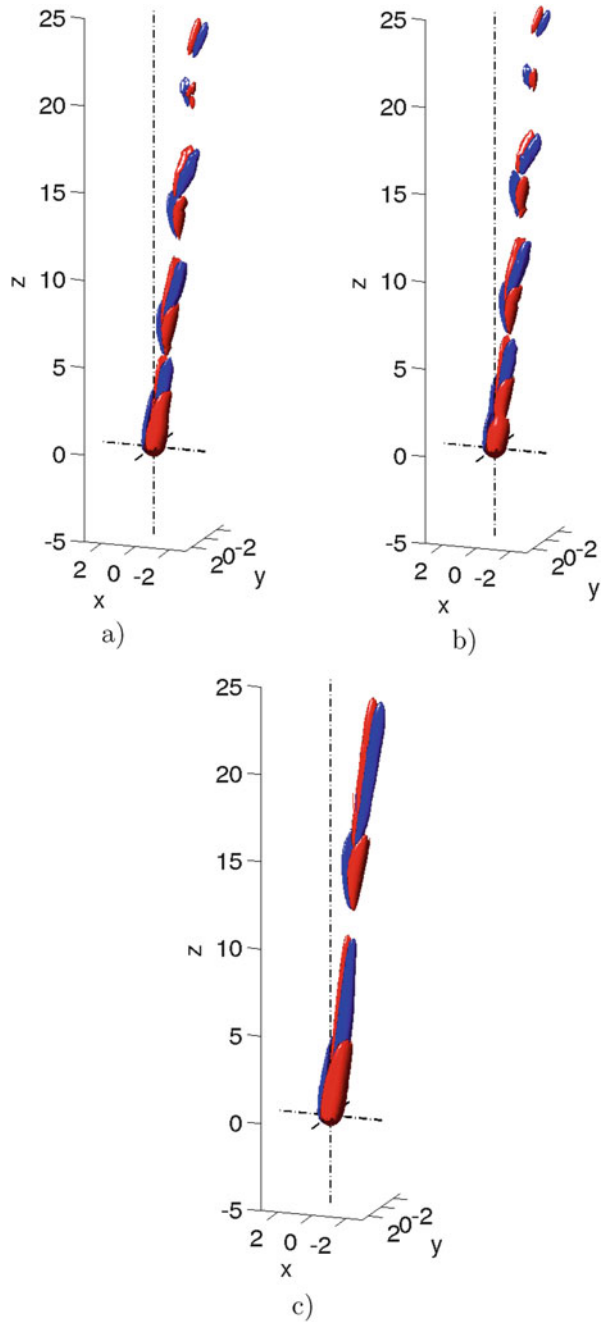
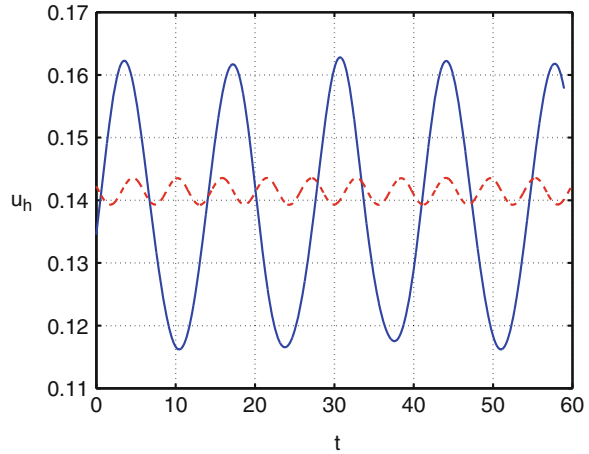


**Fig. 7.15** Comparison of amplitudes of oscillations of the low frequency regime  $\rho_s/\rho = 2, G = 196$  (full blue line) and high frequency regime  $\rho_s/\rho = 3, G = 199$  (dashed red line). Note that the mean values are comparable



opposite levels  $\pm 0.15$ . Figure 7.14c provides analogous information for a sphere of density ratio 2 at a similar Galileo number (196). The difference of the length of vortical structures (shorter in Fig. 7.14a than in Fig. 7.14c) is related to the lower vortex shedding frequency in the wake of the lighter sphere. More importantly, to have a similar picture, the levels of the vorticity used for plotting Fig. 7.14c had to be taken three times lower ( $\pm 0.05$ ) than in Fig. 7.14a. I.e. the stream-wise vorticity generated in the wake of the lighter sphere is much smaller than that of the denser one. In contrast, Fig. 7.15, comparing the oscillations of the horizontal velocities of both spheres, shows that the oscillation amplitude is much larger for the light sphere. The presence of modes characterized by large and small amplitude of oscillations of the free body was recently predicted by linear analysis [19]. The modes where the free body strongly interacts with the fluid were called ‘solid’, whereas those where the solid presents few motion were called ‘fluid’. Clearly, the low frequency mode is a solid one and the high frequency mode a fluid one. This statement is further confirmed by Fig. 7.14b representing the vorticity at the same levels as in Fig. 7.14a for a sphere the translation velocity of which has been frozen and the rotation inhibited. This fixed sphere configuration presents the same vorticity structures. The notion of fluid and solid (a more accurate designation would be solid-fluid) modes is also very important for the understanding of some regimes of discs, flat cylinders and oblate spheroids.

The two primary bifurcating states (oblique and oblique oscillating) are easy to observe in experiments (see Fig. 7.2 and references [20] and [11]). They are, however, limited to a narrow interval of Galileo numbers. A further investigation of what happens at higher Galileo numbers is thus necessary to understand the transition scenario.



**Table 7.3** Estimates of critical Galileo numbers  $G_{crit}$  and corresponding mean vertical velocities at the onset of chaos

$\rho_s/\rho_f$	0	0.2	0.5	1	1.3	
$G_{crit1}$	171	175	179	192	202	
$u_{z1}$	1.350	1.356	1.361	1.381	1.392	
$\rho_s/\rho_f$	1.7	2	2.5	3	4	10
$G_{crit1}$	228	224	228	230	234	240
$G_{crit2}$	212	216	215	215	213	219
$u_{z1}$	1.429	1.424	1.430	1.436	1.439	1.447
$u_{z2}$	1.409	1.410	1.413	1.413	1.412	1.417

For subcritical transition two values (upper and lower limit of bi-stability) are provided

### 7.4.2 Onset of Chaos

Table 7.3 presents some critical Galileo numbers at which chaotic behavior sets in. It is clearly seen that the way how chaos sets in is different for ‘light’ and ‘dense’ spheres. The same is also hinted in the state diagram (Fig. 7.13) by representing a patch of early chaotic states of light spheres in cyan color.

#### Light Spheres

In the early paper [14] it was observed that the amplitude of oscillations of the oblique oscillating regime of buoyant spheres could become large enough to compensate the mean value of the horizontal velocity. When this happens the sphere rises temporarily vertically. In the somewhat coarse parametric study of [14], it happened that at the investigated point  $\rho_s/\rho = 0.5, G = 180$ , the trajectory kept its planarity and each time the horizontal velocity became zero the sphere started to drift in the opposite direction of the vertical axis. This resulted in a perfect zig-zagging motion (see Fig. 7.16 which was erroneously considered to exist in a whole region of the parameter space). Such perfectly periodic planar trajectory is an exception among a large variety of non planar non-periodic trajectories some samples of which are represented in Figs. 7.17, 7.18, 7.19, 7.20, and 7.21. It can be seen that the temporary verticality of the trajectory brings about a situation of an arbitrary selection of the symmetry plane of the wake we described in Sect. 7.2.3. Various cases are possible: planar trajectory but intermittent selection of the drift direction (Fig. 7.17) and a large variety of non planar trajectories due to a selection of a different symmetry plane after the vertical stage. Such trajectories are zig-zagging on short time scales but globally three-dimensional and aperiodic (Fig. 7.18), intermittent and zig-zagging in an oblique plane (Figs. 7.19 and 7.20) or characterized by a completely arbitrary angle of selection of the new symmetry plane resulting in chaotic three-dimensional paths. The common feature of all these cases is the small scale order interrupted by intermittence during the vertical

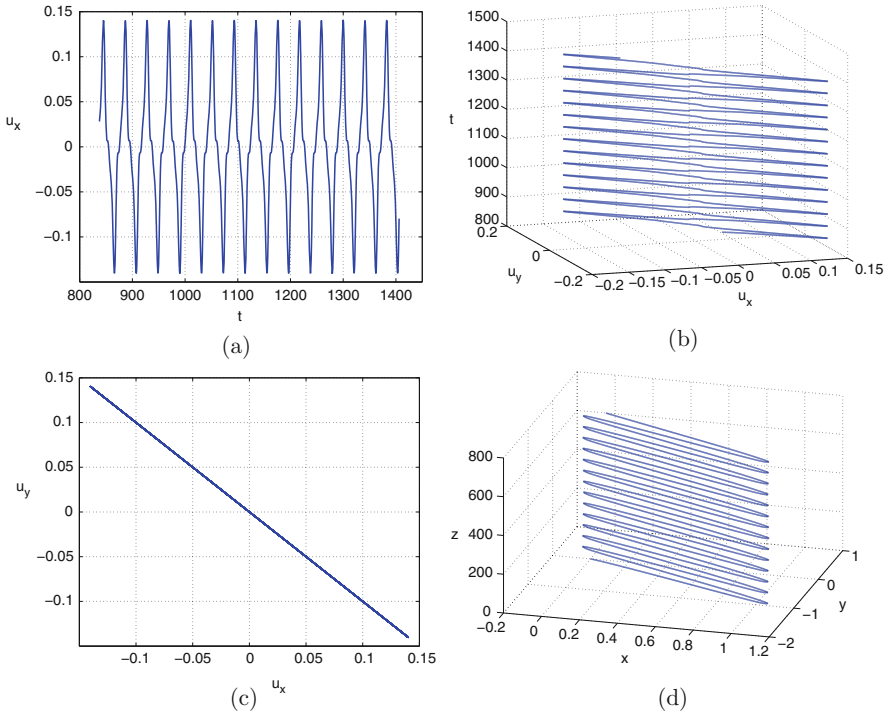


**Fig. 7.16** Perfect zigzagging trajectories of spheres  $\rho_s/\rho = 0.5$ ,  $G = 180$ . (a), (b) Horizontal velocities as a function of time, (c) projection of the velocity vectors onto the horizontal plane, (d) trajectory

stages. Such behavior can be qualified as chaotic intermittent. There is no bistability at the onset of chaos of light spheres (the oblique oscillation regime re-appears at the same critical Galileo number when the Galileo number is decreased back), the thresholds in the first part of Table 7.3 are easily determined by detecting the vanishing horizontal velocity. Since the paths are chaotic starting at the critical Galileo numbers of Table 7.3 the cyan area of the state diagram (Fig. 7.13) is not separated from fully chaotic states by any well defined threshold. The choice to make a difference was given by the small scale regularity of the trajectories making them appear as regular in too short simulations. With increasing Galileo numbers even the short scale regularity disappears.

## Dense Spheres

The different secondary bifurcating state for denser spheres has a significant impact on the scenario of onset of chaos. For density ratios  $\rho_s/\rho \geq 1.7$  there is a region of bistability of planar quasi-periodic paths and helical trajectories. The critical Galileo number  $G_{crit1}$  in Table 7.3 corresponds to the loss of stability of planar

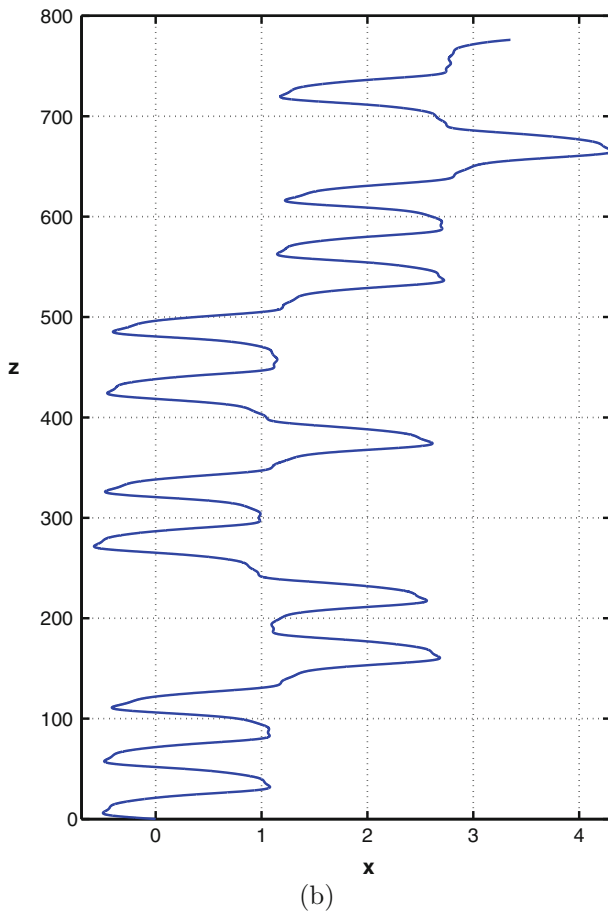
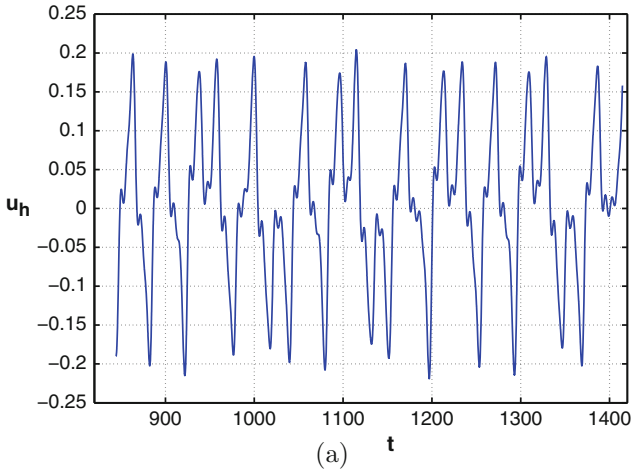


**Fig. 7.17** Horizontal velocity and trajectory of very light spheres at  $\rho_s/\rho = 0.2$ ,  $G = 180$ . (a) Velocity as a function of time and (b) trajectory

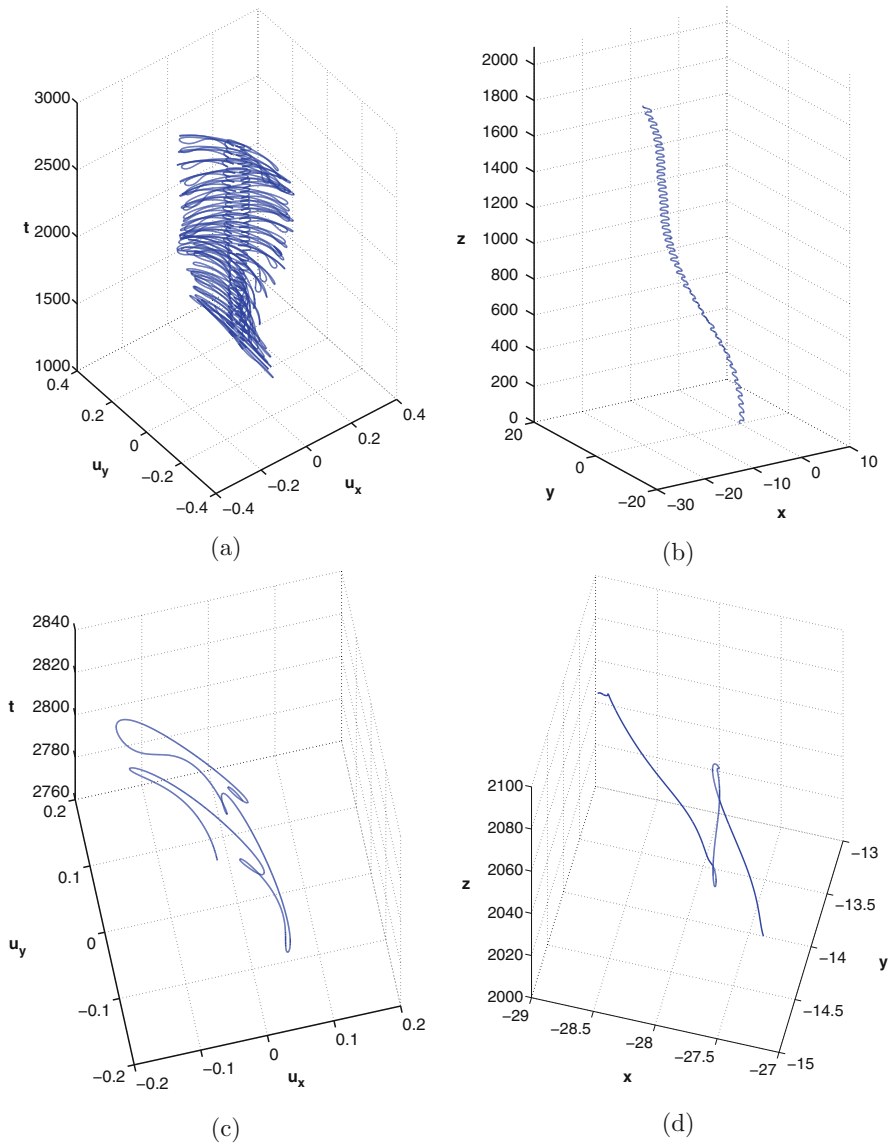


**Fig. 7.18** Velocities and trajectories of very light spheres at  $\rho_s/\rho = 0.2$ ,  $G = 190$ , (a) horizontal velocities as function of time (vertical axis), (b) trajectory, (c),(d) zoom on last 50 time units of figures (a) and (b)

trajectories (becoming suddenly chaotic). When, the Galileo number is decreased, the chaotic trajectories become oscillating and helical. The critical Galileo number  $G_{crit2}$  indicates when these helical trajectories stop to rotate to return to oblique oscillating regime.

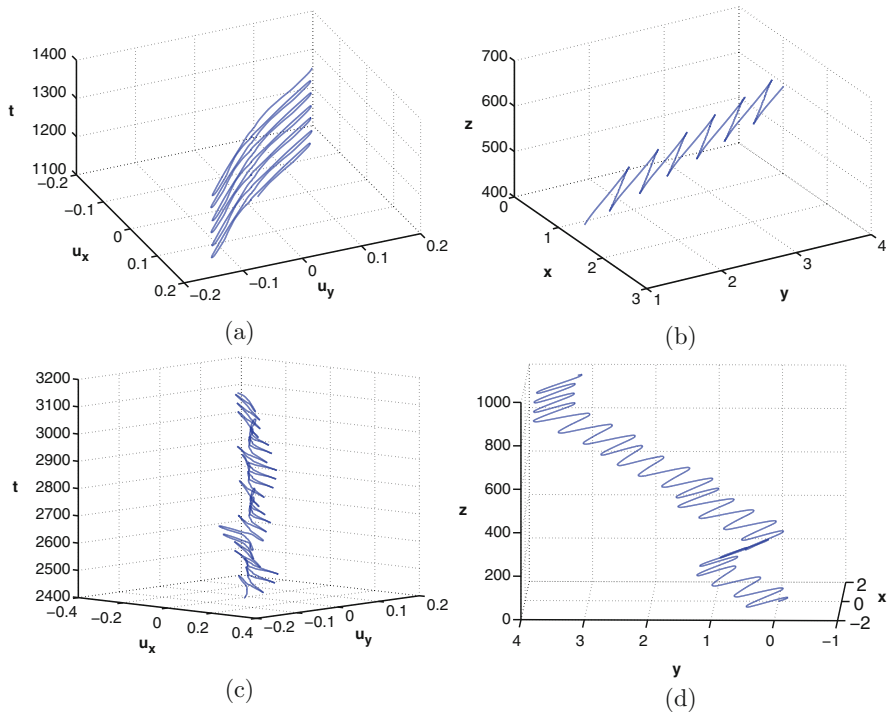


**Fig. 7.19** Velocities and trajectories of heavier but still buoyant spheres. *Left column:* horizontal velocities as a function of time, *right column:* trajectory. (a),(b)  $\rho_s/\rho = 0.5$ ,  $G = 190$  (last six periods), (c),(d)  $\rho_s/\rho = 0.65$ ,  $G = 195$

Both thresholds are also represented in the state diagram (Fig. 7.13). See the green full line delimiting the “low frequency quasi-periodic oblique oscillating” states on the right ( $G_{crit1}$ ) representing the upper limit of stability of planar trajectories and the full magenta line to the left of it ( $G_{crit2}$ ) indicating the lower limit of existence of three-dimensional (helical) trajectories. The scenario can be described in the following way. Consider e.g. a density ratio of 3. At  $G = 215$ , the stable state still corresponds to the high frequency fluid mode described in Sect. 7.4.1. See Fig. 7.22. Recall that the trajectory is planar and oblique oscillating. When the Galileo increases, first the upper limit of stability of the purely periodic fluid mode (full yellow line) is reached and the low frequency of the solid mode appears. This results, in general, in quasi-periodic dynamics except when both frequencies lock in with the integer ratio of 3. This is what actually happens at  $G = 220$  where we observe a periodic oscillation with frequency 0.06 strongly marked by a third harmonic. At  $G = 225$  the dynamics is quasi-periodic with two incommensurate frequencies. What happens when the critical Galileo number  $G_{crit1}$  is reached is seen in Fig. 7.23 representing a simulation for a density ratio 2 starting from a planar quasiperiodic regime at  $G = 230$ , i.e. above the critical

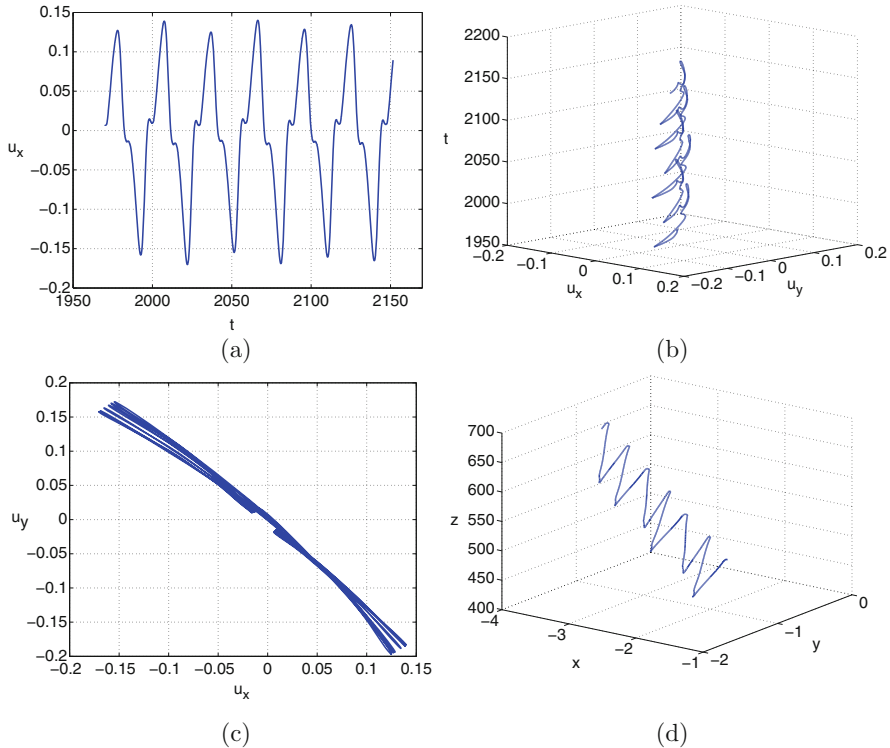


**Fig. 7.20** Quasi-periodic zigzagging trajectories of heavier spheres at  $\rho_s/\rho = 0.5$ ,  $G = 200$  (last six periods). **(a)**, **(b)** Horizontal velocities as a function of time, **(c)** projection of the velocity vectors onto the horizontal plane, **(d)** trajectory

Galileo number of 224 (see Table 7.3). The graph of Fig. 7.23a, representing the horizontal velocity as function of time, shows the initial planar quasiperiodic regime becoming completely chaotic. This makes the originally oblique oscillating path become chaotic and three-dimensional (Fig. 7.23b).

In the paper [14], it has already been noted that the chaotic trajectories of dense spheres have a strong resemblance with helices. If the Galileo number is lowered back from a chaotic regime, the trajectories progressively become perfect helices with superimposed oscillations. As can be seen in Figs. 7.24 and 7.25, the latter are of the same nature for planar trajectories (low and high frequency, quasi-periodic). The difference is given by the very regular rotation of the plane of oscillations, i.e. of the symmetry plane of the vortex shedding. Figures 7.24a, c and 7.25a, c show how the thresholds  $G_{crit2}$  were determined. In Figs. 7.24a and 7.25a the rotation exponentially decays whereas in Figs. 7.24c and 7.25c the rotating state is still clearly stable. For the density ratio 10 and  $G = 220$ , the helix has especially large diameter and pitch which is due to the very large period of rotation (more 200 times larger than the period of oscillation). In the state diagram (Fig. 7.13), the sub-

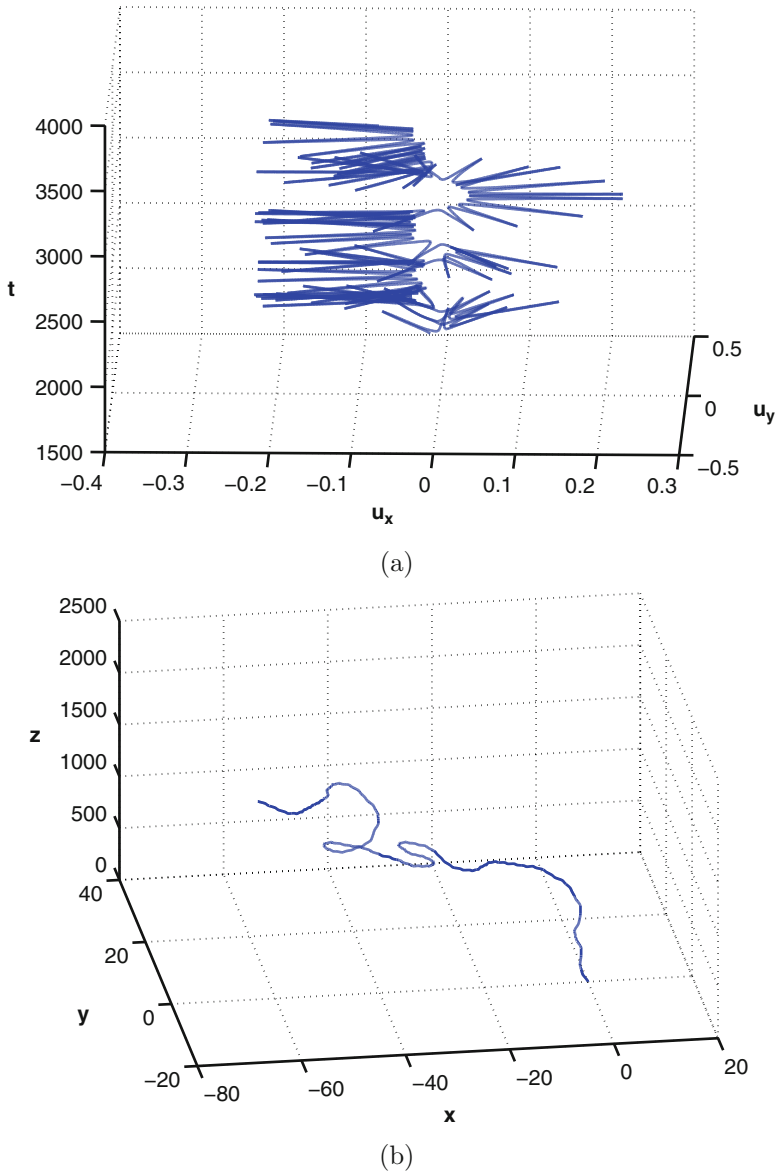


**Fig. 7.21** Horizontal velocities (a) and trajectory (b) of heavier but still marginally buoyant spheres at  $\rho_s/\rho = 1$ ,  $G = 195$ .

domain of slowly rotating states is represented in light gray between the lines of the critical Galileo numbers  $G_{crit2}$  (magenta line) and  $G_{crit1}$  (green line). It overlaps not only with the region of quasi-periodic planar oblique oscillating trajectories but even partly with that of periodic high frequency oblique oscillating states. This

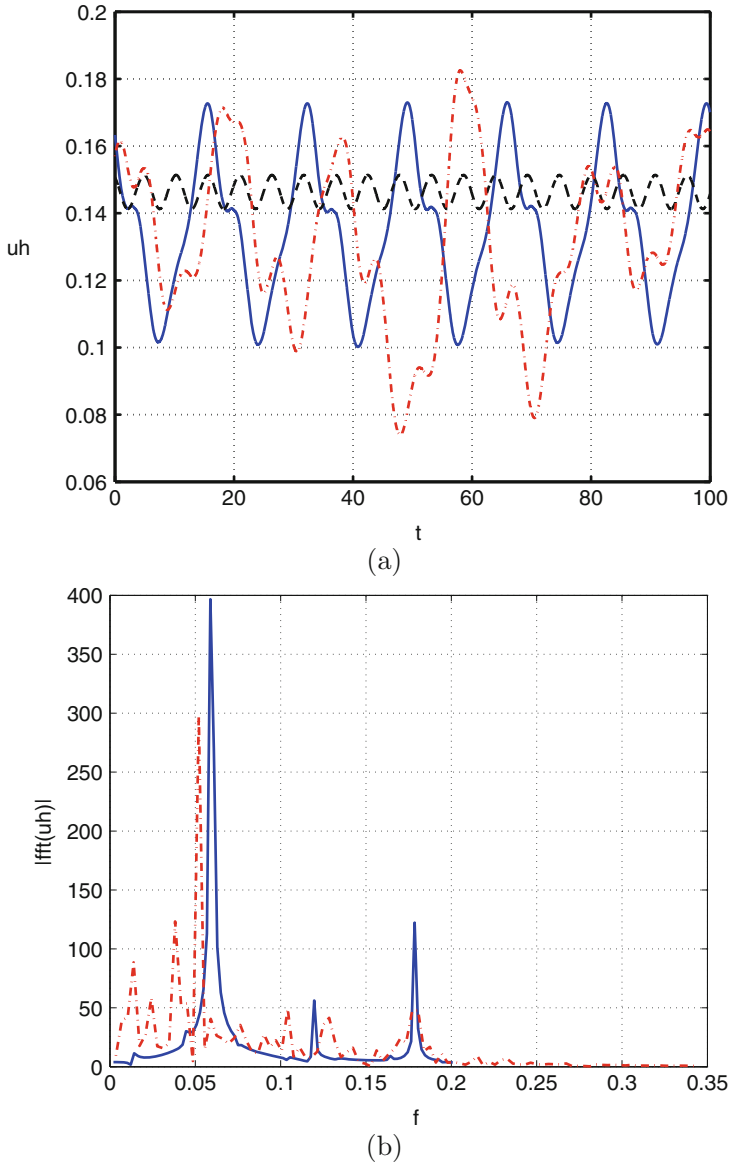


**Fig. 7.22** (a) Horizontal velocity for the density ratio  $\rho_s/\rho = 3$ . *Solid blue line*: periodic low frequency oscillations at  $G = 220$ ; *dashed black line*: high frequency oblique oscillating state at  $G = 215$  (frequency: 0.186); *dash-dotted red line*: quasi-periodic state at  $G = 225$ . (b) Power spectrum of horizontal velocity for  $G = 220$  (*solid blue line*) and  $G = 225$  (*dash-dotted line*)



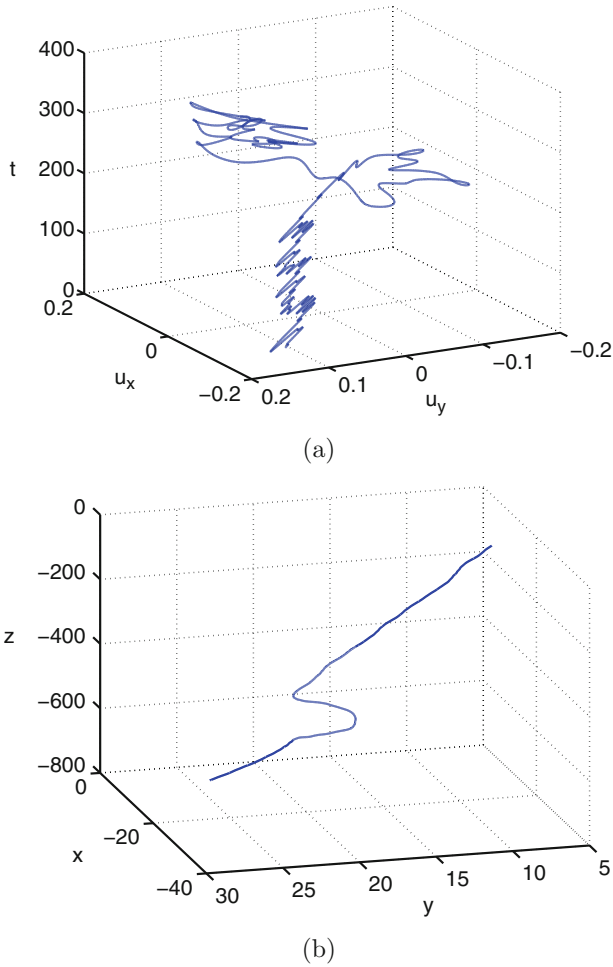


**Fig. 7.23** Loss of stability of the symmetry plane at  $\rho_s/\rho = 2$  and  $G = 230$ . **(a)** Horizontal velocity components as a function of time in a false 3D plot, **(b)** trajectory

typically subcritical feature was absent in early stages of transition of the sphere but is omnipresent for flat bodies.

### 7.4.3 Order in the Chaos: Vertical Oscillating Paths and Helical Paths

The chaotic trajectories also significantly differ depending on the problem parameters. Since by definition no simulation of chaotic trajectory can be repeated, their quantitative characterization requires a statistical treatment. Some statistical

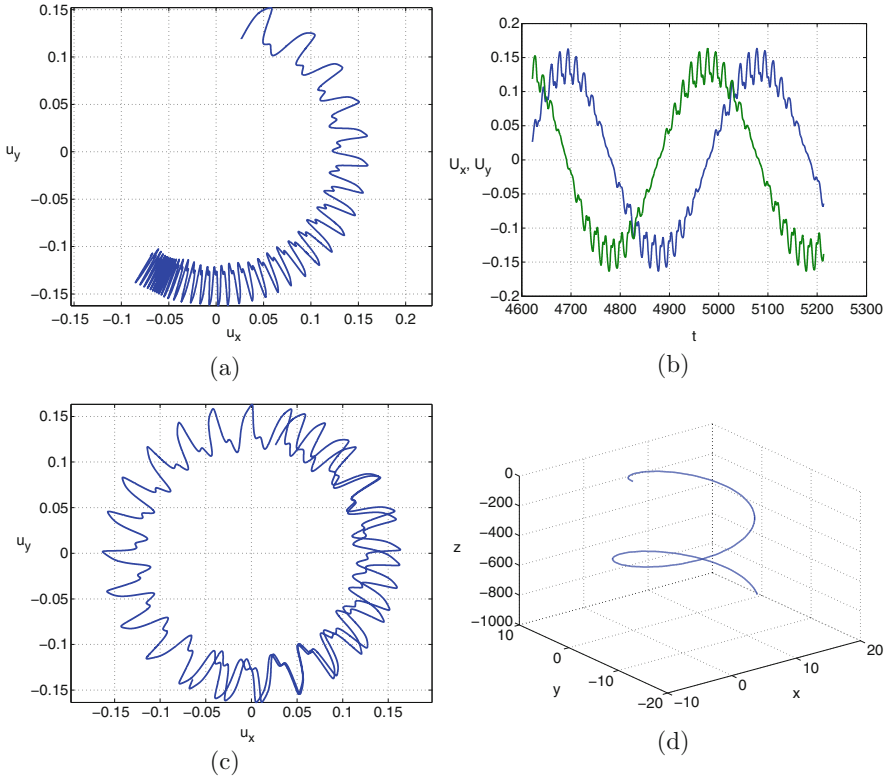


**Fig. 7.24** Velocities and trajectories of spheres of density ratio  $\rho_s/\rho = 4$  on the rotating bi-stability branch. **(a)**  $G = 212$ : Settling to oblique oscillating state. **(b–d)**  $G = 214$ : slowly rotating symmetry plane and periodic low frequency oscillations, **(b)** horizontal velocity components as a function of time, **(c)** projection of the velocity vectors onto a horizontal plane, **(d)** trajectory

quantities were suggested and tested in [21]. In this section we limit ourselves to mentioning two regular regimes representing what might be considered as windows of order in the chaotic domain. Some other isolated ordered states are also mentioned in the caption of Fig. 7.13 but, since they have a minor importance, we invite the interested reader to consult [21] for more details.

### Vertical Oscillating Regime

The domain of vertical oscillating trajectories represents a remarkable feature of the state diagram (Fig. 7.13). It is completely embedded in the chaotic domain delimited roughly by Galileo numbers ranging from 250 and 300 and intermediate density ratios between 0.5 and 2. Some of the neighboring chaotic states present a very slow intermittent behavior difficult to capture unless simulation over very long time are executed. The erroneous conclusion to be avoided is that these states

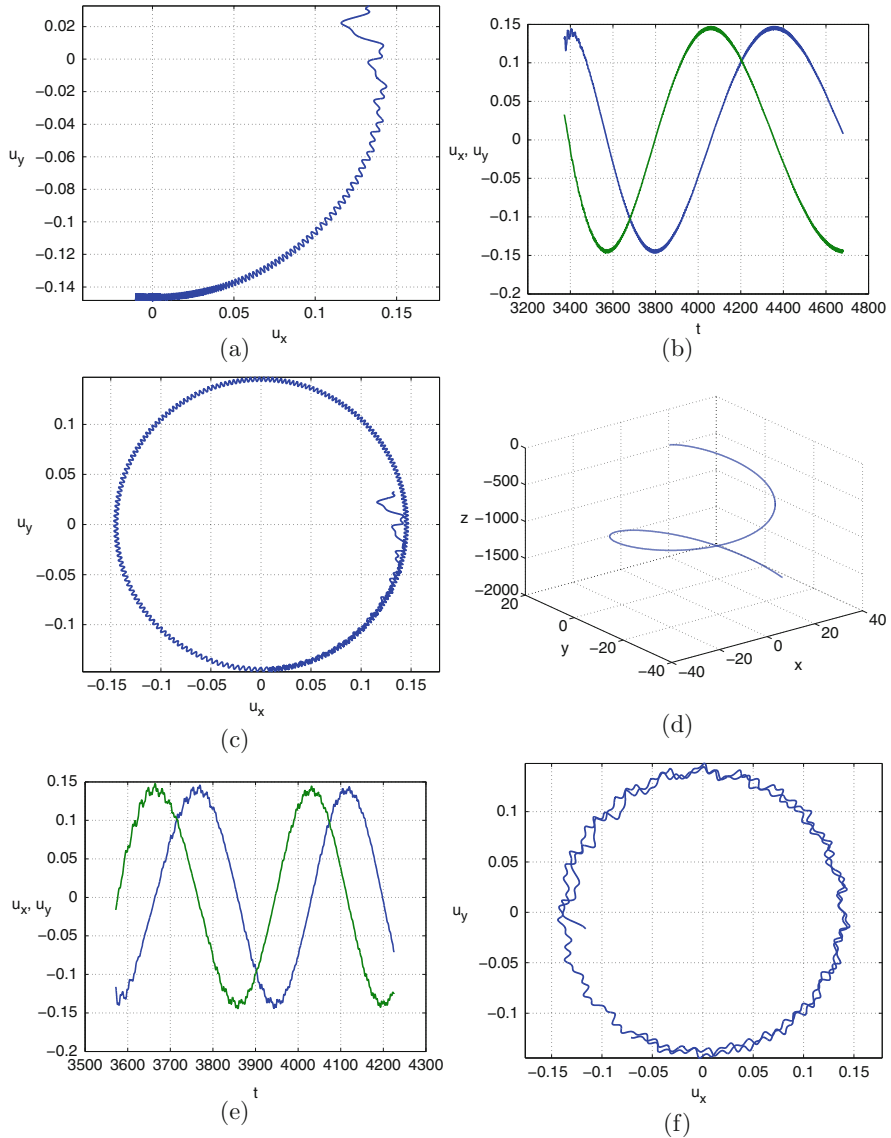


**Fig. 7.25** Velocities and trajectories of spheres of density ratio  $\rho_s/\rho = 10$  on the rotating bi-stability branch. (a) Settling to oblique oscillating state at  $G = 215$ , (b–d) slowly rotating symmetry plane and periodic high frequency oscillation at  $G = 220$  (same types of figures as Fig. 7.24b–d), (e) horizontal velocity components as a function of time, (f) projection of the velocity vectors onto a horizontal plane in the case of quasi-periodic oscillation at  $G = 225$

are bi-stable: vertical oscillating and chaotic. Very long simulations allowed to discard all such bi-stable cases except three on the side of lower Galileo numbers. A typical vertical oscillating trajectory represented in Fig. 7.26a, b at  $\rho_s/\rho = 0.5$

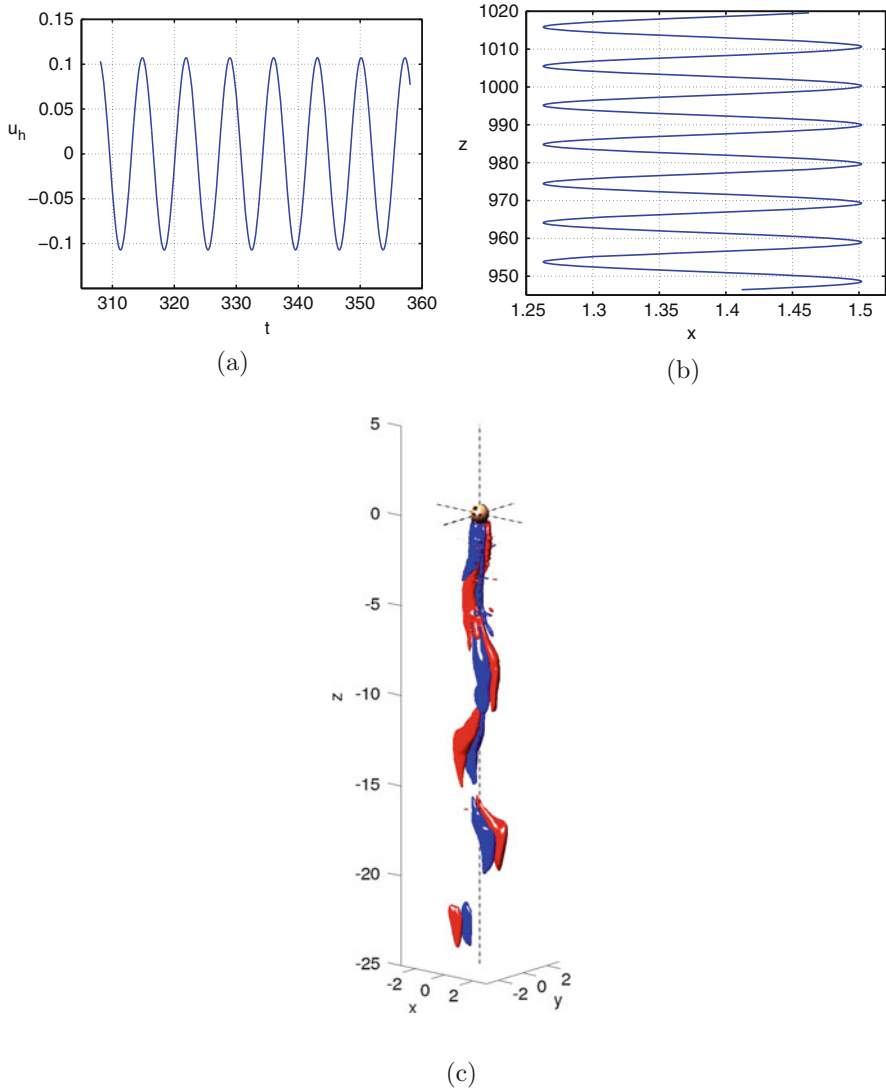


**Fig. 7.26** Vertical oscillating regime at  $\rho_s/\rho = 0.5$ ,  $G = 260$ . (a) Horizontal velocity in the trajectory plane as a function of time, (b) trajectory in its plane. (c) vortical structure of the wake at  $\rho_s/\rho = 0.5$  and  $G = 250$ . The represented levels of vorticity are  $\pm 0.25$

and  $G = 260$  is very accurately vertical. Figure 7.26a shows that the oscillation amplitude of the velocity barely exceeds 0.1 (0.105), the period of oscillation is about 7, more accurately, the frequency is 0.1416. The high frequency (not much lower than the frequency of the high frequency oblique oscillating regime—0.18) and the relatively small horizontal velocity amplitude (as compared to chaotic

fluctuations of neighboring chaotic states) yields a small amplitude of oscillations of the trajectory with respect to the vertical direction (see Fig. 7.26b): 0.12 of the sphere diameter. The vertical oscillating regime is characterized by very small and fast oscillations and its planarity and verticality are remarkably accurate. This behavior is due to a symmetric vortex shedding analogous to planar oscillating state of a fixed spheroid of aspect ratio 6 represented in lower Fig. 7.10. Indeed, the typical wake structure represented in Fig. 7.26c is very similar.

It can be considered that the effect of the primary bifurcation is overridden by the rapid oscillations forcing an almost axisymmetric wake. As the result, the flow wake dynamics is driven essentially by the pair of complex eigenvalues. Interestingly enough, already in the early paper [14], the mentioned frequency of 0.14 was identified as corresponding to the imaginary part of the complex eigenvalue of the Navier-Stokes operator linearized with respect to axisymmetric flow, found, indeed, unstable at Galileo numbers and density ratios corresponding to the vertical oscillating regimes.

## Helical States

Helical states represent another type of ordered state deep inside the chaotic domain. Several case have been evidenced for spheres of very small density ratio and higher Galileo numbers (see the filled blue circles in Fig. 7.13). Similarly as the vertical periodic ones, they correspond to one of the prototypical states enumerated in Sect. 7.3.3.

The most striking feature of the helical regime is the high regularity of the trajectory despite the high Galileo numbers, i.e. also the Reynolds number (750 for  $\rho_s/\rho = 0.1$  and  $G = 500$ ). The characteristics of a typical trajectory ( $\rho_s/\rho = 0.1$  and  $G = 500$ ) are represented in Fig. 7.27a–c. Figure 7.27d shows the typical twisted wake. The helical regime stands out for an exceptionally large horizontal velocity. While the typical horizontal velocity represents less than 10% of the vertical one in oblique regimes, the same ratio amounts to 30% for the massless sphere and 20% for the sphere of density ratio 0.1. The helical shape of the trajectory is not very far from an ideal spiral having a circular horizontal projection (Fig. 7.27b). The norm of the velocity vector is practically constant (within about 1%). The horizontal projection turns regularly with less than 2% r.m.s. fluctuations, the vertical component is constant with about a half percent accuracy. The large horizontal velocity is correlated with a drop of vertical velocity. The helical paths present some common features with the planar vibrating states reported in experiments [11]. They are perfectly vertical in the average, the pitch is very similar to the reported wavelength of the vibrating states, the radius is in qualitative correspondence with the r.m.s. of the horizontal projection of the vibrating trajectories and they are very accurately periodic. However, numerical experiments showed that planar trajectories are strongly unstable in the same region of parameter plane and that the vertical velocity is considerably higher.

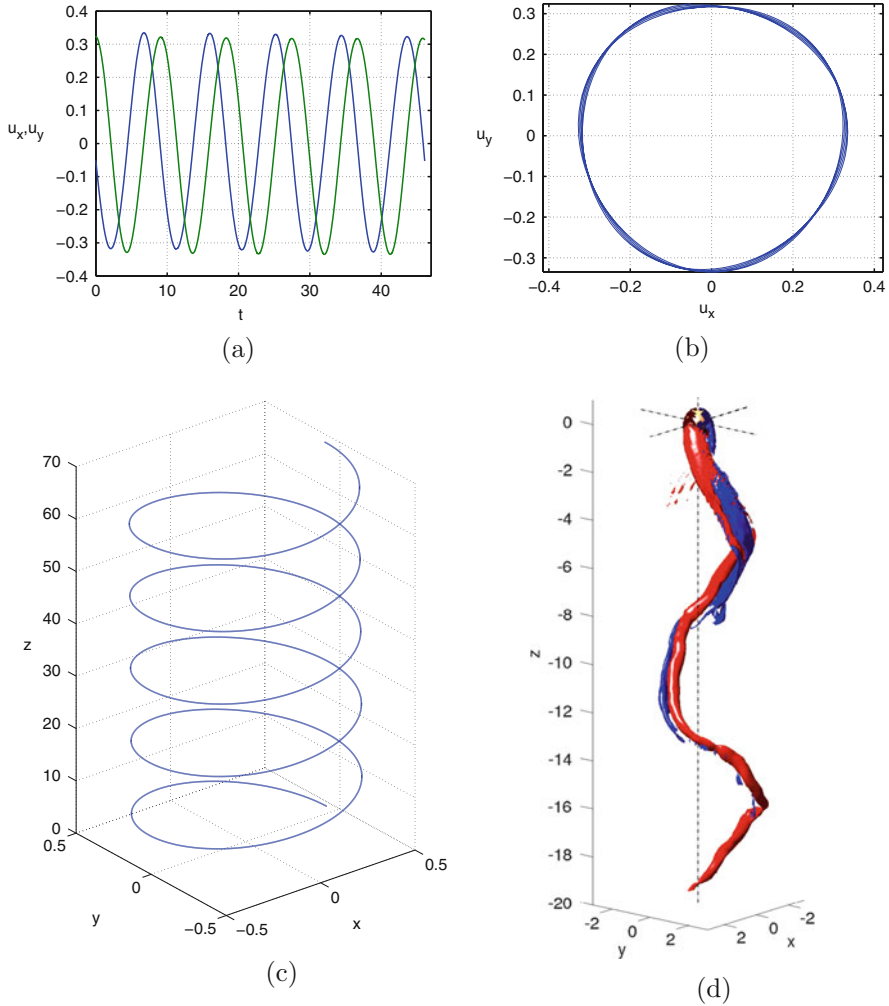


**Fig. 7.27** Five periods of helical trajectory for  $\rho_s/\rho = 0.1$  and  $G = 500$ . **(a)** Horizontal velocity components as functions of time, **(b)** path of the horizontal velocity vector, **(c)** trajectory. **(b)** Shows the very small deviations from periodicity and from circular form. **(d)** Represents iso-surfaces of stream-wise vorticity at levels  $\pm 1$  at the end of the time interval of **(a)**

#### 7.4.4 Conclusion

The above presentation focused essentially on ordered states of falling or rising spheres and on the way how chaos sets in this system. The most important feature of the transition scenario of spheres is the very fast onset of chaos. This, together with the difficulty of assuring a perfect sphericity and homogeneity of experimental spheres, is very likely at the origin of disagreements between the

numerical simulations and experimental observations as soon as the regimes leave the restricted domain of primary and secondary bifurcation states. It is interesting to note that all the theoretically predicted regimes listed in Sect. 7.3.3 can, actually, be evidenced as stable ordered states. This will also be the case for flat bodies but in a different order and within a totally different scenario.

## 7.5 Homogeneous Thin Disc

As shown in Fig. 7.1, path instabilities of flat bodies, namely of very flat cylinders considered approximately as nominally infinitely thin discs, are very easy to observe. An experimental Nature paper [8] from late nineties, sums up experimental observations of paths of falling discs found to depend on the relative solid/fluid inertia and the reached Reynolds number. A more rigorous choice of problem parameters is necessary to formulate the problem mathematically. Moreover, the numerical method described in Sects. 7.2.3 and 7.3.1 needs to be generalized to account for the arbitrary disc inclination.

### 7.5.1 Mathematical Formulation and Numerical Method

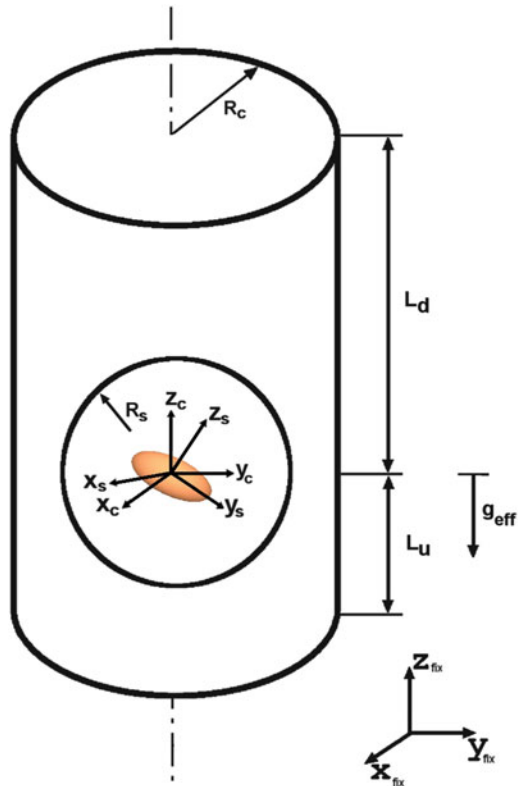
Since our numerical method is limited to axisymmetric geometry, the computational domain is decomposed into a spherical subdomain with polar axis defined by the revolution axis of the body (in the present case of the disc) and into a remaining vertical cylindrical domain. The numerical configuration is schematized in Fig. 7.28 with indications concerning the choice of numerical parameters defining the domain geometry. The spherical sub-domain is allowed to rotate with respect to the cylindrical one. The reconnection uses a spherical function expansion and corresponding rotation matrices (see [2] for technical details). The choice of the domain decomposition was stimulated by the physics of the configuration requiring to capture an essentially vertical far wake together with the boundary layer and the detached flow close to the body. In both subdomains, the velocity field is defined with respect to a fixed frame. In the rotated spherical subdomain, the velocity vector is projected onto the rotating frame attached to the body axis.

In order to allow for the limit case of infinitely flat bodies, we can no longer keep the density ratio as a convenient parameter. We replace it by the non-dimensionalized mass

$$m^* = \frac{m}{\rho d^3}, \quad (7.36)$$

where  $d$  is the diameter of disc (or more generally of the projection onto a plane perpendicular to the axis of revolution) and  $m$  is the mass of the body. For a given

**Fig. 7.28** Geometry of the problem.  $g_{eff}$ : vertical vector of effective gravity oriented downward or upward for falling or ascending bodies,  $(x_{fix}, y_{fix}, z_{fix})$ : fixed reference frame,  $(x_c, y_c, z_c)$ : vertically translated frame, and  $(x_s, y_s, z_s)$ : frame of the spherical sub-domain rotating with the body. Numerical parameters: radius of the spherical sub-domain  $R_s = d$ ,  $R_c = 8d$ ,  $L_u = 12d$ ,  $L_d = 25d$



body shape, an equivalent choice consists in considering the non-dimensionalized moment of inertia with respect to an axis perpendicular to the axis of revolution of the body (see [8])  $I^* = I/(\rho d^5)$ . For a disc,  $I^* = m^*/16$ . For the same reason, the velocity scale is more conveniently defined using the resultant of the weight and buoyancy:

$$U = \sqrt{|m^* - V^*|gd} \tag{7.37}$$

where  $V^* = V/d^3$ . The flow equations then write

$$\frac{\partial \mathbf{v}}{\partial t} + [(\mathbf{v} - \mathbf{u} - \boldsymbol{\omega} \times \mathbf{r}) \cdot \nabla] \mathbf{v} + \boldsymbol{\omega} \times \mathbf{v} = -\nabla p + \frac{1}{G} \nabla^2 \mathbf{v} \tag{7.38}$$

and

$$\nabla \cdot \mathbf{v} = 0 \tag{7.39}$$



where  $\mathbf{u}$  is the translation velocity of the body center and  $\boldsymbol{\omega}$  is the angular velocity of the rotating spherical sub-domain. The Galileo number  $G$  appearing in Eq. (7.38) is given by

$$G = \frac{Ud}{\nu} = \frac{\sqrt{|m^* - V^*| \mathbf{g} d^3}}{\nu} = \frac{\sqrt{m^* \mathbf{g}_{eff} d^3}}{\nu}. \quad (7.40)$$

The solid body motion equations are:

$$m^* \left( \frac{d\mathbf{u}}{dt} + \boldsymbol{\omega} \times \mathbf{u} \right) = \mathbf{F}_{fl}(\mathbf{v}, p) + \mathbf{k}_{fix}, \quad (7.41)$$

$$\alpha I^* \frac{d\Omega_3}{dt} = M_{fl_z}, \quad (7.42)$$

$$I^* \left( \frac{d\Omega_+}{dt} - i\alpha \Omega_+ \Omega_3 \right) = M_{fl_+} \quad (7.43)$$

where  $\mathbf{k}_{fix}$  is the vertical unit vector pointing downward or upward for falling or ascending bodies, respectively. Equations (7.42) and (7.43) are written for complex coordinates [18] of angular velocity  $\Omega_+ = \Omega_x + i\Omega_y$  and torque  $M_{fl_+} = M_{fl_x} + iM_{fl_y}$ . The angular velocity vector of the spherical sub-domain has the components  $\boldsymbol{\omega} = (\Omega_x, \Omega_y, 0)$ . Due to the axisymmetry of the body, the body fitted mesh is not required to follow the rotation about its axis. As already mentioned, for a homogeneous disc, the non-dimensionalized moment of inertia is equal to  $m^*/16$ , in general the ratio  $I^*/m^*$  is given by the body shape and the mass distribution and appears as an additional external parameter of the problem. For a disc, the full system of Navier-Stokes equations (7.38) and (7.39) and of motion equations (7.41)–(7.43) depends only on two dimensionless parameters and a similar two parameter investigation as for the sphere is sufficient to characterize all its possible regimes.

### 7.5.2 Description of Regimes of Falling Discs

Depending not only on the choice of external parameters  $G$  and  $m^*$  but, due to sub-critical effects and many cases of bistability or even multiple stability, also on initial conditions, a variety of trajectories has been evidenced. We start with their description before situating them in a comprehensive state diagram.

#### Periodic Flutter

Periodic flutter is the regime of Fig. 7.1. Since ‘flutter’ refers rather to a relatively fast oscillating motion it is also called zig-zagging. “Flutter” originates from the motion of confetti or cards in the air. The physical time-scale is, however, irrelevant

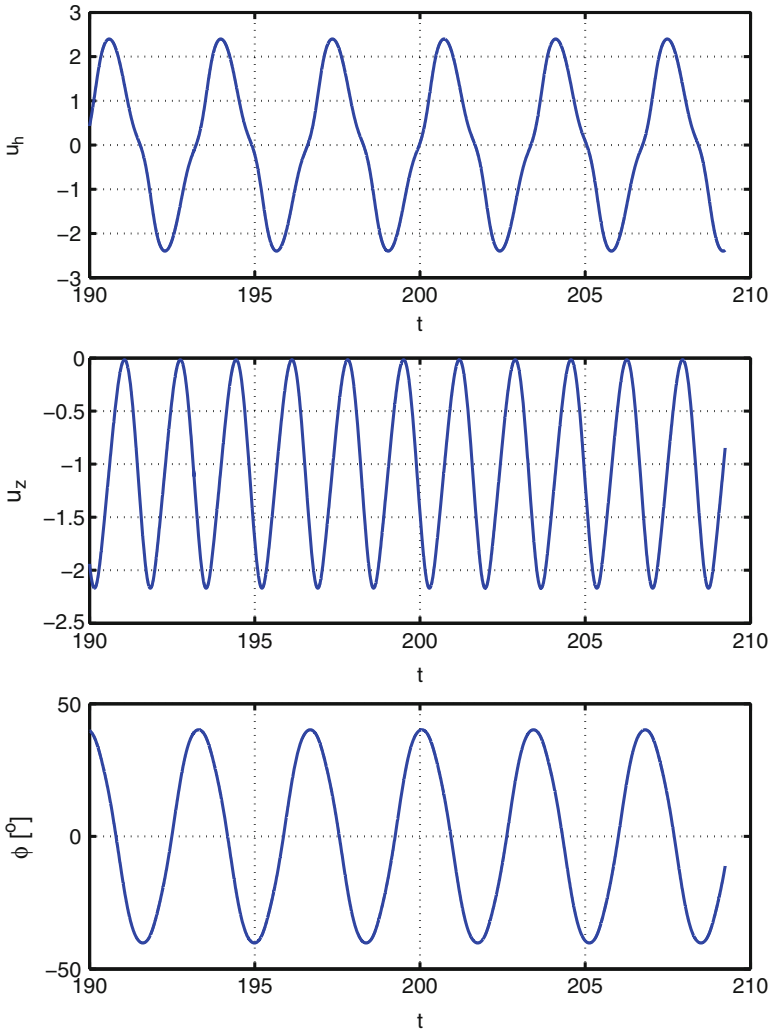
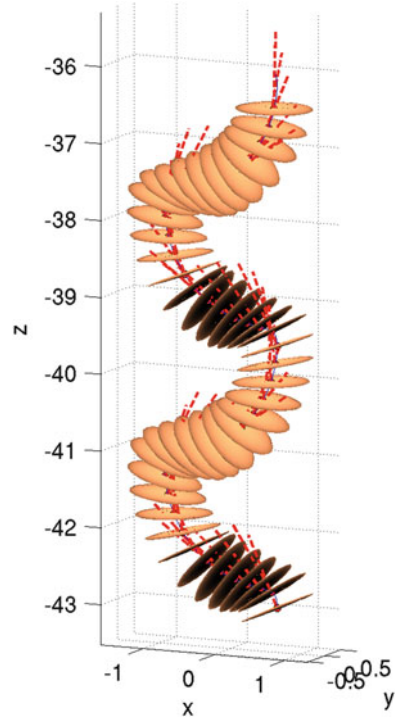


**Fig. 7.29**  $m^* = 0.1$ ,  $G = 200$ . (Top) Horizontal component of the velocity; (middle) Vertical component of the velocity; (bottom) inclination of the disc defined as an angle between the disc axis and the vertical direction

in the non-dimensional formulation. The important features of this regime are planar, vertically oscillating trajectories accompanied by a significant amplitude of inclination of the disc. A quantitative idea of typical dynamics is provided by Fig. 7.29. In the represented case the horizontal motion dominates, similarly as in Fig. 7.1. The amplitude of the horizontal velocity is larger than the maximal value of the vertical one. The mean value is strictly zero which results in a vertical trajectory. Twice by period, the disc flies horizontally, i.e. its vertical velocity is

**Fig. 7.30** Fluttering periodic state,  $m^* = 0.1$ ,  $G = 200$ ,  $z$ —vertical position,  $x, y$ —horizontal positions as multiples of  $d$ . The *red dashed line* represents a half-axis of the disc



practically zero. This happens when the disc is not far from a horizontal position (zero inclination angle). The maximal inclination of the disc exceeds  $40^\circ$ . At this moment, the disc falls the fastest. Qualitatively, the motion is visualized by the kino-gram of Fig. 7.30. The flutter is a solid (solid-fluid) mode where the motion of the fluid strongly interacts with that of the solid body. For an infinitely flat disc, the fluid modes are rare and limited to very small non-dimensionalized masses. In these regimes, the motion of the solid is almost invisible (see the next paragraph). For the purpose of demonstrating the difference between the flutter and a periodic fluid mode we use the example of a flat spheroid of aspect ratio  $d/(2a)$  ( $a$ —small of half axis of elliptical section). The right Fig. 7.31 is very similar to that of Fig. 7.30. The left Fig. 7.31 shows the vortex shedding influenced by the motion of the solid. Figure 7.32 represents the streamwise vorticity and kino-gram of a fluid mode. The oscillations of the body are very small but the vorticity in the wake is almost as intensive as for the solid mode. Some quantitative data is given in Table 7.4. The maximum inclination angle of the disc in this regime is at least  $20^\circ$  and reaches  $90^\circ$  when the intermittently tumbling regime sets in. The frequency expressed in terms of Strouhal number is high (higher than characteristic frequencies of the sphere scenario) for very light discs but considerably decreases with growing inertia (as can be expected from motion equations). The “flying” described above, concern discs of moderate non-dimensionalized mass for high enough Galileo numbers. As

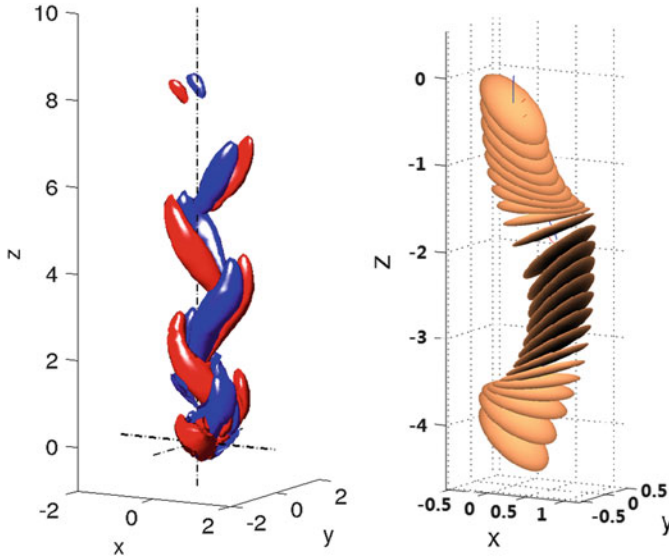


**Fig. 7.31** Vorticity structures and trajectory of a flutter of spheroid of aspect ratio 10 at  $m^* = 0.25$ ,  $G = 115$ ;  $\sin \psi_{max} = 0.75$ , vorticity level  $\omega_z = \pm 0.8$

soon as inertia becomes larger the flutter is replaced by the intermittent and tumbling regimes.

### Quasi-Vertical States (Fluid Modes)

For an infinitely flat disc, the fluid modes have been evidenced as primary bifurcation states in a very narrow range of small non-dimensionalized masses  $m^* \leq 0.05$ . They become very rapidly chaotic as the Galileo number increases. The typical trajectories are thus rather chaotic deviating very few from vertical direction and accompanied by a small inclination of the disc (see Fig. 7.33). Such a chaotic motion was attributed to experimental noise in experiments and the trajectories were considered as vertical. This lead to the conclusion that the free body degrees of freedom have a very strong stabilizing effect on the primary instability. Actually, the primary bifurcation threshold can be slightly shifted upward for flat cylinders but the effect is very limited (see the discussion in [4]). It is interesting to note that, unlike for spheres, the fluid modes of discs have a much smaller frequency than the flutter. The Strouhal number of oscillations characteristic for the quasi-vertical states (main peak of spectra of velocity of chaotic trajectories) at  $m^* = 0$  is about 0.1 whereas, the Strouhal number of the flutter grows from 0.4 (at  $G = 140$ ) to 0.6 (at  $G = 500$ ) for the same infinitely small non-dimensionalized mass (see Table 7.4). The amplitude of oscillation of the disc is very small from all viewpoints, vertical and horizontal velocity, angular velocity and inclination (not more than  $1^\circ$ ).

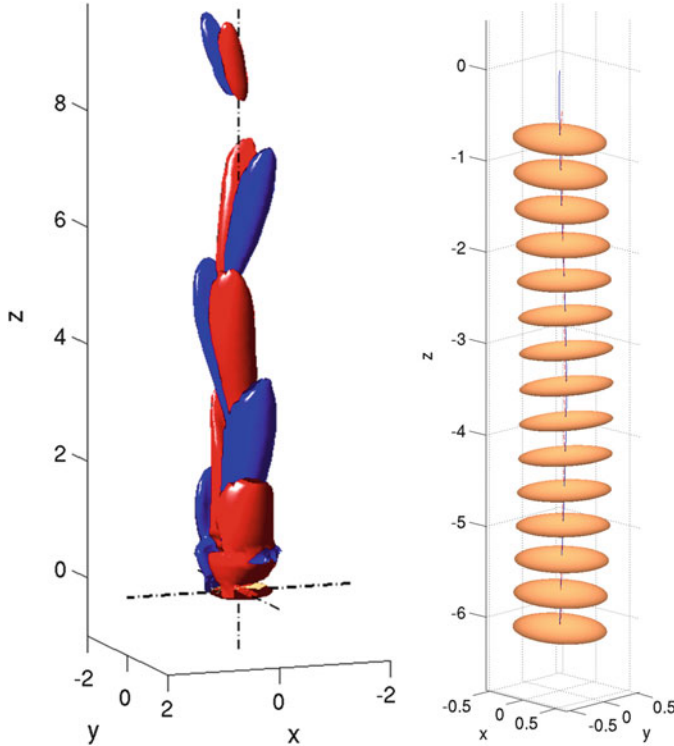


**Fig. 7.32** Vorticity structures and trajectory of vertical periodic state (fluid mode) of spheroid of aspect ratio 10 at  $m^* = 0.25$ ,  $G = 100$  ( $\sin \psi_{max} = 0.1$ , vorticity level:  $\omega_z = \pm 0.4$ )

**Tumbling State**

The trajectories of the tumbling states are planar like for the flutter. The tumbling regime can be understood as resulting from the flutter when the inclination angle exceeds  $90^\circ$  due to the increase of inertia ( $m^*$ ) or decrease of viscous effects (increase of  $G$ ). In that case, the disc tumbles over edge and continues rotating in the same direction. This results in a globally oblique trajectory with horizontal translation and angular velocities which do not change the sign. A kino-gram conveying the idea of the motion is represented in Fig. 7.34. Quantitative information on the translation and rotation velocities can be obtained from Fig. 7.35. For the relatively ‘light’ disc of Figs. 7.34 and 7.35, the angular velocity presents strong oscillations (between zero and 2). The regime lies at the threshold of stable tumbling states in the state diagram (Fig. 7.40). The rotation almost stops once per period. With growing inertia the fluctuations decrease and, at  $m^* = 10$ , the disc rotates almost with a constant angular velocity.

Some quantitative data is provided in Table 7.5. It can be seen that the Strouhal number is much less sensitive to inertia which is easily understood considering that

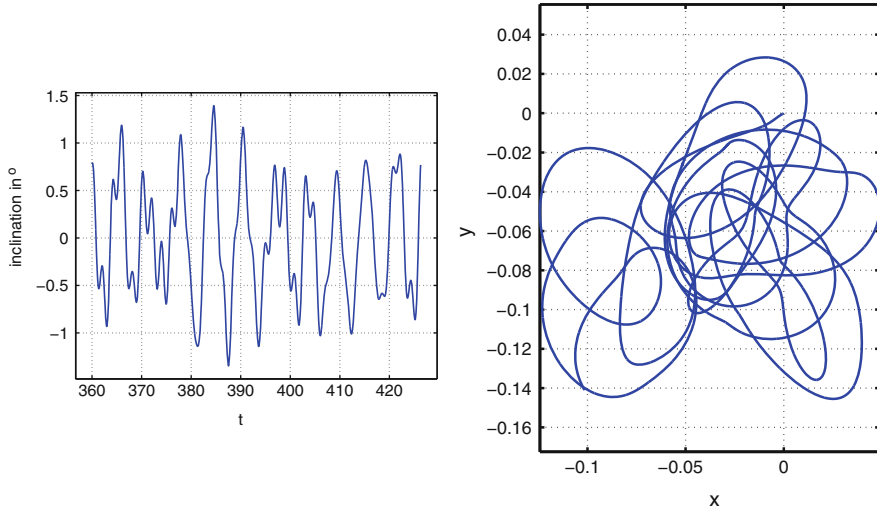


**Fig. 7.33** Chaotic quasi-vertical trajectory for  $m^* = 0$  at  $G = 140$ . *Left figure*: inclination along the horizontal  $x$ -axis as a function of time. *Right figure*: horizontal projection of the trajectory

the frequency is that of a rotating and not oscillating motion. The inertia reduces unsteady fluctuations. The latter tend to zero for large non-dimensionalized masses and the rotation tends to be uniform. The average trajectory is oblique. Its average inclination can be inferred from the ratio of the mean horizontal,  $u_h$ , and vertical,  $u_z$ , velocity. The inclination angle varies between  $20^\circ$  and  $40^\circ$ .

### Intermittent State

The flutter and tumbling are separated by a region of regimes where the disc ‘hesitates’ between both. This results in mostly non periodic trajectories presenting intermittent switching between tumbling in two opposite directions. In some cases the switching becomes periodic. In that case, the disc tumbles the same number of times in the same direction before the sense of the rotation changes. Such trajectories still have a zig-zagging aspect and their mean direction is vertical. A non periodic intermittent state is represented in Figs. 7.36 and 7.37.

### Non Planar, Three-Dimensional Trajectories

The zig-zagging (flutter), tumbling and intermittent states represent a specificity of flat bodies. Their shape makes them interact strongly with the flow in the manner of a propeller. In all the three mentioned regimes, the trajectories remain planar in a large interval of Galileo numbers, i.e. the wake keeps a fixed symmetry plane. We

**Table 7.4** Some quantitative data for selected periodic fluttering and quasi-vertical (fluid modes—marked by \*) regimes of a disc

$m^*$	$G$	$u_z$	$\Delta u_z$	$\Delta u_h$	$\Delta \omega_h$	$\Delta s_h/d$	$St$	$\phi_{max}[\text{rad}]$
0*	90	-1.439	0.003	0.046	0.019	0.043	0.105	0.019
0*	100	-1.444	0.004	0.055	0.030	0.061	0.100	0.022
0	150	-1.374	0.307	1.109	1.467	0.287	0.437	0.392
0	200	-1.363	0.401	1.380	1.649	0.328	0.477	0.415
0	300	-1.343	0.476	1.682	1.712	0.370	0.528	0.407
0	500	-1.292	0.546	2.035	1.693	0.411	0.598	0.380
0.1	80	-1.250	0.408	0.991	1.648	0.370	0.304	0.685
0.1	100	-1.232	0.502	1.181	1.759	0.427	0.306	0.731
0.1	200	-1.199	0.972	2.097	1.863	0.797	0.292	0.962
0.1	300	-1.255	1.333	2.778	1.876	1.199	0.246	1.102
0.1	500	-1.339	1.839	3.759	1.826	1.974	0.190	1.227
0.25	90	-1.347	0.924	1.602	2.213	0.749	0.182	1.362
0.5	38	-1.166	0.106	0.343	0.865	0.209	0.208	0.555
0.5	50	-1.254	0.365	0.737	1.626	0.410	0.184	1.057
0.75	45	-1.271	0.284	0.595	1.482	0.379	0.154	1.040
0.75	50	-1.377	0.432	0.774	1.791	0.527	0.131	1.340
1	40	-1.222	0.160	0.396	1.107	0.287	0.160	0.867
2	34	-1.165	0.043	0.173	0.568	0.165	0.137	0.532
2	38	-1.243	0.095	0.267	0.856	0.251	0.123	0.822
10	45	-1.250	0.006	0.050	0.173	0.094	0.067	0.332

Meaning of symbols:  $u_z$  mean vertical velocity,  $\Delta u_z, \Delta u_h, \Delta \omega_h$  amplitude of oscillation of vertical and horizontal velocity and of angular velocity,  $\Delta s_h$  maximum horizontal displacement,  $St$ —Strouhal number and  $\phi_{max}$ —maximal inclination

have, however, seen that the stability of the symmetry plane was quite weak for a spherical body. For discs, except for the particular case of chaotic quasi-vertical paths, the symmetry plane is relatively stable. Nevertheless, at sufficiently high Galileo numbers the flow symmetry also gets lost. The flutter loses its symmetry due to the loss of stability of states characterized by equal amplitudes  $B_{\pm}$  in Eqs. (7.34) and (7.35) in favor of purely helical states with only one of the two helical components. This results in spiral trajectories of the type represented in Fig. 7.38. For tumbling regimes, the symmetry plane starts to rotate in a similar manner as for spheres. The rotation velocity is constant, the trajectories remain very regular and assume a globally helical shape, albeit with a large rotation period, large radius and pitch (see Fig. 7.39). The onset of non-zero helicity could be observed also for intermittent states. Interestingly enough, up to Galileo number of 500, we did not evidence any truly chaotic paths except for quasi-vertical trajectories. The strong solid–fluid interaction has obviously a stabilizing effect.

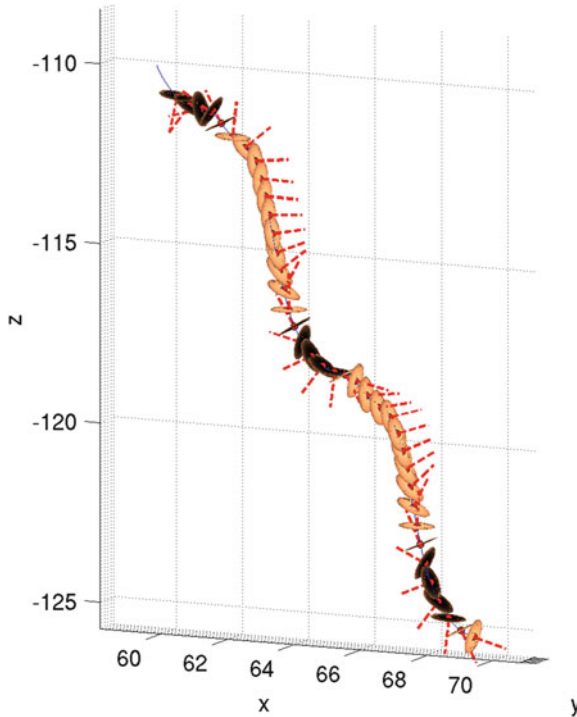


**Fig. 7.34** Kino-gram of the tumbling state at  $m^* = 0.5$ ,  $G = 160$ . The red dashed line represents a half-axis of the disc

### 7.5.3 Transition Scenario of Discs

A comprehensive picture of the transition scenario for thin discs is provided by the state diagram of Fig. 7.40. As can be seen at first glance, there is practically no common feature with Fig. 7.13 referring to a spherical body. The differences can be summed up as follows.

The vertical trajectories are much less stable than for a sphere. To make this statement clear, it is necessary to mention the Reynolds numbers at the primary instability threshold represented by the thick black line in Fig. 7.40. The non-dimensionalization defining the Galileo number (7.40) was chosen so that the non-dimensional vertical velocity remains close to one. It varies roughly between 1.2 and 1.4 as can be seen in Table 7.4. The highest value of critical Galileo number (78) was found for the onset of quasi-vertical regime at  $m^* = 0$  and 0.05. Given the vertical velocity 1.44, this yields a critical Reynolds of 112, slightly less than for a fixed disc placed perpendicularly to the flow (117—see [3]). This, about half as high, value than for a sphere is explained by the sharp edges of the disc and the strongly detached flow. At higher non-dimensionalized masses ( $m^* \geq 0.1$ ), the primary bifurcation is of Hopf type yielding directly an oscillating regime. The latter



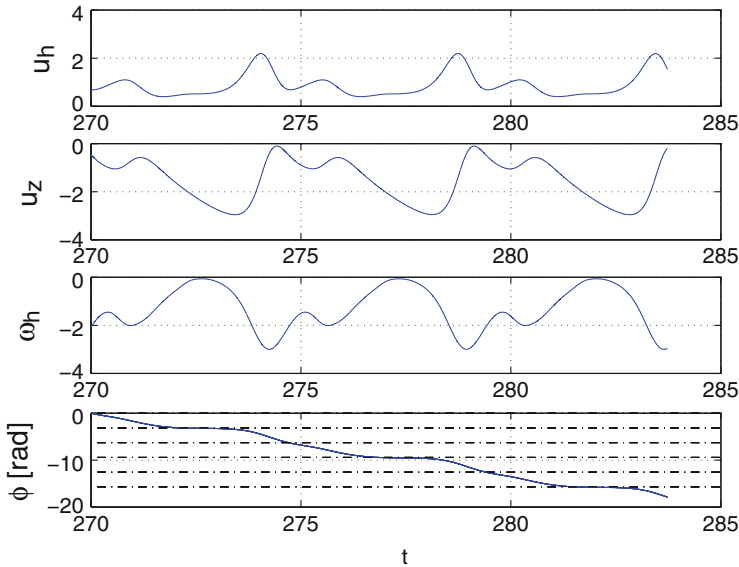


**Fig. 7.35**  $m^* = 0.5$ ,  $G = 160$ . *Top*: horizontal component of the velocity; *second row*: vertical component of the velocity; *third row*: angular velocity; *bottom*: inclination of the disc defined as an angle between the disc axis and the vertical direction over three periods of rotation. The *dotted lines* in the bottom figure mark the rotation by  $k\pi$ , where  $k = 1, 2, \dots$

has a strongly destabilizing effect, making the threshold drop to a minimum critical Galileo of 30 (at  $m^* = 2$ ). The corresponding Reynolds number is only 33. This extremely low critical Reynolds number appears to be specific for very thin bodies. Oblate spheroids of as large aspect ratio as 10 have a minimum critical Reynolds number of primary instability of 115 ( $m^* = 1.5$ ). The explanation comes certainly from a very small drag of a horizontally moving disc, with only skin friction and no pressure drag.

On the other hand, as has already been mentioned, virtually no chaotic regimes were evidenced in spite of relatively large Reynolds numbers (about 800) corresponding to the highest Galileo number (500) considered in the parametric study. The explanation is, again, easily at hand. Both for light and massive discs, when viscous effects become weak, the inertia of the organized oscillation (for light discs) or rotation (for massive discs) prevents the system from becoming chaotic. In the case of light discs the inertia is that of the moving fluid but the final effect is similar. Only when the motion of the disc is very small, chaotic behavior is possible, as it is the case for the quasi-vertical chaotic states.

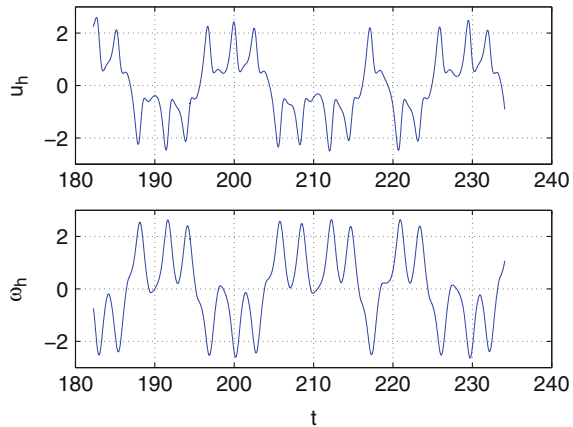
Strictly speaking, intermittency is a form of chaos so that the intermittent regime may also be qualified as chaotic. The main difference consists, however, in the fact that the trajectories remain planar. The existence of the intermittent regime can be rather linked to the subcritical effects characterizing the whole scenario. A subcritical bifurcation leads to coexistence of two (or more) stable states. The loss

**Table 7.5** Some quantitative data for selected tumbling states

$m^*$	$G$	$u_z$	$\Delta u_z$	$u_h$	$\Delta u_h$	$\omega_h$	$\Delta \omega_h$	$St$
0.75	90	-1.224	0.504	-0.929	0.351	1.292	0.721	0.315
0.75	100	-1.202	0.534	-0.929	0.349	1.317	0.689	0.333
0.75	200	-1.067	0.461	-0.941	0.347	1.533	0.538	0.443
0.75	300	-1.014	0.451	-0.939	0.343	1.599	0.502	0.490
0.75	400	-0.987	0.449	-0.937	0.344	1.626	0.487	0.515
1	80	-1.267	0.424	-0.631	0.203	0.875	0.477	0.283
1	100	-1.213	0.397	-0.858	0.270	1.259	0.570	0.320
1	150	-1.139	0.367	-0.863	0.264	1.389	0.479	0.381
1	200	-1.099	0.359	-0.861	0.259	1.463	0.441	0.418
1	300	-1.059	0.352	-0.858	0.257	1.529	0.423	0.458
1	400	-1.035	0.353	-0.859	0.258	1.552	0.418	0.476
2	50	-1.412	0.283	-0.690	0.167	0.865	0.595	0.176
2	54	-1.399	0.280	-0.702	0.165	0.894	0.563	0.187
2	58	-1.374	0.264	-0.712	0.163	0.921	0.534	0.199
5	40	-1.497	0.158	-0.499	0.104	0.600	0.421	0.113
10	50	-1.474	0.079	-0.459	0.056	0.565	0.219	0.118
10	80	-1.419	0.061	-0.538	0.044	0.765	0.141	0.170
10	150	-1.330	0.047	-0.584	0.035	1.035	0.088	0.246
10	200	-1.297	0.045	-0.594	0.033	1.143	0.076	0.279

For the meaning of symbols, see Table 7.4

**Fig. 7.36** Intermittent state,  $m^* = 0.25, G = 110$ . (Top) Horizontal component of the velocity; (bottom) the angular velocity  $\omega_h$



of stability of the subcritical state does not correspond to that of the super-critical one (for the bifurcation parameter evolving in opposite sense), which can remain stable below the bifurcation threshold. The intermittent subdomain corresponds to an opposite situation where neither of the neighboring ordered states is stable.

In all other cases, the typical subcritical overlapping is observed. Already the primary bifurcation was found subcritical in the interval  $0.05 \leq m^* \leq 2$ . For

**Fig. 7.37** Kino-gram of intermittent state,  $m^* = 0.25$ ,  $G = 110$ . The *red dashed line* represents a half-axis of the disc

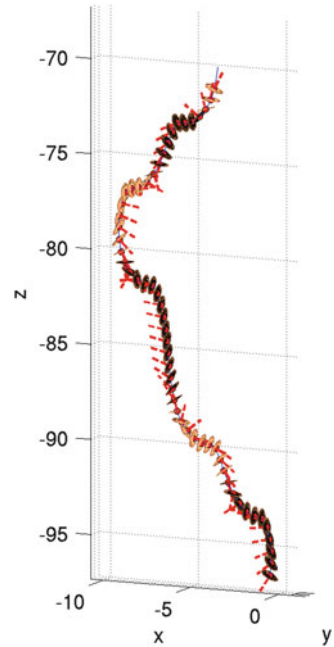
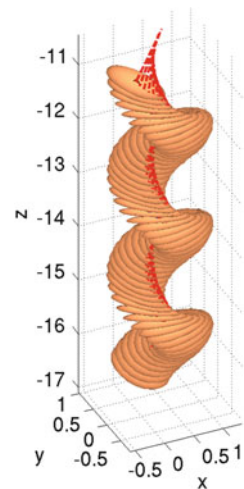


**Fig. 7.38**  $m^* = 0.05$ ,  $G = 300$ ; Spiral state



these intermediate non-dimensionalized masses, the vertical state loses its stability at settles immediately to a developed flutter with significant amplitude of oscillation. This state remains stable, albeit in a limited interval of Galileo number, when the Galileo number drops again under the critical value. A similar bi-stability was observed at the transition from the quasi-vertical chaotic regime to the flutter for very light discs. The rotation makes the tumbling very stable, able to resist to a considerable increase of viscous effects (decrease of Galileo number) as soon as

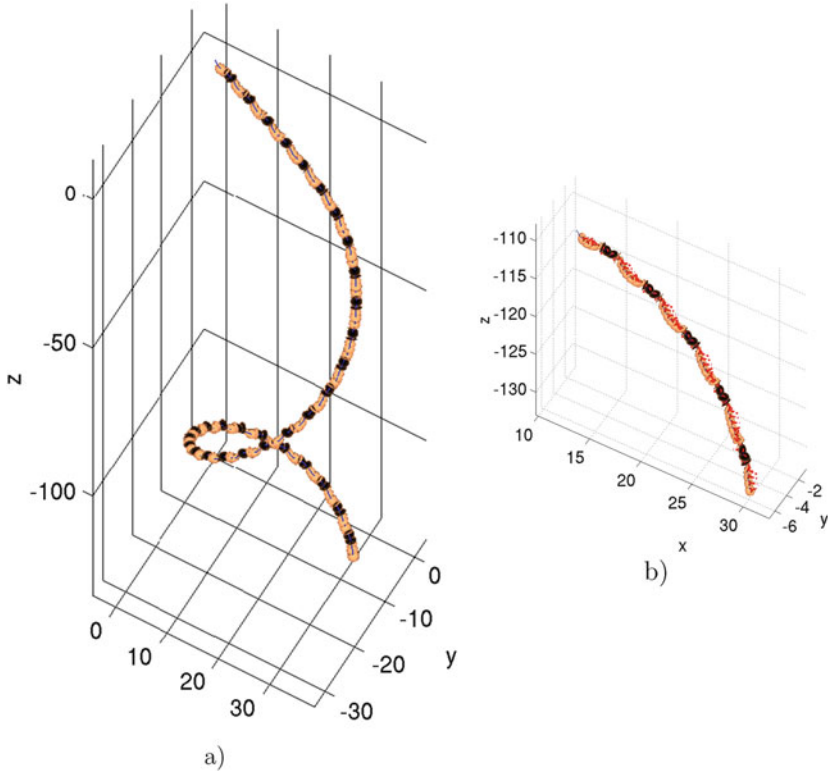


**Fig. 7.39**  $m^* = 0.5$ ,  $G = 400$ ; spiral tumbling state. (a) The disc is enlarged by a factor of 2. (b) Detail of figure (a). The disc is on the scale in this figure

the inertia of the solid body sufficiently exceeds that of the fluid ( $m^* > 1$ ). This explains the disappearing of the intermittent regime and overlapping not only with the oscillating regime (flutter) but also partly with the vertical one at high  $m^*$ .

It must, of course, be expected that for very high Galileo numbers (outside the scope of our investigation) turbulence ends up by dominating the dynamics and makes the trajectories chaotic. The loss of planarity resulting in helical trajectories mentioned in Sect. 7.5.2 of the trajectories can be considered as initial stage of this transition. Non planar (helical) fluttering, intermittent and tumbling trajectories are marked by filled markers in the state diagram (Fig. 7.40).

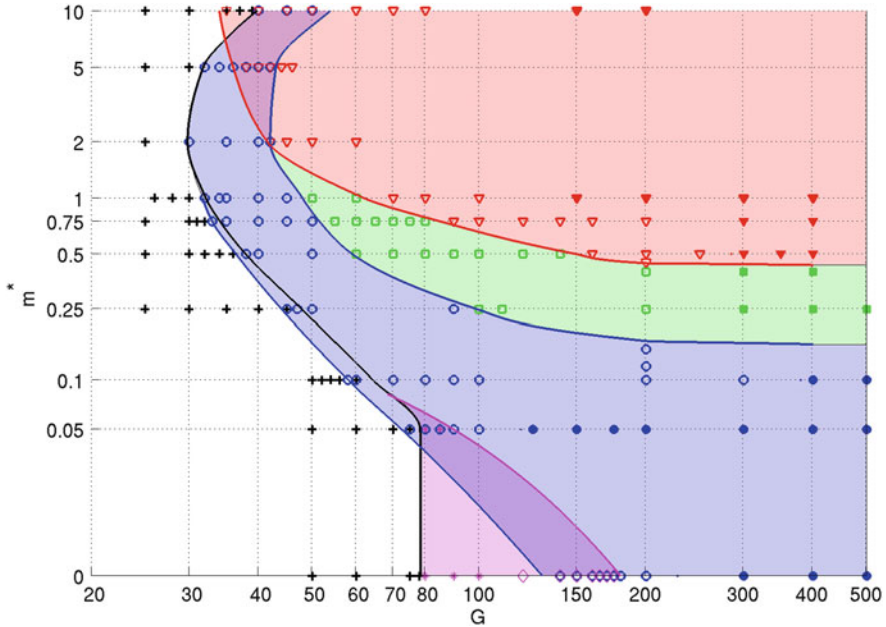


**Fig. 7.40** State diagram for infinitely thin disc. Meaning of symbols: *red triangles*: tumbling; *green squares*: intermittent; *blue circles*: flutter; *black crosses*: vertical. *Filled symbols*: helical trajectories. *Magenta symbols*: (*dots and diamonds*) periodic and chaotic quasi-vertical states

### 7.5.4 Conclusion

The vertical trajectories of discs give way to an oscillating regime. The trajectory remains vertical in the average but, except for very light discs, the disc oscillates with significant inclination amplitude. This amplitude grows mostly due to increasing inertia of the body. When the inclination of  $90^\circ$  is reached, the disc starts to tumble over edge. Initially, the tumbling itself and its direction are intermittent. For higher inertia, it becomes perfectly periodic and results in an oblique trajectory accompanied by a regular rotation of the body. The importance of inertia is particularly obvious for Galileo numbers exceeding 200 when the separation between these three regimes becomes practically independent of the Galileo number. In spite of the early onset of non-vertical trajectories, the transition to chaos is considerably delayed due to the inertia of body rotation.

## 7.6 General Conclusion and Perspectives

The significant difference between the transition scenario of a sphere and of a disc raises the question of behavior of less idealized bodies. Some results concerning flat cylinders [4, 19] are available and show the importance of the aspect ratio of the body. To shed more light on this effect and to establish a clear relation between an ideally flat disc and an ideally spherical body a detailed parametric investigation of spheroids of aspect ratio decreasing from infinity (ideally flat spheroid) to almost one (sphere) has been performed and will be published in the near future. Recently, also prolate spheroids were brought to the spotlight due to applications concerning the sedimentation of fibers. Since the prolate spheroids (and long cylinders) fall with horizontal revolution axis in the fundamental vertical state of trajectory, the early stages of transition are no longer about characterized by axisymmetry breaking and are thus outside the scope of the described approach.

Another topic involving axisymmetry breaking concerns the motion of drops and bubbles in quiescent ambient fluid. Gas bubbles in liquids have dynamics mainly driven by the free surface with negligible effect of the gas motion. An ideal bubble can be modeled as a void in a liquid delimited by a deformable surface at which a free surface boundary condition can be imposed. A numerical treatment of the problem is complicated by the dynamically changing, potentially three-dimensional geometry, however the physical background is still given by axisymmetry breaking and only two external parameters are sufficient. Extensive experimental effort to investigate the dynamics of freely ascending bubbles showed a large variety of non-vertical trajectories. The instabilities giving rise to non-vertical ascension have, however, not yet been clearly identified in spite of the availability of numerical tools.

## References

1. G. Bouchet, M. Mebarek, J. Dušek, Hydrodynamic forces acting on a rigid fixed sphere in early transitional regimes. *Eur. J. Mech. B Fluids* **25**, 321–336 (2006)
2. M. Chrust, Etude numérique de la chute d'objets axisymétriques dans un fluide newtonien. PhD thesis, Université de Strasbourg, 2012
3. M. Chrust, G. Bouchet, J. Dušek, Parametric study of the transition in the wake of oblate spheroids and flat cylinders. *J. Fluid Mech.* **665**, 199–208 (2010)
4. M. Chrust, G. Bouchet, J. Dušek, Effect of solid body degrees of freedom on the path instabilities of freely falling or rising flat cylinders. *J. Fluids Struct.* **47**, 55–70 (2014)
5. M. Chrust, C. Dauteuille, T. Bobinski, J. Rokicki, S. Goujon-Durand, J.E. Wesfreid, G. Bouchet, J. Dušek, Effect of inclination on the transition scenario in the wake of fixed disks and flat cylinders. *J. Fluid Mech.* **770**, 189–209 (2015)
6. D. Fabre, F. Auguste, J. Magnaudet, Bifurcations and symmetry breaking in the wake of axisymmetric bodies. *Phys. Fluids* **20**, 051702 (2008)
7. D. Fabre, J. Tchoufag, J. Magnaudet, The steady oblique path of buoyancy-driven disks and spheres. *J. Fluid Mech.* **707**, 24–36 (2012)
8. S.B. Field, M. Klaus, M.G. Moore, Chaotic dynamics of falling disks. *Nature* **388**, 252–254 (1997)

9. B. Ghidersa, J. Dušek, Breaking of axisymmetry and onset of unsteadiness in the wake of a sphere. *J. Fluid Mech.* **423**, 33–69 (2000)
10. M. Golubitsky, I. Stewart, *Singularities and Groups in Bifurcation Theory*, vol. II (Springer, New York/Berlin/Heidelberg/London/Paris/Tokyo, 1988)
11. M. Horowitz, C.H.K. Williamson, The effect of Reynolds number on the dynamics and wakes of freely rising and falling spheres. *J. Fluid Mech.* **651**, 251–294 (2010)
12. M. Jenny, J. Dušek, Efficient numerical method for the direct numerical simulation of the flow past a single light moving spherical body in transitional regimes. *J. Comput. Phys.* **194**, 215–232 (2004)
13. M. Jenny, G. Bouchet, J. Dušek, Nonvertical ascension or fall of a free sphere in a Newtonian fluid. *Phys. Fluids* **15**, L9–L12 (2003)
14. M. Jenny, J. Dušek, G. Bouchet, Instabilities and transition of a sphere falling or ascending freely in a Newtonian fluid. *J. Fluid Mech.* **508**, 201–239 (2004)
15. M. Kotouč, G. Bouchet, J. Dušek, Transition to turbulence in the wake of a fixed sphere in mixed convection. *J. Fluid Mech.* **625**, 205–248 (2009)
16. P. Meliga, J.M. Chomaz, D. Sipp, Global mode interaction and pattern selection in the wake of a disk: a weakly nonlinear expansion. *J. Fluid Mech.* **633**, 159–189 (2009)
17. R. Natarajan, A. Acrivos, The instability of the steady flow past spheres and disks. *J. Fluid Mech.* **254**, 323–344 (1993)
18. S.A. Orszag, Fourier series on spheres. *Mon. Weather Rev.* **102**, 56–75 (1974)
19. J. Tchoufag, D. Fabre, J. Magnaudet, Global linear stability analysis of the wake and path of buoyancy-driven disks and thin cylinders. *J. Fluid Mech.* **740**, 278–311 (2014)
20. C.H.J. Veldhuis, A. Biesheuvel, An experimental study of the regimes of motion of spheres falling or ascending freely in a Newtonian fluid. *Int. J. Multiphase Flow* **33**(10), 1074–1087 (2007)
21. W. Zhou, J. Dušek, Chaotic states and order in the chaos of the paths of freely falling and ascending spheres. *Int. J. Multiphase Flow* **75**, 205–223 (2015)

# Chapter 8

## Microbubbles: Properties, Mechanisms of Their Generation

V. Tesář

**Abstract** This chapter discusses microbubbles—small gas bubbles in liquid medium of diameter less than 1 mm. Although they were known to offer a number of advantages, until recently they could be generated only by methods energetically inefficient. New horizons became open by the discovery of generation by aerators provided with an oscillator in their gas supply. Chapter provides in particular an information about no-moving-part fluidic oscillators, recently already almost forgotten but now demonstrated to offer benefits like low manufacturing cost, reliability, long life and absence of maintenance. The empirical fact that small bubbles cannot be obtained simply by making small passages in the aerator is here explained by conjunction of several microbubbles. Because the velocity of bubble motion decreases with decreasing size, small microbubbles tend to dwell near the aerator exits. They then coalesce there into a much larger single bubble (the effect promoted by the latter possessing lower surface energy). The fact that the oscillator prevents this conjunction and thus keeps the microbubbles small has been explained by high-speed camera images which show the effect of oscillatory motions.

**Keywords** Bubble conjunction • Fluidic oscillators • Fluidics • Instability • Microbubbles • Shape oscillation • Surface tension

**MSC2010:** 76T10, 74K15, 76R50, 74A50, 76D45, 74Q10, 76D25

Microbubbles gained recently an importance in many areas of chemical and process engineering, biotechnology, and other industrial as well as medical applications. Their mathematical description typically follows similar principles as when dealing with heavy particles in liquids, but there remain several characteristic aspects of bubbles and especially microbubbles where a specific approach has to be adopted. The aim of this chapter is to provide phenomenological description of generation and initial stages of existence of microbubbles—as well as description of oscillators recently introduced to generate them. It should serve as an overview and motivation for future theoretical investigations in this area.

---

V. Tesář (✉)

Institute of Thermomechanics, Czech Academy of Sciences, Dolejškova 1402/5, 18200 Prague 8, Czech Republic

e-mail: [tesar@it.cas.cz](mailto:tesar@it.cas.cz)



## 8.1 Basics of Gas Bubbles

### 8.1.1 Importance of Microbubbles

Small bubbles of gas in a liquid may not seem to be of any particular use—perhaps just an object of idle observation of their rising motion in one’s drink. Yet they are actually an objects of very serious scientific investigations—and of substantial importance in a large number of branches of practical engineering. Especially important are sub-millimetre sized *microbubbles*, the main subject of discussion in this chapter, Fig. 8.1. The limiting definition of 1 mm diameter is admittedly somewhat arbitrary, but it actually quite well represents the size scale below which the tiny bubbles can exhibit a behaviour in some aspects quite different from the processes in larger bubbles. At the other, small size end of the scale is a similar definition limit, also associated with qualitative difference in behaviour. Smaller than 1  $\mu\text{m}$  are *nanobubbles*—e.g. [26, 60]. Immediately apparent extraordinary property of nanobubbles is the longevity of their existence in the liquid. While bubbles and microbubbles exist only for the time it takes to rise to the surface, nanobubbles can stay for days and even months. Their practically non-existent rising—which is overtaken by omnidirectional Brownian motion—is remarkable, but some other properties are even more strange. Nevertheless, they are not discussed here since it would require a whole monograph of its own.

The subject of the present chapter are the less enigmatic microbubbles. Testimony to their importance is the number of publications presented in Fig. 8.2, recently increasing in exponential manner. Prior to about the year 1995 they were a little known subject and the term “microbubble” was mentioned worldwide in scientific publications at a small, rather constant rate, on average  $\sim 30$  times per year. Even though their potential advantages were then already known, applications were limited by ineffectiveness of then existing methods of microbubble generation (e.g., by ultrasonic generators). It was the idea of using the fluidic oscillators

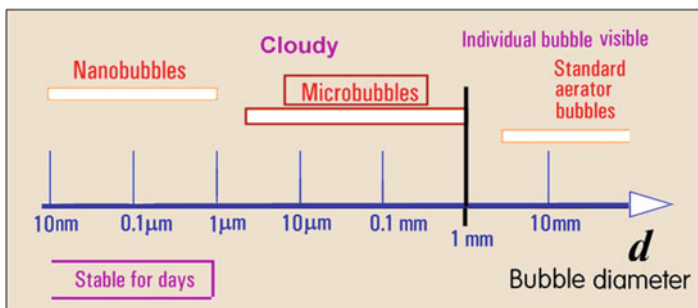


**Fig. 8.1** Size scales of bubbles. Discussion topic in this chapter are *microbubbles*, of diameter less than 1 mm. They are difficult to generate—standard aerators produce larger bubbles. Current interest in microbubbles is due to discovery of conjunction-suppressing effect of fluidic oscillators placed into gas inlet

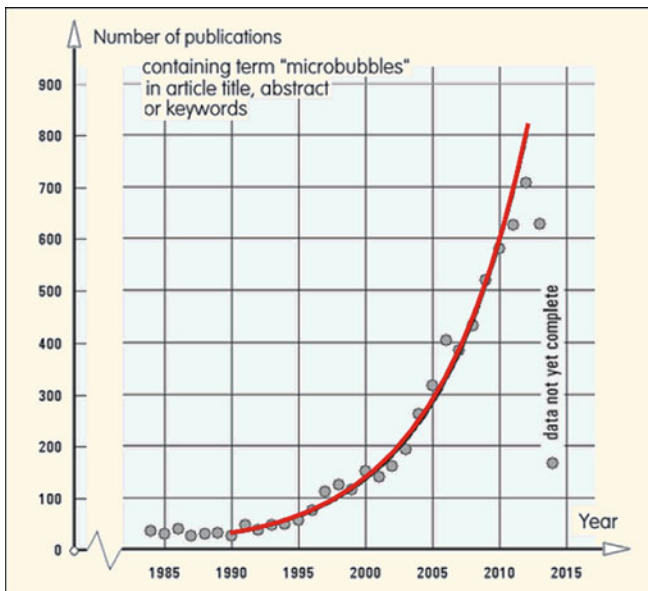


**Fig. 8.2** Increasing importance of microbubbles both in practical engineering applications and in theoretical studies is reflected in the exponential growth of the numbers of publications devoted to this subject

generating flow pulsation in the aerator passages that changed the situation. Today the studies of microbubbles appear with exponential growth rate characterised by the doubling every 4.66 years (Fig. 8.2).

The engineering application developments based on the use of microbubbles are nowadays in several not infrequent cases described as literary revolutionary. To provide a rough idea about them (far from complete), some present-day uses may be mentioned as follows:

- (a) An important application area is that part of chemical engineering and biochemistry, in which the performed operations and reactions depend on diffusion transport of gas into liquid. The large total collective surface of small microbubbles, together with their slow ascent velocity (which rapidly decreases with decreasing size) and hence long time of travel to the surface, can intensify the transfer rate substantially. A typical example that benefited from the use of microbubbles is transfer of oxygen into processed waste water [35] or delivering  $\text{CO}_2$  to unicellular algae grown in a bioreactor [59].
- (b) Important increase in effectiveness of the process is offered by microbubbles in separation of substances by flotation. By their strong clinging to contaminants like oil or grease the microbubbles made possible environmentally friendly removal of such contaminants from processed water. Microbubbles also exhibit a remarkable washing effect [51] without chemical detergents. In paper [56] is discussed typical successful use of microbubbles in de-contamination of silicon

wafers. Their current high yield losses, over 50%, are mainly caused by microcontamination which may be removed by treating them with microbubbles. In fact, microbubbles were demonstrated [47] to be able to perform efficient medical disinfection.

- (c) In food industry microbubbles can extend shelf-life of products of foamy character—whipped cream, ice-cream, sorbets and mousses—in addition giving them interesting taste properties. Microbubble foam was demonstrated to remain stable for up to a year. Also of interest for food industry is water evaporation ability of microbubbles [61] without the applied heat reaching the dried product.
- (d) Hydrodynamic resistance of ships and boats may be reduced by air microbubbles injected into boundary layers. McCormick and Bhattacharya [20] demonstrated a 30% reduction in the frictional resistance. Lack of further progress was due to their method of generation of hydrogen microbubbles by electrolyzing. This consumed more energy than was saved. The problem of suitable microbubble generation at the required large scale plagued also other attempts at ship improvement, including those able to show reductions up to 80%—i.e. decrease to only one fifth of the original value [3, 18]. Recent ship tests with microbubbles are now already made with very large models [15, 18, 21, 52], very near to the practical use (such as Indonesian Navy fast patrol boat described in [57]). For process engineers may be of importance the analogous decrease of friction factor of flow in tubes and pipes [25, 31].
- (e) A wide spectrum of microbubble uses has been found in medicine. Microbubbles can convert energy of ultrasonic vibration into a local thermal therapeutic effect [11]. Streaming effect on microbubbles in ultrasonic field can destroy cancer cells [13] and can cause permeability of cell membranes for drugs [22]—in particular, the anti-cancer ones [53]. Microbubbles were also demonstrated to make possible measuring absolute values of blood pressure [46].
- (f) Many currently developed techniques of using microbubbles aim at microfluidic scale. A use was found in gene manipulation [33], in biosensors [14], mixing of reactants [16] or sorting [48]. Important progress is expected in optofluidics, where ordered arrays of microbubbles can create tuneable optical components [2, 9].

### 8.1.2 *The Main Reason for Desirable Small Scale*

Although bubbles—especially larger ones—are not of exactly spherical shape, everyday experience documents a strong tendency towards sphericity. Thus a useful model for working with bubbles in first approximation is the following dependence between diameter  $d$  and the bubble surface area  $F$  ( $\text{m}^2$ ).

$$F = \pi d^2 \tag{8.1}$$

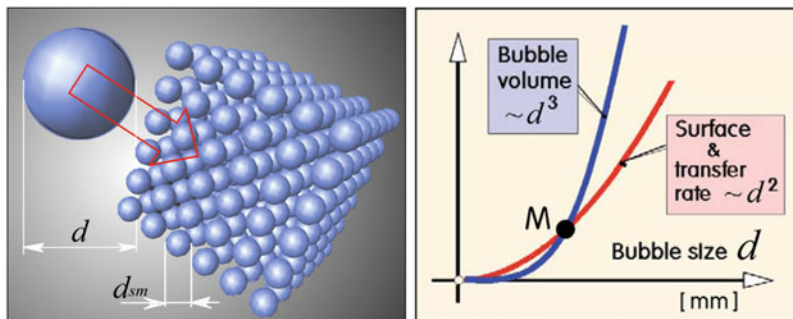


**Fig. 8.3** Single bubble decomposed into small bubbles of equal total volume. Surface decreases with decreased diameter less rapidly than volume—resulting in more efficient diffusion across the total surface

There are many engineering processes involving gas transport by diffusion from the bubbles across their boundary into the surrounding liquid. The available total collective surface area often provides the limiting factor to effectiveness of the process. As a consequence of the non-linearity of Eq. (8.1) this limitation may be overcome by dividing the available gas volume  $V$  ( $\text{m}^3$ ) into a larger number of smaller bubbles. Gas volume in the spherical bubble model is

$$V = \frac{\pi}{6} d^3 \quad (8.2)$$

Let us now assume a distribution of the available gas volume  $V$ —as presented in Fig. 8.3-left—into  $n$  smaller bubbles, each having the surface below the intersection  $M$  as presented in Fig. 8.3-right.

Division of volume  $V$  of gas into  $n$  bubbles increases the total surface across which the gas diffuses from the bubbles into liquid. Since diffusion transport depends on the surface size, bubbles smaller than the intersection  $M$  of the two curves exhibit more intensive total transport across their boundaries.

Assuming also the ability to make the resultant ensemble of small bubbles isometric—i.e. with all the bubbles of the same diameter  $d_{sm}$ .

$$d_{sm} = \sqrt[3]{\frac{6V}{\pi n}} \quad (8.3)$$

then equating  $V$  in Eqs. (8.2) and (8.3) results in the relation between the number  $n$  of small bubbles and their size

$$\frac{d_{sm}}{d} = \sqrt[3]{\frac{1}{n}} \quad (8.4)$$

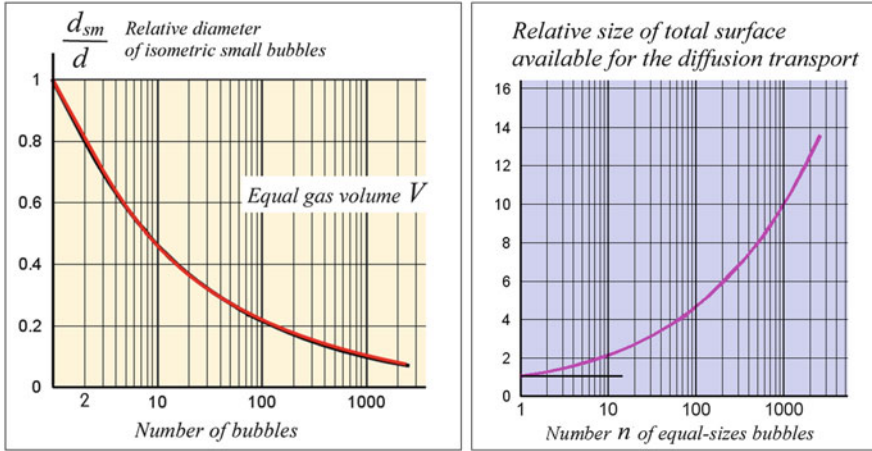


**Fig. 8.4** Dependence of the relative size (*left*) and relative total surface (*right*) of isometric (equal diameter) bubbles on their number  $n$ , when they are all produced from the same given gas volume. Note the semi-logarithmic character of this presentation

Using the expression Eq. (8.1) for the surface area  $F$  converts the diagram shown in Fig. 8.4-left, into the dependence of the total surface on the number  $n$  of resultant small (isometric) bubbles. This is presented in Fig. 8.4-right.

It shows that division of a single large bubble into, e.g.,  $n \sim 1000$  microbubbles increases the total transport area 10-times. No doubt this is a welcome improvement. In addition, as discussed in the next Sect. 8.1.3, a significant increase in the total diffusion transport is also obtained due to the fact that smaller bubbles move slowly. This increases the time during which the bubbles are available for the transport across their boundaries.

On the other hand, the beneficial effect of small bubbles is not obtained at no cost. Distribution of the gas volume into small bubbles is associated with increase of total surface energy. This energy must be supplied from an external source. Fortunately, in contrast to earlier approaches, fluidic oscillators—the main subject discussed here—can deliver this energy with remarkable effectiveness.

### 8.1.3 Another Reason: Velocity

Because the specific volume of the gas inside the bubbles is much larger—roughly by three decimal orders of magnitude—than that of the surrounding liquid, bubbles tend to move upwards in the gravitational field of the Earth. If the available height is sufficient, they finally reach a constant rising speed, the terminal velocity. It is determined by difference between Archimedes' lift and steady-flow hydrodynamic resistance. For small bubbles the resistance is nearly the same as if it were a motion

of a solid body, governed by the Stokes law. There are actually influences of various secondary effects, mainly varying somewhat the conditions on the surface. They are discussed in numerous publications—e.g. references [54, 55] identify, besides the obvious and expected influence of Reynolds number, also the influences of other non-dimensional criterial parameters like the Weber, Eötvös, Morton, and Tadaki numbers. The velocity thus slightly depends, e.g., on chemical composition and purity of the liquid. For the present purpose of discussing microbubbles and their role in generation of biofuels, these effects may be practically neglected. An idea of the magnitudes of terminal velocities may be gained from the data in Fig. 8.5. It is a collection of experimental values from references [8, 17, 23, 24, 34, 55]. There are two important facts.

The first is the general trend of the velocity decreasing significantly with decreasing bubble or microbubble diameter  $d$ . The smaller are the bubbles, the more they are available for the gas transport. In the microbubble range  $d < 1$  mm the terminal rising velocity is more or less exactly proportional to the second power of the bubble diameter. This is in agreement with the Stokes law.

The other fact is the evident change in the character of the motion at the microbubble size upper limit  $d = 1$  mm. This limit was introduced as a more or

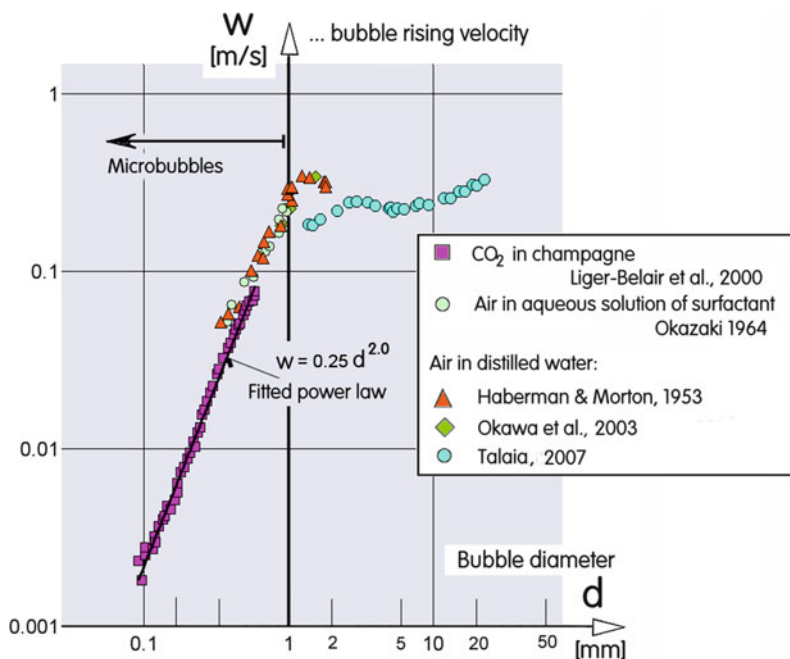


**Fig. 8.5** Measured terminal rising velocity of gas bubble in a liquid in dependence on its diameter  $d$ . There is some dependence on chemical compositions, but it is rather weak and may be neglected in this discussion. Much more important is the change of the character at the microbubble limit boundary at  $d \sim 1$  mm

less simple and convenient value, nevertheless the remarkable change at this limit is apparent. It is one of the examples of the general fact that microbubbles do not behave in the qualitatively same manner as larger bubbles. Other examples of similar analogous behaviour change are more complicated. As an example may be named the change in evaporation dynamics [61]. The transitions in Fig. 8.5 at  $d = 1$  mm of the overall character of the flowfield past slowly moving objects is due to formation of the wake vortices as well as the shear-stress deformation of the bubble shape. The behaviour is governed by the magnitude of Reynolds number

$$Re = \frac{wd}{\nu} \tag{8.5}$$

—where  $w$  (m/s) is the velocity and  $\nu$  ( $m^2/s$ ) is (kinematic) viscosity of the liquid. Presented in the next Fig. 8.6 is the Reynolds number dependence on microbubble size (sub-millimetre diameter in stationary regime) for the case of main interest, the transport of carbon dioxide into water. Evident is the extremely rapid  $Re$  values decrease, especially below  $d = 0.2$  mm, i.e. in the viscosity-dominated creeping flows.

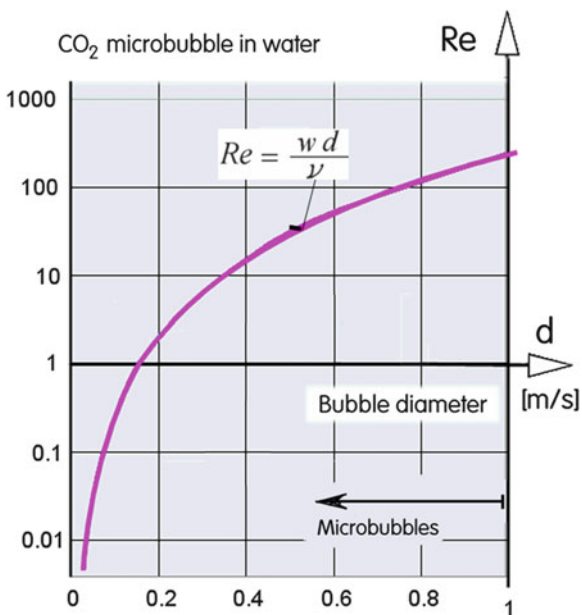


**Fig. 8.6** Reynolds numbers of steady upwards motion of microbubbles decrease substantially with decreasing bubble size  $d$ . The flowfield at small  $Re$  is of creeping-motion character, dominated by viscous effects

### 8.1.4 Surface Tension

Character as well as size of gas bubbles in a liquid are significantly influenced by the phenomena taking place on the boundary between the gas and liquid—i.e. on the surface of each bubble. There seems to be an extremely thin layer, behaving as if it were made of additional elastic material spread on the surface. This apparent elasticity causes a tendency of the bubble to assume minimum surface area. In reality there is no such foreign material. Observed effects are a consequence of missing molecular cohesion forces on the gas side of the boundary, cf. Figs. 8.7 and 8.8.

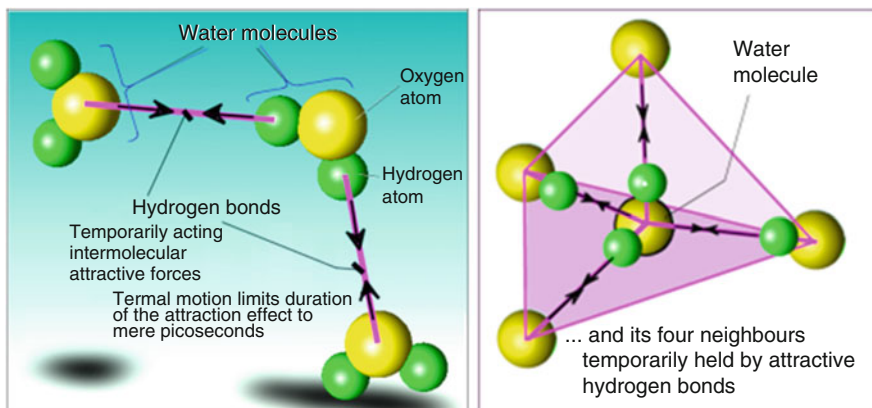


**Fig. 8.7** *Left:* Non-uniform distributions of electric charge on water molecule generates temporary cohesion forces between the residual charge in oxygen atom of a molecule and hydrogen atoms in its neighbour. *Right:* Molecule of water can attract four neighbours

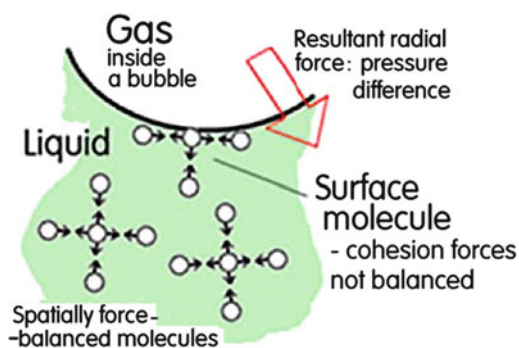


**Fig. 8.8** Shape of bubbles is determined by uncompensated forces on molecules at the interface. Inside the liquid are intermolecular cohesion forces balanced but on the boundary the balancing cohesion force on the gas side is missing



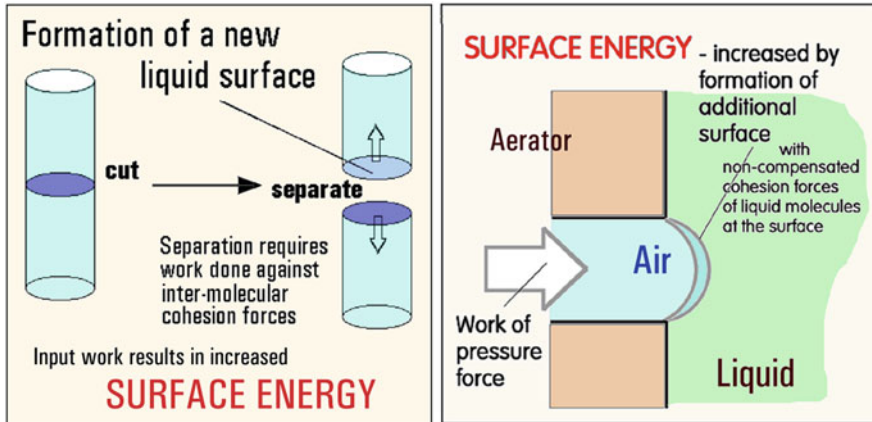
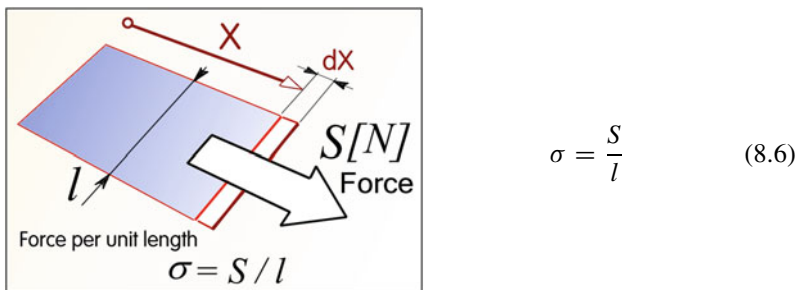


**Fig. 8.9** What seems to behave as an elastic layer at the surface of a liquid is particularly apparent if a new surface is formed e.g. by cutting the liquid-filled volume into two halves. The work done and converted into the surface energy in creation of new gas/liquid interface is a particularly important factor in generating bubble at the exit from an aerator

This missing force effect is found whenever a new liquid surface is formed, Fig. 8.9-left. The case in this illustration, i.e. making a new surface by cutting a liquid column, is easy to understand but in practice rarely encountered. It should be considered, however, that in principle the same creation of additional new liquid surface takes place at the initial formation stage of generated bubble, as shown schematically in Fig. 8.9-right.

For setting up a mathematical model and it is useful to introduce the idea of surface tension  $\sigma$  (N/m),—defined as the force  $S$  (N) acting on the unit transversal length  $l$  (m) of the surface.



Here is this definition of surface tension  $\sigma$  (N/m) that characterises physical properties of the liquid and gas demonstrated on a model of constant-width strip elongated by action of force  $S$ . Magnitude of  $S$  is proportional to the strip width  $l$ . The surface energy increases with the product of  $S$  and the traveled distance  $dx$ .

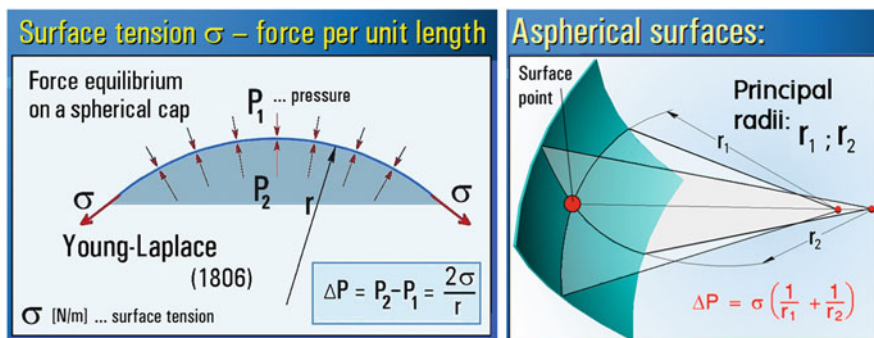


**Fig. 8.10** Basic law of surface tension, formulated independently by Young and Laplace in 1806. The pressure difference between both sides of an interface is inversely proportional to the interface curvature radius  $r$ . Surface of a bubble exposed to a force field (e.g. due to gravity) is not spherical. The Young-Laplace law has to be in that case re-arranged in terms of principal radii

This idea is particularly useful for interpretation of the basic Young and Laplace law

$$\Delta P = P_1 - P_2 = \frac{2\sigma}{r} \tag{8.7}$$

defining the pressure difference between both sides of a spherical surface cap segment dependent on the surface tension  $\sigma$  and curvature radius  $r$  of the spherical surface shown in Fig. 8.10. Since the pressure difference is inversely proportional to the radius, it is obvious that inside microbubbles with small radii the gas is under quite large pressure—which may explain the diffusion transport away from the bubble.

The sphericity condition assumed in Eq. (8.7) is on a free bubble (not in contact with other objects) satisfied only on the top (apex) and antapex (bottom) points. Elsewhere the conditions are more complex and it is there necessary to adapt the Young-Laplace law to the form with two principal radii, as shown in Fig. 8.10-right. This is also the case of surfaces of bubbles exposed to a force field (e.g. due to gravity), having a non-spherical shape, exhibiting at general surface point different principal radii. The Young-Laplace law (8.7) adapted in terms of principal radii to account for this fact is.

$$\Delta P = \sigma \left( \frac{1}{r_1} + \frac{1}{r_2} \right) \tag{8.8}$$

Magnitudes of the surface tension depend predominantly on the chemical composition of the liquid. Values for first-approximation calculations-not including thermal effects-are listed in the diagram in Fig. 8.11 (note the logarithmic vertical scale). More precise calculations have to account apart from temperature dependences also

**Fig. 8.11** Values of the surface tension  $\sigma$  as the proportionality factor in the Young-Laplace law here listed for the case of air bubbles in various liquids

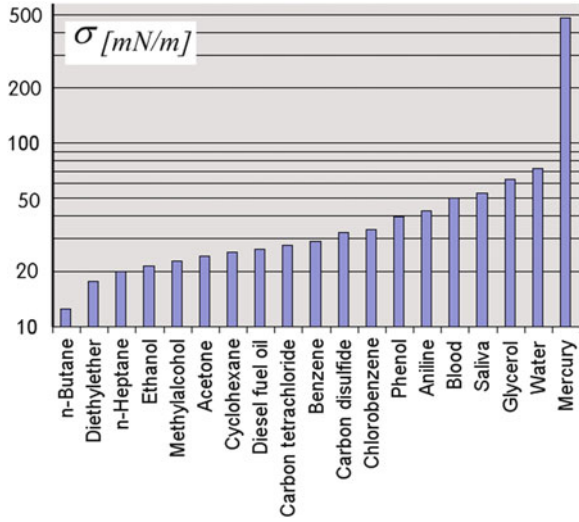
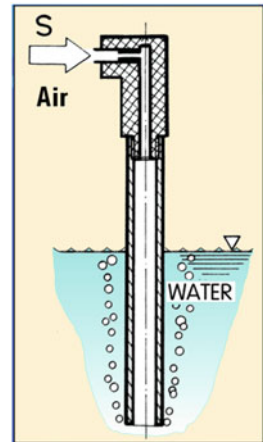


**Fig. 8.12** Traditional method of air input into the liquid. It is simple and inexpensive, but generated bubbles are large (typical diameter for air in clean water is  $d \sim 4\text{--}10\text{ mm}$ ). The aeration is also ineffective due to large bubbles moving fast to the surface, providing not enough time for diffusion transport



influence of pressure. For applications in microfluidics were developed devices [36] employing also surface tension dependences e.g. on applied electric field.

### 8.1.5 Bubbles Generated by An Aerator

Bubbles may be generated extremely simply, by inserting an end of gas supplying tube or pipe into the liquid. The drawing Fig. 8.12 presents a solution of a technically higher standard. However, in most applications this approach, without any attempt at limiting the bubble size, would generate too large bubbles, of the order of millimetres. Typically, such simple designs are used, e.g. in waste-water processing.

Actual decomposition of the contaminants is performed by bacteria. The aerobic ones need oxygen from the air bubbles—the waste water containing almost none—but the air transport into the fast moving large bubbles is so ineffective that the bacteria often die. To keep them and letting them doing their job puts so high demands on the electric energy to drive the air compressors that their running costs typically represent the largest percentage of the operating cost of the whole facility.

The inefficiency of the solution from Fig. 8.12 did not escape attention. An improvement in the bubble size has been often sought in making the air exit channels very narrow—in a belief that the bubbles will be correspondingly small. To produce the required total gas throughput, it is necessary to provide a large number of the small channels. They are usually arranged in parallel in a submerged body called aerator, Fig. 8.13. The channels through which the gas is percolated are results of sintering the aerator body from small solid particles. As long as the mechanical stressing due to gas pressure difference across the channels allows it, the aerator is preferably made in the form of a rather thin porous barrier or membrane. Even with a thin sintered barrier, the length of air paths relative to their small transversal dimensions is large. High hydraulic losses in them are inevitable, adding to the generally low overall energetic efficiency.

What may be surprising to a newcomer, the idea of generation of small bubbles by the percolation method is always a failure. In fact, no really better idea occurred even to professionals, as demonstrated by the fact that the percolation-type aerators

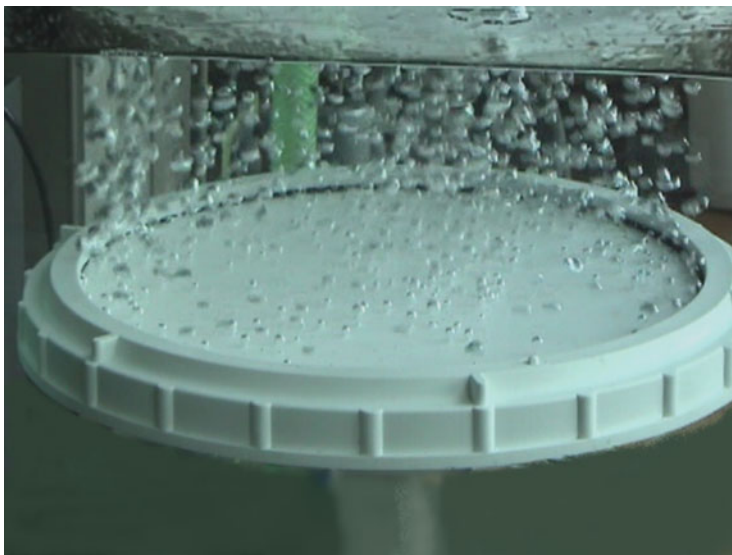


**Fig. 8.13** Photograph of a typical present-day aerator in operation. Despite the equivalent diameter of the exits in this case only 0.12 mm, the produced bubbles are more than an order of magnitude larger. Note that only small minority of pore channels actually produce the bubbles. This is a consequence of instability of parallel bubble formation, Sect. 8.2.3

are still manufactured and supplied commercially in large numbers. Apart from the operational problems caused by the small channels becoming easily clogged, the device does not do what it is expected: the bubbles are not small. Note in the photograph of an example in Fig. 8.13, that only few from the available passages actually do produce the bubbles at their exits.

The typical example of present-day aerator photographed in Fig. 8.13 was found to use for bubble generation only less than 40% of its upper sintered membrane surface. It is immediately apparent that the generated bubbles are much larger than the passages cross sections—the average bubble size in this case was 5.7 mm. This discrepancy is the consequence of a phenomenon called *instability of parallel bubble formation* discussed in the next part of this chapter.

### 8.1.6 Bubble Shapes

When the bubble (and the surrounding liquid) is exposed to an acceleration, it is elongated—or compressed—in the direction of the acting force. Let us investigate the case of stationary bubble in gravitation field, still attached according to Fig. 8.14 to the exit from either upwards or downwards directed aerator passage at which it was formed. The two configurations in Fig. 8.14 differ only in the sign of the acting gravitation. Geometry of the problem is shown in Fig. 8.15. The bubble is rotationally symmetric with respect to the vertical axis. Because of the symmetry, position of a typical point  $P$  (coloured red in Fig. 8.15) on the bubble surface is determined by only two Cartesian co-ordinates,  $X_1$  and  $X_2$ . Their origin is located in the apex point. The co-ordinate  $X_1$  is the radial distance from the symmetry axis while  $X_2$  is the vertical distance from the apex. The law governing the bubble shape is Eq. (8.8) and to use it, it is necessary to evaluate the magnitudes if the two

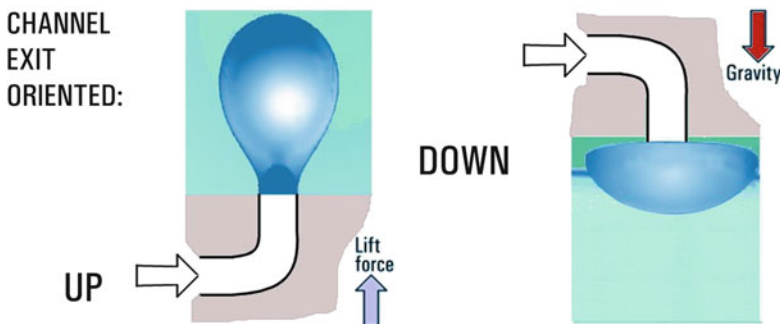
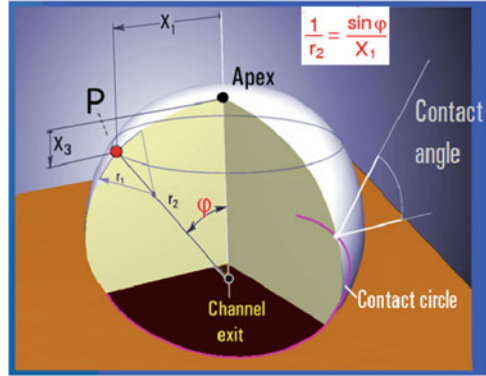


**Fig. 8.14** Shapes of gas bubbles are influenced by hydrostatic lift force. In the case of vertical orientation of the exit channel (either up or down) the shape is axisymmetric and computation of its contour simplifies to solution of ordinary differential equations

**Fig. 8.15** Bubble sessile at the exit of aerator channel at which it was generated (with one quarter removed for access to the co-ordinates and curvature radii). Investigation of the bubble shape starts from the simple conditions ( $r_1 = r_2$ ) prevailing in the apex point



principal radii  $r_1$  and  $r_2$ . It should be noted that they are equal only in the apex point, where they are

$$r_1 = r_2 = r_A \quad (8.9)$$

To determine  $r_2$ , it is useful to use spherical coordinates, radius  $r_2$  and angle  $\varphi$ , where

$$X_1 = r_2 \sin \varphi \quad (8.10)$$

so that Eq. (8.8) becomes

$$\Delta P = \sigma \left( \frac{1}{r_1} + \frac{\sin \varphi}{X_1} \right) \quad (8.11)$$

The pressure difference  $\Delta P$  consists of two parts. The first one is the value  $\Delta P_{apex}$  in the apex, Eq. (8.7)

$$\Delta P_{apex} = \frac{2\sigma}{r_A} \quad (8.12)$$

and the second one is the difference in hydrostatic pressures increasing with the depth below the apex. Hydrostatic pressures are evaluated as

$$\Delta P_{hydro} = \frac{gh}{v} \quad (8.13)$$

where  $g = 9.81 \text{ m/s}^2$  is the gravitational acceleration,  $h$  (m) is the depth, in the present case  $h = X_2$  and  $v$  ( $\text{m}^3/\text{kg}$ ) is the specific volume of the liquid. In Eq. (8.4) there is the difference between the hydrostatic increase on both liquid and gas sides.

Of course, on the gas side it is practically negligible, but it is included into the equation so easily that it may be left. Thus the governing Eq. (8.11) is re-written as

$$\Delta P = \sigma \left( \frac{1}{r_1} + \frac{\sin \varphi}{X_1} \right) = \frac{2\sigma}{r_A} + \left( \frac{g}{v_w} - \frac{g}{v_o} \right) X_2 \quad (8.14)$$

—where  $v_w$  is the specific volume of the liquid (water) and  $v_o$  is the specific volume of the gas. The result may be converted into two first-order ordinary differential equations

$$\frac{dX_1}{d\varphi} = \frac{\sigma X_1 \cos \varphi}{-\sigma \sin \varphi + (g/v_w - g/v_o) + \Delta P_{apex} X_1} \quad (8.15)$$

$$\frac{dX_1}{d\varphi} = \frac{\sigma X_1 \sin \varphi}{-\sigma \sin \varphi + (g/v_w - g/v_o) + \Delta P_{apex} X_1} \quad (8.16)$$

These equations are non-linear and their analytic solution is not known. They may be solved numerically for any particular combination of the parameters, but this does not provide an overall universal picture of the solutions. It is useful, for obtaining some degree of universality, to convert them into introduced dimensionless variables. The key factor is the capillary length scale

$$l_{cap} = \sqrt{\frac{\sigma}{g/v_w - g/v_o}} \quad (8.17)$$

The other is the pressure parameter

$$p = \frac{\Delta P_{apex}}{(g/v_w - g/v_o) l_{cap}} \quad (8.18)$$

This means the apex pressure difference related to difference of hydrostatic pressure values at the depth  $l_{cap}$ . The Cartesian co-ordinates of the bubble surface are thus converted into non-dimensional

$$x = X_1/l_{cap} \quad (8.19)$$

$$y = X_2/l_{cap} \quad (8.20)$$

In these co-ordinates, the surface shape equations to be solved are

$$\frac{dx}{d\varphi} = \frac{x \cos \varphi}{xy + xp - \sin \varphi} \quad (8.21)$$

$$\frac{dy}{d\varphi} = \frac{x \sin \varphi}{xy + xp - \sin \varphi} \quad (8.22)$$

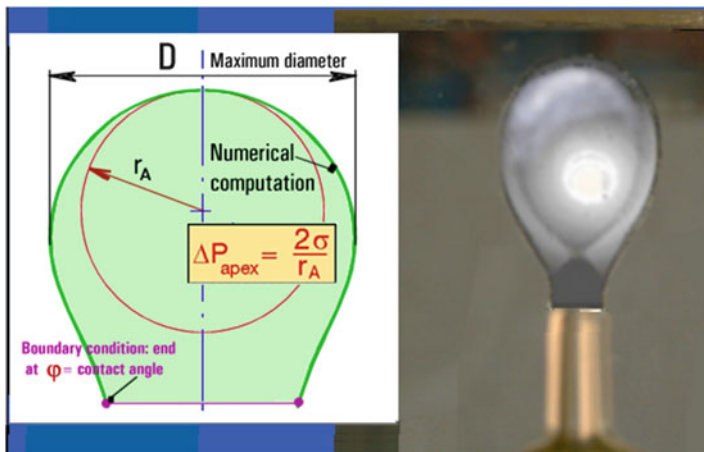


**Fig. 8.16** Numerical solution of Eqs. (8.21) and (8.22) in the “sessile” bubble case. Solution starts in the apex point on top and progresses down with gradually increasing principal radius  $r_2$ . Of interest is the largest diameter  $D$ , found in the location where the radial distance  $x$  reaches its maximum

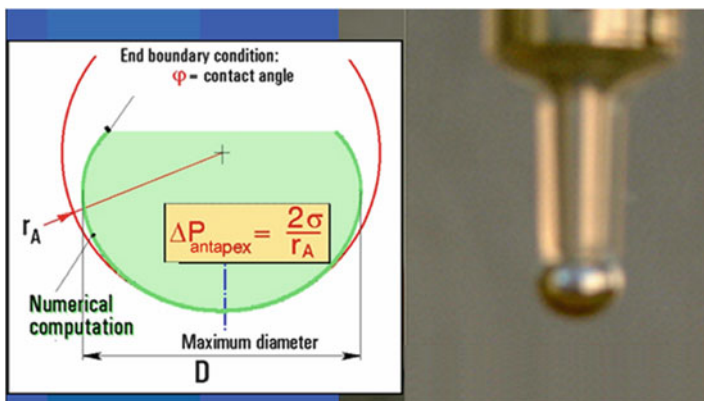


**Fig. 8.17** The numerical solution of the “pendant” case. The solution starts at the antapex and progresses upwards

Author performed numerical solutions (by the Runge-Kutta method) of the pair of simultaneous Eqs. (8.21), (8.22), following the ideas presented in Figs. 8.16 and 8.17. The pictures in this picture pair differs in the orientation of the acting accelerations. They may be called “sessile” (Fig. 8.16) and “pendant” (Fig. 8.17)—the terms which were originally introduced for the two basic orientations of attached liquid drops and do not perfectly fit the character of attached bubble (Figs. 8.18, 8.19, and 8.20).



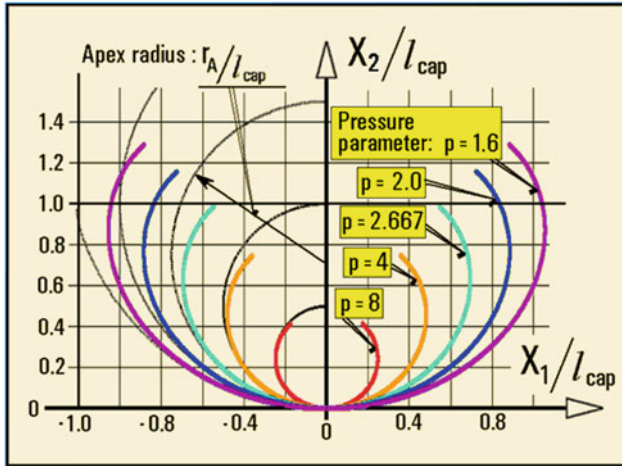


**Fig. 8.18** Computed bubble shapes according to Fig. 8.17. This is a single-parameter family of solutions, each for a certain numerical value of the pressure parameter defined in Eq. (8.18)

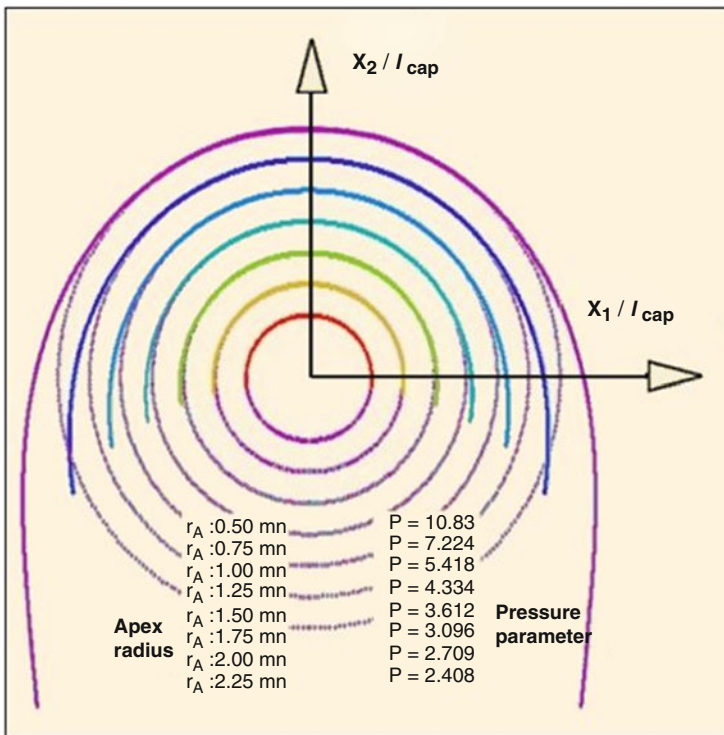


**Fig. 8.19** From the practical point of view more important solutions of the sessile cases, cf. Fig. 8.16

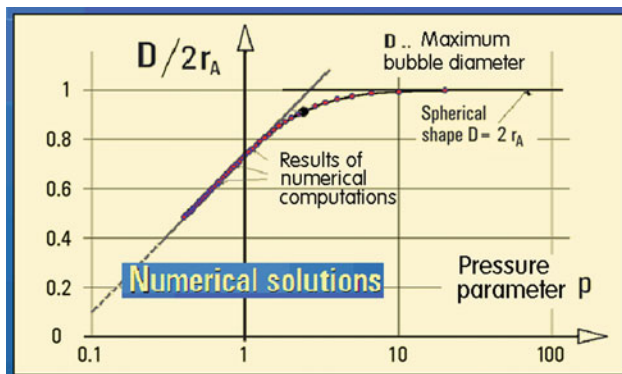


**Fig. 8.20** In this author's series of numerical "sessile" bubble solutions (Figs. 8.16 and 8.19) was evaluated the dependence of the relative magnitude of the diameter  $D$  (cf. Fig. 8.19) on the pressure parameter

### 8.1.7 Shape Oscillation

Problems associated with generation of microbubbles are clearly seen in the typical Fig. 8.13. It is the inefficient use of most passages in the aerator and, more importantly, generation of too large bubbles out of any proportion to the passages cross section. The solution of the problem by oscillating the gas flow into the aerator was discovered by a chance and the mechanism of the improvement was initially not recognised. It benefited from existing previous positive experience with available fluidic oscillator, the properties of which were the crucial factor. Since the oscillator in the original tests was designed for use in a different application, it soon became necessary to design and build a new one.

The starting point in designing any oscillator is the oscillation frequency at which it is going to operate. In the case discussed here, the choice of frequency depends upon the basic idea of what the oscillation actually does with the bubbles. Observations of the rapid decrease of bubble size once the oscillator was switched on has led quite naturally to idea of the oscillator causing fragmentation of the bubbles. It seemed that an initially large bubble was by the acting pulsation decomposed into a group of smaller ones. Such decomposition, of course, would request very high amplitudes of the oscillatory motion. This can be achieved in practice only by pulsating the initial bubble in some higher-mode, using its natural resonant frequency. The oscillation was to be at least in the second mode, i.e. with two alternatively appearing amplitude maxima at the bubble surface (Fig. 8.22). In that case the initial bubble would decompose into two smaller daughter bubbles. Considering the desirable small scale of the microbubbles, it was immediately apparent that the natural frequency is likely to be quite high. A higher bubble oscillation mode, with decomposition into more than only two daughter bubbles,

would be, of course, better—but it was obvious that this would necessitate an even higher frequency. With fluidic oscillators this might be a problem.

It should be emphasised that the shape oscillations discussed here are different from the volume oscillation involving the gas compressibility, which was studied already as long ago as in 1917 by Rayleigh [28]. This oscillation, mainly in association with the cavitation problem of importance in pumps and ship propellers, was since then often studied and the original equation derived by Rayleigh gradually improved by later authors. The present case of shape oscillation is obviously different. The pressure amplitude levels are very much smaller than those necessary for producing a significant compression of the bubble.

To obtain a first-hand information about the much less studied shape oscillation, present author performed an independent study [42]. The oscillation under investigation was transitional, following a sudden formation of a bubble by conjunction of two bubbles in a bubble chain rising from the exit of a single passage, as seen in images presented in Fig. 8.21. Since the bubbles (in this case indeed microbubbles) at the aerator passage exit were very small, they moved upwards rather slowly (cf. Fig. 8.5). It was no problem to adjust conditions so that the follower bubble (generated later) came into conjunction with its predecessor bubble. Such conjunction produced a very strong shape disturbance, from which the resultant bubble recovers in oscillation driven by the released excess surface energy. It finally assumed its spherical shape as seen in the images presented in Fig. 8.21, recorded by a high-speed camera. In the images was chosen a reference point on the bubble, the instantaneous position of which was manually measured in the camera images. In this case the reference was the bottom antapex of the oscillating bubble. Evidently—as seen in Fig. 8.22—the oscillation studied was of the second mode, with two amplitude maxima taking alternatively place at the bubble top and bottom (there were some small sideways motions, but these were neglected as unimportant). Camera provided to each image the precise time which the image was recorded (it is written at the bottom of Fig. 8.21). Plotted instantaneous positions of the reference point as a function of the time instants were fitted by a continuous line. This was fitted with a sixth power polynomial. The result was then differentiated to provide the instantaneous velocity  $w$  of the reference point movements. This recording and evaluation of the vertical velocity was repeated six times under slightly different

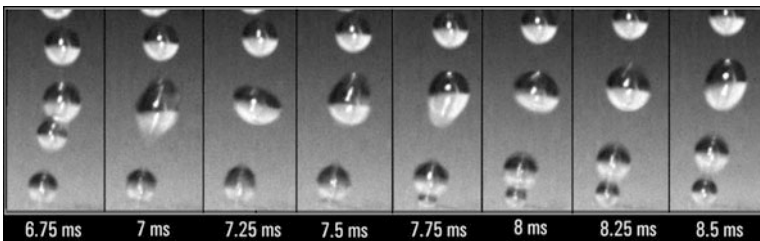


**Fig. 8.21** High-speed camera images of conjunction of two microbubbles (*extreme left*) and subsequent oscillatory motions of the resultant larger microbubble

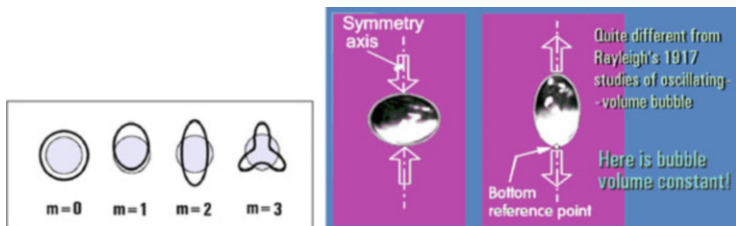


**Fig. 8.22** Bubbles behave in the studied oscillation as if they were elastic incompressible objects. The easiest excitation of constant-volume oscillation is obviously in the lowest axisymmetric mode  $m = 2$ . This (apart from some skewness caused by the generated bubbles slowly moving horizontally) was found in the images of the oscillation in Fig. 8.21

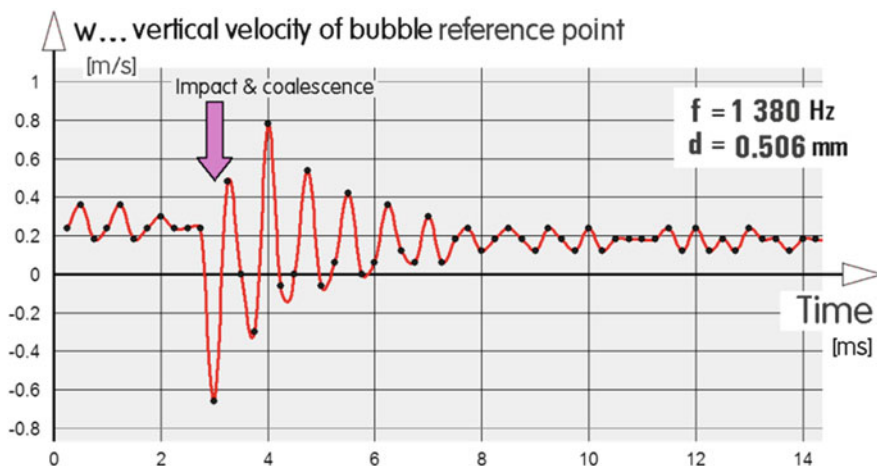


**Fig. 8.23** Oscillatory motions after the conjunction—Typical fit to velocities computed from measured positions of the bottom reference point in data points in images similar to Fig. 8.21

conditions. One of the six velocity diagrams obtained is presented in Fig. 8.23. Even though the oscillation was rather strongly damped—it practically disappears in less than  $10\ \mu\text{s}$  (Fig. 8.23)—in the first approximation it was possible to neglect the damping. Thus the governing equation of the oscillatory movements could be written, as shown in Fig. 8.24, with only two terms. It was the inertial term, with inertance  $J$ , and the accumulation term, with capacitance  $C$ . Natural frequency of such oscillation is

$$f = \frac{1}{\sqrt{JC}} \tag{8.23}$$

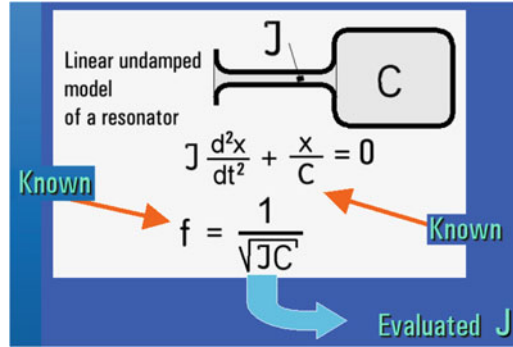


**Fig. 8.24** Fluidic model of undamped oscillating bubble. Capacitance  $C$  may be evaluated from surface energy variations of measured bubble deformation, Fig. 8.25. The frequency  $f$  is measured in a diagram similar to Fig. 8.23. Thus the only not directly measurable quantity was the inertia  $J$  representing inertia of the liquid

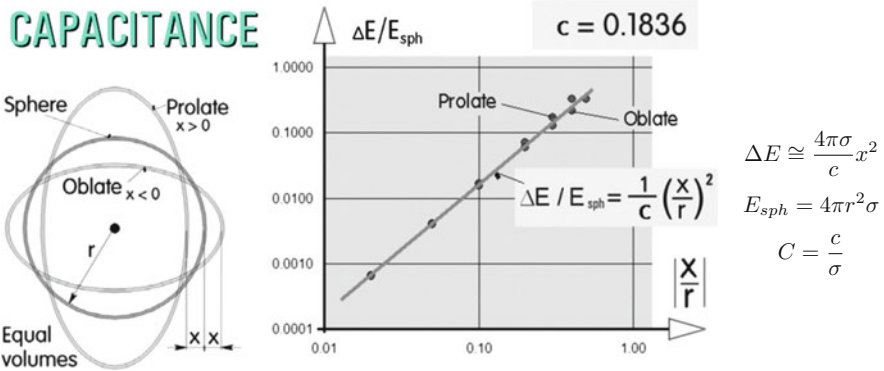


**Fig. 8.25** Capacitance of the bubble oscillating as an elastic body between the oblate and prolate ellipsoid shape was evaluated by computed surface area directly proportional to surface energy (the excess of which the bubble tends to minimise)

From these two known variables ( $f$  and  $C$ ) in Eq. (8.23) it was possible to determine the missing quantity  $J$  (Figs. 8.25 and 8.26).

### 8.1.8 Oscillation Frequency

Dynamics of fluid mechanical processes involving a boundary between gas and liquid is characterised by Weber number  $We$ , a dimensionless parameter

$$We = \frac{w^2 d}{2\nu\sigma} \tag{8.24}$$

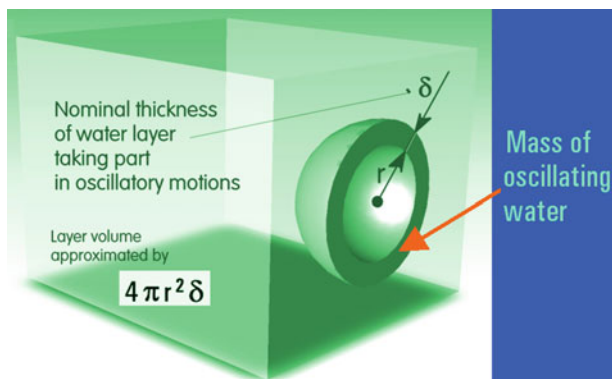


**Fig. 8.26** Inertance evaluated as the missing parameter of the model in Fig. 8.23 made possible estimating how thick boundary layer of liquid is associated with the motion of an oscillating bubble

introduced in 1919 [54]. It is apparent in Eq. (8.24) that  $We$  is defined as a ratio of specific kinetic energy  $w^2/2$  of the fluid flow and specific surface energy, which is the ratio of bubble surface energy Eq. (8.42) and  $\pi d^3/V$ , the mass of the liquid volume occupied by the bubble.

While  $We$  was introduced and has been used earlier for steady bubbles, in analysis of the bubble oscillation, discussed here, this author has introduced a closely related parameter for oscillatory processes at frequency  $f$ . For the oscillating bubbles of diameter  $d$  this parameter is

$$We_o = \frac{f^2 d^3}{2\nu\sigma} \quad (8.25)$$

Available numerical data obtained in the analysis of the six shape oscillation experiments were inserted into the definition Eq. (8.25), with the result presented in Fig. 8.27. Evidently, the bubble oscillation is characterised by a constant  $We_o$  value, in these experiments the average

$$We_o = 1.27 \quad (8.26)$$

The corresponding frequency is plotted in the next diagram, Fig. 8.28. The most important conclusion obtained is the fluidic oscillator for excitation of the lowest  $m = 2$  mode for generation of microbubbles by fragmentation microbubbles has to oscillate at a frequency of the order of kilohertz. This is a demanding requirement, especially if the oscillator is requested to generate considerable output power—and hence it has to be not very small.

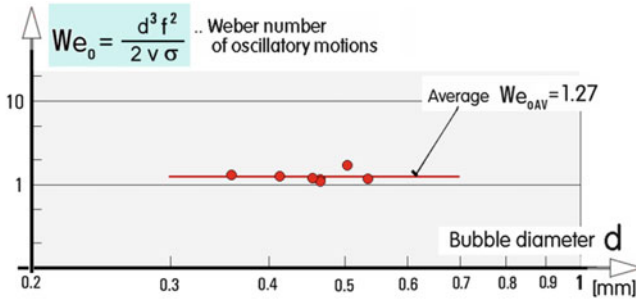


**Fig. 8.27** Author’s measurements of oscillatory Weber number  $We_0$  in high-speed camera images like those in Fig. 8.21. The values are nearly constant, which justifies evaluating their average value

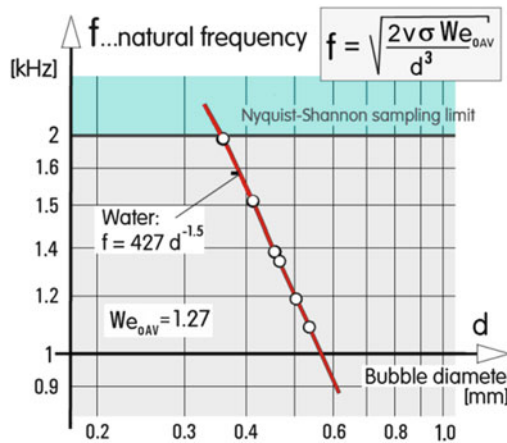


**Fig. 8.28** Natural frequency of photographed microbubbles as a function of their diameter  $d$ , using the average result in Fig. 8.27. The frequencies are above 1 kHz, very high for generation by typical standard fluidic oscillators

## 8.2 Problems and Solutions

### 8.2.1 Gas Diffusion from the Bubble

Most gases can in a significant measure dissolve in liquids. Aquatic animals, after all, are known to depend on the oxygen dissolved in water. The case of main interest here is carbon dioxide which, in addition to its dissolution, reacts with water and forms carbonic acid. In most engineering processes working with bubbles the aim is to transport the gas into the liquid.

Exact solutions of the problem of diffusion transport from a bubble moving in the liquid are very difficult. It may be, however, useful to apply a simplified approximate analysis to obtain some knowledge of magnitudes of parameters and variables.

Let us assume small bubble of surface  $F$  ( $\text{m}^2$ ), across which the gas molecules propagate away. The law governing this spatial transport is one of two expressions derived by Fick in 1855 [6]. One is the law which governs the time dependences and may be neglected in the present discussion which assumes quasi-steady regime—since the diffusion transport from a bubble is a quite slow process. It is the other law, on spatial distributions, which is here applied. Its basic idea is dependence of the intensity of the transport of an  $i$ th component in a multi-component mixture on the local spatial gradient of its concentration. The concentrations considered here are

$$m_i = M_i/M \quad (8.27)$$

where  $M_i$  (kg) is the mass of the investigated gas, the specific volume of which is  $v_i$  ( $\text{m}^3/\text{kg}$ ), while the total mass of the mixture in the same volume is  $M$  (kg).

Let us consider a spherical bubble of diameter  $d$  (m) and surface area  $F$  ( $\text{m}^2$ ) It moves in the direction of axis  $X$ . It is a creeping motion, so slow that it is acceptable to neglect the resultant deformation of the concentration field. Thus the problem may be reduced to a one-dimensional one—with all variables varying only along the axis  $X$ , measured from the bubble surface. Inside this bubble the concentration of the studied  $i$ th gas is  $m_{ib}$ . The bubble exists in liquid in which the concentration of this gas (at sufficiently large distance from any bubbles) is lower,  $m_{ie}$ . Due to the general tendency toward the same concentration everywhere, molecules of the  $i$ th component gas diffuse and move away. Thus results in the concentration field with most changes taking place in the rather thin boundary layer (Fig. 8.30) surrounding the bubble surface.

Total intensity of the transport is evaluated as the mass flow rate  $\dot{M}_i$  (kg/s) of the  $i$ th gas from the bubble. It is also acceptable to use for this purpose the volume flow rate  $\dot{V}_i$  ( $\text{m}^3/\text{s}$ ),

$$\dot{V}_i = \dot{M}_i v_i \quad (8.28)$$

In the approximation here applied, variations of the specific volume may be neglected, so that the two approaches differ only by a multiplication constant. With the one-dimensionality assumption also the intensity of transport is the same over the whole surface area  $F$  ( $\text{m}^2$ ).

The Fick's law of transport intensity dependence on the local spatial concentration gradient  $\frac{dm_i}{dX}$  assumes the simplest, linear dependence, so that it may be written as

$$V_i \sim - \frac{dm_i}{dX} F \quad (8.29)$$

The negative sign is there to remind the fact that the diffusion transports the gas towards the region with lower concentration, attempting to equalise the concentration  $m_i$  everywhere. Of course, the intensity of the transport also depends



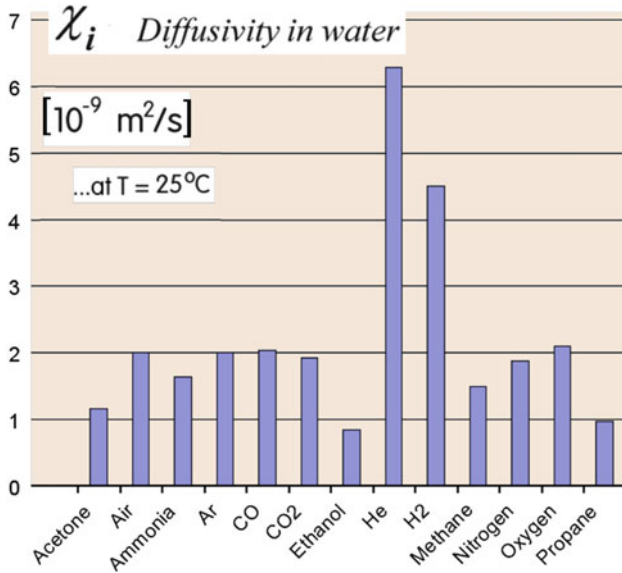


**Fig. 8.29** Diffusivity  $\chi$  was introduced as the factor characterising influence of fluid chemical composition in diffusion problems

on the properties of the gas. This, is expressed by introducing a multiplicative constant, at any rate necessary for proper units of the quantities. The constant in the proportionality is diffusivity  $\chi$  ( $\text{m}^2/\text{s}$ ).

There is practically no way how to find value of this quantity other than by performing experiments with various gases and liquids. In real situations the introduction of diffusivity is used to cover various other effects nor expressed in the transport intensity equation—and as a result  $\chi$  may be not a simple constant. Nevertheless in the discussed problem of slow laminar flow past the moving bubble the assumption of its invariance is acceptable. Diagram in Fig. 8.29 presents a number of values for diffusion of fluids (mainly gases) into water.

The complete expression for the Fick’s law is thus

$$M_i = - \frac{dm_i}{dX} \frac{\chi_i}{v_i} F \tag{8.30}$$

It may be useful in problems of convective transport to compare the mass diffusivity  $\chi$  with the viscosity  $\nu$  ( $\text{m}^2/\text{s}$ ), which has the same role in momentum transport in the liquid—both have the same dimensions. Their ratio

$$Sc = \frac{\chi_i}{\nu} \tag{8.31}$$

—is called Schmidt number [30].

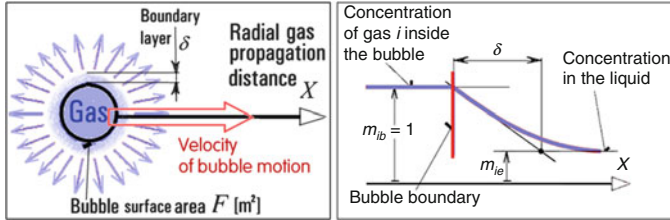


**Fig. 8.30** Assumption of one-dimensional distribution of the gas concentration outside the bubble surface

A simplified version of the transport equation (8.30) is based on the idea of thickness  $\delta$  of the boundary layer (Fig. 8.30) and the corresponding effective mean gradient  $(m_{ib} - m_{ie})/\delta$ .

The aim of most investigations of diffusion problems is determining the mass transport rate Eq. (8.30). Especially in experimental determination the basic complication is unknown spatial distribution of the concentration. This is circumvented by working with the mean gradient above:

$$M_i \sim - \frac{m_{ib} - m_{ie}}{\delta} \frac{\chi_i}{v_i} F \quad (8.32)$$

Again, the proportionality (8.32) becomes equation by introducing the mass transport factor  $\alpha_m$  (m/s)

$$M_i = (m_{ie} - m_{ib}) \frac{\alpha_m}{v_i} F \quad (8.33)$$

and for the spherical boundary, [Eq. (8.1)],

$$M_i = (m_{ie} - m_{ib}) \frac{\alpha_m}{v_i} \pi d^2 \quad (8.34)$$

It is useful to transform the factor  $\alpha_m$  into non-dimensional Sherwood number  $Sw$  [32]

$$Sw = \frac{\alpha_m d}{\chi_i} \quad (8.35)$$

It may be interesting to view the physical meaning of  $\alpha_m$  from comparison of Eqs. (8.30) and (8.33):

$$\alpha_m = \frac{\chi_i}{\delta} \quad (8.36)$$

—so that the inverse of Sherwood number in Eq. (8.35) expresses the effective thickness of the boundary layer related to the diameter  $d$  of the bubble

$$\frac{1}{S_w} = \frac{\delta}{d} \tag{8.37}$$

The solution of the transport problems concentrates on determination of  $\alpha_m$ — usually sought in its dimensionless form Eq. (8.35). Other variables in Eq. (8.35) are usually known, so that the diffusion mass flow rate  $\dot{M}_i$  from the bubble is determined by evaluating  $S_w$ . The influence of the liquid flow on  $S_w$  is characterised by the magnitude of Reynolds number  $Re$ , Eq. (8.5). According to recent investigators, e.g. Aissa et al. [1], it is now accepted that the diffusion from moving bubbles is described, with accuracy sufficient for engineering purposes, by the Ranz–Marshall [27] correlation

$$S_w = 2 + 0.6Re^{1/2}Sc^{1/3} \tag{8.38}$$

Some consequences of Eq. (8.38), computed using the known microbubble rising velocity above in Fig. 8.5, are presented in Figs. 8.31 and 8.32 as the dependence on the microbubble diameter of the diffusion transport factor  $\alpha_m$  and of the Sherwood number.

**Fig. 8.31** Magnitudes of the gas diffusion transport factor  $\alpha_m$  depend very strongly (note the logarithmic scale) on the bubble size

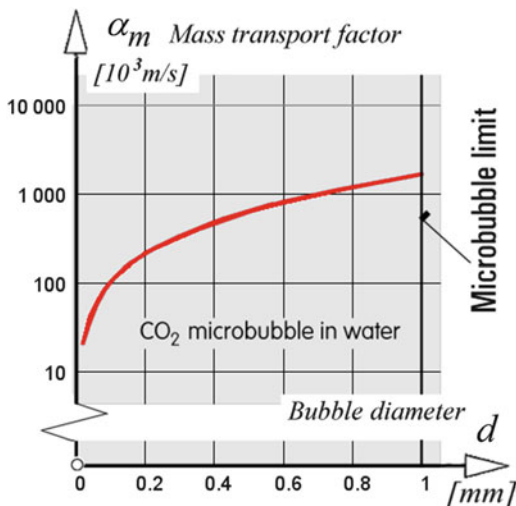
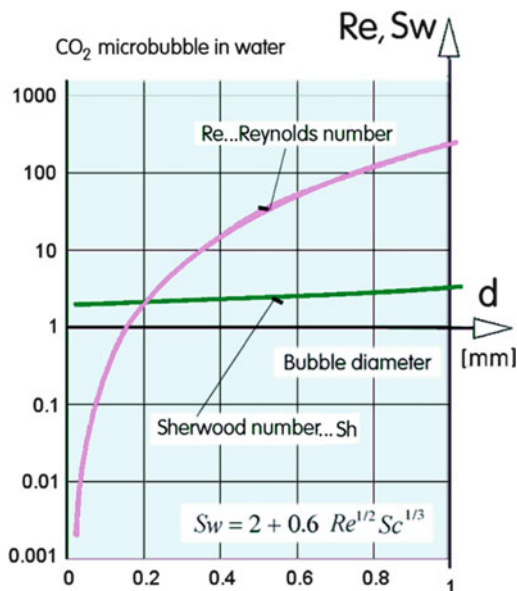


**Fig. 8.32** Reynolds and Sherwood numbers of the derived approximate solution of the diffusion problem for very slowly rising  $CO_2$  microbubble in water



### 8.2.2 Surface Energy

Why it is difficult to generate very small bubbles? And also, why the small bubbles, when we finally manage to produce them, tend to coalesce into a single large bubble? One of the reasons is very fundamental. It is a consequence of general trend of processes in Nature towards the lowest accessible energetic potential.

Derivation of the energy stored in the bubble during its formation begins by considering the definition of the surface tension  $\sigma$  (N/m), in Eq. (8.6). Shown there is an element of the bubble surface in the form of a strip of constant width  $l$ . The strip is elongated by the force  $S$  that moves in the direction  $X$  perpendicular to  $l$ . The magnitude of the force is  $S = \sigma l$ . In the course of the movement by the distance increment  $dX$ , the force does an infinitesimal work—which is equal to infinitesimal increase of the stored energy  $dE$ . It is evaluated as the product of the force and distance

$$dE = S dX = \sigma l dX \tag{8.39}$$

while the increase of the surface area is

$$F = l dX \tag{8.40}$$

so that

$$dE = \sigma dF \tag{8.41}$$

**Another point of view: energy**

$\sigma$  [N/m] = [J/m<sup>2</sup>]

... surface tension = energy per surface unit

A bubble of radius  $r$   
has surface  $F = 4\pi r^2$   
- and surface energy  $E = 4\pi r^2 \sigma$

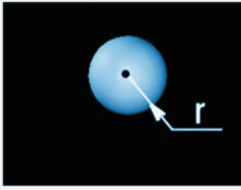


**Fig. 8.33** Alternative interpretation of the meaning of the surface tension  $\sigma$  (N/m) that may be useful for solution of some problems. It may be thought of as the local value of the surface energy per unit area. Here the surface energy is evaluated for the simple case of perfectly spherical bubble

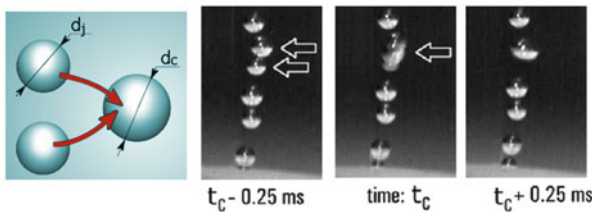


**Fig. 8.34** *Left:* Conjunction of two gas bubbles of the same diameter  $d_j$  into a single larger bubble of diameter  $d_c$  is due to the decrease of resultant total surface energy—and the fact that all processes in Nature tend to reach the energetic minimum. *Right:* An example of conjunction in a chain of rising microbubbles. Note the very short time difference between images. The energy released during the conjunction is dissipated by damped high-speed oscillation (Fig. 8.23)

—evidently, the surface tension  $\sigma$  has now another physical interpretation. It is  $\sigma = dE/dF$  (J/m<sup>2</sup>) energy of cohesion of surface molecules per unit of bubble surface. Because of the almost complete spherical symmetry of microbubbles, magnitude of  $\sigma$  on their surface is everywhere the same, so that the result of integrating Eq. (8.41) over the whole liquid/gas interface is simply (Fig. 8.33)

$$E = \sigma F = \pi d^2 \sigma \tag{8.42}$$

Let us now consider the conjunction of two bubbles as they are presented in Fig. 8.34-left, both of the same diameter  $d_j$  in a bubble chain, rising to the liquid surface above from the exit of aerator passage. Images taken by high-speed camera before, during, and after the actual conjunction of two neighbour microbubbles in the chain are presented in Fig. 8.34. It explains how the used high intensity LED source illuminated the bubbles from above so that their “spherical lens” shapes focused the light onto the bottom parts of microbubbles. The indicated time in Fig. 8.34 at which the images were taken show how fast is the conjunction process. It starts and is finished in mere fractions of a millisecond.

Prior to their merger, the combined surface of the two pre-conjunction bubbles was

$$F_{total} = 2\pi d_j^2 \quad (8.43)$$

so that their total surface energy  $E_{total}$  considering Eq. (8.42) was

$$E_{total} = 2\pi d_j^2 \sigma \quad (8.44)$$

Volume of each of the bubbles assuming spherical shape was Eq. (8.2)

$$V = \frac{\pi}{6} d_j^3 \quad (8.45)$$

The resultant large bubble after the conjunction is of diameter  $d_c$  and volume

$$V_c = \frac{\pi}{3} d_j^3 = \frac{\pi}{6} d_c^3 \quad (8.46)$$

and hence surface area

$$F_c = \pi d_c^2 = 2^{2/3} \pi d_j^2 \quad (8.47)$$

This is smaller than the original  $F_{total}$

$$F_c = 2^{-1/3} F_{total} = 0.794 F_{total} \quad (8.48)$$

In the same proportion is decreased the surface energy. The difference between Eqs. (8.43) and (8.47),—the energy released in the conjunction process, is

$$\Delta E = (2 - 2^{2/3}) \pi d_j^2 \sigma \quad (8.49)$$

—which is dissipated by the oscillation inside the much larger volume of the stationary liquid surrounding the resultant bubble (of course, the bubble oscillates as well, but the energy of its motion is very much smaller).

This negative energetic balance of the conjunction is also reflected in the opposite, energy increase that must be input into each bubble if it is desired to fragment it and make smaller. Since this means an extremely larger number of bubbles—and perhaps smaller in size than obtained by mere halving—this explains many of the difficulties so far met in all attempts at producing microbubbles.

### 8.2.3 *Instability of Parallel Bubble Formation*

Although it has been known for quite a long time that the desirable generation of small bubbles cannot be achieved by making exits from aerator passages more narrow, there are many aerator designers still believing in that approach

and maintaining that the success must be within sight. The failure of these hopes is demonstrated by the example photograph of contemporary commercially available aerator in Fig. 8.13. This does not mean the narrow-passages in aerator are useless—they generate bubbles visibly smaller than what can be expected by simple submerged end of a large-diameter pipe (Fig. 8.12). Nevertheless the steady percolation of air through sub-millimetre passages makes the desired goal of microbubbles inaccessible. Another closely associated problem is the most of the aerator surfaces—typically more than 60%—being visibly inactive, the bubbles being produced by only remaining active aerator exits.

A complicating fact is that there is not only a single cause. Why the bubble generation is unevenly distributed over the aerator outer surface could not be explained by comparing the geometry of the active and inactive passages. What the observations show is the effect of inactivity generally becomes more pronounced if the aerator passages, in an attempt to decrease the hydraulic friction losses in the aerator passages, are made short in the flow direction. The explanation at least of one of the problems is actually simple: this reason is a direct result of the very basic Laplace-Young’s law of surface tension, Fig. 8.10. It is called instability of parallel bubble formation [36].

Presented in Fig. 8.35-left are two stages of bubble (and microbubble) generation. Both show the situation with the gas supplied from below into the formed bubble. The gas flow causes gradual increase in the bubble volume (coloured blue) of the yet “pre-natal” bubble—i.e. a bubble still attached to the aerator passage exit. The left-hand side of the illustration shows an earlier stage, with the interface radius of curvature  $r$  gradually decreasing from the starting situation at which the radius

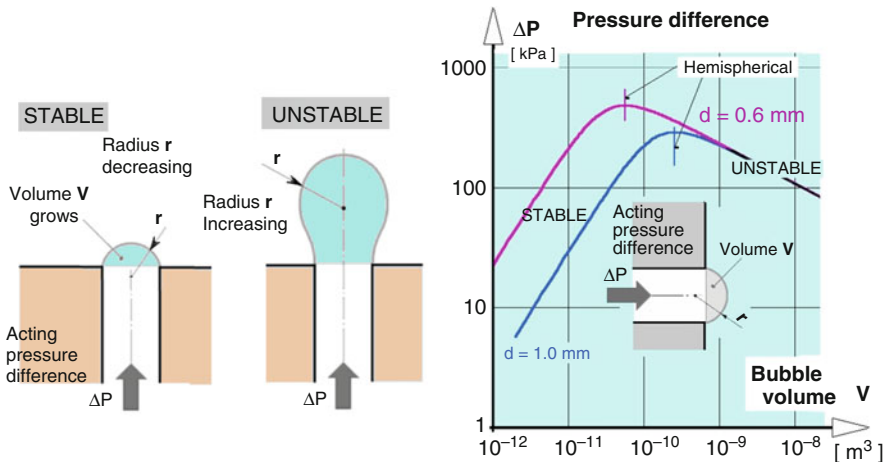


**Fig. 8.35** Bubble formation at an exit from the aerator passage. According to the Young-Laplace law, Fig. 8.10, the pressure difference  $\Delta P$  between the gas inside the exit and the outer liquid makes stable the initial phase of bubble growth. Stability is lost when the bubble surface attains the hemispherical shape  $r = d/2$

is practically infinite. This condition of decreasing radius is short lived while the bubble is still attached to the aerator exit. As shown in the right-hand side of the illustration, representative of a later stage, the still sessile bubble grows with the interface radius of curvature  $r$  increasing.

The limiting situation between the two stages shown in Fig. 8.35, presenting a diagram of pressure difference across the liquid/gas interface as a function of volume of growing bubble. In the initial stages, when the surface curvature radius  $r$  is less than one half of the exit orifice diameter  $d$ , is stable. The increasing gas volume in the bubble meets the increasing opposing pressure. Once, however, the hemispherical limit state is reached, the unstable conditions cause the growing bubble to decrease its internal pressure. Entering gas meets less opposition to its flow. Thus it grows faster, up to the separation condition in which the surface tension on the bubble base ceases to hold in its vertical position the hydrostatic lift inside the bubble.

The differences in behaviour may be now observed in the generation of bubbles in two neighbour parallel orifices—the model shown in Fig. 8.36. As soon as one of the bubbles increases, perhaps by some chance disturbance, beyond the hemispherical shape  $r = d/2$ , its further volume growth is assisted by the continuous decrease in the pressure difference  $\Delta P$  that is to be overcome by the supplied gas (air). Because of the instability, such a bubble grows fast at the expense of the other bubble at the parallel passage, which stops growing or even experiences a opposing pressure force that pushes the generated bubble back, into the passage.

This instability is less effective if the aerodynamic resistance of the passages is high in relation to the Laplace-Young pressure. This resistance makes the conditions nearer to equal, i.e. may even cease to produce the unstable condition. This is the reason why the problem of parallel bubble instability is more pronounced in the case of thin aerator walls (i.e. with short passages). Typical is its presence in those cases where the aerator is formed—in an attempt at decreasing the necessary gas driving power—from metal textile, made by weaving thin wires.

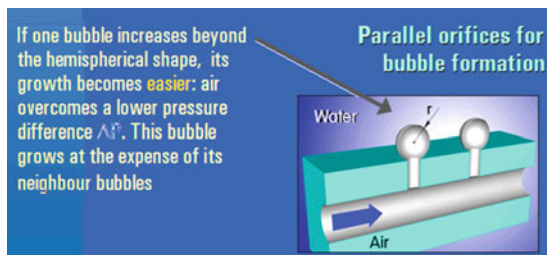


**Fig. 8.36** Formation of two bubbles from the same air flow source in two parallel exits. It is impossible to generate in the two exits bubbles of identical radii  $r$ . As was seen in the photograph Fig. 8.13 of generated bubbles, some channels that started forming the bubble later do not produce any bubble at all—while others generate bubbles out of any proportion to the channel diameter



### 8.2.4 Conjunction of Microbubbles

The instability discussed in the previous section is not the only reason for the observed large size of bubbles—so large to make impossible generating, by aerator percolation, the desirable microbubbles. An interesting bubble growing mechanism acting at the small, microbubble size scale very near to the aerator exits was discovered only recently—and seems to remain unrecognised until the publications of [39]. It is the growth by repeated conjunctions with bubbles formed later in the same aerator passage exit. It escaped attention due to two reasons. First, because it is a high frequency phenomenon impossible to follow by naked eyes. Second, it takes place at very small distances above the exit. Mostly it is seen in camera images at heights above the aerator exits less than  $\sim 0.3$  mm. This very small distance makes the observation and photography very difficult because of the light diffraction on various nearby aerator walls and edges. At the distances  $> 1$  mm, where bubbles are normally accessible for being observed and measured, the effect cannot be seen at all. What is visible there are the quite large bubbles produced at not very high repetition frequency. Only by using a very high speed camera with special optics was discovered the fact that these values are a result of a quite complex process.

The conjunctions are due to the very small rising velocities of microbubbles. They linger near the exit in which they were made and easily come into contact with subsequently produced microbubbles. An example obtained with this camera is presented in Fig. 8.37. It is a diagram of bubble centre height (on vertical axis) dependence on time (on horizontal axis). In this case the final bubbles consist

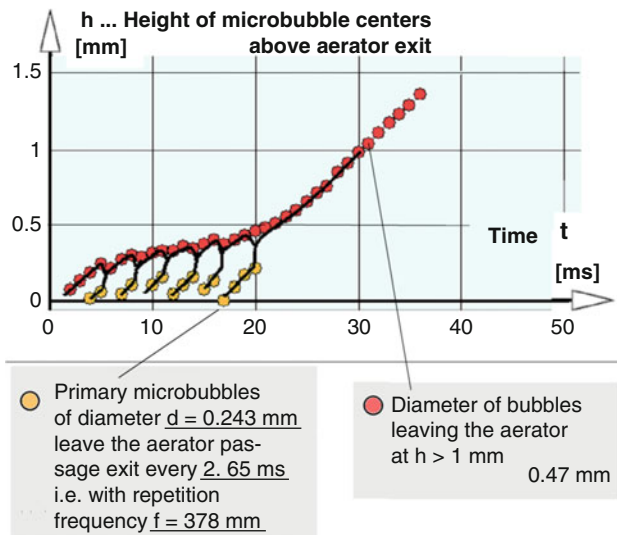


**Fig. 8.37** Height/time history of growth of larger bubbles from microbubbles by conjunction. Note the very small heights  $h$

of seven coalesced primary microbubbles. They were leaving the same particular aerator at the period  $2.65 \mu\text{s}$ . Their diameter was  $d = 0.243 \text{ mm}$ . The microbubbles at this size, as shown in Fig. 8.5, rise so slowly that their vertical distance above the aerator at the appearance of the next bubble from the same exit is comparable with the bubble diameter. As a result of this proximity, the two microbubbles touch and then coalesce, forming a larger bubble. The surface energy released in this conjunction causes the resultant bubble to oscillate—and the oscillation increases the hydrodynamic resistance. This practically stops or slows down the natural upwards motion of the resultant bubble. Its remaining near the exit at the time of appearance of third primary bubble causes another, second conjunction—and later third and other repeated conjunctions.

Another example history of the repetitive conjunctions, again presented by showing the height/time trajectories, is in the next Fig. 8.38. In this case there

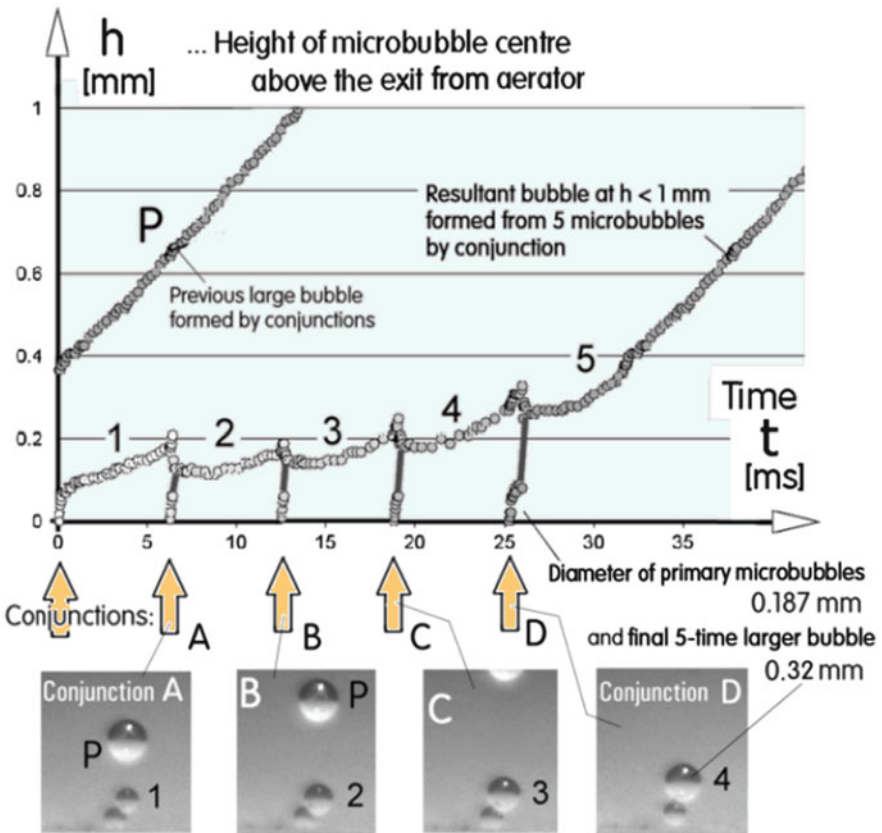


**Fig. 8.38** Details of experimentally investigated repetitive conjunctions, in this case making the final bubble from five primary microbubbles. *Top*: the height vs time trajectories, *bottom*: images of the primary bubbles 1, 2, 3, and 4 prior to the conjunction recorded by high-speed camera

were only five primary microbubbles. The improved lighting (which is usually the limiting factor for high-speed camera recording) made possible better resolution of the positions and speed of motions than was the case above in Fig. 8.37. The primary microbubbles produced at the aerator exit were now of diameter  $d = 0.187$  mm. Apart from the trajectories, in the bottom part of Fig. 8.38 there are also high-speed camera images of the microbubbles, taken at the critical times just before the conjunctions. The primary microbubbles are in this picture numbered from 1 to 5 (the microbubble 1 was one that appeared first while the microbubble 5 was the last one) that finally left the near-exit space and thus finished the cycle. These numbers correspond to the numbered trajectories in the height/time diagram. The four images in the bottom part of Fig. 8.38 are labeled A, B, C, and D and the same letters indicate above, under the diagram, the appearance of additional primary microbubbles in the aerator exit.

- (A) This image was recorded just prior the first conjunction—that of the two primary microbubbles, which are visible in the bottom part of the image. Also seen in the image is the ascending large bubble P which is the result of the previous cycle.
- (B) The same photographed scene as in precious image A was here recorded after elapsed period lasting 6.2 ms. The microbubble 2 created by the previous conjunction is visibly larger than the primary microbubble (or the microbubbles in the image A). Note how the large—and therefore faster rising—bubble P has in the meantime already ascended to the top part of the image while the bubble 2, because of its shape oscillation, still remains at practically the same height as the microbubble 1 in the image A.
- (C) Taken after another 6.2 ms time increment. Another primary microbubble emerges from the aerator exit and will soon coalesce with the bubble 3. The bubble P has moved so fast that it has already left the scene (only its bottom is seen at the top of the image). Note that bubble 3 is already significantly larger than the microbubble 2 in previous image B.
- (D) At the total time 19.2 ms after the first conjunction A of this cycle. The microbubble 4 has already ascended to the height (0.25 mm above the aerator exit) at which the subsequent conjunction D becomes the last one in the series.

### 8.2.5 *Microbubbles with Fluidic Oscillation*

After the discovery of the growth by repetitive conjunctions, the essential question remained not fully answered. It was the question of the role actually played by the oscillation generated by the fluidic oscillator. After all, the capability of the oscillation—under some conditions—to produce microbubbles was clearly demonstrated at the very beginning of this study.

At that time it was believed that the pulsation somehow causes fragmentation of the bubbles. This would need applying the oscillation at the natural frequencies of the microbubbles. As demonstrated by the measurements the results of which were

presented above in Fig. 8.28, these frequencies are very high, typically between 1 and 2 kHz. These values are high above the typical frequencies of fluidic oscillators, which—with air, dependent on the lengths of the feedback loops and flow rate—are in the range from 50 to 300 Hz. In accordance with the universal trend in Nature—high frequency associated with small size of the device—author devoted considerable effort to development of extra high frequency oscillators. Figure 8.62 in the Sect. 8.3.5 demonstrates achieving frequency near to 2 kHz with quite large oscillator, of 2 mm supply nozzle width. Unfortunately, no visible reduction of generated bubbles could be observed with this oscillator.

After the failure of unequivocal experiences with the fragmentation idea, another explanation—and consequent development direction—was sought in suppressing the instability of parallel formation [36]. It was considered quite possible that the oscillation allows the bubble growth only during one half of the oscillation period. This means the bubbles stay within their stable regime, i.e. not growing past the hemispherical stability limit discussed in the Sect. 8.2.3. The weak point of this idea is how these hemispherical bubbles separate from their aerator exit. A proviso explanation was in the flip-flop character of the oscillation. The sudden switching of the jet attachment to the attachment walls can apply a strong sudden airflow pulse, causing the bubble separation.

The discovery of the growth by repetitive conjunctions made the problem of microbubbles visible in a new perspective. The it became apparent that the oscillatory motion with suitably adjusted parameters can prevent the contact and coalescence between freshly formed microbubbles. To investigate validity of this idea, author's study [40] was made again with the high-speed camera and a slightly scaled up (0.6 mm exits) model aerator which could be adjusted to generate  $d = 0.6$  mm diameter microbubbles. In contrast to standard sintered glass dust aerators with stochastic geometry of the passages, the passages in this aerator model were made regular, by drilling them arranged in line.

The immediately apparent fact that was really not expected was the back-and-forth motion of the bubbles, as seen in the photograph in Fig. 8.39. The bubbles that were formed in the first part of the oscillation period are, after their completed separation from the exit, in the subsequent part of the period pulled back into the aerator passage. Of course, once they were there, they became protected from the conjunctions. The dynamics of their motions was evaluated again from the height vs. time trajectories, by measuring positions of bubble centres manually in camera images. Results of this data processing are plotted in the diagram in Fig. 8.39.

Instead of being pushed, after formation, towards mutual proximity, the microbubbles are moved away from one another. The suction is a short-range effect. It influences the nearby freshly formed microbubble while the microbubble formed in the previous cycle is no more influenced—in fact it is moved away, together with ejected water.

Understanding the motion of water during the oscillation period is very important. The well visible bubbles attract attention, but really crucial is the water which has much more mass and hence much more inertia. In the next three illustrations, from Figs. 8.40, 8.41, and 8.42, show schematic representation of the conditions

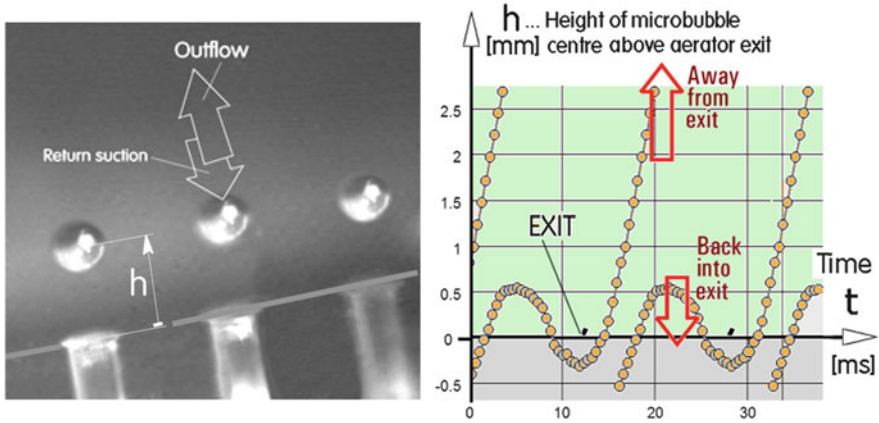


**Fig. 8.39** *Left:* High-speed photograph of 0.6 mm dia microbubbles formed at exits from passages in model aerator. Conjunction of microbubbles at the passage exit is here prevented by fluidic oscillator causing suction return motion of the bubble. *Right:* Height/time trajectories of the microbubbles. In the suction part of oscillation period the motion of the nearest bubble reverses while the bubble formed previously is accelerated away

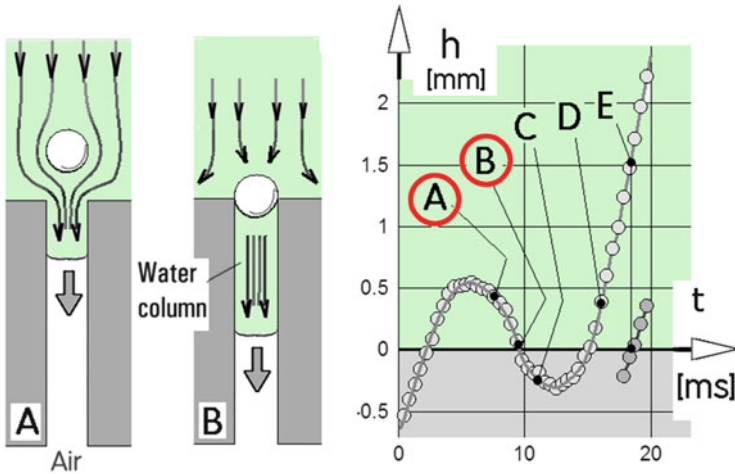


**Fig. 8.40** In stage A the flow is just past its reversal. Because the bubble is quite far, the suction pulls into the passage the surrounding water. At B the microbubble has returned into the passage and closes the water column

at and near to the flow reversal. Five points in the trajectories from Fig. 8.38 were chosen for the analysis, labeled A, B, C, D, and E and at the left-hand side of the pictures are shown positions of the freshly made bubble in space in addition with hand-drawn water flowpaths.

In the first drawing, Fig. 8.40, the bubble in the position A just begun moving back (i.e. opposite to the general upwards motion). The downwards suction moves

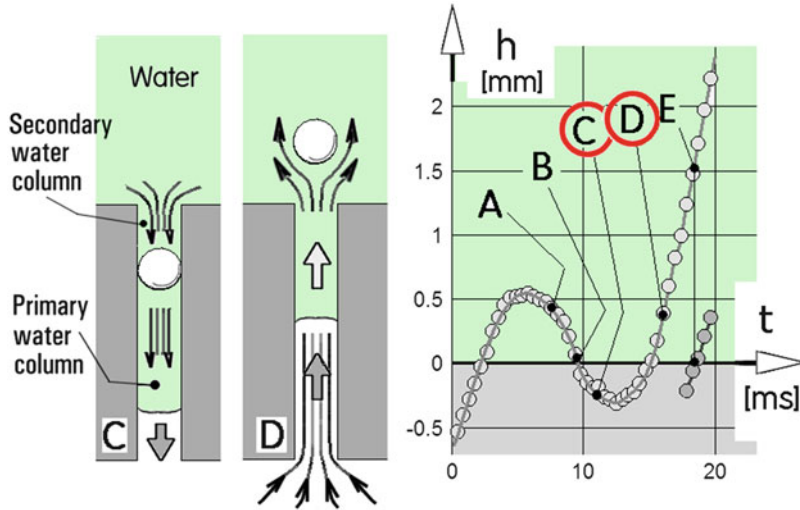


**Fig. 8.41** In the stage C the microbubble is protected from conjunctions inside the aerator passage. Secondary water column is formed. In the next stage D both the microbubble and water columns are expelled. Momentum of the water columns plays decisive role in moving the microbubble away

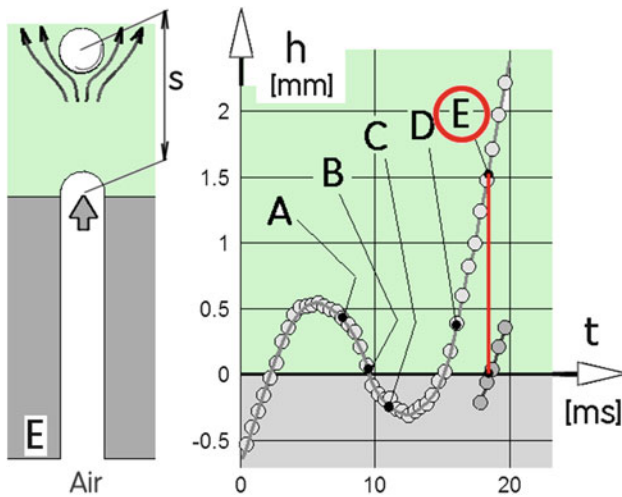


**Fig. 8.42** The stage E at which starts the formation of the next microbubble. Note the separation height  $s$  from the bubble formed previously. It is moved away from the aerator by the accelerated water columns

into the aerator passage water, especially the water that is near to the suction mouth—and with it, also the freshly formed bubble. Inside the aerator passage the water forms a liquid column. The drawing, Fig. 8.40, marks as B the situation when the returning bubble reaches the passage. There it forms the upper lid of the water column below.

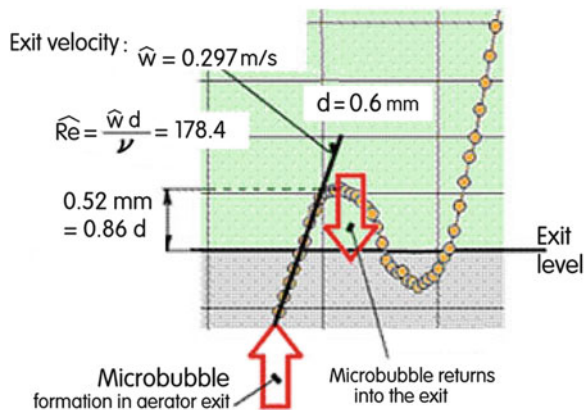
The accelerated water at and above the bubble continues moving down. Thus the bubble reaches the point C shown in Fig. 8.41. Being inside the passage, it is inaccessible for any contact with bubbles formed earlier. No conjunction hence can take place. Very soon after the point C, however, comes another reversal of the flow direction. Both water columns (primary below the bubble as well the secondary above it) start moving upwards. The microbubble operates as a piston. Illustration Fig. 8.41 represents the state D in which the aerator passage is emptied by its contents moving upwards.

Especially the primary water column is accelerated by the air “piston”. While the bubble itself, due to its small and indeed almost negligible mass, would not possess any significant inertia, with the liquid columns it is different. The inertia of their upwards motion affects also the bubble. In Fig. 8.42, when the subsequent bubble is formed and is already seen in its starting hemi-spherical shape, the originally studied bubble has moved into the position E which, due to the water inertia, is at the large vertical distance “e”.

Real fluidically generated oscillations are expected to operate under different conditions than the above discussed scaled up model. The conditions, however, have to fulfil the request of constancy of some dimensionless criterial parameters. Especially the criteria for initial formation of the bubble will be important and this is the reason why they were evaluated for the successful case from Fig. 8.39. The local slopes of the time/height diagram trajectories make it quite easy—by fitting a tangent to selected data points—to evaluate the bubble motion velocity. The heavy black straight line in Fig. 8.43 was evaluated to obtain the velocity

$$\hat{w} = 0.297 \text{ m/s} \tag{8.50}$$

**Fig. 8.43** Parameters of the initial bubble formation driven by the gas pressure. Low Reynolds number indicates laminar character of the flowfield



Compared with the general expression for Reynolds numbers, Eq. (8.5), the aerator exit Reynolds number for this case

$$\widehat{Re} = \frac{\widehat{w}d}{\nu} \quad (8.51)$$

Its numerical value is

$$\widehat{Re} = 178.4 \quad (8.52)$$

Evaluated from the same velocity Eq. (8.50) was also Strouhal number

$$\widehat{Sh} = \frac{fd}{\widehat{w}} \quad (8.53)$$

—the numerical value of which was

$$\widehat{Sh} = 0.121 \quad (8.54)$$

The same role of similarity as the Reynolds number of steady flows plays in the periodic oscillation flows Stokes number

$$Sk = \frac{fd^2}{\nu} \quad (8.55)$$

In the above analysed experiment its value was

$$Sk = 21.6 \quad (8.56)$$

Finally, it may be interesting and at the same time useful to evaluate the oscillatory-motion Weber number, Eq. (8.25) which in the shape oscillation bubble motions had the value  $We_o = 1.27$ , Eq. (8.26). Now in the generation of microbubbles by the oscillatory flows in aerator passage, the value is very much smaller

$$We_o = 0.0054 \quad (8.57)$$

### 8.2.6 Consequences of the Discovered Effects

Critical aspect of the discussed problem is understanding the mechanism of microbubble formation in the exits of aerator passages, supplied by airflow with flip/flow oscillation. It is not a trivial problem and it has to be admitted that full understanding is still missing. Generating microbubbles is a demonstrated fact, but it is still not possible to say in advance whether and at what combination of oscillator parameters the desirable phenomenon will be achieved.



The very basic parameter upon which there is so far no agreement is the oscillation frequency. Initially the development effort concentrated of achieving—in a not very small body—very high frequencies. This direction, however, has been deserted. The successful model study discussed in Sect. 8.2.5 has demonstrated, that the desirable performance will most probably need the protection by bubble flow reversal, including the back-and-forth bubble movement. These somewhat complicated motions cannot be done at high frequencies. To the very opposite, the new fluidic oscillator principles had to be developed at frequencies lower than previously expected.

## 8.3 Fluidic Oscillators

### 8.3.1 *Development History of Fluidics*

Fluidics is technique of generating and handling fluid flows. In its broad general meaning the term may be applied to activities that have been there since time immemorial. Man always had to handle fluids (i.e. either liquids or gases—and their two-phase mixtures) and control their flows. Initially distinguished were terms “hydraulics” for handling liquids and “pneumatics” when the handled medium was gas. The unifying term *fluidics* for both is nowadays used in a narrow sense, applied to devices without mechanical parts. Earlier devices operating with moved or deformed components are now described as mechano/fluidic ones. Devices with mechanical components are generally easier to design—while pure fluidic action requires a deeper knowledge about sensitive spots in flowfields. Nevertheless, apart from being expensive (they are made separately and inserted in an additional assembly operation) mechanical components can cause problems in operation. They may be broken, get stick or become loose—and may need maintenance (oiling, tightening the seals). Most importantly, because of their inertia, they limit the speed of response. In pure fluidic devices that were invented in the middle of the last century the absence of such components thus brought obvious advantages. Particularly apparent were the advantages in the key devices of control systems—in the no-moving-part fluidic amplifiers. These are capable of operating in a similar manner as vacuum-tube electric amplifiers, which at that time still had to grapple with the competition of earlier moving-part relays. Vacuum tubes won by being capable of operating at very high frequencies, but were so unreliable that they had to be used in sockets for easy replacement. Only the later invented transistors has solved the painstaking reliability problems. By a direct analogy with electronic amplifiers were then invented fluidic relaxation oscillators [58] and feedback-loop oscillators [49]. More attention, however, was then paid to fluidic binary counters and other digital circuits (as discussed, e.g., in [7]). In the competition with electronics has fluidics lost because of its two drawbacks: (1) size of fluidic devices cannot be decreased so much as it is possible with transistors (because of

the adverse effects of low resultant Reynolds numbers and also the need of smooth channel shapes)—and (2) upper limit of operating frequency in fluidics is the speed of sound, incomparably lower than the speed of light of moving electrons in electric circuits. Some of these former drawbacks could be recently solved or by-passed by the emerging microfluidics [37]. Nevertheless, the speed limit prevented building large systems which became necessary for solving many control tasks. Of course, the universally valid history of inventions, with the “ditch of disillusion”, was also a factor. As a result, fluidics became at about two decades ago practically forgotten.

It was at that time of near-extinction that a remarkably useful application was found for the fluidic oscillators. They were employed to generation of pulsation in the fluid flow passing through various devices. Compared with steady flows the agitation improves the efficiency—and compared with traditional oscillation generating methods, fluidic oscillators are easy to manufacture, reliable and maintenance-free. Their use in generation of microbubbles has a revolutionary consequences in a number of process engineering tasks.

### 8.3.2 The Key Component: Amplifier

Although there are oscillations in fluid flows the action principle of which may be difficult to recognise and identify, deeper analysis always shows that all fluidic oscillators contain two essential components:

1. a fluidic amplifier—device generating a flowfield that can be changed substantially in response to a weak input flow signal, and
2. feedback loop bringing a part of the output flow to the input. It must be a negative type of feedback, suppressing the action by which it was previously generated.

Schematic block-diagram representation of the amplifier is presented in Fig. 8.44. The two variants shown there differ in absence or presence of their venting of

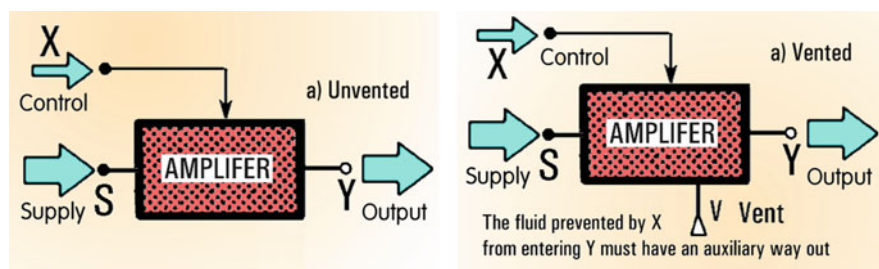


**Fig. 8.44** Schematic block-diagram of simple fluidic amplifier with supply S, control inlet X, and single output terminal Y. In many device types there must be also the vent V—as the alternative exit path

internal cavities (opening them into the outside atmosphere, if the fluid is air). The device has three essential terminals. By the first of them, the supply terminal **S**, enters into the device the working fluid. It passes through and leaves at controlled variable intensity through the output terminal **Y**. It is this terminal to which is connected the process or object influenced by the fluid flow. The amplification property means that the powerful output flow in **Y** is controlled by a much weaker input flow applied in the control terminal **X**.

At first sight, the presence of the vent may be not necessary. The unvented amplifier (top in Fig. 8.44) may suffice. After all, its electronic analogue, transistor, also suffices with only three terminals. The output flow in the terminal **Y** of the amplifier varies in dependence on the intensity of the control flow in **X**. Closer examination, of course, shows two problems. The supply flow is normally expected to stay constant. If there were no vent, however, its constancy is impossible as it has to vary also in response to the control signal in **X**. Second and more important fact is the limited extent of amplifier flow rate in the unvented device. Evidently, if the flow rate through **S** decreases to zero, as a consequence disappears the very hydrodynamic phenomenon upon which the amplification effect is dependent. No flow rate means no flowfield—and no amplification effect. In fact, with gradually decreasing flow the hydrodynamic mechanism would stop working much earlier because of the inevitable dominance of viscous friction at low Reynolds numbers.

The other configuration, vented amplifier in Fig. 8.44, avoids these problems. The supply flow remains constant—and the control action may remain effective even in zero output flow in **Y**. The device may be described as a diverter. Through the vent terminal **V** leaves the fluid diverted by the control action from entering the output **Y**. Of course, the cavities inside the amplifier have to be designed so that the venting does not mean losing the working fluid when it is needed in **Y**.

The most popular amplifiers currently used are based on the diverter principle using the deflected jet, as presented in Fig. 8.45. The jet flow is generated by letting the supplied fluid to issue from a nozzle into a more or less free space (**A** in Fig. 8.45). Typical feature of nozzles is the cross section of the flowpath decreasing in the flow direction. Thus the fluid pressure is converted in a nozzle into its increased kinetic energy. The control acting on the jet is provided by control nozzle, usually oriented perpendicular to the jet as shown in the case **B** in Fig. 8.45. This deflecting effect employs the jet sensitivity to actions applied at the nozzle exit. The output terminal **Y** is connected to the collector placed opposite the nozzle, **C** in Fig. 8.45. Its task is to capture there the jet fluid. Deflection by the control flow varies the captured amount—and this varies the output flow in the terminal **Y**. The collector is usually shaped as a diffuser, performing an effect which is the reverse to that taking place in the nozzle. The flow velocity in the diffuser decreases in the flow direction and the kinetic energy of the jet is used in **Y** to increase the fluid pressure. One of the reasons for these pressure conversions are the losses in connecting channels bringing the fluid into the amplifier and out of it. Very roughly, the losses in channels are proportional to the square of velocity. It is therefore desirable to keep the velocity in them at a minimum. There are other reasons for the conversions to be discussed in the following Sect. 8.3.5.

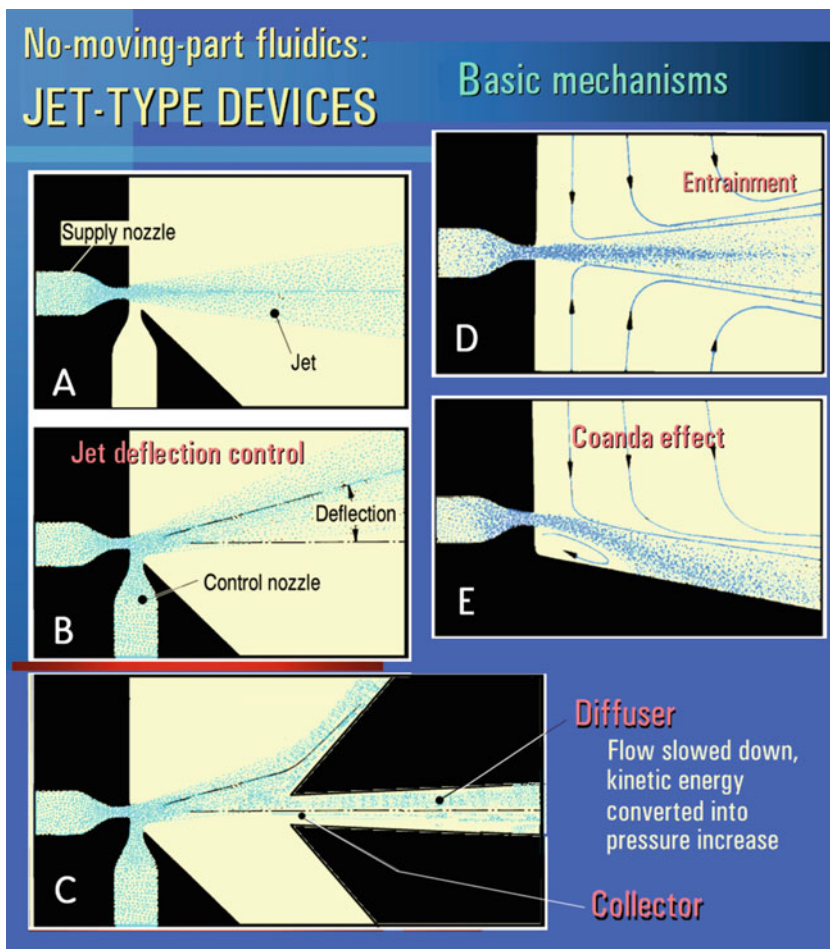


**Fig. 8.45** The most popular mechanism employed in fluidic amplifiers is the fluid jet A issuing from a nozzle. Acting in its sensitive spot near the nozzle exit, the control flow deflects it, B. This may be used to controlled decrease of the output flow C, the device becoming an amplifier. Issuing into stagnant surrounding fluid causes an entrainment, D. If there is a suitably oriented nearby wall, the jet attaches to it deflected by the pressure difference between its two sides, E

Early researchers who investigated the idea of jet-deflection amplifiers were disappointed by an unpleasant effect. Instead of the expected jet deflection continuously increased with increasing control flow, some jets became instantly fully deflected, with the control flow having no influence. These jets attached to a nearby wall of the interaction cavity and remained there deflected even when the control flow stopped completely. It was recognised as manifestation of the effect described in a patent filed by Coanda in 1936 [5]. It is a consequence of the jet-pumping effect—the entrainment of surrounding fluid (D in Fig. 8.45). Presence of the wall

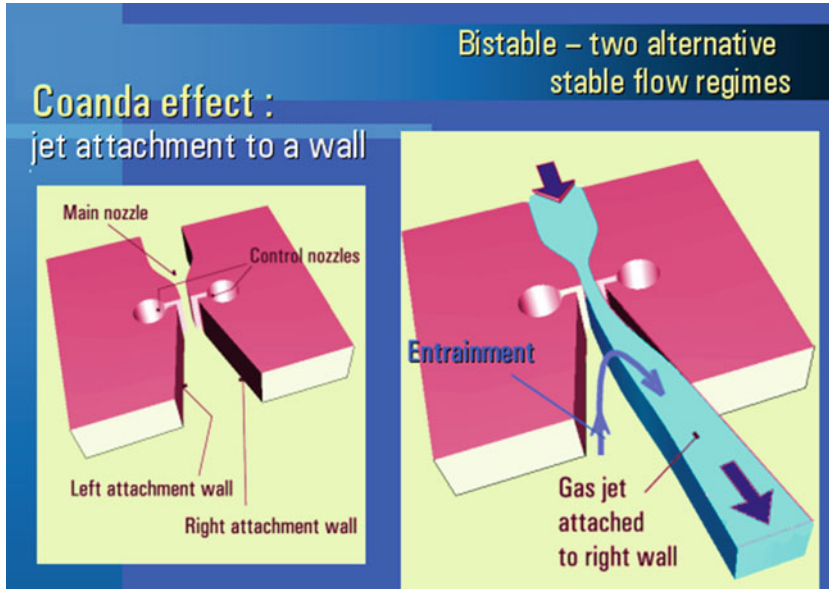


**Fig. 8.46** If there are two attachment walls symmetrically located on both sides of the jet path, the flow can attach alternatively to one of them and may be switched to the other one by a short flow pulse applied in the corresponding control nozzle

at one side of the jet limits there the removal of the fluid by entrainment. The jet-pumping suction decreases pressure on that side of the jet. The permanent full deflection (the Coanda effect E in Fig. 8.45) is due to the pressure difference acting between both sides of the jet.

Rather than a nuisance, the Coanda effect was soon found useful. Layouts with its use in fact dominate current jet-type amplifiers. They are operated not in the continuous mode but as bistable devices, with the jet switched between two attachment walls, Fig. 8.46. The switching control action needs only short flow pulses. The captured flow in the collector—as well as in Y and the downstream devices connected to it—has character of a train of rectangular pulses. These rapid changes are beneficial for the agitation of the fluid in the devices connected downstream.

If there is only a single attachment wall, the amplifier exhibits monostability. This means the jet with control action absent attaches always to this single wall. As is apparent from the schematically represented transfer characteristics in Fig. 8.47, the configurations with attachment are typical by the presence of hysteresis loop in their characteristic curves.

There are two possibilities how to control the jet attachment, presented as A and B in Fig. 8.48—shown there on the examples of monostable amplifiers. In the much more often used case A, the separation from the attachment wall is obtained by the control flow acting on the main flow at the location where the main flow leaves

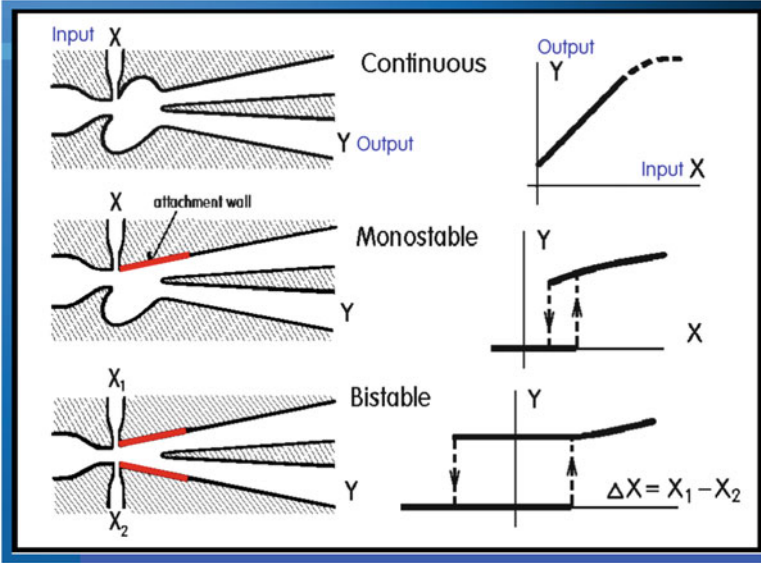


**Fig. 8.47** Depending on the presence or absence of the attachment walls, the jet may be controlled as shown in the transfer characteristics at right. The response may be continuous (no attachment wall), monostable, or bistable (as in Fig. 8.46)

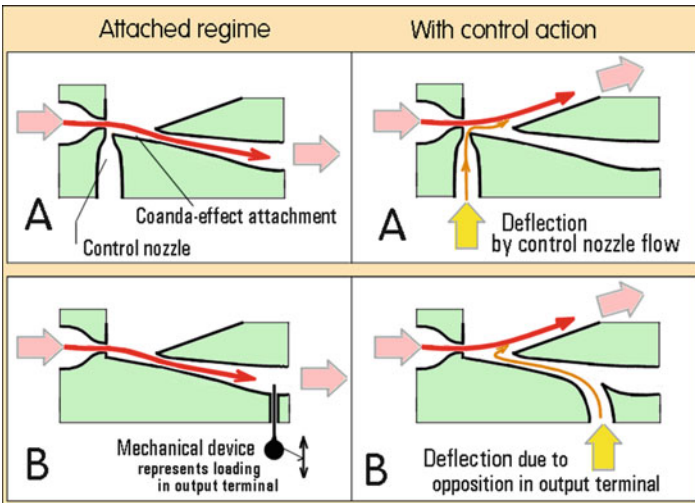


**Fig. 8.48** Control of output flow in a jet-deflection fluidic amplifier by a weak input flow. Separation of the jet from the attachment wall switches the character of the flowfield. There are two control action alternatives, A and B, the former used much more often



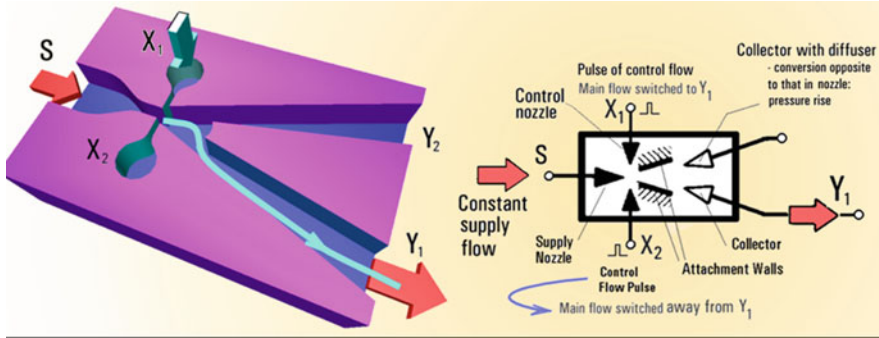


Fig. 8.49 Typical planar bistable amplifier and its schematic representation

the supply nozzle—as in the case B of Fig. 8.45. The other switching mechanism, case B in Fig. 8.48, is based upon the idea of making it difficult for the main flow to pass through the output terminal. This switching mechanism may be caused by connecting the terminal to a downstream device called load. The Coanda attachment to the wall simply is not strong enough if the output is blocked by flow-restricting load. This is why this control effect is called *load switching*.

### 8.3.3 Bistable Diverter with Jet Deflection Control

The most common symmetric version of a jet-deflection amplifier based on the bistable Coanda effect is presented in Fig. 8.49—both as a drawing of its cavities in the left part of the picture and the schematic representation in the right part. This representation stresses the difference between nozzles (triangular symbols filled black) and the diffusers downstream from the collector (triangular symbols not filled). Also represented in the schematic symbol of the amplifier are the two attachment walls, indicating the use of Coanda effect. While the continuously operating as well as the monostable amplifier versions may have only single control nozzle, the bistable amplifier must have two control nozzles. Each can separate the jet from the attachment wall on its side (note how in Fig. 8.49 the flow pulse in  $X_1$  switches the main flow into  $Y_1$ ).

As is generally known, the streamwise increase in the cross section area in a diffuser must be smooth and gradual. If the area were increased suddenly, the flow would separate from the diffuser walls—and the diffuser effect would be lost. No such danger is there in the nozzles, in which the streamwise cross-section change can be quite rapid. It is thus a characteristic feature of fluidic jet-type amplifiers that most of their layout is occupied by the long diffusers. Quite upstream in the amplifier body are the nozzles and the interaction cavity into which the nozzle exits are oriented.

Bistable amplifiers are always symmetric (otherwise they would tend to behave in the monostable manner). There may be, however, asymmetry in the outputs loading. For example the case in Fig. 8.49 may be used with only one output terminal  $Y_1$  while the other terminal  $Y_2$ , on the opposite side, has then the role of a vent. The control action tends to be by differential pressure (or to the same effect by difference in control flow rates). Thus the switching effect of control nozzles  $X_1$  and  $X_2$  in the bottom part of Fig. 8.47 may be achieved by the differential control signal  $\Delta X = X_1 - X_2$ . Similarly, the resultant output signal may be the difference  $\Delta Y = Y_1 - Y_2$ . The operation with the differential signals may at first sight appear to be an unnecessary complication, but it is actually very convenient with differential-type loads and also with amplifier cascades, as is the case in the schematically drawn Fig. 8.50.

The planar configuration example in the left part of Fig. 8.49, with the constant-depth cavities for fluid flow made in a planar material, is quite common. Another example are the amplifiers photographed in Fig. 8.51. In this shown case they were made by numerically controlled laser light cutting in a teflon plate (for operation with hot air). The following Fig. 8.52, shows another case. In the upper right corner of the picture is a larger amplifier version made by the 3D printing, with

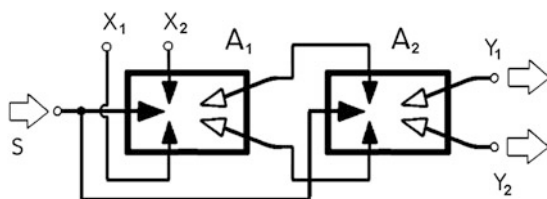


**Fig. 8.50** The differential input signal in  $X_1$  and  $X_2$  as well as the differential output in  $Y_1$  and  $Y_2$  are suitable for amplification cascades—here in the continuous version without Coanda attachment. Overall gain of the cascade is the product of the amplification gains in  $A_1$  and  $A_2$

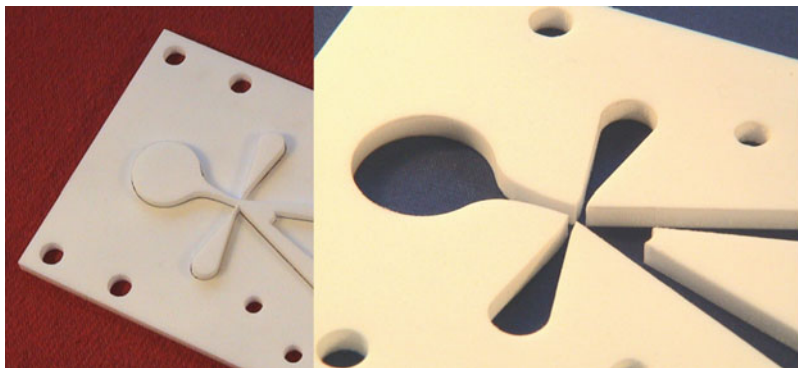


**Fig. 8.51** Popular method of manufacturing fluidic devices is numerically controlled laser light cutting in a planar material



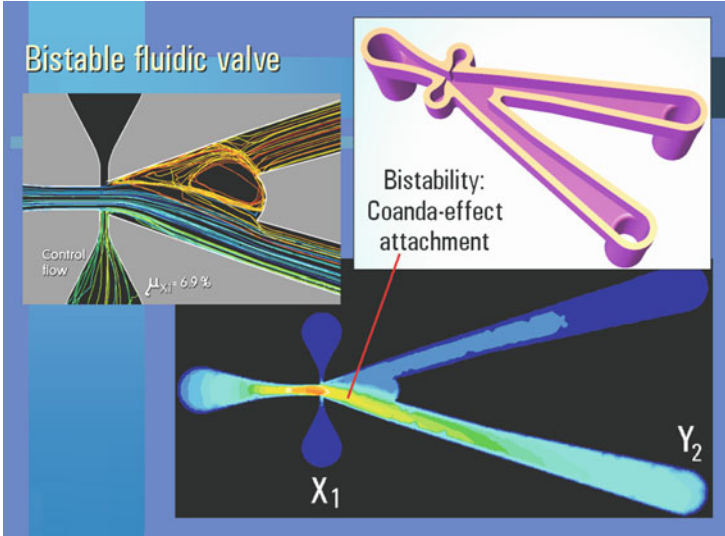


**Fig. 8.52** Character of the flowfield in bistable amplifiers as it was obtained by numerical solutions

constant thickness walls surrounding the internal cavities. The other two images in Fig. 8.52 show typical results of numerical flowfield computations—flowpath trajectories and coloured contours of computed pressure field. Usual amplifier size and flow velocities are of magnitudes at which the Reynolds number values tend to be within the region of transition into turbulence. This complicates the computations by difficulties in turbulence modelling. It is necessary to use modified turbulence models, with additional constants (usually not known in advance) and not particularly reliable model equations. This is why the computation procedures in amplified development, Fig. 8.52 have to be usually supported by experiments. Experimental data consisting of the flow rates and pressure levels in the terminals may not suffice and really useful results for comparisons with the computation may need investigation of the whole internal flowfield. While the flows may be visualised, as shown in Fig. 8.53, equally important pressure measurements need making pressure tap holes in the laboratory model body. Reading there the pressure values using a manometer is shown in Fig. 8.54. This may be neither easy nor fast done. Sometimes the discovered flow phenomena do not agree with expectations. As discussed above, the starting point in design of an amplifier was idea of increase of pressure in the nozzle and its subsequent rise in diffusers. Figure 8.54 shows the surprising fact that the pressure rise in the tested diffuser between the beginning B and end Y is unexpectedly small—and there is an unexplained significant rise between the points A and B at the diffuser entrance. Fluidic amplifiers may seem to be simple and easy to design. The opposite is true. In fact, it was the underestimation of the associated time and effort that were one of the reasons behind some of the failures in fluidics.

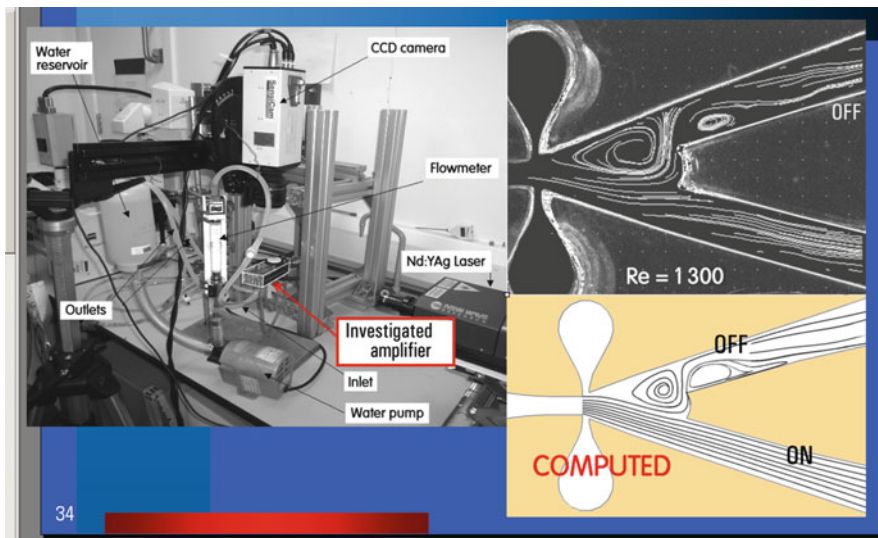


**Fig. 8.53** Example of laboratory experiments with jet-deflection amplifier models. Trajectories of tiny particles carried with the fluid (here liquid) visualised by laser light are recorded by camera, processed by PIV software and compared with numerical computations

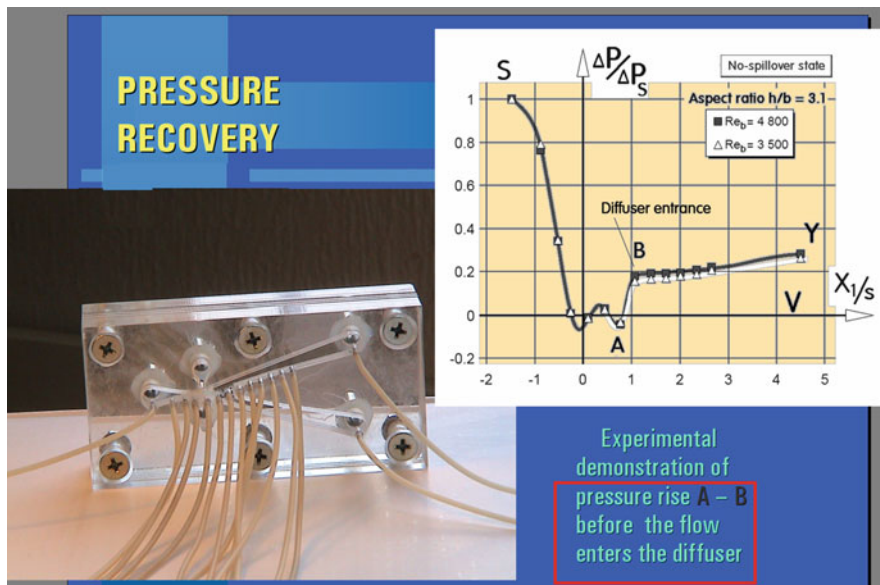


**Fig. 8.54** Another example of author’s laboratory investigations of a fluidic amplifier models. Pressure measurements in small drilled tap holes—connected by the small diameter tubes to digital manometer—were performed in attempts to understand the pressure recovery mechanism

### 8.3.4 The Feedback

Schematic representation in Fig. 8.55 in comparison with Fig. 8.44 shows how the amplifier becomes an oscillator. The change is by addition of a feedback. In oscillating flowfields, like the vortex street downstream from a blunt body, the feedback effect may be a result of an impulse carried by vortices. In the present case of fluidic circuit built from individual devices the term “feedback” describes cavity or channel connecting the output terminal Y with the control terminal X. The diverted part of the output flow is brought through X as a control flow into the interaction cavity of the amplifier. The feedback causing oscillation has to act there in a negative sense—it causes the flow in Y to decrease. An important factor in this configuration is the phase shift taking place in the feedback, Fig. 8.55. If it were not present, the configuration would finish as a steady flow regime. With the delay, the amplifier can for a brief time remain in one of its two regimes before the feedback action switches it to the other regime.

The oscillator presented in Fig. 8.56 corresponds to the schematic representation in Fig. 8.55. It is drawn so that even the locations of its terminals are in agreement with the scheme in Fig. 8.55. The amplifier is a monostable one—which means it is switched between two regimes of which only one is stable. The working fluid enters this oscillator through the supply terminal S. It issues from the supply nozzle and forms a jet. Downstream from the nozzle exit there is an asymmetric interaction cavity. On the upper side of the jet there is the attachment wall p. It is located near the jet so that it can easily attach to the latter. On the opposite, bottom side of the jet there is a larger space. This is also bounded by a wall, but this wall is quite far from

**Fig. 8.55** Fluidic oscillator: the vented variant of a simple amplifier shown in Fig. 8.44 is provided with the feedback connection from Y to X

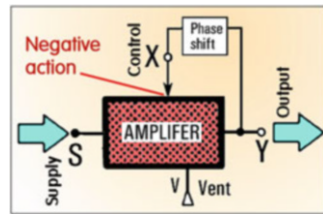
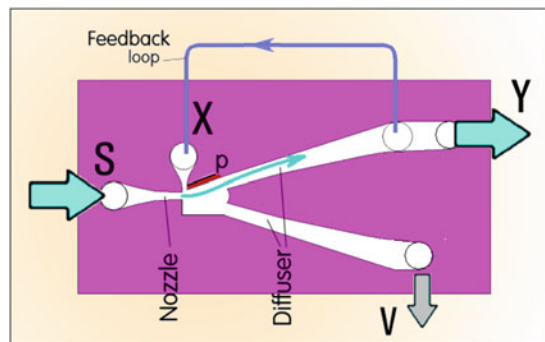


**Fig. 8.56** An example of a monostable jet-deflection amplifier converted into the self-excitation oscillator. The configuration corresponds to the schematic representation in Fig. 8.55



jet flowpath. Thus in this monostable amplifier the jet not acted upon by the control effect always adheres to the attachment wall  $p$ . From it the jet may be separated by the fluid flow coming through the control terminal  $X$ . When the jet is separated from  $p$ , the fluid leaves the amplifier body through the vent  $V$ .

In the oscillator, the two terminals  $X$  and  $Y$  are mutually connected by the feedback loop channel (the channel is made at a different level of the oscillator body and therefore in Fig. 8.56 not drawn in detail). The  $Y$  end of the feedback channel is at the end of the diffuser. Thus the fluid flowing through it is at this end at a higher pressure level than the interaction cavity. This pressure difference generates the feedback flow from  $Y$  to  $X$ . Because of the inertia of the fluid inside the feedback channel, it takes some time before this feedback flow reaches a significant intensity. This is the phase shift effect as presented schematically in the feedback loop in Fig. 8.55. When after the phase shift time the necessary intensity is reached, the jet is separated from the attachment wall  $p$ . It is then diverted into  $V$ . This jet deflection stops the flow in the diffuser and thus eliminates the source of fluid driven through the feedback loop. The control flow in  $X$  then ceases. The jet can return to its attachment wall  $p$ —and then the whole jet deflection process can be repeated. The result in the terminal  $Y$  are repeated flow pulses.

The example as presented in Fig. 8.56, with the monostable amplifier, was chosen for simplicity of explanation and does not correspond to typical oscillator configurations as they are used in practice. Experience has shown that monostable amplifiers are not easy to tune into proper operation. They are also sensitive to various disturbances. Typical configuration used with positive experience has the bistable amplifier. This corresponds to the Warren’s design [50] patented in 1962 and presented in the left part of Fig. 8.57 (the picture is the original drawing from

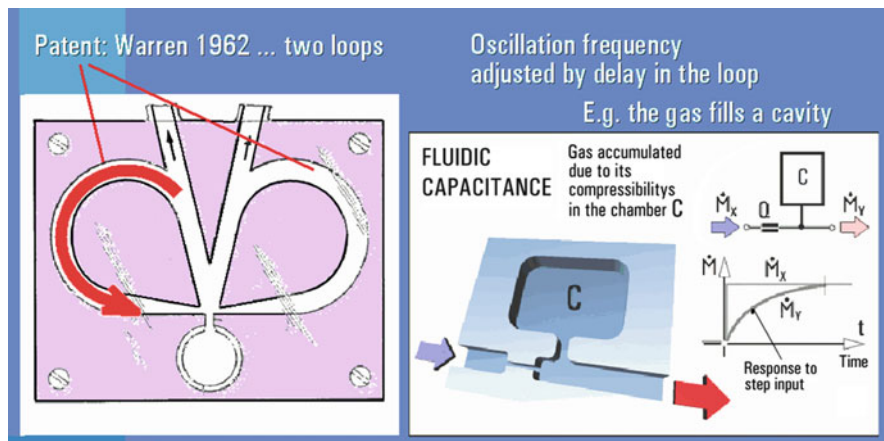


**Fig. 8.57** The most popular fluidic oscillator configuration invented by Warren in 1962: a bistable jet-deflection amplifier with two feedback loops [50]. Sufficient phase shift is due to finite flow velocity in the loop (indicated by the *thick red arrow line*). The frequency may be decreased by incorporating the camber filling in the QC sub-circuit

the US Patent). In principle this configuration may be thought of as a pair of monostable amplifiers, with common supply nozzle but each with its attachment wall and its feedback loop. Thus the flow processes may be studied following the above description of monostable case.

If the feedback loop channels are short, as is the case in Fig. 8.57, then the generated oscillation frequency may be quite high. There are situation where high frequency pulses are not welcome. They may be strongly damped or there may be other reason for demanding lower frequency. The right-hand side of Fig. 8.57 presents an example of feedback with frequency decrease. Included into the feedback loop (or loops) is a cavity  $C$  in which the fluid pressure increases by fluid flow at a magnitude restricted by a fluidic restrictor  $Q$  (a local decrease of the flowpath cross-section area). The time needed to fill the initially empty cavity  $C$  increases the phase shift in the loop and thus decreases the frequency.

### 8.3.5 Other Oscillators: Usual and Unusual

Some popularity have gained fluidic oscillators with the bistable diverter amplifiers having only single feedback loop as shown in Fig. 8.58. They may be somewhat difficult to adjust proper operating conditions, but the existence of only single loop channel may be an advantage simplifying the control circuit. Inventor of this oscillator configuration was also Warren, who patented the ides in 1960, i.e. 2 years earlier than the two-loop version [49]. The single feedback loop channel here

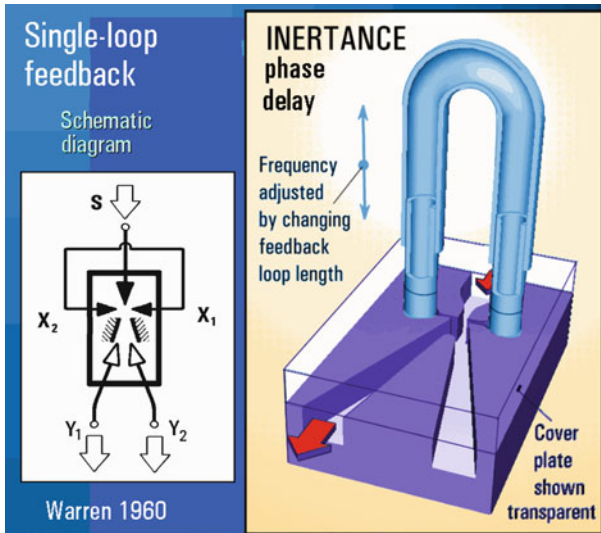
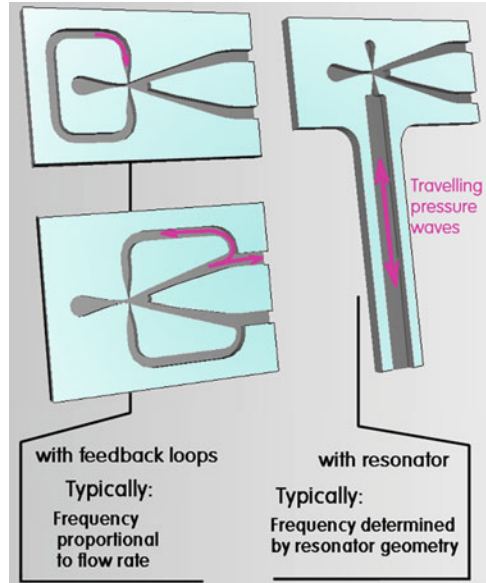


**Fig. 8.58** The single-loop oscillator, with the flow in the tube generated by the pressure difference between the two sides of the jet deflected. Invented by Warren in 1960 [49]

**Fig. 8.59** Most popular oscillator principles use the bistable jet-deflection amplifier. At *left* are the alternative loop configurations from Figs. 8.57 and 8.58. At *right* is the recent high-frequency oscillator based on pressure pulse reflection and propagation in a resonator channel



connects the control nozzles,  $X_1$  and  $X_2$ . The pressure difference driving the flow in the loop is the same difference between sides of the jet that is responsible for Coanda effect attachment, Fig. 8.45.

Yet another, relatively new feedback idea—Tesař, Zhong and Fayaz, 2013 [45]—is shown at the right-hand side of Fig. 8.59. This oscillator operates with compressible fluid, usually air. One of the control nozzles of the bistable amplifier is open to atmosphere. To the other one is connected a resonator pipe. The pulses switching the jet in the amplifier are derived from the travelling compression and expansion waves in the resonator, reflected from its open end. Typical property of this oscillator is the practically constant oscillation frequency, dependent on the resonator length and velocity of pressure signal propagation—but not varying with supplied flow rate. On the other hand, both single-loop and two-loops oscillators, shown at the left-hand side of Fig. 8.59, have their oscillation frequency increasing in linear proportion with increasing flow. An example of this proportionality is shown in Fig. 8.60. The planar geometries of the three tested laser-cut single-loop oscillators differ solely in their size. One of them, the smallest, differed in generating oscillation at the second harmonic—and also by exhibiting a range of constant frequency. This was certainly a consequence of resonance and propagating pressure wave effect in the feedback loop. Similar locking to resonance in feedback loop was found also in [44].

The rather complex internal geometry of the amplifier—and hence also of the oscillator—cavities provides an opportunity and freedom for detail design. Discussing some accumulated examples may provide useful guidance for future designs. Eight oscillator examples found in literature are presented in Fig. 8.61. All of them are of the planar configuration—with cavities of constant depth everywhere



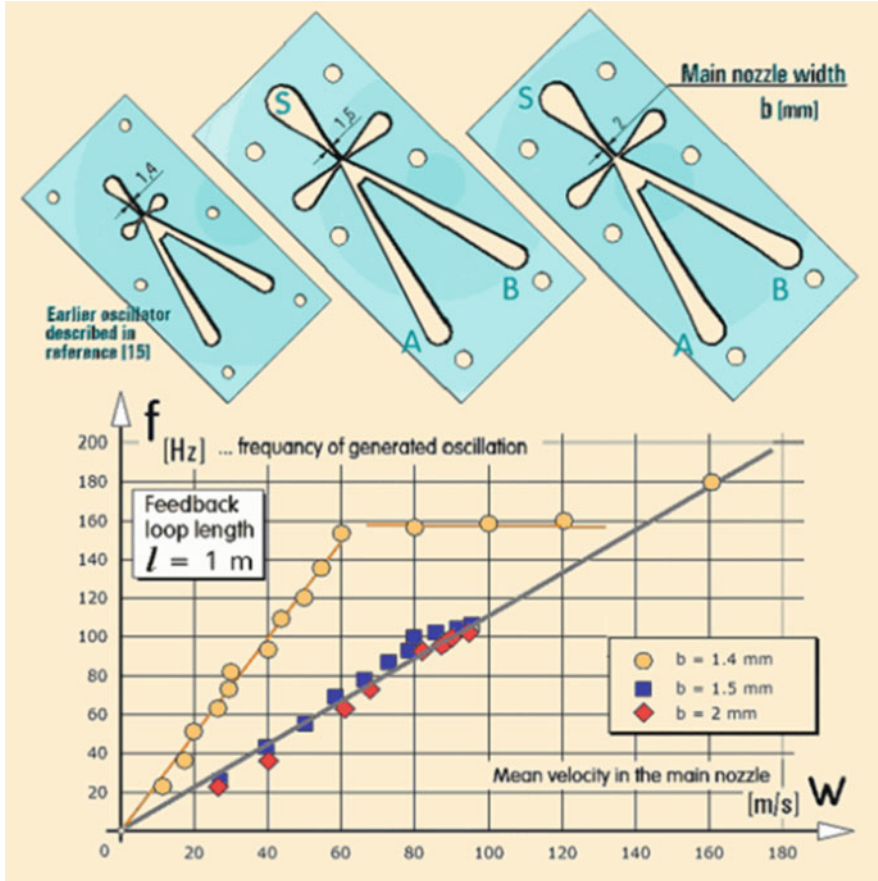


**Fig. 8.60** Author’s three oscillators with the single loop feedback. They differ only in size—and yet the behaviour of the smallest one differs, locking to a constant-frequency resonator behaviour over a range of flow velocities

made by removal of the material from a thin plate. The geometry of the first example **A** is the original Warren’s two-loop geometry from Fig. 8.57. Note the smooth course of the feedback channels, certainly beneficial for keeping the oscillation on even at small flow rates. What has to be said against this design of the amplifier is lack of understanding the meaning and importance of the pressure recovery downstream from collectors. This recovery is to take place in diffusers characterised by channel cross-section increasing in the flow direction. Such channels are in example **A** missing. Obviously, some recovery was present, most probably due to the rise **A–B** shown above in Fig. 8.54. Better understanding of the processes inside the jet-deflection amplifier is demonstrated in the next **B** of Fig. 8.61 by Markland et al. [19], patented in 1986 for the purpose of using it in fluidic digital flowmeters. At least there are, downstream from the collectors, visible diffuser shapes—though

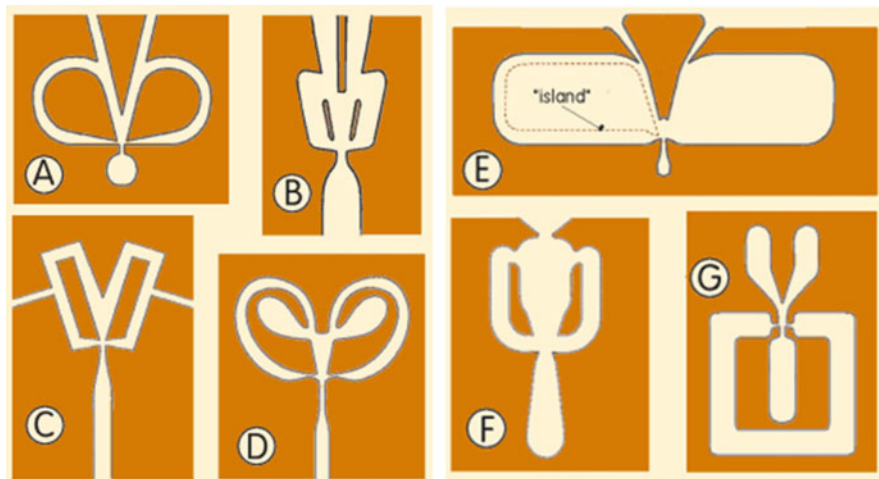


**Fig. 8.61** Several examples of oscillators in the configuration with bistable amplifiers: A—The original Warren’s (1962) Patent [50] geometry of two-loop version; B—Markland et al., 1986 [19] layout for fluidic flowmeters; C—Ries et al., 2009 [29], obviously with cavalier disregard for flows past smooth contours; D—Cerretelli and Kirtley 2009 [4], oscillator for turbine blade flow control; E—Tesař 2014 [43] vortex cavities replacing feedback channels; F—Koklu 2013 [12], US Patent for NASA; flow control by a sweeping jet actuator; G—Warren’s 1960 [49] single-loop version is the oldest known fluidic oscillator

they are obviously too short for any efficient pressure rise. Also, the entrances into the diffusers are there too far downstream and thus the diffusers cannot produce the desirable pressure rise for driving the feedback flows.

What is no doubt the worst among the designs in this collection in Fig. 8.61 is the oscillator **C**, by Ries et al. [29], discussed as used for control of flow separation in low-pressure stage of a turbine. Since this design was published as late as 2009, after widespread existence of efficient designs, it is very difficult indeed to find out what has led the authors to the horrible geometry with the sharp corners and outputs connected as an afterthought at right angles to the feedback channels. Very probably there was in their turbine stage enough available pressure difference for brute force pushing the fluid into the strangely positioned output terminals despite the inescapable huge losses that are evident at first sight.

Perhaps some more understanding for the need of fluid flows is manifested in Fig. 8.61 in the case **D**. This, however, applies only to the design of the smooth-contoured feedback loop channels. There is, as in the oscillator case **C**, a visible disregard for efficiency of the fluid flow into the output terminals. There may be some, nevertheless extremely small, diffuser effect in the outputs, evidently negated by the flow direction change at almost right angle at the inlet into the “diffuser”. The lack of diffuser effect upstream from the entry into the feedback channels is here circumvented by placing the feedback entrances opposite to the supply nozzle and generating thus in them an impingement effect.



The unusual features of the geometry in the case **E** of Fig. 8.61 are a result of a change made with what was originally a quite conventional configuration. The geometry shown is the result of removing the “islands” on the inner side of the two feedback channels, present in all two-loop designs. The removal of “islands” means elimination not only of the feedback channels, but also of the essential feature of the Coanda-effect amplifiers—the attachment walls. To a general surprise this configuration not only did not stop oscillating, but actually [41] managed to generate oscillation at very high frequencies, then called for. Example of properties found by laboratory investigations is in Fig. 8.62. The diagram of oscillation frequency as a function of mass flow rate shows the frequency of generated pulsation as high as reaching nearly to  $f = 2$  kHz—and with very small dependence on the flow rate.

The configuration **F** in Fig. 8.61 was intended to a different mode of flow control past bodies. The configurations like **C** or **D** above were employed for this task in the usual mode of flow alternatively switched between the two outlets. In the case **F** there is only a single outlet through which the flow issues at constant intensity—but at direction varying in each oscillation period by approximately by  $90^\circ$  forth and back. Finally in configuration **G** of Fig. 8.61 is a single-loop oscillator Fig. 8.58. This particular geometry shows typical design errors: too short diffusers of too wide angle and the quadratic feedback channel shape with sharp turns in the corners.

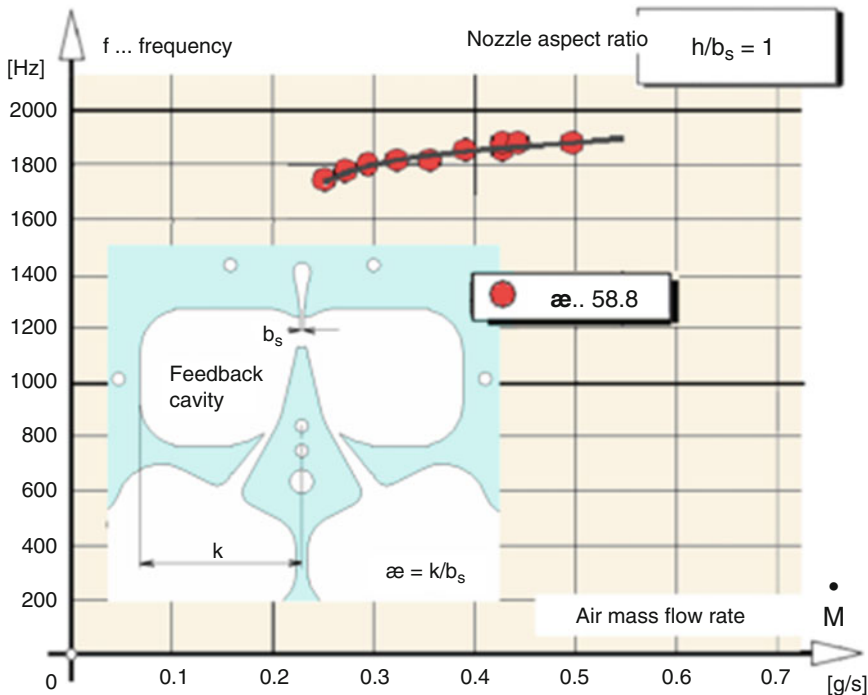
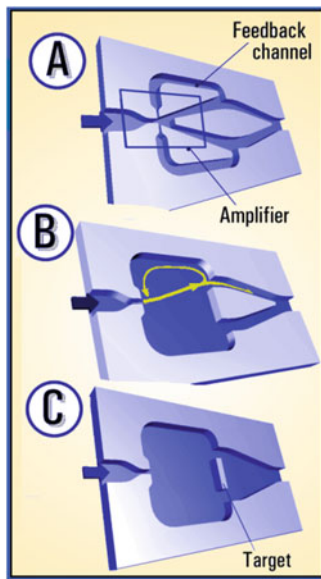


**Fig. 8.62** Demonstration of the possibility to obtain very high oscillator frequencies with quite large oscillator size. Feedback channel flows replaced by vortices in recessions, Fig. 8.61 E

**Fig. 8.63** Jet flow impinging on a blunt target body generates strong and particularly regular oscillation, making this configuration popular for use in fluidic digital flowmeters [10]. Its configuration may be seen as a gradual development from the standard two-loops oscillators a A and B to C



Special class of fluidic oscillators represent those intended for use in digital flowmeters. The frequency of generated oscillation must be in these cases strictly linearly dependent on the supplied fluid flow rate down to very low Reynolds numbers. Their typical geometries are characterised by a blunt-body target opposite to the nozzle—and empty spaces on the both sides of jet flowpath, very similar same as in the geometry of the case E of Fig. 8.61. In the picture Fig. 8.63 is suggested the gradual development from the standard geometry of two-loop oscillator.

### 8.3.6 Relaxation Oscillators

There is a little known family of fluidic oscillators characterised by gradual increase of pressure (usually in QC sub-circuit, Fig. 8.57) followed, upon reaching a limit, by sudden discharge in the rest of the oscillation period. Typical representative may be the earliest fluidic oscillator of them all, patented in the US in December 1959 [58]. It is shown in Fig. 8.64 where it is obvious that the basic idea came from elsewhere—from the flow separation on the upper surface of an airplane wing as a response to a spoiler. The flow from the nozzle in the upper part of Fig. 8.64 is a jet which attaches to the top surface of the “wing” body and continues into a collector. This is connected directly to an accumulation chamber—with the accumulation of air made possible by its compressibility. Pressure in the chamber gradually increases until it equals to the dynamic pressure of the jet. At that moment the opposition to the jet flow causes a sudden change. The jet then separates from the “wing” surface and becomes directed away from the collector. The pressure in the vicinity of the collector then becomes so low that the air flows from the chamber.

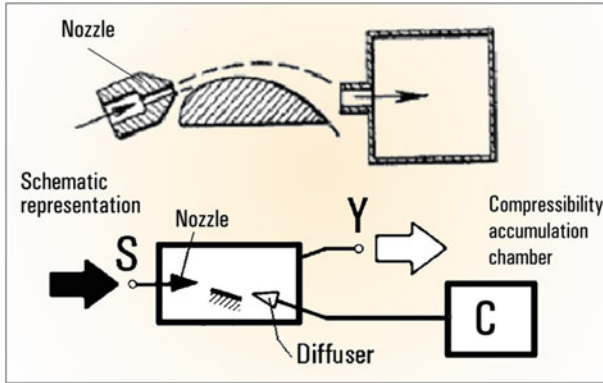


**Fig. 8.64** The first pure fluidics oscillator patented by Zalmanzon in December 1959 [58]. It uses relaxation principle for which it did not find followers

Its collision with the jet flow from the nozzle supports keeping the separated flow regime. This regime lasts for the rest of the period until the reversal flow from the chamber ceases and the jet re-attaches to the “wing”. Despite the old history, this relaxation oscillator design did find practically no followers. Possible explanation is the very small compression capacitance values obtainable with reasonably sized accumulation vessels or chambers. Compared with the frequency formula presented above in Fig. 8.23, it was obvious that the Zalmanzon’s oscillator inevitably operated at inconveniently large frequencies.

The bottom part of Fig. 8.64 shows the configuration drawn using the standard symbols for fluidics. Obviously, the upper surface of the “wing” functions as the Coanda-effect attachment wall. The whole fluidic valve is thus equal to a monostable configuration, which in the standard fluidic device manufacturing technique would correspond to the device shown at right in Fig. 8.65. This valve has no control inlet—instead, the flow is switched—separated from the attachment wall—by the load-switching (cf. Fig. 8.48). Useful load-switched valves developed in [38], have output characteristic as schematically represented in the next Fig. 8.66. Its intersections with the load characteristic curve labelled *Load A* determine the instantaneous flow rate and output pressure. Increasing load is in this diagram represented by more steep characteristics, like the curve labelled *Load B*—and finally this progress reaches the load-switching point at which the flowfield suddenly changes to the main flow deflected away from the attachment wall.

The results summarised in Sect. 8.2.3 lead to the obvious conclusion that the goal of generating microbubbles by blowing gas through the passages in aerator requires a fluidic oscillator operating at much lower frequencies than was expected earlier. Also desirable, for practical reasons, is compactness of the design. Standard oscillator designs do not fulfil these requirements. It is true that the single-loop standard configuration oscillator discussed in [44] was demonstrated to be capable of operating at periods lasting as long as 358 ms, i.e. frequency slightly below 3 Hz (at  $f = 2.79$  Hz), but this was achieved with feedback formed by a Tygon tube of

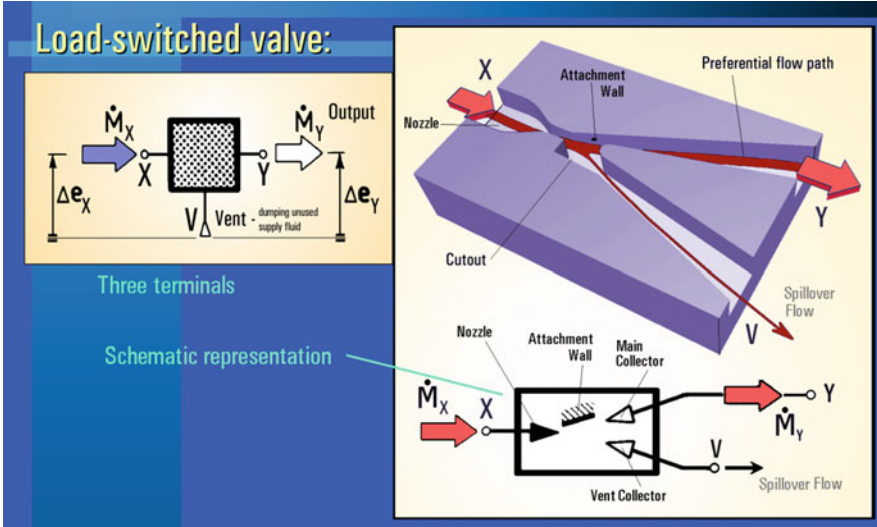


**Fig. 8.65** Monostable diverter valve with flow controlled by the load-switching (the case B in Fig. 8.48). The jet attaches in unloaded regime to the wall that leads it to the output terminal Y. Increased fluidic resistance of the connected load causes initially a spillover flow into V and finally a separation from the wall

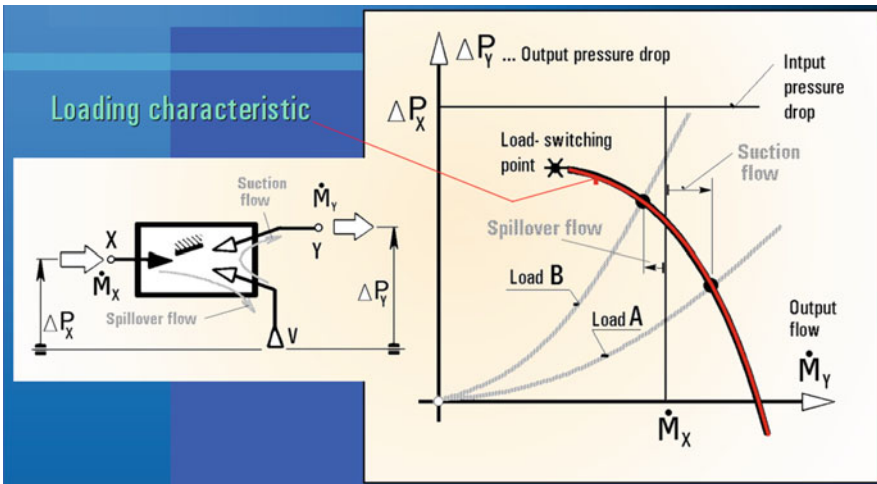


**Fig. 8.66** Loading characteristic of the valve shown in Fig. 8.65. It is the red curve with two intersection points with characteristics (gray) of two different loads connected to Y

inner diameter 10 mm and length 50 m. The very volume of this tube shows that any compactness is out of question. Also economy of handling the compressed air must be poor, because of the inevitable friction-type losses in so long tubes. It was thus concluded that because of these limitations of standard designs—and also because

of the advantages of potential patent protection—it was desired to develop a new oscillator concept for microbubble generation purposes.

The desirable operating frequency was estimated to be at or near to  $f = 3$  Hz. For the sake of compactness, the design was chosen to be based on the so far little known relaxation principle, with the load-switching. Because of the requirement of low frequency, the monostable principle of Figs. 8.64 and 8.65 was to be replaced by bistable, symmetric version—which means achieving roughly twice the period, i.e. one half of the frequency magnitude.

The key problem was finding a suitable load, characterised by gradual increase of pressure drop. Solution was found in the vortex diode, shown in Fig. 8.67. It is a flat cylindrical cavity with tangential inlet and central exit. In the **CLOSED** direction, the inlet flow gradually increases the intensity of fluid rotation until it reaches the magnitude at which it is difficult to overcome the centrifugal force. In the other, **OPEN** flow direction there is no rotation and the negative pressure drop is small. According to Fig. 8.68, the vortex diodes are placed at the two exits from the load-switched diverter. The red line shows the starting flow into the vortex chamber with initially non-rotating fluid. The tangential direction of the inlet forces the fluid to spin up. On the opposite side, the jet-pumping effect into the main flow, together with the small flow resistance in the **OPEN** direction, generates the return flow which is required for moving the microbubble back into its protected position inside the aerator passage. As the rotation intensity inside the vortex chamber increases, the centrifugal force makes it increasingly difficult for the fluid to get into the exit in the chamber centre. Finally the difficulty becomes to effective that the Coanda effect no more manages keeping the jet attached. It switches to the opposite attachment wall and the spin-up process now becomes taking place in the other chamber. That this principle really works and makes it possible to obtain the desirable frequency near to  $f = 3$  Hz is demonstrated by the measured spectrum in Fig. 8.69.

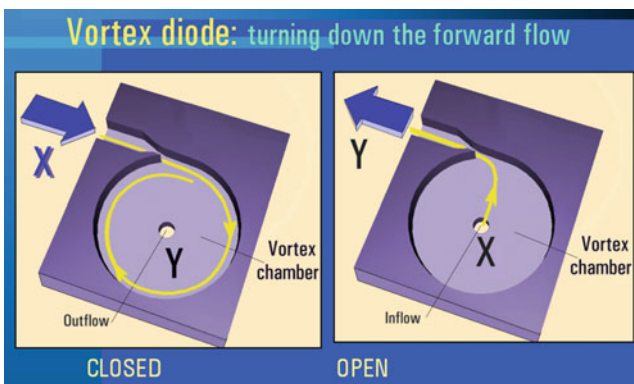


**Fig. 8.67** Behaviour of vortex chamber depends upon the direction of flow. In the **OPEN** regime the overall hydraulic resistance is quite low and constant. If the flow direction changes into the **CLOSED** regime, then the resistance gradually increases as the fluid inside the chamber spins up—and finally can reach high values since the flow is opposed by centrifugal force

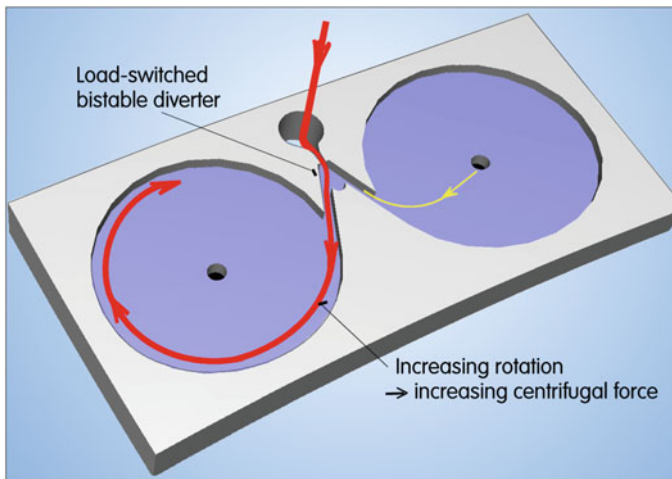


**Fig. 8.68** Author’s recently invented double-relaxation oscillator (Patent: Tesař [43]) developed for operation at very low oscillation frequencies. The diverter is load-switched when fluid rotation in the vortex chamber develops high enough centrifugal resistance

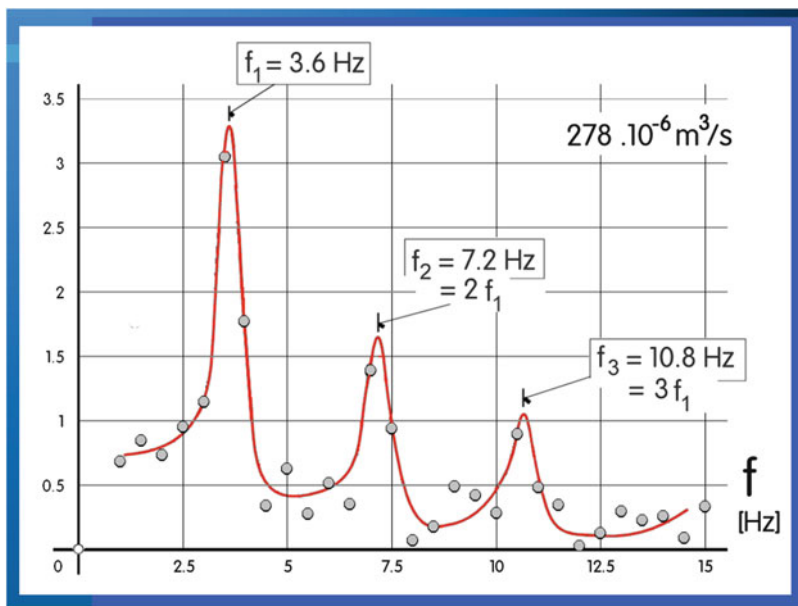


**Fig. 8.69** An example of frequency spectrum of pulsation in one of the output terminals of the relaxation oscillator shown in Fig. 8.68. The capability of oscillating at low frequencies is obvious. The higher harmonics  $f_2$  and  $f_3$  determine the shape of oscillation pulses

## 8.4 Conclusions

Subject of this chapter, sub-millimetre gas bubbles in liquids, were until recently not of particular interest—because methods of their generation then known were energetically inefficient. Standard aerator-generated bubbles are an order of magnitude larger than the size of microbubbles. A new era begun by discovery of microbubble generation by oscillation of the supplied gas—especially by using for the task no-moving-part fluidic oscillators. This opened roads towards many microbubble applications with considerable advantages so that interest in this matter is increasing exponentially. For a considerable time, however, the oscillator-driven generation of microbubbles was led by the wrong idea of fragmentation. As demonstrated here, the main problem was elsewhere. It was the slow velocity motion (decreasing with decreasing bubble size) that has led to small distances between the microbubbles. They get into contact and coalesce—an effect supported by the fact that the conjunction decreases the overall surface energy. The role of the fluidic oscillation was thus elucidated as preventing the coagulation and this way keeping the bubbles small.

The chapter discusses the basics of bubble formation, such as explanation of surface tension by uncompensated inter-molecular forces. Also presented is solution of bubble shape, instability of parallel bubble formation, and mechanism of shape oscillation. In its next part, the chapter presents a survey of the nearly forgotten art of making fluidic oscillators.

The main reason behind the present interest in oscillator-generated microbubbles are the potential geopolitical consequences of renewable liquid fuel. The problem of worldwide distribution of crude oil sources different from locations where the fuel is needed has been recently demonstrated solvable by generating biofuel from primitive green plants—mainly algae. These can produce combustible liquids (or precursors) using only minimal input substances. What they need for their growth by photosynthesis are merely water and  $CO_2$  (the latter, of course, from atmosphere). The energy driving this process is obtained from sunshine. The main advantage of the primitive plants is their extremely rapid growth. There are arid areas where sunshine and even water (the latter perhaps with salt and thus unsuitable for agriculture) are plentiful. The reason why mankind is as yet not employing algae at a massive scale is the fossil fuel, imported mostly from politically unstable regions, is at present significantly cheaper. To make liquid fuel from algae economically competitive needs improving efficiency of all production steps. In two steps, cultivation and harvesting, a considerable efficiency improvement may be obtained by using the properties of microbubbles.  $CO_2$  transport intensification was already demonstrated to increase the algae growth quite rapidly when using microbubbles—at the same time also stripping from the liquid medium the oxygen generated as a by-product in photosynthesis (which at a higher concentration blocks the growth).

**Acknowledgements** Author's work was supported by research grant No. 13-23046S by GAČR as well as also institutional support RVO:61388998.

## References

1. A. Aissa, M. Abdelouahab, A. Noureddine, M. Elganaoui, B. Pateyron, Ranz and Marshall correlations limits on heat flow between a sphere and its surrounding gas at high temperature. *Therm. Sci.* **19**(6), 1521–1528 (2015)
2. A. Allouch, K. Bourmine, A. Monmayrant, O. Gauthier-Lafaye, S. Geoffroy, A.-M. Gué, P. Joseph, Microbubbles for optofluidics: controlled defects in bubble crystals. *Microfluid. Nanofluid.* **17**(3), 549–560 (2014)
3. V.G. Bogdevich, A.R. Evseev, A.G. Malyuga, G.S. Migirenko, Gas saturation effect on near-wall turbulence characteristics, in *Proceedings of 2nd International BHRA Fluid Engineering Drag Reduction Conference (1977)*, pp. 25–37
4. C. Cerretelli, K. Kirtley, Boundary layer separation control with fluidic oscillators. *J. Turbomach.* **131**(4), 041001 (2009)
5. H. Coanda, Device for deflecting a stream of elastic fluid projected into an elastic fluid. US Patent, No. 2052869. Filed in September 1936
6. A. Fick, Über diffusion. *Ann. Phys.* **170**(1), 59–86 (1855)
7. K. Foster, G.A. Parker, *Fluidics: Components and Circuits* (Wiley, New York, 1970)
8. W.L. Haberman, R.K. Morton, An experimental investigation of the drag and shape of air bubbles rising in various liquids. Technical Report 802, NS 715-102, Navy Department, The David W. Taylor Model Basin Washington 7, DC, September 1953
9. M. Hashimoto, B. Mayers, P. Garstecki, G.M. Whitesides, Flowing lattices of bubbles as tunable, self-assembled diffraction gratings. *Small* **2**(11), 1292–1298 (2006)
10. S. Honda, H. Yamasaki, A new hydrodynamic oscillator type flowmeter, in *Proceedings of the International Symposium on Fluid Control and Measurement, Tokyo 1985* (Pergamon, Oxford, 1986), pp. 623–628
11. T. Kanagawa, Focused ultrasound propagation in water containing many therapeutical microbubbles, in *Proceedings of FLUCOME 2013, 12th International Conference on Fluid Control, Measurements, and Visualization*, Nara (2013). Paper OS6-04-4
12. M. Koklu, Fluidic oscillator having decoupled frequency and amplitude control. US Patent, No. 9339825. Filed in March 2013
13. K. Kooiman, M. Foppen-Harteveld, A.F.W. van der Steen, N. de Jonga, Sonoporation of endothelial cells by vibrating targeted microbubbles. *J. Control. Release* **154**(1), 35–41 (2011)
14. L.A. Kuznetsova, W.T. Coakley, Applications of ultrasound streaming and radiation force in biosensors. *Biosens. Bioelectron.* **22**(8), 1567–1577 (2007)
15. R. Latorre, A. Miller, R. Philips, Micro-bubble resistance reduction for high speed craft. *Trans. Nav. Archit. Mar. Eng.* **110**, 259–277 (2002)
16. J.H. Lee, K.H. Lee, J.M. Won, K. Rhee, S.K. Chung, Mobile oscillating bubble actuated by AC-electrowetting-on-dielectric (EWOD) for microfluidic mixing enhancement. *Sensors Actuators A Phys.* **182**, 153–162 (2012)
17. G. Liger-Belair, R. Marchal, B. Robillard, T. Dambrouck, A. Maujean, M. Vignes-Adler, P. Jeandet, On the velocity of expanding spherical gas bubbles rising in line in supersaturated hydroalcoholic solutions: application to bubble trains in carbonated beverages. *Langmuir* **16**(4), 1889–1895 (2000)
18. N.K. Madavan, S. Deutsch, C.L. Merkle, Reduction of turbulent skin friction by microbubbles. *Phys. Fluids* **27**(2), 356–363 (1984)
19. E. Markland, G.M. Tofield, G.P. Lucas, H.S. Kalsi, Fluidic oscillator flowmeters. US Patent, No. 4838091. Filed in June 1986
20. M.E. McCormick, R. Bhattacharyya, Drag reduction of a submersible hull by electrolysis. *Nav. Eng. J.* **85**(2), 11–16 (1973)
21. Y. Moriguchi, H. Kato, Influence of microbubble diameter and distribution on frictional resistance reduction. *J. Mar. Sci. Technol.* **7**(2), 79–85 (2002)
22. J.S. Oh, Y.S. Kwon, K.H. Lee, W. Jeong, S.K. Chung, K. Rhee, Drug perfusion enhancement in tissue model by steady streaming induced by oscillating microbubbles. *Comput. Biol. Med.* **44**, 37–43 (2014)



23. T. Okawa, T. Tanaka, I. Kataoka, M. Mori, Temperature effect on single bubble rise characteristics in stagnant distilled water. *Int. J. Heat Mass Transf.* **46**(5), 903–913 (2003)
24. S. Okazaki, The velocity of ascending air bubbles in aqueous solutions of a surface active substance and the life of the bubble on the same solution. *Bull. Chem. Soc. Jpn.* **37**(2), 144–150 (1964)
25. M.J. Pang, J.J. Wei, B. Yu, Numerical study on modulation of microbubbles on turbulence frictional drag in a horizontal channel. *Ocean Eng.* **81**, 58–68 (2014)
26. T. Prevenslik, Stability of nanobubbles by quantum mechanics, in *Proceedings of Topical problems of Fluid Mechanics 2014* (Institute of Thermomechanics, Czech Academy of Sciences, 2014), pp. 113–116
27. W.E. Ranz, W.R. Marshall, Evaporation from drops, part 1. *Chem. Eng. Prog.* **48**, 141–146 (1952)
28. L. Rayleigh, On the pressure developed in a liquid during the collapse of a spherical cavity. *Philos. Mag. Ser. 6* **34**(200), 94–98 (1917)
29. T. Ries, F. Mohr, J. Baumann, M. Rose, U. Rist, I. Raab, S. Staudacher, LP turbine laminar separation with actuated transition: DNS, experiment and fluidic oscillator CFD, in *ASME Turbo Expo 2009: Power for Land, Sea, and Air*. Volume 7: Turbomachinery, Parts A and B, Orlando, FL (The American Society of Mechanical Engineers, New York, 2009), pp. 917–927. ASME Paper No. GT2009-59600
30. E. Schmidt, Einführung in die Technische Thermodynamik und in die Grundlagen der chemischen Thermodynamik, 10th edn. (Springer, Berlin, 1963)
31. M.M. Shams, M. Dong, N. Mahinpey, Friction factor of microbubbles in capillary tubes at low Reynolds numbers. *Chem. Eng. Sci.*, **112**, 72–78 (2014)
32. T.K. Sherwood, R.L. Pigford, C.R. Wilke, *Mass Transfer* (McGraw-Hill, New York, 1975)
33. R.R. Sun, M.L. Noble, S.S. Sun, S. Song, C.H. Miao, Development of therapeutic microbubbles for enhancing ultrasound-mediated gene delivery. *J. Control. Release* **182**, 111–120 (2014)
34. M.A.R. Talaia, Terminal velocity of a bubble rise in a liquid column. *Int. J. Math. Comput. Phys. Electr. Comput. Eng.* **1**(4), 220–224 (2007)
35. K. Terasaka, A. Hirabayashi, T. Nishino, S. Fujioka, D. Kobayashi, Development of microbubble aerator for waste water treatment using aerobic activated sludge. *Chem. Eng. Sci.* **66**(14), 3172–3179 (2011)
36. V. Tesař, Fluidics applied to generation of small aeration bubbles, in *Proceedings of FLU-COME 2007*. 9th International Conference on Fluid Control, Measurements, and Visualization, Tallahassee, FL (2007)
37. V. Tesař, *Pressure Driven Microfluidics* (Artech House, Norwood, 2007)
38. V. Tesař, No-moving-part valve for automatic flow switching. *Chem. Eng. J.* **162**(1), 278–295 (2010)
39. V. Tesař, Mechanisms of fluidic microbubble generation Part I: growth by multiple conjunctions. *Chem. Eng. Sci.* **116**, 843–848 (2014)
40. V. Tesař, Mechanisms of fluidic microbubble generation Part II: suppressing the conjunctions. *Chem. Eng. Sci.* **116**, 849–856 (2014)
41. V. Tesař, Microbubble generator excited by fluidic oscillator's third harmonic frequency. *Chem. Eng. Res. Design* **92**(9), 1603–1615 (2014)
42. V. Tesař, Shape oscillation of microbubbles. *Chem. Eng. J.* **235**, 368–378 (2014)
43. V. Tesař, Fluidic oscillator. Czech Patent No. CZ 306604 (2016). Filed on December 15, 2014
44. V. Tesař, C.-H. Hung, W.B. Zimmerman, No-moving-part hybrid-synthetic jet actuator. *Sensors Actuators A Phys.* **125**(2), 159–169 (2006)
45. V. Tesař, S. Zhong, F. Rasheed, New fluidic oscillator concept for flow separation control. *AIAA J.* **51**(2), 397–405 (2013)
46. C. Tremblay-Darveau, R. Williams, P.N. Burns, Measuring absolute blood pressure using microbubbles. *Ultrasound Med. Biol.* **40**(4), 775–787 (2014)
47. H. Tsuge, P. Li, N. Shimatani, Y. Shimamura, H. Nakata, M. Ohira, Fundamental study on disinfection effect of microbubbles. *Kagaku Kogaku Ronbunshu* **35**(5), 548–552 (2009)

48. C. Wang, S.V. Jalikop, S. Hilgenfeldt, Efficient manipulation of microparticles in bubble streaming flows. *Biomicrofluidics* **6**(1), 012801 (2012)
49. R.W. Warren, Fluid oscillator. US Patent, No. 3016066. Filed in January 1960
50. R.W. Warren, Negative feedback oscillator. US Patent, No. 3158166. Filed in August 1962
51. K. Watanabe, Washing effect of microbubbles, in *Proceedings of FLUCOME 2013*. 12th International Conference on Fluid Control, Measurements, and Visualization, Nara (2013). Paper OS1-01-1
52. O. Watanabe, A. Masuko, Y. Shirose, Measurements of drag reduction by microbubbles using very long ship models. *Nippon Zosen Gakkai Ronbunshu (J. Soc. Nav. Archit. Jpn)* **183**, 53–63 (1998)
53. Y. Watanabe, A. Aoi, S. Horie, N. Tomita, S. Mori, H. Morikawa, Y. Matsumura, G. Vassaux, T. Kodama, Low-intensity ultrasound and microbubbles enhance the antitumor effect of cisplatin. *Cancer Sci.* **99**(12), 2525–2531 (2008)
54. M. Weber, Die Grundlagen der Ähnlichkeitsmechanik und ihre Verwertung bei Modellversuchen. Ph.D. thesis, Technischen Hochschule zu Braunschweig (1919)
55. K. Wichterle, K. Smutná, M. Večeř, Shape and rising velocity of bubbles, in *Proceedings of 36th International Conference of SSCHE*, Tatranské Matliare (Slovak Society of Chemical Engineering, Bratislava, 2009)
56. X. Xi, Controlled translation and oscillation of micro-bubbles near a surface in an acoustic standing wave field. Ph.D. thesis, Imperial College London, Department of Mechanical Engineering (2012)
57. Yanuar, Gunawan, Sunaryo, A. Jamaluddin, Micro-bubble drag reduction on a high speed vessel model. *J. Mar. Sci. Appl.* **11**(3), 301–304 (2012)
58. L.A. Zalmanzon, Method of automatically controlling pneumatic or hydraulic elements of instruments and other devices. US Patent, No. 3295543. Filed in December 1959
59. W.B. Zimmerman, M. Zandi, H.C.H. Bandulasena, V. Tesař, D.J. Gilmour, K. Ying, Design of an airlift loop bioreactor and pilot scales studies with fluidic oscillator induced microbubbles for growth of a microalgae *Dunaliella salina*. *Appl. Energy* **8**(10), 3357–3369 (2011)
60. W.B. Zimmerman, V. Tesař, H.C.H. Bandulasena, Towards energy efficient nanobubble generation with fluidic oscillation. *Curr. Opin. Colloid Interface Sci.* **16**, 350–356 (2011)
61. W.B. Zimmerman, M.K.H. Al-Mashhadani, H.C.H. Bandulasena, Evaporation dynamics of microbubbles. *Chem. Eng. Sci.* **101**, 865–877 (2013)